Johannes Löhner-Böttcher

Wave phenomena in sunspots

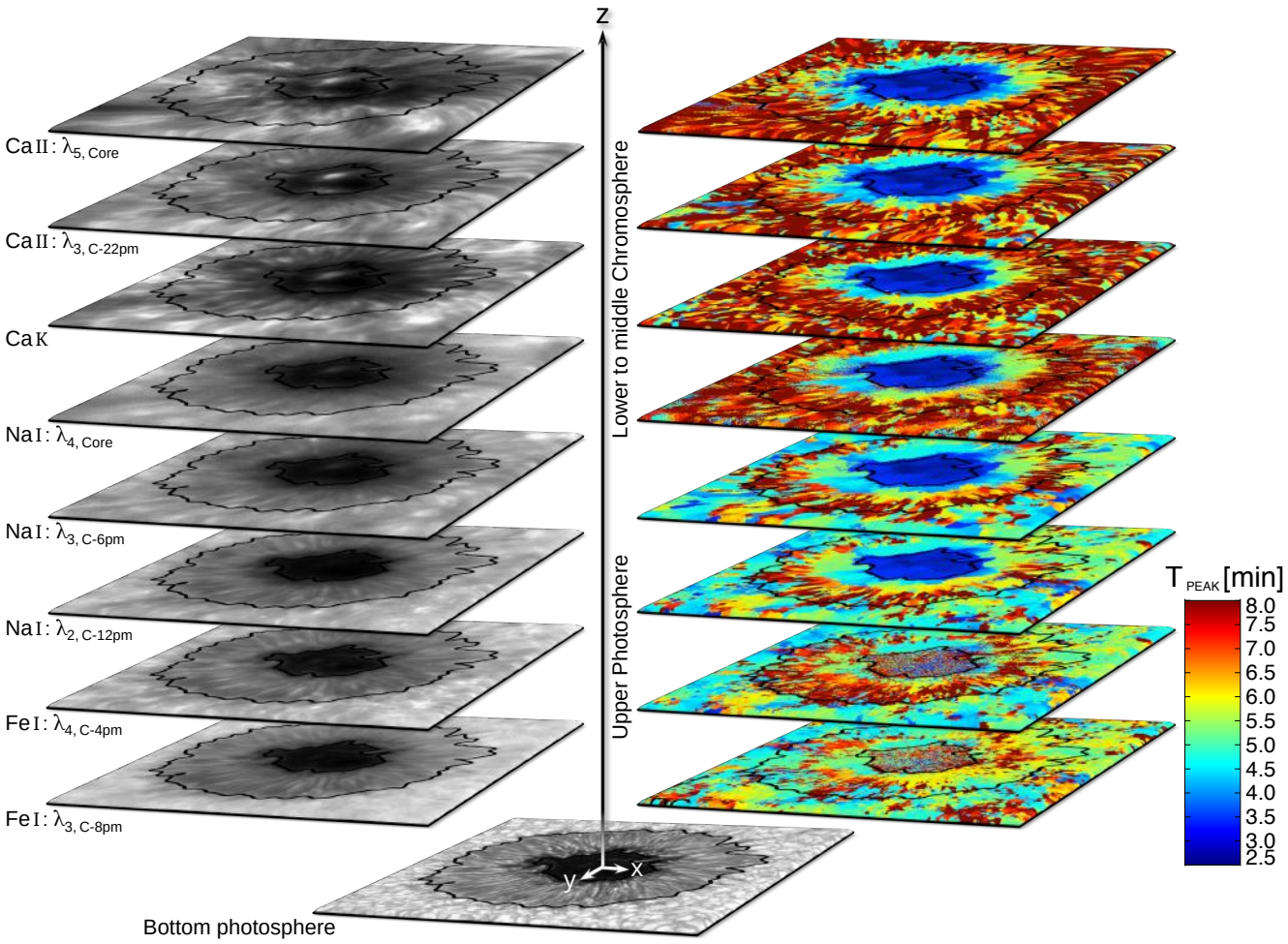

Dissertation

Albert-Ludwigs-Universität

Freiburg im Breisgau

Cover image: Three-dimensional distribution of spectral intensities (left) and dominant wave periods (right) in the sunspot atmosphere. The fully-developed sunspot of active region NOAA11823 was observed on August 21st 2013 at 15:00:06UTC with the Interferometric Bidimensional Spectrometer at the Dunn Solar Telescope. The spectral intensities (grayscale) in the upper photosphere and lower chromosphere exhibit a bright shock wave in the sunspot umbra. The peak periods T_{PEAK} of the intensity oscillations present the characteristic wave modes which scale from 2.5 min (blue color) in the umbra to 8 min (red color) in the outer penumbra. The black contours indicate the sunspot boundaries from continuum intensity (bottom). The positions along the z-axis are not to scale.

Wave phenomena in sunspots

DISSERTATION

zur

Erlangung des Doktorgrades

„Doctor rerum naturalium“

der

Fakultät für Mathematik und Physik

der

Albert-Ludwigs-Universität,
Freiburg im Breisgau

vorgelegt von

Johannes Löhner-Böttcher

aus Nürnberg

Freiburg, 2015

Dekan:	Prof. Dr. Dietmar Kröner
Referent:	Prof. Dr. Wolfgang Schmidt
Korreferent:	Prof. Dr. Markus Schumacher
Datum der Disputation:	24. Februar 2016

To Bella.

Contents

Abstract

Context. The dynamic atmosphere of the Sun exhibits a wealth of magnetohydrodynamic (MHD) waves. In the presence of strong magnetic fields, most spectacular and powerful waves evolve in the sunspot atmosphere. Allover the sunspot area, continuously propagating waves generate strong oscillations in spectral intensity and velocity. The most prominent and fascinating phenomena are the 'umbral flashes' and 'running penumbral waves' as seen in the sunspot chromosphere. Their nature and relation have been under intense discussion in the last decades.

Aims. Waves are suggested to propagate upward along the magnetic field lines of sunspots. An observational study is performed to prove or disprove the field-guided nature and coupling of the prevalent umbral and penumbral waves. Comprehensive spectroscopic observations at high resolution shall provide new insights into the wave characteristics and distribution across the sunspot atmosphere.

Methods. Two prime sunspot observations were carried out with the Dunn Solar Telescope at the National Solar Observatory in New Mexico and with the Vacuum Tower Telescope at the Teide Observatory on Tenerife. The two-dimensional spectroscopic observations were performed with the interferometric spectrometers IBIS and TESOS. Multiple spectral lines are scanned co-temporally to sample the dynamics at the photospheric and chromospheric layers. The time series ($1-2.5\,\mathrm{h}$) taken at high spatial and temporal resolution are analyzed according to their evolution in spectral intensities and Doppler velocities. A wavelet analysis was used to obtain the wave power and dominating wave periods. A reconstruction of the magnetic field inclination based on sunspot oscillations was developed.

Results and conclusions. Sunspot oscillations occur continuously in spectral intensity and velocity. The obtained wave characteristics of umbral flashes and running penumbral waves strongly support the scenario of slow-mode magnetoacoustic wave propagation along the magnetic field lines. Signatures of umbral flashes and running penumbral waves are found already in the middle to upper photosphere. The signal and velocity increases toward the chromosphere. The shock wave behavior of the umbral flashes is confirmed by the evolving saw-tooth pattern in velocity and the strong downward motion of the plasma right after the passage of the shock front. The power spectra and peak periods of sunspot waves vary significantly with atmospheric altitude and position within the sunspot. In the vertical field of the umbra, the mixture of wave periods in the lower photosphere transforms into a domination of the 2.5 min range in the upper photosphere and chromosphere. In the differentially inclined penumbra, the dominating wave periods increase with radial distance. The acoustic cut-off frequency which blocks the propagation of long-period waves is considered to increase with the field inclination and the ambient sound speed. The reconstruction of the sunspot's magnetic field inclination based on the peak period distribution yields consistent results with the inferred photospheric and extrapolated coronal magnetic field.

Zusammenfassung

Kontext. Die aktive Sonnenatmosphäre weist eine Fülle an magnetohydrodynamischen (MHD) Wellen auf. Bedingt durch die starken Magnetfelder in Sonnenflecken können sich höchst spektakuläre und kraftvolle Wellen entwickeln. Diese breiten sich kontinuierlich im gesamten Sonnenfleckenbereich aus und rufen starke Schwankungen in spektraler Intensität und Geschwindigkeit hervor. Die bedeutendsten und faszinierendsten Phänomene sind die sogenannten 'umbral flashes' und 'running penumbral waves' in der Chromosphäre von Sonnenflecken. Über ihren Ursprung und Beziehungen wurde in den letzten Jahrzehnten viel diskutiert.

Ziele. Es wird davon ausgegangen, dass sich Wellen in Sonnenflecken nach oben entlang der Magnetfeldlinien ausbreiten. Um die feld-geleitete Natur und Verknüpfung der vorherrschenden umbralen und penumbralen Wellen nachzuweisen oder zu widerlegen, wurde eine experimentelle Studie durchgeführt. Dabei sollen umfassende spektroskopische Beobachtungen bei hoher Auflösung neue Einblicke in die Eigenschaften und Verteilung von Wellen über die Sonnenfleckenatmosphäre liefern.

Methoden. Die zwei zentralen Sonnenfleckenbeobachtungen wurden mit dem Dunn Solar Telescope am National Solar Observatory in New Mexico und dem Vakuum Turm Teleskop am Teide Observatorium auf Teneriffa durchgeführt. Die zweidimensionalen spektroskopischen Daten wurden mit den interferometrischen Spektrometern IBIS und TESOS gewonnen. Um die Dynamik in photosphärischen und chromosphärischen Schichten zu ermitteln, wurden mehrere Spektrallinien zyklisch nacheinander abgetastet. Die Zeitserien ($1-2.5\,\mathrm{h}$) zeichnen sich durch ihre hohe räumliche und zeitliche Auflösung aus. Sie wurden hinsichtlich der Entwicklung ihrer spektralen Intensitäten und Dopplergeschwindigkeiten analysiert. Aus einer Waveletanalyse ergaben sich die Leistungsspektren und dominierende Perioden der Wellen. Auf der Grundlage von Sonnenfleckenoszillationen ließ sich die Inklination des Magnetfeldes rekonstruieren.

Ergebnisse und Fazit. Die Atmosphäre von Sonnenflecken oszilliert kontinuierlich in spektraler Intensität und Geschwindigkeit. Die für Umbra und Penumbra ermittelten Welleneigenschaften sprechen sehr für das Szenario, dass es sich um langsame (engl.: slow-mode) magnetoakustische Wellen handelt, die sich entlang der Magnetfeldlinien ausbreiten. Bereits in der mittleren bis oberen Photosphäre finden sich erste Anzeichen von umbralen Blitzen (engl.: 'umbral flashes') und laufenden penumbralen Wellen (engl.: 'running penumbral waves') wieder. Ihre Signalstärke und Geschwindigkeit nehmen zur Chromosphäre hin zu. Das Schockwellenverhalten von 'umbral flashes' wird durch das ausgeprägte Sägezahnmuster des Geschwindigkeitsverlaufs und die verstärkte nach unten gerichtete Plasmabewegung unmittelbar nach dem Passieren der Schockfront gestützt. Die Leistungsspektren und dominierenden Perioden variieren signifikant mit der atmosphärischen Höhe und der Position im Sonnenfleck. Zur Chromosphäre hin geht das durchmischte Wellenspektrum der unteren Photosphäre im vertikalen Feld der Umbra in ein uniformeres Spektrum im $2.5\,\mathrm{min}$-Bereich über. In der stärker geneigten Penumbra nimmt die dominierende Wellenperiode radial zu. Es kann davon ausgegangen werden, dass die akustische Abschneidefrequenz, welche die Ausbreitung von Wellen mit längerer Periode begrenzt, mit der Inklination des Feldes und der lokalen Schallgeschwindigkeit zunimmt. Die Rekonstruktion der Magnetfeldinklination des Sonnenflecks mittels der Verteilung der dominierenden Perioden stimmt mit dem abgeleiteten photosphärischen und dem extrapolierten koronalen Magnetfeld überein.

1. A brief history of solar science

"If I have seen further, it is by standing on the shoulders of giants."

— Sir Isaac Newton, in a *letter to Robert Hooke*

When Isaac Newton used the metaphor 'on the shoulders of giants', he referred to the groundbreaking discoveries of earlier scientists in appreciation of their accomplishments. Only by the previous research and progress, the next generation can build on and move forward with their own vision. As Newton himself climbed on the shoulders of his predecessors like Copernicus, Galileo or Kepler, he was able to see farther and advance towards discovering the truth. For this reason, I will also try to climb on some shoulders and start this work with a brief summary of the most important achievements in the field of physics and especially astrophysics which led to our today's understanding of the Sun. Honoring one of these giants, Steven Hawking, the title of this chapter borrows the style of the classic book *A brief history of time* (Hawking 1988). The following historical outline bases on the research and books of Hufbauer (1991), Eisberg (2002), Hawking (2002), and the synopsis in *HAO's Solar Physics Historical Timeline*. The illustrative figure (see Fig. 1.1) lists some of the most important achievements in the history of solar physics.

The good old days: The roots of solar observations can be traced back to ancient times and beyond. Before the telescope was invented, the study of the Sun had to confine itself on observation of the solar dynamics visible to the naked eye. By nature, the most impressive astronomical events – the solar eclipses – were the first to be recorded by the Babylonians from the 13th century BC on. The observation of the dark sunspots has a long tradition, too. Under suitable viewing conditions, large sunspot formations can even be seen by the naked eye. The oldest plausible record of such a sunspot observation dates back to around 800 BC and was made by Chinese astronomers. An explanation for these darkenings of the Sun was not given. Later, when Aristotle (384–322 BC) and Claudius Ptolemaeus (100–170 AD) developed the geocentric model of the cosmos with a fixed Earth at the center surrounded by the Sun and the planets on spheres, the heavens were seen as perfect and unvarying. In this believe, a spot on the solar surface was not possible and utterly out of question. Instead, in line with eclipse scenarios, when the moon covers the Sun, the small darkenings were explained by the passage of Mercury or other transients in front of the Sun.

Moving a millennium further to the Middle Ages, the first sunspot drawing (see Fig. 1.1) was made in 1128 by the monk John of Worcester in his chronicles. The drawing shows two black circles with a distinguished dark core and a brighter annulus. This early sunspot drawing illustrates the division of the sunspots into umbrae and penumbrae.

The Sun moves into focus: After the end of the medieval era, the time was ripe for a new understanding of the Sun. In 1543, in his major work *De Revolutionibus Orbium Coelestium*, Nicolaus

[1] Images of Fig. 1.1 from *HAO's Solar Physics Historical Timeline*, 1609: http://galileo.rice.edu/sci/instruments/telescope.html, 1817 http://www.briefmarken-bilder.de/brd-briefmarken-1987/lichtspektrum-joseph-frauenhofer-optiker, 1645–1715: http://solarscience.msfc.nasa.gov/SunspotCycle.shtml, 1858: http://www.kis.uni-freiburg.de/en/research/the-sun/structure/, 1908: Hale (1908b), 1960s: ttps://heasarc.gsfc.nasa.gov/docs/heasarc/missions/images/oso_images.html

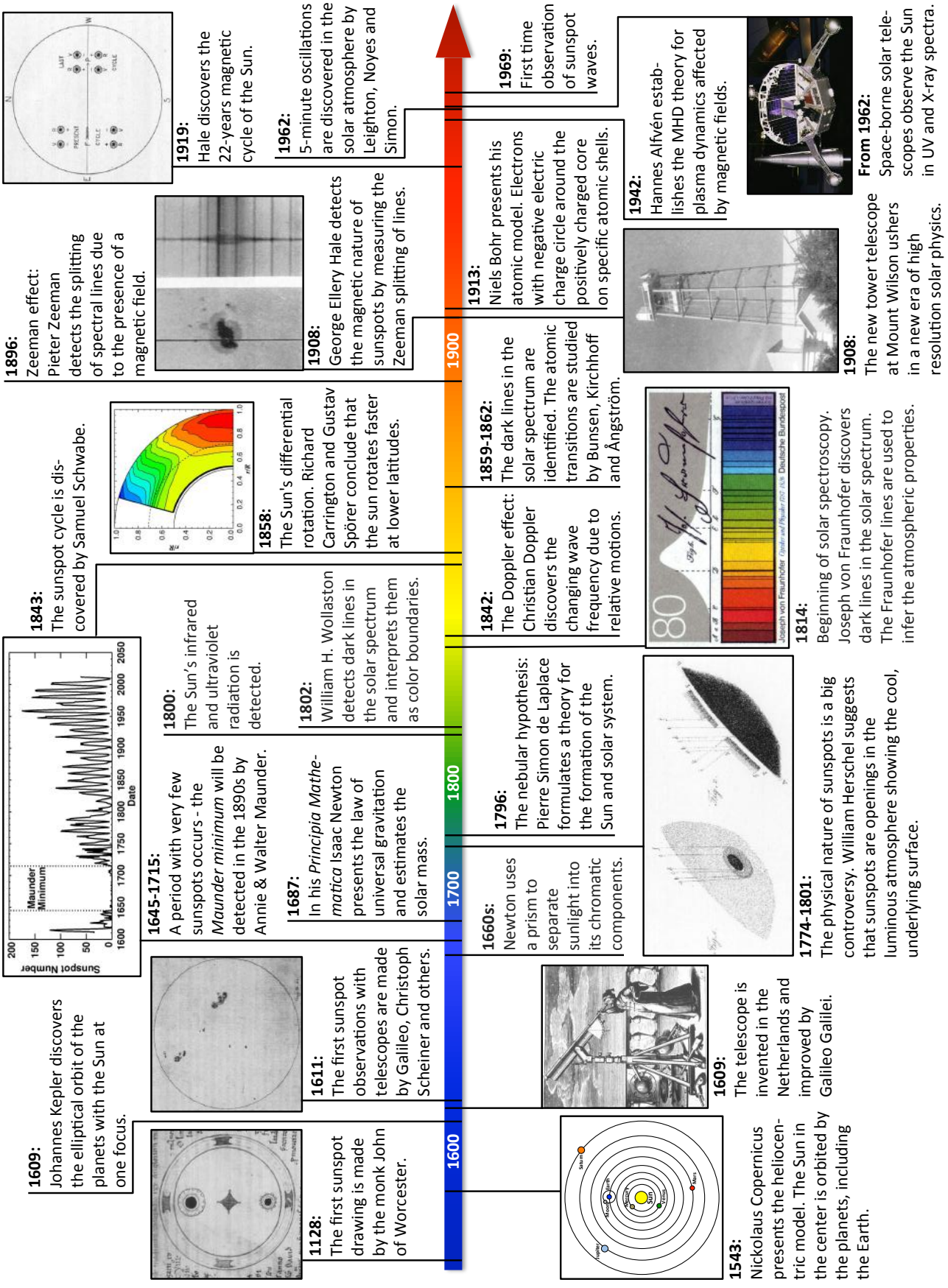

Figure 1.1.: Timeline of important achievements for solar science.[1]

Copernicus (1473–1543) developed the heliocentric model and declared the Sun as the center of the solar system. The planets – including the Earth – orbit the Sun on circular trajectories. In addition, the Earth rotates around its own central axis. As this new model would have been considered as heresy by the Church, Copernicus waited until near his death to publish the theory. After a long struggle, it replaced the geocentric model of Ptolemaeus and Aristotle with the Earth as the center of the solar system and universe.

At the beginning of the 17th century, several astronomical milestones were set to modernize the human understanding of the Sun. The first was in 1609, when Johannes Kepler (1571–1630) expanded the heliocentric system to include elliptical orbits of the planets with the Sun at one elliptical focus. In the same year, the telescope was invented in the Netherlands by Hans Lippershey (1570–1619), Zacharias Janssen (1585–1632) and Jacob Metius (1571–1631). As indicated in the greek name *teleskopos*, which means *far-seeing*, it was build to visibly enlarge far objects in order to see them better with the eye. First, a light-gathering lens was used as an objective (refractor), shortly later also a mirror (reflector). Only some weeks after the invention of the refractor, Galileo Galilei (1564–1642) built his own telescope and improved its design in 1610. The invention of the telescope became the starting shot in a new era of solar and stellar observations.

Already from 1610 to 1612, the first sunspot observations with telescopes were performed: At the end of 1610 by Galileo and Thomas Harriot (1560–1621), just some months later also by Johannes Fabricius (1587–1616) and the Jesuit Christoph Scheiner (1573–1650). In the spring of 1611, Galileo showed his observation to a number of people at a visit in Rome. In the autumn of the same year, Johannes Fabricius was the first to publish his results on sunspots. In April 1612, Galileo started his deeper investigations on the solar spots and concluded from the spot's apparent motion across the solar disk that the Sun had a rotation around its own axis. The answers to the question about the nature of sunspots were diverse. They reached from Scheiner's interpretation that they are objects orbiting the Sun, to Galileo's understanding that they are most likely clouds in the solar atmosphere. Galileo's letters from 1613 and Scheiner's *Rosa Ursina* from 1630 – in which he revised his opinion on the nature of the spots and illustrated the motion and changing appearance of spots – became the standard works for the 17th century.

In the second half of the 17th century, the progress of sunspot studies had slowed down. This was not due to the observers, but had a natural reason. Based on the investigations of Gustav Spörer (1822–1895), in the 1890s Edward Walter Maunder (1851–1928) and his wife Annie (1868–1947) discovered that a period with very few sunspots had occurred. That time from 1645 to 1715 will later be referred to as the *Maunder minimum*. The low activity of the Sun coincided with a main part of the *Little Ice Age* with lower average temperatures and very cold winters in Europe and North America.

Still in the 17th century, further essential discoveries have been made on the way to modern solar physics. One important conclusion was drawn by Johannes Kepler in 1619, when he explained the orientation of comet's tails by a directed solar wind. Other basic observations were made by a real giant of physics himself, Isaac Newton (1642–1727). In the late 1660s, Newton used a prism to separate sunlight into its chromatic components and concluded that the colors are not introduced by the prism but are the real composition of the visible light itself. This finding acted as the basis for solar spectroscopy. The second substantial achievement was the law of universal gravitation, which Newton presented in 1687 in his *Principia Mathematica*. Based on the gravitational theory, Newton gave a first quantitative estimate for the solar mass.

In the late 18th century (1774–1801), the physical nature of sunspots was a big controversy. After suggestions that they could be cloud-like structures or dense objects in the solar atmosphere, William Herschel (1738–1822) hypothesized that sunspots are holes in the luminous atmosphere showing the cool, underlying solid body. According to him, the surface could be a habitable zone on the Sun if it was shielded from the fiery topmost atmosphere. A reproduction of Herschel's diagram on the nature of sunspots is shown in Fig. 1.1 in top and side view.

With his large telescopes, William Herschel also made night-time observations and found various

cloud-like diffuse structures in the night sky. He suggested these Nebulae to be different evolutionary steps of a gravitational collapse into a star. In 1796, Pierre Simon de Laplace (1749–1827) formulated the nebular hypothesis, proposing a gravitational collapse of a large, slowly rotating gas cloud as the formation mechanism of the Sun and the solar system.

The 19th century – the birth of solar spectroscopy: In the 19th century, a revolution in the field of solar and astronomical research started. The reason was the birth of spectroscopy. Before, astronomical studies focused almost exclusively on examination of the motion of celestial bodies. Thereafter, the newly raised spectroscopical methods became a prime tool of astrophysics allowing the deep investigation of the physical nature of the stars, planets and especially our Sun.

By the beginning of the new century, it was known for more than 130 years that white sunlight can be separated into its chromatic components. Now the groundbreaking discoveries followed in quick succession. In 1800, William Herschel detected the Sun's invisible infrared radiation adjacent to the red side of the visible rainbow color spectrum. In the following year, Johann Wilhelm Ritter (1776–1810) emulated Herschel's deeds and discovered the invisible radiation adjacent to the blue side of the visible solar spectrum, the ultraviolet radiation. Another year later, William Wollaston (1766–1828) confirmed the existence of both invisible radiations. Also in 1802, Wollaston detected a number of dark lines crossing the so far continuous solar spectrum. He interpreted the lines as the marked boundaries between the natural colors of the spectrum. The next step – certainly one of the most important ones for Solar Physics – was made in 1814. The optician Joseph von Fraunhofer (1787–1826) rediscovered the dark lines in the solar spectrum and thanks to a very high dispersion mapped more than 500 spectral lines, later called the *Fraunhofer lines*. It was obvious to him, that these lines could not be spectral boundaries of colors. A German postage stamp honoring the achievement is shown in Fig. 1.1. In 1823, John Herschel (1792–1871) was the first to compare the dark absorption lines in the solar spectrum with the bright emission lines in the spectrum of flames. He concluded that lines in the solar spectrum could reveal the chemical composition of the Sun's atmosphere. In the following years, many more lines even beyond the visible range were measured in the solar spectrum. In 1842, the first photograph of the visible solar spectrum by Edmond Becquerel (1820–1891) initiated a new and reproducible method for solar spectroscopical measurements. The entry of photography as an astronomical tool increased the scientific opportunities by multiples. The first photograph (by then known as a *daguerrotype*) of the Sun was made in 1845 by the physicists Louis Fizeau (1819–1896) and Léon Foucault (1819–1868). In the years between 1859 and 1862, the new recording technique helped to identify the element-specific dark lines in the solar spectrum which allowed to infer the chemical composition of the Sun's atmosphere. Main contributors were Gustav Kirchhoff (1824–1887), David Brewster (1781–1868), Robert Bunsen (1811–1899) and Anders Jonas Ångström (1814–1874). Especially Kirchhoff established the young spectroscopy as a valid scientific field. By comparing the D-lines in the Fraunhofer spectrum (today known as sodium lines) with the emission lines of a flame containing sodium, Kirchhoff managed not only to confirm the element specific solar lines, but – by adding both spectra and getting even deeper absorption lines as result – renewed the solar model. The Sun has to have a hotter interior and a cooler, absorbing atmosphere.

Apart from the first steps of solar spectroscopy, the middle of the 19th century became a fundamental era for Solar Physics. The activity of the Sun was studied in detail. Starting in 1838, the solar luminosity was measured for the first time. Again, John Herschel was one of the pioneers who defined the Sun's energy output as the 'solar constant'. In 1842, Christian Doppler (1803–1853) discovered a change in wave frequency due to motions of a sound source relative to the observer. The Doppler effect was named after him and became one of the major measurands in Solar Physics. One year later, in 1843, the German pharmacist and amateur astronomer Heinrich Schwabe (1789–1875) published his 17-year ongoing analysis of the number of sunspots on the solar disk. By analyzing his meticulous sunspot observations and consulting recent records, he discovered that the number of sunspots changes periodically in time. He proposed a sunspot cycle with a period of ten years, later corrected by Rudolf

Wolf (1816–1893) to eleven years. A diagram showing the number of sunspots for the last 400 years can be seen in Fig. 1.1. A decade later, in 1852, Edward Sabine (1788–1883) followed Schwabe's results and was the first to prove that the sunspot cycle is directly linked to geomagnetic activity. Also in the 1850s, the energetic source of the Sun was still a mystery. In 1853, Hermann von Helmholtz (1821–1894) and William Thomson (later Lord Kelvin, 1824–1907) suggested a new theoretical solar heating mechanism. They proposed that only contraction due to gravitation could provide enough energy to heat the Sun for such a long life time.

At the end of the 1850's, two major discoveries based on sunspot observations should revise the understanding of the Sun and its activity. In 1858, Richard Carrington (1826–1875) and Gustav Spörer (1822–1895) both mapped the daily sunspot appearances and discovered that their location and motion vary with latitude and time. They found that the absolute latitudes of sunspot appearance shifted from around 35° to 5° throughout the sunspot cycle. In addition, sunspots are tracked faster across the solar surface when they are situated at latitudes closer to the solar equator. The higher the latitude, the slower the motion. Carrington concluded from these observations that the Sun rotates differentially. Ten years later, this result was confirmed with spectroscopical methods using the Doppler shift of spectral lines. In Fig. 1.1, the differential rotation is shown as a function of latitude and depth in the convection zone, with rotation rates ranging from 24 days (red) at the equator to 38 days (blue) near the poles.

In 1859 and the following year, further pioneering observations of the very active solar atmosphere were made. Carrington was the first to observe a solar flare. He monitored an intense and rapidly occurring brightening in the middle of a sunspot group, which will later be interpreted as an acute heating of the ambient atmosphere caused by the reconnection of magnetic fields. One year later, a coronal mass ejection was observed for the first time.

The 20th century – a deeper look at the Sun: At the beginning of the 20th century, Solar Physics reached the next evolutionary step. This time it were the smaller scales which delivered a deeper insight into the nature of the Sun. In hand with new theories and the technological progress, new kinds of telescopes and instruments were invented and constructed. In the United States, George Ellery Hale (1868–1938) devoted his life to study the Sun and became one of the most important solar physicists of modern times. In 1889 he developed the first spectro-heliograph[2] for the Kenwood Astrophysical Observatory, the personal observatory at the family home in Chicago. Together with his assistant Ferdinand Ellerman (1869–1940), Hale used it extensively to study the solar dynamics in monochromatic light. In 1908, he invented a new kind of tower telescope with a Coelostat mirror system and increased optical resolution (as shown in the reproduction in Fig. 1.1 from Hale (1908b)). Placed at Mount Wilson, the telescope ushered in a new era of high resolution solar physics. In the same year, Hale made a ground-breaking discovery for solar science. He detected the magnetic nature of sunspots by measuring the Zeeman splitting of spectral lines in the cooler and therefore darker umbral region and concluded on strong magnetic fields. Just a decade before (in 1896), Pieter Zeeman (1865–1943) explained that the intensity profile of some spectral lines can split from a one-component into a more-component shape when a strong magnetic field is present. An exemplary case is shown in Fig. 1.1 reproduced from Hale et al. (1919). In the following years, Hale became one of the chief investigators of sunspot phenomena, made significant contributions to modern observation techniques for solar physics and raised several solar observatories like the Yerkes Observatory in Wisconsin and the Californian Mount Wilson Observatory and Palomar Observatory.

In 1911 and the following years, nuclear physics built the fundament for modern solar spectroscopy. The new atomic models of Ernest Rutherford (1871–1937) described the atom as consisting of an electrically positively charged tiny nucleus surrounded by electrically negatively charged electrons. Two

[2]The spectroheliograph is an astrophysical instrument to produce a photographic image of the Sun at a single wavelength. This monochromatic light is retrieved by a combination of a diffracting medium, a prism or optical grating, and a narrow slit which moves across the solar projection to complete a full disk solar image.

years later, Niels Bohr (1885–1962) included specific and discrete atomic shells on which the electrons circle around the positively charged core. The spectral emission was explained by the transition of electrons to the lower atomic shells representing the lower energy states. An explanation for the spectral lines was found.

After the pioneering discovery of the sunspot's magnetic field, it was again Hale and his collaborators Ferdinand Ellerman, Seth B. Nicholson (1891–1963) and Alfred H. Joy (1882–1973) who were the first to find a systematic and periodic behavior of the sunspot magnetic field. The illustration of *Hale's polarity laws* in Fig. 1.1 stems from their original article (Hale et al. 1919). It shows not only the drift of spots within a sunspot cycle towards lower latitudes but also the magnetic field orientation of sunspot pairs. During one cycle, the leading and following spot always have the same magnetic polarity pattern in one hemisphere. In the other hemisphere the orientation is just reversed. But the really important result was that at the end of one sunspot cycle the large-scale magnetic field reversed itself and switched the magnetic polarity pattern. Consequently, the activity cycle of the magnetic field covers two sunspot cycles and therefore has a period of 22 years. The reason for this phenomenon opened a still ongoing debate and a new field of theoretical research for the *solar dynamo*.

More than half a century after Helmholtz and Kelvin had suggested gravitational contraction as the energy source of the Sun, a new explanation for the solar heating mechanism was necessary. The contraction as the single energetic source could last for only 20 million years, way shorter than the time span needed to explain the geological discoveries. Rutherford suggested radioactive decay as the internal source for the solar heating. In 1920, Arthur Eddington (1882–1944) found the (from today's view) right answer to the energetic problem. Under extreme pressure and temperature in the hot solar interior, a nuclear fusion of hydrogen nuclei into helium cores releases the required energy. Some years later, the astrophysicists Subrahmanyan Chandrasekhar (1910–1995), Hans Bethe (1906–2005) and others developed the theory of nuclear fusion which powers the Sun.

Till 1931, the solar corona had only been observed during solar eclipses. In this year, the French solar physicist Bernard Lyot (1897–1952) developed the first coronagraph. The telescope had an integrated diaphragm shadowing the solar disk so that Lyot was able to observe and photograph the solar corona at full daylight. The field of modern coronal physics was born.

Three fundamental discoveries from the middle of the 20th century are remaining. They are already named in this paragraph, as the scientists behind the discoveries complete the exquisite group of 'giants' on which shoulders my work is based on. The first is the establishment of the magnetohydrodynamic (MHD) theory by Hannes Alfvén (1908–1995) in 1942 (see Alfvén 1942). It explains how magnetic fields affect the plasma dynamics of the solar atmosphere, implicitly the generation and the essentials of magnetoacoustic waves which are the topic of this work (Chapter 3). Secondly, the discovery of the five-minute oscillations in the solar photosphere by Robert B. Leighton (1919–1997) and his colleagues in 1962 (see Leighton et al. 1962). With these so-called p-mode oscillations detected all over the solar surface, a new field to study the solar interior was born, the Helioseismology. And thirdly, the first time observation of waves in the sunspot umbra by Jacques Beckers and Paul Tallant in 1969 (see Beckers and Tallant 1969). They called these shock waves *umbral flashes* (Chapter 2).

Solar telescopes in space: Another major step for Solar Physics was made from 1962 on. Space-borne solar telescopes were developed to observe the Sun in UV and X-ray spectra. These bands of the electromagnetic spectrum are largely blocked by the Earth's atmosphere and could therefore only be observed by satellites. Another big advantage of space-borne telescopes is that the observations do not suffer from turbulent motions introduced by the Earth's atmosphere. However, it was ever since complicated to construct robust satellite telescopes which could deal with the enormous heat and intense radiation in space. The first successful space missions with solar telescopes were the Orbiting Solar Observatories (OSO) in the 60's (see Fig. 1.1), the German-American space probes Helios A & B in the 70's, and the Japanese Hinotori satellite in the 80's. From 1990 on, systematic observations of the Sun with long-term space telescopes began. For one decade, the Japanese-American-British

Yohkoh (or Solar-A) satellite observed the Sun continuously in several X-ray ranges. The Ulysses spacecraft orbited the Sun three times between 1994 and 2008 with changing inclination to make solar observations at all latitudes. And the Solar and Heliospheric Observatory (SOHO), a joint NASA/ESA probe which was launched in 1995, is still in operation. Its continuous and comprehensive observation of the solar atmosphere at various wavelength domains and especially the publicly available data led to further extensive research and novel findings. At the beginning of the 21st century, the amount and capabilities of solar space observatories even multiplied. With the Solar Dynamics Observatory (SDO), Hinode (SOLAR-B), the Interface Region Imaging Spectrograph (IRIS) and ESA's Solar Orbiter just a few of these newest generation's solar telescopes are mentioned.

Solar Physics – a diverse discipline: The detection of the dark lines in the solar spectrum by Joseph von Fraunhofer and their connection to the solar atmosphere must be seen as one of the most revolutionary events in the history of astronomy and as the prime milestone of a new scientific field, the solar spectroscopy.[3] To distinguish this new field of research from the established astronomy, it was diversely called *physical astronomy*, *astrophysics*, *astrochemistry*, *solar physics* or even *New Astronomy*. However, especially in its early stages of development, the pioneering field of astrophysics was disdained by many astronomers and physicists. Until then, astronomy had addressed to the motion of the heavenly bodies, their cataloging, classification and the visible events on the Sun. The new astrophysical studies aiming to define the nature of the objects and events were dismissed as pure speculation. Only when further groundbreaking discoveries substantiated the astrophysical science, the young field obtained more acceptance, but still not the appreciation to be due. At the beginning of the 20th century, the aspiring field of solar physics developed into an entrepreneurial science. Especially in America and thanks to the visionary George Ellery Hale, modern telescopes, improved cameras and spectroscopic instruments were developed and contributed to the gain of observational knowledge. Together with the nuclear models developed by the European community, astrophysics became a well established discipline. Today, solar physics accommodates a wide number of research areas with the Sun as the perfect real-life laboratory: from astrophysics, astronomy, atomic physics, plasma physics and spectroscopy over radiative transfer, seismology, fluid dynamics and magnetohydrodynamics to applied optics, signal processing and computer science.

The Sun – today's view of our unique star: Indeed unique? Actually, the Sun is a very ordinary star. With an effective photospheric temperature of 5778 K and an absolute magnitude of +4.83, a quick look on a Hertzsprung-Russell diagram[4] reveals that the Sun is as a common main-sequence dwarf star of spectral type G2. So far, so good. Like so many other stars, it has formed approximately 4.6 billion years ago under the gravitational collapse within a large and slowly rotating molecular cloud.

So what makes the Sun so unique for us? Of course, it is the mysterious star in the center of our planetary system. It spends and preserves life by being the most important energy source on Earth. Ever since it has fascinated human kind and nourished the scientific curiosity to understand its nature. Also from the scientific point of view, the Sun is incomparable for us. By nature, it is the only star we can observe in high spatial and temporal resolution. We can observe small-scale structures and very dynamical events in real-time as well as middle-term changes by statistical records. It is possible to observe the different atmospheric layers up to the outer corona or to derive insight into the sub-surface convective zone using continuous observations and mathematical methods. We can gain a vast knowledge of our ordinary star from the measurable processes and conditions and investigate the impact of its activity on the climate of the orbiting planets. Going one step further, we can then adapt these findings and probe the structure of other stars and planetary systems. The Sun as our laboratory for plasma physics provides the basis.

[3] Most of this paragraph is adapted from Eisberg (2002).

[4] A diagram showing the distribution of stars according to their stellar luminosity and effective temperature or spectral class. It consists of a main sequence of dwarf stars and several side branches of giant stars.

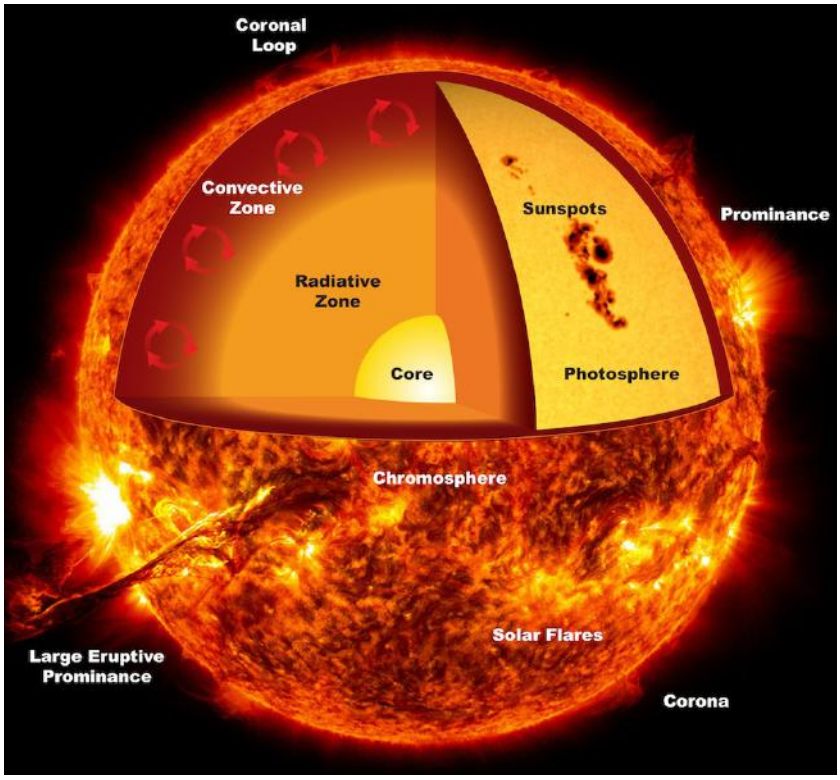

Figure 1.2.: Today's view of the Sun. The interior of our star is separated into four zones (starting from inside): The core, the radiative zone, the interface layer (tachocline) and the convection zone. The solar atmosphere is composed of the photosphere, the chromosphere, a transition region and the corona. Several dynamical events like sunspots, flares, prominances and coronal loops are shown. Image from NASA (b).

In the last centuries, our knowledge of the Sun's nature and dynamics has become very broad. In Fig. 1.2 the Sun is shown in a schematic view as we see it today.[5] Our star is an almost spherical star made of hot gas plasma located in a mean distance of around 150 million km from the Earth.[6] For illustration, the emitted photons traveling with the speed of light arrive at the Earth around 8 min and 19 s later. The Sun has a diameter of almost 1.4 million km and a mass of almost $2 \cdot 10^{30}$ kg. Compared to the Earth, it is 109 times bigger in diameter and about 330,000 times more massive. Chemically, the Sun consists by three quarters of hydrogen, almost one quarter of helium and a small rest of heavier elements.

The source of the Sun's energy is nuclear fusion. Through the large gravitational force, the solar core exhibits densities which are up to 150 times larger than the density of water, enormous pressures up to 265 billion bar and extreme temperatures up to 15 million degrees Celsius. Under these unimaginable conditions hydrogen nuclei are fused into helium cores releasing the enormous amounts of energy to heat the Sun. This hydrogen fusion will persist for another 4 billion years. After this process has stopped, nuclear fusion of Helium to heavier elements will transform the Sun from a dwarf star into a cooler, red giant.

The energy that is produced in the solar core is transported outward by different processes. The innermost is radiation. The radiative zone spans from the margin of the solar core to the interface layer at the lower edge of the convection zone. In the radiation zone, the photons carrying the energy in

[5] Numbers and facts taken from NASA (a).
[6] The mean distance of the Sun to the Earth is defined as one astronomical unit (1 AU).

kinetic form collide so frequently with the dense particles that it effectively takes them about a million years to escape this inner zone. In the interface layer the way of energy transport is converted from radiation into the more effective convection.[7] In the convection zone, a temperature gradient from two million Kelvin at its base to around 6000 K at the solar surface drives the rapid upward motion of the hot gas plasma. The convection stops a the solar surface since the atmosphere gets transparent and radiation becomes effective. At the solar surface, we can identify the convective motions as granules, supergranules and large-scale flows. As the hot gas plasma reaches the solar surface in the form of bright granules, a large fraction of the heat is radiated. Since the gas cools down, it sinks back into the darker intergranular lanes. When strong magnetic fields rise up and pierce through the solar surface, the convection is suppressed and less heat can be formed into radiation. These cooler and therefore darker areas are called pores or – when a filamentary penumbra has been formed – sunspots.

The investigation of magnetic fields is the quintessence of Solar Physics. From today's perspective, the solar magnetic field is generated in the lower convective zone by a magnetic dynamo. Due to shear flows across the convection zone, the magnetic field can be enhanced. The Sun rotates differentially with periods of 25 days at the equator to 34 days at the poles. Therefore, the magnetic field lines are stretched, wounded up like a coil, form dense bundles of field lines and by buoyancy drift up to the surface.

In the solar atmosphere, these strong magnetic fields are responsibly for a diversity of dynamical activity, from large eruptive events like shock waves in sunspots, solar flares and coronal mass ejections to filaments, solar prominences and the beautiful coronal loops. The solar atmosphere consists of different layers, mainly distributed according to their density and ambient temperature. The first atmospheric layer following the convection zone is the photosphere. Most of the emitted light of the Sun is coming from this layer. The granular pattern, flows, surface waves, the differential rotation, sunspots and an intensity variation from the center to the limb can be observed. In these first 500 km of altitude above the surface, the temperature decreases with height by some 2000 Kelvin and reaches a temperature minimum. In the following roughly 1500 km thick chromosphere the temperature increases again. At the top of the chromosphere, the atmosphere is heated up to 10,000 Kelvin. In this zone, the appearance is dominated by the magnetic field. The chromospheric network, prominences, spicules, waves, filaments and flares are observed. The layer that separates the chromosphere from the solar corona is called the transition region. It is a thin and irregular layer in which the temperature can increase up to a million Kelvin. The even hotter corona is the Sun's outermost atmosphere. Due to its temperature, the present atoms are highly ionized. The coronal spectrum is characterized by strong emission lines in the ultraviolet and X-ray domain. Magnetic fields induce magnificent phenomena like coronal loops, dynamics in prominences and coronal mass ejections. A more detailed description of the solar atmosphere will be given in section 2.3. For more information on the Sun and Solar Physics, a very broad and detailed introduction is given in Stix (2002).

[7] Due to outward decreasing temperatures, the ionization of the heavier atoms decreases and the radiation fails to pass the gas plasma of increasing opacity.

2. Sunspots

"The diversity of the phenomena of nature is so great, and the treasures hidden in the heavens so rich, precisely in order that the human mind shall never be lacking in fresh nourishment."

— Johannes Kepler, quoted in *Cosmos* by Carl Sagan

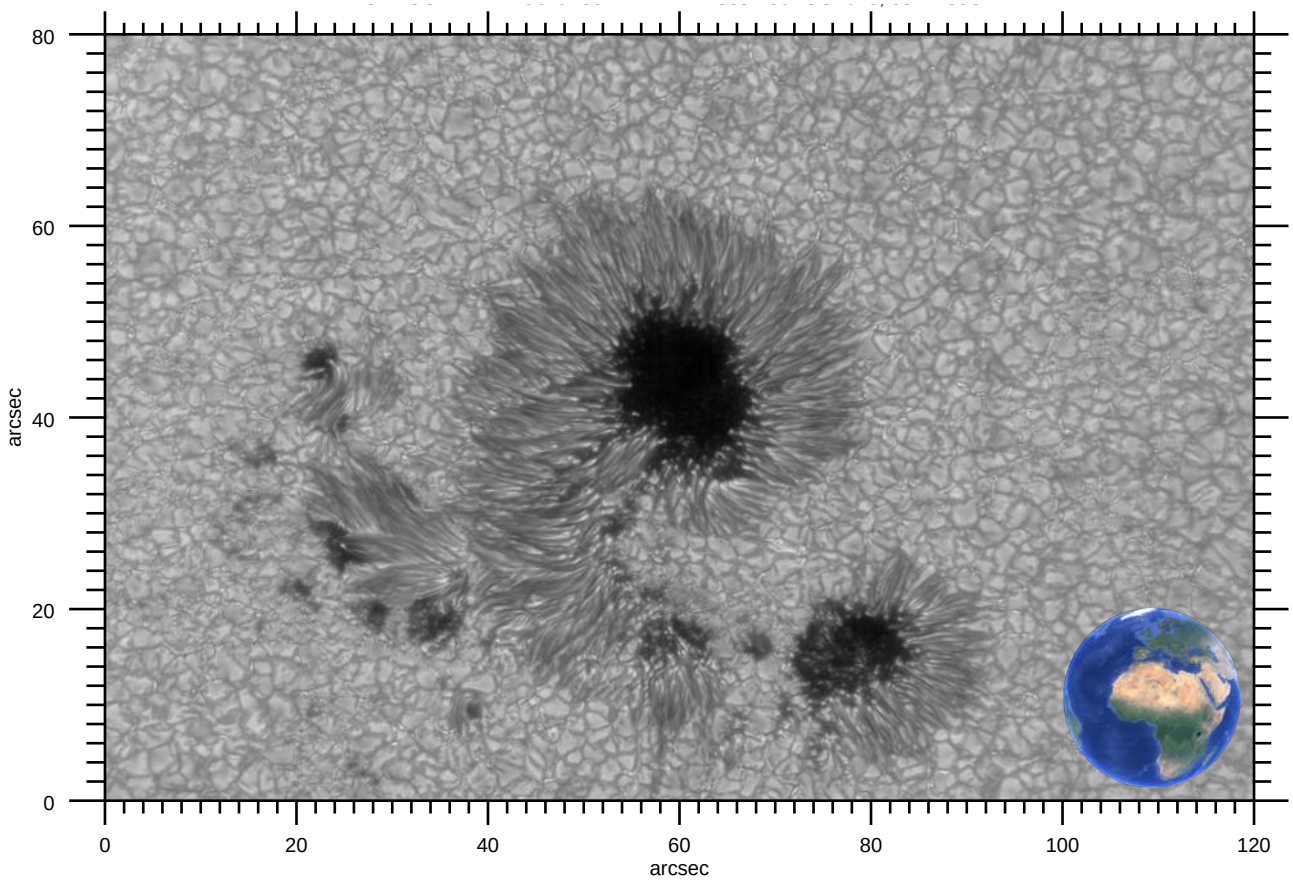

Figure 2.1.: Sunspots in active region NOAA 11835, observed with the Broad-Band Imager (BBI) at the GREGOR telescope on Tenerife. The observation was performed on August 30th 2013 at 08:27:35UTC with a broad (4 nm) continuum band centered at 486 nm. The overplotted Earth scales in size.

As outlined in Chapter 1, the history of solar physics is greatly dominated by sunspot observations. More than four centuries ago, the dark spots were the first solar objects to be observed with a telescope (see Fig. 1.1). From their motion across the solar disk, the rotation of the Sun became evident. Moreover, the solar rotation was determined as differential, as sunspots closer to the solar equator rotate with a higher rate. The temporal variation of sunspot numbers allowed the detection of the 11-year sunspot cycle. Sunspots were also the first solar objects where a Zeeman splitting of spectral

lines was measured. This was the first step to reveal the magnetic nature of the Sun. Furthermore, the discovery of the sunspot magnetic field and its temporal evolution disclosed the 22-year solar cycle of magnetic activity. At the beginning of a sunspot cycle, the spots occur preferentially at heliographic latitudes of around ±35°. Toward the end of the sunspot cycle they migrate to latitudes of typically ±5°. At the transition to the next sunspot cycle, the bipolarity of the paired sunspots switches its sign. In addition, the global magnetic field changes its polarity as well, so that two sunspot cycles make one solar cycle. According to its shape, the diagram of this temporal variation is called 'butterfly' diagram (Hathaway 2015). With the technical progress and excellent solar telescopes, the established phenomena in sunspots can be investigated at the highest resolution which allows the detection of new small-scale dynamics and fine-structures. Like at the times of Galileo Galilei or William Herschel, sunspot phenomena are still a up-to-date subject of debate.

This chapter introduces the observed wave phenomena in sunspots which are the cover topic of this work. To get an easy access, the basic structures and dynamics in sunspots are described in Section 2.1. The fine structure of sunspots and their magnetic field topology are discussed in Section 2.2. In Section 2.3, the basic properties and physical quantities of the solar atmosphere above sunspots are illustrated. The traditional classification of sunspot oscillations is presented in Section 2.4 with the division in photospheric 5-min oscillations (Section 2.4.1), chromospheric 3-min oscillations and umbral flashes (Section 2.4.2), and running penumbral waves (Section 2.4.3) in the sunspot chromosphere. Following this, the modern sunspot wave scenario is presented in Section 2.5. At the end of this section, the leading questions about sunspot waves are formulated.

2.1. Essentials and dynamics

A first impression of sunspots is that they are distinctly darker features on the bright surface of the Sun. Their sizes range from 3.5 Mm to more than 60 Mm in diameter, while the largest formations are even visible to the naked eye (Solanki 2003). Sunspots appear darker because the convection of hot gas is suppressed. Consequently, sunspots are cooler and radiate less than the surrounding quiet sun. Since the detection of the Zeeman splitting of spectral lines in sunspots by Hale (1908a), it is known that strong magnetic fields and their magnetic forces reduce the convective motion of the plasma. The appearance of a sunspot is dominated by the strength and topology of the magnetic field.

The basic structure and evolution of sunspots are linked. When an accumulation of magnetic flux tubes rises to the outer convection zone and pierce through the solar surface, the footpoints of the magnetic loop are observed as small sunspot pores suppressing the granular convection. For strong magnetic field concentrations, a complex active region can develop. It is classified according to the size, distribution, penumbra, and magnetic field properties of its sunspots (McIntosh 1990). After its emergence which often takes only few hours, it can decay again within several hours or days, or develop into a stable sunspot with a lifetime of several weeks. Fig. 2.1 shows a complex sunspot region observed with the 1.5 m GREGOR telescope (see Fig. 4.3) at the highest spatial resolution available. In general, a sunspot is divided into the umbra which is the darkest part of spot, and the penumbra with its brighter filamentary structure surrounding the umbra. In the center of Fig. 2.1, a large umbra with a strong magnetic field strength of around 3 kG (or 0.3 T) dominates the active region. Its size with a diameter of around 10 Mm is only slightly smaller than the overplotted size of the Earth. Strong umbral cores exhibit typical field strength from 1.8 kG to 3.7 kG (Livingston 2002). The average atmospheric temperature of around 4400 K in the low photosphere is almost 2000 K cooler than in the vicinity of the sunspot (see Fig. 2.4). The spectral intensity in the visible range is reduced to less than 25% compared to the quiet sun continuum (see lower right panel of Fig. 2.7). In the blue and violet range, the decreased intensity can go even down to 5%. As shown in Fig. 2.1, the umbrae can be surrounded by penumbral filaments. Umbral cores with a strong magnetic field strength often develop a fully-surrounding penumbra (e.g., Jurčák et al. 2015). As displayed by the lower right umbra, smaller sunspots sometimes form only a half-sided penumbra (e.g., Schlichenmaier et al. 2010) or no penumbra

at all. In the latter case, they are called pores. On the other hand, as shown in the lower left part of the field, an orphan penumbra can also form even without an adjacent umbra. In average, the penumbra yields a photospheric temperature of around 5500 K and a heat flux of around 75% compared to the quiet sun continuum. The penumbral filaments have a typical thickness of 0.2″ to 0.6″ and a length up to 2 Mm and more. The magnetic strength decreases smoothly with radial distance from the umbra (see Fig. 5.4) to around $1.4-2.2$ kG at the inner and $0.7-1$ kG at the outer penumbral boundary (e.g., Balthasar and Schmidt 1993).

As illustrated in Fig. 2.2, the photospheric magnetic flux tubes (brown lines) of the penumbra harbor a strong magnetized flow, commonly known as the Evershed effect. It is a mainly horizontal outflow toward the outer penumbra with absolute average velocities of around 3 km s^{-1}. At the inner penumbra it exhibits a more vertical up-flow component, at the outer penumbra the Evershed flow sinks slightly to deeper layers (e.g., Schlichenmaier and Schmidt 2000; Bellot Rubio et al. 2003). The line-of-sight velocities in a sunspot feature the typical appearance shown in Fig. 5.1 of spectral blue-shifts for the center-side penumbra and red-shifts for the limb-side penumbra. In the vicinity of the sunspot, the Evershed effect disappears and the moat flow sets in. It is also a radially outward directing flow, but compared to the penumbral flow it is non-magnetized and has horizontal velocities decreasing from 1 km s^{-1} (e.g., Löhner-Böttcher and Schlichenmaier 2013). In addition, moving magnetic features follow the moat flow across the granular motion of the lower photosphere. As described in Section 6.1.1, the solar pressure waves or commonly called *p-modes* in the convection zone and lower photosphere can run through a sunspot. Thereby, a portion of their wave power is absorbed and converted into magnetoacoustic waves (Braun et al. 1987).

In the chromosphere and the layers above, the structure and dynamics of sunspots are governed by the magnetic field (low plasma-β in Section 3.3). As shown in Fig. 2.3, the appearance of a sunspot changes dramatically for different atmospheric layers (described in Section 2.3). The granular convection of the lower photosphere (left panel) gets reversed toward the upper photosphere (middle panel). The umbra and penumbra exhibit less convective fine-scale structure. In the chromosphere, the distinction of the umbral and penumbral area is less pronounced (right panel). The elongated filaments of the superpenumbra exceed the photospheric penumbral boundaries. The dynamics in the upper sunspot atmosphere are quite unlike to the photospheric case, too. Oscillations, waves, and highly energetic eruptive events are prevalent. Umbral flashes and running penumbral waves (see Section 2.4) continuously propagate across the sunspot chromosphere with a periodicity from 2.5 min to 10 min. Bright sunspot jets at the outer penumbra occur up to several times per hour (e.g., Morton 2012). Bright Ellerman bombs happen preferentially in the low chromospheric vicinity of the sunspot (e.g., Bello González et al. 2013a). Highly energetic solar flares can dominate the active region when it gets to reconnection of the magnetic field lines, especially when a torsion of the sunspot exists. The formerly radially outward directed Evershed flow of the photosphere translates into an inverse Evershed flow of gas plasma along the superpenumbral filaments in the chromosphere (e.g., Dere et al. 1990). In the transition region above sunspot umbrae, a steady down-flow to deeper layers is present (e.g., Straus et al. 2015). Above, coronal loops exhibit a wide range of wave dynamics and eruptive events. The sunspot dynamics in the performed observations of NOAA11823 and NOAA11455 are presented in Sections 4.3.1 and 4.3.2. Further information and references on sunspots and their dynamic phenomena can be found in the excellent reviews by Stix (2002), Schmidt (2002) and Solanki (2003).

2.2. Magnetic field topology and fine-scale structure

Magnetic field strength: The magnetic field topology and fine-scale structure of sunspots affect the present flows and waves. Sunspot waves and the penumbral Evershed flow are oriented along the magnetic field lines. As explained in Section 2.1, the magnetic field concentration in the umbral core can reach field strength of up to 3 kG and more. Toward the outer edge of the penumbra the field strength decreases smoothly to below 1 kG. But the magnetic field strength also exhibits a negative vertical

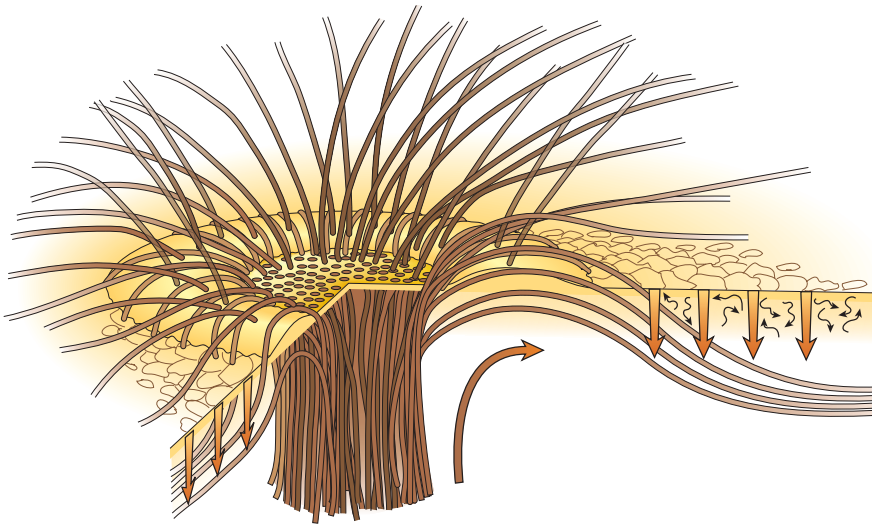

Figure 2.2.: Sunspot structure and magnetic field topology. The distribution of magnetic field lines (brown) close to the solar surface is shown schematically for the umbra (inner circle), penumbra (surrounding ring) and granular vicinity of the spot. The arrows indicate convective motion. Image from Thomas et al. (2002)

gradient. In the umbra, the total field strength decreases as a function of height by $1-3\,\mathrm{G\,km^{-1}}$ in the lower photosphere and by $0.3-0.6\,\mathrm{G\,km^{-1}}$ in the average photosphere and chromosphere (e.g., Wittmann 1974; Balthasar and Schmidt 1993). In the penumbral atmosphere, the field strength decreases with a smaller gradient (see review by Solanki 2003). The magnetic field fans out very rapidly in the lower sunspot atmosphere so that the average magnetic field strength of 3 kG in an umbra drops below 1.5 kG in the chromosphere and lower corona (e.g., Rueedi et al. 1995b).

Magnetic field topology: In Fig. 2.2, a sketch of the magnetic field lines illustrates the three-dimensional topology of sunspots in the lower solar atmosphere. In the dark core of the umbra, the magnetic field lines (brown) are close to vertical. As shown in Fig. 5.4 c), the field inclination increases with radial distance from the core of the sunspot. The photospheric inclination depicts an almost linear increase with outward decreasing field strength. In the lower photosphere, the azimuthally averaged zenith angle rises to typical values around 30° at the umbral boundary and a more horizontal orientation of $70-80°$ at the outer penumbral edge. With increasing height, the magnetic field is getting more homogeneous and less inclined compared to the lower photospheric penumbra (e.g., Keppens and Martinez Pillet 1996; Westendorp Plaza et al. 2001). Inferring the total magnetic field topology in the chromosphere requires the measurement of the full-Stokes signal of chromospheric lines, the consideration of scattering polarization, and the inversion of non-local thermodynamic equilibrium. In addition, the presence of sunspot waves can even lead to changing polarities of the polarization signals (Socas-Navarro et al. 2000; López Ariste et al. 2001) and therefore complicates the determination of the magnetic field vector. However, observations agree that the zenith angles in the penumbra decreases with height. From radio observations (Alissandrakis and Kundu 1984), the reconstructed coronal field inclination in the outer penumbra yields angles of around 40°. As indicated by the penumbral filaments in Fig. 2.3 and the inferred azimuth in Fig. 5.4 d), the magnetic fields of a regular symmetric sunspot have an almost radial extent. As reviewed in Solanki (2003), the penumbral field in the photosphere often exhibits an azimuthal twist of up to $10-15°$. In the chromosphere, the torsion of the superpenumbral filaments is even stronger with up to 30° at larger radial distances.

Magnetic canopy: The magnetic field does not stop abruptly at the sunspot boundary seen in continuum intensity (Solanki et al. 1992). It decelerates continuously and extends far beyond the sunspot, making up the chromospheric superpenumbra. The weak ($\approx 100\,\mathrm{G}$) and almost horizontal

magnetic field in the spot's vicinity describes a layer covering the relatively field-free solar surface. It it commonly known as the magnetic canopy. As reviewed by Steiner in Murdin (2001), the base height of the canopy is located in the upper photosphere and lower chromosphere. In the vicinity of sunspots, the layer forms around 400 km above the continuum optical depth unity. In the quiet sun, it is based at $600 - 1000$ km above the solar surface. Physically, the canopy results from the decreasing plasma pressure toward the chromosphere and the expansion of the magnetic field structure. In terms of wave propagation, the canopy layer can influence the formation of acoustic shock waves and wave frequencies of p-mode oscillations over the solar cycle.

Fine-scale structure: Till here, the magnetic field was described by its global properties. However, the sunspot and its magnetic field feature a wide range of small-scale structures which become increasingly prominent for high-resolution observations better than $1''$. As shown in Fig. 2.1, the left panels of Fig. 2.3, and Fig. 4.17 (a,b), small features like umbral dots, light bridges, penumbral filaments and grains appear in a rich variety and influence the dynamics and magnetic distribution in the sunspot photosphere. An overview on fine-scale structures in sunspots is given by Solanki (2003) and references therein.

Umbral dots: Almost no fine-scale structure is visible in the darkest cores of the umbra with the strongest magnetic field. The rest of the umbral area is covered with small umbral dots. The bright point-like features have a typical size ranging from $0.2''$ to $0.5''$, or a few hundred km (e.g., Denker 1998). They are embedded in the diffuse umbral background and cover $3 - 10\%$ of the umbral area (Sobotka et al. 1993). Umbral dots feature up-flows with Doppler velocities of a few hundred $\mathrm{m\,s^{-1}}$ and seem to result from narrow magneto-convection in the umbra. In addition, the temperature in umbral dots ranges from $4900 - 5900$ K, which is significantly hotter (~ 700 K) than in the umbral core (Tritschler and Schmidt 2002). With respect to the background field, the magnetic field strength is reduced by $5 - 20\%$, depending on the dot's position in the umbra (e.g., Schmidt and Balthasar 1994). This decrease can be real or apparent. The latter could be caused by a higher formation altitude and the negative vertical gradient in field strength. By the steeper temperature gradient toward the upper photosphere, the brightness and temperature contrast of umbral dots to the umbral background decreases. The dots have a lifetime of up to one hour and oscillate in brightness.

Light bridges: As shown in Fig. 4.17 a), the sunspot umbra can be divided into multiple cores. The light bridges separating the umbrae appear as bright lanes of convection at photospheric heights. Since up to 20% of the plasma in light bridges is field-free, the magnetic field strength compared to the umbral cores is significantly reduced by $200 - 1500$ G at the arc-second scale (e.g., Leka 1997). The magnetic field components of light bridges are shown in Fig. 4.17 (panels f–h). In accordance with literature (e.g., Rueedi et al. 1995a), the magnetic field is more inclined than in the nearby umbral cores. Zenith angles in light bridges are up to 30° larger. The azimuth of the field differs from the radial symmetry of the sunspot, too. As supported by Fig. 4.17, the appearance of the light bridges in the upper photosphere (panel c) and chromosphere (panel d) gets less pronounced. So does the gradient in magnetic field strength and inclination. Light bridges also influence the oscillations in the sunspot chromosphere (e.g., Sobotka et al. 2013). As reported by Yuan et al. (2014a), the waves cannot propagate across the light bridge from one umbral core to another. But as umbral oscillations in the multiple umbrae seem to be in phase, it is suggested that the oscillations share the same driving source below the light bridge in a probably connected umbra. Moreover, while thin light bridges at low chromospheric layers reveal a standing wave behavior, wider light bridges exhibit running waves along the long axis towards the center of the LB with propagation speeds of $10 - 20\,\mathrm{km\,s^{-1}}$. Within the light bridge, strong localized down-flows of up to $1.5\,\mathrm{km\,s^{-1}}$ have been measured (Rueedi et al. 1995a). It is suggested that the inverse wave propagation in light bridges can be considered as the counterpart of running waves along the penumbral filaments. A possible explanation considers light bridge oscillations as standing acoustic waves trapped by the atmospheric non-linearities.

Penumbral filaments and grains: The penumbra in the low photosphere displays one of the most conspicuous fine-structures of the Sun (see Fig. 2.2). Elongated bright and dark filaments cover most

of the penumbral area. Bright, point-like penumbral grains feature the inner end of the fibrils. The filaments have a typical thickness of $0.2 - 0.6''$ and a length up to $2''$ and more. The velocities in the flux tubes are dominated by the Evershed effect. The magnetic field inclination at the small scales is fluted. This means that the zenith angle of the field fluctuates along the penumbral azimuth. With variations of the zenith angle in the $10 - 40°$ range within less than an arc-second, Schmidt et al. (1992) and Title et al. (1993) provided evidence for this 'uncombed' structure. It is suggested that the bright and dark filaments systematically differ in inclination, field strength, and temperature. Especially the temperature in the penumbral fine structure fluctuates by up to 700 K (Suetterlin and Wiehr 1998). Further, it is argued that dark, cool filaments are oriented more horizontally. Together with the less inclined and hotter flux tubes, they are embedded in the penumbral background field (Schlichenmaier and Collados 2002). The penumbral filaments have a lifetime between 10 min and 4 h, during which their magnetic structure is very stable. The bright penumbral grains are located mainly at the inner penumbra. They are noticed not only in continuum intensity but also in Doppler velocity, magnetic field strength and inclination. The temperature in grains can even exceed the quiet sun temperature. At the inner penumbra, the grains have an apparent inward motion with velocities around $0.4\,\mathrm{km\,s^{-1}}$ and more (Lites et al. 1998). In the outer penumbra, also outward motions are detected.

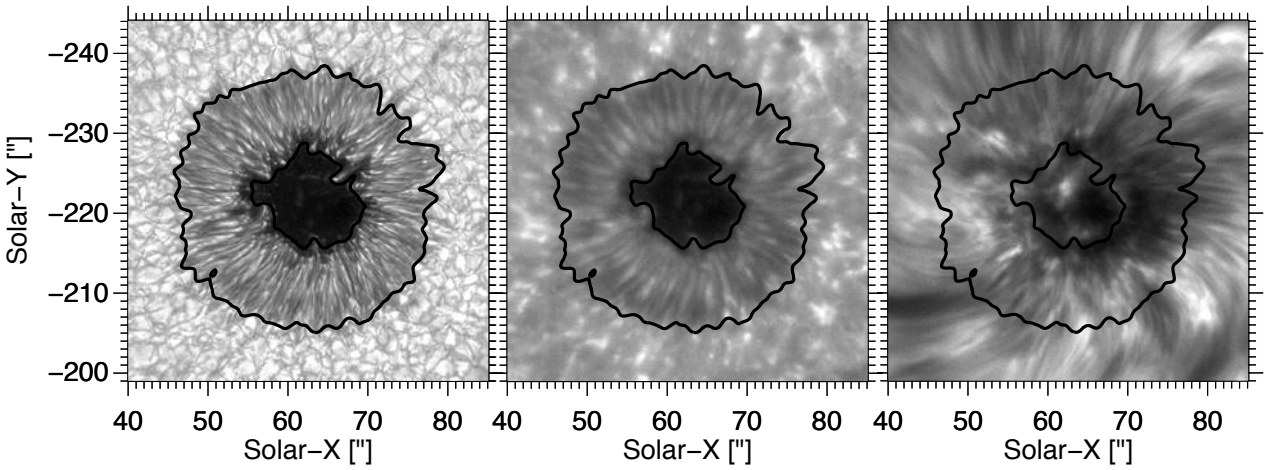

Figure 2.3.: Sunspot appearance in different atmospheric layers. The fully-developed sunspot (NOAA11823, see Section 4.3.1) is shown in spectral intensities of the solar surface (left panel), upper photosphere (middle panel), and chromosphere (right panel) with a bright umbral flash. The sunspot boundaries are contoured as black lines.

Chromospheric fine-structure: Although the magnetic field fans out with atmospheric height, there are still a number of noticeable structures in the sunspot chromosphere at arc-second scale and below. The chromospheric appearance of a sunspot at high spatial resolution is shown in the right panel of Fig. 2.3. With modern high-resolution telescopes and fast imaging spectroscopy, transient jet-like brightenings have been observed recently in the umbra and inner penumbra (Rouppe van der Voort and de la Cruz Rodríguez 2013; Bharti et al. 2013; Yurchyshyn et al. 2014). They are called umbral spikes or umbral micro-jets. The features have a typical width of less than $0.3''$ and an extension of around $0.5 - 1.0''$, with lowest sizes measured at the innermost umbra. First a dot-like structure appears which then gives rise to a narrow elongated jet. In a space-time diagram, the clear parabolic trajectories hint at decelerating velocities. The apparent structure is moving up and down in an oscillatory motion with periods around $2 - 3$ min. The more extended micro-jets at the outer umbra and penumbra exhibit longer oscillatory periods. It is suggested, that the potentially more inclined magnetic field can be the reason. Their characteristics hint at a generation by acoustic shocks and magnetoacoustic waves with longer periods propagating upward along the magnetic field of the sunspot. A possible link between umbral dots and chromospheric micro-jets is still unsettled. As shown in the right panel

of Fig. 2.3, the superpenumbral filaments exhibit a fine-structure at slightly larger spatial scales than in the photosphere. The bright and dark fibrils have a width of around $0.5 - 3.0''$ and an extension of around $15''$. Superpenumbral filaments are dynamical and live for about 20 min. They harbor the outward directed running penumbral waves and also the inverse Evershed flow.

2.3. Properties of the sunspot atmosphere

The dynamical solar atmosphere is diverse in its intrinsic appearance and its physical quantities. The atmospheric properties primarily depend on the atmospheric altitude above the solar surface and on the present magnetic configuration. As discussed above and displayed in Fig. 2.3, the morphology of sunspots changes from the low photosphere to the chromosphere. In the following, the average physical quantities and atmospheric models are introduced.

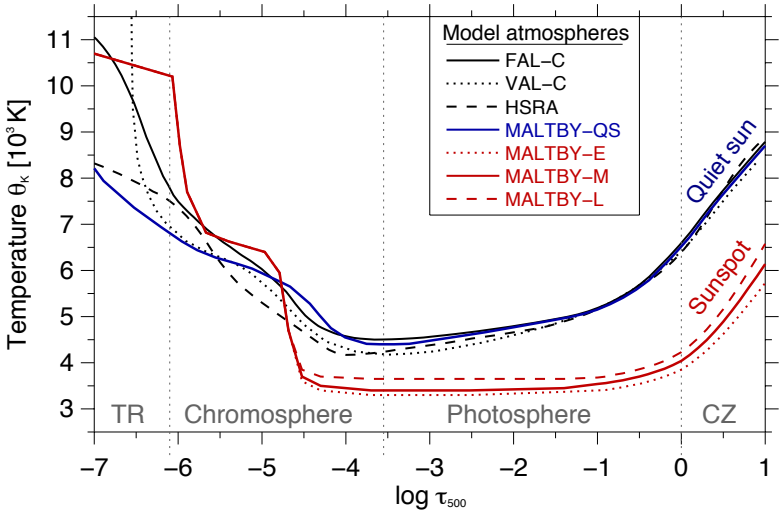

Figure 2.4.: Model atmospheres of the quiet sun and sunspot umbra. The temperature stratification θ_K, is plotted against the optical depth τ at 500 nm. The quiet sun models FAL-C (Fontenla et al. 1993), VAL-C (Vernazza et al. 1981), and HSRA (Gingerich et al. 1971) are displayed as black curves in solid, dotted and dashed line style. The models of Maltby et al. (1986) compare the quiet sun atmosphere (blue solid) with the umbral atmosphere at an early (red dotted), middle (red solid) and late (red dashed) stage of the sunspot cycle. The gray dotted lines indicate the estimated transitions between the convection zone (CZ), photosphere, chromosphere and transition region (TR).

The solar atmosphere is hot and bright with characteristic temperatures of several thousands to a million Kelvin and a luminosity of $3.8 \cdot 10^{26}$ W. But compared to the Earth's atmosphere, the solar atmosphere has a very low density which is several orders of magnitude thinner. The physical quantities of the Sun's atmosphere, more precisely the temperature, density, pressure, and magnetic field essentially change as a function of height. According to the behavior of the temperature, the solar atmosphere is traditionally characterized by four main layers. With increasing heights these are 1) the photosphere, 2) the chromosphere, 3) the transition region, and 4) the corona.

Whereas the density and gas pressure drop exponentially from the inner photosphere to the outer corona (see Fig. 2.5 b), the atmospheric temperature behaves in a strange fashion. The model atmospheres of the quiet sun (Gingerich et al. 1971; Vernazza et al. 1981; Fontenla et al. 1993) and sunspot umbra (Maltby et al. 1986) are plotted in Fig. 2.4 as a function of optical depth τ_{500} at a wavelength

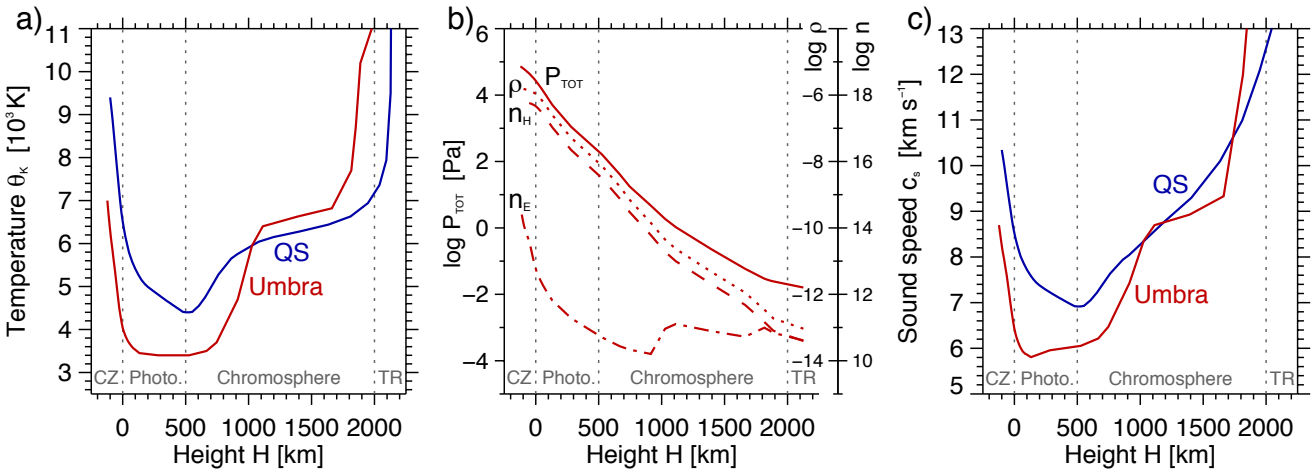

Figure 2.5.: Physical parameters of the atmosphere above the quiet sun (QS, blue curves) and sunspot umbra (U, red curves) of the middle spot cycle (models QS and M from Maltby et al. 1986). The temperatures θ_{K} (panel a) and sound speeds c_{s} (panel c) are plotted as a function of geometrical height H. In panel b), the gas pressure p_{tot} in Pa, gas density ρ in $\mathrm{g\,cm^{-3}}$, total hydrogen number density n_{H} and electron number density n_{e} in $\mathrm{cm^{-3}}$ are displayed at logarithmic scales for the umbral atmosphere. The gray dotted lines indicate the estimated transitions between the atmospheric layers.

of 500 nm.[1] From the convection zone ($\log\tau > 0$) to the solar surface ($\log\tau = 0$), the temperature decreases to below 6500 K in the quiet sun (blue and black curves) and significantly cooler temperatures of around 4000 K in the dark umbral core (red curves). From the lower to the upper photosphere, the temperatures decrease to minimum values of around 4300 K in the quiet sun and around 3400 K in the umbra. This temperature minimum typically defines the transition from the photosphere to the chromosphere at around 500 km above the continuum optical depth unity (see Fig. 2.5 a). In the chromosphere, the temperature starts to increase again. At an average height of 1000 km above the surface it reaches a mid-chromospheric plateau with around 7000 K. Importantly, the umbral temperature begins to exceed the temperature of the sunspot surroundings. In the upper chromosphere which reaches an altitude of more than 2000 km, the increase gets steeper to some 10000 K at its upper boundary. The transition region describes the layer between the chromosphere and corona. It is only a tens to hundreds of kilometers thick but features at sudden increase up to several hundred thousand to a million Kelvin. The atmospheric distribution of temperatures ϑ_{K}, gas pressure p, and plasma density ρ also affects the local speed of sound which is defined as

$$c_{\mathrm{s}} = \sqrt{\gamma \cdot \frac{p}{\rho}} \overset{(3.13)}{=} \sqrt{\frac{\gamma \cdot R_{\mathrm{M}} \cdot \vartheta_{\mathrm{K}}}{M}}\,, \tag{2.1}$$

with the ratio of specific heats γ, molar gas constant R_{M} and mean molar mass M. The resulting sound speed in the quiet sun (blue) and umbral core (red) is plotted in Fig. 2.5 c). While the sound speed in the quiet sun decreases from around $8\,\mathrm{km\,s^{-1}}$ in the lower photosphere to around $7\,\mathrm{km\,s^{-1}}$ at the temperature minimum height, the sound speed in the photosphere and lower chromosphere above the umbra is rather constant at around $6\,\mathrm{km\,s^{-1}}$. Toward the middle chromosphere, the speeds increase to

[1] The temperature inferred from the Sun's intensity brightness is wavelength dependent, especially for sunspots. As stated by Maltby et al. (1986), this is due to the optical depth. While in the visible to near-infrared range (0.5−1.2 μm) the continuum temperature of dark umbral cores is only around 4000 K, the obtained temperature increases to a maximum of 5000 K in the infrared at around 1.6 μm. At longer wavelengths in the infrared one could look into deeper and therefore hotter layers.

around $9\,\mathrm{km\,s^{-1}}$, and significantly faster sound velocities with up to several ten to hundred $\mathrm{km\,s^{-1}}$ in the transition region and corona.

The one-component model describes the physical quantities in the dark cores of large umbrae extremely well. This is also the case for the dark and relatively homogeneous umbral background or the average umbra. However, this one-dimension umbral model has its limits. At high spatial resolution the umbra shows a greatly inhomogeneous and complex structure. Then a refined two-component model would be required to describe the umbral quantities (see Solanki 2003).

As shown in Fig. 2.4, the temperature models for the umbra (red curves) differ for sunspots at the early (dotted), middle (solid) and late (dashed) phase of the sunspot cycle (Maltby et al. 1986). Already Albregtsen and Maltby (1978) noted that the temperature of the umbral photosphere increases toward the late phase of the cycle, even after the correction of the latitudinal temperature dependence. In addition, the temperature of sunspot umbrae decreases almost linearly for increasing umbral sizes and with the square of the magnetic field strength. As demonstrated by Martinez Pillet and Vazquez (1993) and Collados et al. (1994), smaller sunspots and pores with umbral diameters below $10''$ often have a minimum temperature which is several hundred Kelvin hotter than the model temperature of Maltby et al. (1986).

Wilson depression: When sunspots are observed near the solar limb, they exhibit a narrower center-side than limb-side penumbra. Already in the 18th century, Alexander Wilson correctly interpreted this effect as a geometrical dip of the solar surface. More precisely, the magnetic pressure in sunspots lowers the gas pressure and temperature. Since the opacity of the atmosphere drops, wee see deeper into the sunspot. This Wilson depression for sunspots ranges between 400 km and 800 km (e.g., Mathew et al. 2004). Therefore, the geometrical temperature profile of the umbra (see Fig. 2.5) has to be shifted downwards by several hundred km relative to the quiet sun profile.

The photosphere and lower chromosphere: Most of the solar radiation in the visible and infrared comes from the photosphere. Since the density decreases exponentially with height, most of the Sun's atmospheric mass is concentrated in this layer, too. The gas of the solar atmosphere mainly consists of hydrogen and helium atoms, and smaller fractions of oxygen, carbon, nitrogen, and other atoms (Asplund et al. 2009). In the sunspot photosphere, the ionization level of the atoms and molecules amounts to $\approx 3\%$. Many of the spectral lines in the visible and near-infrared range are formed only in the lower photosphere. Most of the lower photospheric spectral lines are iron, magnesium, sodium, calcium, silicon, and aluminum lines. Upper photospheric and lower chromospheric lines often result from transitions in sodium, ionized calcium, and magnesium. Some of the spectral lines formed at these layers are described in Section 4.2.

The chromosphere: In the 2000 km thick layer above the photosphere, the plasma temperature increases outwards. The density and gas pressure have already decreased by several orders of magnitude compared to the photosphere (see Fig. 2.5 b). The total mass of the chromosphere has the order of the Earth's atmosphere. In the upper chromosphere, the transitions in the hydrogen and helium atoms dominate the spectral radiation. The chromosphere is very dynamical and inhomogeneous. Besides radiation, a considerable proportion of the energy and mass transport into the upper atmosphere is done by magnetohydrodynamic waves (see Section 3.2). Due to the decreasing density, and energy conservation, upward propagating magnetoacoustic waves can steepen into shock waves of high amplitude and force the already inhomogeneous chromosphere and layers above to oscillate in temperature (3000–10000 K), plasma pressure, and geometrical height (e.g., Carlsson and Stein 1997; Leenaarts et al. 2007). Therefore, line formation and radiative cooling are strongly nonlinear. A review of chromospheric properties and dynamics is given by B. Schmieder in Murdin (2001).

The transition region and corona: The transition layer between the chromosphere and corona is characterized by its steep increase in temperature (from 10^4 K to almost 10^6 K). Due its extreme inhomogenities it is appropriate to characterize it as a temperature layer, rather than as a geometrical layer(Stix 2002). The structures in the lower transition region are very similar to the chromospheric ones. Toward the corona, the spatial inhomogenities get less pronounced and the temperature increases

monotonically. The heating of the transition region and corona is still one of the biggest mysteries in solar physics, a non-radiative energy supply is required. Due to the extreme temperatures, the atoms of the gas plasma are highly ionized. Strong emission lines especially in the ultraviolet characterize the spectrum of the transition region and corona. As shown in the lower panel of Fig. 5.9, the corona features wide coronal loops especially above sunspots and active regions.

2.4. Sunspot oscillations: Traditional classification

The investigation of solar oscillations started with the detection of pressure waves in the overall photosphere (Leighton et al. 1962). As we know today, these acoustic p-modes propagate within the convection zone and photosphere. The most prominent wave modes have periods of 4–8 min and horizontal wavelengths of up to hundred Mm. In Helioseismology, the discrete mode pattern of wavenumbers and frequencies is used to obtain information about the interior of the Sun. When studying a local region in the lower photosphere, the periods of the characteristic p-modes peak at 5 min. The predominantly vertical oscillations have typical amplitudes of more than $0.5\,\mathrm{km\,s^{-1}}$ in Doppler velocity and a few percent in relative spectral intensity (Stix 2002).

Only few years after the detection of p-modes in the solar atmosphere, significant oscillations were measured also in the sunspot atmosphere (Beckers and Tallant 1969; Giovanelli 1972; Zirin and Stein 1972). Periodic fluctuations of Doppler shifts and intensities of spectral lines provide evidence for compressional waves in sunspots. The power and frequency of the oscillations depend on the part of the sunspot and the atmospheric layer. As shown in Fig. 2.6, the dominating peaks in the umbral power spectra shift from the 3.5 mHz ($\sim$ 5 min) range in the photosphere to the 6 mHz ($\sim$ 3 min) range in the chromosphere. Compared to the p-mode oscillations in the quiet sun, the magnetic field of sunspots damp the oscillatory amplitude in the photospheric umbra. Toward the chromosphere above the umbra, the wave power increases by more than a magnitude. In addition, the observation of sunspots at chromospheric spectral intensities reveals the visual appearance of fast propagating waves. Traditionally (Lites 1992), the wave phenomena in sunspots are classified as 1) five-minute oscillations in the sunspot photosphere, 2) three-minute oscillations and *umbral flashes* in the umbral chromosphere, and 3) *running penumbral waves* in the penumbral chromosphere.

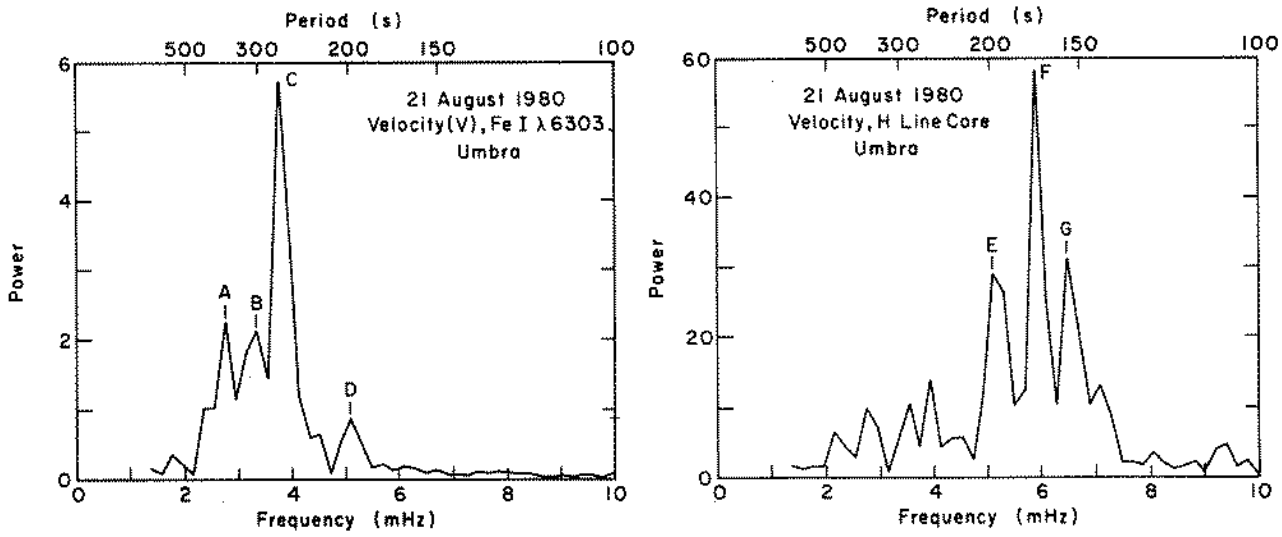

Figure 2.6.: Velocity power spectra in a sunspot umbra from the photospheric Fe I 630.25 nm line (left panel) and chromospheric Ca II H 396.85 nm line (right panel). The units of power are $10^3\,\mathrm{m^2\,s^{-2}\,mHz^{-1}}$. The maximum power in the chromospheric case is one order of magnitude larger than in the photospheric case. Image from Thomas et al. (1984).

The following outline is based on the reviews on observational aspects of sunspot oscillations by Bogdan (2000) and Bogdan and Judge (2006). In addition, the recent work in the field of research is included. The basic wave phenomena and propagation characteristics are discussed in Sections 2.4.1 – 2.4.3. Sunspot oscillations have been measured in a broad spectral range, from radio wavelength of a meter to hard X-rays at the picometer-scale. Here, the observational results of wave signals in absorption lines of the visible and near-infrared spectrum are detailed. Emphasis is put on the small-scale appearance of sunspot waves and the dominating periods in the sunspot atmosphere. In Section 2.5, the classification is revised and the modern sunspot wave scenario is discussed.

2.4.1. Five-minute oscillations

Various spectral lines of simple molecules (e.g., TiO) and non-ionized metals (e.g., Fe I, Si I, Ti I, Ni I, Mg I) have been applied to measure oscillations in the cool umbral photosphere.[2] The observation and analysis of their spectral intensities and Doppler shifts yielded the same basic results (e.g., Thomas et al. 1984; Abdelatif et al. 1986; Balthasar et al. 1987; Lites et al. 1998; Balthasar et al. 1998; Bellot Rubio et al. 2000). Like in the case of p-modes in the quiet sun, the umbral photosphere features a broad mixture of wave modes with dominating oscillations in the five-minute range. The left panel of Fig. 2.6 shows a power spectrum of velocity oscillations in the umbral photosphere as inferred from the Fe I 630.15 nm line core. Several individual peaks are centered at periods of around 300 s. The power peak at 197 s (D in the left panel, E in the right panel), as well as all other photospheric modes, have obvious counterparts in the chromospheric power spectrum (right panel). According to Thomas et al. (1984), this suggests a strong coherence between the oscillations in the umbral photosphere with the wave modes at higher layers. Comparing the dimensions of the photospheric net wave power in the 2–5 mHz range, the numbers have solely doubled toward the chromosphere. Because of the exponential decrease of the atmospheric density, the kinetic energy density of the five-minute waves is actually several magnitudes larger in the photosphere.

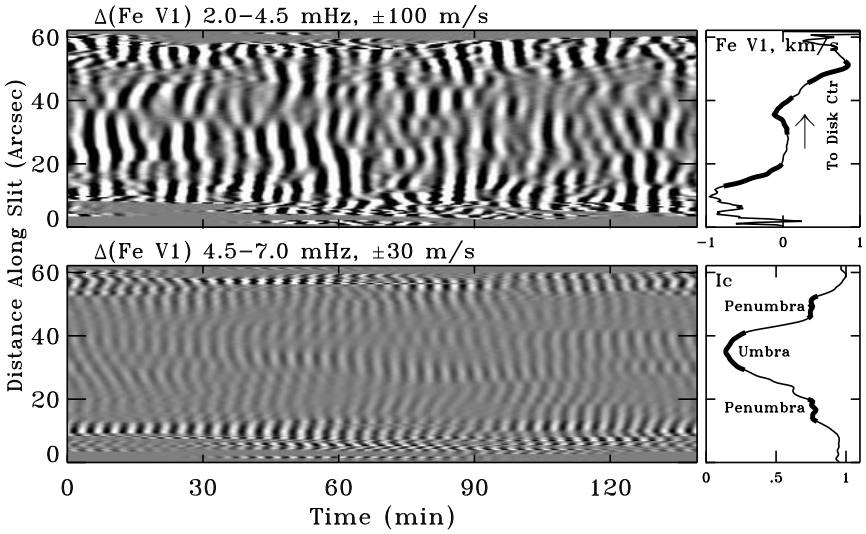

Figure 2.7.: Doppler velocity oscillations in the sunspot photosphere filtered for the 5-min (upper left) and 3-min (lower left) period range. A slit was centered at the sunspot. The velocities were obtained from the Fe I 630.15 nm line and plotted against time. The displayed values were scaled to $\pm 100\,\mathrm{m\,s^{-1}}$ and $\pm 30\,\mathrm{m\,s^{-1}}$. The time-averaged continuum intensity and Doppler velocity are shown in the lower and upper right panels. Image from Lites et al. (1998).

[2] A selection criterion for the investigation of sunspot oscillations with weak photospheric lines is given in Section 4.2.1.

In Fig. 2.7, the temporal diagrams show the evolution of the photospheric Doppler velocities along a slit centered in a sunspot (Lites et al. 1998). In the upper panel, the velocity oscillations were filtered in the 2.0–4.5 mHz (4–8 min) range. The time-series emphasizes the dominating five-minute oscillations. In general, the five-minute oscillations are largely coherent in the sunspot umbra and often also in a considerable part of the penumbra (Kobanov 1990). The velocity amplitudes typically reach values up to $\pm 100\,\mathrm{m\,s^{-1}}$ and more. However, compared to the amplitudes of the p-modes in the surrounding of the sunspot, the oscillatory velocity in the umbral photosphere is reduced at least by a factor of two or three (e.g., Abdelatif et al. 1986; Balthasar et al. 1998). In the penumbra, the suppression of five-minute wave power is more modest. All in all, this damping of the velocity power in the sunspot region makes the main distinction of five-minute waves in the sunspot region and the p-modes in the quiet sun. But even more important than their distinction is the connection between p-modes and sunspot waves. Observational evidence was given that propagating p-modes in the active region photosphere can cross the entire sunspot region (e.g., Kobanov and Makarchik 2004). When the inward and outward traveling p-mode waves in a sunspot are separated (Braun et al. 1987), it is evident that sunspots indeed absorb up to half of the incoming power of wave power. As proposed by Thomas (1981), it seems natural that the five-minute oscillations in the sunspot photosphere could be forced by the p-mode oscillations in the surrounding convection zone. Moreover, the absorbed acoustic wave power in sunspots is proposed for mode conversion into upward propagating magnetohydrodynamic waves (Bogdan 2000). The MHD waves (Section 3.2) and their possible driving mechanisms in sunspots are discussed in more detail in Section 6.1.

2.4.2. Three-minute oscillations and umbral flashes

Three-minute oscillations in the umbral atmosphere are already present in the photosphere. Yet, as shown in the lower panel of Fig. 2.7, the oscillations in Doppler velocity in the frequency range of 5–7 mHz are hard to the detect. With velocity amplitudes below $\pm 30\,\mathrm{m\,s^{-1}}$, the photospheric three-minute oscillations are overpowered by the sunspot's five-minute oscillations. This is also reflected in the power spectrum shown in the left panel of Fig. 2.6. Sunspot pores yield the same photospheric three-minute oscillations (Centeno et al. 2009; Stangalini et al. 2012).

Toward the umbral chromosphere, the situation alters dramatically. The upward propagating waves in the three-minute range start to dominate the wave power in sunspot umbra (Lites 1984). As shown in the right panel of Fig. 2.6, the wave modes in the 5–7 mHz frequency range (2.4–3.3 min) increase in velocity power by two orders of magnitude compared to the low photospheric case (e.g., Thomas et al. 1984). Especially oscillations with periods at around 2.8 min govern the chromospheric umbra. The average velocity amplitudes reach values of around $\pm 1\,\mathrm{km\,s^{-1}}$. The power peak (D/E) at 5.2 mHz is assigned to the acoustic cut-off frequency (Eq. 3.32). Due to exponentially decreasing plasma density with increasing altitude, the kinetic energy density of the photospheric three-minute oscillations is in fact above the chromospheric level.

The studies on umbral three-minute oscillation mainly focus on the chromosphere and upper photosphere where the waves dominate. Numerous observations were performed with spectral absorption lines which cover these layers. Bogdan (2000) gives a list of the applied spectral lines. As the chromospheric oscillations are very present in the cores of strong resonance lines, the most used spectral lines are Hα, Hβ, Ca II H and K, the Ca II infrared triplet, and transition in He I and Mg I. Some of these lines are applied in this work and described in Section 4.2.1.

Toward the transition region and lowest base of the corona, the velocity amplitudes and intensity fluctuations of the three-minute oscillations even increase, but with less concentration. In addition, the vertical phase speed increases (e.g., O'Shea et al. 2002; Kobanov et al. 2013b; Tian et al. 2014; Sych and Nakariakov 2014; Freij et al. 2014). In the hot corona with temperatures above 10^6 K, the intensity oscillations seem to vanish. The three-minute oscillations allover the umbral atmosphere exhibit a high degree of spatial and temporal coherence. The area of wave coherency covers large parts of the umbra (Abdelatif et al. 1986). From the lowest photosphere to the chromosphere (and transition

region up to the base of the corona), the phase shifts of the recorded signals increase as a function of height (e.g., Centeno et al. 2006; Tziotziou et al. 2007; Felipe et al. 2010b; Reznikova and Shibasaki 2012). It is strongly suggested that coherent wave packets propagate vertically upward with velocities of the order of the local sound speed ($6 - 15\,\mathrm{km\,s^{-1}}$). They can leak into the transition region and corona (Brynildsen et al. 1999; De Moortel et al. 2002; Marsh and Walsh 2006; Tian et al. 2014). As discussed in the following paragraphs, the linear upward propagating waves steepen in amplitude when the atmospheric density drops, and eventually form magnetoacoustic shock fronts in the chromosphere and transition region (Kneer et al. 1981; Maltby et al. 1999; Centeno et al. 2006).

Umbral flashes

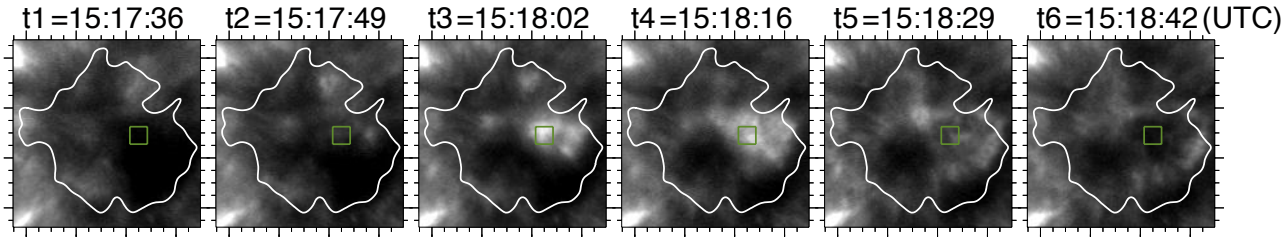

Figure 2.8.: Appearance of a bright umbral flash in the sunspot chromosphere. The umbra area (white contour) of the spot (NOAA11823 in Section 4.3.1 and Fig. 2.3) in line core intensity of Ca II 854.21 nm is shown for six sequential time steps.

Umbral flashes are bright upward propagating shock waves which are most prominent in the umbral chromosphere. They were the first wave phenomenon detected in the sunspot atmosphere. Beckers and Tallant (1969) measured them as bright emissions in the chromospheric blue emission cores (K2v, see Section 4.2) of the Fraunhofer Ca II K and H lines. In Fig. 2.8, an umbral flash appears in the line core intensity of Ca II 854.21 nm. The barycenter of the shock front is located at the position of the green square within the umbral area which is contoured in white. At time step $t1$, the chromospheric umbra is at rest. In the next step after around 13 s, the first signatures of the shock front arrive at the spectral formation layer. At time step $t3$, the maximum emission of the umbral flash sets in and distributes radially toward the umbral boundary in the following three steps. As already described by Beckers and Tallant (1969) and confirmed by numerous subsequent studied (e.g., Tziotziou et al. 2002; Rouppe van der Voort et al. 2003; Centeno et al. 2009; de la Cruz Rodríguez et al. 2013; Madsen et al. 2015), the spectral signal of umbral flashes in the middle chromosphere is characterized by

- a periodical appearance of around 150 s, or 2.5 min,
- a non-sinusoidal light curve with a faster increase than decrease in intensity,
- an apparent horizontal motion of the wave with around $40\,\mathrm{km\,s^{-1}}$ toward the penumbra,
- a periodical Doppler shift of up to $\pm 6\,\mathrm{km\,s^{-1}}$,
- a spectral blue-shift after the flash and a red-shift just before the next flash.

In a spatio-temporal diagram of chromospheric intensity or velocity, like, e.g., Fig. 2.9 from Rouppe van der Voort et al. (2003), umbral flashes arise in the central umbra as a characteristic pattern of 'nested bowls'. They have a spatial extent and coherence of several arc-seconds. Their shape hint at a rapid spatial spreading. Often, it is followed by a fast quasi-circular expansion toward the umbral boundary and beyond. From the space-time analysis, the inferred horizontal velocities decrease from $20 - 50\,\mathrm{km\,s^{-1}}$ close to the center of the initiation point, down to $10 - 20\,\mathrm{km\,s^{-1}}$ in the outer umbra. Some of the bowls extend as running penumbral waves (Section 2.4.3) into the penumbra. There, the herringbone pattern reveals much slower apparent propagation speeds of $4 - 7\,\mathrm{km\,s^{-1}}$.

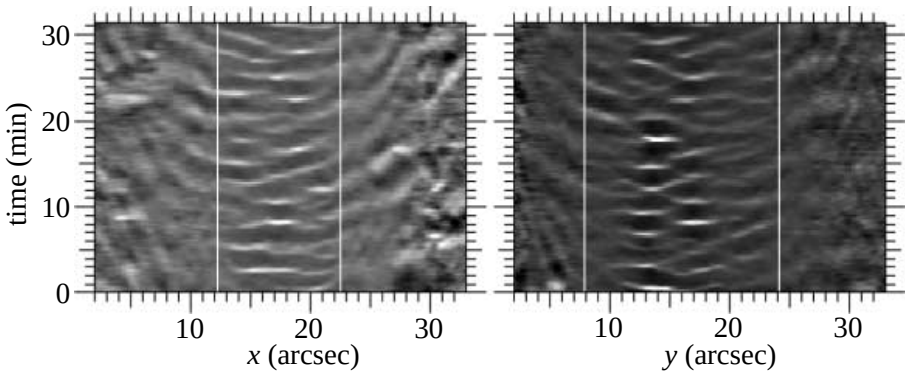

Figure 2.9.: Umbral flash appearance in a spatio-temporal diagram of chromospheric brightness in a sunspot. The variations in spectral intensities of the line core of Ca II H are shown for a horizontal (left panel) and vertical (right panel) cut through the sunspot. A five-minute running mean was subtracted for each pixel. The vertical lines mark the umbra boundary. Image from Rouppe van der Voort et al. (2003).

When the umbral chromosphere is observed in spectral core intensity of strong Ca II lines, like the Ca II K line at 393.3 nm or the near-infrared line at 854.21 nm, the Stokes signals reveal the powerful dynamics of umbral flashes. In the left panels of Fig. 2.10, the spectral intensity (Stokes I) and circular polarization signal (Stokes V) are shown as $\lambda - t$ diagrams for one position in the shocked umbra. The temporal series in intensity exhibits bright emission peaks in the blue core of the line (e.g., Socas-Navarro et al. 2000; Rouppe van der Voort et al. 2003; de la Cruz Rodríguez et al. 2013). The pattern for umbral flashes is identical to the one for bright grains measured in the blue emission peak of the Ca H and K lines in the quiet sun chromosphere (Carlsson and Stein 1992, 1997). The rapid brightening of umbral flashes and the spectral blue-shift is attributed to a fast compressible motion in form of an upward propagating acoustic shock (Bard and Carlsson 2010). Due to the nonlinear steepening and

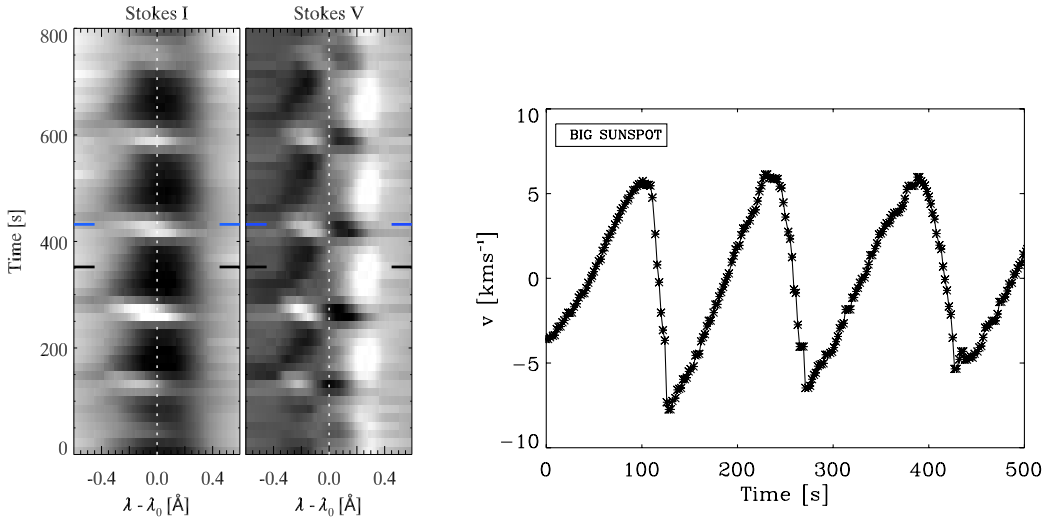

Figure 2.10.: Spectral appearance of umbral flashes. Left two panels: The temporal variations in line core intensity of Ca II 854.21 nm (left) and Stokes V signal (right) are plotted against wavelength. Image from de la Cruz Rodríguez et al. (2013). Right panel: The temporal evolution of chromospheric Doppler velocities (in $\mathrm{km\,s^{-1}}$) during the passage of umbral flashes exhibits the characteristic saw-tooth shape of acoustic shock waves. Image from Centeno et al. (2009).

strong compression of the plasma during the passage of the shock front, the temperature experiences a steep increase of up to 1500 K (de la Cruz Rodríguez et al. 2013; Felipe et al. 2014). An additional attribute of the acoustic shock wave behavior of umbral flashes is represented by the coupling to strong line-of-sight velocity oscillations. As shown in the right panel of Fig. 2.10, the temporal evolution of the velocity profile resembles a saw-tooth shape (e.g., Centeno et al. 2006; Tian et al. 2014). The sudden spectral blue-shift (negative line-of-sight velocities) is followed by a slower shift toward the red (positive velocities). The oscillatory amplitude of Doppler velocities reaches up to $\pm 6\,\mathrm{km\,s^{-1}}$. In smaller sunspot umbrae with less magnetic field strength, the shock wave pattern of umbral flashes is less pronounced. In pores, the chromospheric velocity oscillations exhibit a sinusoidal curve (Centeno et al. 2009). Another surprising characteristic of umbral flashes is found in the temporal evolution of the circular polarization. In the left panels of Fig. 2.10, the co-temporal Stokes V signals in the line core of Ca II 854.21 nm is shown in addition to the intensity signal of the umbral flashes. The Stokes V polarization signal, from which the line-of-sight magnetic field strength can be inferred, switches its polarity during the passage of umbral flashes (Socas-Navarro et al. 2000; de la Cruz Rodríguez et al. 2013; Rouppe van der Voort and de la Cruz Rodríguez 2013). Socas-Navarro et al. (2000) proposed that this anomaly is not caused by a change in the field polarity but is the result of a differential velocity along the line-of-sight. The authors suggest a two-component scenario with opposite velocities in one resolution element. In addition to the resolved component, a second unresolved component with opposite direction is superposed (Centeno et al. 2005). It can also be argued that the sign of the Stokes V signal is simply caused by the change from absorption to emission in the core of the chromospheric line. It is further suggested that the strongly compressive wave changes the opacity of the plasma and could therefore lead to fluctuation in the chromospheric magnetic field signal. Besides the low sensitivity of chromospheric spectral lines to magnetic fields, the misleading fluctuations in the Stokes signals make it difficult to measure the full vector magnetic field in the sunspot chromosphere.

Recently, the observation of chromospheric oscillations at high spatial resolution identified small-scale fluctuations in the sunspot umbra (Socas-Navarro et al. 2009; Rouppe van der Voort and de la Cruz Rodríguez 2013; Bharti et al. 2013; Yurchyshyn et al. 2014). The umbral micro-jets display a filamentary structure at the sub-arc-second scale and feature the same periodicity as umbral flashes (see Section 2.2). The excitation and possible driving mechanisms of umbral flashes are discussed in Section 6.1. The observational results of this study on umbral flashes are described in Section 6.3.

2.4.3. Running penumbral waves

The dynamics in the chromospheric penumbra are dominated by running penumbral waves. In spectral intensity of a chromospheric line, they appear as bright coherent quasi-circular bands which propagate radially outward across the sunspot penumbra. The running penumbral waves and their periodical oscillations were discovered shortly after the detection of umbral flashes. While Zirin and Stein (1972) observed them allover the penumbra in spectral intensity of Hα, Giovanelli (1972) measured the oscillating Doppler velocities coupled to the wave propagation. Since then, numerous observational and theoretical studies have been performed to determine their nature and properties (e.g. Nye and Thomas 1974; Lites et al. 1982; Alissandrakis et al. 1992; Marco et al. 1996; Tsiropoula et al. 1996; Sigwarth and Mattig 1997; Kobanov 2000; Georgakilas et al. 2000; Christopoulou et al. 2000, 2001; Rouppe van der Voort et al. 2003; Kobanov et al. 2006; Tziotziou et al. 2006, 2007; Bloomfield et al. 2007a; Rouppe van der Voort and de la Cruz Rodríguez 2013; Sobotka et al. 2013; Jess et al. 2013; Yuan et al. 2014a; Madsen et al. 2015; Löhner-Böttcher and Bello González 2015).

Most observational studies on running penumbral waves focus on the spectroscopic signals and wave properties at chromospheric and upper photospheric layers. In the lower and middle chromosphere, the appearance and propagation of running penumbral waves is most prominent. Therefore, the waves are predominantly observed in the line core and wings of Hα, Ca H and K, and the Ca II lines in the near-infrared. At sampled atmospheric altitudes of around 1000 km, the waves appear as circular bands at the umbral boundary and seem to be excited by the bright flashes inside the umbra. Visually,

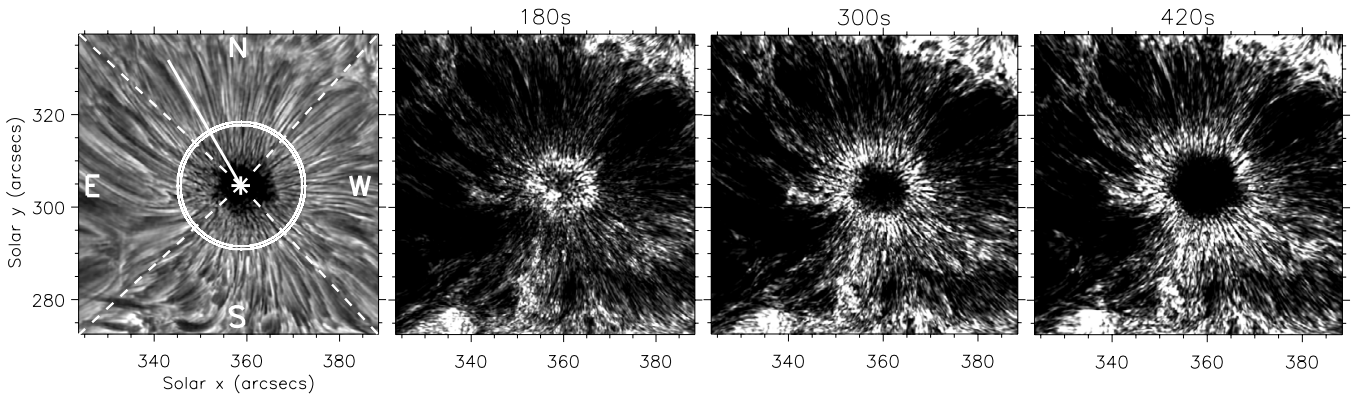

Figure 2.11.: Characteristic wave power distribution in the sunspot chromosphere. In the left panel, the sunspot is shown in Hα line core intensity. The power distribution in the filtered period ranges around 3 min, 5 min, and 7 min (second left to right panel) features the ring-like period increase of running penumbral waves, with high power in bright color. Images from Jess et al. (2013).

they propagate as relative intensity fluctuations of the order of $10-20\%$ from the inner to the outer penumbra. The intensity signal decays smoothly with radial distance. The horizontal wavelength at the inner penumbra range from $3''$ to $5''$. For a spot close to disk center, the measured Doppler velocities reach up to $\pm 1\,\mathrm{km\,s^{-1}}$. The spatial coherence of the wavefronts is large and amounts to a considerable fraction of sunspot's total circumference. At the inner penumbra, the circular wave pattern yields an apparent horizontal velocity of typically around $10-20\,\mathrm{km\,s^{-1}}$. At the umbral boundary, wave speeds of sometimes up to $40\,\mathrm{km\,s^{-1}}$ are reported (e.g., Kobanov and Makarchik 2004). With increasing radial distance, the apparent phase speed decreases steadily and saturates at $5-7\,\mathrm{km\,s^{-1}}$ at the outer penumbral boundary. In addition to the changing horizontal velocities, the dominating wave frequencies (or peak periods) shift conspicuously with radially increasing distance from the umbra. Whereas the oscillatory periods peak at around 3 min in the outer umbra and at 4 min in the inner penumbra, the dominating wave period increases systematically to above 10 min in the outer penumbra and beyond. The case is illustrated in Fig. 2.12 by the scaled power spectra as a function of radial

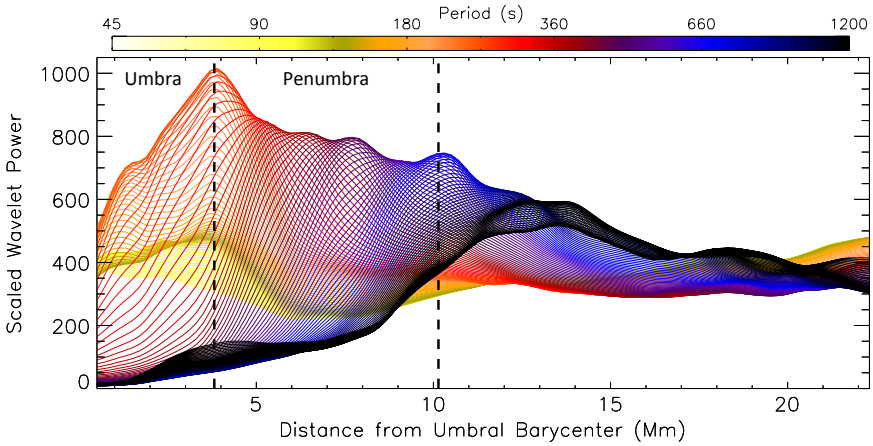

Figure 2.12.: Distribution of wave periods in a sunspot. The azimuthally averaged and scaled wavelet power at periods from 45 s (bright yellow) to 1200 s (dark blue) are plotted as a function of radial distance from the umbral barycenter. The sunspot boundaries are indicated by the vertical dashed lines. Image from Jess et al. (2013).

distance from the chromospheric umbral barycenter. When the oscillatory time series is filtered within a narrow period bandpass at each position of the sunspot region, the wave power shows a typical ring-shaped distribution. As displayed in Fig. 2.11, the radius of the filamentary power rings increases for longer wave periods (e.g., Jess et al. 2013).

At chromospheric height, running penumbral waves propagate along the superpenumbral filaments and can reach distances of 15″ outside the sunspot's white light boundary (Kobanov 2000). Towards photospheric layers, the spectral signal of the running penumbral waves decreases. In the upper photosphere, the signal is immediately overpowered by solar p-mode oscillation at the outer penumbra. In addition, the strong Evershed flow at the outer penumbral edge gives the impression of merging with the waves. Only few attempts have been made to determine a lower photospheric signature of the wave phenomenon (e.g., Marco et al. 1996; Lites et al. 1998; Bloomfield et al. 2007a; Zhao et al. 2015). The detection is difficult since the Doppler velocity oscillation is expected to be low. Moreover, strong p-modes can propagate across the sunspot and reduce the significance of a signal from the weaker running penumbral waves.

In recent studies (Sobotka et al. 2013; Freij et al. 2014), running penumbral waves were also measured in the chromospheric fibrils of pores, which lack a penumbra in the photosphere. They have therefore been classified more generally as 'sunspot running waves' or 'upwardly propagating waves'.

2.5. Modern sunspot wave scenario

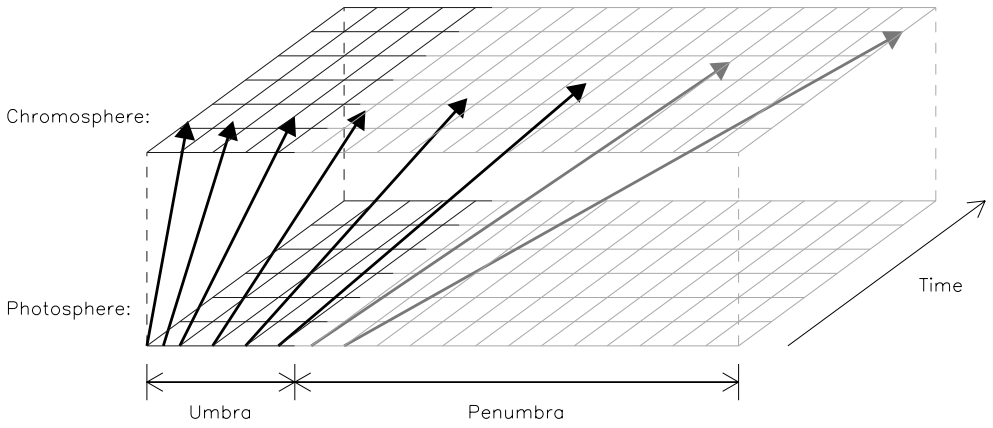

Figure 2.13.: Schematic space-time diagram of sunspot waves. The magnetoacoustic waves (arrows) propagated upward from the photosphere to the chromosphere along the inclined magnetic field lines. The path length to the chromospheric sampling height increases for the more inclined waveguides which delays the arrival time of the wave front. Image adapted from Bloomfield et al. (2007a).

Evidence has been provided that umbral waves and flashes propagate upward along the vertical magnetic field of the sunspot's umbra (see Section 2.4.2). According to their propagation characteristics they are identified as slow-mode magnetoacoustic waves (see Section 3.2.2) in the low-β regime (see Section 3.3) of the umbral field. By the upward decreasing gas density, the umbral waves can form quasi-acoustic shock fronts. From the visual appearance at chromospheric altitudes, a connection of the umbral disturbances and running penumbral waves (see Section 2.4.2) seems to be obvious (Lites et al. 1982). The link between umbral flashes and running penumbral waves is still under discussion. However, from the observational studies, three main scenarios of wave propagation have been developed to describe the apparent propagation and characteristics of running penumbral waves:

1. **Chromospheric trans-sunspot propagation**: The pure visual appearance in chromospheric intensity suggests that running penumbral waves could be excited by umbral flashes. Originating

at the barycenter of the umbral flash, chromospheric trans-sunspot waves propagate horizontally outward across the penumbra. The compressive waves spread across the magnetic field lines of the sunspot. The fast apparent phase speeds approaching the Alfvén velocity are regarded as real. Therefore, the compressive disturbances are interpreted as propagating fast-mode magnetoacoustic waves (see Section 3.2.2) in the low-β regime of the sunspot.

2. **Upward propagating fast magnetoacoustic waves**: In this scenario, running penumbral waves are identified with gravity-modified fast-mode magnetoacoustic waves (see Section 3.2.2 which are vertically trapped at photospheric levels (Nye and Thomas 1974). The basically photospheric waves share the same driving source as umbral flashes which is located in the sub-photospheric umbra. The wave energy of the penumbral fast-modes is centered in the photosphere and below. However, the photospheric signal is assumed too small to be measured. At chromospheric levels where the waves become evanescent, the signal has increased to its maximum values and can therefore be observed.

3. **Visual pattern of upward propagation slow magnetoacoustic waves**: In agreement with the previous scenario, umbral flashes and running penumbral waves are proposed to be generated by the same sub-photospheric driving source within the umbra (Moore 1973). Both sunspot wave phenomena are interpreted as slow-mode magnetoacoustic waves which propagate upward into the chromosphere and higher layers. In the low-β environment of the sunspot, the upward propagating slow-mode waves are guided and influenced by the magnetic field lines (see Section 3.2.2). The isotropic quasi-acoustic waves propagate with phase velocities close to the ambient sound speed. Visually, running penumbral waves spread radially outward across the penumbra and seem to be excited after the appearance of umbral flashes. This visual pattern can be explained by the inclination of the sunspot's magnetic field. As discussed in Section 2.2, the magnetic field lines of the central umbra are oriented predominantly vertical. From the inner to the outer penumbra, the zenith angle of the magnetic field increases significantly. Therefore, a coherent wave front which propagates along the magnetic field lines reaches a chromospheric response layer first in the vertically oriented umbra (Rouppe van der Voort et al. 2003). Due to the increasing path length, the travel time of the wave increases with radial distance from the umbra (Bloomfield et al. 2007a). This wave scenario is illustrated in Fig. 2.13. In addition, the increasing zenith angles and wave paths explain also the fast super-sonic horizontal wave speeds in the umbra and inner penumbra (Madsen et al. 2015). Moreover, the apparent motion in the slow-mode scenario can explain the strong decrease of horizontal phase speeds of running penumbral waves toward the outer penumbra and higher layers. The outstanding shift in wave period from 3 min in the umbra to 10 min in the outer penumbra is accounted for the modified acoustic cut-off (Section 3.4). In the vertical magnetic field of the umbra, only waves with periods below the effective cut-off period of around 3 min can propagate unhindered into the chromosphere and transition region. The increasing zenith angles of the penumbral magnetic field shifts the acoustic cut-off to longer periods (Bel and Leroy 1977). This permits the initially evanescent wave with longer periods to propagate along the magnetic waveguides into the higher atmosphere. As the longer-period waves overpower the three-minute oscillations, the power spectra and its peak periods are affected (Jess et al. 2013).

In the last decades, numerous observational investigations have taken a straightforward path to provide evidence for the latter field-guided slow-mode wave scenario, or called the *modern sunspot wave scenario* (e.g., Christopoulou et al. 2000, 2001; Rouppe van der Voort et al. 2003; Centeno et al. 2006; Kobanov et al. 2006; Tziotziou et al. 2007; Bloomfield et al. 2007a; de la Cruz Rodríguez et al. 2013; Jess et al. 2013; Madsen et al. 2015). On the other hand, the theory has described more of an 'intellectual random walk' (Bogdan and Judge 2006). To recapitulate, the most prominent sunspot oscillations which were classified in Section 2.4 are merely different manifestations of the same wave phenomenon. Since running penumbral waves are guided by magnetic field lines, Bloomfield et al.

(2007a) suggested that the waves should also be detectable at big pores with sufficiently inclined field lines. And indeed, high-resolution observations displayed the running waves in the chromospheric fibrils above pores (Sobotka et al. 2013; Freij et al. 2014). The nature of running penumbral waves and umbral flashes seems to be revealed. But still, there are some missing pieces of this jigsaw puzzle. As always in nature, one single-case scenario will not be able to describe the overall picture. Mode conversion and mixture of fast and slow magnetoacoustic waves are certainly abundant in the sunspot atmosphere (Khomenko and Collados 2009). Further details on sunspot waves and the modern wave scenario will be given in Section 6.

Leading questions:

After five decades of investigations of sunspot oscillations, there is profound knowledge about the present wave phenomena. But still, there are a number of open questions which are important for the overall understanding of the sunspot dynamics. Modern high-resolution observations shall clarify the character and properties of the waves in sunspots and provide evidence or disprove the current theoretical models. Some of the most important questions are:

- How are umbral flashes and running penumbral waves related to each other?
- Can the scenario of upward propagating field-guided slow-mode magnetoacoustic waves be verified for all sunspot waves?
- How do the wave characteristics in the umbra and penumbra differ and how do they change for the atmospheric layers?
- How deep down in the sunspot photosphere can one find spectral signatures of umbral flashes and running penumbral waves?
- As the magnetic field inclination influences the acoustic cut-off in the solar atmosphere, can the magnetic field topology of sunspots be reconstructed from the wave characteristics?
- How far can sunspot waves propagate and what are the wave characteristic in the transition region and corona?
- How do umbral flashes manifest in different spectral lines?
- How does the plasma behave during the passage of the shock front of an umbral flash?
- Do umbral flashes exhibit a sonic boom like in the case of acoustic shock waves?
- Do sunspot pores without a penumbra feature running penumbral waves, too?
- What is the fine-scale structure of sunspot waves?
- What is the physical driving mechanism of sunspot waves? Is the absorbed energy from p-mode oscillations converted into magnetohydrodynamic waves or are the waves excited by magnetic field oscillations? And how deep down in the atmosphere or convection zone is the wave source located?
- How do sunspot waves contribute to the chromospheric heating?
- What is the role of umbral flashes with regard to the super-sonic down-flows observed in the transition region above umbrae?
- How strong is the interaction between sunspot waves and strong plasma flows, e.g., with the Evershed and inverse Evershed effect in the photospheric and chromospheric penumbra.

- Do the plasma dynamics and wave properties change during the evolution of sunspots? What happens during the decay of sunspots?
- Is there a long-term evolution of sunspot waves, e.g., a dependence on the sunspot cycle?
- Can a broad statistical study of sunspot waves reveal significant relations with further sunspot characteristics like spot size or magnetic flux?
- Beyond, do starspots feature similar wave phenomena in the stellar atmosphere?
- What can we learn from the magnetoacoustic waves in sunspots with regard to other plasma experiments or atomic fusion reactors?

In this work only some of these questions can be addressed, of course. But with the high-resolution spectroscopic observations (Chapter 4) and state-of-the-art analysis techniques (Chapter 5), several answers and suggestions will be given in Chapters 6 and 7.

3. Wave theory

"Any physical theory is always provisional, in the sense that it is only a hypothesis: you can never prove it. Each time new experiments are observed to agree with the predictions the theory survives, and our confidence in it is increased; but if ever a new observation is found to disagree, we have to abandon or modify the theory."

— Stephen Hawking, *A Brief History of Time*

In nature, waves are the prime mechanism to transfer information and energy over a long distance. The variety of the overall wave spectrum allows the communication through all kinds of mediums. Electromagnetic waves propagate through gas, liquids, solids, plasma and naturally vacuum.[1] Besides these transversal waves, longitudinal acoustic waves can propagate with sound speed through a medium in the form of compressions and rarefactions. Further kinds of hydrodynamic wave components are introduced by magnetism. These magnetohydrodynamic (MHD) waves depend on the magnetic field properties of the medium. All of the mentioned waves are present in the Sun and its atmosphere. As the sunspot's atmosphere is covered by magnetic fields, MHD waves may play a crucial role in the transport of energy and heating of the chromosphere and corona. In this chapter, the basic fundamentals of magnetohydrodynamic wave theory are introduced.

3.1. Basic magnetohydrodynamics

Magnetohydrodynamics (MHD) is the theory of fluid dynamics in the presence of magnetic fields. When the temperature of a gas is raised so that the ionization of the atoms increases, positive ions and negative electrons can move around freely. The gas becomes electrically conducting and a current can form. The dynamics of the plasma is then intimately coupled to the present magnetic field and vice versa. Therefore, the magnetohydrodynamic theory is essentially based on the theories of fluid mechanics and electromagnetism. The MHD approximation reduces an electrically neutral plasma to its macroscopic processes in order to describe the local thermodynamic quantities. By that, the electrically conducting plasma is described as a continuous fluid. As discussed by Priest and Forbes (2000), the assumption of a continuous medium holds for length scales larger than the mean-free path of particle collisions in the plasma. For the solar chromosphere this is typically above 3 cm, in the corona around 30 km. Especially in the lower solar atmosphere, this is way below the resolution limit of solar telescopes.

In the strong magnetic field of sunspots, the interactions between the plasma and magnetic field become especially important. Strong flows are driven, magnetoacoustic waves are excited (see Section 3.2). To outline the basic equations of ideal MHD processes for a perfectly conducting fluid, I refer to the introductions to magnetohydrodynamics by Spruit (2013) and Priest and Forbes (2000). As described in the following paragraphs, MHD theory is a reduced combination of the equations of slow electromagnetism and the hydrodynamics of fluids.

[1] The electromagnetic spectrum exhibits a wealth of different wave energies and frequencies, from the ionizing radiation (γ-rays, X-rays and UV) over the visible light and infrared to the long micro and radio waves.

Like in the case of electromagnetism, the electric field $\boldsymbol{E}$, magnetic field $\boldsymbol{B}$, and velocity $\boldsymbol{v}$ of the plasma are intimately linked by

$$\boldsymbol{E} = -\boldsymbol{v} \times \boldsymbol{B}/c \tag{3.1}$$

when the fluid motion in ideal MHD is measured by an observer at rest. In most astrophysical applications, the magnetic permeability μ and permittivity ε of the plasma are ignored. This valid assumption allows to abandon the distinction between magnetic field strength and magnetic induction ($\boldsymbol{B} = \mu\boldsymbol{H}$), and between electric field strength and electric displacement ($\boldsymbol{D} = \varepsilon\boldsymbol{E}$). The phenomena of electromagnetism are then described by the Maxwell's equations in the form of

$$\begin{aligned} 4\pi\boldsymbol{j} + \partial\boldsymbol{E}/\partial t &= c\boldsymbol{\nabla} \times \boldsymbol{B} && (3.2)\\ \partial\boldsymbol{B}/\partial t &= -c\boldsymbol{\nabla} \times \boldsymbol{E} && (3.3)\\ \boldsymbol{\nabla} \cdot \boldsymbol{B} &= 0 && (3.4)\\ \boldsymbol{\nabla} \cdot \boldsymbol{E} &= 4\pi\sigma\,, && (3.5) \end{aligned}$$

with the electrical current density $\boldsymbol{j}$, the charge density σ, the speed of light c, and nabla operator $\boldsymbol{\nabla} = (\frac{\partial}{\partial x_1}, \ldots, \frac{\partial}{\partial x_\mathrm{n}})$. The first law states that electric currents and changes of the electric field are coupled to the circulating magnetic field of an area. The divergence of this equation yields the conservation of charge:

$$\partial\sigma/\partial t + \boldsymbol{\nabla} \cdot \boldsymbol{j} = 0\,. \tag{3.6}$$

The second law, the induction equation, demonstrates that a changing magnetic field induces a closed circuit in an electric field. Replacing the electric field by Eq. 3.1, returns the *induction equation of ideal MHD*:

$$\frac{\partial \boldsymbol{B}}{\partial t} = \boldsymbol{\nabla} \times (\boldsymbol{v} \times \boldsymbol{B})\,. \tag{3.7}$$

It is important to notice, that the equation now describes the direct evolution of a magnetic field when it is embedded in a perfectly conducting fluid with velocity $\boldsymbol{v}$. The divergence of the induction equation is $\frac{\partial}{\partial t}\boldsymbol{\nabla} \cdot \boldsymbol{B} = 0$. It incorporates the condition $\boldsymbol{\nabla} \cdot \boldsymbol{B} = 0$, the third of Maxwell's laws (Eq. 3.4). The zero divergence of the magnetic field reveals the nonexistence of magnetic monopoles. The magnetic field lines have no end so that the total magnetic flux of a closed areal element is zero. Therefore, the magnetic field strength cannot change only locally but rather involves global changes in the field shape and strength. The fourth law (Eq. 3.4) describes the proportionality of a diverging electric field of a volume with its charge inside.

The electrical current in a non-relativistic ($v \ll c$) regime can be obtained by substituting Eq. 3.1 into Eq. 3.2. The second term on the left hand side of

$$4\pi\boldsymbol{j} - \frac{\partial}{\partial t}(\boldsymbol{v} \times \boldsymbol{B})/c = c\boldsymbol{\nabla} \times \boldsymbol{B} \tag{3.8}$$

is the displacement current which approaches zero for non-relativistic velocities $\boldsymbol{v}$. Accordingly, the electric current reduces to

$$\boldsymbol{j} = \frac{c}{4\pi}\boldsymbol{\nabla} \times \boldsymbol{B}\,. \tag{3.9}$$

Within this approximation, the divergence of the electric current, $\boldsymbol{\nabla} \cdot \boldsymbol{j} = 0$, implies a conservation of charge density $\partial\sigma/\partial t = 0$ (see Eq. 3.6).

The Lorentz force describes the effect of a magnetic field $\boldsymbol{B}$ on a conducting plasma carrying an electrical current $\boldsymbol{j}$. In an electrically neutral unit volume, the acting Lorentz force $\boldsymbol{F}_\mathrm{L}$ with the approximated current density (Eq. 3.9) becomes

$$\boldsymbol{F}_\mathrm{L} = \frac{1}{c}\boldsymbol{j} \times \boldsymbol{B} = \frac{1}{4\pi}(\boldsymbol{\nabla} \times \boldsymbol{B}) \times \boldsymbol{B}\,. \tag{3.10}$$

To go one step further, the force can be written as a sum of the magnetic pressure gradient, $-\frac{1}{8\pi}\boldsymbol{\nabla}B^2$, and the magnetic curvature force, $\frac{1}{4\pi}(\boldsymbol{B}\cdot\boldsymbol{\nabla})\boldsymbol{B}$.

In MHD, the Lorentz force is of supreme importance because it describes the force of the magnetic field acting on the fluid. It therefore couples the equations of electromagnetism and fluid mechanics. While viscosity is often ignored in ideal MHD, the equation of motion for the plasma adds up to

$$\rho\frac{\mathrm{d}\boldsymbol{v}}{\mathrm{d}t} = -\boldsymbol{\nabla}p + \frac{1}{4\pi}(\boldsymbol{\nabla}\times\boldsymbol{B})\times\boldsymbol{B} + \rho\boldsymbol{g}\,, \tag{3.11}$$

with the gradient in gas pressure p, the Lorentz force $\boldsymbol{F}_\mathrm{L}$, and the gravitational force $\boldsymbol{F}_\mathrm{g} = \rho\boldsymbol{g} = -\rho\boldsymbol{\nabla}\varphi$. In this, g is the gravitational acceleration, φ the gravitational potential, and ρ the density in the unit volume. The total derivative of the motion is described by $\mathrm{d}/\mathrm{d}t$. Note that the plasma motion is invariant under a changed sign of the magnetic field. As the Lorentz force is perpendicular to the magnetic field, only the fluid motion along the magnetic field is purely hydrodynamical.

Further equations of fluid dynamics in MHD are the equation of mass continuity

$$\frac{\partial\rho}{\partial t} + \boldsymbol{\nabla}\cdot(\rho\boldsymbol{v}) = 0 \quad \text{or} \quad \frac{\mathrm{d}\rho}{\mathrm{d}t} + \rho\boldsymbol{\nabla}\cdot\boldsymbol{v} = 0 \tag{3.12}$$

which expresses that no plasma is created or destroyed, and the chosen perfect gas law

$$p = R\,\rho\,\vartheta_\mathrm{K} \tag{3.13}$$

with the plasma pressure p, plasma density ρ, temperature ϑ_K, and gas constant R. In case of a diverging flow of plasma from the unit volume in Eq. 3.12, the density decreases and the gradient gets negative. Together with the conservation of energy, the given equations are used to determine the density, pressure and temperature of the plasma.

The key statement of this section is that in MHD the processes and motions of the conducting plasma and magnetic field are strongly coupled. The appearance and dynamics of the solar atmosphere can be approximated by the above equations. As it will be discussed in Section 3.3, in some part of the atmosphere the plasma properties dominates the magnetic field, in other parts it is vice versa. In the case of a uniform medium, the total pressure is in equilibrium $\boldsymbol{\nabla}(p_0 + \frac{B_0^2}{8\pi}) = 0$ for ideal MHD. All variations in magnetic pressure, $\frac{B_0^2}{8\pi}$, are balanced by the plasma pressure, p_0, and vise versa. When two adjacent regions have different magnetic field strengths (B_1, B_2) and gas pressures (p_1, p_2), the equilibrium is maintained:

$$p_1 + \frac{B_1^2}{8\pi} = p_2 + \frac{B_2^2}{8\pi}\,. \tag{3.14}$$

In case of a small magnetic field in the quiet sun, the gas pressure is very high and the magnetic forces are weak. To uphold Eq. 3.14 in the strong magnetic field inside a sunspot, the increasing magnetic pressure forces have to reduce the gas pressure of the convective plasma.

3.2. Magnetohydrodynamic waves

In hydrodynamics, a non-magnetized fluid facilitates the isotropic propagation of acoustic waves at the speed of sound. On the contrary, a compressible magnetized plasma supports several new kinds of wave components. These magnetohydrodynamic (MHD) waves depend on the several plasma parameters, in particular on the strength of the magnetic field. MHD waves are characterized by an anisotropic distribution of wave speeds and fluid displacements with respect to the magnetic field orientation.

In principle, there are three types of MHD waves in a magnetized fluid. The waves can propagate with or without compressing the plasma and differ in terms of velocities (see Fig. 3.2) and restoring forces. They are commonly known as:

- **Alfvén waves**: The intermediate MHD mode describes an linear wave with incompressible propagation along the magnetic field. It has a characteristic velocity which is called Alfvén velocity v_A. The wave and its speed are named after its constitutor, Hannes Alfvén (1942). While fluctuation in gas and magnetic pressure are wholly absent, the wave is driven by synchronous transverse perturbations of the magnetic field lines. The magnetic tension force acts to straighten these distortions and serves as the restoring force for the field's curvature. By this, the tension force determines the speed of wave propagation. The theoretical description of Alfvén waves is given in Section 3.2.1.

- **Slow magnetoacoustic waves**: The slow MHD wave is one of the two compressible magnetoacoustic modes. It is excited by fluctuations in plasma pressure and magnetic pressure which act in opposition. The propagation of the longitudinal wave is anisotropic relative to the orientation of the magnetic field. Along the magnetic field lines, the slow-mode wave propagates like an acoustic wave but with velocities which are smaller than the sound and Alfvén speed. Comparable to a sound wave, the slow magnetoacoustic wave can steepen to a slow-mode shock which strongly compresses and heats the plasma. In addition to the magnetic tension force and gravity, the pressure forces act as resilience for the acoustic perturbations. Further characteristics of the slow-mode wave are described in Section 3.2.2.

- **Fast magnetoacoustic waves**: The fast MHD wave is the second of the compressible magnetoacoustic modes. Alike the slow-mode wave, it features fluctuations in gas and magnetic pressure. On the contrary, the two interacting pressure forces are in phase. The fast-mode wave describes a longitudinal wave which propagates quasi-isotropic relative to the magnetic field orientation. By that, the fast mode closely resembles the characteristics of an hydrodynamic wave. As its name indicates, the propagation velocity exceeds the sound and Alfvén speed. The restoring forces for the magnetoacoustic perturbations are the pressure forces, gravity, and also the tension force of the magnetic field lines. The theoretical description of fast-mode waves is given in Section 3.2.2.

Even if one of the itemized wave types dominates in the observations, in reality there is natural mixing of wave modes. As described in Section 3.3, the three kinds of MHD modes convert at sharp boundaries in the magnetized solar atmosphere.

In nature, MHD waves are found in a wide range of astrophysical plasmas as well as in experimental plasma fusion devices. In our solar system, they can be detected in the Earth's magnetosphere, the solar wind, and especially in magnetic structures in the solar atmosphere like in sunspots, magnetic flux tubes, coronal loops and solar flares. Their measured properties match with the theoretically postulated ones. Of course, the ideal MHD approximations need refinement for the often strongly inhomogeneous space plasmas.

For now, a simple scenario of MHD wave excitation in a uniform plasma is adequate to describe the basic properties of the three wave types. The following theoretical outline of MHD waves was extracted from the introduction to *Essential magnetohydrodynamics for astrophysics* by Spruit (2013) and Chapter 1.8 therein. Further information was included from the review articles on MHD waves by Roberts (2000) and Bogdan (2000).

In a simple scenario, a uniform plasma is permeated by a homogeneous magnetic field. The field vector, $\boldsymbol{B} = B\boldsymbol{z}$, is pointing along the z-axis of the Cartesian coordinate system. At first, the magnetized fluid with plasma pressure p and density ρ is at rest. In the next step, small perturbations of the magnetic field ($\delta\boldsymbol{B}$), plasma pressure (δp), and density ($\delta\rho$) are introduced. Expanding to first order in the small perturbations and in the fluid velocity $\boldsymbol{v}$, the linearized equations of induction (Eq. 3.7)

and motion (Eq. 3.11) become

$$\frac{\partial \delta \boldsymbol{B}}{\partial t} = \boldsymbol{\nabla} \times (\boldsymbol{v} \times \boldsymbol{B}) \,, \tag{3.15}$$

$$\rho \frac{\partial \boldsymbol{v}}{\partial t} = -\boldsymbol{\nabla} \delta p + \frac{1}{4\pi} (\boldsymbol{\nabla} \times \delta \boldsymbol{B}) \times \boldsymbol{B} \,. \tag{3.16}$$

The equation of mass continuity (Eq. 3.12) with constant background density gets

$$\frac{\partial \delta \rho}{\partial t} + \rho \boldsymbol{\nabla} \cdot \boldsymbol{v} = 0 \tag{3.17}$$

with the total derivatives of the density replaced by the partial derivative of its perturbation. When the changes in pressure δp and density $\delta \rho$ are assumed as adiabatic by $\delta p = \delta \rho \, (\frac{\partial p}{\partial \rho})_{\mathrm{ad}} \equiv c_{\mathrm{s}}^2 \delta \rho$, the sound speed for an ideal gas becomes

$$c_{\mathrm{s}} = \sqrt{\gamma \cdot \frac{p}{\rho}} \,, \tag{3.18}$$

with the gas pressure p and density ρ. The adiabatic index $\gamma = c_{\mathrm{p}}/c_{\mathrm{V}}$ then defines the ratio of specific heats[2] of a gas at constant pressure c_{p} or constant volume c_{V}.

To further simplify the setting, the two directions perpendicular to the initial magnetic field $\boldsymbol{B}$ are considered as equivalent. In Cartesian coordinates, the perturbations δq of the physical quantities along either the x-axis or y-axis can be ignored, here $\partial_y \delta q = 0$. In principle, this makes the wave problem two-dimensional. The axial components of the equations of induction (Eq. 3.15) and motion (Eq. 3.16) are

$$\frac{\partial \delta B_x}{\partial t} = B \frac{\partial v_x}{\partial z} \quad , \quad \frac{\partial \delta B_y}{\partial t} = B \frac{\partial v_y}{\partial z} \quad , \quad \frac{\partial \delta B_z}{\partial t} = -B \frac{\partial v_x}{\partial x} \,, \tag{3.19}$$

$$\rho \frac{\partial v_x}{\partial t} = -\frac{\partial \delta p}{\partial x} + \frac{B}{4\pi} \left(\frac{\partial \delta B_x}{\partial z} - \frac{\partial \delta B_z}{\partial x} \right) \quad , \quad \rho \frac{\partial v_y}{\partial t} = \frac{B}{4\pi} \frac{\partial \delta B_y}{\partial z} \quad , \quad \rho \frac{\partial v_z}{\partial t} = -\frac{\partial \delta p}{\partial z} \,. \tag{3.20}$$

The fact that the y-components only involve derivatives of δB_y and v_y will be one of the key aspects in solving the equations. The mathematical solutions for the Alfvén wave and the magnetoacoustic modes will be given in Section 3.2.1 and Section 3.2.2, respectively.

3.2.1. Alfvén waves

As itemized in Section 3.2, linear Alfvén waves are magnetohydrodynamic waves which propagate along the magnetic field without affecting the plasma pressure or density. As shown in the left panel of Fig. 3.1, for each plane magnetic surface, a synchronous transverse motion $\boldsymbol{v}$ and corresponding perturbation of the field lines excites linear Alfvén waves which propagate ($\boldsymbol{k}$) along the initial magnetic field $\boldsymbol{B}$.

To obtain the characteristics of Alfvén waves from the two-dimensional scenario above, one has to solve the coupled equations of induction and motion (Eqs. 3.15 and 3.16), or more specifically their axial components constituted in Eq. 3.19 and Eq. 3.20. The most trivial solution for the y-z plane can be found by setting v_x, v_z, δB_x, δB_z, δp, $\delta \rho$ all to zero. As the y-components of induction and motion only involve v_y and δB_y, the two equations can be combined by a multiplication. The Alfvén wave equation can be written as

$$\left(\frac{\partial^2}{\partial t^2} - v_{\mathrm{A}}^2 \frac{\partial^2}{\partial z^2} \right) (v_y, \delta B_y) = 0 \quad , \tag{3.21}$$

[2] For monoatomic gases, kinetic theory yields $\gamma = 5/3$. For diatomic gases it is $\gamma = 7/5$.

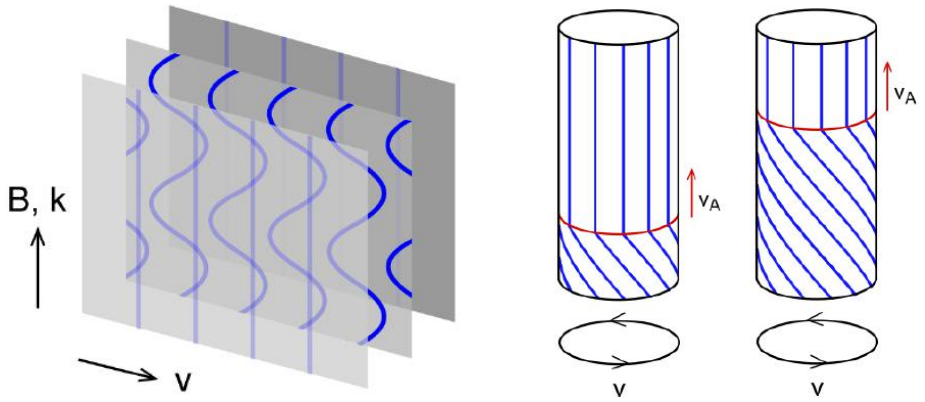

Figure 3.1.: Alfvén wave propagation. Left panel: Linear excitation of Alfvén waves along a plane magnetic surface moving back and forth ($\boldsymbol{v}$). The magnetic field $\boldsymbol{B}$ (blue lines) and wave vector $\boldsymbol{k}$ point perpendicular. Right panel: Torsional propagating with Alfvén speed v_A along a cylindrical magnetic surface (blue lines). Images from Spruit (2013).

with the characteristic Alfvén velocity

$$v_\mathrm{A} = \frac{B}{\sqrt{\mu_0 \cdot \rho}} \quad . \tag{3.22}$$

Essentially, the wave speed increases with the magnetic field strength B. Moreover, a decreasing density ρ accelerates the wave. The permeability of free space is given as $\mu_0 = 4\pi \cdot 10^{-7}$ (SI-system). The amplitudes of the wave are coupled by $\delta B_y / B = \pm\, v_y / v_\mathrm{A}$. Decomposing the perturbations of the physical quantities q into plane waves

$$q = q_0 \exp[i(\omega t - \boldsymbol{k} \cdot \boldsymbol{x})] \tag{3.23}$$

written as complex exponential functions with amplitude q_0, time t, and space $\boldsymbol{x}$, yields the circular frequency ω and the direction of the wave vector $\boldsymbol{k}$. Inserting this representation with the actual quantities into the wave equation (Eq. 3.21), the dispersion relation of Alfvén waves becomes

$$\omega^2 = k_z^2 v_\mathrm{A}^2 \ . \tag{3.24}$$

The wave therefore travels along the magnetic surface with a frequency that depends on the wavenumber component k_z along the magnetic field (see Fig. 3.1). For arbitrary directions, the phase velocity $u \equiv \omega / k$ of the single Alfvén modes with the dispersion $k_z = k \cos\phi$ becomes: $u = v_\mathrm{A} \cos\phi$. Their anisotropic distribution is shown in green in Fig. 3.2. Thus, the phase velocity decreases with increasing angle of incidence (ϕ) against the magnetic field. In accordance to Eq. 3.22, for lower plasma-β values (compare Eq. 3.30) the phase speeds are faster. By the exponentially decreasing gas density, they can vary from a few kms^{-1} in a small flux tube in the dense photosphere up to several hundreds of kms^{-1} in strong magnetic fields in the light upper atmosphere above a sunspot. Linear Alfvén waves describe an incompressible propagation. The group speed defines the propagation direction of the wave energy and is given by $\partial\omega / \partial\boldsymbol{k} = v_\mathrm{A} \boldsymbol{z}$. In contrast to the anisotropic phase speed, the energy is transmitted along the magnetic field lines while the wave vector $\boldsymbol{k}$ can differ from the $\boldsymbol{z}$-direction. Since an Alfvén wave describes a harmonic oscillation, the magnetic and kinetic energy are in equipartition.

3.2.2. Magnetoacoustic waves – slow and fast modes

As itemized in Section 3.2, the magnetoacoustic slow-mode and fast-mode waves are compressible longitudinal waves driven by fluctuations in plasma and magnetic pressure. Both modes have similar-

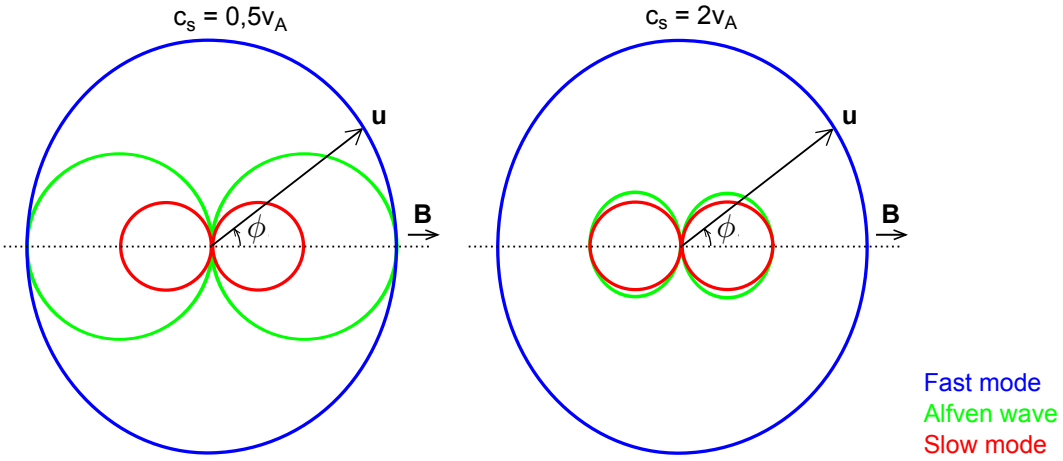

Figure 3.2.: Phase speeds of MHD wave propagation in a uniform medium. The phase velocities u depend on the angle of incidence θ of the wave vector (black arrow) against the magnetic field $\boldsymbol{B}$ (black dotted line). The distribution for the fast mode (blue), slow mode (red) and Alfvén wave (green) are shown for the low-β ($c_\mathrm{s} = 0.5 v_\mathrm{A}$) and high-$\beta$ ($c_\mathrm{s} = 2 v_\mathrm{A}$) regime. Image adapted from Spruit (2013).

ities to hydrodynamic waves, but differ explicitly in propagation velocity and direction relative to the magnetic field orientation.

To obtain the wave equations and dispersion relations of the magnetoacoustic modes, the equations of induction and motion (Eqs. 3.15 and 3.16) have to be solved. According to the simplified scenario above (see Section 3.2), the axial components constituted in Eq. 3.19 and Eq. 3.20 contain the wave solutions. In contrast to the Alfvén ansatz (compare Section 3.2.1), the y-components are now set to $v_y = \delta B_y = 0$, while δp, $\delta \rho$ are non-zero. The physical quantities $\boldsymbol{q} = (v_x, v_z, \delta B_x, \delta B_z)$ involve the existing non-trivial solution by substituting their exponential wave functions (Eq. 3.23) into the x- and z-components of Eqs. 3.19 and 3.20. The equation of mass continuity (Eq. 3.17) with adiabatic changes in plasma pressure and density yields the pressure perturbation, $\delta p = c_\mathrm{s}^2 \rho \, \boldsymbol{k} \cdot \boldsymbol{v} / \omega$, with the wavenumber $\boldsymbol{k}$, motion $\boldsymbol{v}$, and speed of sound c_s. It has to be inserted into the system of the four linear equations. This yields the dispersion relation of magnetoacoustic waves

$$\omega^4 - \omega^2 k^2 (c_\mathrm{s}^2 + v_\mathrm{A}^2) + k_z^2 k^2 c_\mathrm{s}^2 v_\mathrm{A}^2 = 0 \; , \tag{3.25}$$

with the circular frequency ω, Alfvén speed v_A (Eq. 3.22) and wavenumber k. This wavenumber can be represented by its axial components, $k_x = k \sin\phi$ and $k_z = k \cos\phi$, with ϕ being the angle of incidence between the direction of wave propagation $\boldsymbol{k}$ to the magnetic field $\boldsymbol{B}$. With the phase velocity $u \equiv \omega / k$ and the axial wavenumbers, Eq. 3.25 becomes

$$u^4 - u^2 (c_\mathrm{s}^2 + v_\mathrm{A}^2) + c_\mathrm{s}^2 v_\mathrm{A}^2 \cos^2\phi = 0 \; . \tag{3.26}$$

With the substitution $u = \tilde{u} (c_\mathrm{s} v_\mathrm{A})^{1/2}$, the four solutions of Eq. 3.26 are the phase velocities of the individual magnetoacoustic modes

$$u^2 = \frac{1}{2} (c_\mathrm{s}^2 + v_\mathrm{A}^2) \left[1 \pm (1 - 4 \cos^2\phi \, / b^2)^{1/2} \right] \; , \tag{3.27}$$

with $b = c_\mathrm{s}/v_\mathrm{A} + v_\mathrm{A}/c_\mathrm{s} \geq 2$. The solutions with the '+'-sign give the fast-mode phase speeds. The '−'-sign corresponds to the slow-mode waves. Each of the two wave modes has two symmetric solution of opposing directions (see Fig. 3.2). It is important to notice that the phase speeds of the magnetoacoustic waves only depend on

1. the direction of the wave propagation ϕ to the magnetic field orientation,
2. the ratio of the sound speed to the Alfvén speed, $c_\mathrm{s}/v_\mathrm{A} = \sqrt{\gamma\beta/2}$, defined by the plasma-$\beta$ value (Eq. 3.30).

The magnetoacoustic phase speeds are illustrated in Fig. 3.2 according to the direction of wave propagation. The velocities are given by the length of the wave speed vector $\boldsymbol{u}$. According to the inclination angle ϕ to the magnetic field, the phase velocities of the fast mode (blue curve) and the slow mode (red curve) yield the characteristic wave propagation in different plasma-β regimes.

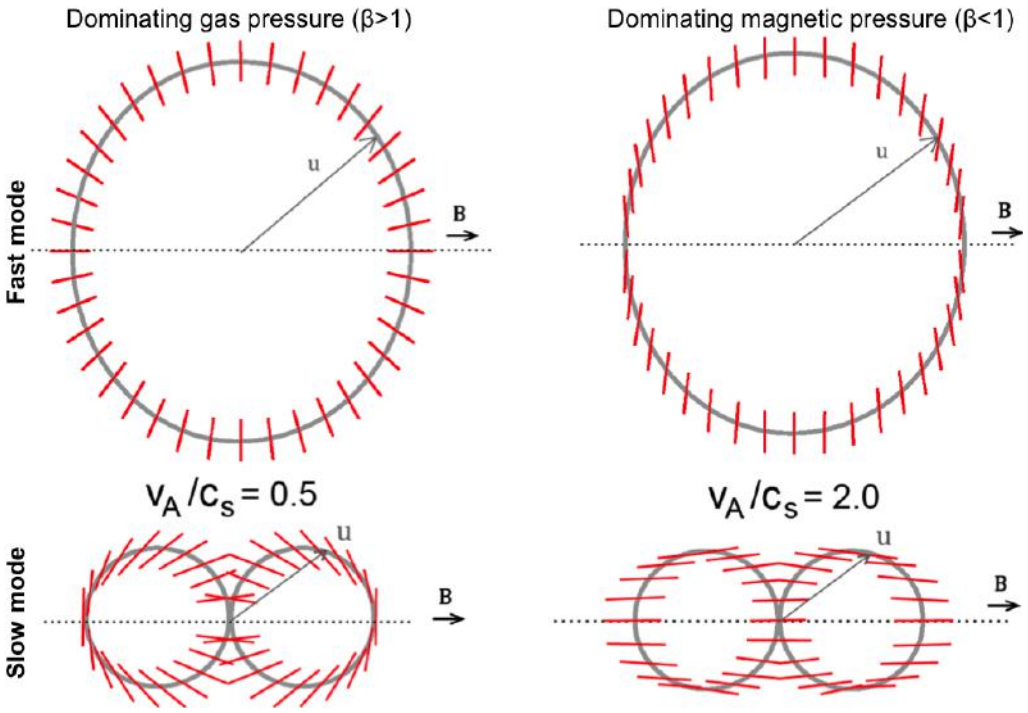

Figure 3.3.: Direction of fluid displacements (red) for the fast mode (upper panels) and slow mode (lower panels) in a high-β ($v_\mathrm{A}/c_\mathrm{s} = 0.5$) and low-$\beta$ ($v_\mathrm{A}/c_\mathrm{s} = 2$) uniform medium. The angular dependence of the phase speed $\boldsymbol{u}$ (gray) is displayed with respect to the magnetic field $\boldsymbol{B}$ (dotted line). See also Fig. 3.2. Image adapted from Spruit (2013).

Slow mode:

The wave characteristic of slow-mode magnetoacoustic waves can be obtained from the dispersion relation (Eq. 3.25). The absolute phase speed u_s of slow-mode waves is given by the negative solution of Eq. 3.27. For the case of a dominating sound or Alfvén speed ($c_\mathrm{s} \gg v_\mathrm{A}$ or $v_\mathrm{A} \gg c_\mathrm{s}$), it becomes

$$u_\mathrm{s}^2 = \frac{c_\mathrm{s}^2 v_\mathrm{A}^2}{c_\mathrm{s}^2 + v_\mathrm{A}^2} \cos^2\phi \ , \tag{3.28}$$

with the cusp speed of the wave at $\cos^2\phi = 1$ for propagation along the magnetic field lines ($\phi = 0°$). As shown in Fig. 3.2, the phase speed of the slow mode (red curve) decreases for growing attack angles ϕ to the initial magnetic field (dotted line). Consequently, there is no propagation perpendicular to the magnetic field lines. The anisotropic distribution of slow magnetoacoustic waves is comparable to the case of Alfvén waves (green curve). For linear wave propagation, the phase velocity of the slow-mode wave is smaller than the sound and Alfvén speed. Exemplarily, in the photosphere of a sunspot (like in Section 4.3.1) with a strong magnetic field strength of around 2000 G, the Alfvén speed can reach

several tens to few hundreds of $\mathrm{km\,s^{-1}}$. In comparison, the sound speed has values of around $8\,\mathrm{km\,s^{-1}}$. According to Eq. 3.28, the phase velocity of the slow-mode wave is slightly sub-sonic. With decreasing density along the atmospheric height, the wave speed can increase by one magnitude and more. Since the magnetoacoustic wave propagation is characterized by longitudinal compression and rarefactions of the plasma just like an acoustic wave, the wave is capable of steepen into a shock front. Toward higher atmospheric layers and growing wave amplitudes, the wave crests can overtake its troughs. According to the group velocity of the slow modes, the wave energy is transmitted along the magnetic field lines. Observationally, the slow magnetoacoustic waves can be verified easily in Doppler velocity. As shown in the lower panels of Fig. 3.3, the spatial fluid displacements (red fluctuations) in the low-β plasma (right case) are aligned with the magnetic field. Due to the dominating magnetic pressure, perpendicular displacements are prevented. For slow-mode waves in the magnetized plasma of a sunspot at solar disk center, the plasma oscillation is along the line-of-sight providing maximum Doppler velocities. The fluctuations in intensity and velocity are in phase. On the contrary, when the gas pressure dominates the magnetic pressure (left case), the fluid displacements are perpendicular to the direction of wave propagation. As discussed in Section 3.4, the upward propagation of the slow-mode wave in the solar atmosphere is limited by the acoustic cut-off frequency.

Fast mode:

Like for the slow magnetoacoustic wave, the wave characteristic of the fast-mode waves are contained in the dispersion relation (Eq. 3.25). The absolute phase speed u_s of the fast magnetoacoustic mode is given by the positive solution of Eq. 3.27. Again, in the limit of a dominating sound or Alfvén speed ($c_\mathrm{s} \gg v_\mathrm{A}$ or $v_\mathrm{A} \gg c_\mathrm{s}$), the phase speeds become

$$u_\mathrm{f}^2 = c_\mathrm{s}^2 + v_\mathrm{A}^2 \ . \tag{3.29}$$

Hence, the phase speed of the fast-mode wave is super-sonic and super-Alfvénic. As shown in Fig. 3.2, the distribution of the wave propagation (blue curve) is quasi-isotropic in the high- and low-β domain. Only in the case when the sound speed approaches the Alfvén speed ($\beta \approx 1$), the phase speeds along the magnetic field are slightly smaller. The fast-mode wave is therefore the only MHD wave which can effectively propagate perpendicular to the magnetic field lines. According to Eq. 3.29, the fast-mode velocity is slightly faster than the assumed Alfvén speed of a few hundreds of $\mathrm{km\,s^{-1}}$. In comparison, the slow-mode velocity was slightly smaller than the sound speed of around $8\,\mathrm{km\,s^{-1}}$. With decreasing density toward the corona, the fast speed can further increase by one magnitude. Several characteristics of the fast-mode wave hint at its acoustic nature. This includes the group velocities which are nearly longitudinal. That implies a wave energy following the roughly isotropic wave vector. Furthermore, the waves can steepen into fast-mode shock waves. Since the waves compress the magnetized plasma, the measurable fluid displacements also exhibit acoustic properties as shown in the upper panels of Fig. 3.3 by the red bars. In the high-β regime (left case) of dominating gas pressure, the plasma oscillates roughly in the direction of wave propagation. The displacements are slightly modified by the magnetic pressure. When the magnetic field strength is strong, the magnetic forces dominate (low-β) the plasma motion. As shown in the top right panel of Fig. 3.3, the displacements become perpendicular to the magnetic field lines. Observationally, the fast magnetoacoustic wave is hard to detect because of its high velocity, weak Doppler signal and isotropic distribution.

3.2.3. Flux tube waves

Till here, the description of magnetohydrodynamics waves has been made for a uniform medium. In this section, the wave modes in magnetically structured flux tubes are briefly discussed. Although the presented modes describe the motion of 'thin' flux tubes, one can develop a feeling for waves in 'thick' tubes or strong umbrae of sunspots. Additionally to the 'body waves' which affect the whole

tube, these thick structures also feature 'surface waves' which do not enter the interior of the magnetic structure. The most prominent flux tube waves are illustrated in Fig. 3.1 (torsional Alfvén wave) and Fig. 3.4 (sausage and kink wave). They are outlined in the following paragraphs.

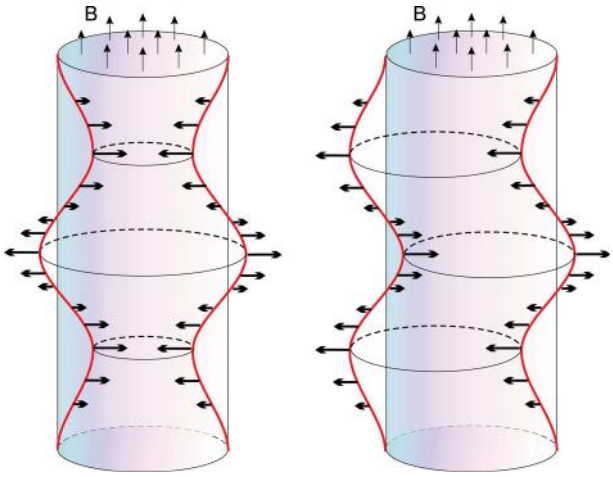

Figure 3.4.: Fast MHD waves in a magnetic flux tube. A schematic diagram of cylindrical magnetic wave guides (red lines) illustrates the longitudinal (sausage) and transversal (kink) modes. The sausage wave (left) is excited by a periodic stretching and squeezing of the magnetic field. The kink wave (right) is characterized by a coextensive displacement of the magnetic flux tube. The thick arrows indicate the velocity amplitudes. The thin arrows point the direction of the background magnetic field. Image from Morton et al. (2012).

When a set of magnetic field lines in the solar atmosphere is concentrated to a bundle, it is called a magnetic flux tube. The magnetic field strength $\boldsymbol{B}$ in the closed surface $\boldsymbol{S}$ defines the strength of a flux tube. The magnetic flux is $F = \int_S \boldsymbol{B} \cdot \mathrm{d}\boldsymbol{S}$. In the solar atmosphere, these flux tubes are the basic components of larger magnetic configurations like sunspots, pores, spicules, or coronal loops. To simplify the mathematical description, a thin cylindrical tube with rotationally symmetric attributes is taken. Perturbations of the flux tube can excite several types of wave modes.

Sausage mode: The longitudinal flux tube wave, or more illustratively called 'sausage'-mode, belongs to the fast magnetoacoustic waves (see Section 3.2.2). The perturbed magnetic waveguides (red lines) of the sausage wave are displayed in the left panel of Fig. 3.4. The initially cylindrical flux tube is periodically stretched and squeezed perpendicular to the magnetic field orientation. The azimuthally symmetric perturbations do not lead to spatial displacements of the tube, but to a change in the size of the loop cross-section. This compressive change induces an oscillation in plasma pressure and spectral intensity inside the tube. The longitudinal sausage wave propagates along the magnetic field, with perpendicular velocity amplitude. Observationally, this wave mode is hard to detect in the solar atmosphere due to the low wave energy flux, but best at high spectral frequencies.

Kink mode: The transversal flux tube wave, or more illustratively called 'kink'-mode, belongs to the fast magnetoacoustic waves (see Section 3.2.2). As displayed in the right panel of Fig. 3.4, the initially unbowed magnetic waveguides (red lines) are periodically swayed perpendicular to the background magnetic field. These asymmetric spatial displacement of the central tube axis do not change the shape of the loop cross-section. Inside the flux tube, the kink wave does not affect the plasma pressure or spectral intensity. An Alfvénic wave can propagate along the magnetic field lines. Due to the perpendicular oscillation of the flux tube and its magnetic pressure and tension, a fast magnetoacoustic wave is excited. This serves as an important example of mode-coupling between Alfvén and magnetoacoustic waves.

Torsional Alfvén wave: When a constant torque is applied to the magnetic flux tube, the bundle of field lines is twisted and a torsional Alfvén wave (see Section 3.2.1) is excited. As illustrated in the right panels of Fig. 3.1, the sharp wave front propagates with the Alfvén velocity v_A (Eq. 3.22) along the rotating field bundle. The Alfvén torsional wave is difficult to observe in the solar atmosphere. They do not change the shape, location, plasma pressure or spectral intensity of the magnetic flux tube. As the wave propagation is not periodically, the wave mode can only be measured as an incoherent Doppler velocity pattern. Further characteristics of flux tube waves are discussed by Roberts (2000).

3.3. Plasma-β regimes and mode conversion

In the solar atmosphere, the gas plasma is naturally interspersed with magnetic fields. As discussed in Section 3.1, the dynamical plasma and magnetic fields strongly affect each other. The solar atmosphere exhibits a plethora of visual manifestations and dynamic phenomena. They depend on the local physical quantities and the interaction of the gas pressure and magnetic energy density of the plasma. The β-value of a magnetized plasma precisely quantifies the dominating atmospheric force. It is defined as the ratio of the local plasma pressure p_gas to the magnetic pressure p_mag of the field configuration:

$$\beta = \frac{p_\mathrm{gas}}{p_\mathrm{mag}} \overset{(3.14)}{=} \frac{p_\mathrm{gas}}{B^2/8\pi} \overset{(3.18)}{=} \frac{\rho/\gamma \cdot c_s^2}{B^2/8\pi} \overset{(3.22)}{=} \frac{2}{\gamma} \cdot \frac{c_s^2}{v_A^2} \approx \frac{c_s^2}{v_A^2} \ , \tag{3.30}$$

with the magnetic field strength B, the plasma density ρ, the adiabatic index γ, permeability of free space μ_0 (here 4π), the local speed of sound c_s (Eq. 3.18), and the Alfvén velocity v_A (Eq. 3.22). The most important consequence is that the dominating regime can be described by the ratio of the sound to Alfvén speed. Consequently, the plasma-β follows the proportionality between the ambient temperature (Eq. 2.1) of the atmosphere and the inverse of the squared magnetic field strength ($\beta \sim \frac{\vartheta_\mathrm{K}}{B^2}$). Accordingly, in a photospheric sunspot region the plasma-β drops by some orders of magnitude at the transition from the hotter and less magnetic vicinity of a sunspot to the dark umbral core with the strongest magnetic field. With rising altitude toward the outer solar atmosphere, the magnetic field strength of the sunspot slightly decreases while the ambient temperature and sound speed rise (see Fig. 2.5). But as the local density decreases more drastically, the β-value according to Eq. 3.30 remains small.

The qualitative derivation of the plasma motion in different atmospheric regimes (Spruit 2013) highlights the importance of the plasma-β. Based on the equation of motion (Eq. 3.11) for an compressible ideal gas with constant temperature, neglecting gravity, and after replacing the physical quantities by dimensionless variables ($\tilde{t}$, $\tilde{\boldsymbol{v}}$, $\tilde{\boldsymbol{\nabla}}$, $\tilde{\boldsymbol{B}}$) of order unity, the plasma motions can be described by

$$\mathcal{M}^2 \frac{\mathrm{d}\tilde{\boldsymbol{v}}}{\mathrm{d}\tilde{t}} = -\tilde{\boldsymbol{\nabla}} \ln\rho + \frac{2}{\beta}(\tilde{\boldsymbol{\nabla}} \times \tilde{\boldsymbol{B}}) \times \tilde{\boldsymbol{B}} \tag{3.31}$$

with the Mach number $\mathcal{M}$ (Eq. 3.36) and the characteristic plasma-β (Eq. 3.30). If the Mach number is low ($\mathcal{M} \ll 1$), the motion is clearly sub-sonic. In this case, the left hand side can be neglected and the solution of Eq. 3.31 is decided by the β-value. If the gas pressure dominates ($\beta \gg 1$), the changes in density caused by magnetic forces have to be small. In solar applications, the density is then often approximated as constant. If the magnetic pressure dominates ($\beta \ll 1$), the magnetic forces have to be small, either when the field describes a potential field with vanishing currents ($\boldsymbol{\nabla} \times \boldsymbol{B} = 0$) or a force-free field with currents parallel to the magnetic field $\boldsymbol{B}$. If the Mach number $\mathcal{M}$ is not negligible, the plasma-β is crucial. The magnetized solar atmosphere can be classified into three plasma-β regimes:

- **High-$\boldsymbol{\beta}$**: The gas pressure of the plasma dominates the magnetic pressure. Therefore, the motion and shape of the magnetic field concentrations are governed by the plasma motion. In the convection zone where $\beta \gg 1$, the magnetic fields are 'frozen' in the convection. The solar convection zone and most parts of the photosphere feature a high plasma-β. In the quiet sun,

granular cell motion of the plasma dominates the magnetic forces. The small-scale magnetic field is pushed to the inter-granular lanes. According to Eq. 3.30, the sound speed exceeds the Alfvén velocity. The wave characteristics of magnetoacoustic modes (see Section 3.2.2) can change dramatically for different plasma-β regimes. In the high-β regime, fast-mode magnetoacoustic waves are equivalent to hydrodynamic sound waves. They can propagate in all directions with aligned fluid displacements (see Figs. 3.2 and 3.3) and phase velocities which are slightly faster than the speed of sound (Eq. 3.29). On the other hand, slow-mode waves exhibit similarities to Alfvén waves. They exhibit an anisotropical distribution of phase speeds relative to the magnetic field lines. They reach their maximum velocities (slightly sub-Alfvénic) when propagating along the magnetic field lines (see Eq. 3.28) and cause fluid displacement perpendicular to the direction of wave propagation.

- **Low-$\boldsymbol{\beta}$**: The magnetic pressure forces dominates the plasma pressure. Due to low gas densities and strong magnetic field strengths, the Alfvén velocity exceeds the sound speed by far (Eq. 3.30). As the magnetic field couples the plasma motion, the solar atmosphere visually appears filamentary or loop-like where $\beta \ll 1$. As the convective pressure and plasma density decrease with altitude, the upper solar atmosphere (from the chromosphere to the corona) features a low plasma-β. In the case of sunspots, the magnetic energy density can exceed the gas pressure also at photospheric heights. This becomes conspicuous when imagining strong plasma flows which follow the magnetic fields in the penumbra or at the suppression of convection in the umbra. The wave characteristics of the magnetoacoustic modes have changed compared to the high-β regime. While the anisotropic propagation of the fast-mode magnetoacoustic wave is still valid (see Fig. 3.2), the phase speeds have become slightly super-Alfvénic (Eq. 3.29). The longitudinal fluid displacements are now orientated perpendicular to the magnetic field lines (see Fig. 3.3). On the other hand, the slow-mode waves have adopted an quasi-acoustic wave behavior. They exhibits an anisotropical distribution of phase speeds with maximum velocities (slightly sub-sonic) along the magnetic field lines (see Eq. 3.28). The pressure fluctuations cause field-aligned displacement.

- **$\boldsymbol{\beta \approx 1}$**: At this characteristic transition level of the plasma-β, the magnetic and plasma pressure are in equipartition. Consequently, in this region the sound speed reaches the Alfvén velocity. This property of the plasma is most important for the mode conversion of magnetoacoustic waves. In the quiet solar atmosphere, the β- unity layer is located at chromospheric heights. In the presence of sunspots, the strongly magnetized atmosphere leads to a depression of the layer. Whereas the penumbral $\beta \approx 1$- level is reached at photospheric heights, the umbral equipartition can by reached already below the surface height of the surrounding area. Between the high-β and low-β domain, the effective mode mixing and conversion of fast- and slow-mode waves occurs. As shown in Fig. 3.5, both magnetoacoustic modes can transform most effectively into each other.

When the plasma-β transits from high to low values the individual magnetohydrodynamic waves can suffer from essential changes in their wave characteristics. When the sound speed approaches the Alfvén velocity, the magnetoacoustic mode conversion occurs. As shown in Fig. 3.5 and discussed by Khomenko and Cally (2012) (and references therein), mode conversions and reflections also play an important role for the wave propagation in the sunspot atmosphere. When a propagating quasi-acoustic fast-mode wave (black curve) propagates upward and reaches the $\beta \approx 1$-layer, a fraction of its wave power is converted into a slow-mode magnetoacoustic wave (red curve) which is then guided by the inclined magnetic field lines. As shown by the different field inclinations in the left and right panel, fraction of the converted energy depends on the attack angle between the initial propagation direction of the fast wave and the magnetic field. The excited slow-mode wave is strongest when the angle of incidence is smallest. The phase difference between the two magnetoacoustic modes could be measured, the fast-mode in terms of magnetic field fluctuations and the slow-mode in terms of field-aligned fluid

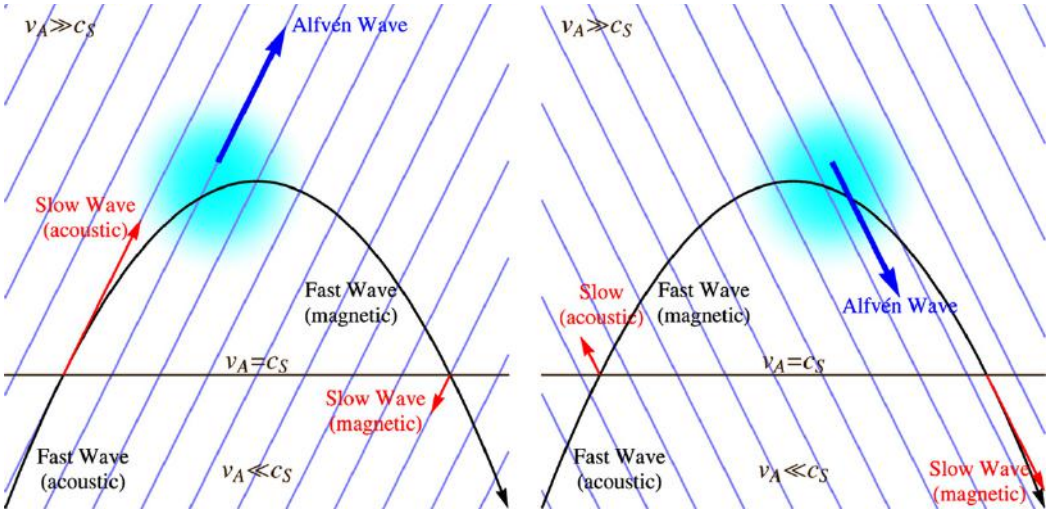

Figure 3.5.: Schematic diagram of MHD mode conversion in the magnetized solar atmosphere. Wave conversions and reflections between fast-mode (black), slow-mode (red) and Alfvén waves (blue) are sketched for different orientations of the magnetic field lines (pale blue). The black horizontal line indicates the Alfvén-acoustic equipartition level ($v_\mathrm{A} = c_\mathrm{s}$) of plasma-$\beta$ unity. It divides the high-β (lower) from the low-β (upper) regime. Image from Khomenko and Cally (2012).

displacements. As it will be discussed in Section 3.4, the wave propagation or reflection of the slow-mode depends on the wave frequency and magnetic field inclination. As further shown in Fig. 3.5, when the magnetic fast-mode wave propagates to even higher atmospheric layers with decreasing plasma-β, the phase speed approaches the Alfvén velocity. Due to the high Alfvén speed gradient, the wave front of the fast-mode wave steepens and is finally reflected downwards. At the turning point of the wave trajectory, fast-to-Alfvén wave conversion is initiated. According to the wave vector and orientation of the magnetic field lines, the Alfvén wave (blue curve) propagates either upward or downward along the field lines. When the magnetic fast-mode wave propagates toward an atmospheric layer with higher plasma-β, fast-to-slow-mode conversion occurs again.

3.4. Wave guiding and the acoustic cut-off

The solar atmosphere oscillates with a number of acoustic eigenmodes. The characteristic mode with the highest frequency determines the upper boundary for resonant acoustic oscillations in the lower solar atmosphere. Therefore, magnetoacoustic waves with frequencies above this eigenfrequency are no longer trapped, but can travel into the chromosphere and even higher layers. This solar eigenmode is therefore called the 'acoustic cut-off' frequency f_cut. In a chromospheric power spectrum, the part with wave frequencies below the cut-off frequency ($f \leq f_\mathrm{cut}$), or wave periods above the cut-off period ($T \geq T_\mathrm{cut}$), are reduced in wave power or as the name suggests are 'cut off'. The waves become evanescent. The filtering cut-off layer can be located roughly at the atmospheric transition from the upper photosphere to the lower chromosphere.

First investigations of the acoustic cut-off in the solar atmosphere were performed by Bel and Leroy (1977). They yielded that the acoustic cut-off for slow-mode magnetoacoustic waves (Section 3.2.2) is caused by the presence of the gravitational field and depends on the local parameters of the gas plasma. Thereby, the acoustic cut-off frequency f_cut in the field-independent case can be calculated as

$$f_{\mathrm{cut},0} = \frac{\gamma\, g}{4\pi\, c_\mathrm{S}} \tag{3.32}$$

or its inverse, the acoustic cut-off period

$$T_{\mathrm{cut},0} = \frac{4\pi}{\gamma\, g} \cdot c_{\mathrm{S}}\,, \tag{3.33}$$

with the speed of sound c_{S} (see Eq. 2.1), the gravitational acceleration g, and the ratio of specific heats γ. Exemplarily, the acoustic cut-off in the upper solar photosphere is calculated. Inserting the gravitational acceleration $g_{\mathrm{Sun}} \approx 274\,\mathrm{m/s}$ of the Sun[3], an isothermal sound speed $c_{\mathrm{S}} = 7\,\mathrm{km/s}$ (see Fig. 2.5 c), and the ratio of specific heats $\gamma = 5/3$ into Eq. 3.32, the acoustic cut-off frequency is $f_{\mathrm{cut},0} = 5.2\,\mathrm{mHz}$. According to that, only slow-mode waves with oscillation frequencies exceeding 5.2 mHz or periods $T < 192\,\mathrm{s} = 3.2\,\mathrm{min}$ (according to Eq. 3.33) can propagate into the chromosphere. With rising atmospheric altitude the density drops and the amplitude of the propagating waves increase rapidly. All modes with periods above 3.2 min are evanescent and suffer from the acoustic cut-off.

In the presence of strong magnetic fields in sunspots (low plasma-β, Eq. 3.30), the slow-mode magnetoacoustic waves propagate along the magnetic field lines with almost the speed of sound and longitudinal fluid displacements (see Figs. 3.2 and 3.3). As suggested by Bel and Leroy (1977) and observationally verified by De Pontieu et al. (2004), the cut-off frequency for the field-guided quasi-acoustic waves depends on zenith angle Φ_{B} of the magnetic waveguides. With Eq. 3.32 and 3.33, the acoustic cut-off becomes

$$f_{\mathrm{cut},\Phi_{\mathrm{B}}} = f_{\mathrm{cut},0} \cdot \cos\Phi_{\mathrm{B}} = \frac{\gamma\, g\, \cos\Phi_{\mathrm{B}}}{4\pi\, c_{\mathrm{S}}}\,, \tag{3.34}$$

in terms of frequencies, and

$$T_{\mathrm{cut},\Phi_{\mathrm{B}}} = \frac{T_{\mathrm{cut},0}}{\cos\Phi_{\mathrm{B}}}\,, \tag{3.35}$$

in terms of wave periods. For a vertical field ($\Phi_{\mathrm{B}} = 0°$), the cut-off values are the same as above. But, for more inclined magnetic field lines ($0° < \Phi_{\mathrm{B}} < 90°$), the cutoff-frequency is reduced significantly. Consequently, this shift in period would especially allow the upward propagation of the overpowering high-period waves which were formerly evanescent. Returning to the example for the photospheric acoustic cut-off, the impact of the magnetic field topology gets clear. Under the same assumptions but a field inclination angle of $\Phi_{\mathrm{B}} = 36°$ at the umbral boundary, the effective cut-off frequency is reduced to $f_{\mathrm{cut},36°} = 4.2\,\mathrm{mHz}$. Now, also the initially evanescent waves with periods $192\,\mathrm{s} < \mathrm{T} < 240\,\mathrm{s}$ (or frequencies $f_{\mathrm{cut},\Phi_{\mathrm{B}}} < f \leq f_{\mathrm{cut},0}$) can penetrate the higher solar atmosphere. For the sunspot atmosphere, several observational studies confirm the shift of the acoustic cut-off from 3 min in the umbra to around 10 min in the outer penumbra (e.g., Tziotziou et al. 2006; Jess et al. 2013). In Section 6.5 the opposite approach is used. The cut-off period deduced from the power spectra indicates the magnetic field inclination in a sunspot.

3.5. Acoustic shock waves

Acoustic waves are longitudinal pressure perturbations which propagate through a non-magnetized medium with the specific speed of sound c_{S} (see Eq. 2.1). When the sound source passes through this medium, it compresses the series of emitted pressure waves in front of it. On the back side of the object, the sound waves are carried along, which leads to an overall decompression compared to the distribution at rest. According to the Doppler effect, when the waves are pushed forward, the wavelength is decreased or blue-shifted. On the other side, when the wave profile is stretched, the wavelength is increased or red-shifted. The left panel of Fig. 3.6 shows the case of a sub-sonic ($v < c_{\mathrm{s}}$) propagation.

When the velocity of the acoustic source approaches the speed of sound ($v \approx c_{\mathrm{S}}$), the emitted waves cannot get out of the way of each other and merge to a single shock front. The same scenario is valid

[3]The gravitational acceleration at the solar surface is about 28 times the gravitation on Earth.

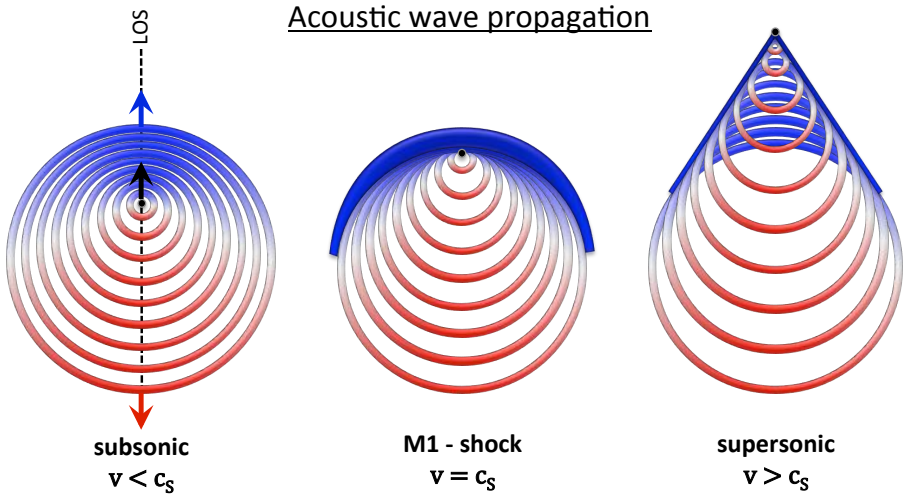

Figure 3.6.: Sketch of the acoustic wave propagation. The object (black source) propagates through the medium along the observer's line of sight. The three scenarios illustrate the wave behavior for sub-sonic (left), sonic (middle) and super-sonic (right) velocities v. The emitted sonic pressure waves are displayed as surrounding circles. The blue colors display upward propagation, red colors indicate downward motion.

for the acoustic-like waves in a magnetized plasma (see Section 3.2.2). When the crest of the wave can propagate faster than its trough, the magnetoacoustic wave steepens progressively and ultimately forms a shock front. As discussed in detail in Dwivedi and Parker (2003), the increasing gradients for the atmospheric parameters makes the dissipation inside the shock important. Due to the enormous compression, the wave energy is gradually converted into heat. The middle panel of Fig. 3.6 displays the formation of a shock wave at the speed of sound. In hydrodynamics, this propagation criterion for which shock formations starts is commonly known as Mach 1. By definition, the Mach number $\mathcal{M}$ of an object moving with velocity v is simply

$$\mathcal{M} = \frac{v}{c_\mathrm{S}} \,, \tag{3.36}$$

where c_S is the local sound speed of the medium. Accordingly, if the sound source is traveling through the medium at twice the speed of sound, it is moving at Mach 2. This super-sonic ($\mathcal{M} > 1$) propagation of an object is illustrated in the right panel of Fig. 3.6. Thus, the faster the acoustic source travels, the more it runs ahead of its emitted sound waves. The shock front gets finer and more pointed. As shown by the blue line in Fig. 3.6, it deforms from a bow to a cone, named Mach cone.

The characteristic shape of the shock front is described by the inverse of the Mach number (Eq. 3.36) as

$$\sin\alpha = \frac{c_\mathrm{S}}{v} \,. \tag{3.37}$$

The half-angle α describes the inclination between propagation direction and the front of the shock wave. For sonic propagation ($v \approx c_\mathrm{S}$), Eq. 3.37 provides an inclination of $\alpha = 90°$, so the shock wave has the form of a bow close to a half-circle. For super-sonic source velocities, the angle decreases and the shock front adopts the shape of a cone with the object at its tip. The case of Mach 2 shock wave is illustrated in Fig. 3.7. Since the source speed is twice the sound speed, the half-angle of the Mach cone (blue line) is $\alpha = 30°$. Inside the cone, a sonic boom of enormous energy is created by the dissipating sound waves. The motion of the sonic boom is in opposite propagation direction. In term of Doppler shifts along the line of sight, this features large spectral red-shifts. In the acoustic description, these sonic booms sound like giant explosions. Thinking about the magnitudes of sonic booms at Earth, e.g.,

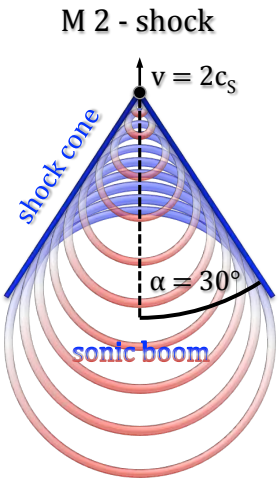

Figure 3.7.: Sketch of an acoustic shock wave with Mach 2. The object (black source) is traveling along the line of sight with twice the sound speed. The shock front has the shape of a cone (blue) with half-angle α. The sonic boom behind the shock front is displayed as the trailed circles. The blue (red) colors display upward (downward) motion of plasma.

of a bullet, a fighter jet, a detonation or even the entrance of the Chelyabinsk meteor into the Earth's atmosphere over Russia in 2013, one can hardly imagine the acoustic effect of an earth-sized sonic boom in the solar atmosphere with several kilometers per second. As it will be discussed in Section 6.3, umbral flashes in the sunspot atmosphere can cause such giant shock waves and sonic booms.

Beyond, in hydrodynamics a double shock in a medium is named 'N-wave'. When the shock wave passes, the overpressure at the shock front leads to a steady decrease in pressure down to negative values behind the shock. The immediate equalization of pressure and return to its unperturbed value leads two a second shock-like wave. Therefore, the temporal pressure profile of such a 'double-shock' at a defined observational position resembles the letter N. The change of the shock direction can even amplify the intensity of the shock wave. This is due to the faster second shock which then can add to the main event.

4. Data and experiments

"Data! Data! Data!" he cried impatiently. "I can't make bricks without clay."

— Sherlock Holmes, in Sir Arthur Conan Doyle's
The Adventures of Sherlock Holmes

With this quote, Sherlock Holmes warns Watson not to jump to conclusions before gathering enough information. First, sufficient data have to be collected as a solid basis, then a significant conclusion can be drawn from the findings. By analogy, one needs clay to build the bricks. In science it has to be the same. Observations have to be performed, the data have to be collected and analyzed. From the results, one can conclude on the nature behind the phenomenon and establish a theory which can reproduce the observations. Therefore, in this chapter, I will first explain the experiments with which the data were acquired and then describe the observations on which this work is based on. In Section 4.1, the telescopes and instruments will be introduced and characterized. Section 4.2 yields the details about spectral lines which are used to investigate the sunspot oscillations. In Section 4.3, the observational data are presented. The applied data calibration is described in Sections 4.3.1 and 4.3.2.

4.1. Experimental devices

As pointed out in Chapter 1, the invention of telescopes and spectroscopic instruments revolutionized the field of solar physics. Their continuous and relentless development has enabled today's high-resolution observations of the Sun and the stars. In this section, the used scientific instrumentation and applied experimental techniques are presented. In Section 4.1.1, a brief description of the different telescopes is given. Section 4.1.2 provides an digression to the functioning of Fabry-Pérot interferometers and the setup of bidimensional spectrometers. Following this, the imaging spectrometers with which the observations were performed are characterized in Section 4.1.3.

Table 4.1.: Characteristics of the solar telescopes.

	DST	**VTT**	**GREGOR**	**SDO**
Location	Sacramento Peak	Teide Observatory, Tenerife		Space (Earth orbit)
Altitude	2800 m	2400 m		35,800 km
Type	Heliostat, z-axis	Coelostat	Gregory	Satellite
Diameter	0.76 m	0.7 m	1.5 m	0.14 m (HMI)
Focal length	54.8 m	46 m	55.6 m	5.0 m (HMI)
Resolving power	0.20″ (600 nm)	0.22″	0.10″	1.0″ (HMI)
Wavelengths	310 nm − 1.0 μm	350 nm − 1.8 μm	350 nm − 2.2 μm	0.1 − 617 nm
Adaptive optics	✓	✓	✓	×

4.1.1. Telescopes

The following high-quality telescopes were used to run the sunspot observations (see Table 4.1). The first observation which is presented in this work (Section 4.3.1) was made with the Dunn Solar Telescope (DST). The second observation (Section 4.3.2) was performed with the Vacuum Tower Telescope (VTT). For both observation, complementary data from the Solar Dynamics Observatory (SDO) were acquired. Beyond the scope of this work, sunspot oscillations were also observed with the GREGOR telescope (see Fig. 2.1).

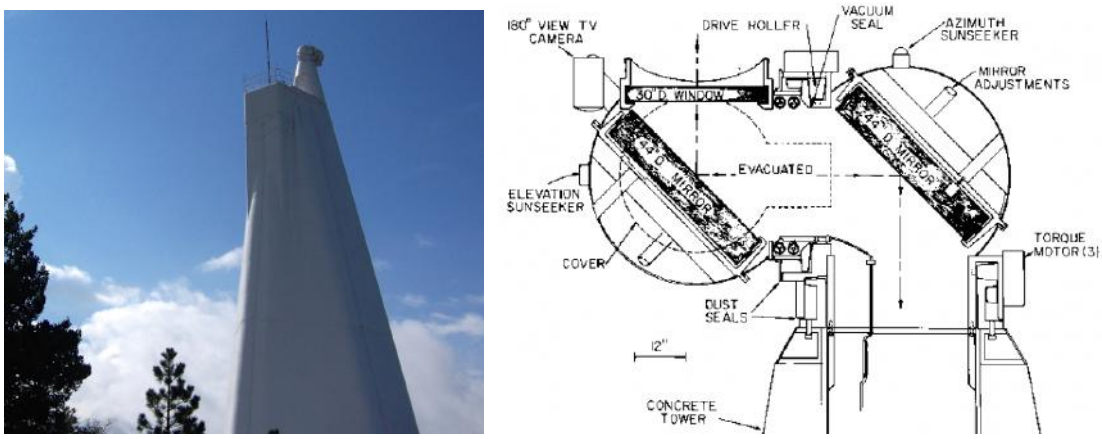

Figure 4.1.: The Richard B. Dunn Solar Telescope (DST) at Sacramento Peak, New Mexico. On top of the 41 m tall tower (left panel) the evacuated dual mirror system (right panel) guides the light into the telescope (Images: NSO/AURA).

Dunn Solar Telescope (DST)

The Dunn Solar Telescope (DST), formerly Vacuum Tower Telescope, was renamed in 1998 after its constructor Richard B. Dunn. The DST was inaugurated in 1969 at Sacramento Peak, New Mexico and is operated by the National Solar Observatory. The telescope is integrated into a 41 m tall tower from ground level (see left panel of Fig. 4.1) with an evacuated heliostat system (right panel of Fig. 4.1) at the top to track the Sun during the daily motion. The turret consists of a 76 cm entrance window and two plane-parallel 1.1 m-mirrors which guide the sunlight to a primary mirror (1.6 m) placed 59 m below ground level. The primary mirror reflects the light with a long focal length of 54.8 m to an optical laboratory close to ground level. The platform has a diameter of 12 m and hosts the scientific instruments. The solar image in the primary focus has a diameter of 51 cm. The angular resolution limit[1] for the effective wavelength range of $\lambda = 310 - 1000$ nm (optical to near-infrared) ranges from 0.1 arcsec to 0.33 arcsec. To compensate the image rotation during the day, the entire 100-meter-long telescope with all the optical elements and the instrumental platform (250 tons in total) rotates along the vertical axis. To eliminate the air distortions due to heat in the telescope and especially in the primary focus, the tube with the optical path of the sunlight is evacuated. To compensate for the Earth's atmospheric distortions, the DST is equipped with a high-order adaptive optics (AO) system (Rimmele and Radick 1998; Rimmele 2004). With this optical system, a high spatial resolution of 0.4 arcsec is achieved on a regular basis. For more information see NSO/AURA webpage.

[1]The angular or spatial resolution, $\theta_R = \lambda/D$, is the minimum distance of two object to still be distinguished by the telescope. It depends on the observed wavelength λ and the aperture D of the telescope. The number in radian can then be converted in arc-seconds.

Figure 4.2.: The Vacuum Tower Telescope (VTT) at the Observatorio del Teide on Tenerife. On top of the tower (left panel) the dual mirror coelostat system (right panel) guides the light into the telescope.

Vacuum Tower Telescope (VTT)

The Vacuum Tower Telescope (VTT) is located at the Teide Observatory on Tenerife at an altitude of 2400 m. The VTT started its scientific operation in 1988 under the lead of the Kiepenheuer Insitute for Solar Physics (Schroeter et al. 1985). Like in the case of the DST, the telescope is integrated in a tall tower (38 m; see left panel of Fig. 4.2) and has an evacuated tube for the optical path. At the top of the tower coelostat system (see right panel of Fig. 4.2) is used to feed the sunlight into the telescope. It consists of two plane mirrors with a diameter of 0.8 m. The first mirror reflect the solar image to the secondary mirror and has to follow the daily motion of the Sun across the sky. Therefore it is aligned with the Earth's rotation axis and rotates with its half rotation velocity. With this setup the solar image is not rotating in time. The secondary mirror then guides sunlight to the primary spherical mirror in the vacuum tank. The mirror has a diameter of 0.7 m and a focal length of 46 m. Before the light enters the instrumental laboratory, it passes a high-order adaptive optics system (von der Luehe et al. 2003) with a wavefront sensor and a deformable mirror. The AO compensates for the image blurring due to distorted wavefronts in the turbulent Earth's atmosphere. In combination with image reconstruction techniques, one tries to reach the theoretical limit for the spatial resolution of the telescope. The resolving power of the VTT ranges from 0.13 arcsec at 350 nm to 0.65 arcsec at 1.8 μm in the near infrared. In the visible range solar structures of less than 150 km could then be distinguished. Fostered by little atmospheric distortions, shortly exposed images, and image reconstruction techniques, the resolution limit can be reached. More information is given on the KIS webpage and listed references.

GREGOR

With a free aperture of 1.5 m, GREGOR is the largest solar telescope in Europe. It is located at the Teide Observatory right next to the VTT and was inaugurated in 2012 (Schmidt et al. 2012). As shown in Fig. 4.3, it is constructed in an alt-azimuthal mounting to track the solar motion. GREGOR is built in a triple-mirror Gregorian configuration with a 1.5 m primary mirror. The light path is folded and has an effective focal length of 55.6 m. To correct for atmospheric wavefront distortions a high-order adaptive optics system has been integrated (Berkefeld et al. 2012). With its large aperture, the telescope can achieve a spatial resolution of 0.1 arcsec at 600 nm. Therefore GREGOR can resolve objects on the sun as small as 70 km. The observable wavelengths extend from 350 nm to 2.2 μm. The corresponding resolving power ranges from 0.1 arcsec to 0.37 arcsec. More information on the telescope

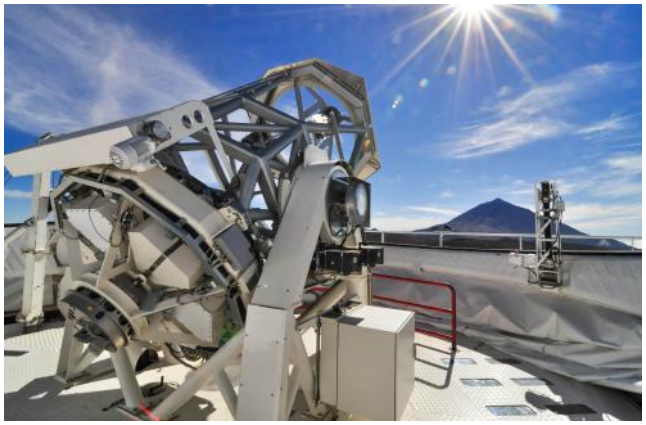

Figure 4.3.: The GREGOR telescope at the Observatorio del Teide on Tenerife. Image from KIS, H.-P. Doerr.

can be found in von der Lühe et al. (2000) and Volkmer et al. (2007).

A sunspot observation with GREGOR is shown in Fig. 2.1. The sunspots of active region NOAA 11835 were observed with the Broad-Band Imager (BBI) at GREGOR on August 30th 2013 at 08:27:35UTC. The observation was performed in a broad (4 nm) band centered at 486 nm. The continuum intensity reveals the small-scale structure of the region at the solar surface. A sequence of 100 shortly exposed (1 ms) images was flat-field calibrated (Eq. B.1). The sequence was reconstructed with speckle techniques (KISIP; Wöger and von der Lühe 2008) to one high-resolution observation. Thanks to the excellent atmospheric conditions and low turbulences (Fried parameter $r_0 > 50$ cm), the reconstruction yields a spatial resolution down to $0.1''$.

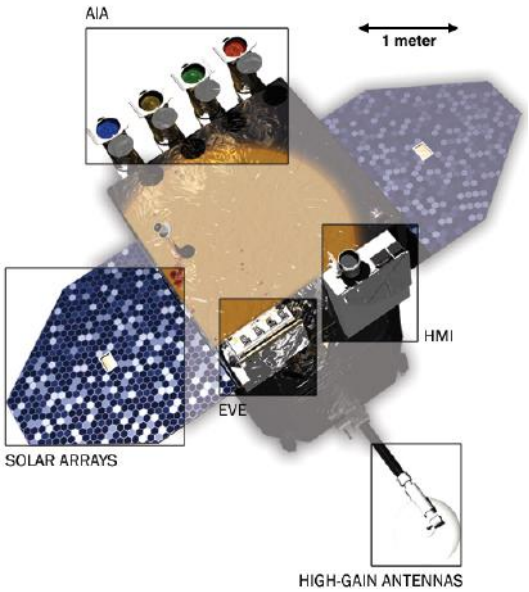

Figure 4.4.: The Solar Dynamics Observatory. Image from Pesnell et al. (2012).

Solar Dynamics Observatory (SDO)

The Solar Dynamics Observatory (SDO) is a NASA space mission to perform solar observations with its onboard instruments. The solar satellite was launched in February 2010 and started its scientific

operation in May 2010 with a mission duration of up to 10 years. The observatory moves in a circular, geosynchronous orbit at an altitude of around 35,800 km. The orbit is inclined by 28.5° to the dedicated ground station of NASA in New Mexico to which the observational data are transferred and from where the spacecraft is operated remotely. As shown in Fig. 4.4, the SDO is therefore equipped with two high-gain antennas. The span of the satellite has a size of 6.1 m × 6.0 m × 4.7 m. Further indicated are the two solar arrays and the three scientific instruments: the Helioseismic and Magnetic Imager (HMI), the Atmospheric Imaging Assembly (AIA), and the Extreme Ultraviolet Variability Experiment (EVE). They operate in different wavelength domains, from the extreme ultraviolet to the visible range, to study all atmospheric layers and dynamical processes of the Sun. The stable observations are performed continuously with a cadence of 12 s to 45 s and a spatial resolution down to 1 arcsec. As listed in Table 4.1, an adaptive optics is naturally not needed as there is no atmospheric distortion between the Sun and the telescope. The listed information were taken from Pesnell et al. (2012).

4.1.2. Spectroscopy with Fabry-Pérot interferometers

Accurate spectroscopic observations are needed to investigate the highly dynamical solar atmosphere. Spectral lines echo the conditions and motions at different atmospheric layers. Therefore instruments were realized to perform observations with a high spectral resolution. In solar physics, the scanning of spectral lines is commonly done with a spectrograph or an imaging spectrometer. Both instruments base on interference to filter very narrow bandwidths. Fabry-Pérot interferometers are very popular realizations of imaging spectrometers in solar physics. They produce two-dimensional solar images recorded at one instant of time in a narrow spectral bandwidth, typically of the order of a few picometer. Of course, such a fine spectral filtering requires sufficient incoming light. Among our celestial bodies only the Sun enable a significant two-dimensional resolution and provides enough photons, so the use of Fabry-Pérot interferometers in astronomy is basically limited to solar observations.[2]

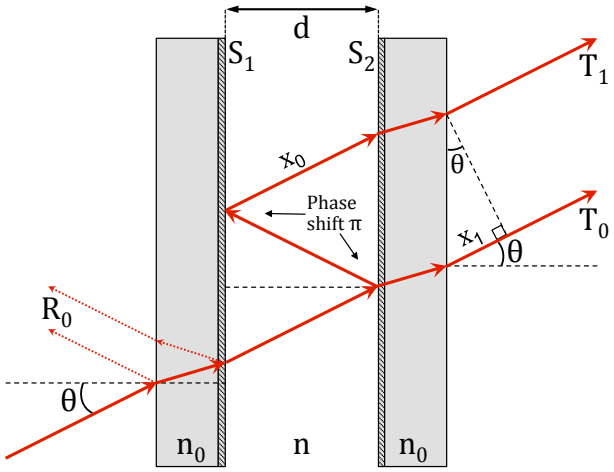

Figure 4.5.: Light path through a Fabry-Pérot interferometer. Two transparent plates with refractive index n_0 face each other with reflecting surfaces S_1 and S_2 in a plate separation d with index n. The light (red arrows) is transmitted (T_i) and reflected (R_i) under an angle of incidence θ.

A Fabry-Pérot interferometer (often abbreviated as FPI) is an optical system of one or two transparent plates with two parallel reflecting surfaces (see Fig. 4.5). In addition, several lenses are added to collimate and focus the light (see Fig. 4.7). The interferometer was named after Charles Fabry

[2]The following paragraphs are based on the descriptions of Fabry-Pérot interferometers by Stix (2002), Hernandez (1986) and Kentischer et al. (1998).

(1867–1945) and Alfred Pérot (1863–1925) who invented the filtering mechanism using two partially reflecting silvered plates (Perot and Fabry 1899). The reflected beams interfere and produce a spectrum of narrow transmission maxima in a regular spectral distance. A narrow interference filter or second FPI isolates one of the transmission peaks at a defined wavelength. Coming from the French word *étalon* (translated as "standard"), the interferometric device is also called Fabry-Pérot etalon.

High-quality etalons are characterized by a very narrow tunable spectral band-pass and a high intensity transmission. To meet these requirements, several parameters have to be taken into account. In Fig. 4.5, the light path through a Fabry-Pérot interferometer is sketched. The incoming beam (red arrow on the left) enters the first plate under an angle of incidence θ. A fraction R_0 of the light is reflected at the first plate's surface under the same angle. Based on Snell's law of refraction, in the medium with the higher refractive index n_0 the transmitted beam is refracted to the perpendicular. Both plates are layered with plane reflecting surfaces (S_1 and S_2) with reflectance R. The surfaces are separated by a distance d, the layer in between has a refractive index n (in case of air: $n \approx 1$). Parts of the light beam are multiply reflected between the mirrors. With each reflection the phase of the reflected beam is shifted by a half period π. At the same time, a fraction T of the light is transmitted. The outgoing beam T_0 exits the second plate under the initial angle of incidence θ. The multiply reflected beams can interfere with each other. In case of two successive outgoing beams T_0 and T_1, the path length difference is $\Delta x = 2x_0 - x_1 = 2nd\cos\theta$. The phase difference δ is given by

$$\delta = \frac{2\pi\Delta x}{\lambda} = \frac{4\pi nd\cos\theta}{\lambda} \tag{4.1}$$

for a wavelength λ. The beams interfere constructively when the path difference Δx is an integer multiple m of the wavelength, so that $\delta = 2m\pi$. As shown in Fig. 4.6, the transmission intensity T_E of the etalon is periodic with the mth maximum at a phase of $2m\pi$ or, in terms of wavelength, at $\lambda = 2nd\cos\theta/m$.

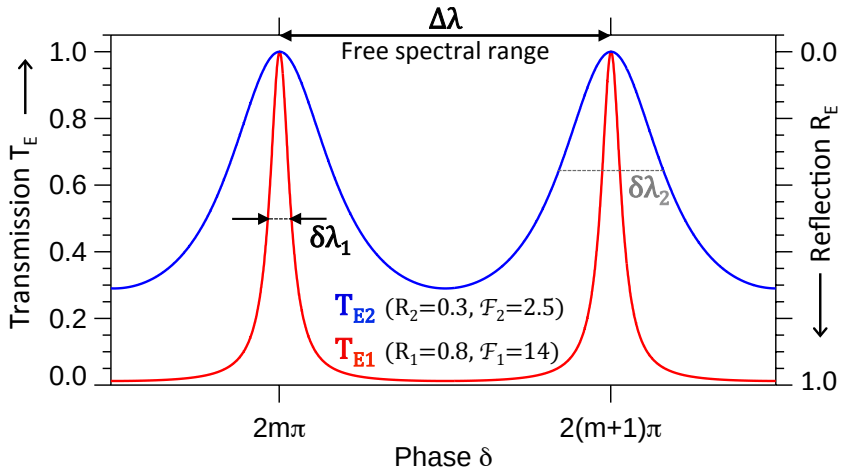

Figure 4.6.: Transmission of a Fabry-Pérot interferometer without absorption. The transmittance functions $T_{\mathrm{E}1}$ (red) and $T_{\mathrm{E}2}$ (blue) for two different reflectance values $R_1 = 0.8$ (finesse $\mathcal{F}_1 = 14.0$) and $R_2 = 0.3$ ($\mathcal{F}_2 = 2.5$) are plotted against the phase δ. The free spectral range $\Delta\lambda$ and the full widths at half maximum $\delta\lambda$ are indicated.

The transmission intensity T_E for the outgoing beam can be derived from the transmitted and reflected waves. Therefore, a geometric series is developed from the multiply reflected and transmitted waves. Its sum can be expressed analytically and written as

$$A = T(1 + Re^{i\delta} + R^2e^{2i\delta} + ...) = \frac{T}{1 - Re^{i\delta}} \quad . \tag{4.2}$$

The amplitude A can be multiplied with its complex conjugate

$$T_{\mathrm{E}} = AA^* = \frac{T^2}{1 - 2R\cos\delta + R^2} \tag{4.3}$$

and results in the transmitted intensity T_{E}. In the absence of absorption ($T + R = 1$), the transmission function of the FPI simplifies to

$$T_{\mathrm{E}} = \frac{(1-R)^2}{1 - 2R\cos\delta + R^2} \tag{4.4}$$

and only depends on the reflectance R and the phase δ. In Fig. 4.6, the transmitted intensity is plotted as a function of the phase δ. The red curve displays the transmittance functions T_{E1} computed for a reflectance value of $R = 0.8$. For comparison, the blue curve shows the intensity T_{E2} with an identical setup but a smaller reflectance value of $R = 0.3$. It can be concluded that an increasing reflectance R narrows the transmission peak and deepens the transmission minimum. The maximum of the reflectivity function $R_{\mathrm{E,max}}$ in the spectrum is reached when the phase is an odd multiple of π and is calculated as

$$R_{\mathrm{E,max}} = 1 - T_{\mathrm{E,min}} = \frac{4R}{(1+R)^2} \quad . \tag{4.5}$$

In Fig. 4.6, the narrowness of the intensity peak is indicated by the full width at half maximum $\delta\lambda$. The wavelength separation between two successive transmission maxima (m and $m+1$) is called the free spectral range $\Delta\lambda$. It is computed as

$$\Delta\lambda = \frac{\lambda}{m} = \frac{\lambda^2}{2nd\cos\theta} \tag{4.6}$$

and depends on the wavelength λ, the plate separation d, the angle of incidence θ and the refractive index n. A qualitative value for the intensity transmission of an etalon is the so called *finesse* $\mathcal{F}$. It is the ratio of the free spectral range $\Delta\lambda$ to the full width at half maximum $\delta\lambda$ and is commonly approximated for equal reflecting surfaces as

$$\mathcal{F} = \frac{\Delta\lambda}{\delta\lambda} \approx \frac{\pi\sqrt{R}}{1-R} \quad . \tag{4.7}$$

The finesses of the etalons illustrated in Fig. 4.6 are $\mathcal{F}_1 = 14.0$ for a reflectance of $R_1 = 0.8$ (red curve) and $\mathcal{F}_2 = 2.5$ for a reflecting index of $R_2 = 0.3$ (blue curve). It is obvious that an exact filtering of narrow wavebands of the order of a picometer requires a very good finesse and high reflectance of the Fabry-Pérot interferometer, as well as a constant plate separation and a well-defined angle of incidence of the incoming light beam. The distance d of the reflecting surfaces has to be tuned with high precision to change the filtered wavelength. In general, the plate separation has to be close to constant allover the field. Already small flatness defects of the surfaces at the order of some nanometer lead to wavelength shifts of several picometer. A detailed description of etalon errors and their effects is given in Section B.2 and illustrated in Figs. B.6 and B.7.

The sunlight can enter the Fabry-Pérot interferometer under various angles of incidence (compare Fig. 4.5). In case of an etalon-based imaging spectrometer, several lenses are used to guide the beam from a solar image through the reflecting plates to the camera. In general, there are essentially two instrumental concepts to design such a FPI spectrometer. In Fig. 4.7, the collimated (upper) and telecentric (lower) optical mounting are sketched (Kentischer et al. 1998).

The classical setup is the collimated mounting (upper panel of Fig. 4.7). The rays (solid lines) excited at a point of the solar image (FS) close to the optical axis pass the first collimating lens (L1) and are guided parallel through the reflecting plates of the Fabry-Pérot interferometer (FPI). The rays which are excited further away from the optical axis (dotted lines) enter the FPI under a larger angle of

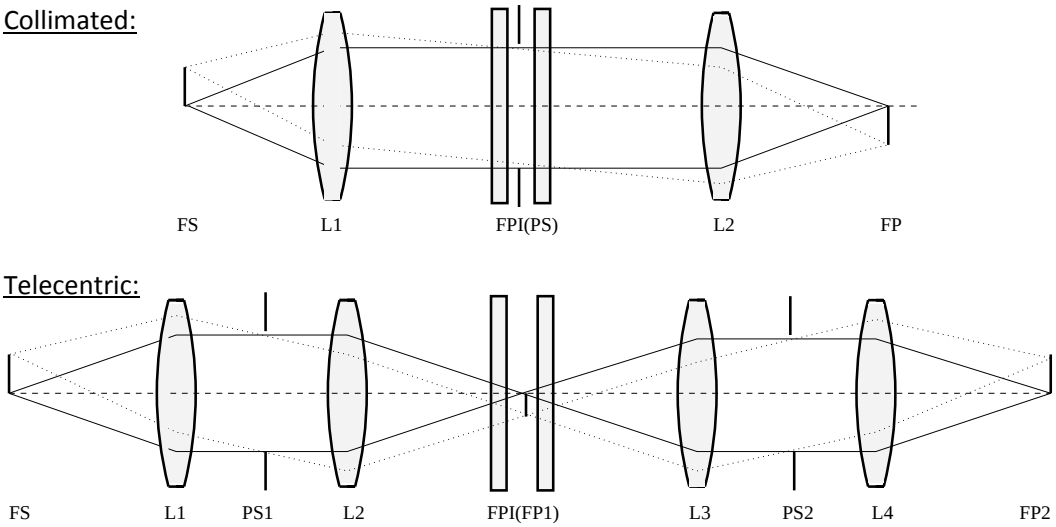

Figure 4.7.: Mounting concepts for Fabry-Pérot interferometers. The two light beams (solid and dotted line) from the solar image (confined by the field stop FS) follow the optical axis (dashed line) and pass a system of several lenses (L1–L4) and an etalon (FPI) until they are detected in the focus point (FP) by the camera. In the collimated setup, the beams are collimated at the FPI location and confined by the telescope aperture (PS). In the telecentric configuration, the beams have their first focus at the etalon. Image adapted from Kentischer et al. (1998).

incidence. As derived in Eq. 4.1 and 4.3, for constructive interference the filtered wavelength decreases with the angle of incidence. In the setup, a second lens (L2) focuses the rays and inverts the original image. The image in the focal plane (FP) exhibits a radial wavelength gradient across the field of view, with an increasing blue-shift towards the edges. As the rays with the same inclination at the FPI will be focused to one image point in the focal plane, the defects in the surface flatness and parallelism errors will distribute over the whole field and broaden the profile of the spectral line.

The second concept is the telecentric mounting (lower panel of Fig. 4.7). In this case, the rays (solid and dashed lines) from the solar image enter the spectrometer and are projected by two lenses (L1 and L2). The Fabry-Pérot interferometer is placed in the first focal plane (FP1). The additional lenses (L3 and L4) re-image the filtered solar image onto the detector of the camera in the second focal plane (FP2). A quick comparison of the light paths through the plates for both mountings tells that a smaller etalon size is sufficient in the telecentric mounting. As the cones of the light beams forming the images have the same angle at the FPI location, the path length of the light through the etalon is equal for the whole field of view. In contrast to the collimated mounting, every position at the etalon corresponds to only one point of the solar image. For perfectly flat and parallel surfaces the filtered wavelength is stable, no systematic line shift should occur. In reality, the surface coating of an etalon has flatness defects of several nanometers and small errors in plate shape and parallelism affect the transmission of the FPI. These small-scale errors locally shift the transmission profile in wavelength. To reduce these inhomogeneities, the etalons are slightly displaced from the focal plane. The imaged displacements are called “orange peel pattern”, as can be seen in Fig. B.7. The larger-scale displacements of the plates lead to transmission shifts and reductions over the full field of view. More information on those errors is given in Section B.2.

Examples for etalon-based solar spectrometers can be found for both optical mountings and have been used extensively within this work. The state-of-the-art representatives with a collimated mounting are the Interferometric Bidimensional Spectrometer (IBIS; Cavallini 2006) at the Dunn Solar Telescope

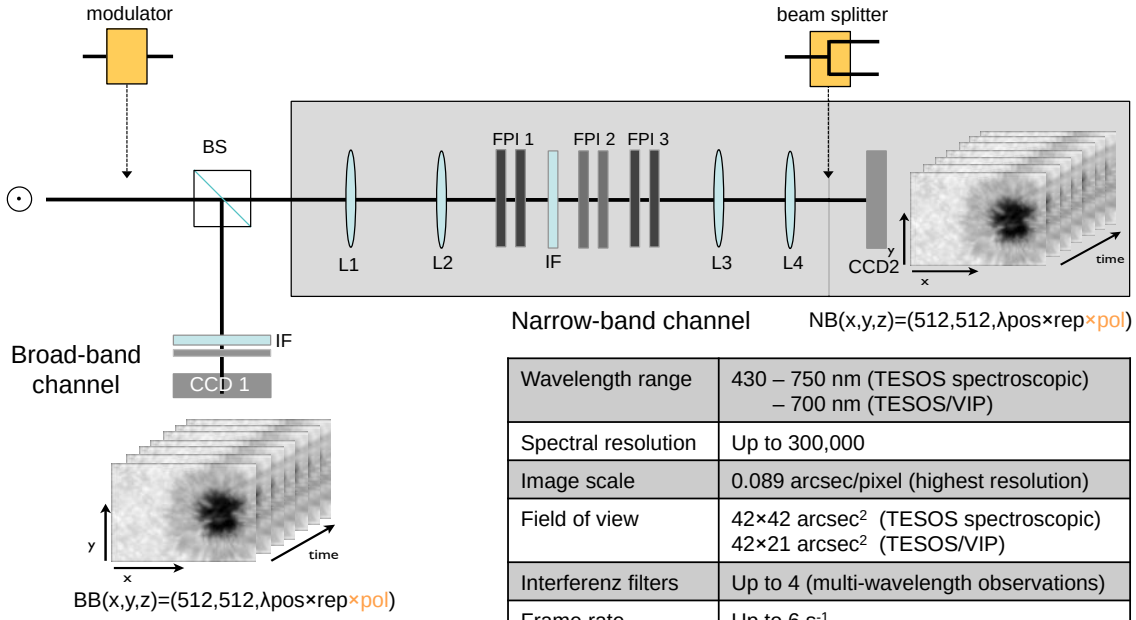

Wavelength range	430 – 750 nm (TESOS spectroscopic) – 700 nm (TESOS/VIP)
Spectral resolution	Up to 300,000
Image scale	0.089 arcsec/pixel (highest resolution)
Field of view	42×42 arcsec^2 (TESOS spectroscopic) 42×21 arcsec^2 (TESOS/VIP)
Interferenz filters	Up to 4 (multi-wavelength observations)
Frame rate	Up to 6 s^{-1}

Figure 4.8.: General setup of a solar etalon-based spectrometer in telecentric mounting. The characteristics and numbers are described for Triple Etalon SOlar Spectrometer (TESOS). The main optical setup consists of an entrance window, a beam splitter (BS), several lenses (L), interference pre-filters (IF), Fabry-Pérot interferometers (FPI) and camera detectors (CCD). For the polarimetric observation, a polarimetric modulator and a beam splitter have to be inserted.

and the GREGOR Fabry-Pérot Interferometer (GFPI; Puschmann et al. 2012) at GREGOR. Their prominent counterparts with a telecentric mounting are the Triple Etalon SOlar Spectrometer (TESOS; Kentischer et al. 1998) at the Vacuum Tower Telescope and the CRisp Imaging Spectro Polarimeter (CRISP; Scharmer et al. 2008) at the Swedish Solar Telescope. The next-generation spectrometer will be the Visible Tunable Filter (VTF; Schmidt et al. 2014) which will start its high-resolution spectro-polarimetric observations at the Daniel K. Inouye Solar Telescope (DKIST) in 2019. It will also have a telecentric mounting.

Common imaging spectrometers base on a system of one to three Fabry-Pérot interferometer for the spectral filtering. A well-calibrated multi-etalon system yields the advantage that the unwanted peaking side-orders of transmission are suppressed while the spectral resolution for the desired order is increased. However, one must be aware that with every additional etalon the instrumental complexity increases and the optical quality of the image decreases. Therefore, most spectrometers use a tandem of Fabry-Pérot interferometers. One FPI has a higher finesse ($\mathcal{F} \sim 30 - 40$, see Eq. 4.7) to filter a series of narrow transmission peaks. The other FPI yields a lower finesse to isolate the transmission peak in a fine spectral range (see Fig. 4.6). The combination of a low-resolution etalon with such a high-resolution etalon gives an even narrower spectral filtering. The resulting transmission curve is the product of the two transmission profiles of the FPIs (see left panel of Fig. B.6).

The combination of Fabry-Pérot interferometers is the heart of the imaging spectrometer. The selection and positioning of collimating and focussing lenses determines the mounting concept for the instrument. In Fig. 4.8, the optical setup of the Triple Etalon SOlar Spectrometer (TESOS; Tritschler et al. 2002) is illustrated exemplarily. The sunlight enters the instrument though a field diaphragm. The beam is guided to the so-called 'narrow-band' channel (highlighted in gray) which contains a system of etalons (FPI) and lenses (L). The Fabry-Pérot interferometers (FPI1,2,3) are mounted close to the focal plane in a telecentric way (setup shown in Fig. 4.7). An interference filter (IF) with a

bandwidth of typically one nanometer is inserted between the etalons to isolate the preferred spectral range. The filter can be tilted to fine-adjust its transmission function to the desired wavelengths or spectral line. The interference filter is integrated into a rotating filter wheel with four placements. For simultaneous observations of multiple spectral lines, the different filters are switched within a second while the etalon settings are adapted. The solar images within the narrow spectral bands are then recorded by a fast camera.

Simultaneously to the spectral scans, an additional camera (CCD1 in Fig. 4.8) records the same field of view in continuum intensity. With a beam splitter (BS), a fraction of the incoming light is guided to the so-called 'broad-band' channel. An interference filter (IF) is inserted to select a broad waveband in the spectral continuum close to the observed spectral line or lines. The resulting data cube $NB(x, y, z)$ of the narrow-band channel consists of the two-dimensional images (in case of TESOS: $[512\,\text{pixels}]^2$; in case of IBIS: $[1007\,\text{pixels}]^2$) made at various wavelength positions λ_{pos} for different spectral lines. The amount of the scan can be multiplied by the repetitive observation (*rep*) at the selected spectral positions. With additional optical devices, the imaging spectrometer can become a spectro-polarimeter (Tritschler et al. 2004). When the observation should be performed spectro-polarimetrically, then a polarimetric modulator and a beam splitter have to be inserted in the setup (see yellow devices in Fig. 4.8). In general, four to six polarimetric modulation states *pol* are enough to retrieve the full-Stokes vector. The states have to be recorded at every wavelength position. Thus the amount of images in the data cube has to be multiplied by this number (indicated in yellow in Fig. 4.8). The data cube $BB(x, y, z)$ of the broad-band channel contains the same field of view and an corresponding amount of images. However, all images are recorded at the same broad waveband and setting. A detailed description of the data calibration of these data cubes is given in Section B.2. For more information on Fabry-Pérot interferometers and imaging spectro-polarimeters in general, I want to refer the reader to the work by Hernandez (1986) and Feller (2007). In the following section, the instrumental specifications of the used imaging spectrometers will be outlined.

4.1.3. Scientific instruments

The principles of imaging spectrometers and Fabry-Pérot interferometry have been elaborately discussed in Section 4.1.2. In this section, I will introduce the imaging spectrometers used in this work. The physical properties and instrumental characteristics are described for the Interferometric Bidimensional Spectrometer (IBIS), the Triple Etalon SOlar Spectrometer (TESOS), the Rapid Oscillations in the Solar Atmosphere (ROSA) instrument, the Helioseismic and Magnetic Imager (HMI) and the Atmospheric Imaging Assembly (AIA).

Interferometric Bidimensional Spectrometer (IBIS)

The Interferometric Bidimensional Spectrometer (IBIS; Cavallini et al. 2000) is an imaging spectrometer working with two synchronized Fabry-Pérot interferometers in a collimated mounting (see Fig. 4.7). A description of the functionality and theory of FPI spectrometers was given in Section 4.1.2. A detailed instrumental characterization of IBIS is given by Cavallini (2006) and Reardon and Cavallini (2008). The polarimetric upgrade is described by Viticchié et al. (2009) and Judge et al. (2010).

The IBIS instrument has been installed at the Dunn Solar Telescope (see Fig. 4.1 and Table 4.1 in Section 4.1.1) at Sacramento Peak in 2003. It was developed at the Osservatorio Astrofisico di Arcetri belonging to the Istituto Nazionale di Astrofisica. IBIS performs two-dimensional solar spectroscopy at high spatial, spectral and temporal resolution. The instrumental characterization is summed up in Table 4.2. The main optical setup differs from the one shown in Fig. 4.8 for TESOS only by the number of etalons, the bigger detector size and the collimated mounting (see Fig. 4.7). When the sunlight enters the instrument, it is fed by a beam splitter to two channels, one for narrow spectral filtering and the other for context observations in continuum intensity. In both channels, interference filters are used to limit the transmitted spectral band. While in the broad-band channel the filters

Table 4.2.: Characteristics of the spectrometers IBIS and TESOS.

	IBIS	**TESOS**
Fabry-Pérot interferometers	2	3
Optical mounting	Collimated	Telecentric
Wavelength range	580 – 860 nm	430 – 750 nm
Field of view (circular)	80″	42″
Detector size	$(1024\,\text{pixel})^2$	$(512\,\text{pixel})^2$
Camera chips	CCD	CCD
Spatial scale	$0.098''\,\text{pixel}^{-1}$	$0.089''\,\text{pixel}^{-1}$
Spectral resolution	200,000 – 300,000	250,000 – 300,000
Transm. bandwidth (FWHM)	2.1 – 4.2 pm	1.4 – 3.0 pm
Minimum step width	0.48 pm	0.25 pm
Etalon aperture	50 mm	50 mm
Etalon reflectance	0.91 – 0.94	0.94
Plate spacings	2.3 mm (#1), 0.6 mm (#2)	1.3 mm (#1), 0.8 mm (#2), 0.57 mm (#3)
Wavelength shifts (radial)	6 – 9 pm	–
Cavity errors	< 10 nm	< 5 nm
Wavelength setting time	$\simeq 20$ ms	$\simeq 20$ ms
Exposure times (S/N ≥ 100)	$10 - 20$ ms	$10 - 20$ ms
Average acquisition rate	$\simeq 6$ frames s^{-1}	$\simeq 6$ frames s^{-1}
Filters per observation	≤ 6	≤ 4
Pre-filter wavelengths [nm]	589.6, 630.2, 656.3, 854.2, ...	543.4, 656.3, 617.3, 709.0, ...
Pre-filter bandwidth	0.3 nm (0.5 nm→ 854.2 nm)	0.3 – 1.0 nm
Continuum channel	✓	✓
Polarimetric upgrade	✓	✓
Detailed descriptions	Cavallini (2006)	Kentischer et al. (1998)

have a bandwidth of several nanometers, the pre-filters in the narrow-band channel have a centered transmission on a spectral line and transmit a bandwidth of only 0.3 nm (or 0.5 nm in case of the broad Ca II line at 854.2 nm). To perform simultaneous multiline observations, up to six filters can be mounted in a filter wheel. The two Fabry-Pérot interferometers have an aperture of 50 mm, plate spacings of 2.3 mm (#1) and 0.6 mm (#2), and reflectivities of around 93%. Fig. 4.9 a) shows that the value of the etalon reflectance depends on the wavelength. In the wavelength range between 580 nm (visible) and 860 nm (near-infrared) it scales between 0.91 – 0.94. According to Eq. 4.7, the transmitted bandwidth $\delta\lambda$ is smallest for high reflectivities. Fig. 4.9 b) depicts how the reflectivity affects this full width at half maximum (FWHM) of the filter transmission. The transmitted bandwidth ranges from values below 2.5 pm in the visible range to more than 4.0 pm in the near-infrared. As indicated by the dashed lines in Fig. 4.9 b), the spectral resolution of IBIS approaches 300,000 for wavelengths between 630 nm and 730 nm, and decreases to a resolution of 200,000 at 860 nm. In panel c) of Fig. 4.9, the transmission profile at $\lambda = 632.8$ nm has a width of $\delta\lambda = 2.4$ nm (gray dashed area), resulting in a spectral resolution of 288,000. The measured profile (gray solid) slightly differs from the calculated

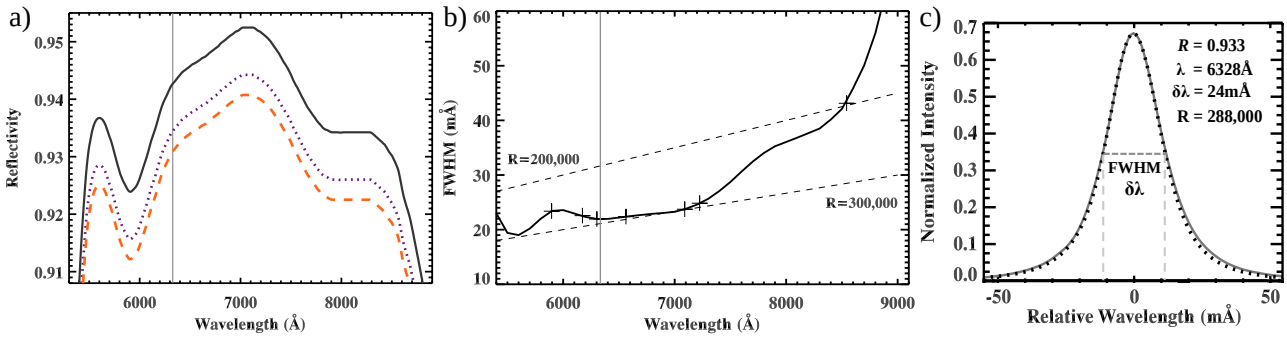

Figure 4.9.: Narrow-band filtering of IBIS. Panel a): The reflectivities of both etalons (first dotted, second dashed) are shown for the wavelengths and compared to the nominal values (black solid). Panel b): The transmission width (FWHM in mÅ) is plotted against the wavelength. The dashed lines indicate spectral resolutions of 200,000 and 300,000. Panel c): The centered transmission peak (in normalized intensity) at $\lambda = 632.8\,\mathrm{nm}$ (marked in panels a and b) has a width $\delta\lambda = 24\,\mathrm{m\AA}$. The measured transmission is shown in solid, the theoretical one in dotted. Images adapted from Reardon and Cavallini (2008).

profile (dotted). When scanning through a spectral line during observations, the instrument needs around 20 ms to set the wavelength. To achieve a signal to noise ration $\mathrm{S/N} \geq 100$, an exposure time of at least 10 ms is needed in continuum intensity and at least 20 ms in spectral lines. With its fast CCD cameras ($1024 \times 1024\,\mathrm{pixel}^2$), IBIS can perform observations at an average acquisition rate of up 6 frames per seconds. The circular field of view has a diameter of 80 arcsec. The image scale amounts to $0.098''\,\mathrm{pixel}^{-1}$ to enable observations at the resolution limit of the telescope of around 0.2 arcsec (0.19 arcsec at 580 nm, 0.28 arcsec at 860 nm). Due to the collimated mounting of the etalons, the transmitted wavelength shifts to smaller values (blue-shifts) with increasing distance from the optical axis. The temporal stability of the instrumental profile is very high and yields a drift of less than $10\,\mathrm{m\,s}^{-1}$ in ten hours. The necessary post-observational data calibration is explained in Sections 4.3.1 and B.2. The sunspot of NOAA11823 was observed with IBIS, the data are shown in the middle row of Fig. 4.14.

Triple Etalon Solar Spectrometer (TESOS)

The Triple Etalon Solar Spectrometer (TESOS; Kentischer et al. 1998) is a high-resolution imaging spectrometer installed at the Vacuum Tower Telescope (see Fig. 4.2 and Table 4.1) at the Teide Observatory. The instrument was developed at the Kiepenheuer-Institut für Sonnenphysik as a double Fabry-Pérot spectrometer in a telecentric mounting (see Fig. 4.7). Later, TESOS was upgraded by a third synchronized high-resolution etalon (Tritschler et al. 2002) and a polarimetric setup (Tritschler et al. 2004). The main optical setup of TESOS is shown in Fig. 4.8. The functionality of the instrument is explained in Section 4.1.2. The instrumental characterization including the spectral, spatial and temporal parameters is listed in Table 4.2.

With three synchronized etalons in the telecentric mounting, TESOS reaches a high spectral resolution of 300,000 in the visible range. The high mean reflectivity of the plate surfaces (94%) enables the narrow bandwidths of 1.4 pm to 3.0 pm of the transmitted light for wavelengths between 430 nm and 750 nm. An additional interference pre-filter with a narrow bandpass (0.3 –1 nm) centered on a spectral line is used to perform the two-dimensional spectroscopy. For quasi-simultaneous scans of multiple spectral lines, up to four filters can be mounted to a filter wheel located after the first etalon. While the switching of the filters is done within two seconds, the setting time of the etalon plates for each wavelength positions takes another 20 ms. During observation, TESOS achieves a mean acquisition rate of six frames per second. The transmitted signal is recorded by a fast CCD camera ($512 \times 512\,\mathrm{pixel}^2$).

In the normal setting, the detector has an image scale of $0.089''$ pixel^{-1}, the circular field of view has a diameter of 42 arcsec. A second setting with a larger field of view (90 arcsec) and lower spectral resolution (150,000) can be selected to observe larger regions on the Sun. The diffraction limited spatial resolution without atmospheric blurring ranges from 0.15 arcsec to 0.27 arcsec across the visible spectrum. As shown in Fig. 4.8, a second channel with the same field of view performs simultaneous observations in the continuum intensity. The interference filter has a broader transmission and should have a central wavelength in the spectral continuum close to the wavelength of the spectral scan. The post-observational calibration process for TESOS data was sketched in Fig. B.3 and described in Sections 4.3.2 and B.2. The most involved part is the reduction of the flatness defects of the etalon plates. In the telecentric mounting close the focus, each position of the transmitted image corresponds to one position of the etalon aperture. Already small errors (< 5 nm) of the etalon plate spacings (1.3 mm, 0.8 mm, 0.57 mm) cause big shifts in wavelength (shown in Figs. B.6 and B.7). On the other hand, the telecentric configuration of TESOS provides an almost constant wavelength passband across the field of view. The temporal wavelength drift is less than 0.3 pm per hour. A data pipeline and calibration program (CASSDA GUI – TESOS; see Section B.3) has been developed. The calibrated TESOS data of NOAA11455 (introduced in Section 4.3.2) are shown in the lower panel of Fig. B.10.

Rapid Oscillations in the Solar Atmosphere (ROSA)

The Rapid Oscillations in the Solar Atmosphere instrument (ROSA; Jess et al. 2010) is installed at the Dunn Solar Telescope (see Section 4.1.1) and was specially designed to observe wave phenomena and explosive events in the Sun's lower atmosphere. ROSA was developed at the Queen's University Belfast as a fast and efficient solar imager. Up to six different wavelength bands can be filtered simultaneously, each recorded with an individual high-speed camera. The six CCD cameras have a detector area of 1004×1002 pixel^2 which can be read out up to 30 times per second. To achieve the highest spatial resolution, wavebands in the blue range of the visible spectrum are chosen. The interference filters used for the photospheric imaging (continuum at 417.0 nm, G-band at 430.55 nm) have a broad transmission width of several nanometers (see Table 4.6). The adjusted exposure times are very short (several milliseconds) and allow for high-cadence observations. For the imaging of higher photospheric to chromospheric layers (Ca II K core at 393.37 nm, H_β at 486.1 nm) filters with a narrow transmission width of less than 0.1 nm are selected. Therefore, the exposure time is larger with some hundreds of milliseconds. To approach the diffraction-limited spatial resolution, the observations are performed with the adaptive optics of the telescope. The accumulated images (typically 20–60) for each waveband are calibrated and reconstructed to single frames (see Section B.2). The resulting spatial ($> 0.15''$) and temporal resolutions (> 2 s) are suitable to observe small-scale wave dynamics larger than 100 km. The field of view has a size of $60''$ (alternatively $120''$) with an image scale of around $0.06''$ pixel^{-1} (or $0.12''$ pixel^{-1}). The resulting images of the different cameras have to be co-aligned, the calibration is described in Sections 4.3.1 and B.2. The sunspot of NOAA11823 observed with ROSA is shown in the upper row of Fig. 4.14.

Helioseismic and Magnetic Imager (HMI)

The Helioseismic and Magnetic Imager (HMI; Schou et al. 2012b) and references therein) is a solar spectro-polarimeter onboard the Solar Dynamics Observatory (see Fig. 4.4 in Section 4.1.1). It was designed as a full-disk solar imager and measures intensities, velocities and magnetic fields in the solar photosphere. HMI was built at the Lockheed Martin Solar and Astrophysics Laboratory (LMSAL) and started its continuous operation in 2010. The instrument's telescope has a primary lens with a diameter of 0.14 m (see Table 4.1) and an effective focal length of 4.95 m in complete. HMI observes the photospheric Fe I spectral line at 617.3 nm. With an effective Landé-factor of $g_{\text{eff}} = 2.5$, the absorption line sensitive to the magnetic Zeeman effect. To filter six wavelength positions across the spectral line (6.9 pm spacing), the optical setup consists of a front-window filter (5 nm bandpass), a blocking

filter (0.8 nm), a Lyot filter with a single tunable element and two tunable Michelson interferometers. The first one filters a broad spectral band, the second transmits only a narrow wavelength position. The combined transmission has a width of 7.6 pm leading to a spectral resolution of 81230. To make polarimetric observations, a set of tuning waveplates is integrated. The final spectro-polarimetric signal is divided by a beam splitter and detected by two equal CCD cameras ($4096 \times 4096\,\mathrm{pixel}^2$) every 3.75 s. At the detectors the solar disk has a size of 4.6 cm. The images are recorded with a scale of $0.5''\,\mathrm{pixel}^{-1}$ to approach the spatial resolution of one arc-second. The first camera measures the left and right circular polarization at the six wavelength positions making an overall scan time of 45 s. With this measurements, full-disk solar maps are created for the continuum intensity, Doppler shifts translated into line-of-sight velocities (Dopplergram), and line-of-sight magnetic fields (LOS magnetogram). The second camera measures the full Stokes vector at the same wavelength positions. To increase the polarimetric accuracy, the Stokes vectors are averaged for a time span of 12 minutes. The inversion (see Section 5.3) uses the Zeeman effect to produce full-disk vector magnetograms at the temporal cadence of 12 minutes. The sunspot of NOAA 11823 observed with HMI is shown in Figs. 4.12 and 4.14 (i, m). The corresponding vector magnetic field is displayed in Fig. 5.4. Since the HMI products are publicly available, the data can serve as context information for any co-temporal observation made with other solar telescopes.

Atmospheric Imaging Assembly (AIA)

The Atmospheric Imaging Assembly (AIA; Lemen et al. 2012) is an array of solar imagers mounted to the Solar Dynamics Observatory (see Fig. 4.4 in Section 4.1.1). The instrument was designed at the Lockheed Martin Solar and Astrophysics Laboratory to make continuous observations of the upper solar atmosphere. The scientific aim is to study the dynamics of the Sun's magnetic field and the response of the coronal plasma on scales from seconds to years. The four AIA telescopes simultaneously record full-disk images of the Sun and its vicinity ($41 \times 41\,\mathrm{arcmin}^2$ or 1.3 solar radii) at a cadence of 12 s. Each of the Cassegrain-type telescopes has an effective focal length of 4.1 m, a primary mirror with a diameter of 20 cm, an active secondary mirror, and an own guiding telescope. To study the atmospheric transition region and solar corona by narrow-band imaging, multiple bandpasses in the extreme ultraviolet are filtered by a combination of multilayer coatings and entrance window filters. The transmitted intensities center on various spectral emission lines formed at temperatures from 10^4 K to 10^7 K. The spectral filters of each telescope can be changed by a filter wheel in front of the focal plane. In total, AIA observes the Sun simultaneously in ten wavebands. The corona is sampled by six emission lines produced by transitions in highly-ionized iron atoms (Fe IX at 17.1 nm, Fe XII,XXIV at 19.3 nm, Fe XIV at 21.1 nm, Fe XVI at 33.5 nm, Fe XVIII at 9.4 nm, Fe VIII,XXI at 13.1 nm). The chromosphere and transition region is observed with the He II line at 30.4 nm. The lower solar atmosphere is recorded by two ultraviolet channels at 160.0 nm and 1700 nm. As the same region looks very different across the atmospheric layers, a visible-light channel (450 nm) observing the photospheric continuum was included for context information and co-alignment with other instruments. The internal field of views of the telescope cameras are well-aligned. Each camera has a CCD detector of $4096 \times 4096\,\mathrm{pixel}^2$. To fulfill the spatial resolution of 1.5 arcsec, an image scale of $0.6''\,\mathrm{pixel}^{-1}$ was chosen. The exposure time of the detector depends on the filtered waveband, but typically ranges from 0.5 s to 3 s. The sunspot of NOAA11823 observed with AIA is shown in Fig. 4.14 (k and l).

4.2. Spectral lines for sunspot oscillations

In 1814, the detection of spectral lines in the visible spectrum of the Sun by Joseph von Fraunhofer was the inauguration of the era of solar spectroscopy (as discussed in Section 1). Spectral lines became a powerful tool of atomic diagnostics for the solar atmosphere. The profiles of spectral lines are used to retrieve the physical parameters of the atmosphere, like temperature, gas pressure, plasma motions and magnetic field strength. The ability to filter narrow wavebands across spectral lines yields the possibility to study the solar dynamics at different atmospheric layers. The sampling of the deepest absorption lines allowed to observe solar phenomena from the deep photosphere to the upper chromosphere. Spectroscopic measurement let to the detection of 5 min-oscillations (p-modes) allover the solar surface (Leighton et al. 1962). Chromospheric observations of the Ca II K line core enabled the discovery of sunspot waves (Beckers and Tallant 1969). From that time on, numerous studies have been performed to investigate the oscillatory dynamics in sunspots. In these almost 50 years, various spectral lines and observational settings have been used to examine the atmospheric waves. A list of observed spectral lines in studies of sunspot oscillations is given by Bogdan (2000).

Line formation: A photon is emitted by the atom when an electron changes from a higher energy level to a lower one (see Fig. 4.10). Vice versa, an electron can be lifted to a higher excited state when the absorbed photon has a wavelength corresponding to the energy difference of both levels. Both processes, can also be induced by the collision of an electron with the atom and the transfer of its kinetic energy to the atom. If the Sun would be a black body without an atmosphere it would have a continuous spectrum of radiation without any spectral lines. If the continuous spectrum passes through a layer of cool gas, the atoms of the gas will absorb photons with discrete wavelengths. The energy can be re-emitted in all directions as photons with the same wavelength or with bigger wavelength by a cascade of electron transitions. In any case, if the opaque atmosphere has a lower temperature than its radiating body, the observed intensity at this wavelength is reduced. Consequently, the spectrum yields dark absorption lines. On the other hand, if the gas cloud is very hot, its atoms would even contribute to incident radiation by additional emission of photons. Then, the continuous spectrum yields emission lines. Naturally, a spectrum observed in the hot atmosphere beyond the solar limb exhibits a low continuum intensity interspersed by emission lines. It is obvious that the formation of spectral lines is dominated by the atmospheric parameters and especially the temperature. As shown in Fig. 2.5 a), the atmospheric models for the quiet sun (blue) and sunspot umbrae (red) reveal an odd behavior for the temperature with height. In the photosphere the temperature cools down with height to a temperature minimum at around 500 km above the solar surface. In the chromosphere the temperature starts to increase again up to 10,000 K at a height of around 2000 km. At the same range, the gas pressure and density decrease by more than four orders of magnitude (Fig. 2.5 b). So how do the profiles of photospheric and chromospheric lines look like? The answer is given by the characteristic source function of the spectral line. It is defined as the ratio of the emitted and absorbed radiation by atoms of the local atmosphere. When the source function decreases, less photons are re-emitted and an absorption line forms. In the photosphere, the source function monotonically decreases as it follows the temperature dependent Planck function. Consequently, photospheric spectral lines are all absorption lines. In the chromosphere, the profile of the source function depends on the physical mechanism leading to the atomic transition and the formation of the spectral line. If the line is controlled by radiation (for example Hα), the source function decreases with height and the line is in absorption even if the temperature increases. However, if the formation is controlled by collisions, the source function increases in the chromosphere and the core of the absorption line is in emission. A more detailed description of spectral line formation and the essentials of radiative transfer is given by Rutten (2003).

Inversion: As discussed above, spectral lines harbor the physical parameters of the solar atmosphere. To extract these quantities across the formation region, an inversion to reproduce the spectral line has to be performed. Based on an atmospheric model (see Fig. 2.4) and several free physical parameters of the plasma, the radiative transfer equations are solved and the best solution is adapted.

While for photospheric lines a local thermodynamic equilibrium (LTE) is assumed, in the case of chromospheric lines the statistical equilibrium of each atom and its levels has to be calculated (non-LTE). Automated codes like the Very Fast Inversion of the Stokes Vector (VFISV, see Section 5.3) have been designed to infer the plasma properties from the spectral profiles.

4.2.1. Absorption lines sampling the lower atmosphere

The solar spectrum exhibits many thousands of spectral lines. Altogether, they hint at the chemical composition, structure and dynamics of the solar atmosphere. The sensitivity of the lines to plasma motions, temperatures and magnetic field varies greatly. The task of picking just a few spectral lines to cover a broad range of atmospheric layers from the lower photosphere up to the corona is a difficult one. To select the best lines to investigate the oscillations in intensity, velocity and magnetic field needs experience and instinct. In this section, I will present and characterize the spectral absorption lines used to observe the wave phenomena in the sunspot photosphere and chromosphere. The atomic transitions are illustrated in Fig. 4.10. The spectral lines and some of their characterizing parameters are listed in Table 4.3.

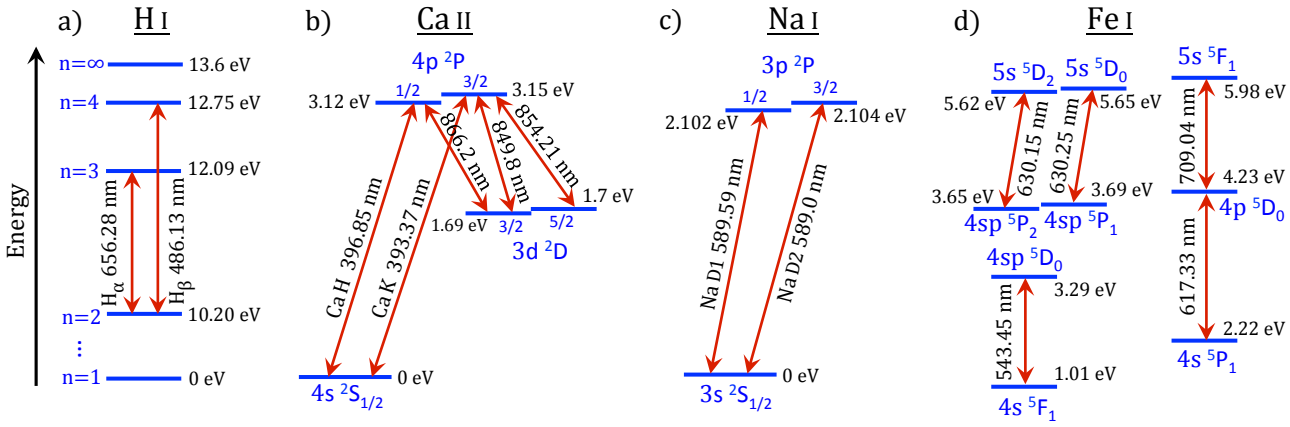

Figure 4.10.: Electron transitions in the a) hydrogen, b) calcium, c) sodium and d) iron atoms. The transitions (red arrows) between two energetic levels (blue) in eV are shown. The corresponding spectral wavelength is indicated. The values were taken from the NIST Atomic Spectra Database (Kramida et al. 2014).

Photosphere

Since the atmospheric temperature and source functions decrease monotonically in the photosphere, all spectral lines formed in this layer are in absorption. The shapes of most photospheric lines resemble the profile of a Voigt function. It is a convolution of the Lorentzian profile caused by the natural broadening[3] and pressure broadening of the transition with the Gaussian profile resulting from the atmospheric Doppler broadening[4]. The spectral width of photospheric lines ($10 - 30\,\mathrm{pm}$) is by far narrower than the width of chromospheric lines. The line depths can also reach large depressions of up to 80% compared to the continuum intensity when the line core is formed in the uppermost photosphere (see Table 4.3).

[3] According to Heisenberg uncertainty principle the uncertainty of energy levels in an atom is related to the lifetime of the excited states. Therefore a shorter lifetime of an atomic transition leads to a larger energy uncertainty and a broader line profile.

[4] The Doppler broadening of spectral lines is cause by the turbulent motion of atoms and molecules during the emittance of photons. The line width depends on the ambient temperature and small-scale motion in the atmosphere.

Table 4.3.: Spectral lines used for the observation of sunspot waves in the lower solar atmosphere. The columns indicate the 1) ion and reference wavelength, 2 and 3) line width and line depth from the Liège atlas, 4) estimated formation height of the line minimum, 5) Landé factor, 6) estimated velocity sensitivity, and 7) the observation run in which the line was employed.

Spectral line Ion, λ_0	**Line width** $\delta\lambda_{\mathrm{FWHM}}$	**Line depth** $A_{\mathrm{core,\,norm}}$	**Height** $z_{\mathrm{core,\,QS}}$ [km]	**Landé** g_{eff}	**V-sensitivity** $\frac{A_{\mathrm{core,\,norm}}}{\delta\lambda_{\mathrm{FWHM}}}\lambda_0$ $[10^4]$	**Obs.** #
H α 656.28 nm	$\simeq$ 130 pm	0.82	1200 – 1800	1.05	(0.41)	2
H β 486.13 nm	$\simeq$ 100 pm	0.85	1000 – 1500	1.0	(0.41)	1
Ca II K 393.37 nm	$\simeq$ 1200 pm	0.95	1000 – 2000	1.17	(0.03)	1
Ca II 854.21 nm	$\simeq$ 200 pm	0.81	1000 – 1400	1.10	(0.35)	1
Na I 589.59 nm	38.0 pm	0.95	700 – 1000	1.33	(1.47)	1
Fe I 630.15 nm	15.0 pm	0.72	$\simeq$ 300	1.67	3.02	1
Fe I 630.25 nm	12.6 pm	0.65	$\simeq$ 200	$(g = 2.49)$	$3.25 \xrightarrow{U} 0.85$	1
Fe I 709.04 nm	13.8 pm	0.51	$\simeq$ 200	0.0	$2.62 \xrightarrow{U} 1.11$	2
Fe I 543.45 nm	17.2 pm	0.86	$\simeq$ 550	0.0	2.72	2
Fe I 617.33 nm	11.0 pm	0.62	$\simeq$ 280	2.5	$3.48 \xrightarrow{U} 1.39$	1, 2
Fe I 1564.85 nm	28.0 pm	0.3	$\simeq$ 100	3.0	$1.68 \xrightarrow{U} 0.65$	– –
Ti I 630.38 nm	11.0 pm	0.08	$\simeq$ 100	0.92	$0.46 \xrightarrow{U} 1.40$	– –

Line selection: Most parts of the photospheric atmosphere are dominated by the gas pressure of the plasma. To retrieve the atmospheric parameters as exact as possible, the spectral line has to feature a very high sensitivity to plasma motions and temperature fluctuations. As it will be discussed in this paragraph, the shape of the spectral line plays an important role for the accuracy of observations of Doppler velocities and intensity fluctuations. In case of sunspot waves, additional consideration has to be given to the magnetic sensitivity of the spectral line. In summary, there is no best spectral line for a comprehensive investigation of sunspot oscillations. Either the observation focusses on one physical parameter, then one single most suitable line can be selected. Or a set of spectral lines with complementary characteristics is chosen to make a simultaneous multi-line observation which can focus on multiple photospheric parameters. As the scientific instrumentation allowed, the latter method was applied in this study of sunspot wave phenomena. In the following, the selection process of the complementary lines is explained.

Naturally, the number of possible spectral lines which can be observed is limited by the available scientific instrumentation. The effective wavelength range of the telescope and instrument defines the observable spectral band. In case of ground-based solar telescopes, the wavelength range is reduced by the Earth's atmosphere to the near-ultraviolet, visible and near-infrared (see Table 4.1). In addition, the working range of the high-resolution Fabry-Pérot spectrometers (Section 4.1.3) limits the effective range to the visible spectrum from around 400 nm to the near infrared at around 860 nm (see Table 4.2). A further exclusion criterion comes from the spectroscopic instrument. The interference filters needed to pre-select the transmitted bandwidth (see Section 4.1.2) are limited in amount and spectral coverage. Therefore, the available spectral lines are in general the most prominent ones. In case of TESOS and IBIS the number of possible lines is still high, so that a criterion for the line selection had to be established.

The first requirement to meet is the comprehensive sampling of the photospheric layer from the solar surface (optical depth unity depending on the wavelength) up to the temperature minimum. This spectral sampling has to be done with a high sensitivity to temperatures and velocities. As the

spectral resolution of the instrument increases with wavelength, often spectral lines in the red part of the visible spectrum or in the infrared are the expedient choice. However, not only the wavelength regime defines the response sensitivity of the spectral line to velocity perturbations. As presented by Cabrera Solana et al. (2005), the response of a photospheric line also depends on the shape of the line. The model is based on the assumption of a constant velocity along the photospheric formation height. As shown in Fig. 2.5 c), this is in good agreement with the sound speed of waves in the photosphere above sunspots. To obtain a rough estimate for the velocity sensitivity of spectral lines, the absorption profile $I(\lambda)$ is approximated by a simple Gaussian

$$I(\lambda) = 1 - A_{\text{core, norm}} \cdot \exp\left[\frac{-(\lambda - \lambda_0)^2}{2(\delta\lambda_{\text{FWHM}})^2}\right] \tag{4.8}$$

normalized to the continuum intensity level with the intensity depression $A_{\text{core, norm}}$ in the core of the line. In this approximation, the line width $\delta\lambda_{\text{FWHM}}$ is described by the full width at half maximum of the profile. The response function RF of the spectral line defines the sensitivity of the Stokes profiles to atmospheric perturbations (Ruiz Cobo and del Toro Iniesta 1994). According to Cabrera Solana et al. (2005), the maximum of the response function for velocity oscillations, RF_{max}, is reached in the line wings. It depends on the shape ratio and position of the spectral line by

$$RF_{\text{max}} \sim \frac{A_{\text{core, norm}}}{\delta\lambda_{\text{FWHM}}} \cdot \lambda_0 \quad . \tag{4.9}$$

Consequently, deep and narrow spectral lines have larger shape ratios. Thus, the shape and the central wavelength λ_0 of the spectral line are equally important for its sensitivity to velocity oscillations. The sensitivity values for various photospheric lines were calculated. The spectral line characteristics (width, depth, and Landé factor) were taken from the Liège spectral atlas of the quiet sun (Delbouille et al. 1973). Therefore, the calculated values represent the sensitivity values of a quiet sun atmosphere. The results for the selected lines are listed in Table 4.3. In the absence of magnetic fields, the narrow Fe I 617.33 nm line has the highest sensitivity to velocities. It is even twice as good as the Fe I line in the infrared at 1564.85 nm. The most sensitive line of this model is the Fe I 524.71 nm line. However, for the observation of sunspot waves, the values are not valid. The umbral atmosphere is a lot cooler than the quiet sun and has a strong magnetic field. Most spectral profiles become less deep compared to the continuum level. In addition, spectral broadening occurs for lines which are sensitive to the Zeeman effect. For most spectral lines the sensitivity to velocity oscillations decreases. In Table 4.3, this effect is shown for an umbral atmosphere with a weak magnetic field. Naturally, lines with a low or zero Landé factor g_{eff} yield a smaller decrease in sensitivity. Comparing the Fe I lines at 630.25 nm ($g = 2.49$) and at 709.04 nm ($g_{\text{eff}} = 0$), the sensitivity factors in an umbra reverse their order. Fe I 617.33 nm still has a higher sensitivity, especially compared to the Fe I 1564.85 nm line. In the last row of Table 4.3, the Ti I 630.38 nm line is listed. In the quiet sun atmosphere, it is very week and has a low sensitivity, but in the umbral atmosphere it becomes deeper and one of the most sensitive spectral lines to observe photospheric velocities. Unfortunately, this line was not available with the employed Fabry-Pérot spectrometers.

The sensitivity of spectral lines to magnetic field and temperature perturbations also differs in a wide range. According to Cabrera Solana et al. (2005), the magnetic field sensitivity $RF^{\text{B}}_{\text{max}}$ depends on several factors and is given by

$$RF^{\text{B}}_{\text{max}} \sim \frac{A^{\text{B}}_{\text{norm}}}{\delta\lambda^{\text{B}}} \cdot g_{\text{eff}}\lambda_0^2 \quad . \tag{4.10}$$

On the one hand, it increases with the effective Landé factor g_{eff}. On the other hand, it is proportional to the square of the central wavelength λ_0 of the line. In addition, the sensitivity also depends on the shape ratio of the Stokes-V signal given by the amplitude $A^{\text{B}}_{\text{norm}}$ and width $\delta\lambda^{\text{B}}$ of the profile lobes.

Consequently, a spectral line with a large Landé factor in the infrared, like Fe I 1564.85 nm, exhibits a high sensitivity to magnetic field oscillations in a sunspot. In the visible solar spectrum, the preferred lines of choice are the Fe I lines at 617.33 nm ($g_{\text{eff}} = 2.5$) and at 525.02 nm ($g_{\text{eff}} = 3.0$). A more detailed description of the computation of spectral line sensitivities to velocity, temperature and magnetic field fluctuations is given by Cabrera Solana et al. (2005). The results for more than twenty photospheric lines are listed and explained.

To summarize the last paragraphs, the sensitivities of the spectral lines vary for the different atmospheric parameters and solar regions in a wide range. After the theoretical calculation of line sensitivities and test observations with numerous lines, a set of five iron lines has been selected to sample the photospheric dynamics above a sunspot with an especially high quality and completion. While the magnetic insensitive Fe I 709.04 nm line samples the lower photosphere, the Fe I 543.45 nm line yields the dynamics in the upper photosphere. In addition, the combination of Fe I lines at 630.15 nm and 630.25 nm yields the information about the middle and lower magnetized photosphere. To perform observations of the magnetic field with a high sensitivity, the Fe I 617.33 nm line was observed for context observations.

Observed Fe I lines: In the following, the observed photospheric lines are characterized. The atomic transitions by which the photospheric lines are formed are shown in Fig. 4.10 d) as red arrows. The energy levels (in blue) are described by the quantum numbers (principal orbital, number of electrons, azimuthal and total angular momentum). The potential energy is given in electron volt. The atomic information was taken from the NIST Atomic Spectra Database (Kramida et al. 2014). It is worth mentioning that the Fe I 709.04 nm and 617.33 nm lines are formed by transitions to or from the same energetic state at 4.23 eV. Therefore, both lines can be formed in a cascade of electron transitions. The widths, strengths and Landé factors of the lines were taken from the Liège atlas (Delbouille et al. 1973) of the solar spectrum. The retrieved values are listed in Table 4.3 and taken to estimate the line sensitivities to velocity oscillations (Eq. 4.9).

Fe I 630.2 nm: The neighboring Fe I lines at 630.15 nm and 630.25 nm are two of the most popular spectral lines for photospheric spectroscopy. As their wavelength separation is very small, they are often observed as a pair (e.g., Lites et al. 1998; Bello González et al. 2005). This yields the advantage that complementary data can be acquired at the same time. Both lines are narrow and deep enough to have a good sensitvity to plasma velocities (see Table 4.3). They complement each other also by their magnetic sensitivity and sampled formation region. While the 630.25 nm ($g = 2.49$, Zeeman triplet) line yields a high response to magnetic fields, the 630.15 nm line ($g_{\text{eff}} = 1.67$) exhibits the higher sensitivity to velocities in the sunspot photosphere. The formation heights of both lines depend on the position within the line and the solar feature. While the wings of the lines are formed in the lower photosphere, the cores are formed higher up in the middle photosphere. The center of the weaker 630.25 nm is formed at an average height of around 200 km, the deeper core of the 630.15 nm is formed at around 300 km above the continuum optical depth unity (e.g., Bruls et al. 1991; Kucera et al. 1998; Bello González et al. 2005; Martínez González et al. 2006). Observations of sunspot oscillations with these lines have been performed for example by Thomas et al. (1984) or (Lites et al. 1998).

Fe I 709.04 nm: This spectral line is a very suitable tool to observe velocity oscillation in the lower photosphere of sunspots. With a Landé factor $g = 0$, the line is insensitive to magnetic fields. The Fe I 709.04 nm line maintains its high sensitivity to plasma velocities even in the strong magnetic field of the umbra (see Table 4.3). The line is formed by an atomic transition between the $5s\,^5F_1$ and $4p\,^5D_0$ level (see Fig. 4.10 d). At the lower state, the transition can be followed by another transition which leads to the Fe I 617.33 nm line. The Fe I 709.04 nm is formed in the lower to middle photosphere. Its line core is formed in a layer around 200 km above the continuum optical depth. Although the line is less often used for sunspot oscillations (e.g., Balthasar et al. 1987, 1998), a combination Fe I 709.04 nm with an upper photospheric line (like Fe I 543.45 nm) yields a very good velocity sampling of the overall photosphere.

Fe I 543.45 nm: Of particular interest for photospheric oscillations in sunspots is the Fe I 543.45 nm line. Its transition is shown in Fig. 4.10 d). As listed in Table 4.3, the line is very deep and has contributions from the entire photosphere. While the outer line wings are formed in the lower photosphere, the inner wings sample the middle photosphere. In the average quiet sun, the line center is formed in the upper photosphere around 550 km above the continuum optical depth unity (e.g., Kucera et al. 1998; Bello González et al. 2010). In the umbral atmosphere the formation height of the line core even rises to 700 km (Bruls et al. 1991). In the umbra, the Fe I 543.45 nm line exhibits contributions of the dominating low-photospheric 5 min oscillations and the increasing 3 min waves toward the chromosphere. An additional advantage of the spectral line for sunspot oscillations is its insensitivity to magnetic fields ($g_{\text{eff}} = 0$). Its high sensitivity to velocity perturbations is decreased only little in the presence of the strong umbral magnetic field. Therefore, the line is widely used for the observation of photospheric waves, especially in the case of sunspots (e.g., Lites 1984; Lites and Thomas 1985).

Fe I 617.33 nm: According to the theoretical response of the spectral line to perturbation, the Fe I 617.33 nm line has a high sensitivity to the photospheric velocities as well as to the magnetic field. This is due to the big shape ratio and high Landé factor ($g_{\text{eff}} = 2.5$) of this narrow line (see Table 4.3). Therefore, Fe I 617.33 nm is highly suitable for modern spectro-polarimetric observations of the solar photosphere. As Fig. 4.10 d) shows, the line is formed by the transition from the same atomic level which is also involved in the formation of Fe I 709.04 nm. While the line wings correspond to the lower photosphere, the core of the line is formed in the middle photosphere at an average height of 280 km above the quiet sun surface. In the umbral atmosphere, the formation height of the core even rises to 380 km above the continuum optical depth (Bruls et al. 1991). Because the Fe I 617.33 nm line provides a very good compromise of sensitvity for different physical parameters and solar regions, it was chosen for the Helioseismic and Magnetic Imager (HMI, see Section 4.1.3) and its continuous spectro-polarimetric observations of the solar photosphere. Also beyond HMI, the line has been chosen frequently to investigate the oscillations in velocity and magnetic field strength of sunspots and pores (e.g., Staude and Horn 1997; Stangalini et al. 2012; Sobotka et al. 2013).

Beyond the set of selected photospheric lines, there are of course further spectral lines which are highly suitable for the research of sunspot oscillations. As discussed in this section and also by Cabrera Solana et al. (2005), the Ti I 630.38 nm is very sensitive to velocities in the lower umbral photosphere (Lites and Thomas 1985; Lites et al. 1998). The same holds for the Fe I lines at 569.15 nm. A good complementary study of the physical parameters across the photosphere can also be achieved by the Fe I lines at 524.71 nm or 525.02 nm. The Fe I line at 557.61 nm yield a high response to temperature fluctuation in the middle photosphere at a zero Landé factor. The exploration of small-scale magnetic field fluctuations in the deep umbral photosphere is very ambitious and requires a high spatial, temporal and spectral resolution. In terms of magnetic sensitivity, the Fe I line at 1564.85 nm would be best suited (Bellot Rubio et al. 2000).

Chromosphere

Above the photosphere, the solar chromosphere reaches an atmospheric height of around 2000 km. Since chromospheric lines show a very strong intensity depression and a broad width compared to the photospheric lines, they were easily identified and labeled in the first Fraunhofer spectrum (see Fig. 1.1). As discussed at the beginning of this section, the line formation and shape of the profile depend chiefly on the atmospheric temperature and the dominating transition mechanism. As indicated in Fig. 2.5, the chromosphere reveals an increase in temperature (by several thousand Kelvin) and a strong decrease in gas pressure and density from the lower to the upper boundary. When the core of a spectral line is formed in the hotter middle to upper chromosphere, the absorption profile can reverse in the central core to one or several emission peaks (e.g., in Ca II H and K). It is obvious that the profiles of most chromospheric lines cannot be approximated by a simple Gaussian function (Eq. 4.8). In addition, in most cases a line bend from the outer to the inner wings of the line indicates the transition from photospheric to chromospheric heights. The assumption of uniform velocities across the whole

photospheric and chromospheric formation layers does not hold anymore. A perturbation in form of an acoustic wave would speed up toward the upper chromosphere because the sound speed increases (see Fig. 2.5 c). Therefore, the line selection criterion (Eq. 4.9) of photospheric lines can not be applied to chromospheric lines. The selection of chromospheric lines for this study was easy. In the wavelength range of the telescopes and instruments from 400 nm to 860 nm (see Table 4.2) only a few spectral lines have contributions from the chromosphere. These lines are all well studied and characterized. The chromospheric lines extensively used for wave observations are Hα (H I 656.28 nm), the extremely broad Ca II H and K lines at 393.37 nm and 396.85 nm, and the Ca II triplet in the infrared (849.8 nm, 854.21 nm, 866.2 nm), as well as He II 30.4 nm in the extreme ultraviolet and He I 1083.0 nm in the infrared. The strong Hβ line (H I 486.13 nm) and the narrower Na I D1 and D2 lines (Na I at 589.59 nm and 589.0 nm) are less often used, but yield a great capability for the investigation of sunspot oscillation at chromospheric heights (Bogdan 2000). The corresponding atomic transitions are illustrated in Fig. 4.10. The spectral range of the Fabry-Pérot spectrometers and available interference filters limit the number of available spectral lines. The chosen chromospheric lines and their characterizing parameters are listed in Table 4.3. The width of the chromospheric lines (0.1 – 1 nm) exceeds the width of the photospheric lines by far. The line depression in the cores reach values of up to 95% of the continuum intensity level. Therefore, often a longer exposure time has to be selected for the spectroscopic scanning of the line. The sensitivity of the lines to velocities in the quiet sun atmosphere was calculated by Eq. 4.9 and is given only for comparison (in brackets). For the observation of chromospheric waves, intensity oscillations are often more important and easier to measure than the oscillating velocities. A high temperature sensitivity of the line increases the quality of shock wave measurements. Therefore, a set of three chromospheric line has been selected for the spectroscopic observations with the Fabry-Pérot instruments. To achieve a complementary sampling of the chromospheric layer, the H α, Ca II 854.21 nm and Na I 589.59 nm lines were chosen (see formation heights in Table 4.3). In addition, fast chromospheric imaging has been performed at the line cores of Ca II K and Hβ.

Hα 656.28 nm: The Hα line is one of the most interesting and noticeable lines of the visible solar spectrum. As illustrated in Fig. 4.10 a), it is formed by the transition between the third and second energy level of the neutral hydrogen atom. Like Hβ, it belongs to the Balmer series. In the 1950's, first observations of the chromospheric layers were performed with Lyot filters within narrow spectral bands in Hα. Till today, Hα is the prime spectral line for investigations of the chromospheric dynamics. In sunspot regions, imaging spectroscopy in the line core and wings features beautiful observations at high resolution of the elongated filaments, the forest-like appearance of small fibrils, as well as umbral flashes and running penumbral waves. The formation of Hα is controlled by radiation, also in the high chromospheric layers. Therefore, the source function is decoupled from the Planck function and decreases with height. Consequently, the line is in absorption even in the deep core which is formed in the hot upper chromosphere. While the line wings of the spectral profile are formed in the photosphere, the line center has contribution mainly from the upper half of the chromosphere. The average formation altitude ranges between 1200 km and 1800 km above the solar surface (e.g., Vernazza et al. 1981; Leenaarts et al. 2012).Hα is a very broad ($\simeq$ 130 pm) and deep line with a low sensitivity to magnetic fields ($g_{\rm eff}$ = 1.05) and Doppler velocities (assuming Eq. 4.9). On the other hand the spectral line exhibits a good temperature response and was therefore used in many studies of sunspot waves. Intensity fluctuations revealed characteristics of running penumbral waves (Jess et al. 2013; Yurchyshyn et al. 2015), umbral oscillations (Tziotziou et al. 2007; Jess et al. 2012; Kobanov et al. 2013a) and umbral fine structures (Yurchyshyn et al. 2014).

Hβ 486.13 nm: The second spectral line of the Balmer series of neutral hydrogen is called Hβ. As shown in Fig. 4.10 a), the line is formed by the electron transition between the fourth and second energetic state of the atom. The spectral line was less used than the Hα line, although both lines are very similar (see Table 4.3). In fact, Hβ is even a bit narrower ($\simeq$ 100 pm) and deeper, but has a smaller wavelength. According to Eq. 4.9, this would result in the same sensitivity to velocity oscillations. The effective Landé factor is $g_{\rm eff}$ = 1.0. When the center of the line is filtered in a broad band (including

the inner wings), the solar image exhibits a mixture of photospheric and chromospheric structures. Like in the case of Hα, the line wings of Hβ have a photospheric origin. The line core is formed in the middle chromosphere (1000 – 1500 km). The imaging of the sunspot atmosphere in Hβ yields a high capability to study sunspot oscillation and especially running penumbral waves (Kobanov 2000; Federspiel and Mattig 1993)

Ca II K 393.37 nm: The strong absorption lines of single ionized calcium at central wavelength of 393.37 nm and 396.85 nm were labeled as the Fraunhofer K and H line. They are the deepest and widest lines in the visible spectrum of the Sun and have contribution from the whole lower atmosphere. Both lines were used for the first chromospheric observations by Hale at the beginning of the 20th century. As illustrated in Fig. 4.10 b), the atomic transitions by which Ca II K and H are formed are closely related. They share the same lower energetic level, the ground state $4s\,^2S_{1/2}$ of Ca II. The upper level of the transition ($4p\,^2P$) differs only by their total angular momentum. As Fig. 4.10 b) shows the lines are also coupled to the infrared triplet. Ca II K was selected for the observations. The line has a central wavelength of 393.37 nm and a width of around 1.2 nm. The broad absorption wings (K_1) are covered by narrower absorption lines. The line formation of Ca II K and H is controlled by collisions. Due to the temperature increase in the chromosphere, the amount of emitted photons increases and therefore also the source function rises. The deep core of Ca II K (5% of the continuum intensity) which is formed in the hot upper chromosphere can be reversed in intensity and exhibits two emission peaks. The central minimum was named K_3, the two adjacent maxima are called K_2. As discussed by Vernazza et al. (1981) and (Mein and Mein 1980), the core at K_3 is formed at an altitude of around 1600 km to 2000 km. The emission peaks K_2 have their main contribution from the middle chromosphere at 800 km to 1400 km. The very broad absorption wings (K_1) have major contributions from the photosphere and to a large fraction from a formation altitude of around 500 km. As it can be inferred from the low shape ratio and the Landé factor ($g_{\text{eff}} = 1.17$), the sensitivity of the line to plasma velocities and magnetic field is very low. On the other hand, the line core is very sensitive to temperature fluctuations. In case of shock waves in sunspots, temperature excesses show up as strong intensity fluctuations. Therefore, the first observations of chromospheric sunspot waves were performed in the line core of Ca II K (Beckers and Tallant 1969). Especially the blue K_2 emission has been used for numerous investigations of umbral flashes, running penumbral waves and so-called Ca II K bright grains (e.g., Kneer et al. 1981; Uexkuell et al. 1983; Thomas et al. 1984; Carlsson and Stein 1997; Rouppe van der Voort et al. 2003). To measure the very dynamical events in the average chromosphere, fast broad-band imaging was performed in a broad spectral band (0.1 nm) in the line core including K_2 and K_3.

Ca II 854.21 nm: The spectral line is a very promising diagnostic tool to study the dynamics of the solar chromosphere. It is a strong absorption line at 854.21 nm formed by the transition between the upper $4p\,^2P_{3/2}$ level and lower metastable $3d\,^2D_{5/2}$ level of singly ionized calcium. As illustrated in Fig. 4.10 b), it has the same upper energy level as the Ca II K line and the infrared line at 849.8 nm. The calcium infrared triplet is completed by the 866.2 nm line. It is obvious that the attributes and observations of the calcium infrared triplet lines resemble each other. As discussed by Cauzzi et al. (2008), most photons in the infrared triplet result from excitation in the Ca II H and K lines. As the formation of the calcium lines is dominated by collisions, the lines feature a high sensitivity to the local temperature.

The characteristics of the Ca II line at 854.21 nm are taken from the Liège atlas (Delbouille et al. 1973) and listed in Table 4.3. In Fig. 4.11 b), the line profile (solid curve) and atmospheric contribution in km (grayscale) are shown for the quiet sun. The broad outer absorption wings of Ca II 854.21 nm are formed in the lower photosphere and dominate the overall line shape (width $\delta\lambda_{\text{FWHM}} \simeq 0.2$ nm). The line bend at around 35 pm from the line minimum position indicates the transition from the photosphere to the chromosphere. The core of Ca II 854.21 nm is deep (19% of the continuum intensity) and originates in the middle chromosphere at an average altitude of 1000 km to 1400 km above the surface (e.g., Cauzzi et al. 2008; Uitenbroek 2006). The local contribution height differs for convective and magnetic

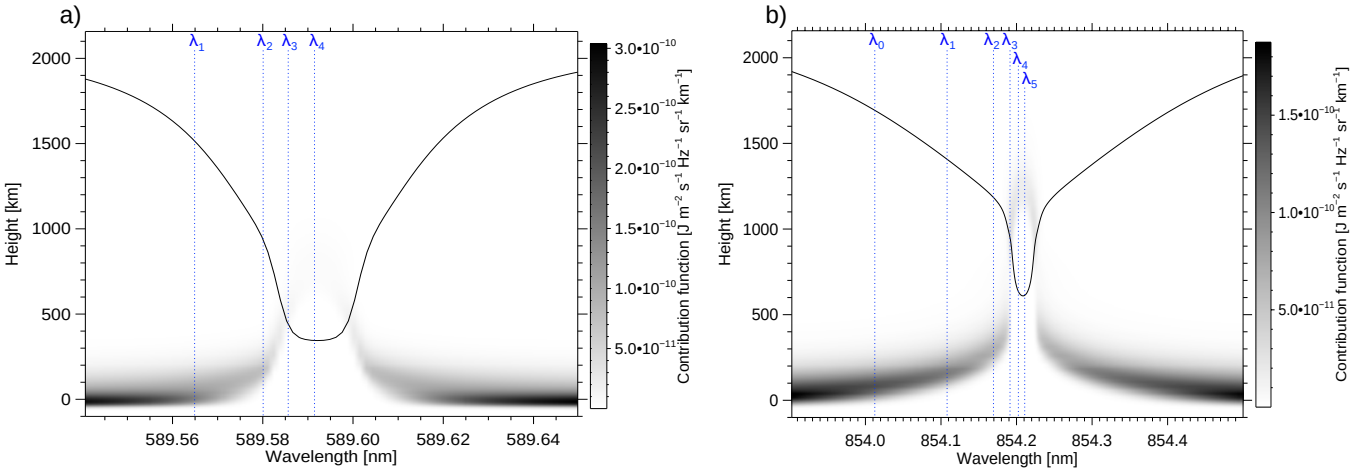

Figure 4.11.: Contribution functions of the chromospheric spectral lines. Panel a): Na I D_1 at 589.6 nm (Uitenbroek 2006); Panel b): Ca II at 854.2 nm (Cauzzi et al. 2008). The contributing heights (in km) are plotted in gray-scale against the wavelength (in nm). The functions were computed using a plane-parallel, hydrostatic, atmosphere of the quiet sun (Fontenla et al. 1993). The height zero levels corresponds to the optical depths $\tau = 1$ at the given wavelength. The solid black curves are the spectral line profiles plotted for context information at an arbitrary scale. The blue dotted lines indicate the wavelength positions λ selected for the observations.

features (Leenaarts et al. 2009). The response of the line depends on the kind of physical perturbation. While the response to temperature fluctuations peaks at an altitude of 1100 km, for velocity fluctuation the height is reached at around 1300 km (Mein and Mein 1980). In addition, the formation altitude depends on the frequency of the oscillating perturbation. When umbral waves propagate upward in the sunspot atmosphere, they steepen and form shock fronts which cause temperature rises and super-sonic velocities. In the chromospheric line core and inner wings, the intensities are especially sensitive to the hot shock waves. During their passage, the line core can go into bright emission. The sensitivity to chromospheric velocities is better compared to other chromospheric lines. The same holds for the response to magnetic fields ($g_{\rm eff} = 1.1$) in the relatively narrow line core. Therefore, Ca II 854.21 nm has become the most widely used spectral line to study umbral flashes in the sunspot chromosphere (e.g., Kneer et al. 1981; Lites 1984; Socas-Navarro et al. 2000; Tziotziou et al. 2007; Kobanov et al. 2013a; de la Cruz Rodríguez et al. 2013; Sobotka et al. 2013).

Na I 589.59 nm: The deep absorption lines at 589.59 nm and 589.0 nm are formed in neutral sodium and were labeled as the Fraunhofer D1 and D2 lines. The energetic transitions giving rise to the spectral lines are shown in Fig. 4.10 c). The Na I D1 line forms between the energetic ground state $3s^2S_{1/2}$ and the upper $3p^2P_{1/2}$ level. The upper energetic level of Na I D2 only differs by its total angular momentum. The characteristics of both spectral lines resemble each other. As the profile of Na I 589.59 nm (D1) is less influenced by line blends, it was chosen for the observations. In Fig. 4.11 a), the line profile (solid line) and atmospheric contribution (grayscale) are shown. The spectral line is very deep with an intensity at line center of only 5% of the continuum intensity. Compared to other chromospheric lines (see Table 4.3), the line width $\delta\lambda_{\rm FWHM} \simeq 38$ pm is rather small. Under the approximation of Eqs. 4.8 and 4.9, the sensitivity of the line core and wings to velocity oscillations is very good. As shown in Fig. 4.11 a), the outer wings of Na I D1 have their major contributions from the lower photosphere. The line bend at around 10 pm from the line minimum position indicates the transition from the photosphere to the chromosphere. The formation height rises for the line core. The deepest line core originates in the lower chromosphere at average altitudes around 700 km to 1000 km above the quiet sun surface (e.g., Schleicher 1976; Uitenbroek 2006). While the response

of the line center to velocity oscillations peaks at 850 km, the response to temperature fluctuations does not exceed the photosphere (Eibe et al. 2001). In addition, line formation altitude can vary for different convective and magnetic features Leenaarts et al. (2010). The sensitivity of Na I D1 to temperatures and magnetic fields ($g_{\text{eff}} = 1.33$) is moderate. Therefore, the line was less used than other lines to study waves in sunspots (e.g., Kneer et al. 1981; Uexkuell et al. 1983; Sigwarth and Mattig 1997). However, an observation of velocity oscillation across the Na I 589.59 nm line in combination with the intensity fluctuation across the temperature sensitive Ca II 854.21 nm or Ca II K lines would yield a complementary investigation of shock waves in the lower sunspot atmosphere. Exactly this observational combination (see Section 4.3.1) establishes the basis of this work.

4.2.2. Emission lines of the transition region and corona

The effective temperature in the solar transition region and corona increases to several hundred thousand degrees. In the corona above active regions it can even rise to several million degrees. The atoms are highly ionized and emit photons with a high energy. Spectral lines of the hot upper solar atmosphere are predominantly in the ultraviolet, extreme ultraviolet and soft X-ray range. As these wavelength ranges are shielded by the Earth's atmosphere, the observations have to be performed from space. Satellites with solar telescopes, like the Atmospheric Imaging Assembly (AIA; Lemen et al. 2012) aboard the Solar Dynamics Observatory (see Fig. 4.4) are used to study the dynamics of the coronal plasma and its response to the Sun's magnetic field.

Contrary to the absorption lines of the lower solar atmosphere, spectral lines of the hot transition region and corona are all in emission. With increasing temperature, the source functions of the lines grow with the formation altitude. The emission maximum at line center corresponds to the hottest and uppermost atmospheric layer. More information on the formation of coronal lines is given by Rutten (2003). In the following, the used spectral emission lines are introduced. As discussed in Section 4.1.3, the Atmospheric Imaging Assembly provides a set of ten wavebands to observe the solar dynamics from the photosphere to the corona. Four of them were chosen to investigate the sunspot waves in the chromosphere, transition region and corona (see Table 4.4). The spectral information was retrieved from laboratory measurements and provided by the atomic database for emission lines, CHIANTI (Dere et al. 1997; Landi et al. 2012).

Table 4.4.: Spectral lines used for the observation of sunspot waves in the upper solar atmosphere (TR: transition region).

Wavelength	Primary ion	Formation region	Temperature	Transition levels	Obs.
160.0 nm	C IV & Cont.	TR, photosphere	$\simeq 10^5$ K	$2s^2S_{1/2} - 2p^2P_{1/2,3/2}$	1
30.4 nm	He II	chromosphere, TR	$\simeq 5 \cdot 10^4$ K	$1s^2S_{1/2} - 2p^2P_{1/2,3/2}$	
17.1 nm	Fe IX	corona, upper TR	$\simeq 6 \cdot 10^5$ K	$3p^6\,{}^1S_0 - 3p^5\,3d\,{}^1P_1$	
21.1 nm	Fe XIV	active-region corona	$\simeq 2 \cdot 10^6$ K	$3p^2P_{1/2} - 3d^2D_{3/2}$	

C IV 154.82 nm: The broad 160.0 nm waveband includes a large fraction of continuum intensity, but also the strong emission lines from the threefold ionized C IV at 154.82 nm and 155.08 nm. While the continuum is formed in the cool photosphere, the C IV lines are formed at temperatures around 10^5 K in the transition region.

He II 30.38 nm: The 30.4 nm waveband in the extreme ultraviolet is dominated by the very strong He II emission line at 30.38 nm. The doublet is formed at characteristic temperatures around $5 \cdot 10^4$ K. The line is very sensitive to temperature fluctuations in the chromosphere and transition region.

Fe IX 17.11 nm: The 17.1 nm waveband harbors the eightfold ionized Fe IX emission line at 17.11 nm. The line is represents the upper transition region and corona at characteristic temperatures around $6 \cdot 10^5$ K.

Fe XIV 21.13 nm: The 21.1 nm waveband is dominated by the strong emission line of the thirteen-fold ionized Fe XIV at 21.13 nm. The line is formed at a characteristic temperature around $2 \cdot 10^6$ K which is reached only in the active region corona or in the presence of flares.

All lines exhibit a high sensitivity to temperature and intensity fluctuations. Therefore, imaging spectroscopy in a waveband centered at the line maximum is a valid method to investigate the visual sunspot waves in the upper solar atmosphere. In this sense, several studies on sunspot waves are based on the continuous AIA observations (e.g., Reznikova and Shibasaki 2012; Kobanov et al. 2013b; Freij et al. 2014).

4.3. Observations

This section introduces the sunspot observations which are the foundation of this thesis. They base on the experimental devices and spectroscopic techniques which were introduced in the previous sections. In the following Sections 4.3.1 and 4.3.2, the two major observation runs are described and the obtained data are presented. The first observation run was performed to investigate a fully developed sunspot close to disk center at high temporal and spatial resolution. The aim is to determine the oscillatory behavior in multiple atmospheric layers by a broad sample of photospheric to coronal lines. The second observation focuses on waves in the photosphere above a more inhomogeneous sunspot with several umbrae and a developing penumbra.

4.3.1. Observation 1: NOAA11823 – Regular sunspot

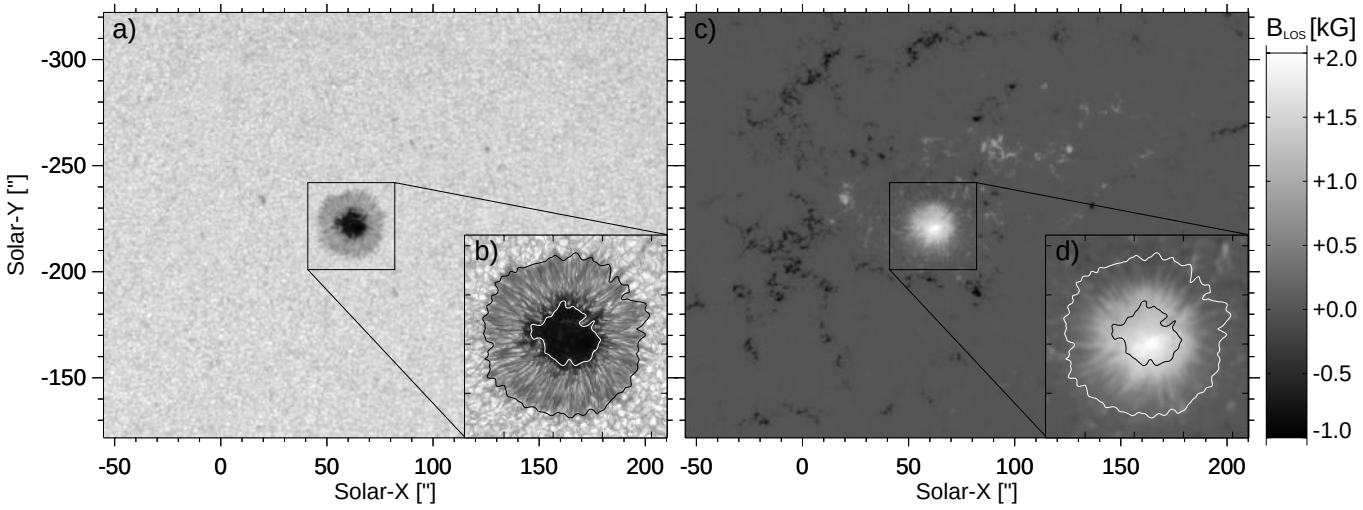

Figure 4.12.: NOAA11823 in continuum intensity (left panels) and line-of-sight magnetic field strength (right panels) on August 21st 2013 at 15:00:45UTC as observed by HMI (a, c, d) and ROSA (b). The black squares mark the analyzed region. The contours in panels b) and d) indicating the sunspot's inner and outer penumbral boundary retrieved from HMI continuum intensity. The HMI magnetogram is scaled from −1 kG (black) to 2 kG (white). Image from Löhner-Böttcher and Bello González (2015).

Observing program

The prime observation of this thesis was carried out on August 21st 2013 at the Dunn Solar Telescope (Fig. 4.1, Table 4.1) at the National Solar Observatory in New Mexico. The active region NOAA11823 is shown in Fig. 4.12 in continuum intensity (left panels) and line-of-sight magnetic field strength (right

panels). The small bipolar group of spots is dominated by a leading sunspot with a strong magnetic field ($\leq +2200$ Gauss) in the dark umbral core and a fully-developed circular penumbra. Several small decaying pores surround the sunspot at a distance of more than $30''$. The region is classified as a *Cso* - group (McIntosh 1990). The main sunspot was very stable during the observation period from 14:50 UTC to 15:53 UTC. The reduced, analyzed region has a dimension of $(50'')^2$, and is highlighted and enlarged (panels b and d) in Fig. 4.12. The sunspot is located close to disk center at heliographic coordinates $(X, Y) \simeq (63'', -222'')$. The position corresponds to a heliocentric angle $\theta = 14°$. With a center latitude of $B_0 = 6.9°$ and a declination $P_0 = 18.2°$ of the solar rotation axis, the heliographic position of the umbral center amounts to 6.7° S and 3.8° W. The vertical magnetic field of the umbra is unipolar and directs almost in the line-of-sight. For this angle of incidence, the spatial displacement Δx over an altitudinal difference $\Delta h = 1$ Mm calculates to $\Delta x = \Delta h \cdot \tan\theta = 0.25$ Mm (or $0.34''$). This displacement is of the order of the spatial resolution and can be neglected in the analysis. The umbral area (inner contour) has a size of 92 Mm^2 and an average radius of around 5.1 Mm, just slightly smaller than the Earth's radius. The circular penumbra has a filamentary structure and yields a radially decreasing magnetic field strength in the line-of-sight. The penumbral boundaries in intensity are indicated by the contours in Fig. 4.12. The sunspot has an average diameter of 24 Mm. The observational information is summarized in Table 4.5.

As listed in Table 4.5, the sunspot was observed simultaneously with four different spectroscopic instruments in various spectral settings (detailed in Table 4.6). The observations at the Dunn Solar Telescope started at 14:53UTC and lasted 58 min for the Interferometric Bidimensional Spectrometer (IBIS), and 54 min for the Rapid Oscillations in the Solar Atmosphere (ROSA) broad-band imager. Both instruments were explicitly introduced in Section 4.1.3. During this almost one hour observation run, the atmospheric conditions were excellent and very stable. This is a crucial demand for ground-based solar observations. The very good atmospheric seeing is described by the average Fried parameter $r_0 \simeq 25$ cm. This effective telescope aperture allows an average spatial resolution of $0.5''$ for the non-reconstructed IBIS data. This corresponds to resolved solar features which are as small as 400 km. It is most illustrative to compare the angular resolution of the telescope with scales on Earth. If it would be possible to point the telescope at Sacramento Peak toward Freiburg with the same atmospheric conditions, one could resolve the tower of the Minster. In case of the reconstructed ROSA data, the spatial resolution even approaches $0.2''$, which makes it possible to distinguish structures as small as 150 km on the Sun's surface. By comparison, pointing the DST to New York would allow to resolve the head and torch of the Statue of Liberty. In addition to IBIS and ROSA at the DST, the instruments HMI and AIA (both described in Section 4.1.3) aboard the Solar Dynamics Observatory (see Fig. 4.4) performed continuous observations. The acquired data cover the temporal span of the DST observations (see Table 4.5). Of course, the performance of the space telescope HMI (and AIA) does not suffer from atmospheric turbulences. Therefore the instruments are able to work close to the diffraction limit. According to the aperture of 14 cm (and 20 cm), the effective spatial resolution of solar structures is stable at $1''$ (and $1.5''$). Due to the Earth orbit, the spatial scale oscillates slightly around $0.505'' \,\mathrm{px}^{-1}$ (and $0.6'' \,\mathrm{px}^{-1}$).

As indicated in Table 4.5, the observations were performed in different instrumental modes. On the one hand, IBIS was operated as a narrow-band spectrometer to perform fast scans of multiple spectral lines. On the other hand, HMI made spectro-polarimetric line scans of one single line. In addition, the instruments ROSA and AIA carried out their fast observations within single broad wavebands centered at the spectral line cores. However, all instruments have in common, that they record two-dimensional images at defined wavelength positions within a short instant of time. The functionality of the imaging spectrometers is described in Sections 4.1.2 and 4.1.3. The next paragraphs report on the spectroscopic settings and spectral lines of this observation run. The settings are summarized in Table 4.6. The characteristics of spectral lines and their selection criteria were detailed in Section 4.2 and listed in Table 4.3.

Table 4.5.: Basic information on observation run 1.

Observation	**1**			
Date	21. August 2013			
Active region	NOAA 11823			
Classification	Cso: Main spot with penumbra, four small decaying pores at large distance			
Sunspot	Unipolar, full circular penumbra			
Position	6.7°S , 3.8°W			
Heliocent. angle	$\theta = 14°$, $\mu = 0.97$			
Size umbra	$92\,\mathrm{Mm}^2$			
Radius umbra	$\simeq 7''$			
Radius spot	$\simeq 16''$			
Field of view	$(50'')^2$			
Evolution	$< 1\%$			
Sunspot cycle	Middle			
Instrument	**IBIS**	**ROSA**	**HMI**	**AIA**
Telescope	DST	DST	HMI/SDO	AIA/SDO
Start (UTC)	14:53:41	14:53:08	14:50:21	14:50:08
Duration Δt_{obs}	58 min	54 min	62 min	62 min
Seeing r_0	$\simeq 25$ cm	$\simeq 25$ cm	(14 cm)	(20 cm)
Resolution	$\simeq 0.5''$	$\simeq 0.2''$	$1''$	$1.5''$
Observ. mode	Spectroscopic	Band imaging	Polarimetric	Band imaging
Spectral lines	Fe I 630.15 nm	Cont. 417.0 nm	Fe I 617.33 nm	C IV+C. 160.0 nm
(→ Table 4.6)	Fe I 630.25 nm	G-band 430.55 nm		He II 30.4 nm
	Na I 589.59 nm	Ca II K 393.37 nm		Fe IX 17.1 nm
	Ca II 854.21 nm	Hβ 486.13 nm		Fe XIV 21.1 nm

Table 4.6.: Spectral settings of observation run 1.

	Spectral lines Ion, λ_0 [nm]	**#λ_{pos}**	**$\Delta\lambda_{\mathrm{pos}}$** [pm]	**$\delta\lambda$** [pm]	**Cadence** dt [s]	**t_{exp}** [ms]	**Scale** [″/px]	**SNR** $\mathrm{U_{core}} - \mathrm{QS_{cont}}$
IBIS	Fe I 630.15	12	4.0	2.2	13.232	35	0.098	$31 - 358$
	Fe I 630.25	11	4.0	2.2				$51 - 416$
	Na I 589.59	10	6.0	2.4				$10 - 502$
	Ca II 854.21	11	9.0	4.3				$36 - 238$
ROSA	Cont. 417.00	1	–	5200	2.123	10	0.059	$10^3 - 10^4$
	G-band 430.55	1	–	920	2.123	15	0.059	
	Ca II K 393.37	1	–	100	5.786	120	0.117	
	Hβ 486.13	1	–	21	13.850	250	0.117	
HMI	Fe I 617.33	6	6.9	7.6	45	150	0.505	400
AIA	C IV+C. 160.0	1	–	15k	24	2900	0.6	> 100
	He II 30.4	1	–	1000	12			
	Fe IX 17.1	1	–	300	12			
	Fe XIV 21.1	1	–	700	12			

IBIS: Quasi-simultaneous observations were performed with the Interferometric Bidimensional Spectrometer (see Section 4.1.3) in the visible to near-infrared spectral range. Four solar absorption lines were scanned cyclically in a purely spectroscopic mode. The continuum intensity was recorded simultaneously at 680 nm. The combination of the Fe I lines at 630.15 nm and 630.25 nm (lower to middle photosphere) with the Na I D1 line at 589.59 nm and the Ca II line at 854.21 nm (lower to middle chromosphere, see Fig. 4.11) yields a complementary sampling of the lower solar atmosphere. As discussed in Section 4.2, the Fe I 630.15 nm (and Na I D1) line have a high sensitivity to velocity fluctuations in the lower (and upper) photosphere. The Ca II line exhibits a very high temperature sensitivity and therefore acts as a perfect tracer of shock waves in the chromosphere. Each spectral line was sampled successively at about 10 to 12 narrow wavelength positions with a combination of interference filters and Fabry-Pérot interferometers (see Sections 4.1.2). The transmission width $\delta\lambda$ depends on the wavelength and amounts to 2.2 pm to 4.3 pm (see Fig. 4.9). The spectral intensity profile (black curve) and filtered wavelength positions (blue asterisks) are shown in Fig. 4.13. Whereas the narrow Fe I lines are scanned with an equidistant step width of 4.0 pm, the Na I D1 line has a fine equidistant sampling of 6.0 pm in the deep core and a non-equidistant gauging in the outer wings. The same holds for the broad Ca II line, the chromospheric core is scanned with equidistant steps of 9.0 pm width while the outer photospheric wings are scanned in a less dense sampling. By this, the highest atmospheric formation layers of each line experience the best probe. The exposure time for each position was fixed to 35 ms. With a recording rate of six frames per second and the time needed to switch the filters on the filter wheel, the temporal cadence for the full multi-wavelength scan adds up to an average value of 13.232 s. With this high temporal resolution, it is possible to analyze high-frequency waves with

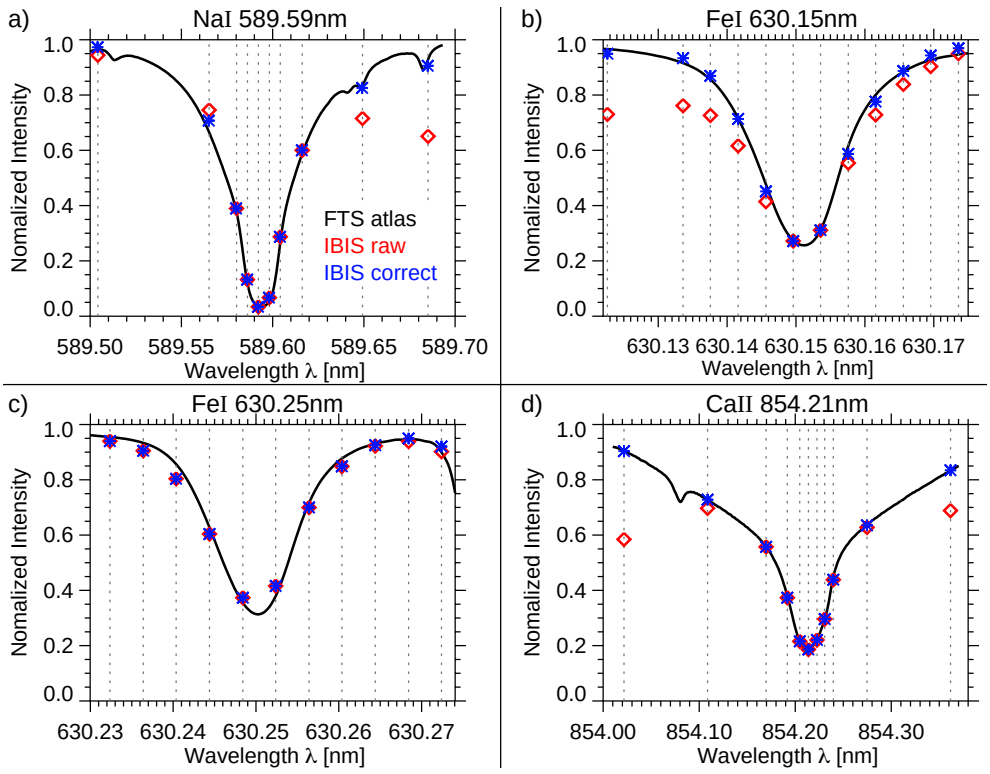

Figure 4.13.: Spectral sampling of the absorption lines with IBIS. The normalized intensities are plotted against the wavelength λ in nm. The selected wavelength positions are indicated by the dotted vertical lines. The average intensity is shown before (red squares) and after (blue asterisks) the correction of the pre-filter transmission. The line profile from the FTS atlas (black curve) serves as context.

smallest periods as small as 26.5 s, according to the Nyquist frequency. The circular field of view has a diameter of 95″ with a pixel scale of 0.098″ px^{-1}. For the overall analysis, the field of view was reduced to a quadratic region of interest with a side length of 50″. The sunspot at the four line core positions is shown in the middle row of Fig. 4.14.

ROSA: Observations were carried out with the broad-band imaging instrument ROSA (see Section 4.1.3) in the blue part of the visible spectrum. Co-temporally with IBIS, the instrument performed observations in four spectral bands (see Table 4.6), each recorded with an own fast camera. One band is centered in the blue continuum around 417.0 nm and has a width of $\delta\lambda = 5.2$ nm. Another band (0.92 nm) is set to the G-band around 430.55 nm. The transmitted intensity of both channels comes from the low photosphere and enables short exposure times of 10 ms to 15 ms. The fast cameras have an image scale of 0.059″ px^{-1} for a chip size of 1004×1002 px and record 30.3 frames per second. The post-observational reconstruction of every 64 consecutive images makes a final cadence of 2.123 s for the blue continuum and the G-band. In addition, two narrower bandpasses (100 pm and 21 pm) are centered on the chromospheric cores of the Ca II K line at 393.37 nm and the Hβ line at 486.13 nm. Consequently, longer exposure times had to be applied. For the Ca II K camera, an integration time of 120 ms was chosen. This leads to a frame rate of 6.22 s^{-1}. One reconstructed image was obtained from 32 consecutive images. This gives a temporal cadence of 5.786 s. For the Hβ camera an exposure time of 250 ms was selected to perform the observation at a rate of 2.63 s^{-1}. Every reconstruction was made from a sequence of 32 consecutive images, giving a final cadence of 13.85 s. The cameras of both channels have an image scale of 0.117″ px^{-1} for a chip size of 512×512 px. The ROSA data are intended to observe the sunspot dynamics at the highest temporal and spatial resolution. The effective spatial resolution of the reconstructed data can reach values down to 0.2″. As discussed in Section 4.2, the chromospheric core of Ca II K is very sensitive to the atmospheric temperature fluctuation induced by propagating waves. Moreover, Hβ turns out to be a very fine tracer of running penumbral waves. To fit the IBIS observation, the circular field of view was reduced to a quadratic region of interest with a side length of 50″. The sunspot in the four bandpasses is shown in the upper row of Fig. 4.14.

HMI: The Helioseismic and Magnetic Imager aboard SDO (see Section 4.1.3 and Fig. 4.4) performs continuous spectro-polarimetric observations of the full solar disk. The Fe I line at 617.33 nm (see Table 4.3) is sampled at six equidistant wavelength positions with a step width of 6.9 pm. The transmission width centered on the wavelength positions is 7.6 pm. The HMI cameras have detector chips with 4096×4096 px and an average image scale of 0.505″ px^{-1}. The integration time at each wavelength position and polarimetric state amounts to 150 ms. The science-ready data products of HMI and AIA are provided by the Joint Science Operations Center on the JSOC webpage. The fully calibrated solar disk maps in continuum intensity, Doppler velocity, and line-of-sight magnetic field strengths have a temporal cadence of 45 s. The full-disk vector magnetograms (see Fig.5.4) are provided with a temporal cadence of 12 min. As discussed in Section 4.2, the Fe I line at 617.33 nm is a very suitable line for the analysis of plasma velocities and magnetic fields in the lower to middle photosphere. Further information on the instrument and data are given in Section 4.1.3 (HMI) and on the LMSAL webpage. In this thesis, the HMI data serve as the polarimetric context for the high-resolution observations from the ground-based telescopes. As the observations are performed continuously, the reduced field of view of the IBIS data was extracted from the full-disk images. The cut-out in continuum intensity and magnetic field strength is shown in Fig. 4.12. The reduced quadratic region has a side length of 50″. The spatial resolution reaches the diffraction limit of 1″. In Fig. 4.14, the sunspot is displayed in continuum intensity (panel i) and line-of-sight magnetic field strength (panel m). The time-averaged line-of-sight velocities are shown in the right panel of Fig. 5.1.

AIA: The Atmospheric Imaging Assembly aboard SDO (see Section 4.1.3 and Fig. 4.4) performs continuous full-disk imaging of the Sun in well-chosen spectral bands in the ultraviolet and extreme ultraviolet. The bandpasses are very broad and include strong emission lines which form in the hot upper solar atmosphere (listed in Table 4.4). To investigate the dynamics in the chromosphere, transition region and corona, a set of four spectral bands was chosen (see Table 4.6). The very broad

(15 nm) bandpass at 160.0 nm includes the spectral continuum of the photosphere and the C IV lines at 155 nm which form in the transition region. The 1 nm-bandpass at 30.4 nm is dominated by the upper chromospheric He II emission line at 30.38 nm. The quiet solar corona and upper transition region is covered by the narrower 17.1 nm bandpass including the Fe IX line at 17.11 nm. Finally, the bandpass at 21.1 nm is dominated by the Fe XIV line at 21.13 nm. It forms in the hot corona above active regions. More information on the observed spectral lines is given in Section 4.2. The four AIA cameras have CCD detectors with a size of 4096×4096 px and an average image scale of $0.6'' \, \mathrm{px}^{-1}$. The spectral intensity is integrated over 2.9 s. The full-disk observations are provided by the Joint Science Operations Center on the JSOC webpage and have a temporal cadence of 12 s (24 s for 160.0 nm). The spatial resolution of the observations reaches $1.5''$. In this thesis, the AIA data serve as the upper atmospheric context for the high-resolution observations of the lower solar atmosphere. The full solar disk in the 17.1 nm-bandpass in shown the lower panel of Fig. 5.9. As AIA performs continuous observations, the reduced quadratic IBIS region ($50''$) was applied to the AIA full-disk image. In Fig. 4.14, the sunspot region is shown for He II 30.4 nm (panel k) and Fe XIV 21.1 nm (panel l).

The quality of the data set is excellent. The contrast and the spatial resolution of the images are very high. The spectral intensity is typically a hundred to thousand times above the average noise. The quantitative value is expressed by an adapted signal-to-noise ratio (SNR) which is calculated by

$$SNR_{\mathrm{x,y}}(\lambda) = \left\langle \frac{I_{\mathrm{x,y}}(\lambda)}{\sigma(D_{\mathrm{x,y}} - \overline{D_{\mathrm{x,y}}})} \right\rangle_{\mathrm{t}} \tag{4.11}$$

for each pixel (x,y) and spectral position λ. The spectral intensity I of the scientific data is divided by the dark noise D of the cameras and background radiation. In case of solar absorption lines, the minimum spectral intensity is reached in the line core at the darkest part of the umbra ($\mathrm{U_{core}}$). The maximum spectral signal is assumed for the continuum intensity of the quiet sun ($\mathrm{QS_{cont}}$). The signal-to-noise ratio was calculated for these two domains and are listed in Table 4.6. In the case of IBIS, the SNR-values range from 10 in the very deep Na I D1 line core at the darkest umbra to above 500 in the continuum of the quiet sun. For the broad-band data of ROSA, the signal is naturally above one magnitude larger. Likewise, the solar signal in HMI and AIA data is two magnitudes above the dark noise level.

Sunspot dynamics

As it can be seen in Fig. 4.14, the appearance of the sunspot differs heavily for the various atmospheric layers. In the lower photosphere (panels a, b, i), the umbra is very dark due to the suppression of radiating hot plasma. The magnetogram (panel m) of the sunspot reveals that the darkest parts are coupled with the strongest magnetic fields as expected. For the umbra, the magnetic pressure dominates the gas pressure ($\beta < 1$). Except from the darkest core in the lower right umbra, bright umbral dots with a size of typically $0.2''$ to $0.5''$ cover the umbral background. A cornered nexus of brighter dots is located in the upper part of the umbra. It is spatially fixed and oscillates slightly in brightness. Its horizontal and vertical edging surround the strongest barycenter of umbral flashes in the higher atmosphere. The photospheric penumbra exhibits a perfectly radial structure of filaments with a thickness of $0.2''$ to $0.5''$ and a length of several Mm. In the vicinity of the sunspot, the convective motion and gas pressure dominate the small scale magnetic fields ($\beta > 1$). The granules have a sizes up to $3''$ and lifetimes of a few minutes. The moat flow pushes the granulation radially away from the spot. The intergranular lanes appear darker with sporadic bright points due to accumulated magnetic fields (G-band).

In the middle photosphere (Fig. 4.14 e and f), the convective structures are getting less pronounced. The brightest umbral dots and structures are still visible. The penumbral area also exhibits the fine-scale filamentary structure of the lower photosphere. However, due to the lower contrast and converging intensity levels, the distinction of the sunspot areas is getting less prominent. For context information,

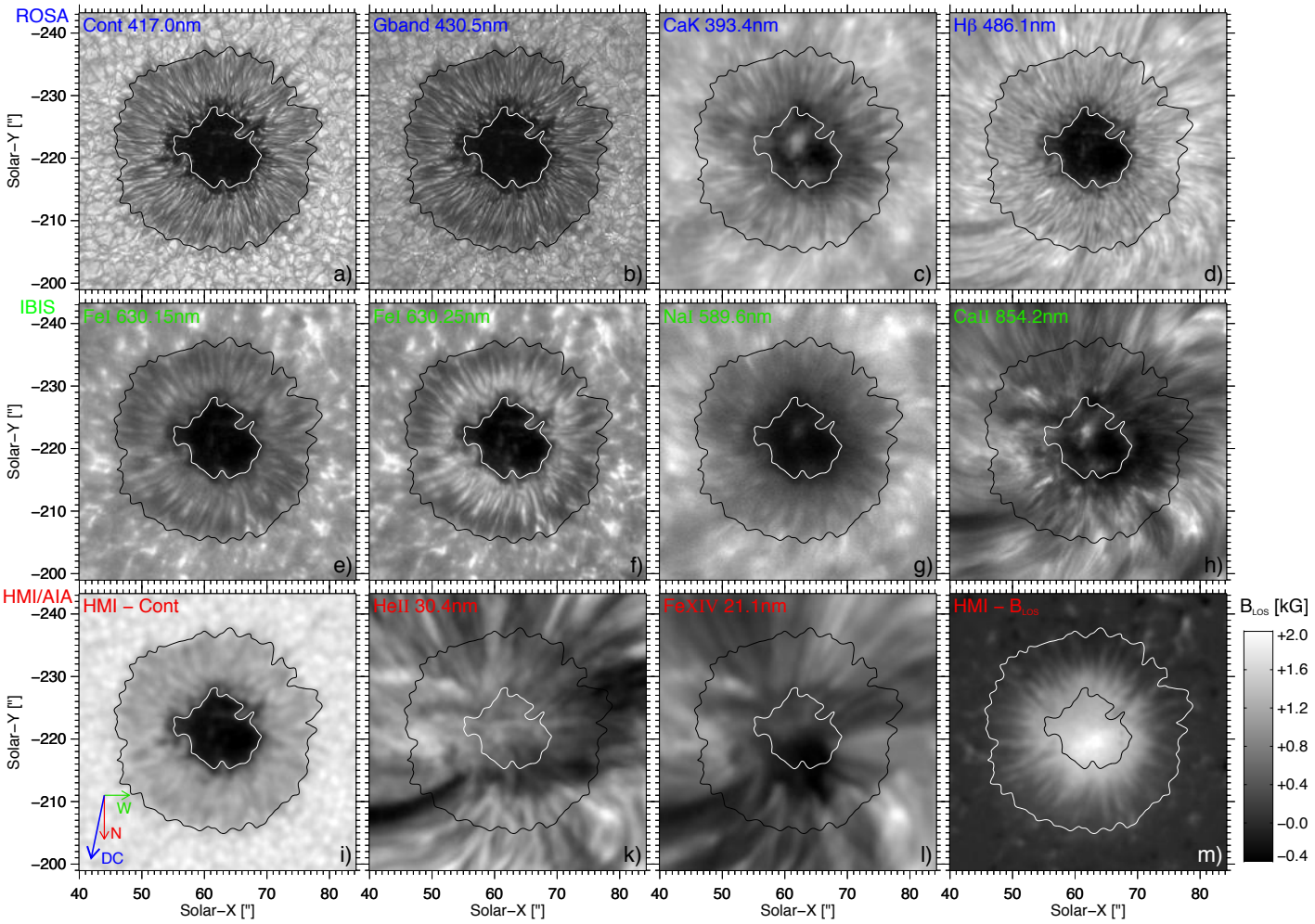

Figure 4.14.: NOAA11823 on August 21st 2013 at 15:00:06UTC as observed by ROSA (a–d), IBIS (e–h), HMI (i, m) and AIA (k, l). The sunspot region is shown in continuum intensity (panels a, b, i), line core intensity (panels c–h, k, l) of various spectral lines, and photospheric line-of-sight magnetic field strength (panel m). The contours mark the penumbral boundaries from continuum intensity. The blue arrow is pointing toward disk center.

the sunspot contours of the lower photosphere are delineated in the figures. In the vicinity of the sunspot, the granular pattern is reversed and less structured. The propagation of waves through the region becomes apparent in spectral intensity.

In the high photosphere to lower chromosphere (Fig. 4.14 c, d and g), the convective structures translate into magnetic field structures. The umbral structures have vanished, just the small-scale umbral spikes appear during the steady occurrence of umbral flashes with a period around 3 min. The bright flash at 15:00:06UTC is clearly visible in the upper part of the umbra. The penumbral structure is still filamentary, but extends beyond the delineated photospheric boundary (black contour). The dynamics of the penumbra is dominated by the running penumbral waves which propagate radially outward and seem to be excited by the umbral flashes. The vicinity of the spot still exhibits a fraction of the reversed granulation. In addition, first bright jet-like events appear in the outer parts of the spot.

In the middle chromosphere (Fig. 4.14 c, d and g), the appearance of the sunspot region is dominated by the magnetic pressure of the chromospheric field ($\beta \ll 1$). The umbra is shocked by very bright umbral flashes. The visual barycenter of the flash at 15:00:06UTC is visible in the upper umbral part.

The umbral flashes continuously appear like exploding fireworks with a period of around 2.5 min. The brightening seems to exceed the umbral area and propagate radially outward. Several bright micro-jets and more pronounced sunspot jets appear in the penumbra.

In the upper chromosphere, transition region and corona (Fig. 4.14 k and l), the magnetic field of the sunspot can be outlined by the spectral intensity. The appearance resembles the chromospheric case. The filamentary structure seems to be widened and exhibits a clockwise torsion of up to 15° within a radial extend of two spot radii. The umbral flashes and running penumbral waves are less apparent than in the lower chromosphere. This is not surprising as the ambient temperature and therefore the sound speed increases dramatically in the outer solar atmosphere. Accordingly, the ratio of the phase speed of the propagating waves to the ambient sound speed decreases.

Data calibration

The data for the scientific analysis were described above. To acquire the science-ready data level, various calibration steps had to be performed on the raw data. The most important processing steps are briefly outlined in this section. The calibration of data from Fabry-Pérot spectrometers like IBIS is detailed in Section B.2.

IBIS data: The time series (58 min) of IBIS raw data consists of 264 successive scan cycles with 44 wavelength positions in four different spectral lines. For the instrumental calibration of the scientific data, a series of flat-field images and background noise intensities were recorded under the same spectral settings (comparable to Fig. B.4). For the co-alignment of the field of views, a series of target grids was observed. The characteristics of the different calibration data and the processing steps are described in Section B.2 and summarized in Fig. B.3. As the dark noise detected by the camera is independent of the wavelength, the two-dimensional background intensity (averaged from 220 single darks) was subtracted from the science data. This was done for the broad-band and narrow-band data. The broad-band data were calibrated by the average flat-field image (from 618 single images) to reduce the instrumental intensity errors (Eq. B.1). The narrow-band data were corrected by the spectral flat-field intensities (averaged from around 1000 images) and radial wavelength shifts of the flat-field profiles across the field of view due to the collimated setup (explained in Section 4.1.2). The overall intensity transmission of the four interference filters was calculated as the ratio of the FTS atlas profiles to the additional line setup profiles which were observed with a denser and wider spectral sampling. In Fig. 4.13, the uncorrected (red squares) and corrected (blue asterisks) average spectral intensities are shown in comparison with the atlas profile (black solid line). The co-alignment of the IBIS channels was done with the average target image (air force grid, line grid, point grid) of each spectral band. The image scale, rotation and shift was computed with respect to the Na I D1 observations. All observations, including spectral and continuum intensities, were then perfectly co-aligned to the Na I D1 observations with sub-pixel precision. In conformity with the ROSA data, a common quadratic region of size 512×512 px ($50'' \times 50''$) was selected from the field of view. In the last step of data calibration the image distortions due to atmospheric turbulences were reduced. As no accumulated observation was performed at the spectral positions, the application of image reconstruction techniques was not possible. However, an iterative distortion mapping technique and image destretching was performed on the data. The best result was achieved by calculating an running average over 8 continuum intensity cycles (106 s) as a reference. Then, with respect to the reference, the distortion parameters are calculated for every single continuum intensity image. To take the isoplanatic patch into account, this mapping is done iteratively starting with the biggest subfield size of $(64\,\text{px})^2$ and halving the subfield for the following three iterations. The distortion parameters are then applied to the corresponding, simultaneously recorded spectral images. This technique yields a stabilized image quality, especially for the central sunspot region.

ROSA data: As ROSA is a broad-band imager, the instrumental calibration of the data is easy. The raw data recorded by the four fast cameras has to be reduced by the individual background intensity and averaged flat-field images (Eq. B.1). Then, the temporal image distortions in the calibrated data

due to atmospheric turbulences are mapped and destretched for each data set individually. To obtain the highest spatial resolution, every 64 (or 32) consecutive images are reconstructed to one high-resolution speckle image. For this, the automated speckle code KISIP (Wöger and von der Lühe 2008) was applied. The reconstruction technique is described in Section B.2 (Image reconstruction). The processed ROSA data were co-aligned with the IBIS observations. The spatial co-alignment to IBIS was done with the average target, grid and dot images for each camera. The adjustment included transposing, rotating and scaling the data. Finally, the same region of interest was selected to coincide with the IBIS observations. An alignment with sub-pixel precision was achieved. As the time stamps of the ROSA observations were defective, the time series also had to be temporally co-aligned. This was done by applying different starting times and cadences to the data sets and correlating them with the most similar IBIS observations. Only values with correlation coefficients greater than 0.998 were fitted by a linear regression. The new temporal alignment of both ROSA and IBIS observations is excellent and has an correlation error of 0.1%. Even if the corrected cadences are only a few percent above the given ones, the lengths of the new overall observation times differ by up to 2 min.

HMI data: The calibrated HMI data were loaded from the JSOC webpage. The data calibration was described by (e.g., Schou et al. 2012a,b; Couvidat et al. 2012). As suggested by Löhner-Böttcher and Schlichenmaier (2013), full-disk Dopplergrams are reduced by the orbital motion, differential solar rotation, center-to-limb variation of the convective blueshift and spatially fixed interference fringes. The active region was tracked across the solar disk for more than one hour. Using the HMI time stamps, the data temporally agrees with the IBIS observations. The sunspot region in continuum intensity was co-aligned with the IBIS continuum intensity. To gain the same orientation, the data had to be rotated, transposed and scaled. Then, the common reduced quadratic region was selected for HMI. The fine spatial co-alignment has a sub-pixel precision. The data alignment was applied to the full range of HMI observables. This includes also the 720 s HMI vector magnetic field inversion (see Section 5.3) obtained with the Fast Inversion of the Stokes Vector (VFISV; Borrero et al. 2011).

AIA data: The calibration of AIA broad-band data is simple. For each channel the dark current and noise is removed and the intensity errors are reduced with a normal flat-field calibration (Eq. B.1). In addition, the intensities of individual pixels are corrected, either because of their systematic error ("bad" pixels) or because of energetic 'spikes'. The calibrated data were downloaded from the JSOC webpage and covers the full observation time. The active region was tracked in time. After an additional spatial fine tuning, the sunspot has a spatial stability at the one-pixel scale. The identical field of view ($50'' \times 50''$) was selected to directly compare the observations with the IBIS, ROSA and HMI data. As the telescope is operated in space, no image reconstruction had to be applied. More information on the instrumental calibration is given by Boerner et al. (2012).

4.3.2. Observation 2: NOAA11455 – Irregular sunspot

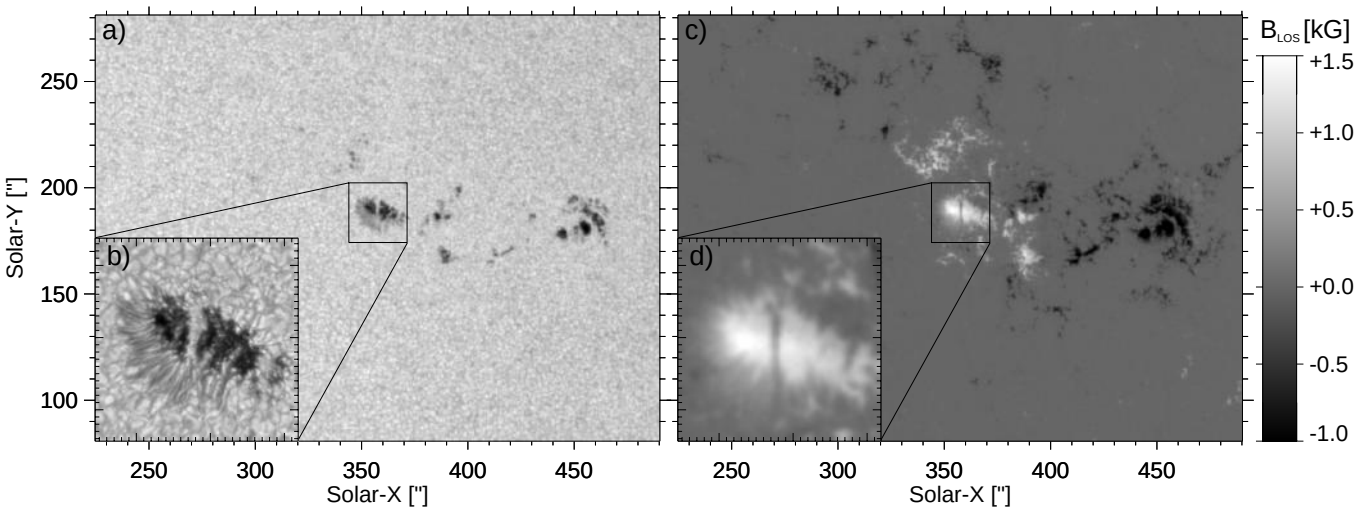

Figure 4.15.: NOAA11455 in continuum intensity (left panels) and line-of-sight magnetic field strength (right panels) on April 14th 2012 at 10:05:29UTC as observed by HMI (a, c, d) and TESOS (b). The analyzed region is marked in black. The HMI magnetogram is scaled from −1 kG (black) to +1.5 kG (white).

Observing program

The second observation was performed on April 14th 2012 from 10:05 UTC till 12:38 UTC at the Vacuum Tower Telescope (Fig. 4.2, Table 4.1) at the Teide Observatory on Tenerife. The active region NOAA11455 is shown in Fig. 4.15 in continuum intensity (left panels) and in line-of-sight magnetic field strength (right panels). The complex bipolar group of more than 15 sunspots consists of a formation of leading spots with a magnetic field orientation toward the convection zone (black color) and a set of following spots with opposite polarity. The magnetic field strength ranges from −1100 G to +1800 G in the dark umbral cores. The active region is classified as a *Dai* - group (McIntosh 1990). The evolving group covers a size of 150″ and features an irregular penumbra for the spot with the strongest magnetic field strength. The analyzed spot is highlighted in Fig. 4.15. The sunspot region observed by TESOS (see Section 4.1.3) has a dimension of 27.4″ × 28.1″ and is shown in panels b). In continuum intensity, a convective light bridge with an extent of 2″ × 7″ basically divides the umbral area (27 Mm^2) into two parts. The HMI magnetogram (Fig. 4.15 d) yields a co-spatial decrease of magnetic field strength from 1800 G in the umbrae to around 800 G in the light bridge and less than 200 G in the vicinity of the sunspot. In the light bridge, the inclination of the field immediately increases by a mean of 20°. Besides this rough segmentation in two umbral cores, several smaller formations of convective features like light bridges and bright points cover the umbral areas. Spatially, these features are at the arc-second and sub-arc-second scale. In Fig. 4.17, the umbral and penumbral boundaries in intensity are indicated by the contours. The small sunspot has a total size of 24″ × 15″ and a irregular filamentary penumbra which extents radially by around 6″ on the center-side of the spot. During the observation period of 153 min, the sunspot was stable with smaller changes in size (< 2%). The sunspot was located on the northern hemisphere at solar disk coordinates $(X, Y) \simeq (358'', 190'')$. This corresponds to a heliocentric angle $\theta = 23°$. With respect to the center latitude ($B_0 = -5.6°$) and declination ($P_0 = -26.0°$) of the solar rotation axis, the heliographic position amounts to 6.4° N and 21.3° W. Assuming a vertical topology of the umbral magnetic field, the angle of incidence at this heliocentric angle toward the line-of-sight causes spatial displacements Δx with height in the images. Over a latitudinal difference $\Delta h = 1$ Mm, these displacements $\Delta x = \Delta h \cdot \tan\theta = 0.42$ Mm (or 0.59″) are of the order of the spatial

Table 4.7.: Basic information on observation run 2.

Observation	2
Date	14. April 2012
Active region	NOAA 11455
Classification	Dai: Bipolar group of 15 small sunspots, largest spot with irregular penumbra
Sunspot	Small, half-side penumbra, several umbrae
Position	6.4°N , 21.3°W
Heliocent. angle	$\theta = 23°$, $\mu = 0.92$
Size umbrae	$27\,\mathrm{Mm}^2$
Radii umbrae	$< 3''$
Extent of spot	$24'' \times 15''$
Field of view	$27.4'' \times 28.1''$
Evolution	$< 2\%$
Sunspot cycle	Middle
Instrument	**TESOS**
Telescope	VTT
Start (UTC)	10:05:23
Duration Δt_{obs}	153 min
Seeing r_0	$\simeq 15$ cm
Resolution	$\simeq 0.8''$
Observ. mode	Spectroscopic
Spectral lines	Fe I 709.04 nm
($\rightarrow$ Table 4.8)	Fe I 543.45 nm
	Hα 656.28 nm

resolution. They are neglected in the spatial analysis. The observational information is summarized in Table 4.7.

As listed in Table 4.7, the sunspot was observed with TESOS (see Section 4.1.3) by scanning three different spectral lines consecutively in each cycle. The spectroscopic settings are detailed in Table 4.8. Simultaneous HMI observations in intensity, Doppler velocity and magnetic field (strength, inclination, azimuth) were consulted. They are displayed in Fig. 4.17. During the 153 min of TESOS observations, the atmospheric seeing at the VTT was good and stable around a Fried parameter of $r_0 \simeq 15$ cm. With clear sky and wind speeds of less than $5\,\mathrm{m\,s^{-1}}$ above an inversion layer, the Adaptive Optics of the telescope stably corrected the atmospheric turbulences over the full observation run. This allows an average spatial resolution of $0.8''$ to resolve solar features which are smaller than 600 km. Again, I would like to illustrate the angular resolution of the telescope with the scales on Earth. Pointing the VTT on Tenerife to the Swedish Solar Telescope on La Palma at a distance of 140 km, one would clearly see the windows of the building. Reconstructing the broad-band data yields a spatial resolution down to $0.4''$ (see panel b in Fig. 4.17). The HMI instrument aboard SDO (see Fig. 4.4) performs continuous observations at a spatial resolution of $1''$, according to the telescope aperture of 14 cm (see Table 4.1).

The spectroscopic setting of this observation run was designed to focus on acoustic wave phenomena in the lower sunspot atmosphere. TESOS operated in a spectrometric setup to perform a fast and dense scanning of different spectral lines. The HMI instrument made two-dimensional spectro-polarimetric line scans of Fe I 617.33 nm to obtain the photospheric magnetic field vector. The detailed functionality of the described imaging spectrometers was discussed in Sections 4.1.2 and 4.1.3. The characteristics of spectral lines and their selection criteria were detailed in Section 4.2 and listed in Table 4.3. In the following paragraphs, the chosen observational settings (summarized in Table 4.8) are explained.

Table 4.8.: Spectral settings of observation run 2.

	Spectral lines Ion, λ_0 [nm]	$\#\lambda_{pos}$	$\Delta\lambda_{pos}$ [pm]	$\delta\lambda$ [pm]	Cadence dt [s]	t_{exp} [ms]	Scale [″/px]	SNR $U_{core} - -QS_{cont}$
TESOS	Fe I 709.04	27	1.6	2.5	30	150	0.089	$\simeq 10^2$
	Fe I 543.45	27	1.8	1.8	|	|	|	|
	Hα 656.28	8	12.3	2.2				
HMI	Fe I 617.33	6	6.9	7.6	45	150	0.505	400

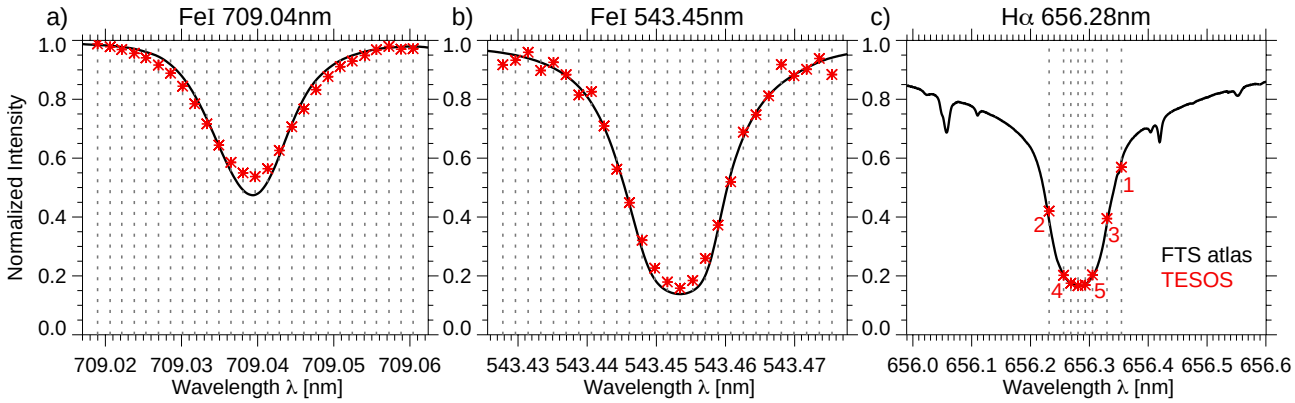

Figure 4.16.: Spectral sampling of the Fe I lines at a) 709.04 nm and b) 543.45 nm, and c) the Hα line core. The average spectral intensities of TESOS (red asterisks) are normalized and plotted against the wavelength positions λ (dotted vertical lines). The FTS atlas profiles is added. The numbers 1–5 in panel c) indicate the nested scan.

TESOS: Quasi-simultaneous observations were performed with the Triple Etalon SOlar Spectrometer (see Section 4.1.3) in the visible spectral range. Three solar absorption lines were scanned in cycles in a spectroscopic mode. The scanning of the lines was performed in a nested mode with alternating line positions. As indicated by the numbers (1–5) in Fig. 4.16, the order of the scanned wavelength positions iteratively approaches the line minimum at the center position. Due to the jumping from one side of the spectral line to the other, the scanning is sometimes figuratively called 'rabbit'-mode. This guarantees that equal atmospheric layers are scanned at roughly the same time. It prevents line asymmetries due to rapidly fluctuating plasma velocities. The narrow Fe I lines at 709.04 nm and 543.45 nm were sampled at 27 equidistant line positions with a narrow step width of $\Delta\lambda_{pos}$ (1.6 pm and 1.8 pm). In Fig. 4.16, the spectral intensities (red asterisks) and filtered positions (dotted vertical lines) are indicated. Both lines have an effective Landé-factor $g_{eff} = 0$. Therefore, their spectral intensity is insensitive to the Zeeman effect in the presence of strong magnetic fields. As discussed in Section 4.2, both lines have a very high sensitivity to velocity oscillations and complement each other by the represented line formation altitude in the solar atmosphere. As listed in Table 4.3, the line core of Fe I 709.04 nm forms in the middle photosphere at an average height of 200 km above the continuum optical depth. The Fe I 543.45 nm covers the whole photosphere and forms at altitudes as high as 550 km. With a combination of interference filters and three coupled Fabry-Pérot interferometers (see Fig. 4.8 and Table 4.2), TESOS reaches a spectral resolution of 300,000. A detailed description of the interferometric spectroscopy was given in Sections 4.1.2. The spectral width $\delta\lambda$ of the intensity transmission (see Figs. 4.6 and B.6) depends on the wavelength and amounts to 1.8 pm to 2.5 pm. In addition to the photospheric iron lines, the core of Hα at 656.28 nm is scanned at eight spectral positions. The average spectral intensities are plotted in Fig. 4.16 c). The step width $\Delta\lambda_{pos}$ of the five points in the

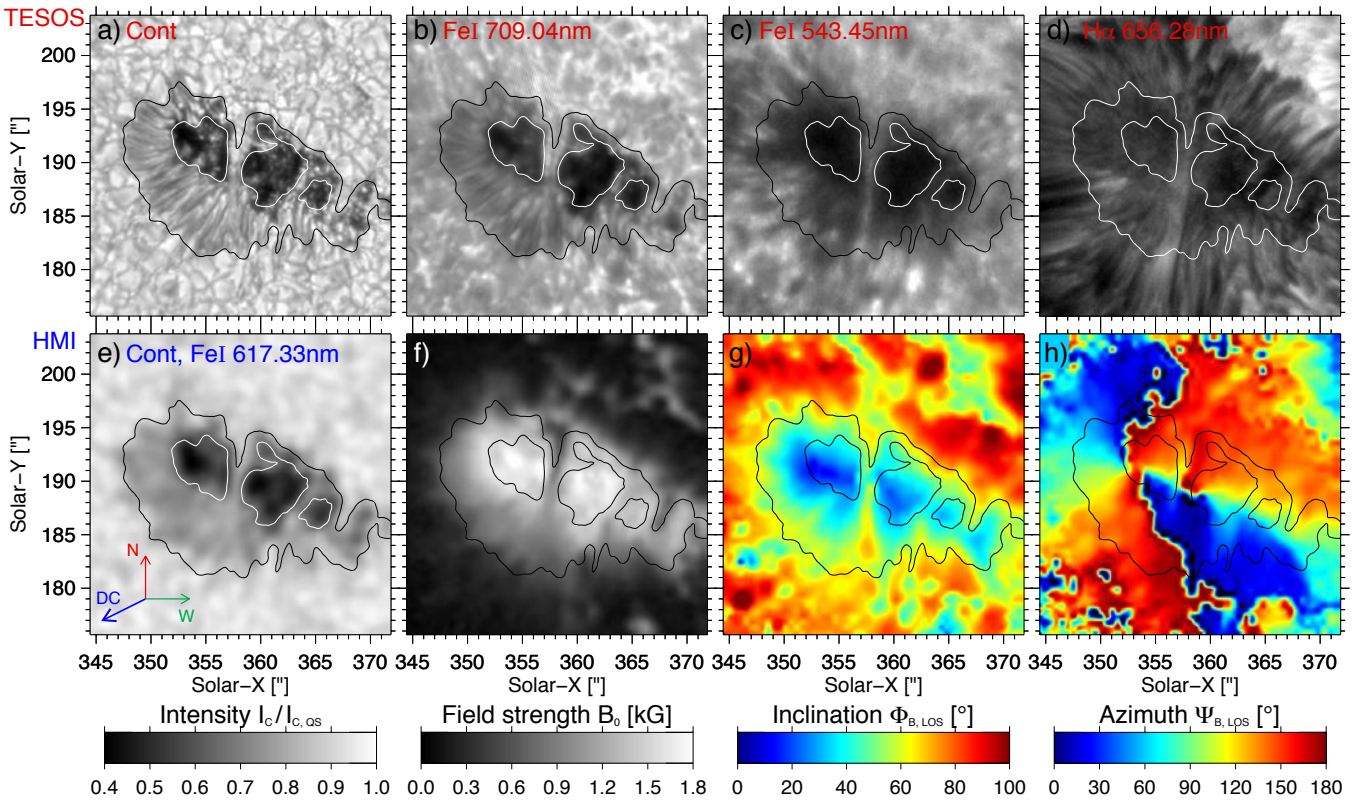

Figure 4.17.: Major sunspot of NOAA11455 on April 14th 2012 at 11:37:34UTC as observed by TESOS (upper row) and HMI (bottom row). Panels a–e) show the region in spectral intensity: continuum (a, e), and line minima of (b) Fe I 709.04 nm, (c) Fe I 543.45 nm, (d) Hα 656.28 nm. The magnetic field parameters from the inversion of the HMI Stokes profiles of Fe I 617.33 nm are displayed in panels f–h) for the field strength B_0, zenith inclination $\Phi_{B,LOS}$, and azimuth $\psi_{B,LOS}$. The black contours mark the penumbral boundaries from continuum intensity. The blue arrow is pointing toward disk center.

middle chromospheric core (see Table 4.3) was set to 12.3 pm. The inner wings of the strong Hα are sampled by additional three points. As discussed in Section 4.2, Hα is one of the prime tools to investigate sunspot waves in the chromosphere and is highly suitable to trace running penumbral waves. As listed in Table 4.8, the exposure time for all spectral positions was set to 150 ms. The iron lines were scanned within 10 s each, the eight Hα positions were recorded in 5 s. Additional time was needed for the cyclical change of the interference filters in the filter wheel and for the processing of the data. The total cycle time adds up to 30.0 s. According to the Nyquist criterion, this temporal resolution allows to analyze waves with the periods down to 1 min. Simultaneously to the narrow-band scans, the continuum intensity was recorded in the broad-band channel at 630 nm (see Fig. 4.8). The reduced rectangular region has a size of $27.4'' \times 28.1''$ at a detector scale of $0.089''\,\mathrm{px}^{-1}$. The quality of the data is good. The spectral intensity shows a clear solar signal and is calculated as two magnitudes above the noise level (Eq. 4.11). In Fig. 4.17, the analyzed sunspot region is shown in continuum intensity (panel a) and spectral intensity at the line minima (panels b–d). More information on the instrument is given in Table 4.2 and Sections 4.1.2 and B.3.

HMI: The HMI data of this observation run have the same instrumental specifications as described in Section 4.3.1 (HMI) for the first observation. Again, the HMI data serve as the polarimetric context for the spectroscopic high-resolution observations from the ground-based telescope. The spectro-polarimetric observations of the Sun are performed continuously at six wavelength positions across the Fe I line at 617.33 nm. The calibration of the data provides Doppler velocities and magnetic field

strength in the line-of-sight in the lower to middle photosphere (see Table 4.3). The active region in continuum intensity and magnetic field strength is shown in Fig. 4.15. The corresponding field of view to the TESOS data ($27.4'' \times 28.1''$) was selected (panel d). The temporally averaged Doppler velocities are displayed in Fig. 5.2 c). The center-side penumbra exhibits a strong blue-shift caused by the strong, preferentially horizontal Evershed flow. The strong light bridge of the sunspot features a strong redshift in its center. The inversion of the full-Stokes vector (see Section 5.3) yields the sunspot's absolute magnetic field strength, zenith inclination and azimuth. The results are displayed in Fig. 4.17. The sunspot has a magnetic field strength of up to 1900 G (panel f). In the dark umbral cores seen in continuum intensity (panel e), the magnetic field inclination (panel g) is close to zenith. In the penumbra, the field strength decreases steadily to below 700 G. Toward the outer penumbral boundary, the inclination angle increases up to 60°. In the vicinity of the spot, the magnetic field strength falls below 200 G. The radial symmetry of the sunspot's azimuth (panel h) is disrupted at the locations of the light bridges.

Sunspot dynamics

The appearance of the sunspot changes from the deep photosphere to the middle chromosphere. When the convection decreases and the magnetic field starts to dominate the gas pressure (see plasma-β regime in Section 3.3), the structure of the sunspot region changes from a granular to a filamentary pattern. In Fig. 4.17, the sunspot region is shown for increasing altitudes (from panel a to panel d). Not only the appearance changes for different atmospheric layers and solar features, but also the dynamics vary significantly.

In the low photosphere close to the convection zone (Fig. 4.17, panels a and e), the umbral area is the darkest part. The strong magnetic field (panel f) suppresses the convection of hot plasma and its radiation. The umbrae exhibit a plethora of small umbral dots with a diameter of $0.2''$ to $1''$ and a lifetime of several minutes. Only the upper left part of the umbrae shows a dark core. Several thin light bridges divide the umbral area. The wide light bridges exhibits convective motion. The strongest one in the center of the spot has an extension at the granular scale ($2''$) and yields a convective current directing from the northern to the southern part of the spot. The filamentary penumbra has developed only on the side of the spot facing the disk center. The filaments have a thickness of $0.3''$ to $0.6''$, a length of several Mm, and a radial structure. The bright points seem to migrate inward to the umbra. In the vicinity of the sunspot, the uprising plasma dominates the magnetic fields ($\beta > 1$). The granular convection has a size of several arc-seconds and a lifetime of a few minutes. On the penumbral side of the spot, the moat flow pushes the granulation radially outward.

The middle photosphere (Fig. 4.17 b) is represented by the line core of Fe I 709.04 nm (see Table 4.3). At an estimated altitude of 200 km above the continuum optical depth, the convective structures are less pronounced. The most prominent convective structures of the umbra and penumbra are still visible. In the vicinity of the sunspot, the granular pattern transforms into a reversed appearance. The dynamics of the sunspot are still similar to the low photospheric case. The propagation of p-mode waves through the region becomes apparent in spectral intensity. For distinction, the sunspot contours from the continuum intensity are delineated in the figures.

The line core of Fe I 543.45 nm is formed in the high photosphere to low chromosphere at an average altitude of 550 km above the optical depth unity (see Table 4.3). The sunspot at the core formation layer is shown in Fig. 4.17 c). The convective structures start to translate into magnetic field structures. The appearance is characterized by a mixture of convective features and filamentary chromospheric structures. The strong light bridge is very distinctive. Umbral flashes dominate the activity in the umbral cores at a period of around 3 min. From the apparent barycenters in the umbrae, running penumbral waves propagate radially outward along the extended penumbral filaments.

The appearance of the sunspot region in the middle chromosphere is shown in Fig. 4.17 d). The line minimum position of Hα is formed at an average altitude of around 1200 km to 1800 km above the optical depth unity. At this height, the magnetic pressure of the chromospheric field ($\beta \ll 1$) dominates

the gas plasma. Therefore, the sunspot appearance is governed by the filamentary structure of the superpenumbral field. On the center-side of the spot it exceeds the field of view. On the limb-side of the spot lacking the photospheric penumbra, the filaments end after 5″ to 10″. The adjoining fibrils are brighter in spectral intensity. Like in the upper photospheric case, the umbra is shocked by very bright umbral flashes with a period of around 2.5 min. Running penumbral waves seem to be excited by the umbral flashes and propagate radially along the superpenumbral filaments. At the main light bridge, the running waves seem to become evanescent.

Data calibration

The observational data acquired with TESOS and HMI require various calibration steps to gain a science-ready state. The most important processing steps are briefly outlined in this section. The detailed calibration of imaging spectrometers are described in Section B.2.

TESOS data: The calibration of the data from the imaging spectrometer was performed with the CASSDA GUI – TESOS. The processing pipeline is described in Section B.3. The calibration steps are detailed in Section B.2. A flowchart of the required data processing is shown in Fig. B.3. For the observation in spectral intensity with the narrow-band channel, fully calibrated science data (Level 1) were obtained. For the observations in continuum intensity with the broad-band channel, it was possible to apply image reconstruction (Level 2). The time series (153 min) of TESOS raw data consists of 306 successive scan cycles with 62 wavelength positions in three different spectral lines (see Table 4.8 and Fig. 4.16). To perform the instrumental calibration, a series of flat-fields (3000 single images) and detector noise intensities (320 dark images) was recorded under the same spectral settings as in the scientific observation (see Fig. B.4). For the spatial co-alignment of the observations, a series of focused target grids was recorded. The spectral intensities were corrected from the average background intensity and calibrated with the average flat-field images of each spectral positions. A simple instrumental calibration in intensity was performed according to Eq. B.1. The narrow-band data required an additional calibration of the pre-filter transmission and the wavelength shifts caused by cavity errors of the telecentric Fabry-Pérot interferometers (see Section 4.1.2). The transmission errors are displayed in Fig. B.6 for a single pixel and in Fig. B.7 for the overall field of view. The average spectral intensities after the correction are shown in Fig. 4.16. Except from the apparent line broadening and minor intensity fluctuations, the intensities (red asterisks) resemble the line profiles of the spectral FTS atlas (black solid line). The spatial co-alignment was done with the average target grid image of each spectral band and has a sub-pixel precision. A co-spatial rectangular region (315 px × 323 px) was selected from the circular field of view. The calibrated data cubes are illustrated in Figs. B.5 and B.8. For the alignment with HMI data, the orientation of the TESOS images had to be flipped horizontally. The broad-band images were reconstructed with speckle techniques taking subfield sizes of 4″.

HMI data: The acquisition and calibration of the HMI data were performed equally to the first observation (see Section 4.3.1). The full-disk Doppler velocities, continuum intensities, line-of-sight magnetic field strengths, and inversions of the magnetic field vector were acquired through the JSOC webpage. The Dopplergrams were additionally reduced by the satellite motion, solar rotation, center-to-limb variation of the convective blueshift and interference fringes. The active region was tracked for the 153 min and spatially co-aligned with the TESOS data at a sub-pixel precision.

5. Analysis techniques

"Mathematical analysis is as extensive as nature itself. It defines all perceptible relations, measures times, spaces, forces, temperatures. It brings together phenomena the most diverse, and discovers the hidden analogies which unite them."

— Jean Baptiste Joseph Fourier, *The Analytical Theory of Heat*

When Joseph Fourier published his *Théorie analytique de la chaleur* in 1822, he established the mathematical tool to analyze the dynamic evolution of signals. The Fourier analysis became prevalent at the investigation of oscillations in numerous fields of research. By the Fourier transformation, a signal which oscillates in time was transferred into the frequency domain. Modern signal processing was born. This achievement opened the door to an extensive and diverse exploration of oscillatory phenomena in technics and nature itself. Of course, this included the study of waves in the solar atmosphere, and especially in sunspots. Therefore, Fourier ought to be named as one of the giants on whose shoulders we stand.

As wave phenomena in sunspots are rich in diversity and appearance, their examination demand a deliberate application of various analysis techniques. The scanning of spectral intensities across multiple spectral lines enables a comprehensive analytical investigation of the atmospheric wave properties. Velocities and temperatures in the solar atmosphere can be inferred from the spectral line profiles. In Section 5.1, the calculated Doppler velocities are presented. Sunspot waves manifest themselves as intensity and velocity fluctuations in the solar atmosphere. The investigation of oscillations by means of wavelet analyses yields the wave power distribution and characteristic periodicities. This technique and its practice are described in Section 5.2. The magnetic field vector can be retrieved from spectro-polarimetric observations via inversion methods for the radiative transfer equation. The inversion technique, its results and errors are discussed in Section 5.3. Further methods are applied to trace the propagation of sunspot waves (see Section 5.4). In Section 5.4.1, a spatio-temporal propagation analysis is developed to obtain the time and space differences of propagating waves between two atmospheric layers. In Section 5.4.2, the temporal diagrams and their usage are presented. For the topological context of the sunspot's magnetic field, coronal field extrapolation based on Maxwell's equations are performed. The technique and its results are discussed in Section 5.4.3.

5.1. Doppler velocities

Plasma motions in the solar atmosphere can be derived from the spectral line profiles. Spectral lines are shifted in wavelength according to the Doppler effect. Motions toward the observer cause a blue-shift of the profile to shorter wavelengths. In case of uniform velocities across the atmospheric formation region, the spectral line is shifted as a whole. If the atmospheric motions are non-uniform, the line shape can become asymmetric as parts of the spectral line are shifted differently. Then, to infer the Doppler velocities, a bisector analysis of the profile is recommended. Under the assumptions of a stable atmospheric motion and a symmetric shape of the line, a Gaussian- or Voigt-approximation can yield a suitable representation of the line profile. To calculate the Doppler velocity v_{dop}, a reference wavelength λ_0 has to be given. The Doppler shifts, $\Delta\lambda = \lambda - \lambda_0$, of the line can be translated into

line-of-sight velocities by

$$\frac{v_{\mathrm{dop}}}{c} = \frac{\Delta\lambda}{\lambda_0}\,, \tag{5.1}$$

referenced to the speed of light c.

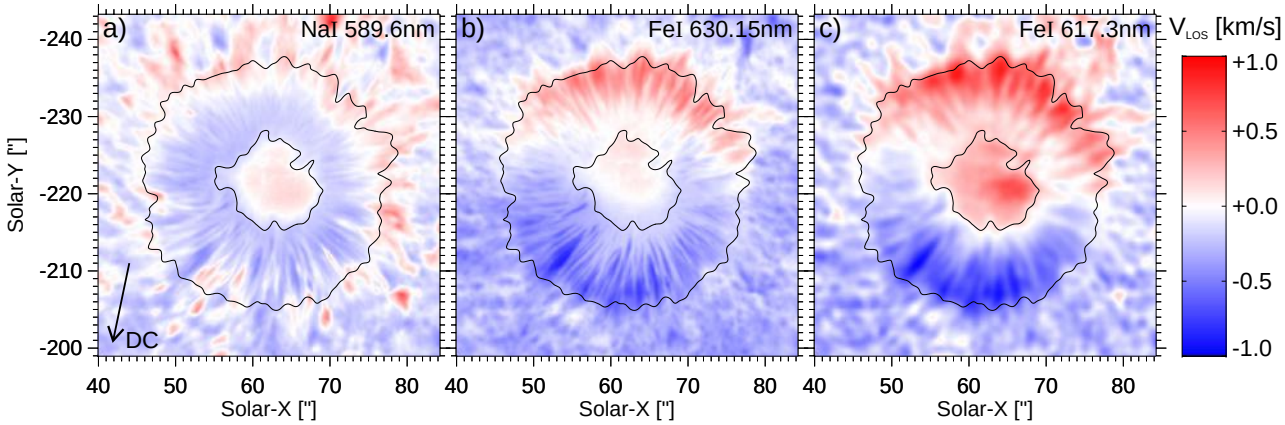

Figure 5.1.: Doppler velocities in NOAA11823 (see Section 4.3.1). The 1h-time averages of the line-of-sight velocities from (a) Na I 589.6 nm, (b) Fe I 630.15 nm, and (c) Fe I 617.3nm lines are scaled to $\pm 1.0\,\mathrm{km\,s^{-1}}$. Negative values correspond to blue-shifts and indicate motions toward the observer. The arrow points to the solar disk center.

IBIS: The Doppler velocities in the IBIS observations were calculated with an unweighted Gaussian approximation to the spectral intensities. As the spectral lines were critically sampled (see Table 4.6), this method proved to yield the most reliable Doppler shifts. The results are the same as from fitting a Voigt function. The line shift was assumed to be roughly uniform, the line minimum position of the Gaussian profile was defined as the central wavelength λ. The reference wavelength λ_0 was identified as the fitted line minimum position averaged for the umbral area and time series. With Eq. 5.1, the Doppler velocities were calculated pixel-wise for the entire data set. It has to be emphasized that the obtained velocities represent the atmospheric motions in the line-of-sight for the average upper formation layer of the line. For the spectral lines Fe I 630.15 nm and Na I 589.59 nm, the velocity results are credible.

In the case of the Fe I 630.15 nm, the formation layer spans the low to middle photosphere up to 300 km (see Table 4.3) above the optical depth unity and is thin enough to assume atmospheric uniformity. The line is very sensitive to velocities (Cabrera Solana et al. 2005). Its magnetic sensitivity is relatively low and allows an investigation of Doppler velocities also in the magnetically strong umbra where the line broadens. The time-averaged Doppler velocities are shown in Fig. 5.1 (panel b).

In the case of Na I D1, the formation altitude spans around 1000 km. It ranges from the low photosphere to the lower chromosphere (see Table 4.3 and Fig. 4.11). The very deep but narrow line is very sensitive to velocity oscillations in the high photosphere to lower chromosphere. With a relatively low Landé-factor of $g_{\mathrm{eff}} = 1.33$, the line preserves its good velocity sensitivity even for the strong magnetic field strength of the umbra. The Na I D1 line reveals the wave dynamics of umbral waves and flashes in the lower chromosphere. The imprint of the intensity amplification due to the flashes is too weak to affect the overall shape of the spectral line and allows for the application of the Gaussian approximation. It has to be noted that the obtained Doppler velocities describe the plasma motion for the average upper photosphere to lower chromosphere. The time-averaged velocities are displayed in Fig. 5.1 (panel a).

For the Fe I 630.25 nm line (see Table 4.6), the splitting in the umbral field is too strong ($g = 2.49$) to perform a reliable Gaussian approximation for the computation of Doppler velocities. A Fourier phase method (Schmidt et al. 1999) was applied to determine the line minimum positions. The results

are in conformity with the Doppler velocities from the line at 630.15 nm. This is valid as both lines form in the lower photosphere (see Table 4.3) and share similar transitions (Fig. 4.10).

The calculation of the Doppler velocities from the Ca II line at 854.21 nm was not possible. The coarse line sampling (see Table 4.6 and Figs. 4.11 and 4.13) and bright emission in the line core during the passage of umbral flashes (see row d in Fig. 6.15) did not allow to perform any kind of simple approximation to the line profile. A non-LTE inversion of the Stokes profiles would be required to infer the plasma velocities from this chromospheric line.

TESOS: The Doppler velocities in the TESOS observations (see Section 4.3.2) were calculated with the same pixel-wise Gaussian approximation to the spectral intensities like for IBIS. The line center λ was defined as the fitted minimum position. Since the spectral lines were sampled by dense equidistant steps (see Table 4.8), a bisector analysis could be applied, too. However, due to the instrumental intensity fluctuations (see Fig. 4.16), the Gaussian fit yields the more consistent results. In contrast to the IBIS Dopplergrams, the reference wavelengths λ_0 for the TESOS data were identified as the fitted line minimum position averaged for the quiet sun and entire time series. The Doppler velocities were calculated with Eq. 5.1. They represent the line-of-sight motions for the average formation layer.

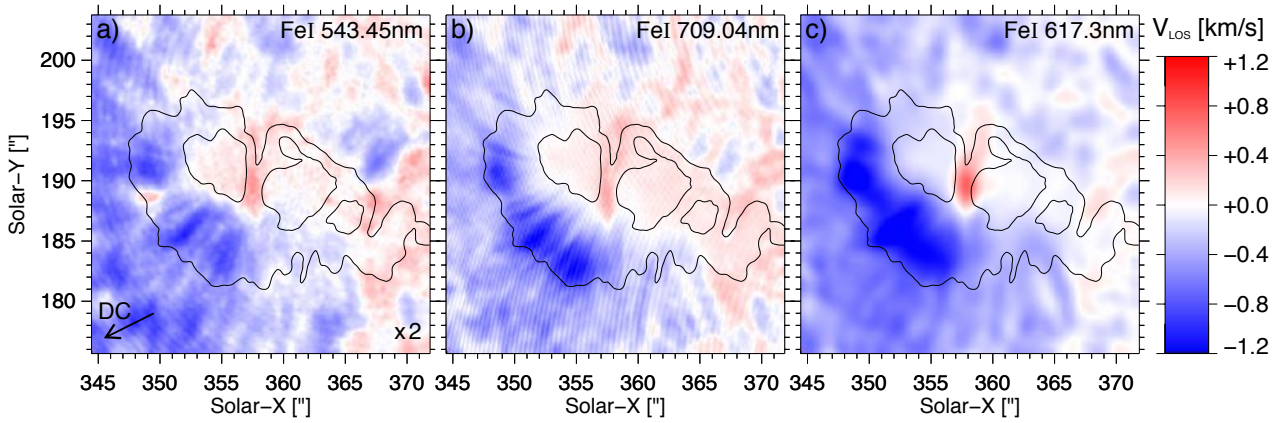

Figure 5.2.: Doppler velocities in NOAA11455 (see Section 4.3.2). The time-averaged line-of-sight velocities of (a) Fe I 543.45 nm, (b) Fe I 709.04 nm, and (c) Fe I 617.3nm are shown. The values are scaled to $\pm 1.2\,\mathrm{km\,s^{-1}}$ (for b and c) and $\pm 0.6\,\mathrm{km\,s^{-1}}$ (for a). Negative values correspond to blue-shifts and indicate motions toward the observer. The arrow is pointing to the solar disk center.

For the spectral profiles of the Fe I 709.04 nm line (see Fig. 4.16 a), the determination of the Doppler velocities worked optimally. As the weak line is formed in the lower photosphere (see Table 4.3), the assumed uniform photospheric velocity and symmetry of the profile are valid. The line is insensitive to magnetic fields ($g_{\mathrm{eff}} = 0$). The sensitivity to velocity oscillations is high, even for the umbral cores of the sunspot. The time-averaged Doppler velocities for NOAA11455 are shown in Fig. 5.2 b).

The determination of the Doppler velocities from the spectral intensities of the Fe I 543.45 nm line (see Fig. 4.16 b) worked properly. As the formation altitude of the iron line spans the entire photosphere (see Table 4.3), the obtained velocities describe the plasma motion in the average middle to upper photosphere. The very deep but narrow line is very sensitive to velocity oscillations. As the line has a zero Landé factor, significant Doppler velocities are gained in the magnetically strong umbra with the emerging umbral flashes. The time-averaged Doppler velocities are displayed in Fig. 5.2 a).

HMI: The HMI Doppler velocities were calculated from the spectral intensities at the six wavelength positions across the Fe I 617.33 nm line (see Table 4.6). The central wavelength was defined as the center of gravity of the line. The Doppler velocities were calculated with the quiet sun average at disk center as the wavelength reference. Additionally, the full-disk Doppler maps were adjusted by the orbital motion of the satellite, solar rotation of the Sun, center-to-limb variation of the convective blue-shift

and instrumental fringes as suggested by Löhner-Böttcher and Schlichenmaier (2013). According to the line synthesis of convective blue-shift at the given heliocentric angle ($\theta \simeq 20°$) a velocity of $-350\,\mathrm{m\,s^{-1}}$ was subtracted. The time-averaged Doppler velocities for NOAA11823 and NOAA11455 are shown in Figs. 5.1 and 5.2 (panels c).

Conspicuous velocities: Flows, waves and convection are present in the Dopplergrams both at short and long time scales. In Figs. 5.1 and 5.2, the time-averaged Doppler velocities are shown for two sunspot regions at various atmospheric layers. The most noticeable phenomenon is the Evershed effect (Evershed 1909), which is characterized by a plasma flow in the penumbra is guided by the filaments. In the lower photosphere (panels b and c), the horizontal flow from the inner to the outer penumbra produces blue-shifts on the center-side penumbra and red-shifts on the limb-side penumbra. The line-of-sight velocity increases with the heliocentric angle. The close distance to the disk center ($\theta = 14°$) explains the relatively low Doppler velocities of $\pm 1.0\,\mathrm{km\,s^{-1}}$. The velocities from HMI exceed the IBIS results in total, but they resemble each other very clearly. The same holds for the moat flow adjacent to the sunspot. In the high photosphere to lower chromosphere (Fig. 5.1 a), the horizontal Evershed flow has disappeared. The velocities in the sunspot converge to a radial symmetry with blue-shifts at the inner penumbra and red-shifts in the outer penumbra. Still, the filamentary structure is evident. For the less inclined magnetic field of the chromospheric inner penumbra, the systematic blue-shifts hint at upward propagating penumbral waves. The red-shift in the outer penumbra and vicinity of the spot could be a superpenumbral down-flow or wave motion.

Besides the penumbral velocities, the average Doppler velocities also contain important information for the umbra. In the HMI Doppler maps (panel c in Fig. 5.1), the lower photospheric umbra is characterized by a systematic red-shift, especially in the darkest part of the umbra with the strongest magnetic field strength (see Fig. 4.14). In the high photosphere to lower chromosphere, the inner umbra yields the same but less intense red-shift. In Fig. 5.2, the umbral areas yield a systematic small red-shift for the lower (panel b) and higher photosphere (panel a) as well. This apparent downward motion can be the imprint of steadily down-falling plasma, the result from umbral flashes and their blowback in the shock cones (see Section 3.5), or simply an instrumental effect.

In Fig. 5.2, the most conspicuous features are the blue-shifts in the center-side penumbra due to the Evershed flow. On the other hand, the main light bridge in center of the spot features strong red-shifts (compare with Fig. 4.17). This apparent downward motion is most intense in the lower photosphere (panel b and c) with line-of-sight velocities up to $1.2\,\mathrm{km\,s^{-1}}$. In the high photosphere (panel a) the red-shift is still present, but with smaller values of a few hundred meters per second.

All in all, the Doppler maps of the lower photosphere resemble each other very well. The accuracy of the calculated Doppler velocities from IBIS and TESOS are confirmed by the HMI observations. The inferred velocities are consistent in their relative values. However, the absolute velocities have to be treated with caution as the calculation of line shifts requires an arbitrary reference. To attain absolute Doppler velocities with an accuracy of $10 - 100\,\mathrm{m\,s^{-1}}$ requires an absolute wavelength calibration, e.g., with a laser frequency comb attached to a spectrograph like LARS (Laser Absolute Reference Spectrograph, Doerr et al. 2012) at the VTT.

5.2. Wavelet analysis

Waves in sunspots feature a wealth of oscillatory modes with a plethora of characteristic frequencies and power. For their detailed investigation, a wavelet power analysis was performed. The time-dependent analysis of the local power spectrum is based on the wavelet techniques provided by Torrence and Compo (1998), which are commonly used in solar physics (e.g., Bello González et al. 2010). Exemplarily, the applied wavelet analysis is illustrated in Fig. 5.3 for an umbral velocity oscillation (panel a) in the low chromosphere.

In a normal Fourier analysis, the Fourier transformation converts an oscillatory signal from the time domain into the frequency domain. The result is a simple power spectrum in frequency or period.

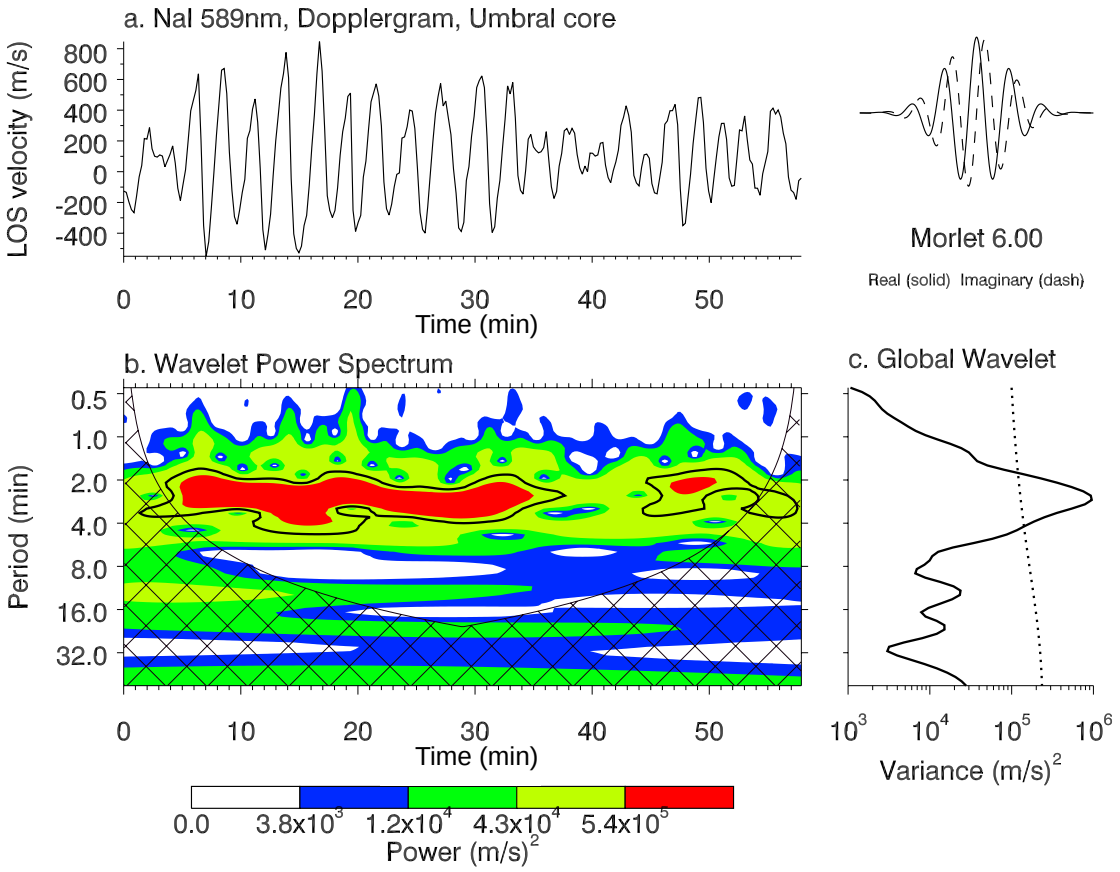

Figure 5.3.: Wavelet analysis with a Morlet wavelet. The wavelet (upper right) is applied to the Doppler velocities (panel a) from Na I 589.59 nm in the umbra of sunspot NOAA11823. Panel b): The obtained wavelet power spectrum displays the oscillatory power in a time-dependent frequency spectrum. High wavelet power is displayed in red color. The region with a significance above 95% is contoured in black. The cone-of-influence is marked by the black line grid. Panel c): The global (time-averaged) wavelet spectrum (solid line) exceeds the significance level (dotted) in the 2–4 min range.

In a wavelet power analysis, a wavelet basis function is used for the successive local sensing of the oscillatory signal (see Fig. 5.3 a). The local wavelet transformation allows the generation of a time-dependent power spectrum, as illustrated in panel b). The wavelet is a compact theoretical wave function. It can have various shapes and qualities. For this study, the Morlet wavelet was selected as it provides the best resolution in frequency. As the analysis has to face the time-frequency uncertainty relation, a better frequency resolution leads to a poorer time resolution, and vice versa. The wavelet is shown in the upper right panel of Fig. 5.3 with its real (solid) and imaginary (dashed) part. The detailed properties of the Morlet wavelet and further wavelet basis functions (e.g., the Paul wavelet or the Mexican Hat) are described in Torrence and Compo (1998).

After the wavelet function has been selected, the period scales for the transformation have to be chosen. By definition, the shortest wave period is fixed by the Nyquist criterion. The Nyquist period is defined as the double cadence ($s_0 = 2 \cdot dt$) of the observation (see cadences in Tables 4.6 and 4.8). In the case of IBIS, this is 26.5 s or 0.44 min. For TESOS the shortest analyzable wave period is 1 min. The general formula for the scale setting s_i is

$$s_\mathrm{i} = s_0 \cdot 2^{i \cdot d_j} \quad , \quad i = 0, 1, \ldots, n \tag{5.2}$$

with $n+1$ periods with a scale spacing d_j. For the power spectrum of IBIS data (cadence $dt = 13.232$ s),

a spacing $d_j = 0.05$ and $n = 100$ was set to obtain a sampling of 101 period scales between 0.44 min and 14.11 min. Consequently, the step sizes of the scales are non-equidistant and increase toward higher periods. As the majority of waves are expected in the $2-6$ min range, it is convenient to have a denser sampling at lower periods. The scale spacing was adjusted to gain a similar sampling of wave periods for the TESOS, ROSA, HMI and AIA data.

With these parameters, the wavelet analysis is performed on the temporal oscillations of Doppler velocity and spectral intensity for each pixel of the sunspot region. As the exemplary case in Fig. 5.3 shows, the analysis works best in the 1 min to 8 min range. The highest power is displayed in red color. The adopted statistical significance level of 95% to the white noise is marked by the black contour. On average, the signal exceeds the significance level in the $2-4$ min range. At lower periods, the time resolution is very sharp, but the noise makes the obtained signal too uncertain. In addition, the influence of the aliasing effect of unresolved oscillation increases. On the other hand, the analysis of wave periods with more than one fourth of the length of the observation time becomes uncertain as well. Too few oscillations contribute to the analysis. This reduces the significance of the transformation. The decreasing resolution in time can be inferred from the horizontal power distribution at periods above 15 min in Fig. 5.3. Due to the finite time of the observations, leakage effects at the edges of the series have to be reduced by an artificial padding of the data. Especially at longer periods, the discontinuities reduce the validity at the edges of the wavelet power spectrum. Therefore a cone-of-influence is delineated to exclude the unreliable region. A detailed description of the applied wavelet analysis is given in Torrence and Compo (1998).

The global wavelet spectrum is the time-average of all local wavelet power spectra (see panel c in Fig. 5.3). It provides an unbiased and consistent estimate for the true overall power spectrum and converges to the Fourier power spectrum. The investigation of the wavelet power in sunspots yields a continuous oscillatory stability. Therefore, I largely confine to the interpretation of the significant power in the global wavelet spectra of sunspot waves.

5.3. Inversions

Spectro-polarimetric observations of the Stokes vector contain the signal of polarized radiation from a magnetized source. In the strong magnetic field of sunspots, the signal in spectral lines is particularly strong. With inversions of the magnetic field vector, the Stokes profiles in intensity (I), linear polarization (Q, U) and circular polarization (V) can be translated into magnetic field strength, inclination and azimuthal orientation. In order to do this, the radiative transfer equations have to be solved. A detailed description of spectro-polarimetric observations and inversion techniques is given by Collados (1999).

Sunspot waves have periods around 1–10 min. A useful observation therefore requires a short temporal cadence. For multi-wavelength observations, the observational settings have to be adapted to provide a cycle with a short cadence. The performance of a polarimetric observation would multiply the cycle time. Therefore, a purely spectroscopic setting was applied for the observations with the ground-based telescopes (see Tables 4.5 and 4.7). For the spatial and magnetic context, HMI performed simultaneous spectro-polarimetric observation at a lower spatial and temporal resolution. The first camera measures the circular polarization for the Fe I line at 617.33 nm ($g_{\rm eff} = 2.5$) at a cadence of 45 s. Based on the Zeeman effect, the line-of-sight component of the magnetic field strength is obtained. The second camera measures the full Stokes vector for the same line at a cadence of 90 s. As suggested by Borrero et al. (2007), an accurate retrieval of the magnetic field vector requires an averaging of the Stokes vector for 12 min. Thereby, the errors are more than halved. Finally, the magnetic field information is retrieved with the Very Fast Inversion of the Stokes Vector (VFISV; Borrero et al. 2011). It was specially designed for the HMI instrument to cope with the large amount of pixels. Within twelve minutes, more than 13.5 million pixels are inverted. This makes almost 19000 processed pixels per second. This challenge is managed in a parallelized manner for the independent

pixels. VFISV is based on the Milne-Eddington approximation of the solar atmosphere (Landolfi and Landi Degl'Innocenti 1982). The synthesized profiles are iteratively converging toward the observed profiles. The final solution yields the resulting physical parameters of the lower photosphere (Borrero et al. 2011).

The inversion results and their errors are provided by the JSOC webpage. The full-disk vector magnetic field was acquired for both sunspot observations (see Sections 4.3.1 and 4.3.2). Fig. 5.4 shows the sunspot NOAA11823 in b) total magnetic field strength B_0, c) the angle $\Phi_{\mathrm{B,LOS}}$ between the line-of-sight and the magnetic field, and d) the azimuth angle $\psi_{\mathrm{B,\,LOS}}$ of the projection of the magnetic field on the plane perpendicular to the line of sight. This azimuthal orientation is ambiguous by 180°. In panel a), the sunspot is shown in continuum intensity I_{C} which is normalized to the quiet sun average $I_{\mathrm{C,\,QS}}$. The stable magnetic field parameters were averaged in time for 5 successive scans (1 h in total). The 1δ-uncertainties δB_0 for the total magnetic field strength, $\delta\Phi_{\mathrm{B,LOS}}$ for the inclination angle, and $\delta\psi_{\mathrm{B,LOS}}$ for the azimuth angle are displayed in Fig. 5.5.

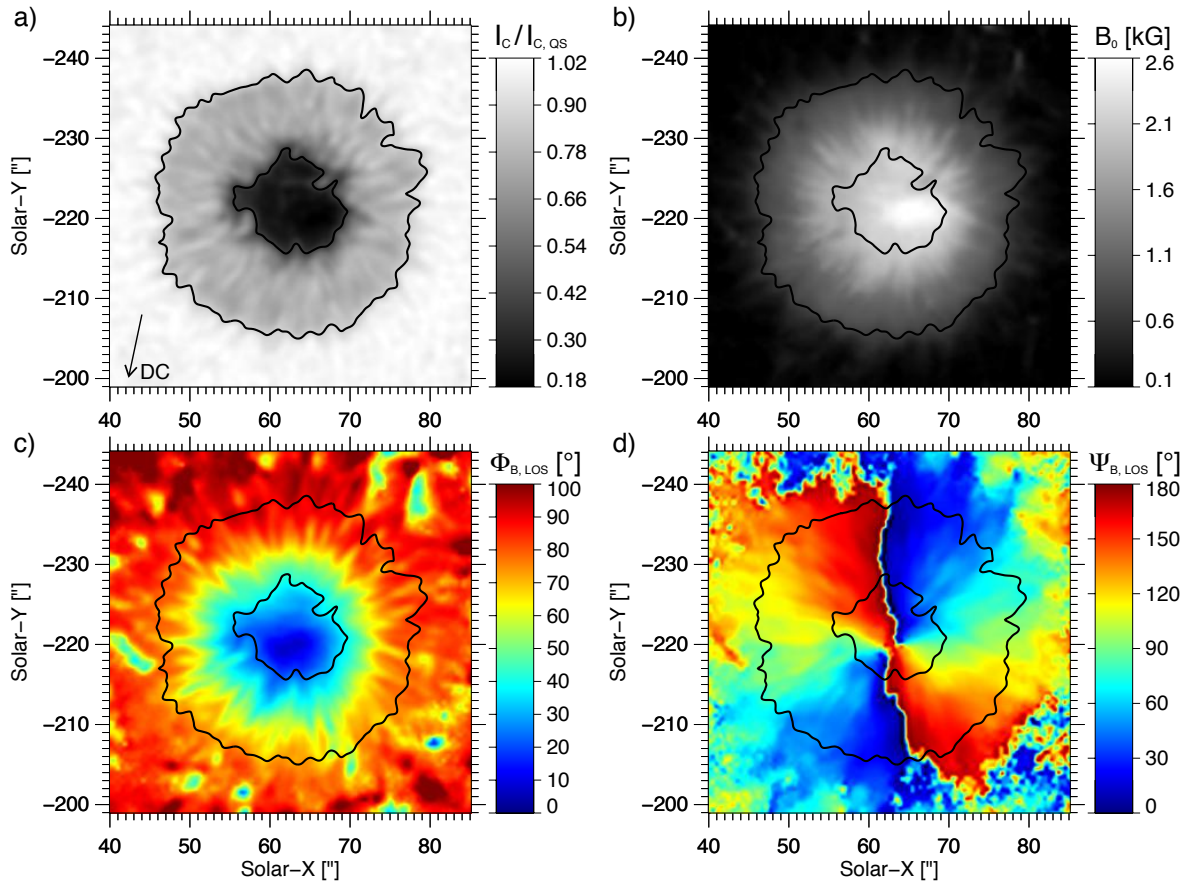

Figure 5.4.: Photospheric magnetic field parameters of sunspot NOAA11823 obtained with HMI magnetic field inversions. The sunspot region is shown in (a) normalized continuum intensity, (b) absolute magnetic field strength B_0, (c) inclination angle $\Phi_{\mathrm{B,LOS}}$ to the line-of-sight, and (d) azimuth angle $\psi_{\mathrm{B,\,LOS}}$ of the magnetic field. The inclination angles are scaled from the line-of-sight direction of 0° (blue) to a roughly perpendicular orientation of 100° to the line-of-sight (red). The azimuth angles $\psi_{\mathrm{B,\,LOS}}$ are ambiguous and range from 0° (blue) to 180° (red). The black contours mark the penumbral boundaries in continuum intensity. The arrow is pointing toward disk center.

As it can be seen in Fig. 5.4 (panels a and b), the darkest part the umbra yields the largest absolute magnetic field strength of almost 2700 G. In the penumbra, B_0 decreases radially to below 1000 G. In

the vicinity of the spot it drops to a few hundred Gauss. The 1δ-uncertainties δB_0 of the field strength (see Fig. 5.5 a) range between 10 G and 20 G in the umbra. In the average penumbra the uncertainties are of the order of 10 G. In patches of the center-side penumbra they reach up to 30 G. The sunspot's magnetic field inclination is displayed in Fig.5.4 (panel c). The angles represent the incidence to the line-of-sight. As the heliocentric angle of the sunspot has an average of 14°, the angular distribution is shifted slightly to the lower left in the disk center direction. Nevertheless, the umbra exhibits its vertical orientation with angles $\Phi_{\mathrm{B,LOS}} < 20°$. At the umbral boundary, inclinations are around 30°. Toward the outer penumbra, the inclination angle monotonically increases to an almost perpendicular orientation of 80° to the line-of-sight. The filamentary structure in the penumbra hints at the diversity of the penumbral field inclinations (Lites et al. 1993). The inversion uncertainty $\delta\Phi_{\mathrm{B,LOS}}$ for the inclination angles (see Fig. 5.5 b) is uniform for the whole sunspot area and has an average value of 0.5°. The azimuth $\psi_{\mathrm{B,LOS}}$ of magnetic field is shown in Fig. 5.4 d). No disambiguation has been performed, so the angles range from 0° to 180° (and not between 0° to 360°). The homogenous distribution of the sunspot's azimuth suggest a radial symmetry of the magnetic field. Again, the calculated uncertainty is very small (see Fig. 5.5 c). In the penumbra, the azimuthal uncertainty has an average below 0.5°. In the umbra and the vicinity of the spot, the uncertainty is bigger with $\delta\psi_{\mathrm{B,LOS}} > 2°$.

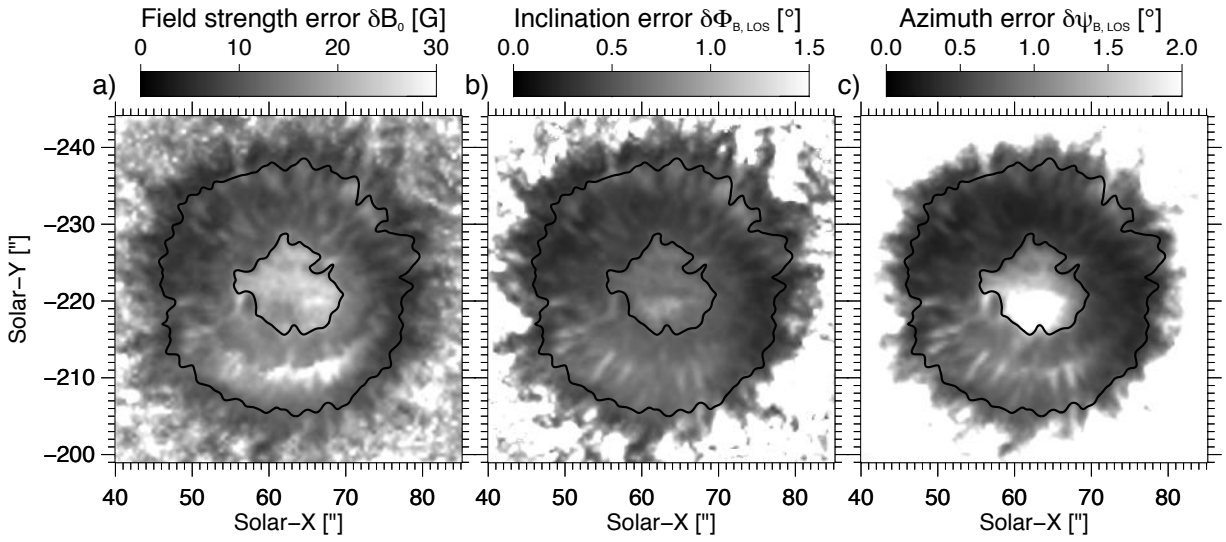

Figure 5.5.: Uncertainties of the HMI vector magnetic field inversion of Fig. 5.4. The panels display the 1δ-uncertainties, (a) δB_0 of the absolute magnetic field strength, (b) $\delta\Phi_{\mathrm{B,LOS}}$ of the inclination angle, and (c) $\delta\psi_{\mathrm{B,LOS}}$ of the azimuth angle of the magnetic field. For a better visualization, the angles are scaled from 0° to 1.5° (and 2°). The black contours mark the penumbral boundaries in continuum intensity.

The results of the vector magnetic field inversion for NOAA11455 are displayed in the lower panels of Fig. 4.17. The vertical umbrae exhibit a total magnetic field strength of up to 1900 G. The topology of the penumbra and light bridges is more complex and will receive further consideration (see Section 6.4.3).

5.4. Further analysis methods

Further analysis techniques were applied to derive additional wave parameters from the data. In Section 5.4.1, a phase difference method is introduced which measures temporal and spatial shifts of sunspot oscillations between different sampling height. This allows to estimate the travel times and the propagation direction of sunspot waves. To expand the investigation of wave characteristics to shock wave propagation, the temporal evolution of spectral lines is analyzed by wavelength-time ($\lambda - t$) diagrams (see Section 5.4.2). To refine the study of apparent velocities, the oscillatory time series are analyzed in regard to the temporal evolution along spatial 1D-slices, circular sectors and radial distances. The diagrams and their physical interpretation are described in Section 5.4.2. For the evaluation of the sunspot's magnetic field structure in the solar chromosphere and corona, potential field source surface extrapolations have been acquired. The technique and the obtained results are reported in Section 5.4.3 for the sunspot region NOAA11823.

5.4.1. Phase differences

I developed a three-dimensional correlation method to keep track of upward propagating waves in sunspots. The temporal wave signatures in spectral intensity and Doppler velocity at different atmospheric altitudes are used to determine the three-dimensional direction of propagation.

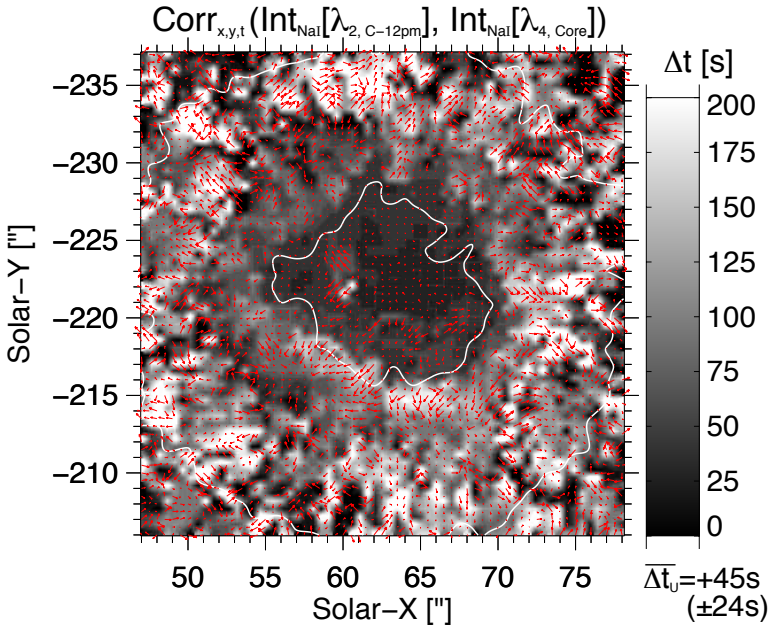

Figure 5.6.: Phase difference map of NOAA11823 between the spectral intensities in the line wing ($\lambda_{2,\,\mathrm{C-12pm}}$) and core ($\lambda_{4,\,\mathrm{Core}}$) of Na I 589.59 nm. The grayscale indicates the time differences across the sunspot region. Larger delays are shown in brighter colors. The red arrows hint at the spatial displacements of the propagating waves. In the umbral area, the wave signature has an average time delay of 45 s with an error of 24 s.

The cross-correlation of the temporal signals at two atmospheric layers yields the travel times and spatial shifts of the waves. The assumption of a linear undisturbed wave propagation has to be satisfied, of course. For each pixel, the overall oscillatory signal of the lower layer is cross-correlated with the signals at the upper layer in a co-spatially centered $5'' \times 5''$ - region. Iteratively, the signals within that box are shifted in time up to ± 200 s. The maximum correlation coefficients define the travel time and spatial shifts from the lower to the upper formation layer. The method yields reliable results for the umbra and inner penumbra. Due to the clear oscillatory signal in the upper photosphere and lower

chromosphere, the correlation coefficients reach values up to 0.9 for adjacent atmospheric layers. The validity of the results is highest in the dark umbra and decreases in the inner penumbra. The analysis in the outer penumbra and vicinity of the spot is too unreliable because of the diffuse oscillatory signal. It should be noted, that the significance of the methods decreases when the acoustic cut-off frequency acts between the two different layers. This mode conversion and atmospheric cut-off is especially present in the upper photosphere which produces severe changes in the oscillatory signal.

The analysis was applied to the spectral intensities and Doppler velocities at the inner part of the sunspot of NOAA11823 (compare Fig. 4.14). In Fig. 5.6, the time delays (grayscale) and spatial shifts (red arrows) are shown for oscillations in spectral intensities of the Na I D1 line 589.59 nm. The lower layer is defined by the spectral intensities at the wavelength position $\lambda_{2,\,\mathrm{c-12pm}}$ in the blue wing of the spectral line (see Fig. 4.11) with a contribution centered at an average formation height of around 250 km in the quiet sun photosphere. The upper layer is represented by the chromospheric spectral intensity at the line minimum position $\lambda_{4,\,\mathrm{Core}}$ of Na I D1. The average formation height is estimated to around 800 km above the continuum optical depth unity. This makes an altitudinal difference of more than 500 km. As shown in Fig. 5.6, the umbral area yields the shortest time differences (in dark color) with an average of $\overline{\Delta t_{\mathrm{U}}} = 45 \pm 24\,\mathrm{s}$. Assuming a constant phase speed, this would hint at upward propagating shock waves with a wave speed of around $12\,\mathrm{km\,s^{-1}}$ in the umbral upper photosphere to lower chromosphere. Except for few occasions, the small umbral displacements (short red arrows) suggest a vertical propagation of umbral flashes along the magnetic field lines (compare Fig. 5.4 c). In the outer umbra and inner penumbra in Fig. 5.6, the travel times increase with radial distance (brighter color). Especially at the lower-left umbral boundary, the longer travel times are coupled to larger spatial displacements. These effects can be explained by the longer travel distances caused by the radially increasing magnetic field inclination (compare Fig. 5.4 c) and the field guided nature of the upward propagating running penumbral waves.

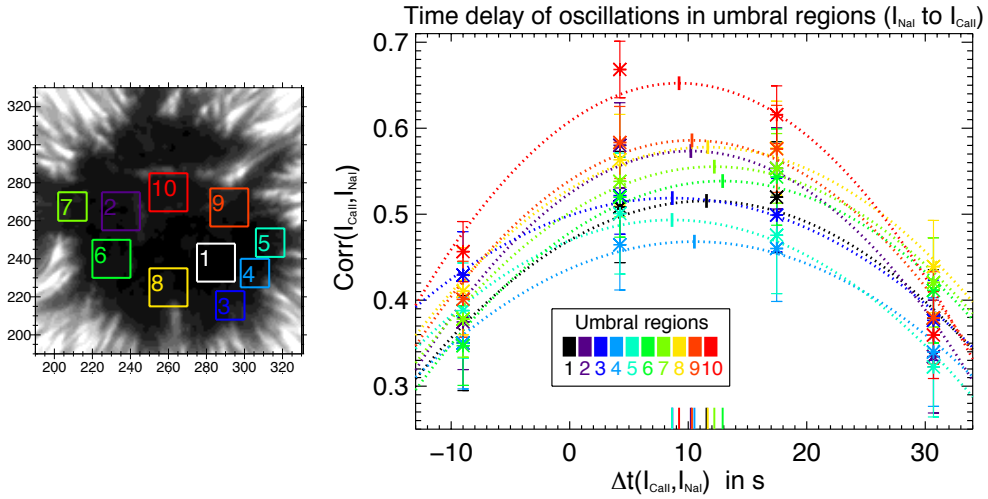

Figure 5.7.: Analysis of time delays in umbral regions (1–10) of NOAA11823. In the right panel, the temporal correlation coefficients are shown for the two time series in spectral intensity at the line minimum positions of Na I 589.59 nm ($\lambda_{4,\,\mathrm{Core}}$) and Ca II 854.21 nm ($\lambda_{5,\,\mathrm{Core}}$). The time delays at the umbral regions were determined by parabolic fits to the temporal coefficients. The umbra is shown in continuum intensity (pixel-scale).

The phase differences of the oscillatory signals were calculated for various pairs of spectral intensities. In all cases, the results hint at a vertical wave propagation in the umbra (see also Fig. A.5). The mean umbral travel times between two atmospheric layers are listed in Table A.1. The large standard deviations stem from the inclusion of the outer umbral area. In addition, the formation height H_{form}

above continuum intensity unity is estimated for the wavelength positions at the inner line wings and cores (compare Figs. 4.11 and 4.13).

Under the assumption of a vertical propagation of waves in the umbra, a refined analysis was performed for differing umbral regions. The left panel of Fig. 5.7 displays the umbral area of NOAA11823 in continuum intensity. The ten analyzed regions are highlighted in color. A purely temporal cross-correlation was calculated for two oscillatory time series. The correlation coefficients were averaged for the spatial region. The standard deviation result from the values within the region. As shown in the right panel of Fig. 5.7, the correlation coefficients next to the maximum value (±40 s) are fitted by a parabola. The maximum of the parabola defines the average time difference in the umbral region. This analysis was done between the spectral intensities at chromospheric line minimum positions of Na I 589.59 nm ($\lambda_{4,\,\mathrm{Core}}$) and Ca II 854.21 nm ($\lambda_{5,\,\mathrm{Core}}$), as well as between the spectral intensities and the Doppler velocities of Na I. The time series are illustrated in Fig. 5.8 (panels c and d).

The refined analysis yields correlation coefficients up to +0.7 for the overall time series. The spatial distribution of the wave correlation for the umbral area is displayed in Figs. 6.17 and A.6. For context information, the umbral area is shown co-spatially in intensity, average power of the oscillation in the 2–3 min range, and magnetic field strength. The lower panels display the correlation values at the given time differences. High correlation coefficients are brighter.

5.4.2. Temporal and periodic diagrams

The dynamics of waves are reflected in the spectral lines. To study of the temporal evolution and periodical distribution of the waves, several kinds of diagrams are studied. In the following, the three main analytical diagrams are presented.

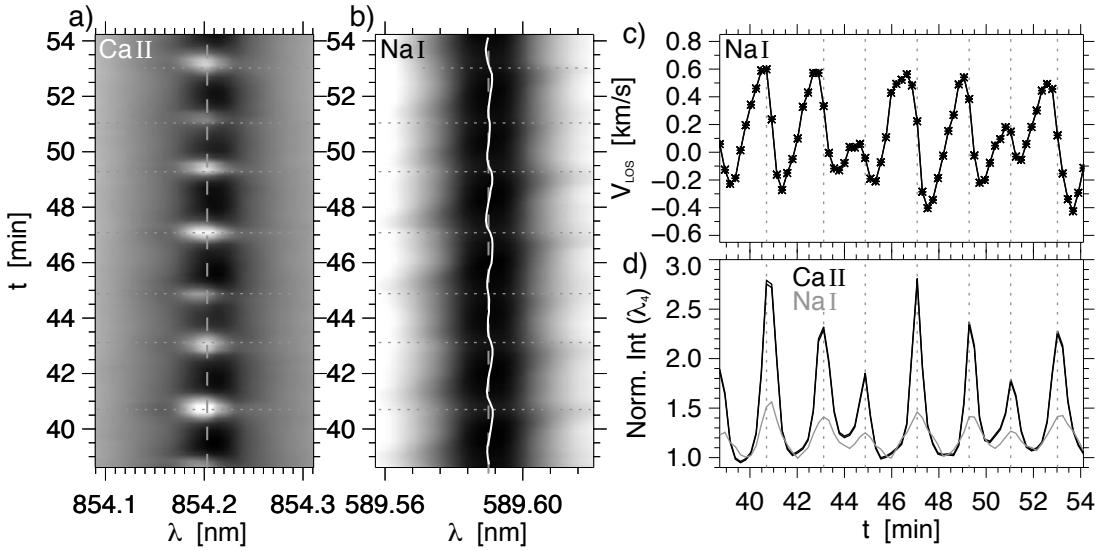

Figure 5.8.: Appearance of umbral flashes in spectral intensity in the umbral core of NOAA11823. Panels a, b): The $\lambda - t$ diagrams for the line cores of Ca II 854.21 nm and Na I 589.59 nm are plotted. The times of the bright maxima in spectral intensity are marked by the gray dotted lines. The nominal line minimum positions are indicated as gray dashed lines. The white solid line shows the oscillating line minimum position. Panel c): The line shifts of Na I D1 are translated into Doppler velocities. Panel d): The normalized line minimum intensity of Ca II (black) and Na I D1 (gray) is plotted.

$\lambda - t$: The temporal chart of a spectral line profile provides information on dynamical line shifts, line broadenings and possible emission reversals in the line core. Traditionally, the wavelength-time ($\lambda - t$) diagram is used to investigate acoustic shocks and their bright emissions (bright points or grains; e.g.,

Rutten and Uitenbroek 1991; Carlsson and Stein 1992) in the blue cores of the Fraunhofer Ca II K_{2v} and H_{2v} lines (see Section 4.2 → Ca II K). In this study, the $\lambda - t$ diagrams focus on the spectral dynamics in the high photosphere and lower chromosphere above a sunspot umbra. As shown in Fig. 5.8, the passage of umbral flashes causes strong emission in the blue core of the Ca II 854.21 nm line (panel a) and strong shifts of the Na I 589.59 nm line profile (panel b). The plots of the Doppler velocities (panel c) and spectral intensities at the central line minimum (panel d) confirm the appearance.

$\boldsymbol{X - t}$: The wave motion and apparent horizontal wave speeds can be inferred from the spatio-temporal diagram. Based on the two-dimensional images in spectral intensity and Doppler velocity, a spatial section of the sunspot can be selected. For the circular sunspot of active region NOAA11823, circular sectors are defined for the analysis. As shown in Fig. 6.20 a), they are centered at the umbral barycenter and extend beyond the penumbral boundary. In case of wave coherency for the sector, the signal can be averaged azimuthally. The evolution of the signal in time t across this radial element is plotted against the radial distance X from the umbral center. An example is presented in Fig. 6.22. The spatio-temporal diagrams of the photospheric (lower panels) and chromospheric (upper panels) Doppler velocities are displayed for three circular sectors. The direction of wave propagation can be obtained from the orientation of the 'herringbone' pattern. The inclination of the local path-time curve gives the apparent horizontal velocity of the wave.

$\boldsymbol{X - T}$: The wavelet analysis (see Section 5.2) of the oscillation in spectral intensity and Doppler velocity yields the global wavelet power spectrum for each position in the sunspot region. As shown in Fig. 6.20 a-c) for the circular sunspot of NOAA11823, a sectorial analysis of the wave power at periods T is performed. The sectors are centered at the umbral barycenter and extend with distance X radially into the vicinity of the sunspot. Under the assumption of azimuthal constancy at radial distances X, the power spectra are azimuthally averaged. The radial distribution of the wave power, as well as eventual shifts or jumps in periods can be easily inferred from the diagrams.

5.4.3. Magnetic field extrapolation

I want to anticipate that the chromospheric magnetic field inclination will be reconstructed (in Section 6.5) with the wave characteristics for the sunspot of active region NOAA11823. To assess the quality of the results, context information on the magnetic field topology is required. The magnetic field topology of the sunspot in the lower photosphere was derived from the HMI magnetic field inversion (see Section 5.3). To present an inherently consistent evaluation of the chromospheric magnetic field, the coronal field geometry was acquired with a potential field source surface extrapolation (PFSS; Schrijver and De Rosa 2003). The field extrapolation is based on the model of Schrijver (2001). The photospheric magnetic field (here from HMI) is used to estimate the magnetic field lines toward an outer source surface with the key assumption of a zero electric current in the corona. For further information on field extrapolations and coronal models, I refer the reader to the review by Mackay and Yeates (2012). The PFSS data were acquired from the LMSAL webpage. In Fig. 5.9, the extrapolated magnetic field lines for the full-disk HMI magnetic field (upper panel) and AIA spectral intensity around 17.1 nm on August 20th 2013 are illustrated. The sunspot region NOAA11823 is highlighted. Additional results of the PFSS are shown in Fig. 6.31 for different days.

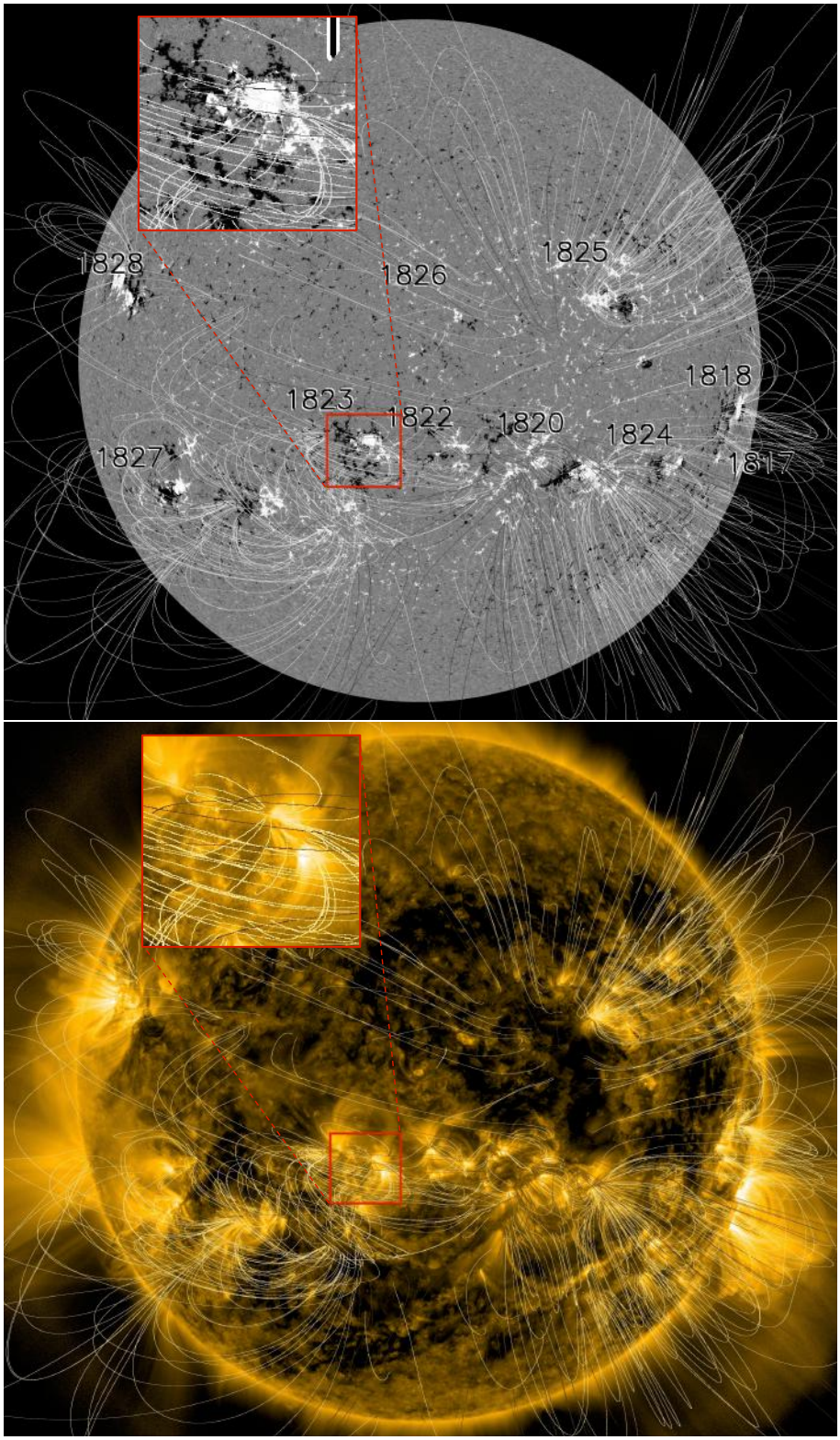

Figure 5.9.: Potential-Field Source-Surface (PFSS) extrapolation of the magnetic field lines on August 20th 2013 at 16:27UTC. The upper panel shows the sun's photospheric magnetic field in the line-of-sight as inferred from HMI data. The strongest field strengths are displayed in black and white color. The lower panel shows the Sun in coronal intensity using the spectral Fe IX line at 17.1 nm of the AIA instrument. The extrapolated field lines are overplotted in gray. The zoomed red box indicates the position of the sunspot's active region NOAA 11823.

6. Sunspot waves

"I insist upon the view that 'all is waves'."

— Erwin Schrödinger, in a *letter to John Lighton Synge*

Of course, the quote of Schrödinger is taken out of context. In fact, Schrödinger wrote it in the sense of quantum mechanics and the wave-particle duality. As such, he complained about his colleagues who supported the Copenhagen interpretation and who ascribe to him that he would insist upon the view that 'all is waves'.

Nevertheless, the quote is suited to underline the importance of waves in the solar atmosphere and interior. Waves can be found indeed in all atmospheric layers and the convection zone. They cover a broad range of wave frequencies and power. Strong acoustic waves with oscillatory periods of several minutes to one hour propagate as p-modes through the outer convection zone and photosphere. Electromagnetic waves are emitted allover the atmosphere and lead to the characteristic spectral radiation of the Sun, from hard X-rays to radio waves. In the presence of strong magnetic field concentrations, magnetohydrodynamic waves gain in importance. In the atmosphere above active regions and especially above sunspots, these magnetoacoustic and Alfvén waves become most prominent. All three kinds of waves are needed to fully describe the oscillatory dynamics in sunspots.

In this chapter, I give my attention to the dominating magnetoacoustic wave phenomena in sunspots which are so remarkable and mysterious. In the following Section 6.1, the possible driving mechanisms of sunspot waves are discussed. In Section 6.2, the most important observational results on oscillatory characteristics and wave propagation are presented from the sunspot photosphere to the corona. Special focus is given on the manifestation of umbral flashes (Section 6.3) in the umbral chromosphere and running penumbral waves (Section 6.4) in the penumbral chromosphere and photosphere. After the determination and confirmation of the nature of both phenomena, the impact of the magnetic field inclination on the atmospheric cut-off frequency is employed to reconstruct the sunspot's magnetic field topology in Section 6.5.

To reach this point, extensive groundwork was done before. As outlined in Chapter 4, the scientific experiments and obtained data covered a wide range of spectroscopic settings, spectral lines and solar dynamics. The two observation runs which form the basis of this work were detailed in Sections 4.3.1 and 4.3.2. The principle properties of the analyzed active regions were included there, too. To obtain significant scientific outcomes, multiple analysis techniques were applied to the data. The methods and preliminary results were reported in Section 5. In the following, the observational findings on wave phenomena in sunspots are brought into context with recent observations (see Chapter 2) and magnetohydrodynamic wave theory (see Chapter 3). Special emphasis is put on the confirmation of the *modern sunspot wave scenario* which was detailed in Section 2.5.

An overview of the common knowledge on sunspot waves was given in Section 2.4. Further information can be found in the review articles by, e.g., Bogdan (2000), Bogdan and Judge (2006), Khomenko and Calvo Santamaria (2013), and Jess et al. (2015).

6.1. Driving mechanism

The permanent and very regular excitation of propagating waves in sunspots requires an unceasing and powerful driving source. This driver is settled in the very deep photosphere or even below the solar surface. The 'prime suspect' for the generation of sunspot waves like umbral flashes or running penumbral waves is the efficient absorption of p-modes transiting the active region. The possible driving mechanism will be discussed in Section 6.1.1. As described in Section 3.2, perturbations of the magnetic field topology and field strength are able to excite magnetohydrodynamic waves, too. Magnetic field oscillations as the possible driving source are considered in Section 6.1.2.

6.1.1. P-mode absorption

The solar photosphere and convection zone is densely covered with powerful acoustic p-modes (Leighton et al. 1962). These longitudinal pressure waves have prominent modes with periods of around 4–8 min and horizontal wavelengths of few to hundred Mm. In the quiet photosphere, waves with periods around 5 min and Doppler velocity oscillations of more than $0.5\,\mathrm{km\,s^{-1}}$ dominate the scene.

When these p-modes approach a sunspot region, they necessarily interact with the strong magnetic field of the spot (Abdelatif et al. 1986). When passing or crossing the sunspot, a significant portion of the acoustic wave power is absorbed (e.g., Braun et al. 1987; Bogdan et al. 1993). The energy of the absorbed p-modes can be converted in a way that magnetoacoustic modes are excited within the sunspot (Spruit and Bogdan 1992; Cally et al. 1994; Bogdan 2000; Cally et al. 2003; Schunker and Cally 2006; Khomenko and Calvo Santamaria 2013). Due to the strong magnetic field in sunspots, a large fraction of the propagating magnetoacoustic waves are slow-modes which can leak into the higher atmosphere guided by the magnetic field (e.g., Bogdan 2000). These upward propagating waves can reach up to coronal heights before becoming dissipated (e.g., De Moortel et al. 2002; De Pontieu et al. 2004; Krishna Prasad et al. 2015).

There are several reasons to assume that efficient absorption and conversion of global solar p-modes is the prime driving source of sunspot waves. First of all, the continuous appearance and propagation of umbral flashes and running penumbral waves necessitates an unceasing and powerful source. The ubiquitous solar p-modes can provide this power. For the sunspot of active region NOAA11823 (Section 4.3.1), the evolution of the photospheric wave power in the filtered 5 min range exhibits p-modes from variant directions which travel partly or completely through the sunspot region. This visual appearance is in line with other studies (e.g., Kobanov and Makarchik 2004). Furthermore, observational evidence was given that sunspots absorb up to half of the incoming wave power of the p-modes (Braun et al. 1987; Penn and Labonte 1993). As proposed by Thomas (1981), it does seem logical that sunspot oscillations in the lower photosphere are dominated magnetoacoustic waves especially in the 5 min domain. Spatially, p-mode absorption and mode conversion were suggested to happen inside the umbra and inner penumbra where the Alfvén speed and local sound speed coincide (Penn and Labonte 1993). This plasma-β equipartition depth is located in the sunspot's lower photosphere. In the darkest umbra, the equipartition can even sink below the surrounding continuum intensity surface. It was found that incident acoustic p-modes are modified into fast magnetoacoustic waves when approaching strong magnetic fields (Bloomfield et al. 2007b). This type of mode conversion, as well as the transformation from fast-mode to slow-mode magnetoacoustic waves, depends crucially on the wave attack angle. The most efficient p-mode conversion is achieved for inclination angles of $30-50°$ between the wave vector and the magnetic field (Cally et al. 2003; Schunker and Cally 2006; Bloomfield et al. 2007b). This has the major consequence that the magnetic field acts like a filter for the incoming p-modes. According to the preferred attack angle and the photospheric magnetic field inclination shown in Fig. 5.4 c), the most effective absorption takes place at the outer umbra and inner penumbra. Consequently, it should be of no surprise that the first visual signatures of sunspot waves appear at exactly this region in the sunspot photosphere (see Section 6.4.2).

The damping of the velocity wave power in the sunspot atmosphere is displayed in Fig. 6.1. As

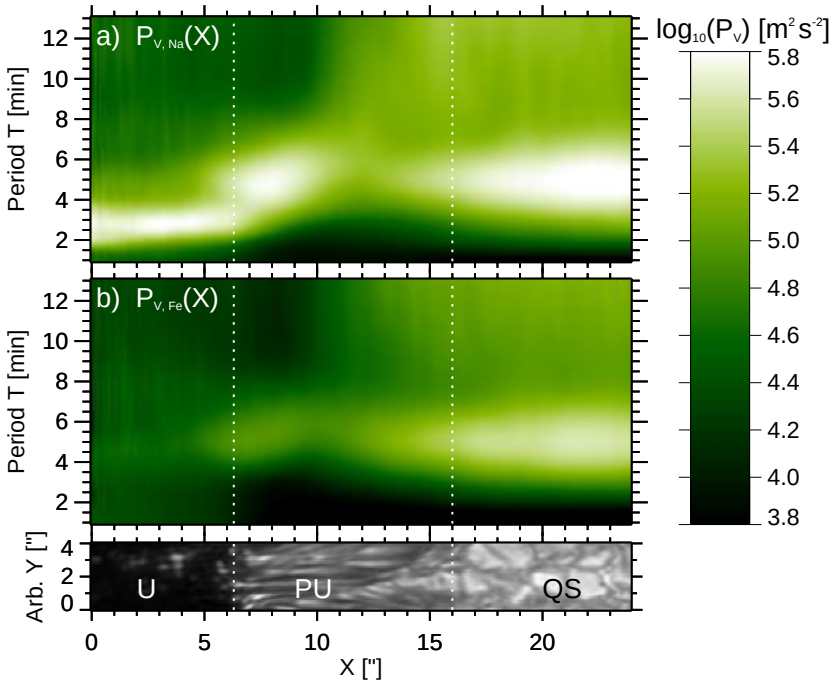

Figure 6.1.: Distribution of velocity wave power $P_{\mathrm{V}}(X)$ in the lower chromosphere (panel a) and lower photosphere (panel b) of sunspot NOAA11823. The wave power was azimuthally averaged and is plotted for the wavelet filtered periods T against the distance X from the umbral barycenter. The Doppler velocities were calculated from the Na I 589.59 nm and Fe I 630.15 nm line. The wave power is shown at a logarithmic scale with bright colors indicating high power. For context information, a slice of the sunspot in continuum intensity is added below. The dotted lines mark the average sunspot boundaries.

described in Section 5.1, the Doppler velocities were calculated for the circular sunspot of NOAA11823 (Section 4.3.1). Thereby, Doppler velocities obtained from the Fe I 630.15 nm line represent the motion of the lower sunspot photosphere up to 300 km above the optical depth unity (see Table 4.3). The Doppler velocities from the Na I 589.59 nm line primarily describe the upper photosphere to lower chromosphere (<1000 km). By means of a global wavelet analysis (see Section 5.2), the wave power and wave periods T were determined from the velocity oscillations. In Fig. 6.1, the azimuthally averaged global wavelet spectra are plotted against the radial distance X from the sunspot barycenter. The high photospheric to low chromospheric wave power $P_{\mathrm{V,Na}}(X)$ is shown in panel a). The lower photospheric wave power $P_{\mathrm{V,Fe}}(X)$ is displayed in panel b). In the lower case, it is evident that the p-modes in the 4–6 min band outside the sunspot yield the highest power. Toward the umbra, the velocity power is damped by at least one order of magnitude. This is in consistency with common knowledge (e.g., Thomas et al. 1984), see Fig. 2.6. As also discussed in Section 2.4.1, compared to the amplitudes of the p-modes in the surrounding of the sunspot, the oscillatory velocity in the umbral photosphere is reduced by a factor of three (e.g., Abdelatif et al. 1986; Balthasar et al. 1998). Of special interest in Fig. 6.1 (panel b) is the slight enhancement of velocity power at the outer umbra and inner penumbra. As it will be described in Section 6.4.2, this increase is the first imprint of running penumbral waves. In the upper photosphere and chromosphere (panel a), the case for acoustic modes outside the spot is very similar. The overall velocity power has increased only slightly. On the contrary, the umbral and penumbral velocity power of magnetoacoustic waves has risen by up to 40 times (see later in Fig. 6.7). Umbral waves in the 3 min range and running penumbral waves in the 4–7 min range dominate the sunspot region. The jump at the umbra-penumbral boundary may be the imprint of efficient absorption

of global solar p-modes (Yuan et al. 2014b). As recent studies have shown (Zhao et al. 2015), the investigation of p-modes with regard to the driving source of sunspot waves is very elaborate and a work by its own. Therefore, I leave a deeper investigation for future cooperations.

6.1.2. Magnetic field oscillations

As described in Section 3.2, perturbations and oscillations of the magnetic field can excite magnetoacoustic waves as well. When the gas pressure of the surrounding plasma interacts with the strong magnetic field concentrations in sunspots, the magnetic flux tubes are shaken, squeezed and stretched, or twisted. This drives Alfvén waves and magnetoacoustic modes which can propagate upward to the higher sunspot atmosphere. Continuous magnetic field oscillations require perturbations by a steady acoustic source like p-modes. Magnetic field fluctuations are proposed the be present in field strength and shape. The latter can occur in the form of kink or sausage modes (see Fig. 3.4), torsional modes (see right panel of Fig. 3.1), and surface modes which deflect only the surface of the magnetic field formation.

Especially at the turn of the millennium, several attempts have been made to measure magnetic field oscillations in the sunspot photosphere. As the results are mixed, no clear consensus on their existence has yet emerged. Most studies report on magnetic field fluctuations in the 3 min to 5 min period band with oscillatory amplitudes of up to 10 G (e.g., Mogilevskii et al. 1973; Gurman and House 1981; Efremov and Parfinenko 1996; Horn et al. 1997; Rueedi et al. 1998; Balthasar 1999; Norton et al. 1999; Kupke et al. 2000; Settele et al. 2002). With full-Stokes measurements, Bellot Rubio et al. (2000) yield significant magnetic field oscillation at a strength of 7–11 G. On the other hand, Lites et al. (1998) are more cautious and argue that in their one-dimensional observations either no magnetic field fluctuations are present or (with an obtained upper limit of 4 G for the rms amplitude) are too small to be detected. However, the case appears more distinct when the complete sunspot region is analyzed. In two-dimensional spectro-polarimetric observations of sunspots at high quality, significant oscillatory power was detected in localized substructures of around 1″ (Rueedi et al. 1998; Balthasar 1999; Norton et al. 1999; Kupke et al. 2000). These inhomogeneously distributed patches of enhanced fluctuation are concentrated in the center of small sunspot and pores. In larger spots, the most significant oscillations are found at the outer umbra and inner penumbra. If the signals of magnetic field oscillations are real, they are limited to much smaller umbral regions than velocity oscillations which are coherent over a large fraction of the sunspot area. As discussed by Rueedi et al. (1998), the magnetic field oscillations vary in frequency across the sunspot region and show no clear correlation with oscillations in other physical quantities. As discussed in the review article by Staude (2002), the detection of magnetic field oscillations which are probably not larger than 10–20 G requires ideal observing conditions and a well-chosen spectro-polarimetric setting.

In recent years, several authors have reported on the detection of magnetoacoustic flux tube waves (see Section 3.2.3) in small pores and other field concentrations. Fujimura and Tsuneta (2009) interpret the measured magnetic flux oscillations in individual elements of plages and pores as magnetoacoustic 'sausage' and 'kink' modes (like in Fig. 3.4). In a small pore, Martínez González et al. (2011) found magnetic field oscillations with periods of 4–11 min and suggest that the motion of the surrounding granules produces these oscillations. The conclusion is based on the finding that the isomagnetic patch area and the magnetic field strength oscillate in anti-phase. Furthermore, they claim that neither velocity nor intensity oscillations are related to fluctuations in the magnetic flux density and isomagnetic area. In addition, Morton et al. (2012) detected magnetohydrodynamic wave modes in a kink- and sausage-shaped horizontal field configuration in the active region chromosphere.

Results from HMI magnetograms: The line-of-sight magnetic field of the circular sunspot of active region NOAA11823 (see Section 4.3.1) was observed with the Helioseismic Magnetic Imager (HMI) onboard of the Solar Dynamics Observatory. The line-of-sight magnetic field strength was derived from the Stokes-V profile of the magnetically sensitive Fe I 617.33 nm lines (see Table 4.3).

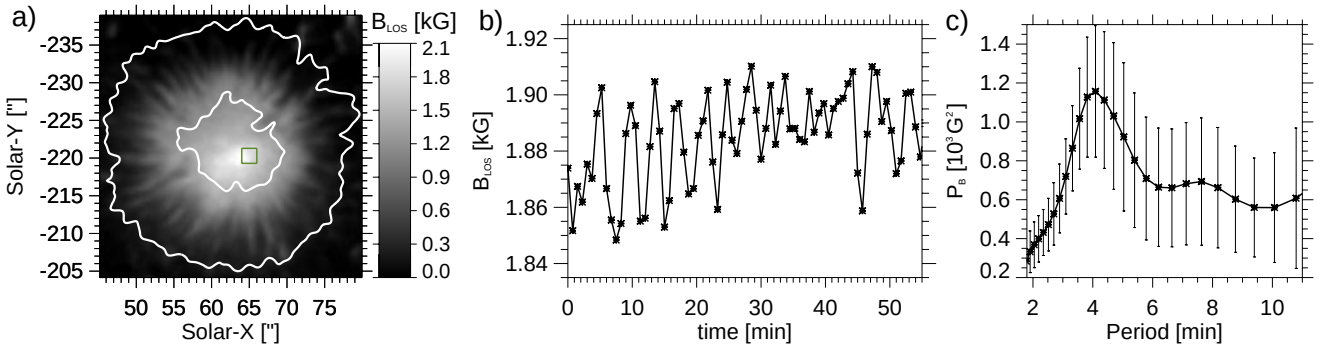

Figure 6.2.: Magnetic field oscillations in the sunspot umbra. The line-of-sight magnetic field strengths B_{LOS} in active region NOAA11823 are shown in panel a). The sunspot boundaries are contoured in white. The green square marks the region for which the 1h-time series of magnetic field strength is plotted (panel b). The oscillatory power P_{B} is shown in panel c) for the spectrum of wave periods. The error bars display the standard deviation within the analyzed region.

The obtained magnetogram for the circular sunspot is shown in Fig. 6.2 (panel a) for the first instant of observation time. As illustrated by the white-light boundaries of the umbra and penumbra, the strongest magnetic field strength is located in the inner umbra where the spot is darkest in continuum intensity. The field strength in the region close to the green square reaches values up to 2 kG. The line-of-sight field strength decreases with increasing radial distance and magnetic field inclination (see Fig. 5.4 c).

At a rough inspection, the magnetic field topology and field strength are very stable in time and spatial arc-second scale. If the investigation of the magnetic field evolution focuses on the short time scales and small spatial scales, the situation is very different. To perform a significant statistical evaluation, the magnetic field strength in a small region of $2'' \times 2''$ (green square in Fig. 6.2 a) in the umbral core is averaged for each instant of time (cadence 45 s) of the 1h-time series. As shown in panel b) of Fig. 6.2, the magnetic field strength describes an oscillatory function when plotted against time. Especially in the first 30 min, the fluctuation are very periodical with amplitudes up to 25 G. The global wavelet analysis of the magnetic oscillation is shown in panel c) of Fig. 6.2. Oscillations in the 3–6 min band dominate the power spectrum from the magnetic field fluctuations. The maximum power $P_{\mathrm{B}} = 1150\,\mathrm{G}^2$ is reached at a period of 4 min. A second increase in oscillatory power is present at 7–8 min. The errors in the power spectrum were calculated for each analyzed period as the standard deviation within the small region.

To determine the spatial signatures of magnetic field fluctuations in the sunspot region, the oscillatory power is averaged in the 3–6 min band. The power distribution $P_{\mathrm{B}}[3-6\,\mathrm{min}]$ in this period range is shown in Fig. 6.3 a). The sunspot region exhibits enhanced magnetic field oscillations (bright color) in the inner umbra core. The region coincides with the strongest umbral magnetic field strength. Moreover, high power is localized in small circular patches with diameters of $1''$ and less. The region in which most fine-scale power accumulates is marked by the green square ($5'' \times 5''$). In this area, the power of the filtered field perturbation in the 3–6 min band reaches an average value of $P_{\mathrm{B}} = 579\,(\pm 298)\,\mathrm{G}^2$. The error is given by the standard deviation within the analyzed region. For the magnetic field of the entire sunspot area, the average oscillatory power amounts to $P_{\mathrm{B}} = 155\,(\pm 122)\,\mathrm{G}^2$. It is important to notice the scales of the localized field fluctuations. Whereas in the average umbra and penumbra, the field fluctuations are around 10 G, the magnetic field in the umbral core can oscillate with up to 20 G. At very localized patches, maximum fluctuations can even reach up to 30 G.

The sunspot's frequency distribution of magnetic field fluctuations is supposed to yield further important impacts for the excitations of magnetoacoustic waves. The circular geometry of the sunspot

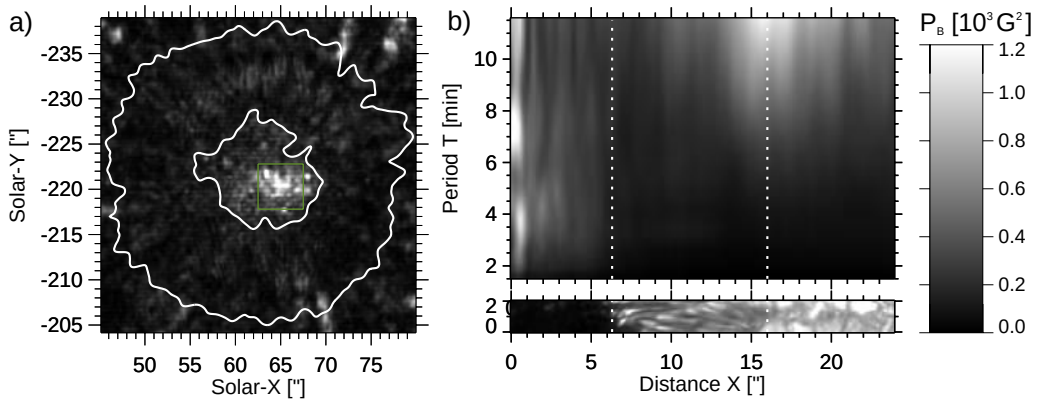

Figure 6.3.: Oscillatory power P_{B} in magnetic field strength. Panel a) shows the power in the filtered 3–6 min range for the entire sunspot region. Panel b) displays the azimuthally averaged power distribution for the entire spectrum with periods $T = 1.5 - 12$ min and radial distances X from the sunspot barycenter. The average sunspot boundaries are marked by the white dotted lines.

allows the computation of the azimuthally averaged power spectrum at each distance from the sunspot barycenter. The azimuthally averaged power P_{B} is plotted in Fig. 6.3 b) as a function of oscillatory periods T and radial distances X from the umbral center. For a better illustration, a slice of the sunspot in continuum intensity is shown at the bottom below the diagram. The inner umbra yields the most conspicuous power enhancement at periods around 3–4 min and 6–8 min. With increasing distance from the spot's center, the power peak shifts from shorter to longer wave periods of around 5 min. Along the radial axis, the patchy distribution of enhanced field fluctuations becomes apparent in the umbra. In the inner penumbra, the field is perturbed only weakly. In the outer penumbra and surroundings of the spot, the power is concentrated at periods longer than 8 min. These analytical field fluctuations are caused by *moving magnetic features* which are excited at the outer penumbra and propagate radially away from the sunspot.

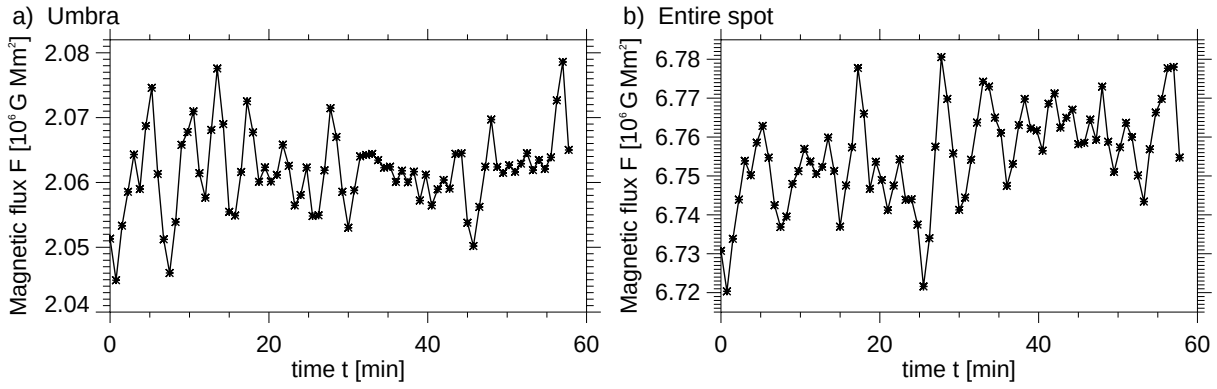

Figure 6.4.: Temporal evolution of the photospheric magnetic flux F in the umbra (panel a) and entire sunspot (panel b) of active region NOAA11823. The flux is plotted in 10^6 G Mm^2.

Another useful parameter for the investigation of magnetic field oscillations is the magnetic flux

$$F = \int \vec{B}(A)\,\mathrm{d}A \tag{6.1}$$

for a magnetic field strength $\vec{B}(A)$ with respect to the spatial area A. For the umbral area, the

magnetic flux was calculated by $F = \sum_{x,y} B_{\mathrm{LOS}}(x,y) \cdot \cos(\theta)$, with the line-of-sight magnetic field strength $B_{\mathrm{LOS}}(x,y)$ for all umbral positions (x,y). The term $\cos(\theta)$ was multiplied for each time step according to the heliocentric angle of the observation. This compensates the projection effects due to the solar rotation. The temporal evolution of the magnetic flux of the sunspot (NOAA11823) is shown in Fig. 6.4. The magnetic flux is plotted as a function of time for the umbral area (panel a) and the entire sunspot (panel b). Especially in the first half of observations, clear signals of oscillating magnetic flux are found for the umbra. Like in the umbral region, the magnetic flux of the entire sunspot is dominated by fluctuations in the 4 min range. The magnetic flux oscillations at this period band amount to 1% for the umbra and less than 0.5% for overall sunspot.

In summary, the magnetic field strength and magnetic flux in the sunspot exhibit significant oscillatory signals. Whether these measured signals are real fluctuations of the magnetic field remains unsolved. As discussed by Staude (2002), various attempts have been made to distinguish the weak magnetic field oscillations from introduced instrumental and atmospheric effects. In the case of ground-based solar observations, temporal image distortions induced by turbulences of the Earth's atmosphere can lead to fluctuations in the spectro-polarimetric signal (Landgraf 1997). The usage of adaptive optics systems and application of image reconstruction techniques reduces the atmospheric impact on the results. Of course, solar observation with space satellites do not suffer from such seeing fluctuations. As investigated by Smirnova et al. (2013), instrumentally-induced systematic magnetic field oscillations in HMI data are only present at longer periods of 12 h and 24 h and are due to the orbital motion of the telescope. No crucial artifacts exist in the temporal band of a few to several minutes. Consequently, a possibly extrinsic oscillation in the magnetic field signal of HMI is proposed to have another reason. Several authors (e.g. Lites et al. 1998; Settele et al. 2002) suggest that spurious magnetic signals can be produced by intrinsic polarimetric cross-talk from the instrument or by the inversion cross-talk between the Stokes signals. Contradictory to the conclusion of Settele et al. (2002) that the magnetic field fluctuations can be caused by a crosstalk from velocity oscillations, Rueedi et al. (1998) argue that the magnetic field fluctuations must be intrinsically solar. Furthermore, the latter authors suggest that the observed phase relations between the magnetic field and velocity oscillations are forced by magnetoacoustic gravity waves in the sunspot photosphere. The waves affect the Stokes signals and consequently the inferred magnetic field vector. The upward propagation of slow-mode magnetoacoustic waves in the umbra introduces compressions and rarefactions of the plasma. Temperature and density fluctuations go in hand with the pressure perturbations from the quasi-acoustic waves. As proposed by several studies (Rüedi and Solanki 1999; Bellot Rubio et al. 2000; Rüedi and Cally 2003), vertical fluctuations in the atmospheric opacity and height of line formation are the reason for the oscillation of the Stokes V signal of circular polarization. The magnetic field in the photospheric umbra yields a negative vertical gradient of at least $-0.1\,\mathrm{G\,km^{-1}}$ (Collados et al. 1994) but often more than $-1\,\mathrm{G\,km^{-1}}$ in the lower photosphere (Wittmann 1974). Consequently, a vertical oscillation in altitude along the magnetic field gradient leads to a periodical variation of the obtained magnetic field strength. Assuming such a field gradient of $-1\,\mathrm{G\,km^{-1}}$ in the lower photosphere sampled by the Fe I 617.33 nm line (see Table 4.3), an altitudinal peak-to-peak oscillation of 50 km of the formation region would cause a magnetic field fluctuation of 25 G, like the values reported for localized patches in the umbral core. By an elaborate theoretical investigation of umbral magnetic field oscillations in synthetic observations, Felipe et al. (2014) obtain significant signals in the 5 min band with amplitudes up to 14 G which are caused by magnetoacoustic wave propagation.

To give a synopsis of the obtained magnetic field fluctuations, I propose that oscillations are indeed intrinsically solar. Whether the signal can be interpreted as a real magnetic field oscillation or the effect of propagating magnetoacoustic waves remains to be clarified. Nevertheless, the fact that one event can affect the other hints at a close relation of magnetic field perturbation and propagating waves in sunspots.

6.2. Wave characteristics in the spot's atmosphere

As introduced in Section 2.4, the observed oscillations are traditionally classified according to the atmospheric layer and characteristic wave frequency. Whereas the sunspot photosphere is dominated by 5 min oscillations (Section 2.4.1), the chromosphere above sunspots features bright umbral flashes and 3 min oscillations in the umbral area (Section 2.4.2) and running penumbral waves in the penumbral area (Section 2.4.3). Throughout the sunspot atmosphere, the observed waves differ systematically in their propagation direction, apparent velocity, and dominant wave period. Contrary to the apparent differences, a modern wave scenario (Section 2.5) unites the wave phenomena as upward propagating slow-mode magnetoacoustic waves which are guided along sunspot's magnetic field lines. The disparities of the wave characteristics are explained by the larger zenith inclination of the penumbral magnetic field and the caused variation of the acoustic cut-off frequency.

In this section, I will present the wave characteristics in the atmosphere above sunspot region NOAA11823. The observations (see Section 4.3.1) permit a complementary determination of the wave properties throughout the sunspot atmosphere, from the photosphere and chromosphere (Section 6.2.1) up to the transition region and corona (Section 6.2.2). The results of wave appearance in spectral intensities and Doppler velocities are displayed and compared. The wave propagation is analyzed with special emphasis on the propagation direction and amplification in the lower sunspot atmosphere. For the first time, a comprehensive three-dimensional wave power distribution is presented. The wavelet power and dominant wave periods in the sunspot region are analyzed at high spatial resolution. Whereas this section will deal with the general wave characteristics in the sunspot region, the subsequent Sections 6.3 and 6.4 will focus on the fine-scale properties of umbral flashes and running penumbral waves.

6.2.1. Photosphere to chromosphere

The most conspicuous wave signatures are observed in the sunspot chromosphere. According to the favored wave scenario, slow-mode magnetoacoustic waves propagate upward along the magnetic field lines and manifest as umbral flashes and running penumbral waves. Consequently, compressive sunspot waves should also be measurable in the photosphere below. According to the higher plasma density in the lower photosphere, the signal is of course weaker and less clear due to the broad mixture of vertically trapped wave modes. Enabled by the high quality and coverage of the observational sequence, the evolution of sunspot waves is analyzed throughout the lower photosphere to the middle chromosphere. With a high spatial ($<0.5''$) and temporal (<14 s) resolution (see Tables 4.5 and 4.6), the spectroscopic observations provide an excellent basis for the analysis of the wave characteristics. The fully-developed, circular sunspot of active region NOAA11823 serves as a typical example to investigate the fundamental wave characteristics in the atmosphere of sunspots. Since the sunspot is very stable and located close to the solar disk center, it guarantees a temporal stability and spatial co-reference for the analysis. Moreover, the simultaneous spectroscopic observation with multiple spectrometers in ten different photospheric and chromospheric spectral bands and lines makes this study of sunspot waves unique and most likely trend-setting. All scientific instruments, spectral settings and observational parameters were described in Chapter 4.

Chromospheric wave appearance

The lower chromosphere serves as a unique laboratory to investigate the appearance and motion of wave phenomena in sunspots. The exponentially decreasing atmospheric gas density (see Fig. 2.5 b) enlarges the amplitude of upward propagating waves toward the chromosphere. In combination with the atmospheric temperature minimum in the upper photosphere to lower chromosphere (Fig. 2.5 a), the speed of sound is smallest in these layers. Magnetoacoustic waves which propagate with high velocity can therefore become sonic or super-sonic in the lower chromosphere and manifest as strong

oscillations in Doppler velocity and spectral intensity.

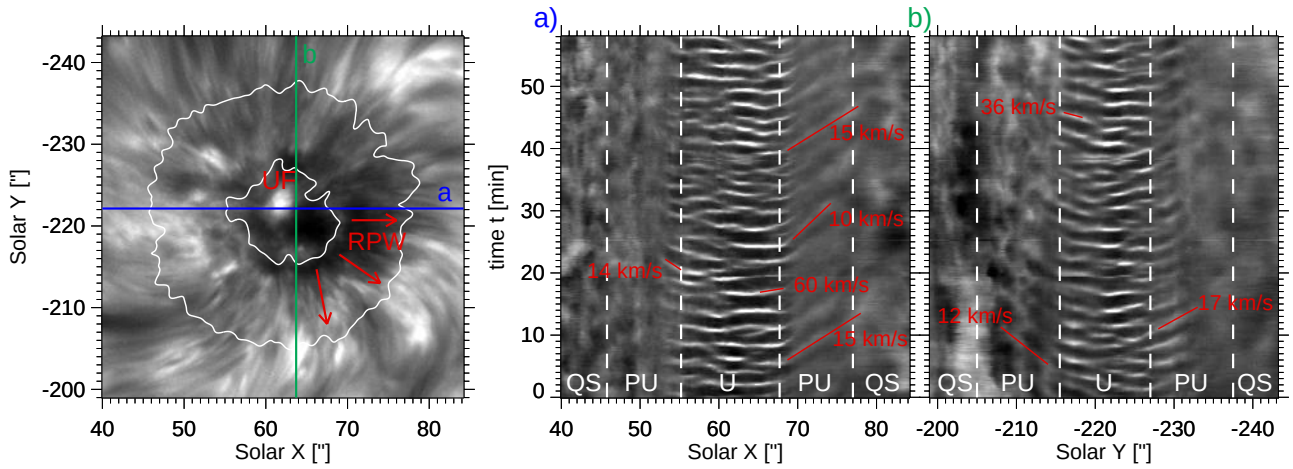

Figure 6.5.: Wave signatures in the temporal evolution of the chromospheric intensity in sunspot region NOAA11823. On the left, the sunspot is shown in spectral line core intensity of Ca II 854.21 nm observed at $t = 6.2$ min. A strong umbral flash (UF) is present in the umbra. Running penumbral waves (RPW) propagate radially outward (red arrows). The spectral intensities along the marked a) horizontal (blue line) and b) vertical (green line) slice are displayed in the right panels as a function of t. The temporal average was subtracted. The intensity fluctuations are normalized and scaled to $I = 1.0 \pm 0.5$. The vertical dashed lines mark the umbral (U) and penumbral (PU) white-light boundaries of the sunspot (QS=quiet sun). The red bars highlight the apparent velocities of running penumbral waves and umbral flashes.

The analysis of oscillations in chromospheric spectral intensity focuses on the line core and inner wings of Ca II at wavelength around 854.21 nm and Na I around 589.59 nm (see Fig. 4.13). The amplitudes of brightness oscillations due to waves in the sunspot region NOAA11823 (see Fig. 4.14) differ significantly for the umbral, penumbral, and surrounding area. In the umbra, the brightest umbral flashes manifest as relative intensity amplifications exceeding the quiescence intensity average by up to 200%. For the average umbral area, the amplitude of periodical intensity oscillations in lower chromosphere amounts to 20%. In the penumbra, the average amplitude of intensity oscillatory from running penumbral waves ranges at 10%.

The apparent wave propagation in the sunspot chromosphere is displayed in Fig. 6.5. On the left-hand side, the sunspot region is shown in spectral line core intensity of Ca II at 854.212 nm. At this instance of time ($t = 6.2$ min), an umbral flash (UF) is present in the upper half of the umbra. Its brightness is 190% above the undisturbed light level. In the lower right quarter of the umbral boundary, running penumbral waves (RPW) with enhanced intensity start to spread out radially (red arrows) along the penumbral filaments. The running penumbral waves seem to be excited together with the preceding umbral flash in the dark core in the lower right part of the umbra. The apparent wave motion is clearly visible when a horizontal (blue) and vertical (green) slice is placed across the sunspot. The temporal evolution of the chromospheric intensity signal along the slices is shown in the corresponding panels (a and b) on the right. For spatial context, the white-light boundaries of the sunspot are drawn as vertical dashed lines. The occurrence of bright umbral flashes is remarkably continuous in the umbral area. The analysis yields an average temporal period $T = 2.8 \pm 0.2$ min. The appearance of umbral flashes in the spatio-temporal diagram resembles the shape of bowls or arcs. The centers of the shock waves appear at different locations in the umbra and exhibit a spatial extent between $2''$ and $5''$. The red bar in Fig. 6.5 a) at $t = 17$ min is placed at a strong umbral flash and indicates an apparent horizontal spreading of around 60 km s^{-1}. In panel b), another trajectory suggest a wave

motion with 36 km s^{-1}. As it can be inferred from the gradients of the arcs of umbral flashes, such high velocities are very common. Some arcs even suggest apparent motions as large as 100 km s^{-1} close to the initiation point of the shock wave. The reason for such enormous apparent velocities is discussed in Section 6.3.3.

The umbral wave motion is followed by running penumbral waves along the chromospheric penumbral filaments. In the spatio-temporal diagrams of Fig. 6.5, the signals of the spreading waves in the penumbral (PU) area are significantly weaker than in the umbra. The herringbone pattern yields an apparent horizontal velocity which is much slower than for umbral flashes. At the estimated height of around 1000 km in the sunspot chromosphere, the apparent velocity ranges between 10 km s^{-1} and 20 km s^{-1}. Several wave trains are marked by red bars in the diagrams. The non-linear gradients of most wave trains reveal that the apparent velocity of the running penumbral waves decreases from the inner to the outer penumbra. In accordance with the results of Jess et al. (2013), the wave speed decreases in average by around 5 km s^{-1} within the first five arc-seconds of the inner penumbra. It can be noticed that some of the running penumbral waves extend beyond the outer white-light boundary of the sunspot and proceed their propagation along the superpenumbral filaments. As it will be discussed later in detail, the temporal period of the wave occurrence increases radially in the penumbra. Obviously, some of the umbral flashes visually proceed as running penumbral waves. Moreover, some pairs of successive umbral waves merge within the first 2″ of the inner penumbra and propagate on as one running penumbral wave.

Upward propagation and wave amplification

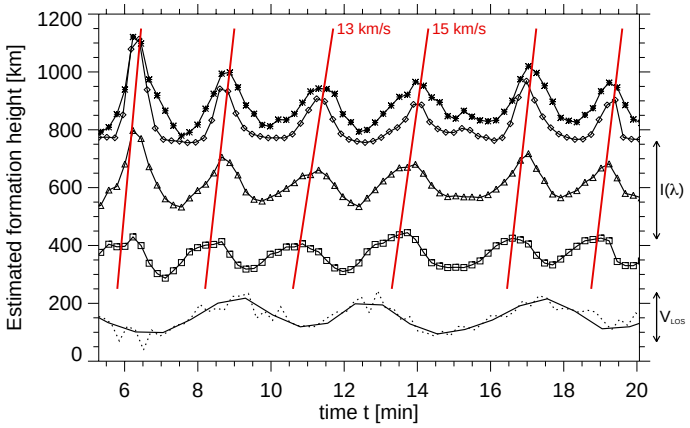

Figure 6.6.: Upward propagation of umbral waves from the photosphere to the chromosphere. The spectral intensities $I(\lambda)$ at four characteristic wavelength positions were averaged for a small 2″ × 2″ region of strong oscillatory signals in the umbral center. The scaled intensity oscillations in the Na I 589.59 nm line at $\lambda_{2,\mathrm{C-12pm}}$ (squares), $\lambda_{3,\mathrm{C-6pm}}$ (triangles), $\lambda_{4,\mathrm{Core}}$ (asterisks) are plotted according to the estimated atmospheric height of formation as a function of time t. The intensity oscillation of Ca II 854.21 nm at $\lambda_{3,\mathrm{C-22pm}}$ (diamonds) are added. The red lines mark the upward propagation of the waves. The scaled oscillations in Doppler velocity v_{LOS} from the lower photospheric Fe I lines at 630.15 nm (dotted) and 617.33 nm (solid) are displayed as context information.

Magnetoacoustic waves in sunspots propagate upward to the chromosphere and upper atmosphere. For umbral waves and flashes, this statement has been proven by various studies (e.g., Centeno et al. 2006; Felipe et al. 2010b). The spectroscopic signal of the compressive waves can be traced in Doppler velocities and spectral intensities between two or more atmospheric layers. A linear wave which propagates upwards along the atmospheric formation height of a spectral line affects the line profile by an intensity enhancements and shift in wavelength. Since a spectral line covers a broad atmospheric

formation layer, the propagating magnetoacoustic wave changes the spectral intensities differentially. In this analysis, the Na I 589.59 nm and Ca II 854.21 nm lines cover a range from the lower photosphere to the lower chromosphere. Whereas the line wings of both lines are formed in the photosphere, the average formation height of the line core reaches up to 1000 km in the chromosphere.

A first simple analysis of the wave signals at different characteristic wavelength positions proves the upward propagation of umbral waves. Fig. 6.6 shows the temporal oscillations in spectral intensity at four wavelength positions corresponding to different atmospheric altitudes. The intensities within a small $2'' \times 2''$ region in the central umbra are averaged. The region is centered on the umbral area which exhibits the highest oscillatory power in 2–3 min band in all layers from the upper photosphere to lower corona (see Fig. 6.17, region 10). To ensure the analysis of the same wavefronts, the investigation is limited to the area with a vertical magnetic field pointing almost directly along the line-of-sight of the observation. For umbral waves which follow the magnetic field lines, the spatial displacements from the photosphere to chromosphere should be below $0.3''$.The amplitudes of the intensity oscillations were scaled and centered according to the estimated formation heights. The comparison of the temporal evolution of the four signal (squares, triangles, diamonds, asterisks) yields a systematic trend. With increasing atmospheric height, the oscillatory signal shifts linearly in time. In the upper photosphere, the brightness variation from the umbral wave describes a clear sinusoidal curve with a period of 2.6 min. Several hundred kilometers higher in the chromosphere, the wave function is described by a basic intensity level with steep periodical peaks. According to the maximum brightness, the waves arrive around one minute later in the chromosphere than in the photosphere. As illustrated in Fig. 6.6 by the red lines, the waves propagate upward with vertical velocities of more than $13\,\mathrm{km\,s^{-1}}$. A more elaborate analysis of the oscillatory time lags was presented in Section 5.4.1. The proposed method aims to infer the three-dimensional wave propagation in sunspot between two atmospheric layers. The oscillatory signals are correlated within a predefined temporal and spatial box. The results of obtained wave propagation and travel times in the umbra are listed in Table A.1 for various wavelengths and their estimated atmospheric formation heights. The results for the overall sunspot region are displayed exemplarily in Figs. 5.6 and A.5 in the appendix. The color code (grayscale) and spatial displacements (red arrows) confirm the assumption that waves in the umbra feature the smallest time delays and spatial shifts. At the umbral boundary and inner penumbra, the temporal differences increase significantly and the arrows of spatial displacements are predominantly oriented radially outward. The results for the outer umbra and inner penumbra suggest an upward but more inclined wave propagation. The increasing time delays hint at longer travel distances. In summary, the findings strongly support the slow-mode wave propagation along the sunspot's magnetic field lines as proposed by Bloomfield et al. (2007a).

I briefly want to recapitulate the wave power distribution in the sunspot atmosphere from Section 6.1.1 which serves as the basis for the examination of the amplification. As shown by the spatio-periodical distribution in Fig. 6.1 (panel b), the azimuthally averaged wave power of velocity oscillations in the lower photosphere decreases from outside to inside the sunspot. Toward the chromosphere (panel a), the velocity power changes dramatically in absolute magnitude and periodical dispersal. A comparison of the wave power at both layers reveals two major results. The first is the general amplification of the velocity power toward the chromosphere. Due to the exponentially decreasing atmospheric density, the wave energy of the modes has to be conserved by the chromospheric velocity power. The second major difference is the disparity of the amplification with respect to the wave period. Especially in the sunspot umbra, the propagating 3 min waves exhibit dramatically enhanced velocity power. When the ratio ($P_{\mathrm{V,\,Na}}/P_{\mathrm{V,\,Fe}}$) of the Doppler velocity power from the Na I 589.59 nm and Fe I 630.15 nm line is calculated, the distribution of wave power amplification from the lower photosphere to the lower chromosphere is very distinct. In Fig. 6.7, the azimuthally averaged amplification is displayed for the analyzed wave periods and radial distances from the sunspot center. For the best visualization, the logarithmic scaling is inverse. The largest amplifications are indicated by dark colors. The diagram presents a diagnostic summary of wave propagation in the lower sunspot atmosphere. In the umbra,

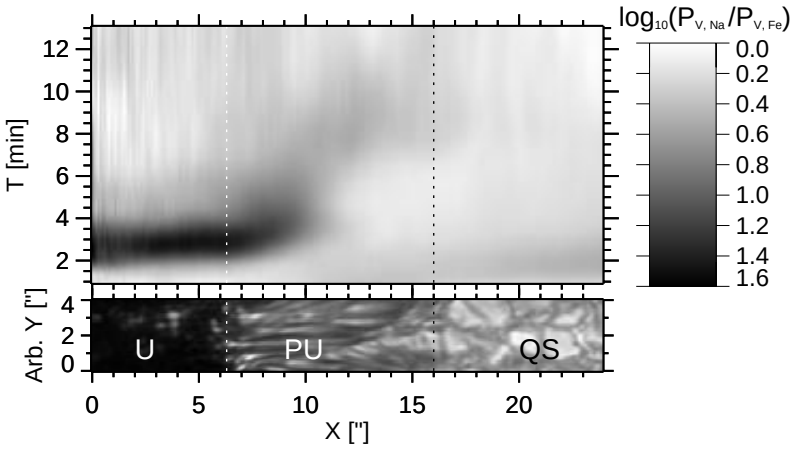

Figure 6.7.: Amplification of the velocity power in the sunspot region NOAA11823 at the transition from the lower photosphere to the lower chromosphere. The ratio ($P_{\mathrm{V,\,Na}}/P_{\mathrm{V,\,Fe}}$) of the Doppler velocity power from the Na I 589.59 nm and Fe I 630.15 nm line (see Fig. 6.1) is displayed at a logarithmic scale. The azimuthally averaged distribution of amplifications is shown for radial distances X from the sunspot barycenter and wave periods T. Dark colors indicate strong amplifications. The average umbral (U) and penumbral (PU) boundaries of the sunspot in continuum intensity (bottom) are marked as vertical dotted lines.

the power ratio is well described by the frequency dependent formulae given by Bogdan and Judge (2006). For waves with frequencies above the acoustic cut-off frequency ($f \geq 5.2\,\mathrm{mHz}$), the relative Doppler velocity power

$$\frac{P_{\mathrm{chromo.}}(f)}{P_{\mathrm{photo.}}(f)} = \frac{\rho_{\mathrm{photo.}}}{\rho_{\mathrm{chromo.}}} \tag{6.2}$$

increases with the inverse ratio of the ambient densities, $\rho_{\mathrm{photo.}}$ and $\rho_{\mathrm{chromo.}}$, from the sunspot photosphere to chromosphere. The density ratio typically amounts to 100–150 between the lower photosphere and middle chromosphere. This explains the strong increase in velocity power by a number of up to $10^{1.8}$ for periods below 192 s. On the other hand, waves with frequencies below the acoustic cut-off frequency are evanescent in the umbral chromosphere. The steep gradients of the atmospheric parameters cause resonances at the reflecting temperature minimum layer. The amplification of the velocity wave power for frequencies $f \leq 5.2\,\mathrm{mHz}$ below the acoustic cut-off value is approximated by

$$\frac{P_{\mathrm{chromo.}}(f)}{P_{\mathrm{photo.}}(f)} = \left(\frac{\rho_{\mathrm{photo.}}}{\rho_{\mathrm{chromo.}}}\right)^{1-\sqrt{1-(f/5.2\,\mathrm{mHz})^2}} . \tag{6.3}$$

For the same density ratio as above, photospheric 5 min waves will solely triple their velocity wave power toward the chromosphere. The kinetic energy density of waves with periods above the acoustic cut-off period therefore decreases significantly. In the penumbra, the approximation has to be refined since the maximum power amplification decreases in amount and shifts toward longer wave periods with increasing distance from the umbra (Fig. 6.7). At the outer penumbral boundary, waves in the 8–10 min band experience a maximum power amplification by a factor of five. The three-minute oscillation are only doubled in velocity power. In the vicinity of the sunspot, the overall amplification does not exceed a factor of two. Only a small fraction of short-period waves experiences a larger increase. The findings are in agreement with the Doppler velocity and power distribution reported by other authors (e.g., Lites 1984; Lites and Thomas 1985; Lites et al. 1998; Centeno et al. 2006; Felipe et al. 2010b) as described in Section 2.4.

Distribution of wave power in a sunspot

The characteristic changes of wave power and oscillatory periods presented in Figs. 6.1 and 6.7 recommend a deeper investigation of the wave power distribution in the sunspot atmosphere. Therefore, I will first perform a spatial analysis of the wavelet filtered velocity power and determine the dominant wave periods for the sunspot region. After that, the investigation will be extended to intensity oscillations at characteristic wavelength position of the spectral lines. Enabled by the diverse spectral formation heights, the three-dimensional variation of the wave distribution is presented. The results are supported by the inferred spatial distribution of the dominating wave periods.

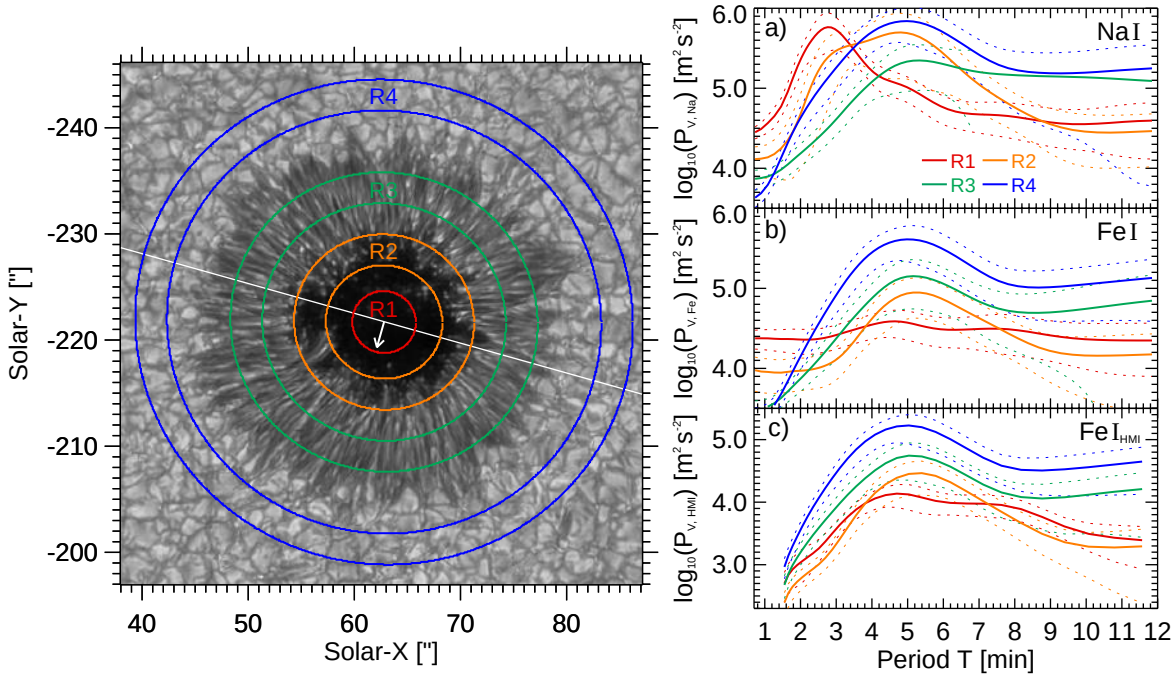

Figure 6.8.: Velocity power distribution in the photosphere and chromosphere of sunspot NOAA11823. On the left, the sunspot is shown in continuum intensity (ROSA, see Table 4.5). The white arrow is pointing toward the disk center. Perpendicular to it, the white line is the line-of-symmetry. The wavelet power was analyzed for oscillations in Doppler velocities of three different spectral lines: the photospheric to lower chromospheric Na I line at 589.59nm (panel a), and the lower photospheric Fe I lines at 630.15nm (panel b) and 617.33nm (panel c). The average global power spectra are shown within four different regions in the sunspot umbra (R1, red), umbra-penumbra boundary (R2, orange), outer penumbra (R3, green), and vicinity (R4, blue). The velocity power P_V is plotted in solid at a logarithmic scale against the wave period T. The error range is displayed by the dotted lines.

Velocity wave power: First, a spatial study of the global wavelet spectra is performed for the Doppler velocity oscillations in the lower photosphere and lower chromosphere. As illustrated in the left panel of Fig. 6.8, three characteristic regions inside and one region outside of the sunspot are analyzed. The Doppler velocities were obtained from the Na I line at 589.59nm (IBIS) for the lower chromosphere and from the Fe I lines at 630.15nm (IBIS) and 617.33nm (HMI) for the lower photosphere. The oscillations are wavelet analyzed pixel-by-pixel for the whole sunspot region. To work out the characteristic differences, the global power spectra were averaged within the indicated regions in the umbra (R1, red sector), at the umbral-penumbral boundary (R2, orange sector), in the outer penumbra (R3, green sector), and in the surrounding area (R4, blue) of the sunspot. The circular regions were foreshortened according to the heliocentric angle $\theta = 14°$ at the sunspot center. The average global wavelet spectra of velocity wave power are shown in panels Fig. 6.8 according to

the spectral lines (panel a–c). The wave power P_V (solid lines) at the logarithmic scale is plotted as a function of wave period T. In the 2–7 min band, the standard deviations (dotted lines) within the respective spatial regions are small compared to the mean power. The power spectra of the lower photosphere (panels b and c) resemble each other very well in shape and size. The power in regions R2–R4 reaches its maximum at periods around 5 min. Only in the umbral region R1 (red curves), the power has two maxima, the stronger peak at 4.5 min and the weaker peak at around 8 min. The magnitude of the power decreases systematically from the vicinity of the spot to the umbral core. Toward the lower chromosphere (panel a), the curves of the wave power spectra alter drastically. The power spectrum of the umbral region R1 exhibits a defined maximum of $P_{V,Na} = 10^{5.8}\,m^2\,s^{-2}$ at around 2.8 min and a second peak at 5 min. At the umbral boundary R2 (orange curve), the power spectrum features the same maxima, but the 5 min peak is overpowering the 3 min peak. The power in the outer penumbra R3 (green curve) and vicinity R4 (blue curve) are similar to the photospheric case. In Fig. 6.9, the velocity power spectra are ordered according to the analyzed regions (R1–R4, panels a–d). By this illustration, the atmospheric changes of the wave power are most obvious for the different regions. In the surroundings of the sunspot (panel d), the overall velocity power increases slightly from the lower photosphere (dotted and dashed dotted lines) to the lower chromosphere (solid line). The shape of the curve remains the same. In the outer penumbra (panel c), the case it very alike to the previous one. In the umbral core (panel a) and umbral boundary (panel b), the strong increase of the 3 min wave power modifies the profile noticeably.

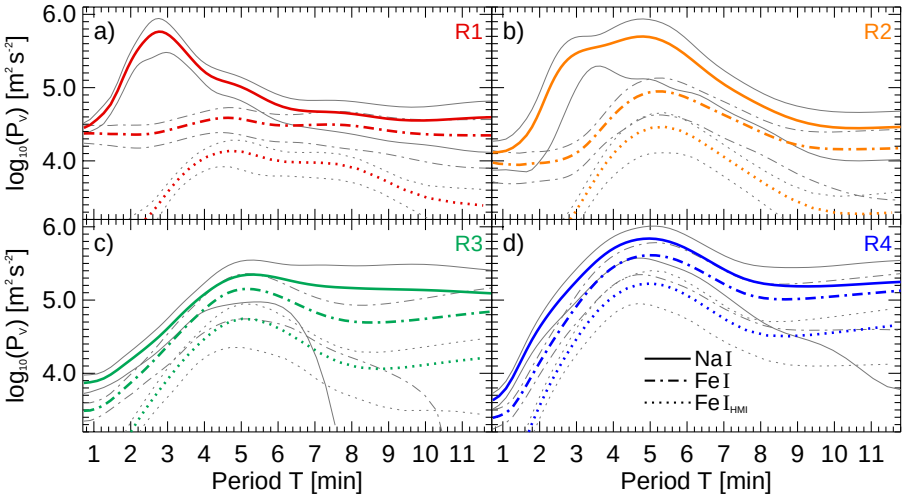

Figure 6.9.: Changes in velocity power from the photosphere to the chromosphere. The power spectra of Fig. 6.8 are ordered according to their spatial region. The distribution of wave power P_V for wave periods T is shown for a) the sunspot umbra (R1, red), b) the umbra-penumbra boundary (R2, orange), the outer penumbra (R3, green), and vicinity (R4, blue). The results from the Na I 589.59 nm (solid), Fe I 630.15 nm (dashed-dotted), and Fe I 617.33 nm lines are plotted in color. The gray lines mark the standard deviations.

Evidently, the dominating oscillatory modes differ within the sunspot. Already the azimuthally averaged power distribution in Fig. 6.1 suggested continuous shifts of the dominating wave periods from the inner to the outer penumbra. In the next step, the two-dimensional spatial distribution of the sunspot's wave power shall be analyzed. Therefore, the filtered wavelet power from Doppler velocity oscillations is averaged over several characteristic period bands. The spatial power distribution in the sunspot region is displayed in Fig. 6.10 for six different ranges from 1.5– 2.5 min (panels a) to 6 – 8 min (panels f). The results from the lower chromosphere (top panels) and lower photosphere (bottom panels) can be compared directly. Evidently, the velocity power in the umbra and inner penumbra

shifts radially outside with increasing wave period. In the lower chromosphere (upper row), the velocity power in the 1.5–2.5 min range (panel a) is concentrated in the inner umbra. In the 2.5–3.0 min band (panel b) with dominant umbral flash occurrence, the power is localized to the umbral center near the accumulation of umbral dots (compare Fig. 6.8) and at the outer umbra. From the filtered 3.0–3.5 min (panel c in Fig. 6.10) to 3.5–4.0 min band, the power shifts quickly from the umbral boundary to the inner penumbra. The radial spreading in the inner penumbra proceeds for wave periods between 4 min and 6 min (panels e). The power in the umbra decreases noticeably. The spatial distribution of the velocity power has a filamentary structure and resembles the penumbral appearance in spectral intensity (see Fig. 4.14 g). In the period band covering 6–8 min oscillations (panel f in Fig. 6.10), the ring-like shape of high wave power has already shifted to the middle penumbra. At even longer wave periods the power distribution approaches the outer penumbral boundary. The results are in line with the ring-shaped power distribution and shift in wave period presented by Jess et al. (2013) for chromospheric intensity oscillations. In the lower photosphere (bottom row of Fig. 6.10), the velocity power in the sunspot is reduced by a factor of five (see Fig. 6.1 b) from the p-mode-dominated vicinity of the spot to the inner umbra. Nevertheless, the enhanced concentration of umbral 3 min oscillations proceeds with a similar radial spreading for the filtered period band between 3.5 min and 6 min (panels d and e). In Section 6.4.2, these first imprints of running penumbral waves in the lower photosphere are analyzed and discussed in more detail.

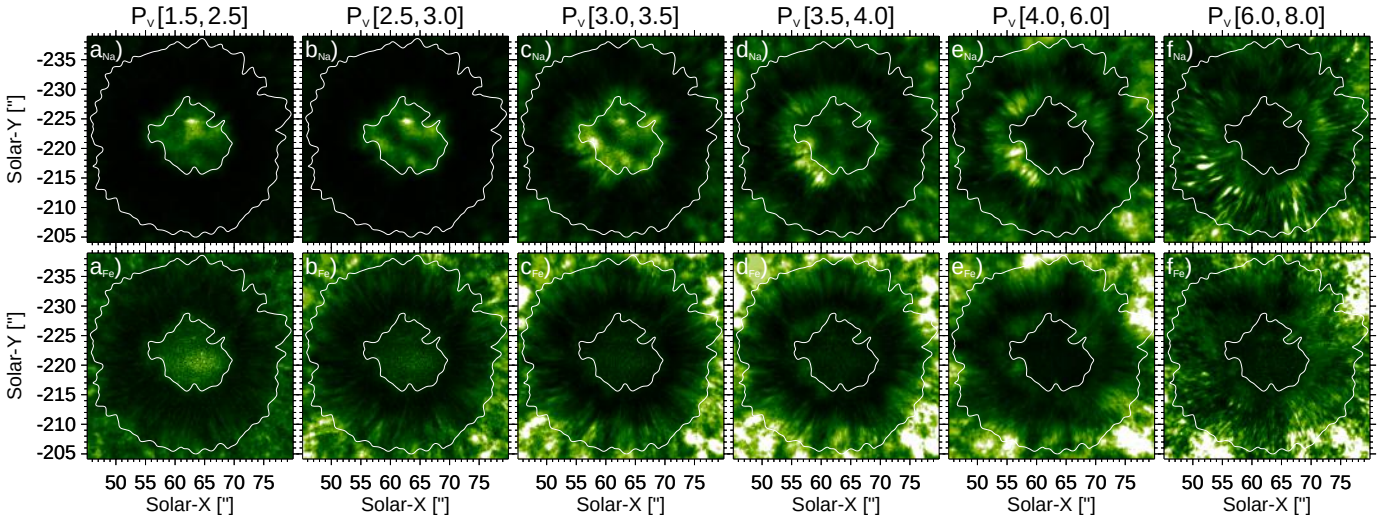

Figure 6.10.: Distribution of the velocity power P_V in the chromosphere (upper panels) and photosphere (lower panels) sunspot region NOAA 11823. The oscillations in Doppler velocity of the Na I 589.59 nm (panels a_{Na}–f_{Na}) and Fe I 630.15 nm (panels a_{Fe}–f_{Fe}) are shown for six different period ranges from 1.5–2.5 min (left) to 6–8 min (right). The power is scaled for best visualization. Brighter colors indicate stronger oscillations. The penumbral boundaries in continuum intensity are contoured in white.

Intensity wave power: Sunspot waves also manifest as brightness oscillations in the upper photosphere and chromosphere. The compressive wave propagation leads to fluctuations in spectral intensity at wavelength positions which represent certain atmospheric formation heights in the chromosphere and upper photosphere. The spectroscopic observations of the sunspot in the line core and wings of Ca II 854.21 nm, Na I 589.59 nm, Ca II K and Hβ, enable the power analysis of oscillations in spectral intensity. The results of the global wavelet analysis are presented in Figs. A.1 – A.4. All cases reveal a very similar behavior to the findings from the chromospheric velocity oscillations. In the chromosphere, the power in the 2–3 min range is concentrated in the inner umbra. With increasing wave period, the ring-like power distribution spreads out radially. From the 3–3.5 min band to the 6–8 min band, the maximum power of intensity oscillations shifts from the umbral boundary to the outer penumbra. The

filamentary distribution in the penumbral area is pronounced (see Fig. A.2). This behavior is in accordance with other observational studies (e.g., Nagashima et al. 2007; Reznikova and Shibasaki 2012; Jess et al. 2013). Besides the obtained properties of the wave power distribution at the chromospheric layers, a second and probably even more important conclusion can be drawn from the spectroscopic high-resolution observation. In Fig. A.1 and A.4, the power distribution is displayed for three characteristic wavelength positions of the Ca II 854.21 nm and Na I 589.59 nm line. The top panels belong to the chromospheric line minimum of each spectral line. The panels in the middle row correspond to the lower chromospheric blue line core and the bottom panels result from the intensity oscillations of the photospheric line wing positions. Like in the chromosphere, the intensity wave power of the middle photosphere is enhanced evidently in the umbra and inner penumbra. A closer inspection of the spatial power distribution in the filtered period bands reveals that the power at the inner penumbra spreads radially for the upward transition from the middle photosphere to the lower chromosphere (from bottom to top panel). As it will be discussed in Section 6.4.1, this spreading of the concentrated power is caused by the propagation of running penumbral waves along the sunspot's magnetic field lines and the effect of the atmospheric acoustic cut-off frequency (described in Section 3.4).

It has to be noted that in a small penumbral section in the upper left half of the sunspot, a penumbral jet has occurred in the middle chromosphere. In the power analysis of intensity oscillations in the line cores of Ca II 854.21 nm (upper row in Fig. A.1) and Ca II K (Fig. A.3), this bright sunspot jet dominates the power in the 3.5–6 min range. As proposed in literature (e.g., Canfield et al. 1996; Morton 2012), the penumbral jet is caused by reconnection and is especially present in the upper chromosphere and transition region.

Dominating wave periods in the sunspot region

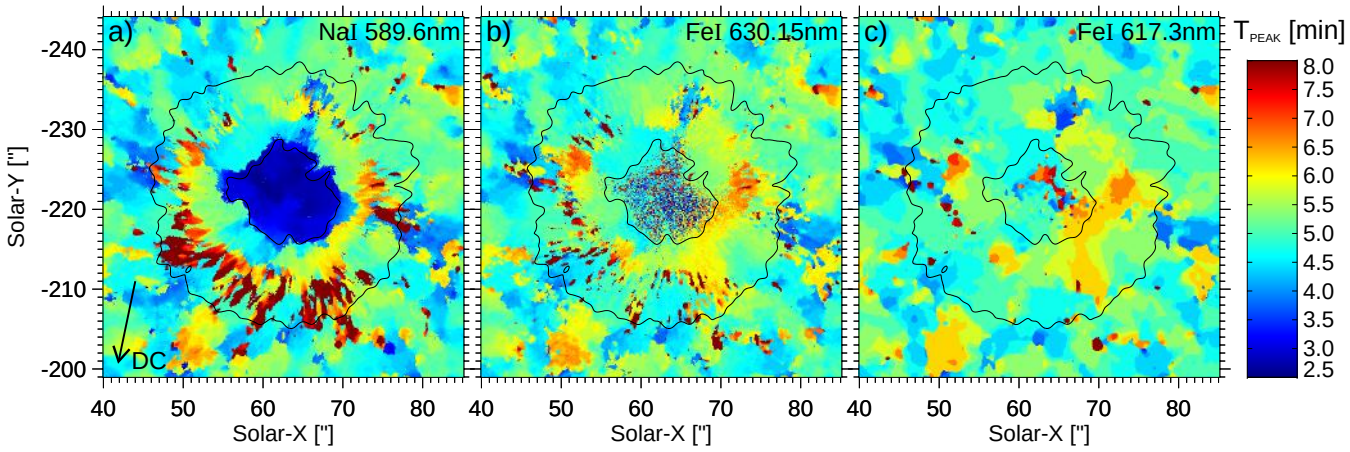

Figure 6.11.: Distribution of dominant wave periods in the sunspot region NOAA11823. The peak periods T_{PEAK} were obtained from the global velocity power spectra of the a) photospheric to lower chromospheric Na I line at 589.59 nm, b) and c) lower photospheric Fe I lines at 630.15 nm and 617.33 nm. The periods are displayed in the range from 2.5 min (dark blue) to 8 min (dark red). The umbral and penumbral boundaries are contoured in black. The black arrow is pointing toward the solar disk center.

The analysis of the power spectra have provided evidence that the dominating wave periods change across the sunspot region. In the next step, I want to determine the two-dimension spatial distribution of the peak periods in a sunspot. Therefore, the maximum value and its position in the power spectrum has to be inferred pixelwise for the whole field of view. To put the emphasis on the period range between 2 min and 10 min, a weighting of the power spectra is introduced (see Section 6.5.1). The evaluation is done for the global wavelet power spectra obtained from Doppler velocities as well as from spectral

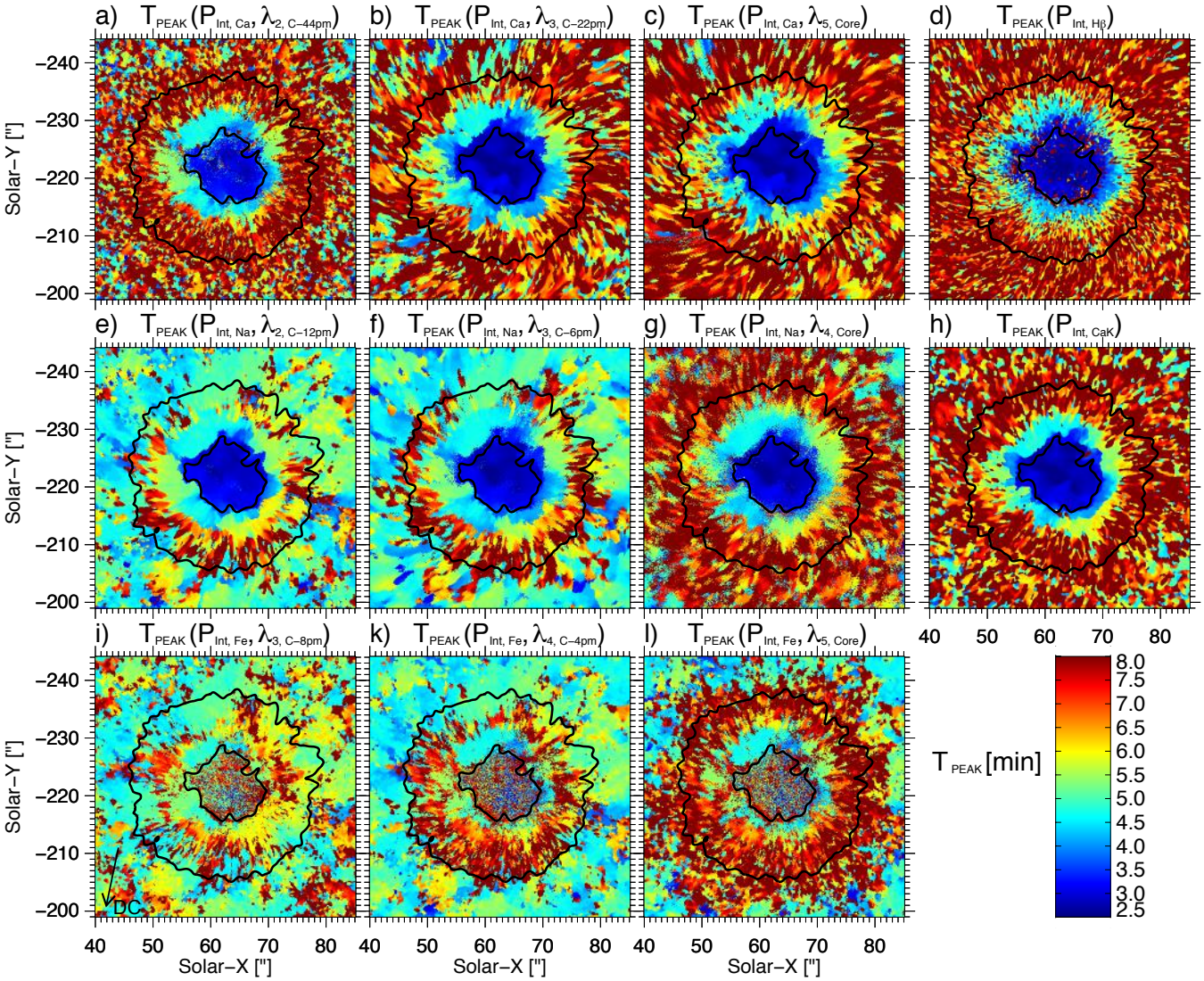

Figure 6.12.: Distribution of dominant wave periods from intensity oscillations in the sunspot region NOAA11823. The peak periods T_{PEAK} were obtained from the global intensity power spectra P_{Int} at characteristic wavelength positions λ (blue line wing, core, and minimum) of five spectral lines. Panels a – c): Ca II 854.21 nm ($\lambda_{2,\mathrm{C-44pm}}$, $\lambda_{3,\mathrm{C-22pm}}$, $\lambda_{5,\mathrm{Core}}$); panels e – g): Na I 589.59 nm ($\lambda_{2,\mathrm{C-12pm}}$, $\lambda_{3,\mathrm{C-6pm}}$, $\lambda_{4,\mathrm{Core}}$); panels i – l): Fe I 630.15 nm ($\lambda_{3,\mathrm{C-8pm}}$, $\lambda_{4,\mathrm{C-4pm}}$, $\lambda_{5,\mathrm{Core}}$). The right panels (d and h) yield the dominating oscillations in the broad line cores of H_β at 486.1 nm and Ca K at 393.4 nm. The peak periods T_{PEAK} are scaled from 2.5 min (dark blue) to 8 min (dark red). The sunspot boundaries are contoured in black. The black arrow is pointing toward the solar disk center.

intensities. The results on the basis of Doppler velocity oscillations are displayed in Fig. 6.11. In panel a), it it easy to notice that the chromosphere above the umbral area is dominated by waves in the 2.5–3 min range (dark blue). At the umbral boundary and first arc-second of the inner penumbral area, the peak period increases sharply. Whereas in the lower half of the sunspot, the period increases more smoothly, in the upper half a jump of more than 1 min to periods around 4.5 min occurs (bright blue). Such a jump in period at the umbral boundary has also been reported in other observational studies (Tziotziou et al. 2007). As shown in Fig. 6.5, some pairs of successive umbral waves merge to one running penumbral wave at the first 2″ of the inner penumbra. This could explain the jump

in wave period from around 3 min to 4 min at the umbral boundary. Further explanations of this steep increase are listed at the end of Section 6.5.5. As further shown in Fig. 6.11 a), with increasing radial distance from the umbra, the penumbral peak periods increase smoothly up to 8 min in the outer penumbra. This behavior is also more distinct in the penumbral side facing the disk-center. The filamentary structure of the penumbra is also present in the dominating wave periods. This suggests a propagation of running penumbral waves along individual, differentially inclined penumbral field lines. The vicinity of the sunspot is dominated by acoustic waves in the 5 min range. A comparison with the peak period maps of the lower photosphere (panels b and c) proves that these oscillations are still the imprint of photospheric p-modes. In panel b), the lower photospheric umbra shows a broad mixture of dominating wave periods. A close inspection reveals an already apparent trend toward 3 min oscillations. In the penumbra, it is important to notice that the linear increase in peak period toward the outer penumbra, which in literature was attributed to the chromosphere, is also present in the photosphere. Moreover, the filamentary structure manifests in the penumbral photosphere as well. In panel c), the lower spatial resolution of the HMI observations limits the analysis to larger spatial scales. In accordance with the ground-based IBIS observation, the smoothing of the middle panel by a factor of five would yield the same distribution as shown in the right panel.

The resulting peak periods from intensity oscillation at characteristic wavelength positions are displayed in Fig. 6.12. Since the results are required for the reconstruction of the magnetic field, the obtained wave periods from brightness oscillation are detailed in Section 6.5.1. To round this section up, I will already describe the basic distribution and differences from the photosphere to the chromosphere. The panels in the top and middle row of Fig. 6.12 show the dominating oscillatory periods in the sunspot's upper photosphere and lower to middle chromosphere. The basic distribution in the sunspot is very similar to the results obtained from oscillation in lower chromospheric Doppler velocities which were displayed Fig. 6.11 a). The peak period in the umbra shifts from around 3 min at the umbral boundary to around 8 min at the outer penumbral white-light boundary. A similar distribution of calculated peak frequencies in the sunspot chromosphere was presented by Socas-Navarro et al. (2009). Whereas in the middle photosphere (panels a, e, i–l) the vicinity of the sunspot is dominated by 5 min p-mode oscillations, the peak periods above 8 min extend along the superpenumbral filaments and are still present at distances of more than 10″ beyond the sunspot's outer white-light boundary. It is important to notice that with increasing atmospheric height from the photosphere to the chromosphere (panels a–c and e–g), the shorter peak periods spread radially. Exemplarily, chromospheric 3 min oscillations exceed the contoured umbral boundary by a few arc-seconds. The estimated altitudinal distribution of peak periods in the sunspot atmosphere is shown on the right side of Fig. 6.28.

6.2.2. Transition region to corona

As demonstrated in Section 6.2.1, the photosphere and chromosphere above the sunspot exhibits vigorous wave phenomena. These compressive waves were proven to propagate upward to higher atmospheric layers. It is suggested that these powerful waves are guided by the magnetic field lines of the sunspot. The direct question emerges whether these waves can reach the transition region and corona above the sunspot. To provide a comprehensive investigation of waves in the sunspot atmosphere, this section includes an analysis of wave signatures in the upper solar atmosphere.

As introduced at the end of Section 2.3, the transition region and corona are better described as temperature layers by the steep increase in temperature from 10^4 K to 10^6 K rather than as a geometrical layer. Due to the extreme temperatures, the atoms of the plasma are highly ionized. Strong emission lines in the ultraviolet, extreme ultraviolet, and X-ray range characterize the spectrum of the transition region and corona (see Section 4.2.2). To perform on-disk solar observations in this frequency range of radiation, satellite telescopes are required. Therefore, the epoch of observations of the upper solar atmosphere started with the launch of the Solar and Heliospheric Observatory (SOHO) and the Transition Region and Coronal Explorer (TRACE) in the late 1990's. Since 2010, the Atmospheric Imaging Assembly (AIA, see Section 4.1.3) aboard the Solar Dynamics Observatory (SDO) provides

continuous observations from the upper chromosphere to corona at a cadence of 12 s and a spatial resolution of 1.5″. In the last two decades, the data of these three solar telescope served as the basis for a number of wave studies in the upper atmosphere, also above sunspots.

To compare the brightness variations in the transition region and corona with the chromospheric oscillations described in the previous section, co-spatial[1] data from AIA were acquired (see Tables 4.5 and 4.6). As listed in Table 4.4, the spectral emission lines dominating the filtered wavelength band of the AIA channels cover different atmospheric layers. The 30.4 nm band represents temperatures around $5 \cdot 10^4$ K and features the dynamics in the transition region and upper chromosphere. The 17.1 nm channel covers the corona and upper transition region at around $6 \cdot 10^5$ K. The brightness in the 21.1 nm band displays the dynamics in the active-region corona with temperatures around $2 \cdot 10^6$ K. The solar evolution in the different temperature regimes is observed co-spatially and co-temporal. The Sun in coronal brightness, as observed with AIA in the wavelength band around 17.1 nm, is shown in Fig. 5.9. Bright coronal loops indicate the arched magnetic field. The analyzed sunspot region is highlighted. The sunspot in transition region brightness is displayed in Fig. 4.14 k), the coronal appearance from the 21.1 nm channel is shown in panel l). The temporal evolution of the spectral brightness reveals upward propagating waves throughout the sunspot atmosphere. Exemplarily, horizontal 1D-slices are centered across the sunspot region (see dashed line in the middle column panels of Fig. 6.14) in the 30.4 nm and 17.1 nm wavelength band. The time series of spectral intensities along the slices are reduced by the time average and plotted as spatio-temporal diagrams in Fig. 6.13.

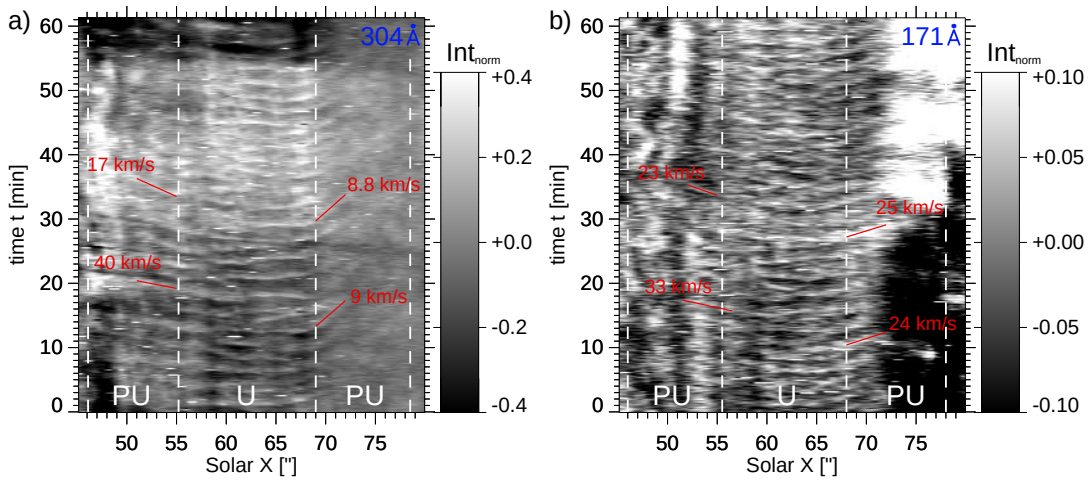

Figure 6.13.: Wave signatures in the temporal evolution of spectral intensities from the sunspot's transition region and corona. The normalized intensities Int_{norm} of the AIA 30.4 nm (panel a) and 17.1 nm (panel b) channels are shown for the horizontal slices which are marked as dashed lines in the middle panels of Fig. 6.14. The temporal average was subtracted from the intensities. The vertical dashed lines mark the umbral (U) and penumbral (PU) white-light boundaries of the sunspot. The red bars highlight the apparent trajectories of running penumbral waves and umbral flashes.

The temporal evolution of spectral intensities from the transition region and corona is displayed in Fig. 6.13. The periodic brightness oscillations serve as clear signatures of wave propagation in sunspots. The evolution in the solar transition region and upper chromosphere is shown in the left panel (a). The appearance of umbral flashes and running penumbral waves in the umbral (U) and penumbral (PU)

[1] At a heliocentric angle of $\theta = 14°$, the sunspot is close to the solar disk center. The investigation of the magnetic field inclination proves the vertical field orientation to the zenith. The projection effects are calculated by $dx = \tan\theta \cdot dH$. The given heliocentric angles and a height difference dH of around 3000 km from the bottom photosphere to the lower corona yields a spatial displacement of less than 750 km or 1″. For AIA data this is around the resolution limit. Spatial displacements are therefore neglected.

area resembles the lower chromospheric case (Fig. 6.5). The umbra exhibits continuous oscillations by up to ±40% and periods around 2.5 min. The spatial coherency of the umbral waves often exceeds 5″. In average, the values are larger than in the lower chromosphere. The bowl shape of the umbral waves in the temporal diagram yields a fast apparent horizontal spreading with often more than 50 km s^{-1}. The shock wave behavior of the umbral waves is less pronounced than in the chromosphere. Like in the lower atmosphere, many of the umbral wave trains proceed into the penumbral region. The existence of running penumbral waves is proven for the transition region above the sunspot. The apparent horizontal velocities (red bars) range between 8 km s^{-1} and 40 km s^{-1}, differing for the right and left half of the sunspot. In average, the apparent horizontal wave motion in the transition region is a few km s^{-1} slower than in the lower chromosphere.

When moving higher up to the sunspot's corona and upper transition region, the wave pattern of umbral oscillations is still noticeable. The temporal evolution of the brightness in the 17.1 nm waveband is shown in the right panel (b) of Fig. 6.13. The coronal waves are predominant with an intensity amplitude of ±10% and wave periods around 2.5 min. The umbral waves extend into the penumbral area. Only minor imprints of running penumbral waves are present. As the magnetic field fans out toward the corona, it is suggested that the observed waves have propagated upward along nearly vertical magnetic field lines. This would also explain the inferred horizontal velocities (red bars) of the wave trains at the inner penumbral area (PU). The velocities of $23 - 33$ km s^{-1} are larger but more consistent than in the chromosphere and lower transition region.

In the hot active-region corona observed by the 21.1 nm waveband channel, the oscillatory signal in the spectral intensity is very low. However, oscillatory amplitudes of ±2% of the average intensity and periods between 2.5 min and 4 min dominate the sunspot area. The time series exhibits several bright sunspot jets which fire out from the inner penumbra into the vicinity of the spot.

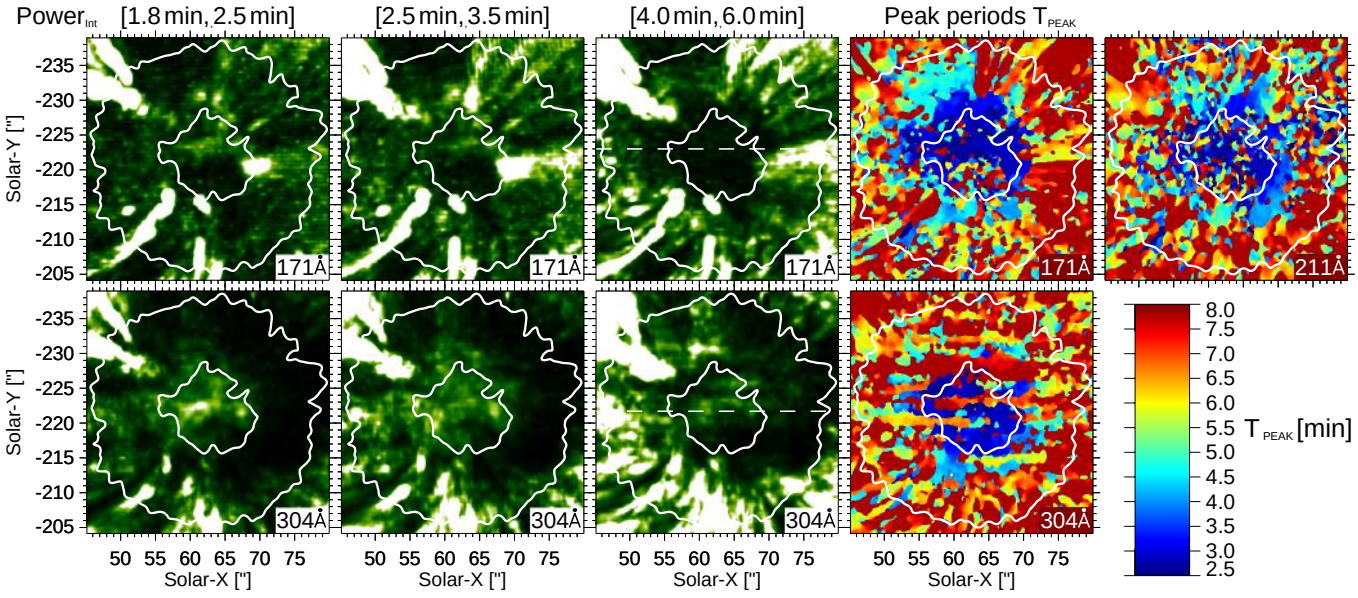

Figure 6.14.: Distribution of the wave power in the upper chromosphere to corona above the sunspot NOAA11823. The six panels on the left show the scaled wave power from intensities in the transition region to corona (upper panels, AIA 17.1 nm) and upper chromosphere to transition region (bottom panels, AIA 30.4 nm) filtered in three period bands (1.8–2.5 min, 2.5–3.5 min, 4 – 6 min). The three panels on the right present the dominant wave periods T_{PEAK} at the same layers, including the coronal distribution (upper right panel, AIA 21.1 nm). The peak periods are scaled from 2.5 min (dark blue) to 8 min (dark red). The umbral and penumbral boundaries are contoured in white. The white dashed lines in the middle panels mark the analyzed horizontal slice for Fig. 6.13.

To examine the characteristics of sunspot waves in the transition region and corona in more detail, the same pixel-wise wave power analysis was performed like in the lower sunspot atmosphere (see Section 6.2.1). The most important results are summarized by Fig. 6.14. The bottom row shows the distribution of wave power and periods in the sunspot's lower transition region and upper chromosphere. The results were obtained from brightness oscillations in the 30.4 nm waveband. The three panels on the left display the intensity wave power in three different period ranges. Bright colors indicate high oscillatory power. The filtered period band at 1.8–2.5 min (left) exhibits high concentrated power in the inner umbra. The region of maximum umbral power coincides with the power found for umbral flashes in the lower chromosphere. For the filtered periods band of 2.5–3.5 min (second left) and 4–6 min (third left), the wave power spreads toward the umbral boundary and inner penumbra. This radial shift in wave period is in line with the findings in the lower chromosphere. The results obtained from brightness oscillations in the coronal 17.1 nm waveband yield very similar results. The three left panels in the top row of Fig. 6.14 show the sunspot region in the same filtered period ranges. At periods around 2–3 min, a concentration of wave power is present in the central umbra. The radial shift of wave power for increasing wave periods is noticeable as well. A qualitative investigation of the dominant wave periods underlines this dependence. The three panels on the right of Fig. 6.14 display the resulting peak periods of the global wavelet spectra. All three atmospheric layers (bottom: 30.4 nm, top left: 17.1 nm, top right: 21.1 nm) reveal peak periods mainly at around 3 min in the umbral area and inner penumbra. With increasing radial distance, the dominating wave period shifts toward longer periods. This trend is visible even for the weak signal in the active-region corona.

One of the most important results is the proof that sunspot waves originating in the deep photosphere can propagate upward into the transition region and corona. Especially, umbral waves in the 2.5–3 min period range leak into the upper sunspot atmosphere. The obtained wave characteristics confirm other wave observations (Brynildsen et al. 1999; Bogdan 2000; De Moortel et al. 2002; Marsh and Walsh 2006; Kobanov et al. 2013b; Tian et al. 2014) in sunspots, pores, and other magnetic configurations. In general, there is controversy whether sunspot waves are present in the hot corona (see Bogdan and Judge 2006). The analysis of coronal brightness oscillations confirms that the wave power decreases rapidly from the lower to upper transition region. But although the signal in brightness oscillation is weak, the power analysis and obtained peak periods prove the existence of sunspot waves in the hot active-region corona. This result agrees with the observed 3 min- and 5 min-oscillations in coronal loops (De Moortel et al. 2002). Moreover, the evident variation of dominating wave periods supports the wave propagation along the magnetic field lines and the influence of the effective cut-off frequency (De Pontieu et al. 2005; Kobanov et al. 2013b; Yuan et al. 2014b). Several authors (e.g., O'Shea et al. 2002; Reznikova and Shibasaki 2012; Kobanov et al. 2013b; Tian et al. 2014; Sych and Nakariakov 2014; Freij et al. 2014) agree that sunspot waves propagate upward with a high degree of spatial and temporal coherence and that the vertical phase speed increases with the ambient sound speed toward the transition region and base of the corona. By investigating the oscillatory signals in the 30.4 nm and 17.1 nm waveband observed with AIA, Kobanov et al. (2013b) found propagation velocities of around $55\,\mathrm{km\,s^{-1}}$ between both layers in the umbral area. The spatio-temporal analysis and calculated time lags for sunspot NOAA11823 from the same AIA channels confirm that result. Furthermore, the wave analysis of spectral intensities in the 30.4 nm waveband proves that umbral flashes are still present in the upper chromosphere and transition region. This in agreement with the results of Tian et al. (2014) who focus on the shock wave appearance in the umbral transition region. In their study, the authors obtain the characteristic saw-tooth shape for Doppler shift oscillations in the transition region. Another reported shock wave behavior from chromospheric observations is the phase shift of intensity and velocity oscillations with the maximum brightness following the maximum redshift. This large red-shift indicates super-sonic downward motion behind the shock front with around $98\,\mathrm{km\,s^{-1}}$. All results obtained for the upper sunspot atmosphere support the same wave scenario as for the lower sunspot atmosphere. Low-β slow-mode magnetoacoustic waves propagate along the magnetic field lines to higher atmospheric layers.

6.3. Umbral flashes: The Sun's amazing fireworks

Umbral flashes dominate the wave dynamics in the sunspot chromosphere. Already Beckers and Tallant (1969) discovered strong periodical brightness fluctuations in the chromosphere above umbrae. When a sunspot umbra is observed spectroscopically at the chromospheric line core of deep spectral absorption lines, like Ca II H and K, umbral flashes visually manifest like bright exploding fireworks (see Fig. 6.15 a and Fig. 2.8). The temporal evolution at the marked region (green square) in the umbra shows a brightness concentration which is first localized at the arc-second scale (panel a, t2) which amplifies and extends with time (t3–t4). Since the first detection, this most spectacular wave phenomena in the solar atmosphere has been studied frequently by observation (e.g., Rouppe van der Voort et al. 2003; Centeno et al. 2006; Felipe et al. 2010b; de la Cruz Rodríguez et al. 2013) and numerical simulations (e.g., Carlsson and Stein 1997; Bard and Carlsson 2010; Felipe et al. 2010a).

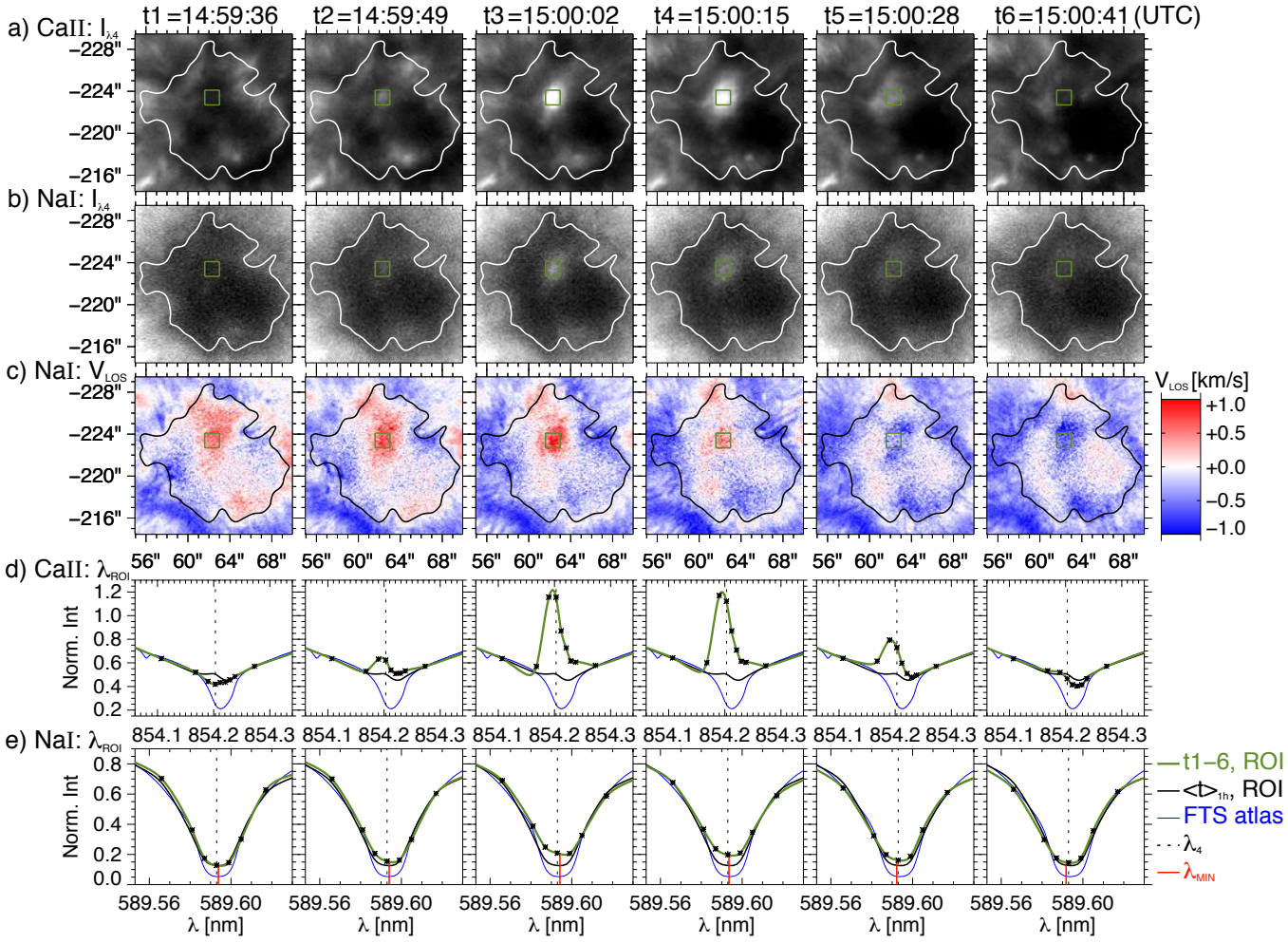

Figure 6.15.: Umbral flash in sunspot NOAA11823. Six consecutive time steps (t1–t6) show the basic characteristics of an umbra flash event. In the upper panels, the umbral region (contoured in white) is shown in chromospheric line core intensities of Ca II 854.21 nm (panels a) and Na I 589.59 nm (panels b). The Doppler velocities from the Na I line are displayed in panels c) between $\pm 1\,\mathrm{km\,s^{-1}}$. In the lower panels, the normalized spectral profiles are plotted for the Ca II line (panels d) and the Na I line (panels e). The profiles were averaged for the small region inside the umbra which is marked in green color. The interpolated profiles are plotted in green, the temporal average in black, and the FTS atlas profile in blue. An umbral micro-jet appears at pixel $(65'' / -218'')$.

6.3.1. Formation and propagation of shock waves

Umbral waves are slow-mode magnetoacoustic waves guided along the magnetic field in the umbral low-β plasma. As suggested in Section 6.1.1, global p-mode oscillations seem to interact with the sunspot's magnetic fields in a way that magnetoacoustic modes can be excited. Turbulent convection and magnetic field oscillation also contribute to the generation of waves in the umbral atmosphere (see Section 6.1.2). As proven by Centeno et al. (2006), the photospheric slow-mode waves perform a linear vertical propagation to higher atmospheric layers. The upward propagating umbral waves exhibit a high degree temporal coherence. The spatial coherence covers patch sized of $\sim 3''$) up to large parts of the umbra (Abdelatif et al. 1986). In the umbra, the magnetic field is vertical. According to the acoustic cut-off frequency (see Section 6.4.1), those oscillations with frequencies below the effective cut-off ($\sim 5.2\,\mathrm{mHz}$) are vertically trapped in the photosphere and evanescent in the chromosphere. Waves with frequencies above the acoustic cut-off frequency can propagate unhindered to higher atmospheric layers. In a sunspot umbra or pore, these waves with periods around 2.5–3 min and below are effectively channeled by the magnetic field lines. When the largely coherent waves propagate upward to the chromosphere, their acoustic energy flux has to be constant. As illustrated in Fig. 2.5, the umbral sound speed in the upper photosphere and lower chromosphere is assumed to be roughly constant at around $6\,\mathrm{km\,s^{-1}}$ (panel b). On the other hand, the density, $\rho \approx \rho_0 \cdot e^{-H/H^*}$, decreases exponentially with increasing geometrical height H (see panel c) or relative height H/H^*. Therefore, the wave power has to be maintained by the relative oscillatory motion, $v \approx v_0 \cdot e^{H/2H^*}$. Consequently, the oscillatory amplitude of an upward propagating wave steepens up to $10\,\mathrm{km\,s^{-1}}$ (Lites 1986). Toward the lower chromosphere, the short-period waves become non-linear and form a magnetoacoustic shock front as shown in Fig. 3.6. The adiabatic compression of the plasma at the shock front is extreme and leads to a rise in temperature by 1500 K and more (de la Cruz Rodríguez et al. 2013). This induces an increase of the atomic ionization and radiative brightness (Havnes 1970; Kneer et al. 1981; Thomas et al. 1984). By this, umbral flashes manifest as increased emission of the local material during the passage of the acoustic shock wave. Simulations of shock front formation and propagation in the solar chromosphere have confirmed the observations (Carlsson and Stein 1997; Bard and Carlsson 2010).

According to the nature of umbral flashes, their appearance in chromospheric line core intensity is deceptive. As shown in Fig. 6.15 (panels a and b), the temporal brightness evolution resemble an exploding firework. Indeed, umbral flashes display shock waves. But by its slow-mode magnetoacoustic character, the compressive motion is oriented along the magnetic field lines and not isotropic. Further examples of umbral flash appearance are given in Figs. A.8 and A.10 in the appendix. In spatio-temporal diagrams like Fig. 6.5 in line minimum intensity of Ca II 854.21 nm, umbral flashes appear as bright cones or bowls. The fine-scale appearance yields vastly super-sonic horizontal velocities of around $40 - 100\,\mathrm{km\,s^{-1}}$. The reasons for the large speeds were discussed in Sections 6.3.3 and 6.4. The apparent velocities are caused by the formation of an inclined shock cone and projection effects by the geometrical configuration (see Fig. 6.19). In this study, the vertical velocities of several umbral flashes in the chromosphere amount to $8 - 15\,\mathrm{km\,s^{-1}}$.

The evolution of the umbral Doppler velocity signal from the lower photosphere to lower chromosphere gives information about the formation height of umbral flashes. A comparison of the wave function of Doppler velocities and spectral intensities is shown in Fig. 6.6. The Doppler velocities in the lower umbral photosphere (below around 300 km) exhibits a sinusoidal oscillation. In contrast, the lower chromospheric Doppler oscillations are displayed in Fig. 6.16 (panel c) and yield the saw-tooth wave function which is characteristic for shock waves. Consequently, the formation of umbral flashes has to happen between the middle photosphere and lower chromosphere. The profiles of brightness fluctuations (Fig. 6.6) further limit the initial shock formation height to the temperature minimum layer. At formation heights around 300 km above the optical depth unity, the wave function of the spectral intensity is almost sinusoidal. At a formation altitude of around 600 km, the temporal evolution of the lower chromospheric brightness already exhibits steep maximum peaks. These findings for the circular sunspot of active region NOAA11823 are in agreement with the results obtained for

the irregular sunspot of active region NOAA11455 (see Section 4.3.2). The Doppler velocities from the upper photospheric Fe I 543.45 nm line ($H < 500$ km) describe an almost sinusoidal wave function with first imprints of a shock pattern.

Magnetoacoustic waves are channeled along all kinds of solar magnetic features. Small sunspots, pores, spicules, and flux tubes exhibits oscillations in the 3 min range as well (e.g., Stangalini et al. 2012). Centeno et al. (2009) have performed a comparative investigation of velocity wave function for different magnetic features. The authors found that field-guided wave propagation in the 3 min band is present for small pores to big sunspots. The amplitude of the chromospheric Doppler velocity oscillations and the formation of umbral shock waves depend on the magnitude of the magnetic field structure. Whereas the pore features amplitudes up to $1-2\,\mathrm{km\,s^{-1}}$ and a sinusoidal wave function, the small sunspot yields oscillations with amplitudes of around $3-4\,\mathrm{km\,s^{-1}}$ and a developing saw-tooth shape. The big sunspot exhibits Doppler velocity amplitudes of $6-10\,\mathrm{km\,s^{-1}}$ and a fully-developed saw-tooth wave function for the umbral flashes.

6.3.2. Manifestation in spectroscopic data

The manifestation of umbral flashes in spectroscopic data is extreme. In chromospheric spectral intensity, the umbral flashes appear as bright shock events in the sunspot umbra. The temporal evolution in the chromospheric umbra is shown in Fig. 6.15 (panel rows a and b), exemplarily for one umbral flash event. The most concentrated and strongest shocks can amplify the brightness by more than 200%. With the arrival of the first shock signatures, the spectral brightness steeply increases to its maximum emission within typically ten seconds. The decay of spectral intensity happens slower, the half-maximum brightness is reached after additional $10-20$ s. The strongest occurrence of umbral flashes is often localized to a small umbral patch of $2-4''$. Consequently, a meaningful observation of umbral flashes requires a high temporal cadence of at least 15 s and a spatial resolution better than $1''$. The lower to middle chromosphere with its relatively low temperature, slow sound speed, and the exponentially decreasing gas density provides perfect conditions for the formation of shock waves. Therefore, the most significant observations of umbral flashes are performed in the line core of chromospheric spectral lines like the Fraunhofer Ca II K and H lines or the Ca II 854.21 nm line in the infrared. Since the shock wave propagates vertically upward, the Doppler effect shifts the emission to shorter wavelength (blue-shift). Therefore, a sparse spectroscopical sampling of the spectral line should include or concentrate on the blue line core around 20–30 pm from the line minimum position (e.g., the K2v peak of the Ca II K line, see Section 4.2).

A comprehensive overview of the spectral manifestation of an umbral flash is presented in Fig. 6.15. The spectral evolution is analyzed for the spatial position in the umbra (green square) where the shock is brightest. It is assumed that this region coincides with the center of the shock cone. The panels of Fig. 6.15 (d, e) show the temporal evolution of the spectral line profiles of Ca II 854.21 nm and Na I 589.59 nm (green curves) during the passage of the umbral flash. The line profile represents the average of all profile within the indicated umbral region. The 1h-time average (black curve) and FTS atlas profiles (blue curve) are plotted as reference. At time step $t1$, the chromospheric umbra seems to be at rest. The spectral profiles of both lines resemble the quiescence profile. In the next step ($t2$) after 13.23 s, the first shock signatures are present. The blue line core of Ca II goes into emission. The emission peak is blue-shifted by 20 pm from the line minimum position (in line with de la Cruz Rodríguez et al. 2013). The Na I line exhibits an overall red-shift by 1.2 pm. As shown by the corresponding Doppler velocity map in panel c, velocities of around $+0.6\,\mathrm{km\,s^{-1}}$ dominate the region. At the next instant of time ($t3$), the umbral flash has reached its maximum brightness in chromospheric intensity. The Ca II line profile exhibits a strong emission peak which is 190% above the quiescence level. The wavelength position of the maximum is less blue-shifted than in the previous instant of time. On the other hand, the Na I line has reached its maximum red-shift of 1.4 pm which corresponds to a line-of-sight velocity of $+0.7\,\mathrm{km\,s^{-1}}$. The positive sign of the velocity indicates downward motion of the plasma behind the shock front. In the following time steps, the umbral flash

spreads across the umbral area. The chromospheric brightness reduces, and the emission peak in the Ca II line core declines gradually to the quiescence profile. The increased intensity in the line core of Na I D1 decreases again. Moreover, the red-shift of the spectral line transforms into a blue-shift of $-1.2\,\mathrm{pm}$ which corresponds to a line-of-sight velocity of $v_{LOS} = -0.6\,\mathrm{km\,s^{-1}}$. The velocities indicate upward motion of the atmospheric plasma. The temporal trajectory of the line minimum of the spectral Na I D1 profile describes a counter-clockwise motion around the average line minimum. The spectral manifestation of other umbral flash events yield an identical behavior. Two more examples are displayed in Figs. A.8 and A.10. A more detailed analysis of the location of the emission peak and the shock wave velocities is given in Section 6.3.3.

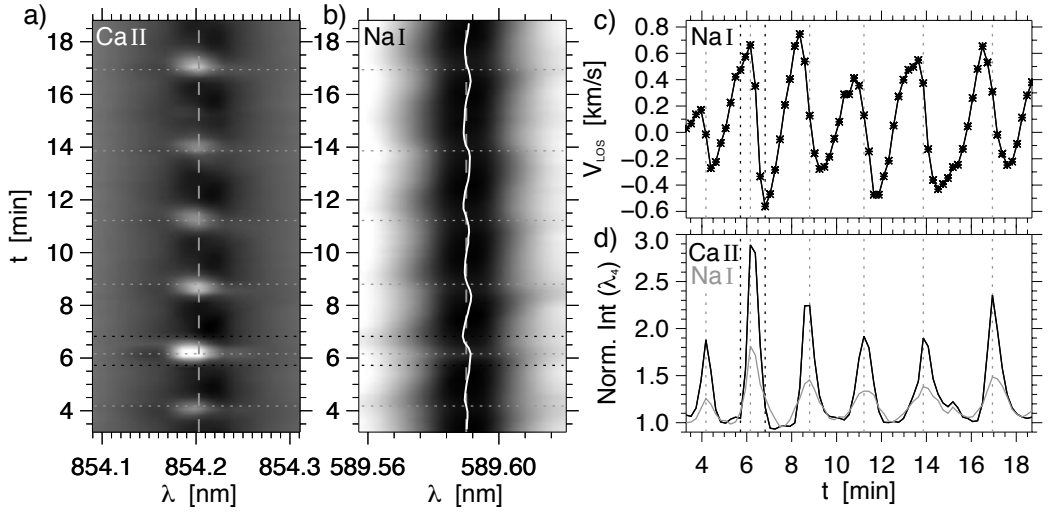

Figure 6.16.: Appearance of umbral flashes in chromospheric intensity in sunspot NOAA11823. The position in the umbra is marked in Fig. 6.15. The spectral profiles of the line cores of Ca II 854.21 nm (panel a) and Na I 589.59 nm (panel b) are plotted for the observation times t. The nominal line minimum positions are indicated as gray dashed lines. The white solid line in panel b) shows the oscillating line minimum position. The times of maximum brightness are marked by the gray dotted lines in all panels. Panel c) displays the Doppler velocities from the Na I line. The normalized line minimum (λ_4) intensities of Ca II (black) and Na I (gray) are plotted in panel d).

To infer the temporal evolution of the spectral lines for a longer temporal range, Fig. 6.16 provides an additional illustration of the oscillatory dynamics in the umbral region. Panels a and b show the evolution of the spectral intensities in the line core and wings of the Ca II and Na I lines. The $\lambda - t$ diagrams highlight the periodicity and effects of umbral flash occurrence in the umbral chromosphere. An interpolation was applied to the diagram. The colors in the diagram correspond to the spectral intensities. The dark colors correspond to low intensities. Evidently, the dark line core of the Ca II line is interrupted by bright umbral flashes. The flashes occur at an average periodicity of 2.5 min. The maximum brightness of the shock occurs in the blue line core. The brightness variation in the line profile of the Na I line is less pronounced. The normalized intensities at the line core of the Ca II (black curve) and Na I (gray curve) line are plotted in panel d) as a function of time. The intensity of the Ca II line core yields a stronger amplification ($\sim 100\%$) than the intensity of the Na I line minimum ($\sim 50\%$). The steep gradients of the brightness peaks are a sign of shock wave propagation. An additional feature of shock waves is the saw-tooth function of Doppler velocities. The temporal evolution of the line core intensity of Na I (panel b), the line minimum position (white solid line), and the inferred Doppler velocities (panel c) reveal the shock wave propagation of umbral flashes. The line profile is mostly preserved but shifted in its entirety in the presence of umbral flashes. The Doppler velocity oscillation

is not sinusoidal but has developed a pronounced saw-tooth shape with rapid blue-shifts and slower red-shifts (in line with Rouppe van der Voort et al. 2003). Shortly before the intensity reaches its maximum brightness, the line shift experiences its maximum red-shift. The amplitude of the upper photospheric to lower chromospheric Doppler velocities from the Na I D1 line reaches up to $1\,\mathrm{km\,s^{-1}}$. Two more examples of spectral manifestation of umbral flashes at other umbral locations and times are displayed by Figs. A.7 and Fig. A.9 in the appendix. Hydrodynamic simulations of chromospheric shock waves managed to reproduce the spectral manifestation of umbral flashes (Carlsson and Stein 1997; Bard and Carlsson 2010).

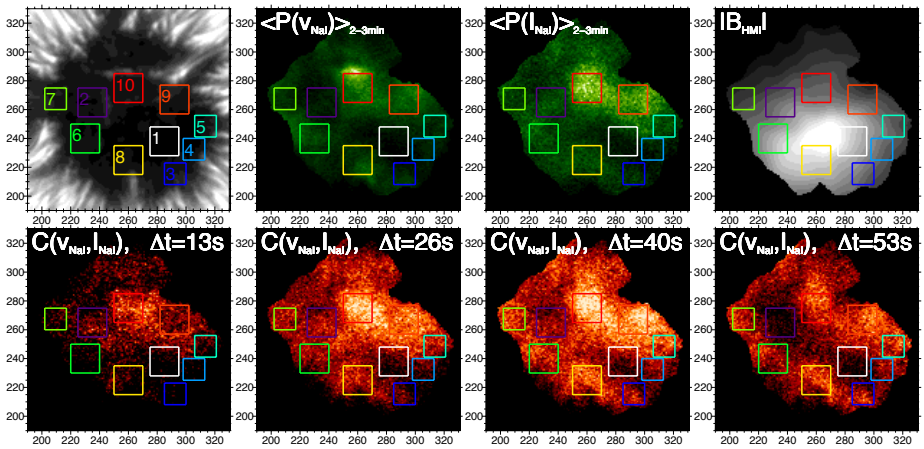

Figure 6.17.: Localized time delays between oscillations in Doppler velocity $v_{\mathrm{Na\,I}}$ and line minimum intensities $I_{\mathrm{Na\,I}}$ at $\lambda_{4,\,\mathrm{Core}}$ in the sunspot umbra of NOAA11823. In the upper panels, the umbra is shown in continuum intensity (left panel). The masked region is displayed in global wavelet power in the 2–3 min period band (middle panels), and line-of-sight magnetic field strength (right panel). In the lower panels, the correlation coefficients $C(v_{\mathrm{NaI}}, I_{\mathrm{NaI}})$ are shown for four given time delays Δt. All values were scaled, bright colors indicate large values. Ten umbral regions are highlighted in color. Compare Fig. A.6.

As shown in Figs. 6.15, A.8, and A.10, strong red-shifts of the Na I D1 line (panels c) seem to be co-spatially coupled to the strongest brightness (panels b) of umbral flashes. The red-shifts indicate downward motion of the plasma with Doppler velocities up to $+1\,\mathrm{km\,s^{-1}}$. A comparison of their appearance and the temporal evolution in Fig. 6.16 reveals that the maximum red-shift in Doppler velocity is slightly preceding the maximum brightness in spectral intensity (in line with Tian et al. 2014). A detailed analysis of the time delays between velocities and spectral brightness is presented by Fig. 6.17. The method was described in Section 5.4.1. The Doppler velocities $v_{\mathrm{Na\,I}}$ obtained from the Na I 589.59 nm cover the photosphere and lower chromosphere. The spectral intensities at the line minimum of the Na I line are formed at a chromospheric altitude of around 800–1000 km above the optical depth unity $\tau_{600} = 1$. A pixelwise correlation of both oscillatory signals for the full observation time is performed for the umbral area. The top left panel in Fig. 6.17 shows the sunspot umbra in continuum intensity. To assure the spatial congruence, the analysis is limited to the inner umbra which exhibits a vertical magnetic field. For the heliocentric angle of 14° and an average formation height difference of 500 km, the horizontal spatial displacements amount to less than 0.2″. The result of the temporal correlation of the oscillatory functions is display in bottom four panels of Fig. 6.17. The obtained correlation coefficients in umbra are shown for four time delays Δt of 13 s, 26 s, 40 s, and 53 s. The correlation coefficients of the time series are normalized to the maximum value of 0.9. Strong correlation are displayed in bright colors. The maximum correlation is obtained for the inner umbra at time delays of 26 s to 40 s. A parabola analysis like the one displayed in Fig. 5.7 yields maximum red-shifts preceding the maximum brightness by a 23–28 s in the umbral center regions (1–2, 6–7, 9–10)

and 30–38 s in the umbral boundary regions (3–5, 8). A comparison with the velocity and intensity power in the 2–3 min band reveals that the umbral region (10, red square) of maximum correlation coincides spatially with the concentration of maximum power from umbral flashes (bright green color). As indicated by the normalized line-of-sight magnetic field strength in the top right panel, the umbral region with the largest wave power and oscillatory correlation does not coincide with the umbral core and its maximum field strength (bright color). The four correlation maps at the bottom of Fig. 6.17 show an apparent motion of maximum oscillatory correlation from the inner to the outer penumbra.

In summary, at the arrival of the shock wave in the chromosphere, the Ca II line exhibits a strongly blue-shifted emission peak. Shortly layer, the emission in the line core reaches its maximum brightness at a less pronounced Doppler shift. The Na I line shows a different behavior. Before the advent of the umbral flash, the spectral line is red-shifted. Around 30 s later, the line minimum intensity reaches its maximum value. At the first glance, the measured signals are contradictory. But as mentioned above, the Doppler velocities were calculated as an average shift of the entire Na I line. Since the spectral line is formed in the photosphere and lower chromosphere up to altitudes of around 1000 km above the continuum optical depth unity, the average line shift has to be assigned to an average altitude of around 500 km. Consequently, the observed signals can be brought in accordance with the suggested upward propagation of shock waves. First of all, one must be aware that the line-of-sight motion of a shock wave consists of two components (Socas-Navarro et al. 2000). The first component of shock propagation is the motion of the shock front toward the observer. The second component is the sonic boom behind the shock front which points in the opposite direction (see Fig. 3.6). For umbral flashes which propagate vertically upward in the sunspot atmosphere, the sonic boom has to point downward, the compressed gas behind the shock front falls back by the downward directed boost and solar gravity. As the spatial and temporal scales of the shock front are small compared to the opposite sonic boom, the shock front component often remains unresolved. This may be the case for the spectral signal of the Na I line. In the line core of Ca II 854.21 nm, the shock front is effectively resolved as a blue-shifted emission peak. The shock wave scenario explains the observed spectral evolution in the following way. The upward propagating shock wave arrives first in the average atmospheric formation layer of the Na I line. The blue-shifted shock front component remains unresolved by the Na I line observations. The opposite sonic boom right after the shock front is resolved and shifts the spectral line toward longer wavelength. When the shock wave propagates at a vertical velocity of around $10 - 15\,\mathrm{km\,s^{-1}}$, it arrives around 30 s later at height of around 900–1000 km in the chromospheric layer. The compressed and heated plasma at the shock front leads to the distinct emission peak in the blue core of the Ca II line. As shown by the time-difference analysis of intensity oscillations at the line minima of Ca II 854.21 nm and Na I 589.59 nm (see Fig. A.6), the maximum brightness in Ca II intensities precede the Na I intensities by around 10 s.

The red-shift component of the down-falling and expanding plasma behind the shock front explains the observed manifestation of umbral flashes. Curiosity arises with regard to the time-averaged Doppler velocities in the sunspot atmosphere. Fig. 5.1 displays the temporal average of Doppler velocities from the lower chromospheric Na I 589.59 nm line (panel a), and the lower photospheric Fe I lines at 630.15 nm (panel b) and 617.33 nm (panel c). The umbral area exhibits a net red-shift of around $200 - 300\,\mathrm{m\,s^{-1}}$ in the first two cases. The Doppler velocities from HMI (panel c) feature systematic red-shifts of up to $300 - 600\,\mathrm{m\,s^{-1}}$. Possible explanations for this average red-shift are the resolution of down-ward motions after the shock waves, the gravitational acceleration, or possible inverse flows along the magnetic field lines.

In spectro-polarimetric sunspot observations of the full-Stokes signal of chromospheric line, the two-component scenario has to be taken into account (Socas-Navarro et al. 2000). The signals of linear and circular polarization are disturbed by umbral flashes (López Ariste et al. 2001). At the maximum emission of the shock wave, the Stokes V signal even switches its polarity (de la Cruz Rodríguez et al. 2013).

6.3.3. Shock front velocities

The upward propagation of umbral waves was proven in Section 6.2 and exemplarily displayed in Fig. 6.6. The analysis of the time lags for estimated differences in spectral formation altitude (Table A.1) yields wave speeds of around $10 - 20\,\mathrm{km\,s^{-1}}$. As discussed in Sections 6.3.1 and 6.3.2, the spectral emission peak in the blue line core and wing of the Ca II 854.21 nm line is caused by the umbral flash event. Since the chromospheric emission signal is significantly shifted from the line center to shorter wavelength, it approves the fast upward propagating nature of a super-sonic shock waves. The temporal evolution of the chromospheric spectral intensity in the Ca II line core is shown in Figs. 6.16, A.7 and A.9, each for one region inside the sunspot umbra. Each case harbors one very bright umbral flash which is marked in time by black dotted lines. In Figs. 6.15, A.8, and A.10, the respective time series is detailed by the spatial appearance in chromospheric brightness (panels a) and by the average spectral line profiles (panels d) for the analyzed region (green square in panels a). It is evident, that all three cases yield strong emission peaks in the blue spectral line core of Ca II 854.21 nm when the umbral flash appears. The wavelength position of the peak emission can serve as an estimate for the shock wave velocity.

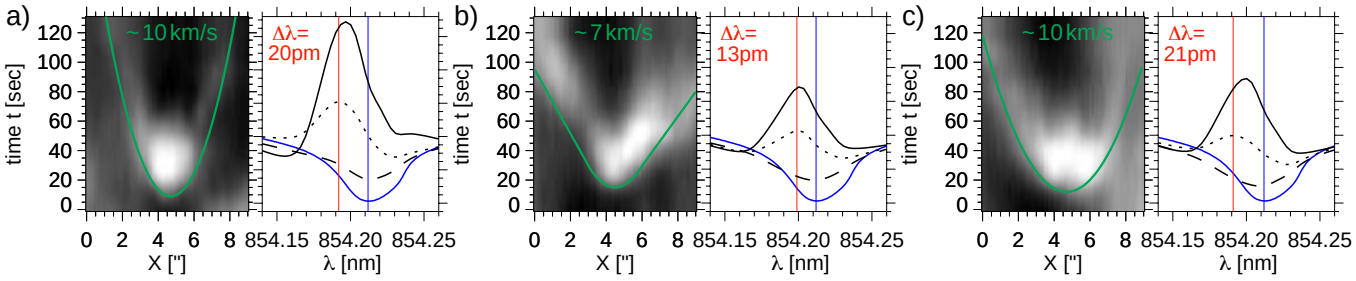

Figure 6.18.: Shock front analysis of umbral flashes. The wave front velocities are determined for the three umbral flashes (panels a–c) illustrated in Figs. 6.15, A.8, and A.10. The left panel of each case shows the spatio-temporal evolution of the bright umbral flash appearance in chromospheric line core intensity of Ca II 854.21 nm. The shock front is marked by the green curve. The right-hand side panels of each case show the spectral line core profiles during the passage of the umbral flash (black curves). Dotted: at the arrival of the flash; solid: at the maximum brightness; dashed: one minute after the flash. The FTS atlas profile is added in blue. The position of the shock front emission is marked by the red vertical line.

A closer inspection of the spectral line profile of Ca II 854.21 nm during the passage of an umbral flash is given in Fig. 6.18. To compare the spectral characteristics of umbral flashes, the three events which were mentioned above are plotted in panels a–c) next to each other. The left diagram of each case displays the arising umbral flash brightness as observed in chromospheric line core intensity. The spatio-temporal plots focus on the small-scale appearance of umbral flashes in the sunspot chromosphere. The right plot of each case shows the corresponding spectral line profiles of Ca II 854.21 nm during the passage of the umbral flash. The line profile from the FTS atlas (blue curve, Neckel 1999) exhibits the undisturbed profile in the quiet sun. For all three umbral flashes, the spectral profiles (black curves) demonstrate the same behavior. Before and distinctly after the umbral flash, the normalized line profile in the umbra (black dashed line) features a similar curve shape like the quiet sun FTS profile. During the umbral flash, the shape in the line core changes dramatically. At the first arrival of the shock front (black dotted line), the core of the line goes into emission. The emission reversal peaks in the blue spectral side of the line core. Shortly later in time, the umbral flash reaches its maximum brightness. The spectral line profile is shown as the black solid line. The wavelength position of the line minimum at quiescence (blue vertical line) and the most blue-shifted emission peak (red vertical line) are marked. The maximum blue-shift belongs to the first arrival of the shock front. The

absolute difference $\Delta\lambda$ between both wavelength positions amounts to $\Delta\lambda_{\mathrm{UF1}} = 20\,\mathrm{pm}$ ($-7.0\,\mathrm{km\,s^{-1}}$), $\Delta\lambda_{\mathrm{UF2}} = 13\,\mathrm{pm}$ ($-4.4\,\mathrm{km\,s^{-1}}$), and $\Delta\lambda_{\mathrm{UF3}} = 21\,\mathrm{pm}$ ($-7.4\,\mathrm{km\,s^{-1}}$) for the three umbral flashes. The results are in good accordance with recent studies from de la Cruz Rodríguez et al. (2013) who also applied the Ca II line at 854.21 nm to obtain the physical properties of the sunspot chromosphere with umbral flashes. The authors present slightly smaller blue-shifts of the core emission and yield chromospheric Doppler velocities of around $-5\,\mathrm{km\,s^{-1}}$ from Stokes inversions of the line profiles.

In a spatio-temporal diagram of the chromospheric spectral intensity in a sunspot as shown in Fig. 6.5, the appearance of umbral flashes resembles the shape of arcs or bowls. The temporal evolution in chromospheric brightness is shown in Fig. 6.18 for the umbral flashes at the smallest scales. The diagrams result from a $9'' \times 9''$ region which is centered on the umbral flash location in the sunspot umbra. In each case, the bright umbral flash appears localized at a size not bigger than $2 - 3''$. With increasing time, the brightness distributes away from the umbral flash barycenter. For a horizontally projected distance of around $4''$, the time for the apparent propagating amounts to 1–2 min. The apparent horizontal motion amounts to typical values between $30\,\mathrm{km\,s^{-1}}$ and $50\,\mathrm{km\,s^{-1}}$ close to top of the shock center. Comparing the three umbral flashes in Fig. 6.18, the slightly different topology of the shock waves becomes obvious. The green curves highlight the estimated shock front of the three umbral flashes. The first and third case (panels a and c) exhibit a very similar behavior. The center of the flash is very strong and is followed by an apparently slow spreading. In the diagrams, the umbral flash evolution can be fitted by a parabola curve. The second umbral flash features a different behavior (panel b). The spreading from the barycenter of the shock wave happens faster and almost linearly. Moreover, the brightness maintains also after a spreading of several arc-seconds. In the diagram, the temporal shape of the umbral flash is approximated by a compound curve. The differences in the spatio-temporal appearance of umbral flashes arises the question if the shape of the shock wave front and its super-sonic velocity can be determined from the spatial topology in chromospheric intensity.

In Section 3.5, the theory of acoustic shock waves was introduced. The geometrical topology of acoustic shock fronts was illustrated in Fig. 3.6. According to the propagation velocity of an object or wave, the acoustic shock front changes from the sonic to super-sonic case. As described by Eq. 3.37, the shape of the shock front depends on the ratio of sound speed to propagation velocity, the inverse of the Mach number $\mathcal{M}$ (Eq. 3.36). The half-angle α, which describes the inclination between axis of propagation and orientation of the shock front, is 90° for sonic wave propagation. With increasing super-sonic speed, the angle of the shock cone decreases and the shock becomes more concentrated. The topology of a super-sonic shock was illustrated in Fig. 3.7. Since umbral flashes are slow-mode magnetoacoustic waves, they share very similar properties with acoustic shocks. Therefore, an attempt can be made to apply this shock wave topology to the spatio-temporal appearance of umbral flashes. For the three umbral flashes shown in Fig. 6.18, this suggests that the more concentrated flashes with slower apparent horizontal spreading (panels a and c) are the manifestation of faster and steeper super-sonic shock waves. The less concentrated flashes with faster and more linear horizontal distribution (panel b) represent slower shock waves in the sonic to slightly super-sonic velocity range. This conclusion is in line with the magnitudes of the obtained relative shifts of the spectral emission peaks caused by the umbral flashes. According to the estimated shock cones (green curves in Fig. 3.7), a Mach number of $\mathcal{M}_{1,3} = 1.4$ is proposed for the first and third umbral flash. The second flash is evaluated with a Mach number of $\mathcal{M}_2 = 1.0$. According to that, the shock cone of the first case would have a half-angle $\alpha \sim 45°$. The sonic shock wave would have a topology as illustrated in the middle panel of Fig. 3.6. At an average formation height of the Ca II line core at around 800–1000 km in the lower solar chromosphere, the umbral model presented in Fig. 2.5 yields a sound speed of around $7\,\mathrm{km\,s^{-1}}$. According to that, the evaluation results in shock wave velocity of more than $10\,\mathrm{km\,s^{-1}}$ for the first and third umbral flash. The second umbral flash is proposed to be sonic to slightly super-sonic with more than $7\,\mathrm{km\,s^{-1}}$. The obtained phase speeds are simplified estimations. The propagation speed of the shock front is possibly underestimated since the shock compression leads to a steep increase of the local temperature which implies an increase of the sound speed by a few $\mathrm{km\,s^{-1}}$.

6.4. Running penumbral waves

As introduced in Section 2.4.3, running penumbral waves dominate the dynamics of the chromospheric penumbra. In chromospheric spectral intensity, they visually appear as bright largely-coherent wave bands which propagate radially outward across the sunspot penumbra and superpenumbra. They were first detected by Giovanelli (1972) and Zirin and Stein (1972) in the line core of Hα. Numerous subsequent studies (e.g., Lites et al. 1982; Alissandrakis et al. 1992; Christopoulou et al. 2000; Kobanov et al. 2006; Tziotziou et al. 2006; Bloomfield et al. 2007a; Jess et al. 2013; Madsen et al. 2015; Löhner-Böttcher and Bello González 2015) analyzed the propagation and oscillation of the compressive magnetoacoustic waves in spectral brightness and Doppler velocity. Visually, the waves appear together with umbral flashes and propagate radially outward from the umbral boundary to the outer edge of the sunspot. At chromospheric height, the apparent horizontal velocity at the inner penumbra amounts to $10 - 20\,\mathrm{km\,s^{-1}}$. Toward the outer penumbra the velocity decreases monotonically.

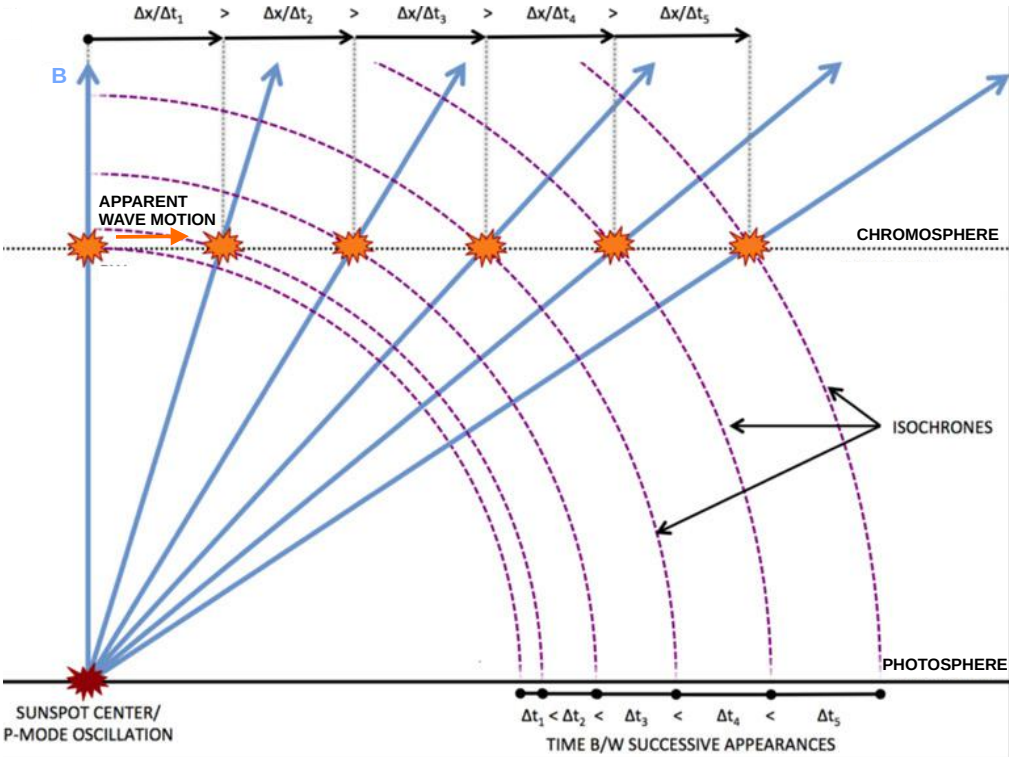

Figure 6.19.: Apparent wave motion of running penumbral waves in the chromosphere. Slow-mode waves are propagating upward along the differentially inclined magnetic field lines (B, blue arrows). When the waves arrive at a constant chromospheric altitude (black dotted lines), they are marked by an flash symbol (orange). The isochrones are displayed as violet dashed lines and reveal the radially increasing travel times Δt and therefore decreasing apparent velocity. Image adapted from Madsen et al. (2015).

The different wave propagation scenarios in sunspots were described in Section 2.5. The first scenario suggests a purely chromospheric trans-sunspot propagation of waves excited by umbral waves and crossing the magnetic field lines of the penumbra. The second option goes back to Nye and Thomas (1974) in which running penumbral waves are described as upward propagating fast-mode magnetoacoustic waves with a driving source in the sub-photospheric umbra. Finally, the third scenario suggests upward propagation of slow-mode magnetoacoustic waves in the low-β regime of the sunspot penumbra (see Section 3.2.2). The waves are guided along the sunspot's magnetic field lines and share the

same sub-photospheric driving source as umbral waves and flashes. At a distinct atmospheric formation altitude, the wave motion projects to a visual pattern of radial outward propagation. In the last years, many observational investigations have favored the slow-mode wave propagation (e.g., Rouppe van der Voort et al. 2003; Kobanov et al. 2006; Tziotziou et al. 2007; Bloomfield et al. 2007a; Jess et al. 2013; Madsen et al. 2015). I would like to anticipate that the obtained results in this work provide evidence for the latter wave scenario. The detection of running penumbral waves throughout the sunspot photosphere (Section 6.4.2), chromosphere (Section 6.2.1), and transition region (Section 6.2.2) disproves the first scenario of purely chromospheric trans-sunspot propagation. Furthermore, the obtained distribution of dominant wave periods in the atmosphere (Section 6.2 and 6.4.3) of both observed sunspots prove the field-guided propagation of sunspot waves. As described in Section 6.4.1, the more inclined magnetic field lines in the penumbra reduce the acoustic cut-off frequency which enables the upward propagation of waves with longer periods. Finally, the properties of the apparent horizontal wave motion shed light on the present magnetoacoustic mode. The inferred velocities vary with radial distance and atmospheric height. Slow-mode quasi-acoustic wave velocities (almost sonic) yield the best accordance with the observations.

The geometrical configuration of the upward-propagating wave scenario is illustrated in Fig. 6.19 after Madsen et al. (2015). Magnetoacoustic waves are excited in the center of the sunspot at the bottom photosphere or sub-photosphere (red flash). Coherent slow-mode waves propagate upward along the magnetic field lines (blue arrows). From the inner umbra (vertical orientation) to the penumbra (diagonal orientation), the zenith inclinations of the magnetic wave-guides increase. Consequently, the path length of a propagating wave to a distinct chromospheric altitude increases from the umbra to the penumbra. In line with Bloomfield et al. (2007a), the travel time of the wave increases too. The coherent wave front first arrives in the umbra and gradually later with increasing distance from the vertical umbral axis (Rouppe van der Voort et al. 2003). Temporally, the projected wave performs a horizontal outward propagation. As demonstrated by the isochrones (violet, dashed circles) for equidistant wave appearances Δx, the required time interval Δt increases for each step. Correlatively, the apparent horizontal velocities $\Delta x/\Delta t$ close to the vertical axis are fastest. With increasing horizontal distance the apparent speed slows down gradually. The illustrated geometrical configuration explains the extremely super-sonic horizontal wave speeds from observations in the umbra and inner penumbra. Toward the more inclined magnetic field of outer penumbra and superpenumbra, the apparent horizontal wave speed approaches the actual phase speed of running penumbral waves. In the chromosphere, these velocities are of the order of $5 - 10\,\mathrm{km\,s^{-1}}$ which is at the scale of the local speed of sound (see Fig. 2.5 c). For fast Alfvén speeds in the low-β atmosphere of the chromospheric penumbra, the quasi-acoustic wave speed coincides with the velocity of slow-mode waves (Eq. 3.28). Fast-mode propagation (Eq. 3.29) yields super-Alfvénic velocities which exceed the sound speed by up to one magnitude.

6.4.1. Characteristic periodicities and the cut-off frequency

The distribution of characteristic wave periods in the sunspot atmosphere of active region NOAA11823 has been described extensively in Section 6.2.1. In this section, I would like to emphasize the importance of the acoustic cut-off frequency for the propagation of sunspot waves. Since the sunspot penumbra exhibits a differentially inclined magnetic field, the interaction of waves with the acoustic cut-off is of particular influence. As described in Section 3.4, the acoustic eigenfrequency of the solar atmosphere scales proportionally with the cosine of the magnetic field inclination angle and inversely with the sound speed of the plasma. For an isothermal sound speed of $c_\mathrm{S} = 7\,\mathrm{km/s}$ in the upper photosphere and a vertical magnetic field, the acoustic cut-off period is often estimated to $T_\mathrm{cut,0} = 192\,\mathrm{s}$ ($f_\mathrm{cut,0} = 5.2\,\mathrm{mHz}$). Following Eq. 3.34, the acoustic cut-off frequency has its maximum value in the vertical ($\Phi_\mathrm{B} = 0°$) magnetic field of the umbra and decreases for more the inclined penumbral field. As sunspot waves are proposed to follow the magnetic field lines, umbral waves with periods above the acoustic cut-off period are evanescent above the filtering layer. On the other hand, the increased cut-off period in the sunspot penumbra enables the propagation of running penumbral waves with longer periods than in

the umbra. The long-period wave modes overpower the short-period oscillations and lead to a shift in the wavelet power spectrum. The peak period defines the position of the maximum wave power in the observed power spectrum. Observations (Tziotziou et al. 2006; Bogdan and Judge 2006) suggest a direct proportionality of the observed peak period in the power spectrum and the acoustic cut-off period, differing by a constant factor of 1.25 between both parameters (Eq. 6.5). The observed distribution of peak periods (Figs. 6.11, 6.12, 6.14, and 6.25) in the sunspot atmosphere is in very good agreement with the proposed theory. From the upper photosphere to corona, the umbral area is dominated by waves in the 2.5–2.9 min band. According to the very vertical magnetic field, this leads to an acoustic cut-off period of around 188–220 s, or an acoustic cut-off frequency around 4.6–5.3 mHz. At the outer penumbra, the peak periods increase to around 8 min with a cut-off frequency of $f_{\mathrm{cut},70^\circ} = 1.7$ mHz.

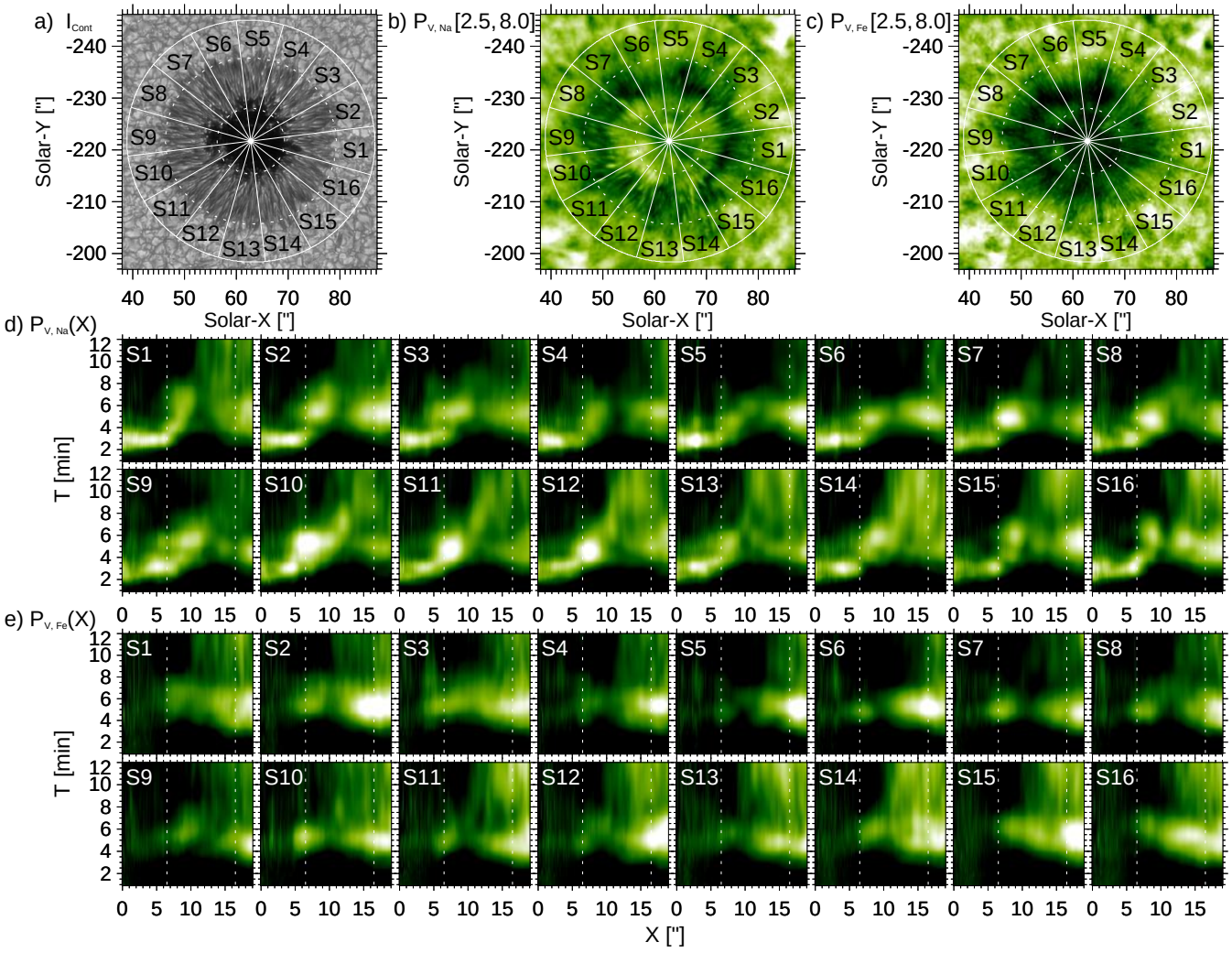

Figure 6.20.: Sectorial analysis of wave power in the lower chromosphere and photosphere of sunspot region NOAA 11823. The sunspot is shown in continuum intensity I_{Cont} (panel a) and velocity wave power P_{V} from the chromospheric Na I 589.6 nm line (panel b) and the photospheric Fe I 630.15 nm line (panel c) in the averaged 2.5–8 min period band. The oscillatory power is scaled in logarithmic (arbitrary) units to assure best contrast in the penumbra. Bright colors indicate largest values. The sunspot is divided into 16 sectors (white solid lines). The azimuthally averaged power distribution of each sector is shown in panels d) and e) for both atmospheric layers. The power is plotted for wave periods T and radial distances X from the sunspot barycenter. The vertical dotted lines mark the average sunspot boundaries.

The obtained distributions of peak periods and cut-off frequencies in the sunspot chromosphere and transition region confirm the theory of Bel and Leroy (1977) in which the cut-off frequency is modified by the inclined magnetic field. The observed wave power, peak periods and acoustic cut-off modifications are in best agreement with the findings of other observational studies (e.g., De Pontieu et al. 2005; McIntosh and Jefferies 2006; Bloomfield et al. 2007a; Jess et al. 2013; de la Cruz Rodríguez et al. 2013; Yuan et al. 2014b). A very comprehensive overview on the distribution of wave power in the sunspot was presented by Fig. 6.1. There the azimuthally averaged velocity power spectra of the circular sunspot is displayed according radial distance from the sunspot center. The results are presented for the Doppler velocities from the lower chromospheric Na I D1 line at 589.59 nm (panel a) and from the lower photospheric Fe I line at 630.15 nm (panel b). The average chromospheric distribution highlight the dominating 2.5–3 min oscillations in the umbra, the jump to 4 min periods at the umbral boundary, the increase in wave period to 6 min in the inner penumbra, followed by an increase to long-period waves with more than 8 min at the outer penumbra, and the dominating p-modes around 5 min in the vicinity of the sunspot. The photospheric distribution yields a similar trend, but less pronounced. The acoustic cut-off period can be read out directly from the diagram. The peak period of the maximum power at each distance only has to be multiplied by a factor of 1.25.

Of course, the azimuthal average of the wave power spectra can only reflect the characteristics for the average umbra and penumbra. To provide information about the individual direction of the circular sunspot, a sectorial examination is performed. The basic concept is illustrated in Fig. 6.20. The sunspot area is divided into 16 sectors which share the same center in the umbra. All sectors have a cone angle of 22.5°, the circumference is slightly foreshortened according to the heliocentric angle of $\theta = 14°$. As shown by the sunspot in continuum intensity (panel a), the sectors are aligned with the penumbral filaments. Sectors 1–16 are ordered counterclockwise with the first sector on the right-hand side. The average velocity power in the 2.5–8 min band is shown for the lower chromospheric Na I D1 line (panel b) and the lower photospheric Fe I line (panel c). The velocity power is scaled, high power is shown in bright color. In the two-dimensional power map, the enhanced chromospheric velocity power covers the umbral area and inner penumbra. In the lower photosphere, amplified wave power is only present at the umbral boundary and inner penumbra. In the following analysis, the velocity power spectra are averaged azimuthally for each circular segment at each radial distances from the sunspot barycenter. The result of each sector is displayed as a spatio-periodical diagram of velocity power $P_V(X)$ in the panels below. The upper 16 panels present the distribution in the lower chromosphere, the lower 16 panels show the case for the lower photosphere. In the chromosphere, all sectors feature the same domination of 3 min oscillations in the umbra ($X \leq 6.3''$). In the vicinity of the sunspot ($X \geq 16.3''$), acoustic 4–6 min oscillation are common within each sector. The velocity power distribution in the penumbral area of the sectors is more diverse. The sectors in the lower right side of the sunspot (S1, S16) reveal a very steep increase from 3 min to 8 min within the first $3''$ of the inner penumbra. On the other hand, many sectors (S10–S14) feature a more smooth increase from 4–5 min at the inner penumbra to 10–12 min at the outer penumbral boundary. Moreover, some segments (S5–S8) yield a smaller increase in wave period from around 4 min to 8 min throughout the penumbra. The dominant wave periods and proportional cut-off periods hint at a differentially inclined magnetic field lines. The spatio-periodical diagrams suggest that the penumbra in the lower half of the sunspot is slightly more inclined than in the upper half. Furthermore, many sectors display a jump in wave period from 3 min to 4–5 min at the umbral boundary. Such a deviation from the linear relation between peak and cut-off frequency at the inner penumbral boundary has also been reported in other observations (Tziotziou et al. 2007; Yuan et al. 2014b). This jump is especially noticeable in sectors S3, S7 and S10. Interestingly, all three sectors feature a larger mixture of umbral structures and penumbral grains and filaments at the outer defined outer umbra and inner penumbra. This directly supports a propagation of sunspot waves along the diverse small-scale magnetic field topology. Beyond, a possible mergence of two consecutive umbral flashes to one running penumbral waves was found in Fig. 6.5. Further reasons for such a non-linearity are discussed at the end of Section 6.5.5.

6.4.2. First imprints at photospheric layers

Running penumbral waves are commonly observed in the chromosphere above sunspots. The modern sunspot wave scenario (Section 2.5) suggests that running penumbral waves are slow-mode magnetoacoustic waves which are channeled upward along the inclined magnetic field lines of the penumbra. According to that, the compressive wave propagation should also be detectable in the photospheric penumbra. An evident imprint of field-guided running penumbral waves in the lower photosphere would prove the proposed wave nature. Whereas most studies on running penumbral waves focused on the chromospheric signal, only few attempts (e.g., Lites et al. 1998; Bloomfield et al. 2007a) have been made to determine the photospheric signatures. Due to the expected weak spectral signal and the presence of acoustic p-modes as well as the strong Evershed flow in the penumbral filaments, no clear evidence has been provided yet for photospheric penumbral waves. Only Marco et al. (1996) and more recently Zhao et al. (2015) found a weak wave signature in the lower photosphere at the inner penumbra. The sunspot observation allows the performance of a novel high-resolution, multilayer study concentrating on the photospheric penumbral wave characteristics. In the following, I will provide strong evidence for running penumbral wave signatures in the lower photosphere. A description of the results is also given in Löhner-Böttcher and Bello González (2015).

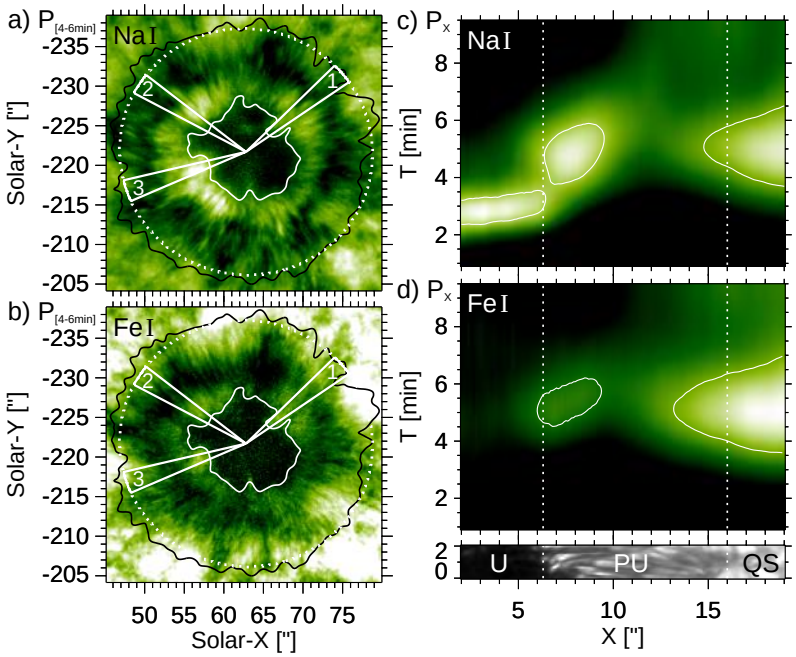

Figure 6.21.: Distribution of velocity wave power in the lower chromosphere and photosphere of sunspot NOAA11823. The oscillatory power of Doppler velocities from Na I 589.6 nm (upper panels) and Fe I 630.15 nm (lower panels) is scaled in logarithmic (arbitrary) units to assure best contrast in the penumbra. Panels a and b show the power in the 4–6 min period band. Bright colors indicate largest values. The sunspot boundaries are contoured in white and black. Sectors 1–3 (white solid) follow the foreshortened projection of a circle (dotted). Panels c and d show the azimuthally averaged global power spectra P_X for periods T and radial distance X from the sunspot barycenter. The important elements in the power distribution are contoured in white. For context information, a slice of the sunspot in continuum intensity is added below. The dotted lines mark the average sunspot boundaries. Image from Löhner-Böttcher and Bello González (2015).

In Section 6.2.1, a first analysis of the Doppler shifts obtained from the lower photospheric Fe I 630.15 nm line was performed for the sunspot region. The visual evolution of the two-dimensional

Dopplergrams indicates radially outward propagating waves at the inner penumbra. In addition, the distribution of photospheric velocity wave power (see Figs. 6.1 and 6.10) has revealed enhanced oscillatory signals in the 3–6 min range at the outer umbra and inner penumbra. Also the distribution of dominant wave periods in the sunspot region supports the presence of running penumbral waves in the lower photosphere. As shown in Fig. 6.11 for Doppler velocity oscillations and in Fig. 6.12 (bottom panels) for brightness variations in the line core of Fe I 630.15 nm, the distribution of peak periods yields a filamentary structure and radial shift toward longer wave periods. In the following, a detailed investigation of photospheric wave propagation provides evidence for the photospheric component of running penumbral waves. The combination of all findings proves the proposed nature of slow-mode magnetoacoustic wave propagation (see Section 2.5).

Evidently, photospheric penumbral waves manifest by a very weak oscillatory signal. To achieve significant results, the penumbral regions with distinct oscillatory power have to be extracted. Therefore, a wavelet power analysis is performed on the photospheric Doppler velocities from Fe I 630.15 nm. The time-averaged wave power $P_{4-6\,\mathrm{min}}$ in the 4-6 min period band is shown in Fig. 6.21 b). For best visualization, the wave power is displayed at a logarithmic scale (total numbers given in Fig. 6.1). To compare the photospheric and chromospheric distribution, the wave power obtained from the Na I D1 589.6 nm line is plotted in panel a) of Fig. 6.21. In contrast to the reduction of total wave power from the sunspot surroundings toward the umbral core, the inner penumbra exhibits an enhancement (bright color) of wave power at the inner $4''$ of the penumbra. Like in the lower chromosphere, the spatial distribution in the lower photosphere follows the filamentary structure of the penumbral magnetic field lines. The panels on the right-hand side of Fig. 6.21 illustrate the azimuthally averaged power spectra of the sunspot region. The power distribution P_{X} in the lower chromosphere (panel c) and lower photosphere (panel d) is plotted for wave periods T as a function of increasing distance X from the umbral barycenter. The contours highlight the dominating wave power in the sunspot region. With increasing distance to the umbra, the power at the inner penumbra shifts towards longer wave periods in the 4–6 min range at both layers. This systematic shift in wave period stands in contrast to the constant p-mode signal in the 4–6 min range at the outer penumbra and quiet sun. It has to be interpreted as the result of the effective acoustic cut-off frequency (see Section 6.4.1), which initially acts on the field-guided wave propagation in the sunspot's middle photosphere. The increasing peak periods at the umbral boundary and inner penumbra are therefore induced by the increasing zenith inclination of the penumbral magnetic field (Bel and Leroy 1977; De Pontieu et al. 2004; McIntosh and Jefferies 2006). More inclined magnetic fields permit the upward propagation of waves with longer periods.

Next, the temporal evolution and apparent wave speeds of photospheric penumbral waves are studied in more detail. The most significant results are obtained for the three sectors shown in the left panels of Fig. 6.21. The sectors with opening angles of 10° are placed at sunspot regions with highest velocity power at the inner penumbra. The oscillation of photospheric Doppler velocities is weak and overlaid by the Evershed flow. First, the time-averaged (58 min) Dopplergram (Fig. 5.1) is subtracted from the individual Dopplergrams. The running penumbral waves seem to follow the filamentary fine-structure of the penumbra. Under the assumption of largely coherent wave trains for nearby fields, the Doppler velocities within each sector are azimuthally averaged at each distance from the spot center. The temporal evolution of the relative velocities along the three sectors is shown in the bottom panels (d–f) of Fig. 6.22. All sectors exhibits continuous and significant oscillation in the inner penumbra. The relative amplitudes in the photospheric penumbra are below $300\,\mathrm{m\,s^{-1}}$. In comparison, the amplitudes in the lower chromospheric penumbra (panels a–c) are at least a factor of two larger. In the inner penumbra close to the umbral boundary, all photospheric waves have a slightly delayed chromospheric counterpart. For both layers, the temporal evolution in the photospheric sectors provides evidence for outward-directed wave propagation in the inner $4''$ of the penumbra. Moreover, the signal can be traced back into the umbra. In the outer penumbra, the direction of apparent wave propagation is often inverse to inward propagation of acoustic p-modes. This is especially noticeable in the last 10 min in Fig. 6.22 (panel d).

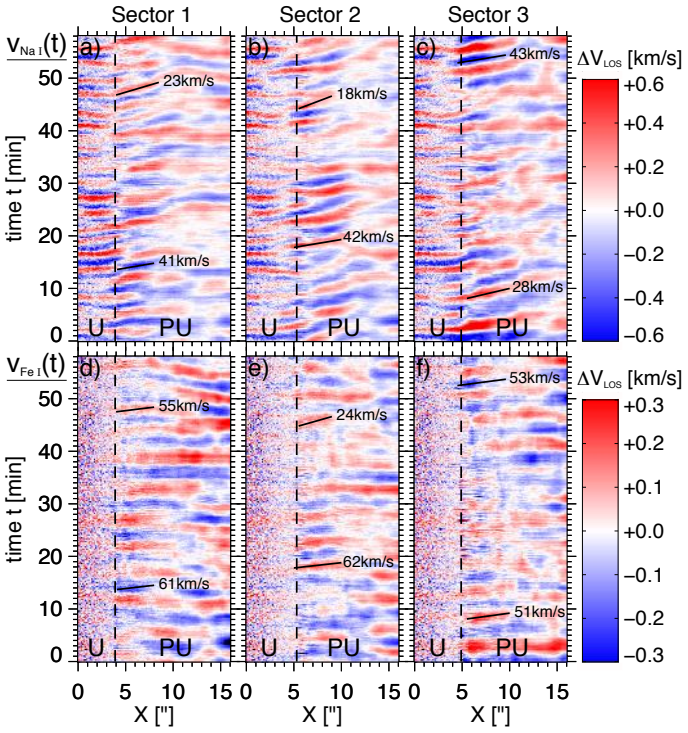

Figure 6.22.: Sunspot oscillations in lower chromospheric (upper panels) and photospheric (bottom panels) Doppler velocities. The temporal evolution of the relative velocities $V_{\mathrm{Na,\,I}}$ from Na I 589.6 nm (panels a–c) and $V_{\mathrm{Fe\,I}}$ from Fe I 630.15 nm (panels d–f) is given for all three sectors marked in Fig. 6.21. The velocities were azimuthally averaged for each sector and plotted in time t and radial distance X from the sunspot barycenter. The black dashed line marks the umbral boundary. The velocity scale $\Delta \mathrm{V_{LOS}}$ ranges between $\pm 0.6\,\mathrm{km\,s^{-1}}$ (a–c) and $\pm 0.3\,\mathrm{km\,s^{-1}}$ (d–f). The black bars highlight apparent wave trains. Image from Löhner-Böttcher and Bello González (2015).

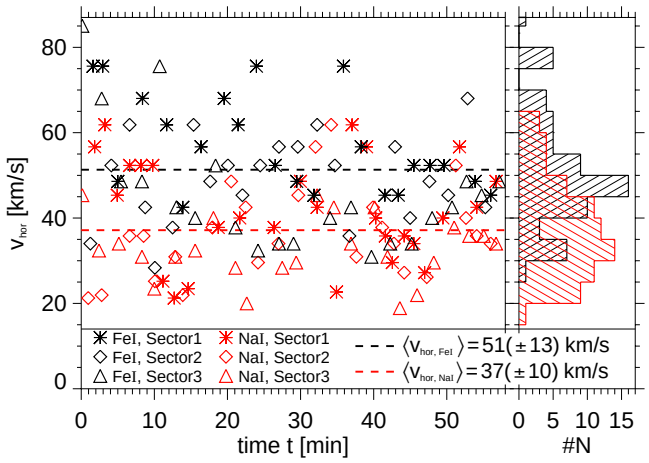

Figure 6.23.: Apparent horizontal velocities, $\mathrm{v_{hor}}$, of running penumbral waves in the photosphere (black) and chromosphere (red). The results were obtained from the inner penumbra of the sectorial analysis shown in Fig. 6.22 for the Doppler velocities from the photospheric Fe I line at 630.15 nm and the chromospheric Na I line at 589.6 nm. The velocities are plotted against the observation time t. The asterisks, diamonds, and triangles represent sectors 1–3. The dashed lines indicate the average apparent velocities $\langle \mathrm{v_{hor}} \rangle$ for both layers. The histogram on the right presents the number $\#N$ of velocity values $\mathrm{v_{hor}}$ within a $5\,\mathrm{km\,s^{-1}}$ binning interval.

The analysis of the apparent wave motion in the lower photosphere yields a very important result. The apparent horizontal velocities of the wave trains in the spatio-temporal diagram are larger than in the upper photosphere and lower chromosphere. As shown in Fig. 6.22, the apparent velocities can be inferred from the slopes of the wave trains over the first 4″ in the inner penumbra. Exemplarily, two cases are marked by black solid bars in each sector. Wave trains highlighted in the lower chromosphere (top panels) and lower photosphere (bottom panels) seem to correspond to the same global wavefront (see Fig. 6.19). In these cases, the apparent horizontal velocities of around $50 - 60\,\mathrm{km\,s^{-1}}$ in the lower photosphere are at least $10\,\mathrm{km\,s^{-1}}$ faster than in the lower chromosphere. The obtained velocities from the extended investigation for all wave trajectories are plotted in Fig. 6.23. In the lower chromosphere, the horizontal velocities $\mathrm{v_{hor}}$ of running penumbral waves range between $20\,\mathrm{km\,s^{-1}}$ and $60\,\mathrm{km\,s^{-1}}$ (red symbols). The average velocity is $\langle v_{\mathrm{hor,\,Na\,I}} \rangle = 37 \pm 10\,\mathrm{km\,s^{-1}}$ (red dashed line). The values are in agreement with recent studies (Tziotziou et al. 2006; Kobanov et al. 2006; Jess et al. 2013). In the lower photosphere, running penumbral waves have apparent velocities $\mathrm{v_{hor}}$ between $30\,\mathrm{km\,s^{-1}}$ and $80\,\mathrm{km\,s^{-1}}$ (black symbols). The average velocity amounts to $\langle v_{\mathrm{hor,\,Fe\,I}} \rangle = 51 \pm 13\,\mathrm{km\,s^{-1}}$ (black dashed line). The histogram on the right-hand side clarifies the dispersion. No temporal trend is evident. The sectorial diagnosis exhibits that running penumbral waves in sector 1 (asterisks) are slightly faster than the average. The values of sector 2 (diamonds) are centered around the overall mean. The velocities in sector 3 are slightly below the average. As shown in Fig. 6.21, the sectors are oriented toward the solar limb (1), disk center (3), and perpendicular to the disk center-to-limb direction (2). The inferred magnetic field inclination in Fig. 6.32, proposes a zenith inclination of $\Phi_{\mathrm{B},1} \sim 35°$, $\Phi_{\mathrm{B},2} \sim 45°$, and $\Phi_{\mathrm{B},3} \sim 55°$ for the inner 4″ of the penumbra in sector 1, 2, and 3.

Consequently, running penumbral waves manifest with faster horizontal velocities when the penumbral magnetic field is more vertical. This is a very important finding which suggests that the observed horizontal wave motion is merely a geometrical projection (Bloomfield et al. 2007a; Madsen et al. 2015). As illustrated in Fig. 6.19, upward propagating waves along inclining waveguides lead to a visual pattern of horizontal propagation at a distinct atmospheric layer. The wave scenario is in agreement with the magnetic field topology obtained in Fig. 6.32, dominant wave periods in the sunspot atmosphere, and maintained horizontal wave velocities. The fast horizontal wave velocities with up to $100\,\mathrm{km\,s^{-1}}$ in the umbra can be explained by the very vertical magnetic field of the sunspot's core. In addition, the strong gradient of increasing zenith inclination at the photospheric umbral boundary clarifies the fast photospheric velocities. As stated by Bogdan and Judge (2006), large horizontal velocities of up to $60 - 80\,\mathrm{km\,s^{-1}}$ for running penumbral waves in the photosphere reflect relative travel time differences for waves guided by the individual less and more inclined magnetic field lines of the outer umbra and inner penumbra. In accord with the topological model of the sunspot's magnetic field (e.g., Westendorp Plaza et al. 1997), the field fans out with increasing atmospheric height which makes the radial increase in zenith inclination more smoothly. Commonly, the apparent propagation speeds decrease radially toward the more inclined outer penumbra. Moreover, as the results at higher chromospheric to transition region layers (Fig. 6.13) have shown that the horizontal velocities decrease to around $10 - 15\,\mathrm{km\,s^{-1}}$ (in line with Madsen et al. 2015). In summary, strong evidence is provided for running penumbral waves in the sunspot photosphere. In conformance with Marco et al. (1996), the waves are aligned with the magnetic field of the penumbra. Consequently, the phenomenon of running penumbral waves is not a chromospheric one. The scenario of chromospheric trans-sunspot propagation excited by umbral flashes is disproved.

To see the bigger picture of sunspot waves in the lower photosphere, further studies on a possible connection between convective flows and magnetoacoustic waves are required. Most sunspot studies focus either on the convective dynamics and magnetized flows or on the wave phenomena. However, especially the magnetized Evershed flow could interact with the magnetohydrodynamic waves. I therefore suggest that upcoming investigations of sunspots have to take the diverse dynamical effects into account (e.g., Esteban Pozuelo et al. 2015). In addition, I propose a statistical study with HMI data on correlations between sunspot waves and the sunspot size, magnetic field topology, and field strength.

6.4.3. Presence in irregular sunspots and pores without a penumbra

The next important question I will answer is whether irregular sunspots and pores without a penumbra also feature running penumbral waves in the chromosphere. Since the propagation is channeled by the sunspot's magnetic field, Bloomfield et al. (2007a) suggested that running penumbral waves should also be detectable in pores with sufficiently inclined magnetic field lines forming a superpenumbra in the chromosphere. Moreover, the investigation of wave propagation in the irregular sunspot of active region NOAA11455 reveals the impact of light bridges on sunspot waves.

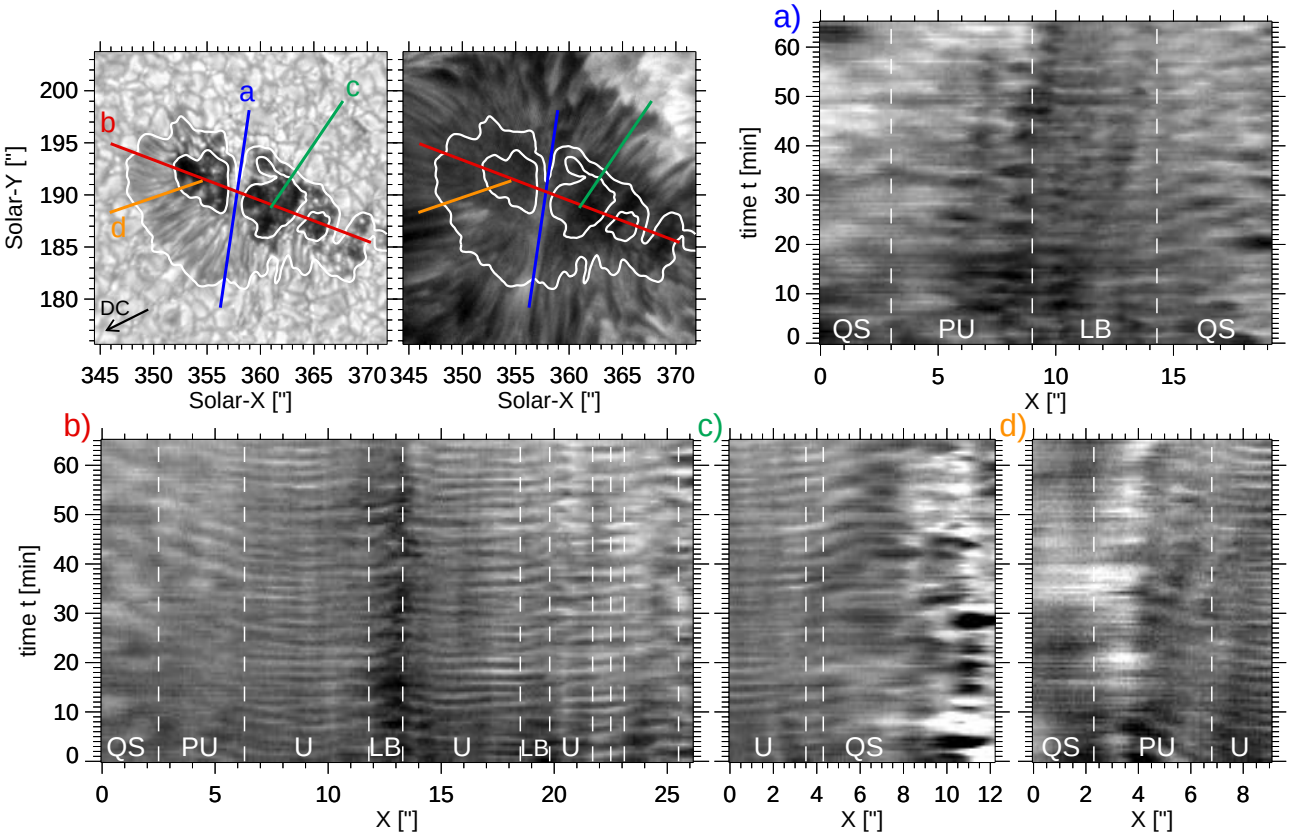

Figure 6.24.: Wave signatures in chromospheric intensities at different regions in the sunspot NOAA11455. On the upper left, the sunspot is shown in continuum intensity (left) and spectral line core intensity of Hα at 656.28 nm. The temporal evolution of the spectral intensities along the four slices (blue, red, green, orange) are displayed in panels a–d. The intensities were reduced by the temporal average and normalized to the average intensity. The vertical dashed lines mark the white-light boundaries (white contour) between umbra (U), penumbral (PU), light bridge (LB), and quiet sun (QS). The black arrow in the upper left panel is pointing toward the solar disk center.

The observations of the irregular sunspot of active region NOAA11455 with the Triple Etalon SOlar Spectrometer (see Section 4.1.3) were described in Section 4.3.2. The observational and spectroscopic settings are listed in Tables 4.7 and 4.8. The spectral intensities and magnetic field parameters of the sunspot region are shown in Fig. 4.17. The sunspot region in the bottom photosphere provided by the continuum intensities (also shown in Fig. 6.24) exhibits a half-sided penumbra toward the solar disk center. Three umbral cores are separated by two convective light bridges. The left one has a width of 2″, the right one is 1″ wide. The sunspot in spectral intensity from the cores of the Fe I lines at 709.04 nm (Fig. 4.17 b) and 543.45 nm (panel c) displays the appearance in the middle and upper photosphere. The sunspot region in chromospheric brightness from the Hα line minimum is displayed in the top, second left panel of Fig. 6.24 (and Fig. 4.17 c). According to the small heliocentric observation angle

of 23°, spatial displacements in the horizontal plane are below 1″ from the bottom photosphere to the middle chromosphere. The spectral intensities from the middle photosphere to middle chromosphere yield significant oscillatory signals in the two umbral cores which characterize by magnetic field strength of up to 1.8 kG and more. As maintained by the magnetogram in Fig. 4.17 (panel f), the wide light bridge which separates the umbrae yields a strong decrease in field strength by around 1 kG.

In the middle chromosphere, the signal of umbral flashes and running penumbral waves in the sunspot region is most notably. A deeper investigation of the characteristics of chromospheric wave propagation in the irregular sunspot region is obtained by the spatio-temporal evolution in the Hα line minimum intensity. The analysis in Fig. 6.24) illustrates the temporal evolution along four characteristic slices. The slices are placed **a)** along the wide light bridge, **b)** across the sunspot umbrae and light bridges, **c)** along the superpenumbral fibrils above the sunspot side lacking a photospheric penumbra, and **d)** along the disk center-side penumbra and superpenumbra. The respective spatio-temporal diagrams are displayed in panels:

a) The temporal evolution along the light bridge (blue slice) is inconsistent. Oscillations in the 5 min range seem to dominate the motion in the light bridge and adjacent superpenumbra above the quiet sun and in the penumbra. In the penumbral region facing the light bridge, an opposite oscillatory motion indicates the convergence and crashing of different wave trains. The overall temporal scale yields a slow apparent shift in intensity from the penumbra toward the light bridge. This motion toward the light bridge center has also been reported by Yuan et al. (2014a). The fact that strong average downward motions with up to 1 km s^{-1} are localized in the center of the photospheric light bridge (see Fig. 5.2) raises questions about a possible linkage. In the upper part of the slice above the quiet sun, outward propagating superpenumbral waves feature apparent horizontal velocities of around $12 - 20$ km s^{-1}.

b) The temporal evolution along the red slice crossing the sunspot umbrae and light bridges is very informative. Continuous oscillations in the 2.5–3.0 min range dominate in the two strong umbral cores. Several umbral flashes are visible by the strong increase in spectral brightness. The spatial coherence of the umbral waves reaches 2–4″. In the area which corresponds to the wide photospheric light bridge, the chromospheric brightness is drastically reduces. Moreover, waves from both umbral cores converge toward the light bridge, overlap and break. Therefore, the oscillatory motion is discontinuous above the wider light bridge. The nearing wave trains yield the characteristics of running penumbral waves but cannot propagate into the opposing umbra. Above the narrower light bridge and small umbral core, a similar but less distinct wave breaking is present. In the left part of the slice, the penumbral area shows clear periodical brightness variations with wave periods around 5 min. According to the trajectories of the wave trains, running penumbral waves feature apparent horizontal velocities of around $10 - 15$ km s^{-1}.

c) The solar limb-side of the sunspot lacks a penumbra in the bottom photosphere. In chromospheric intensity, the region at the green slice features superpenumbral fibrils which extend up to 8″ beyond the white-light boundary of the sunspot. The temporal evolution along that slice exhibits umbral oscillation with a periodicity of 2.5 min and running penumbral waves with a wave period of around 5 min and an apparent horizontal propagation with around $10 - 15$ km s^{-1} in average. The running superpenumbral waves seem to originate in the umbral area and proceed up to 4″ into the umbral vicinity. At a distance $X \sim 8 - 10''$, they break with the opposite oscillatory motion from the surrounding spicules.

d) The orange slice is placed above a regular umbral-penumbral region. The umbra features oscillations with a periodicity of 2.5 min. In the penumbra, running penumbral waves propagate radially outward to a distance of around 3″ from the umbral boundary.

In summary, the wave propagation in the irregular sunspot proves that running penumbral waves do not require a photospheric penumbra. An inclined chromospheric superpenumbra is sufficient for the

existence of running penumbral or better called superpenumbral waves. In support of that statement, Sobotka et al. (2013) and Freij et al. (2014) measured running penumbral waves in the chromospheric superpenumbra of solar pores which lack a photospheric penumbra at all. The authors have classify the wave propagation more generally as 'sunspot running waves' or 'upwardly propagating waves'. The analysis of sunspot waves or running penumbral waves above light bridges reveals that waves from the two umbral cores converge and break above the light bridge. This finding is in accordance to the results obtained by Yuan et al. (2014a) for the upper chromosphere and transition region above a sunspot's light bridge. As it can be inferred from the zenith inclination and azimuth of the photospheric magnetic field (Fig. 4.17 g and h), the magnetic field in the light bridges is not only reduced in strength but also differs to the umbral cores by its topology. Within one arc-second, the zenith inclination of the magnetic field with respect to the local normal increases from around $20-30°$ at the outer umbrae to $50-60°$ at the center of the light bridge. This is in line with other observations (e.g., Rueedi et al. 1995a; Leka 1997). In addition, the azimuth inclination shows a large diversity of magnetic field orientations. The magnetic field topology indicates the presence of a more horizontal small-scale

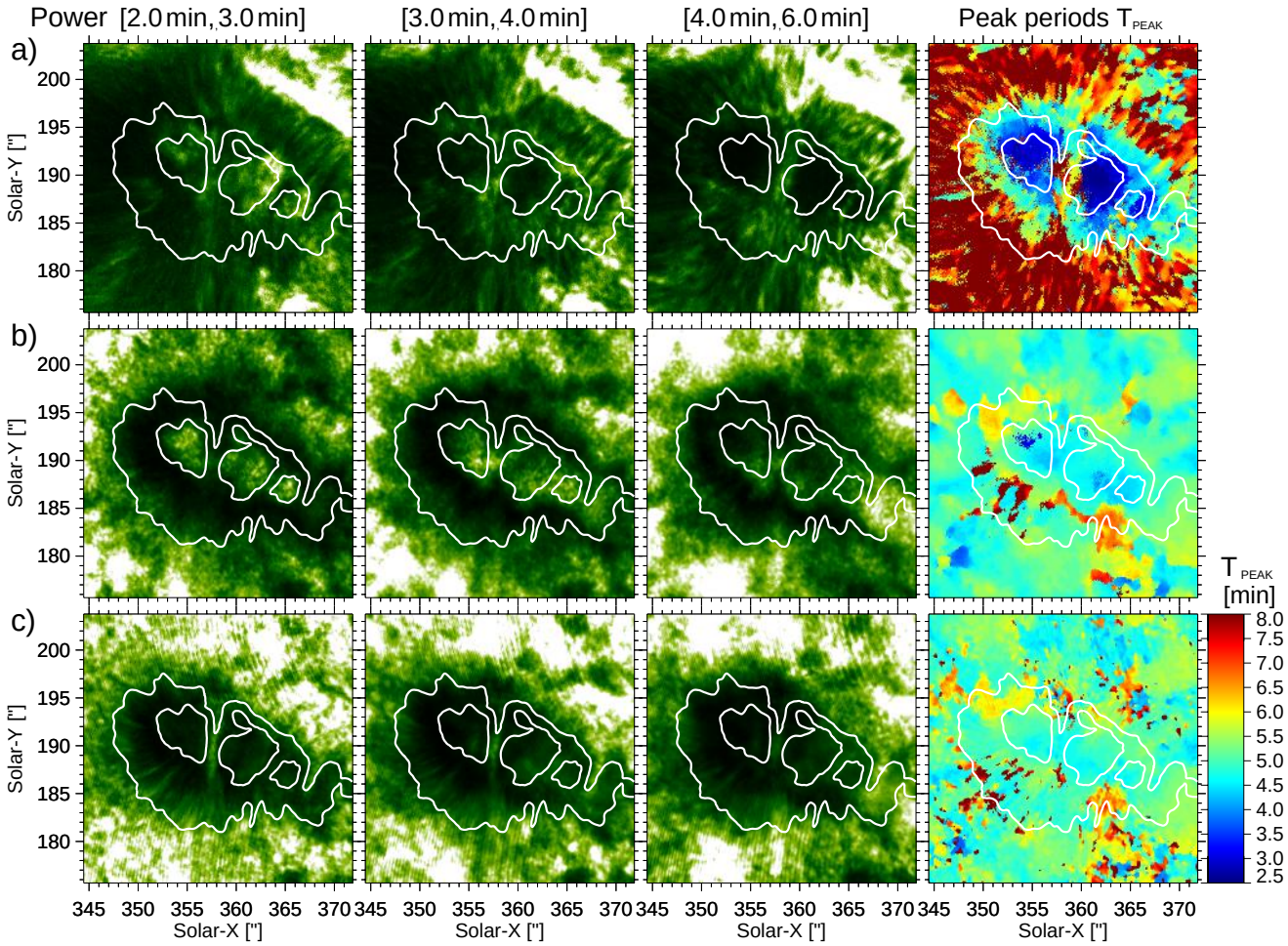

Figure 6.25.: Distribution of wave power in the middle chromosphere (top row), upper photosphere (middle row), and lower photosphere (bottom row) in sunspot region NOAA11455. The nine panels on the left show the scaled wave power from a) line core intensity of Hα at 656.28 nm, and b, c) Doppler velocity oscillations from the Fe I lines at 543.45 nm (b) and 709.04 nm (c), filtered in the 2–3 min, 3–4 min, 4–6 min period bands. The panels on the right present the dominant wave periods T_{PEAK}, scaled from 2.5 min (dark blue) to 8 min (dark red). The umbral and penumbral boundaries are contoured in white.

magnetic canopy in-between the very vertical magnetic field of the umbral cores.

In the following, I will address the question if the increased magnetic field inclination in light bridges leads to the same characteristic increase to longer wave periods like it is the case for the inclined penumbral field. The wavelet analysis of the spectral intensity at the Hα line minimum yields conclusive results. The two-dimensional distribution of the global intensity wave power is shown in the top row of Fig. 6.25. The intensity power is averaged in the 2–3 min (left panel), 3–4 min (second left panel), 4–6 min (second right panel) periods bands to highlight the prime differences. In the 2–3 min band, the chromospheric power inside the sunspot region is concentrated in the umbral cores. At periods between 3 min and 4 min, the wave power has shifted toward the umbral boundaries and parts of the light bridge. In the 4–6 min band, the intensity power in the umbral cores is lowered. Now, the power concentrated in the area of the light bridges and inner superpenumbra. The enhanced power in the upper left region results from the adjoining spicules in the active region. Co-spatially contoured white-light boundaries of the sunspot suggest that the location of the light bridges has shifted by around $1.5''$ to the lower right. In the next step, the peak periods of dominating oscillations are extracted from the global wavelet spectra (see Section 6.5.1). The result are displayed in the top right panel of Fig. 6.25. Whereas the left and right umbral cores are dominated by waves in the 3 min period, the central umbra yields peak periods T_{Peak} in the 2.5 min range. In contrast to the short periods in the umbrae, the wide light bridge characterizes by a steep increase to wave periods around 5–6 min. In the narrow light bridge, an immediate increase to oscillations in the 4.5 min range is noticeable. According to these results, the answer to the question on the characteristic increase in oscillatory period and magnetic field inclination is clear. The magnetic field above a light bridge in more inclined against the zenith than above the umbrae and therefore features the propagation of waves with longer periods. In the peak period map, this shows up by a rapid increase in wave periods. The results confirms earlier studies of light bridge oscillations in sunspots and pores (Sobotka et al. 2013; Yuan et al. 2014a).

The next point I want to emphasis is the overall distribution of wave power and peak periods in the sunspot chromosphere and photosphere. As further shown in the top right panel of Fig. 6.25, the dominating wave periods in the sunspot penumbra and superpenumbra increase with radial distance from the umbrae. This shift in peak period is almost linear. Within a distance of $5''$ from the umbral boundary, the periods increase from around 3.5 min to 8 min for all direction. Consequently, the distribution is not affected by the lack of the limb-side penumbra. In addition, the filamentary structure of the power and period distribution suggests the propagation of magnetoacoustic waves along the sunspot's chromospheric superpenumbra. According to the cut-off theory described in Section 6.4.1, the radially outward increasing peak periods proportional to the acoustic cut-off period are enabled by the increasing zenith inclination of the superpenumbral magnetic field. The distribution of velocity wave power in the photosphere supports the scenario. The wave power of Doppler velocity oscillations from the upper photospheric Fe I line at 543.45 nm and the lower to middle photospheric Fe I line at 709.04 nm is analyzed. The distribution of velocity wave power in three period bands and the peak periods of the global wavelet spectra are shown in Fig. 6.25 for the upper (middle row) and lower to middle (bottom row) photosphere. Evidently, p-mode oscillation in the 4–6 min range dominate the vicinity of the sunspot. The velocity power is reduced in the sunspot. In the lower photosphere, enhanced velocity power is spatially localized to the wide light bridge. Toward the upper photosphere, the spatial distribution of velocity power changes. In the 2–3 min band, the velocity power in the umbral cores is amplified. For the 3–4 min and 4–6 min band, the concentration spreads out toward the outer umbra, inner penumbra, and center of the light bridges. In addition, the distribution of photospheric peak periods suggests that the effective acoustic cut-off layer of the solar atmosphere acting on the wave propagation has to start in the middle sunspot photosphere. The sunspot region in the lower photosphere (bottom right panel) is dominated by 5 min oscillations. In the upper photosphere (middle right panel), the umbrae exhibit 3 min oscillations. The penumbra shows first filamentary imprints.

6.5. Reconstruction of a sunspot's magnetic field

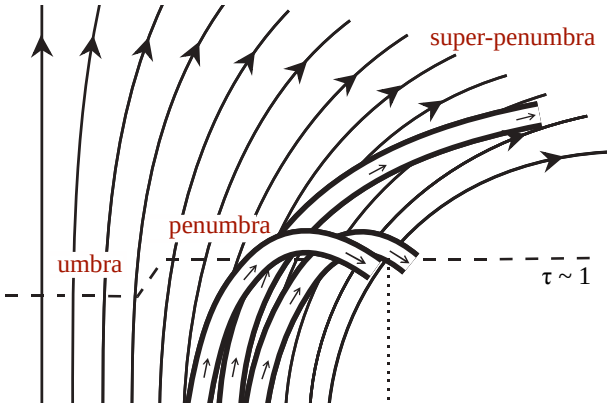

Figure 6.26.: Magnetic field topology in a sunspot. The solid lines sketch the magnetic field lines. The arrows in the magnetic tubes indicate the mass flux in the penumbra. The continuum optical depth unity is illustrated by the dashed line. The vertical dotted line represents the outer penumbral boundary in continuum intensity. Image adapted from Westendorp Plaza et al. (1997).

In the previous sections, it was demonstrated that the most prominent wave phenomena in sunspots are slow-mode magnetoacoustic waves which are guided upward along the magnetic field lines. The umbral and penumbral waves exhibit compressive fluid displacement parallel to the direction of the magnetic field. In Section 6.2, it was shown that the wave power spectra are influenced by the properties of the atmospheric layer and the position within the sunspot. In Sections 6.3 and 6.4, the characteristic wave properties of umbral flashes and running penumbral waves were studied. On the basis of Section 3.4, it was proven in Section 6.4.1 that the acoustic cut-off significantly affects the wave propagation in sunspots. Waves with periods longer than the local cut-off period are evanescent, reflected, or suffer from mode conversion. On the other hand, short-period waves below the acoustic eigenfrequency of the atmosphere can leak into higher atmospheric layers. As the density decreases exponentially, their wave amplitudes increase fast to maintain most of the wave energy. Those upward propagating waves with periods slightly shorter than the critical cut-off value then dominate the oscillatory power spectrum. As shown in Fig. 6.12, the peak periods obtained from intensity oscillations yield increasing periods when shifting from the inner umbra to the outer penumbra. As proposed by Bel and Leroy (1977) and confirmed by, e.g., De Pontieu et al. (2004), the inclination of the magnetic field lines against the zenith strongly impacts the acoustic cut-off period. From the vertical field of the umbra toward the more inclined sunspot penumbra the periods of the dominating oscillations evidently increase from 3 min up to 8 min at the outer sunspot boundary.

The impact of the physical properties of the local plasma on the acoustic cut-off has already been described in Section 3.4. As indicated by Eq. 3.33, the acoustic cut-off period $T_{\mathrm{cut},0}$ increases linearly with the local speed of sound c_{s}. In terms of frequencies, the acoustic cut-off frequency is of course inverse proportional to the sound speed (Eq. 3.32). Since the velocity of acoustic waves scales with the square root of the ambient temperature $\sqrt{\vartheta_{\mathrm{K}}}$ (Eq. 2.1), the same holds for the acoustic cut-off period. Even more important than the gas properties is the effect of the magnetic field inclination on the atmospheric eigenfrequency. According to Bel and Leroy (1977), the cut-off period increases with the magnetic field inclination Φ_{B}. Following Eq. 3.35, the effective cut-off period $T_{\mathrm{cut},\Phi_{\mathrm{B}}}$ in the sunspot's low-β regime becomes

$$T_{\mathrm{cut},\Phi_{\mathrm{B}}} = \frac{4\pi \cdot c_{\mathrm{S}}}{\gamma \cdot g \cdot \cos \Phi_{\mathrm{B}}}\,, \tag{6.4}$$

with the solar gravitational acceleration $g \approx 274\,\mathrm{m/s}$ and adiabatic index $\gamma = 5/3$ (monoatomic gas).

It is assumed that waves with periods slightly below the acoustic cut-off dominate the power spectrum. Observationally, the empirical formula

$$T_{\mathrm{cut},\Phi_\mathrm{B}} = 1.25 \cdot T_\mathrm{Peak} \tag{6.5}$$

describes the relation between the effective cut-off period $T_{\mathrm{cut},\Phi_\mathrm{B}}$ and the measured peak period T_Peak in the power spectrum (Tziotziou et al. 2006). For observations at chromospheric altitudes the proportionality serves as an indicator for the acoustic cut-off (Bogdan and Judge 2006).

The combination of Eqs. 6.4 and 6.5, and substitution of the sound speed (Eq. 2.1) yields the dependencies of the peak period

$$T_\mathrm{Peak} = \frac{T_{\mathrm{cut},\Phi_\mathrm{B}}}{1.25} = \frac{4\pi \cdot \sqrt{\frac{\gamma \cdot R \cdot \vartheta_\mathrm{K}}{M}}}{1.25 \cdot \gamma \cdot g \cdot \cos\Phi_\mathrm{B}} \tag{6.6}$$

on the atmospheric properties and magnetic field topology. Transposing and inverting Eq. (6.6) gives the zenith inclination

$$\Phi_\mathrm{B} = \cos^{-1}\left(\frac{4\pi \cdot \sqrt{\frac{\gamma \cdot R \cdot \vartheta_\mathrm{K}}{M}}}{1.25 \cdot \gamma \cdot g \cdot T_\mathrm{Peak}}\right) \tag{6.7}$$

of the magnetic field lines which guide the propagating sunspot waves. With this equation, the zenith angles are reconstructed from the peak periods T_Peak (in s) of the power spectra, and the atmospheric temperature ϑ_K in Kelvin. Further input parameters are the heat capacity ratio $\gamma = 5/3$ (for monoatomic gases), the specific gas constant R/M, and the solar gravitational acceleration $g_\mathrm{Sun} \approx 274\,\mathrm{m/s}$. In the following, Eq. 6.7 and the assumptions above are applied to reconstruct the magnetic field topology of the observed sunspot in active region NOAA11823.

New approach: In spectro-polarimetry, the determination of the magnetic field inclination requires sensitive measurements of the polarimetric full-Stokes signals. In general, the signal of linear polarization in spectral lines which form in the chromospheric layer is weak. In addition, as demonstrated in Section 6.3.2, the presence of umbral flashes leads to abnormal fluctuations in the polarimetric signal, e.g., in the line core of Ca II lines. Therefore, little contribution has been made to identify the sunspot's magnetic field topology in the chromosphere. A new kind of analytical technique is required to examine the magnetic field parameters of sunspot, pores and other magnetic features in the chromosphere and transition region. The elation established in this work (Eq. 6.7) opens up new possibilities for the determination of the geometric configuration of solar magnetic fields. Spectroscopic observations at high resolution provide the necessary wave periods as the main input parameter for the reconstruction of the magnetic field inclination. Of course, the inference is limited to the layer in which the acoustic cut-off of the solar atmosphere affects the wave propagation. The best results are obtained for the upper photosphere, chromosphere and parts of the transition region. To my best knowledge, such a three-dimension reconstruction of the magnetic field topology on the basis of sunspot oscillation in purely spectroscopic data has not been done before. The successful performance of this pioneering work will contribute to the overall understanding of sunspots.

In Section 6.5.1, I will describe the evaluation of the dominating wave periods in the power spectra. The peak period T_Peak is, by definition, the most sensitive parameter for the computation of the field inclination. The second crucial component for the variable acoustic cut-off is the ambient atmospheric temperature. In Section 6.5.2, umbral and quiet sun atmospheric models are applied and an estimate for the temperature of the sunspot atmosphere is given. In Section 6.5.3, I will describe the first attempt of inference using the standard formula (Eq. 6.7) for chromospheric layers. In Section 6.5.4, the obtained magnetic field inclinations are compared to the results from the magnetic field inversions in the lower sunspot photosphere. To provide a comprehensive study, the coronal magnetic field is extrapolated and matched with the chromospheric field topology. The evident vertical orientation of the magnetic field lines in the umbral core is employed to perform the final refined reconstruction. The results are presented in Section 6.5.5.

6.5.1. Evaluation of dominating wave periods

According to Eq. 6.6, the acoustic cut-off period is most sensitive to the zenith inclination of the magnetic field. Consequently, the same hold for the oscillations which dominate the power spectrum. In the following, the period at which the wave power reaches its maximum value is called the peak period. Vise versa, when the magnetic field inclination Φ_B shall be inferred from the spectroscopic observables (Eq. 6.7), the peak period T_Peak is the most important variable. Therefore, the possibility and performance of a magnetic field reconstruction by wave signatures requires a precise calculation of the wave power and peak periods at each position in the sunspot region.

As introduced in Section 5.2, a wavelet analysis was performed on the temporal signal of the spectral intensities and Doppler velocities. The global wavelet spectrum was calculated for each spectral position at each spatial position within the sunspot region. The determination of the maximum in the power spectra would already yield the peak period. However, as the temporal cadences of the observation of NOAA11823 differ (see Table 4.6) and the wavelet analysis features best results in a limited range of periods, a weighting of the power spectra is applied first.

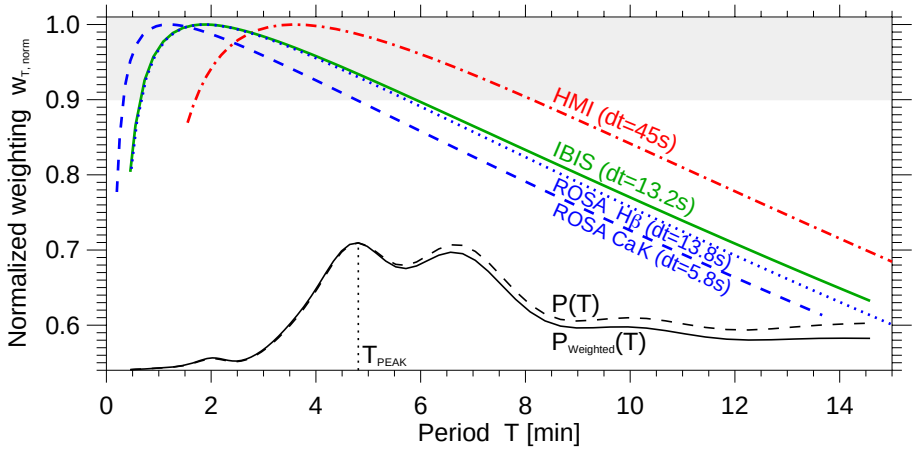

Figure 6.27.: Weighting functions $w_{\mathrm{T,\,norm}}$ applied to the power spectra in order to retrieve the peak period T_PEAK. The weighting is plotted against the period T (in min) for the input parameters of the IBIS (solid green), ROSA CaK (dashed blue), ROSA Hβ (dotted blue) and HMI (dashed-dotted red) observations. The induced change of an exemplary power spectrum P(T) (black dashed) towards its weighted power spectrum P_Weighted(T) is added (black solid). The power is given in arbitrary units to fit the scaling range.

Weighting functions: To achieve an undisturbed retrieval of the peak period in the power spectrum, a normalized weighting function $w_{\mathrm{T,\,norm}}$ was applied on the wave power P(T) at periods T. The weighting function is defined as

$$w_\mathrm{T} = \left(1 - \frac{T}{\Delta t_\mathrm{obs}}\right)^2 \cdot \left(1 - \frac{dt}{T}\right)^{1/2} \quad , \qquad w_{\mathrm{T,\,norm}} = \frac{w_\mathrm{T}}{\max(w_\mathrm{T})} \tag{6.8}$$

and depends on the total observation time Δt_obs (IBIS: 58 min) and the temporal cadence of observations dt (IBIS: 13.23 s, others see Table 4.6). For the computation of the weighting function w_T in Eq. 6.8, the first squared term reflects the decreasing significance level of the power analysis toward longer periods. It is based on the cone-of-influence of the wavelet analysis. Within the given observation time Δt_obs, only a few oscillations with long periods can contribute to the final power analysis. The consideration of this uncertainty is crucial for the quality of the peak period analysis. Therefore, the term is assessed quadratically. The second term for the weighting function w_T in Eq. 6.8 affects the weighting of the shorter periods. The shortest period which can be sampled in the observations is

defined by the Nyquist period, or two times the temporal cadence dt of the observational scan. For periods approaching this criterion, the sampling gets critical and noise gains influence on the power analysis. Since the noise level is well below the amplitude of the solar signal, the impact of this term on the power spectrum is reduced by taking the square root. Finally, the weighting function w_{T} is normalized to its maximum value (Eq. 6.8, right).

The normalized weighting curves $w_{\mathrm{T,\,norm}}$ on the basis of total observation times Δt_{obs} and cadences dt are shown in Fig. 6.27 as a function of period T. The green solid curve is obtained for the IBIS observations used for the magnetic field reconstruction. In addition, the weighting curves of ROSA (CaK in dashed blue, Hβ in dotted blue) and HMI (dashed-dotted red) power spectra are overplotted. In all cases the characteristic weighting in the 2–5 min band exceeds 90%. In case of the IBIS observations the maximum weight is given to 2 min oscillations. For the crucial range between 1 min and 5 min the weighting factor is still bigger than 93%. Toward longer periods than 9 min, the weighting function decreases to less than 80%. The same happens to oscillations close to the Nyquist period. Beyond, the shape of the weighting curves resembles that of an A-frequency weighting which is commonly used for instrumental sound level measurements.

In the lower part of Fig. 6.27, a power spectrum $P(\mathrm{T})$ is shown in black dashed line-style. It was obtained from the lower chromospheric penumbra. In this critical case, two main peaks at 4.8 min and 6.7 min dominate the spectrum with almost equal power. The determination of the peak period can become ambiguous. By applying the weighting function $w_{\mathrm{T,\,norm}}$, the weighted power spectrum, $P_{\mathrm{Weighted}} = P \cdot w_{\mathrm{T,\,norm}}$, yields a distinct and significant peak at $T_{\mathrm{PEAK}} = 4.8$ min. According to the almost linear decease of the weighting function toward longer periods, the power in this range is noticeably reduced. In summary, the applied method enhances the reliability of the results, considers noise and reduces uncertainties to achieve quantitative measurements of the peak period.

Peak periods T_{PEAK}: The peak periods of oscillations in Doppler velocity were shown in Fig. 6.11 for the Na I 589.59 nm line from IBIS observations (panel a) which covers the photosphere and lower chromosphere. As discussed in Section 6.2, it is evident that the umbral area in the lower chromosphere is dominated by waves in the 2.5–3.0 min range. At the umbral boundary, the peak periods increase rapidly to around 4 min. From the inner to the outer penumbra, the periods shift continuously toward longer values. At the outer penumbral boundary, the wave periods reach up to 8 min and have doubled within less than $10''$. The filamentary structure of the penumbra is also obvious in the dominating oscillatory period. In panels b) and c) of Fig. 6.11, the peak periods are shown for velocity oscillation in the lower sunspot photosphere. The umbra exhibits a mixture of dominating wave periods, 3 min and 5 min oscillation seem to govern the region. In the penumbra, the shifts in peak period are also present but less pronounced compared to the chromospheric case.

In Section 6.2, it was demonstrated that sunspot waves lead to oscillations in spectral intensity. Especially in the upper photosphere and lower chromosphere, the oscillatory signal is well above the observational noise level. On this basis, the global wavelet spectrum was calculated at each spectral position of the spectroscopically sampled solar absorption lines (see Fig. 4.13). As described above, the peak period of the weighted power spectrum was determined for each spatial position of the sunspot region. The most significant results are shown in Fig. 6.12. In the upper photosphere and lower to middle chromosphere (upper and middle row), the distribution of peak periods resembles the distribution obtained from lower chromospheric Doppler velocities. Again, the peak periods shift from around 3 min in the umbra to 8 min at the outer penumbral boundary. In the lower to middle photosphere (panels a, e, i–l), the vicinity of the sunspot is dominated by oscillations in the 5 min band. Due to the low spectral signal, the period distribution in the sunspot can be rather noisy. At the transition from the photosphere to the chromosphere (panel f), the intensity signal from p-modes outside the sunspot and magnetoacoustic waves within the sunspot is clear and the analysis yield significant results. In the lower to middle chromosphere (panels b–d, g–h), the distribution and shift in peak periods follows the chromospheric penumbra and superpenumbra.

Since the wavelength positions of the spectral lines have contributions from certain atmospheric formation layers (see Fig. 4.11), the obtained peak period maps can be ordered according to their estimated atmospheric altitude given in Table A.1. The altitudinal distribution of peak periods is shown on the right side of Fig. 6.28. On the left side, the spectral intensities are displayed as context information during the passage of an umbral flash. The positions along the z-axis are not to scale. The lower three panels of peak periods are correspond to estimated altitudes up to 300 km in the photosphere, the fourth lower panel is attributed to a temperature minimum height of around 600 km, and the upper panels show the chromospheric distribution at around 800–1000 km above the optical depth unity. A closer examination of the altitudinal peak period suggests that short-period oscillations fan out. Exemplarily, chromospheric 3 min oscillations exceed the contoured umbral boundary. The shifts in peak periods appear to happen more smoothly toward the outer penumbra.

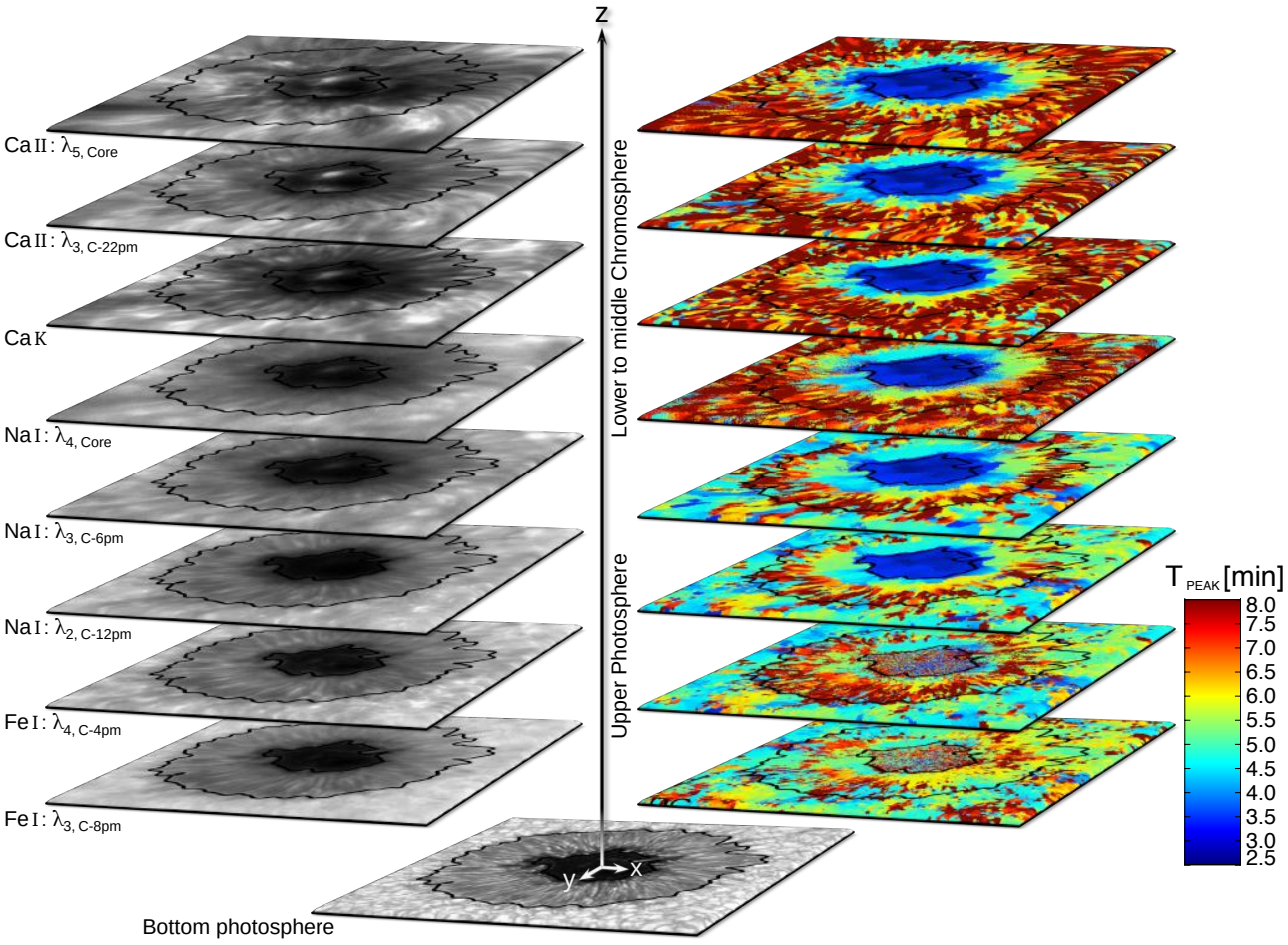

Figure 6.28.: Three-dimensional view of intensities (left) and peak periods T_{PEAK} of intensity wave power (right) of NOAA11823 at photospheric to chromospheric heights. The intensities (left) show an umbral flash event on August 21st 2013 at 15:00:06UTC. The panels along the z-axis belong to line core and wing positions of Fe I 630.15nm, Na I 589.6nm, Ca II 854.2nm, and the Ca K 393.4nm observation. The time-averaged distribution of peak periods T_{PEAK} of the intensity wave power is shown in the right panels for the same wavelengths. The periods are scaled from 2.5min (dark blue) to 8min (dark red). The umbral and penumbral boundary from continuum intensity (bottom panel) are contoured in black. Whereas the length of the axis arrows represent distances around 1.5Mm, the positions of the panels along the z-axis are not to scale.

6.5.2. Estimation of atmospheric gas temperatures

The next step of reconstructing the magnetic field inclination, according to Eq. 6.7, is the inference of the local sound speed c_S of the plasma. As given in Eq. (2.1), the sound speed itself increases with rising gas pressure and decreasing density. The sound speed scales with the ambient atmospheric temperature ϑ_K. Following Eq. 6.7, the result of the magnetic field inclination therefore depends on the local ambient temperature of the sunspot's atmosphere.

An accurate determination of the atmospheric temperature ϑ_K contributes to the best inference of the magnetic field inclination. The most elaborate way to obtain the physical parameters from the line profiles is the use of inversion codes like SIR (Ruiz Cobo and del Toro Iniesta 1992), NICOLE (Socas-Navarro 2015), or HAZEL (Asensio Ramos et al. 2008). These Stokes inversion codes use spectro-polarimetric profiles and model atmospheres as starting parameters to retrieve the atmospheric parameters from the observed signal. A robust inversion can yield very precise results. However, the calculations are very time-consuming for large data sets and often yield ambiguous outcome. Especially for purely spectroscopic observation with a critical sampling for the spectral lines, the results from the codes can contain large uncertainties. Therefore, I decided to take a very basic and fast approach to estimate the temperature in the sunspot atmosphere.

According to Eq. 6.7, the temperature is included with a square root. Therefore, a change in temperature causes a way less significant change of the obtained field inclination angle than a shift of the dominating wave period would cause. To give an example, a relative change from a typical temperature of 6500 K in the quiet sun to 4300 K in the dark umbral core would result in a factor of $\sqrt{4300\,K/6500\,K} = 0.81$ within the bracket of Eq. 6.7. In comparison, a rather small shift of the peak period from 3 min to 3.7 min would cause the same variation for the inclination angle of the magnetic field. A precise determination of the peak period has to have priority over the inference of the temperature. But still, a good estimate of the ambient temperature for each atmospheric layer and position within the sunspot region is important.

A simple estimate of the atmospheric temperature ϑ_K in continuum intensity can be performed with the Stefan–Boltzmann law

$$j = \sigma \cdot {\vartheta_K}^4 \,, \tag{6.9}$$

which describes the radiative power j of a black body in terms of its thermodynamic temperature. σ describes the Stefan–Boltzmann constant. In Fig. 5.4 a), the sunspot of active region NOAA11823 is shown in normalized values of continuum intensity. At the solar surface, the average quiet sun or vicinity of a sunspot has a typical temperature of around 6500 K. Using Eq. 6.9, a relative intensity of 0.19 in the umbra (at around 600 nm) normalized to the quiet sun intensity would corresponds to a temperature of $\vartheta_K = 4300$ K. In literature, this umbral temperature is often given as an appropriate value. A fast estimation of the temperature in the brighter penumbra with a relative intensity of 0.73 gives a temperature of around 6000 K. The values obtained by this law can be seen as a good first estimate. However, the wavelength dependence of the solar radiance can not be neglected.

According to Planck's law, the spectral radiation of a black body depends on the absolute temperature ϑ_K. Expressed in terms of wavelengths λ, the Planck's law for spectral radiance $S_\lambda(\lambda, \vartheta_K)$ can be written as

$$S_\lambda(\lambda, \vartheta_K) = \frac{2hc^2}{\lambda^5} \frac{1}{e^{hc/(\lambda k_B \vartheta_K)} - 1} \,, \tag{6.10}$$

with the Boltzmann constant k_B, the Planck constant h, and the speed of light c in the medium. In the limit of short wavelength ($e^{hc/(\lambda k_B \vartheta_K)} \gg 1$), this law for thermal emission can be simplified by the Wien approximation:

$$S_\lambda(\lambda, \vartheta_K) = \frac{2hc^2}{\lambda^5} \cdot e^{-\frac{hc}{\lambda k_B \vartheta_K}} \,. \tag{6.11}$$

As detectors cannot count single photons, the values of intensity observations I_λ have to be multiplied by a factor m to fulfill the radiance equations. Then, to retrieve the absolute temperature ϑ_K, the

equation

$$\vartheta_{\mathrm{K}} = \frac{hc}{\lambda k_{\mathrm{B}}} \cdot \frac{1}{\ln\left(\frac{2hc^2}{\lambda^5 m I_\lambda}\right)} \tag{6.12}$$

has to be solved. The factor m has to be calculated for a known temperature by $m = {}^{S_\lambda(\lambda,\vartheta_{\mathrm{K}})}/_{I_\lambda}$, e.g., in the quiet sun. If the reference is not at disk center, then the limb darkening effect, $\frac{I_\lambda(\cos\theta)}{I_\lambda(\cos 0°)} \approx \frac{2+3\cdot\cos\theta}{5}$, has to be applied for the given heliocentric angle θ of the sunspot. For the sunspot of active region NOAA11823, the heliocentric angle $\theta \sim 14°$ gives a relative darkening of 0.98.

A temperature estimate for the sunspot atmosphere is calculated in the following way:

1. A reference position within the sunspot region is defined.
2. According to the spatial position, an atmospheric temperature model is chosen.
3. The formation height is estimated for the observed wavelength position within the spectral line.
4. The model temperature is extracted for the estimated formation height.
5. According to Planck's law and the Wien approximation, a two-dimensional temperature map is calculated from Eq. 6.12 for the observational wavelength and spectral intensities.

The approach was performed on the temporal average for each spectral positions of the IBIS and ROSA observations in sunspot NOAA11823 (see Table 4.6 and Fig. 4.13). The inference of the atmospheric temperatures was performed for two reference positions, 1) in the average sunspot vicinity and 2) in the average umbral core. For the first reference case, the atmospheric parameters of the quiet sun model of Maltby et al. (1986) are applied. As shown in Fig. 2.5 a) by the blue curve at $\lambda = 500$ nm, the temperature falls with increasing photospheric height from 6500 K at the designated surface layer to a temperature minimum of 4400 K at around 500 km above the optical depth unity of the quiet sun. In the chromosphere the temperature increases again to around 6000–7000 K in the middle chromosphere. For the umbral core as reference, the umbral core model M of Maltby et al. (1986) at the middle of the sunspot cycle is applied. The red curve in Fig. 2.5 a) exhibits the evolution of the average temperature in the umbral atmosphere. Due to the suppression of plasma convection, the temperature at the continuum optical depth unity is only 4300 K. The temperature minimum of 3400 K is reached between 280 km and 530 km. This temperature layer is interpreted as the region where the acoustic cut-off affects the umbral wave propagation (Jess et al. 2013). Toward the umbral chromosphere, the atmospheric temperature features a stronger increase than in the quiet sun. The temperatures of 6500–7000 K in the middle chromosphere already exceed the quiet sun temperature. In Fig. 2.5 c), it is presented how these strong atmospheric variations affect the local sound speed which enters the inference of the magnetic field inclination.

The average line formation heights of the spectral lines can be calculated by response function of the solar atmosphere to physical perturbations. Especially in the chromosphere, the formation height and atmospheric opacity will vary strongly caused by the presence of magnetoacoustic sunspot waves. For the estimation of the average temperature, the atmospheric contribution functions of the spectral lines are used to define a value for the formation height of the observed spectral position. The contribution functions of Na I 589.59 nm and Ca II 854.21 nm are plotted in Fig. 4.11. The filtered wavelength positions are indicated as vertical dotted lines. In accordance to the wave travel times, the estimated formation altitudes are listed in Table A.1. More information on the spectral lines and line formation is given in Section 4.2.1 and Table 4.3. In the lower sunspot photosphere, the Wilson effect (see Section 2.3) was taken into account. It reduces the opacity of the sunspot's opacity which can be interpreted as an atmospheric depression by several hundred km (e.g., Solanki et al. 1993; Mathew et al. 2004). Therefore, the geometrical temperature profile of the umbra has to be shifted downwards by several hundred km relative to the quiet sun profile. In the chromosphere and upper photosphere, the depression is neglected. Under these assumptions, the atmospheric temperatures are calculated with Eq. 6.12 as an average three-dimensional temperature distribution.

6.5.3. First inference of the magnetic field inclination

The magnetic field inclination Φ_B is calculated with Eq. 6.7. The inference is based on the peak periods and estimated temperatures which were determined in Section 6.5.1 and 6.5.2. A fast approximation of the magnetic field inclination can be given by $\Phi_B = \cos^{-1}\left(2.41\,\mathrm{s\,K^{-1/2}} \cdot \frac{\sqrt{\vartheta_K}}{T_{Peak}}\right)$.

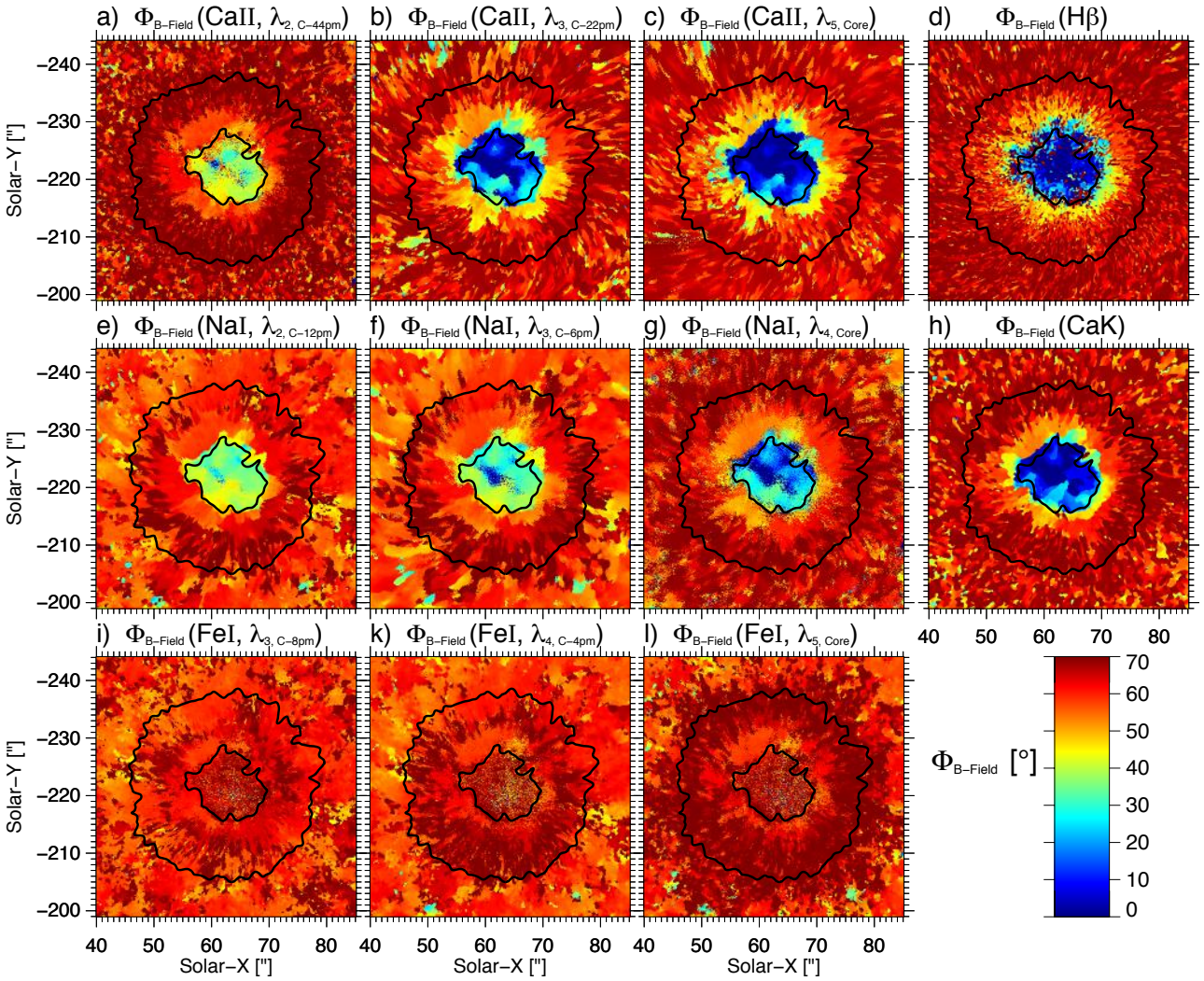

Figure 6.29.: Zenith inclination angles Φ_B (in deg) of the sunspot's magnetic field at various photospheric to chromospheric wavelength positions. The inclination maps (also shown in Fig. 6.33) were reconstructed on the basis of the peak period maps displayed in Fig. 6.12. The degree scale ranges from 0° (dark blue) to 70° (dark red). The umbral and penumbral boundary from continuum intensity is contoured in black. a–c): Ca II 854.212 nm at wavelength positions $\lambda_{2,C-44pm}$, $\lambda_{3,C-22pm}$, and $\lambda_{5,Core}$; e–g): Na I 589.590 nm at $\lambda_{2,C-12pm}$, $\lambda_{3,C-6pm}$, and $\lambda_{4,Core}$; i–l): Fe I 630.147 nm at $\lambda_{3,C-8pm}$, $\lambda_{4,C-4pm}$ and $\lambda_{5,Core}$. Panels d) and h) show the distribution for the H_β line core at 486.1 nm and the Ca K line core at 393.4 nm.

As described in Section 6.5.2, the temperature distribution in the sunspot atmosphere was calculated on the basis of two models, an umbral model of the middle sunspot cycle and a quiet sun model. For both models, the zenith inclinations are inferred separately. The comparison of both model calculations are in very good agreement. The results for the middle to upper photospheric zenith inclinations differ in average by less than 3°. Therefore, a connection of both models seem to be appropriate. Fig. 6.29

shows the average distribution of magnetic field inclinations Φ_B in the sunspot atmosphere. In the following, I will describe the obtained distribution starting from the uppermost layer and moving down to the lowermost layer. The estimated atmospheric altitudes are given in Table A.1.

In the chromosphere, the reconstruction of the magnetic field inclination yields the best and most reliable results. At estimated average altitudes of around 800–1000 km, the intensity signatures of sunspot waves in the spectral line cores of Ca II 854.21 nm (panels b and c), Hβ (panel d), Na I 589.59 nm (panel g), and Ca II K (panel h) are very clear. As demonstrated in Section 6.5.1, the horizontal shift of the peak periods toward longer periods is significant in the sunspot chromosphere. Therefore, Eq. 6.7 produces a well-suited distribution of zenith angles. The umbral area exhibits angles of $0 - 30°$ (vertical field, in dark blue). These small inclinations can extend beyond the umbra. Toward the outer penumbra, the zenith inclination of the magnetic field increases up to $60 - 70°$. The penumbra and superpenumbra exhibits a filamentary structure which resembles the appearance in chromospheric intensity. The diversity of field inclinations along the azimuth provides further evidence for the 'uncombed' structure of the penumbral field lines (see Section 2.2).

At upper photospheric to lower chromospheric heights, the results of the magnetic field reconstruction by Eq. 6.7 are still acceptable but less significant than in the middle chromosphere (see Fig. 6.29). At atmospheric altitudes of around 250–600 km, the intensity signal of sunspot waves in the spectral line wings of Ca II 854.21 nm (panel a) and Na I 589.59 nm (panels e and f) are conspicuous. As discussed in Section 6.5.1, the increase in peak period toward the outer penumbra is significant. However, the obtained field inclinations in the umbra and inner penumbra are too large. Especially in the umbra core, there is no reason why the zenith angles should be larger than in the co-spatial chromospheric region. Therefore, I establish the assumption that the magnetic field orientation in the umbral core is vertical and introduce a correction factor to Eq. 6.7 to refine the reconstruction in the photosphere.

For the lower photosphere, the magnetic field reconstruction yields insufficient results (see Fig. 6.29). Yet, the radial increase of the penumbra field inclination is apparent. On the other hand, the vertical orientation of the umbral magnetic field is absent. The disputable quality of the inference has simple reasons. First of all, the signal of sunspot waves in spectral intensities is very weak and causes noise for the wavelet analysis. Secondly, the Fe I 630.15 nm is sensitive to the strong magnetic field of the umbra what leads to further uncertainties at the sampled wavelength positions. The final and most important reason comes from the Sun itself. The lower photosphere features a broad mixture of wave periods. To retrieve a vertical magnetic field inclination, peak periods of around 3 min would be required for Eq. 6.7. However, the short-period waves are not dominating yet since the acoustic cut-off has no noticeable effect at atmospheric heights of less than 250 km above the optical depth unity. Consequently, the suggested inference of magnetic field inclination can only be applied to the upper photosphere, chromosphere, and possibly the transition region.

6.5.4. Photospheric inversion and coronal extrapolation of the magnetic field

In Section 6.5.3, a vertical magnetic field orientation was suggested for the umbral core of sunspot NOAA11823. This assumption shall be introduced to Eq. 6.7 by a correction factor. In this section, the vertical topology of the chromospheric and upper photospheric umbra is verified by the analysis of the vector magnetic field inversion of the lower photosphere and the magnetic field extrapolation into the corona. In addition, the determination of the photospheric and coronal field topology enables the qualitative evaluation of the final field reconstruction in Section 6.5.5.

Vector magnetic field inversions: The inversion of the full magnetic field vector was described in Section 5.3. The Very Fast Inversion of the Stokes Vector (VFISV) was applied to the HMI observation of polarization signals in the spectral Fe I 617.33 nm line. As described in Section 4.2.1 and Table 4.3, the magnetically sensitive iron line describes the lower photosphere. Its line core is formed in the middle photosphere at an altitude of around 280 km above the continuum optical depth unity. The

temporal averages of the magnetic field parameters (field strength, zenith inclination and azimuth) are shown in Fig. 5.4. The inversion errors $\delta\Phi_{\mathrm{B,\,LOS}}$ for the zenith inclination are below 1° (Fig. 5.5 b).

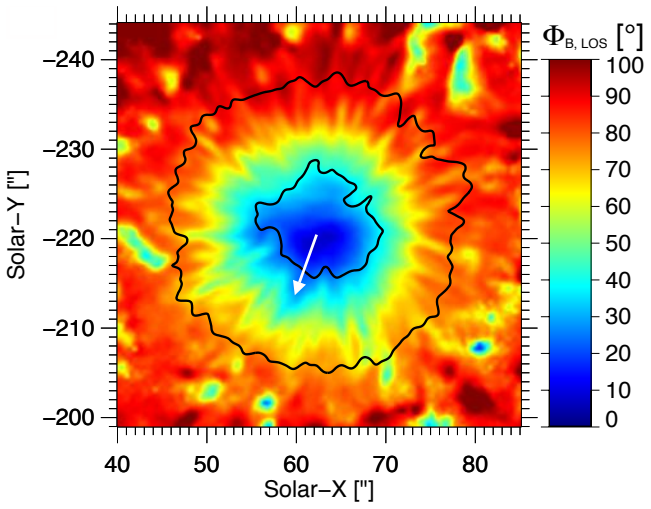

Figure 6.30.: Magnetic field inclination in the sunspot photosphere. The inclination angles $\Phi_{\mathrm{B,LOS}}$ (in degrees) against the line-of-sight were obtained with HMI field inversions. The values are scaled from $\Phi_{\mathrm{B,LOS}} = 0°$ (dark blue) to 100° (dark red). The black contours mark the penumbral boundaries in continuum intensity. The white arrow is pointing toward disk center.

The obtained zenith inclination $\Phi_{\mathrm{B,\,LOS}}$ of the magnetic field is displayed again in Fig. 6.30. It has to be noticed that the inferred field inclination is relative to the line-of-sight. Therefore, the obtained distribution of zenith angles appears to be shifted against the contoured sunspot boundaries from continuum intensity. The heliocentric angle of the sunspot position is $\theta = 14°$. As illustrated by the white arrow, the disk center is located toward the lower left which explains the direction of the spatial shift. The azimuthal average of the photospheric zenith inclination is plotted in Fig. 6.34 (panel a, red curve) as a function of radial distance from the umbra barycenter. Taking the line-of-sight into account, the zenith inclination in the umbral core amounts to below 10°. This proves the vertical orientation of the umbral magnetic field lines. Toward the umbral boundary, the angles increase smoothly to around 30°. The smooth rise of the field inclination continues within the penumbra. At the outer penumbra, the inclination has increased to an almost horizontal orientation of $70 - 80°$. The filamentary distribution of inclination angles verifies the 'uncombed' structure of the penumbral field lines.

Magnetic field extrapolation: To present an inherently consistent evaluation of the chromospheric magnetic field, an extrapolation of the sunspot's magnetic field was performed. As described in Section 5.4.3, the magnetic field lines in the corona were extrapolated with a Potential-Field Source-Surface (PFSS; Schrijver and De Rosa 2003) model. The photospheric magnetic field from the global HMI observations serves as the basis. The data were acquired from the LMSAL webpage. A full-disk magnetic field extrapolation is shown in Fig. 5.9.

In Fig. 6.31, a sample of extrapolated magnetic field lines in active region NOAA11823 is displayed. The coronal field of the sunspot is shown for three different dates within six days. As the sunspot evolution is in a very stable cycle, the magnetic field of the sunspot is assumed as constant at the large scale during this time. The first date (panels of row a) exhibits the sunspot close to the eastern limb (7° S, 44° E). The second date (panels of row a) presents the sunspot closer to disk center (7° S, 16° E). At the third date, the location of the sunspot is on the western side (7° S, 34° W). For all three case,

the active region is shown in continuum intensity (panels of left column), line-of-sight magnetic field strength (middle column), and spectral intensity of the corona (right column). The coronal intensity was recorded by the 17.1 nm channel of AIA (see Table 4.4).

In all three cases in Fig. 6.31, the topology of the magnetic field lines is almost symmetrically distributed. The field fans out and declines toward the solar surface at a distance of several tens to hundred arc-seconds. As illustrated by the disk-center-to-limb line (blue dashed) and the projection effects for larger heliocentric angles, the magnetic field of the sunspot umbra is vertical with respect to the solar surface. Co-spatially to the outer penumbral boundary, the magnetic field in the lower corona yields an inclination of up to 40°.

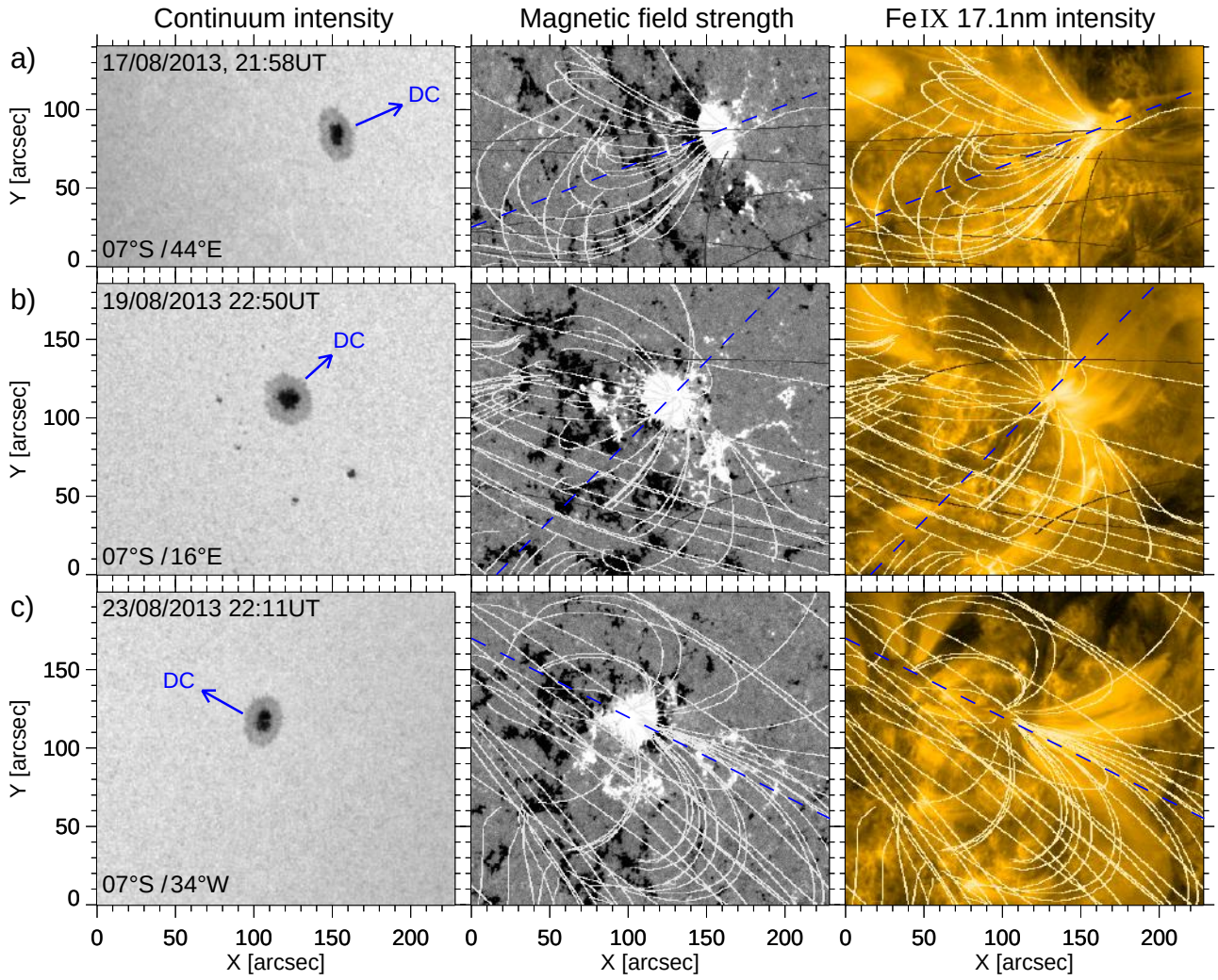

Figure 6.31.: Potential-Field Source-Surface (PFSS) extrapolation of the magnetic field lines for the active region NOAA 11823. The results are given for three dates (row a–c) with strongly differing positions on the solar disk. The sunspot and its vicinity are shown in continuum intensity (left-hand panels) and magnetic field strength in the line-of-sight (middle column panels) as observed with HMI. Strong magnetic fields are displayed in black and white. The right-hand panels show the coronal intensity using the spectral Fe IX line at 171 Å of the AIA instrument. The extrapolated field is drawn as bright solid lines. Drawn in blue color, the arrows are pointing toward disk center with the length corresponding the distance, the dashed connecting line of disk center and limb gives the context for the field orientation.

6.5.5. Final results for the chromospheric magnetic field topology

In Section 6.5.3, the initial inference of the magnetic field inclination was performed. According to Eq. 6.7, the zenith inclination Φ_B was calculated from the obtained peak periods of the power spectra and the modeled temperatures in the sunspot atmosphere (Sections 6.5.1 and 6.5.2). The results were shown in Fig. 6.29. In the chromosphere, the reconstruction of the magnetic field topology yielded the best results. In the upper photosphere, the umbral field orientation differs from the vertical. Therefore, I suggested the assumption of a vertical field in the umbral core. In Section 6.5.4, evidence for the assumption was provided by photospheric magnetic field inversion and coronal field extrapolations. To fulfill the criterion of a vertical magnetic field in the umbral core, a correction factor has to be introduced to Eq. 6.7. According to Eq. 6.5, a constant factor of 1.25 was suggested to connect the acoustic cut-off and peak period in the power spectrum. To obtain a vertical umbral field, the applied factor has to decrease from 1.25 in the middle chromosphere to 1.05 in the middle photosphere.

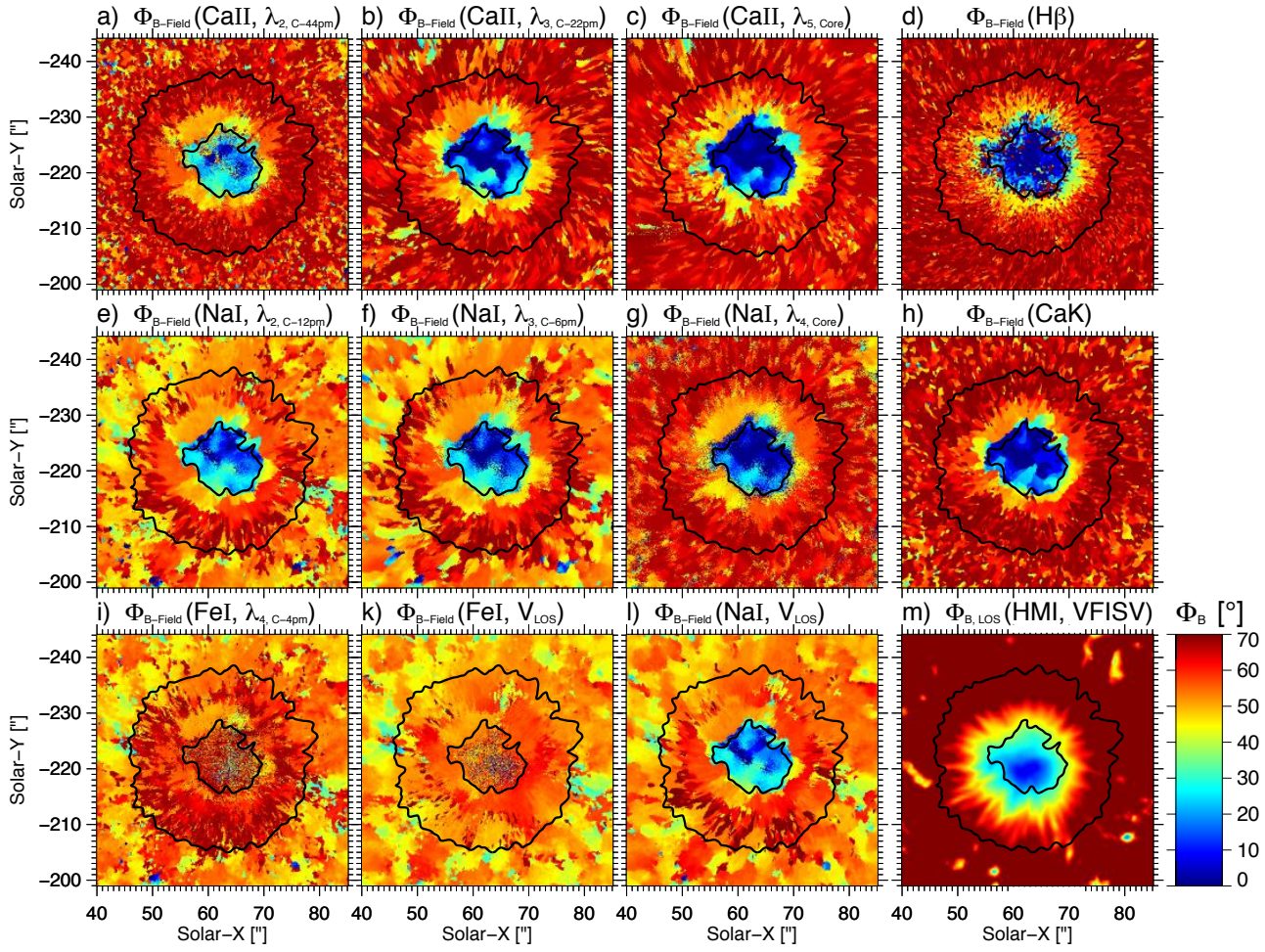

Figure 6.32.: Magnetic field inclination angles Φ_B of NOAA11823 at various photospheric to chromospheric wavelength positions. Compared to Fig. 6.29 the results were obtained with an adapted factor in Eq. 6.5. The range for the angles is scaled from 0° (dark blue) to 70° (dark red). The inclination angles based on intensity variations are shown for a–c) Ca II 854.2nm at wavelength positions $\lambda_{2,C-44pm}$, $\lambda_{3,C-22pm}$ and $\lambda_{5,Core}$ = 854.212nm, d) H_β at 486.1nm, e–g) Na I 589.6nm at $\lambda_{2,C-12pm}$, $\lambda_{3,C-6pm}$ and $\lambda_{4,Core}$ = 589.590nm, h) Ca K at 393.4nm, i) Fe I 630.15nm at $\lambda_{4,C-4pm}$. The results based on Doppler velocities oscillations are shown for k) Fe I 630.15nm and l) Na I 589.6nm. m) The lower photospheric zenith inclination in the line-of-sight was obtained from HMI magnetic field inversions.

Like in Section 6.5.3, the zenith inclination of the magnetic field Φ_B is calculated separately on the basis of two temperature models, one of them for a strong umbra in the middle of a sunspot cycle and the other for a quiet sun atmosphere. The inclination angles resulting from the umbral model are shown in Fig. A.11. The results obtained with the quiet sun model are displayed in Fig. A.12. Again, the calculated angles from both model are in very good agreement with each other and differ in average by less than 3°. The averaged distribution of zenith inclinations Φ_B in the sunspot atmosphere is shown in Fig. 6.32. Comparing the final results with the initial inference (Fig. 6.29), the corrected distribution of field inclinations in the upper photosphere (panels a, e, f, and l) ultimately yields consistent results. A first comparison of the reconstructed magnetic field inclination in the upper photosphere with the inverted field inclinations of the lower photosphere (see Section 6.5.4) gives a good agreement of the spatial distribution. The obtained magnetic field inclination in the upper photosphere and lower to middle chromosphere (panels b–d, g–h) are intrinsically consistent. When the zenith inclination maps are ordered according to their estimated atmospheric formation height (see Table A.1), the altitudinal evolution of the magnetic field inclination can be identified. The magnetic field fans out.

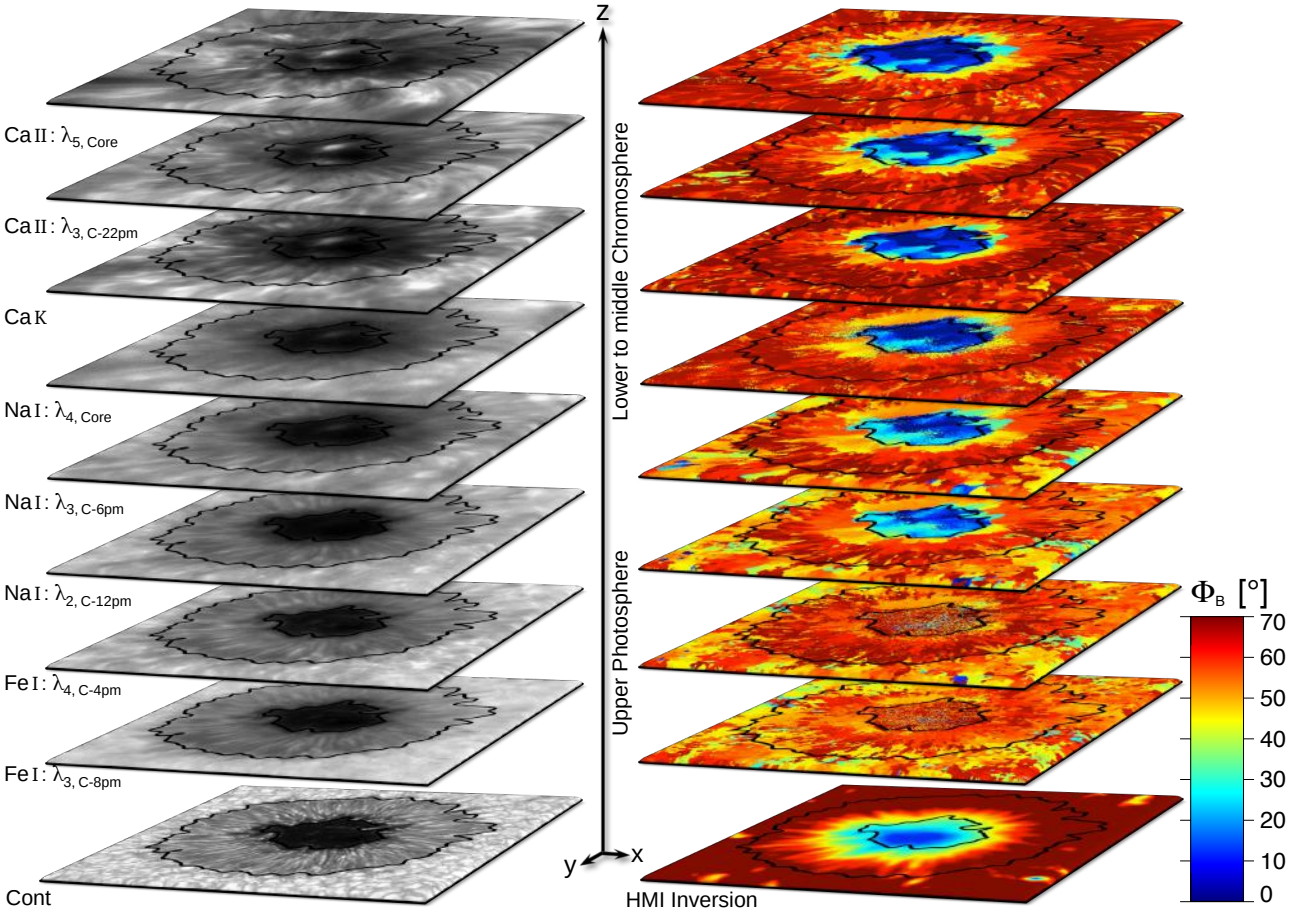

Figure 6.33.: Three-dimensional view of intensities (left) and reconstructed magnetic field inclination angles Φ_B (right) of the sunspot at photospheric to chromospheric heights (positions from Fig. 6.32). The zenith inclination angles (in deg) are scaled from 0° (dark blue) to 70° (dark red). The black contours indicate the location of the umbral and penumbral boundaries in continuum intensity in the bottom left. The inferred line-of-sight inclination obtained from the lower photospheric HMI inversion is added to the bottom right. The inclinations can be compared to the peak periods of Fig. 6.28.

As shown in Fig. 6.33, with increasing height in the solar atmosphere, smaller zenith inclination extend to larger radial distances. Especially, the almost vertical magnetic field lines which are charac-

terized by small zenith inclinations $\Phi_B < 15°$ (dark blue) fan out quickly within the relatively short altitudinal distance of around 700 km in the lower solar atmosphere. The overall distribution of zenith inclinations in the sunspot atmosphere hints at a magnetic field topology as illustrated in Fig. 6.26.

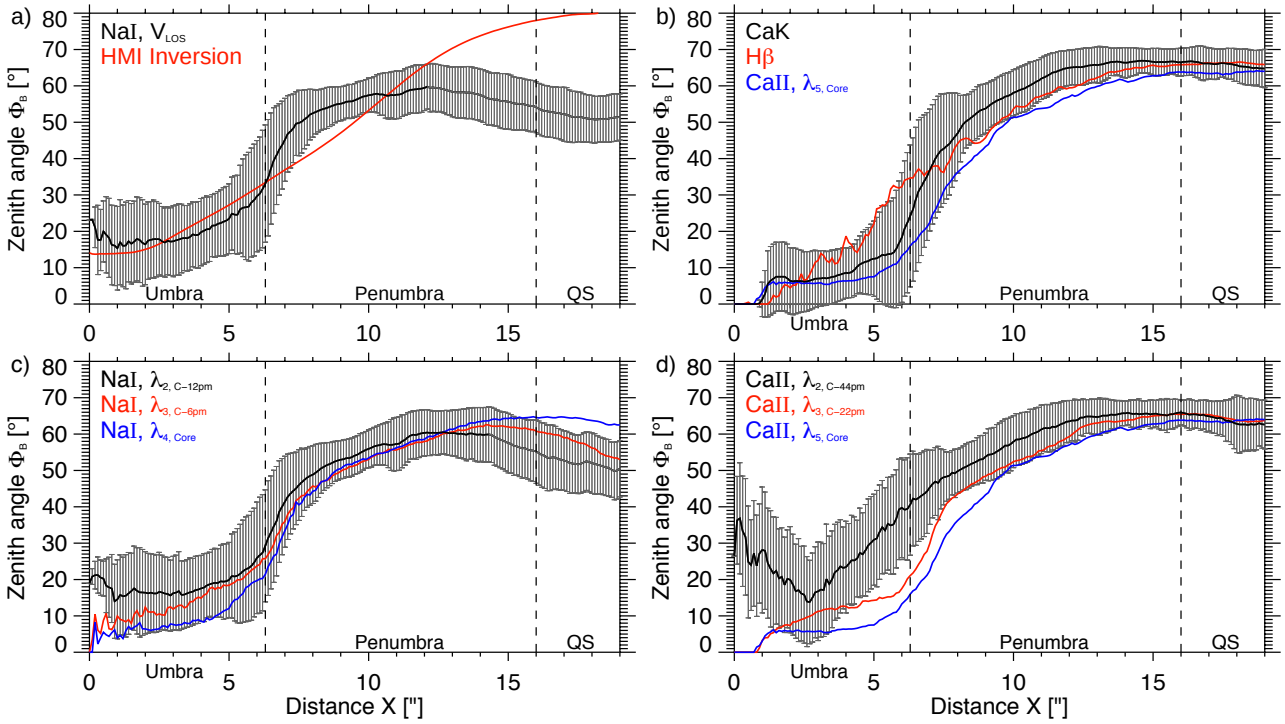

Figure 6.34.: Azimuthally averaged zenith inclinations from different spectral line positions. The zenith inclinations Φ_B are plotted as a function of radial distance X from the umbral barycenter. Panel a): Comparison of the results from the lower photospheric spectro-polarimetric HMI inversion (red curve) and the lower chromospheric reconstruction from Na I 589.59 nm Doppler velocities. Panel b): Results from the chromospheric line cores of Ca II K (black curve), Hβ (red curve), and Ca II 854.21 nm. Panels c and d): Altitudinal evolution from the middle photosphere (black curve) to the lower chromosphere (red and blue curves) as obtained from the line wing, core, and minimum of Na I 589.59 nm and Ca II 854.21 nm. Error bars illustrate the standard deviations along the azimuth. They are shown only for the black curves. The dashed vertical lines mark the average umbral and penumbral boundaries. The two-dimensional distributions of zenith inclinations were shown in Fig. 6.32. The spectral positions are described therein.

For a qualitative analysis of the reconstructed field topology, the two-dimensional maps of zenith inclination can be azimuthally averaged on the basis of a circular sunspot. In Fig. 6.34, the azimuthal average of the magnetic field inclination is plotted as a function of radial distance from the umbral barycenter. In panel a), the reconstructed zenith inclinations Φ_B of the upper photosphere to lower chromosphere (black curve) are compared to the inferred lower photospheric angles (red curve). The former were obtained from the average Na I 589.59 nm line, the latter from the Fe I 617.33 nm line (see Section 4.2.1). The standard deviation along the azimuth is plotted for the Na I line. The errors do not exceed 10°. The increase of the photospheric field inclination from the almost vertical umbra to an zenith inclination of 30° at the inner penumbra and 80° at the outer penumbra is in line with other studies (e.g., Westendorp Plaza et al. 2001). Comparing the photospheric and chromospheric case, the radial distributions exhibit that the field inclination of the inner umbra is the same. Toward the umbral boundary, the photospheric field inclination increases more rapidly. Then at the umbra

boundary, the reconstructed chromospheric inclination jumps to larger inclination and increases more smoothly with increasing radial distance.

Fig. 6.34 b) displays the chromospheric field inclinations which were reconstructed from intensity oscillations in the line cores of Ca II K (black curve), Hβ (red curve), and Ca II 854.21 nm (blue curve). The curves resemble each other within one standard deviation. In the inner umbra, the zenith inclination is below 15°. Toward the outer penumbra, the inclinations increase up to 65°. The gradient of the Hβ curve is similar to the lower photospheric case from HMI inversion. This could be explained by the greater impact of the photospheric layer on the spectral intensities of Hβ (see Section 4.2.1). The curves of Ca II K and the line core intensity Ca II 854.21 nm are very similar in the umbra. In the penumbra, the zenith inclination of Ca II K are larger by up to 10°. Normally, the line cores of both spectral lines are formed at an equal height of around 1000 km in the solar chromosphere. Therefore, the difference in zenith inclination has to be the result of the broad waveband in Ca II K which has been filtered in the ROSA observations (see Table 4.6). Consequently, the narrowly filtered line minimum position of Ca II 854.21 nm describes a greater atmospheric height.

The scenario in which the magnetic field inclination decreases with atmospheric height is confirmed in the following. As shown in the lower panels of Fig. 6.34, three different spectral positions within the Na I 589.59 nm line and Ca II 854.21 nm line were analyzed. In panel c), the three characteristic line wing and core positions belong to the middle photosphere at around 250–300 km (black curve), the temperature minimum height at around 600 km (red curve), and the chromosphere at around 1000 km (blue curve) above the optical depth unity at $\tau_{590,850}$. A co-spatial comparison of the curves yield that the field inclination at higher atmospheric layers is smaller at all umbral and inner penumbral position. In the panel d), the scenario is confirmed by the analysis of the Ca II 854.21 nm line. The black curve is obtained for the line wing position formed at an average atmospheric height of around 200–250 km. It exhibits by far larger field inclination angles than the curves corresponding to chromospheric heights of around 900–1000 km above the optical depth unity.

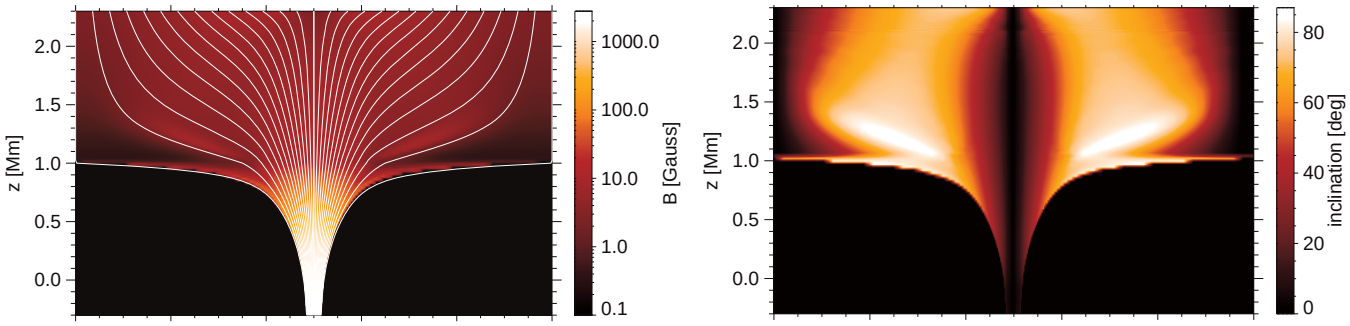

Figure 6.35.: Topology of a magnetic field concentration in the lower solar atmosphere. In the left panel, the magnetic field strength is shown on scale from 0.1 G to 2500 G. The field lines are plotted as white solid lines. In the right panel, the inclination angles are displayed for photospheric to chromospheric altitudes. The horizontal axis covers a size of 10 Mm. Image adapted from Uitenbroek (2011).

Several major conclusions can be drawn from the results. The zenith inclination of the sunspot's magnetic field lines can be reliably reconstructed from the oscillatory signals of sunspot waves in the chromosphere and middle to upper photosphere. In summary, the performed inference of the magnetic field topology by means of a purely spectroscopic investigation yields convincing results. The increasing magnetic field inclination from the umbra to the outer penumbra was confirmed for all atmospheric heights. From the evident fluctuation of the zenith inclination along penumbral azimuth at the arcsecond scale, the 'uncombed' structure of the penumbra magnetic field is supported (Schmidt et al. 1992; Title et al. 1993). Moreover, it was proven that the magnetic field fans out with increasing atmospheric altitude. In comparison to the lower photosphere, the zenith inclination of the magnetic

field in the outer chromospheric penumbra is $10 - 20°$ smaller than in the photosphere. This finding is in line with literature (e.g., Keppens and Martinez Pillet 1996), in which a more homogeneous and less inclined magnetic field topology is obtained for the upper photosphere compared to the lower photosphere. The trend is in accordance with the observed and extrapolated magnetic field inclinations of around 40° in the corona above the outer penumbra (Alissandrakis and Kundu 1984; Reznikova and Shibasaki 2012). According to the results, the general magnetic field topology in a sunspot is very similar to the structure in smaller field concentrations as illustrated in Fig. 6.35. The displayed structure just have to be extended by a multiple and depressed by several hundreds of kilometer.

A comparison of the azimuthally averaged sunspot parameters is presented in Fig. 6.36. The distribution in continuum intensity and magnetic field strength is shown in panels a and b. The characteristic evolution of the zenith inclination and dominant wave period is highlighted in panels c and d.

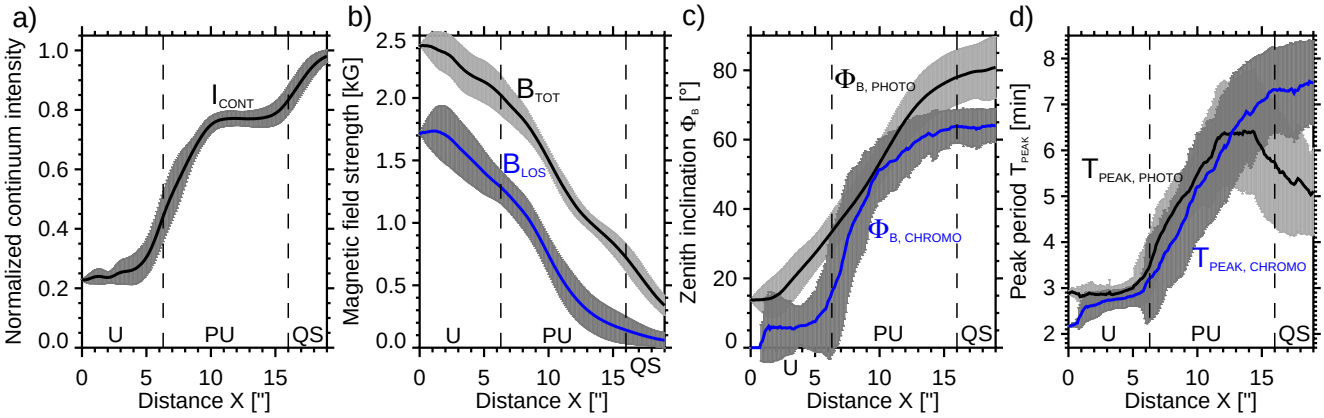

Figure 6.36.: Azimuthally averaged parameters of the sunspot of active region NOAA11823 as a function of radial distance from the sunspot barycenter. The distribution is plotted for a) normalized continuum intensities, b) total (B_{TOT}) and line-of-sight (B_{LOS}) magnetic field strength, c) zenith inclination of the magnetic field in the lower photosphere and middle chromosphere, d) peak periods of oscillations in the middle photosphere and middle chromosphere. The average sunspot boundaries are marked by the vertical dashed lines.

As any method of inferring the chromospheric field inclination, the oscillation-based reconstruction of the magnetic field also bears its deficiencies. One of them is the apparent jump in peak period and atmospheric temperature at the umbral-penumbral boundary. This steep gradient is also reflected in the reconstructed zenith inclination of the magnetic field. However, this steep increase to larger inclination is in contrast to the more homogeneous field topology suggested for the chromosphere. The mentioned jump in peak period from the umbra to the penumbra has also been reported by other observational studies (Tziotziou et al. 2007; Yuan et al. 2014b). Several factors can lead to such an steep transition in period and zenith inclination. Possible causes are:

- a real and very rapid increase of the magnetic field inclination at the umbral boundary,
- the averaging of strongly differing zenith inclinations at the umbral boundary,
- the method of inferring the peak period which is based on the selection of the dominating mode at the maximum power whereas the power spectrum can feature several distinct peak,
- the observed merging of pairs of consecutive umbral waves to one running penumbral wave,
- a possible wave conversions at the umbral boundary,
- the underestimation of the Wilson depression and changing line formation height in the sunspot,
- a changing line formation height for different wave periods (Mein and Mein 1980).

If the deficit is attributed to the fine-scale structure of the sunspot's magnetic field, future studies will overcome this attribute and refine the reconstruction of the zenith inclination. A dense sampling of oscillating spectral lines and the application of advanced inversion codes will provide more precise atmospheric parameters. In addition, an exact determination of the spectral formation height, dynamic opacity, and inclusion of the Wilson effect can yield a very significant reconstruction of the sunspot's magnetic field topology.

7. Conclusions – Picturing sunspot waves

"Physics is puzzle solving, too, but of puzzles created by nature, not by the mind of man."

— Maria Goeppert-Mayer

I can only agree with Maria Goeppert-Mayer, the second female Nobel laureate in Physics. Indeed, doing science is like playing an overwhelming jigsaw puzzle with innumerable pieces and without knowing the final picture. But once you have started, ordered some pieces and maybe found some connections, you are hooked. The same happened to me when studying the dynamical phenomena in the solar atmosphere. I learned about the current knowledge, ordered the findings of my dear colleagues, performed my own studies and searched for the connections. In this section, I will summarize my conclusions on the observed wave phenomena in sunspots. Hopefully, I have added some missing pieces to this overwhelming jigsaw puzzle. But, as always in science, the picture can only be complemented and not completed. In the following, the observational results from the previous chapters are listed and brought in context to the supported sunspot wave scenario. To my best knowledge, I illustrate my conclusion in Fig. 7.1.

Wave phenomena in sunspots were studied by two sophisticated observation runs with spectroscopic two-dimensional data. The Fabry-Pérot spectrometers IBIS and TESOS at the ground-based Dunn Solar Telescope in New Mexico and Vacuum Tower Telescope on Tenerife, provided observations at superb temporal and spatial resolution. The simultaneous scanning of multiple spectral lines in the visible to near-infrared range allowed a fine sampling of the photosphere and chromosphere above two sunspots. Co-temporal observations with the satellite telescopes aboard the Solar Dynamics Observatory enabled the comprehensive examination of the sunspot dynamics in the upper chromosphere, transition region, and corona. In addition, the magnetic field parameters in the sunspot photosphere were determined and served as magnetic context information. The observation of one regular fully-developed sunspot and one irregular sunspot with a half-sided penumbra and light bridges accomplished the task of a complementary investigation of sunspot waves. The extensive wave analysis and employment of diverse methods yield substantial results. The findings and discussion were described in Chapter 6. In the following, the conlusions are listed and briefly summarized according to their logical order.

Omnipresence: Sunspot waves are detected throughout all atmospheric layers, from the lower photosphere to the upper transition region and corona. Umbral flashes and running penumbral waves are most prominent in the sunspot chromosphere. All oscillations in spectral intensity and Doppler velocity occur unceasingly at periods of a few minutes for the observational timespan.

Driving mechanism: The permanent excitation of sunspot waves requires a sustained and powerful driving source. The most likely driving mechanism is the absorption of p-modes by the sunspot in the upper convection zone and lower photosphere (Abdelatif et al. 1986). Measurements of the velocity power in the lower photosphere show that acoustic 5 min oscillations are strongly damped within the sunspot region: From the vicinity of the sunspot to the umbral core, the oscillatory amplitude of the Doppler velocities reveals a decrease by a factor of three. It is therefore considered that a fraction of the p-mode power must be converted into magnetoacoustic wave modes. Enhanced wave power is obtained in the outer umbra and inner penumbra in the

lower photosphere where the mode conversion is expected. A deep investigation reveals that the oscillatory signal stems from the first signatures of running penumbral waves along the magnetic field lines.

Magnetoacoustic waves are also driven by perturbations of the magnetic field lines. Measurements of the line-of-sight magnetic field exhibit oscillatory signals in the 1%-range for the magnetic field strength and magnetic flux in the lower sunspot photosphere. In the umbral core, localized patches with a size of 1″ feature magnetic field oscillations with periods around 3–6 min and field strength of up to 25 G. The results are in general agreement with other observational studies which report on average oscillatory amplitudes of around 10 G (Horn et al. 1997; Rueedi et al. 1998; Balthasar 1999; Norton et al. 1999; Bellot Rubio et al. 2000). As discussed by Staude (2002), the apparent field fluctuation have to be treated with caution since they could also result from atmospheric changes induced by the sunspot waves. The waves introduce vertical fluctuations of the atmospheric pressure which leads to a variation in the opacity and height of line formation. When the parameters oscillate along the negative vertical gradient of the magnetic field strength of around $-1\,\mathrm{G\,km^{-1}}$ in the lower photosphere (Wittmann 1974), it causes apparent oscillations in magnetic field strength which are comparable with the measured magnitude.

Upward propagation and shock formation: Time delays of oscillatory signals and the appearance of

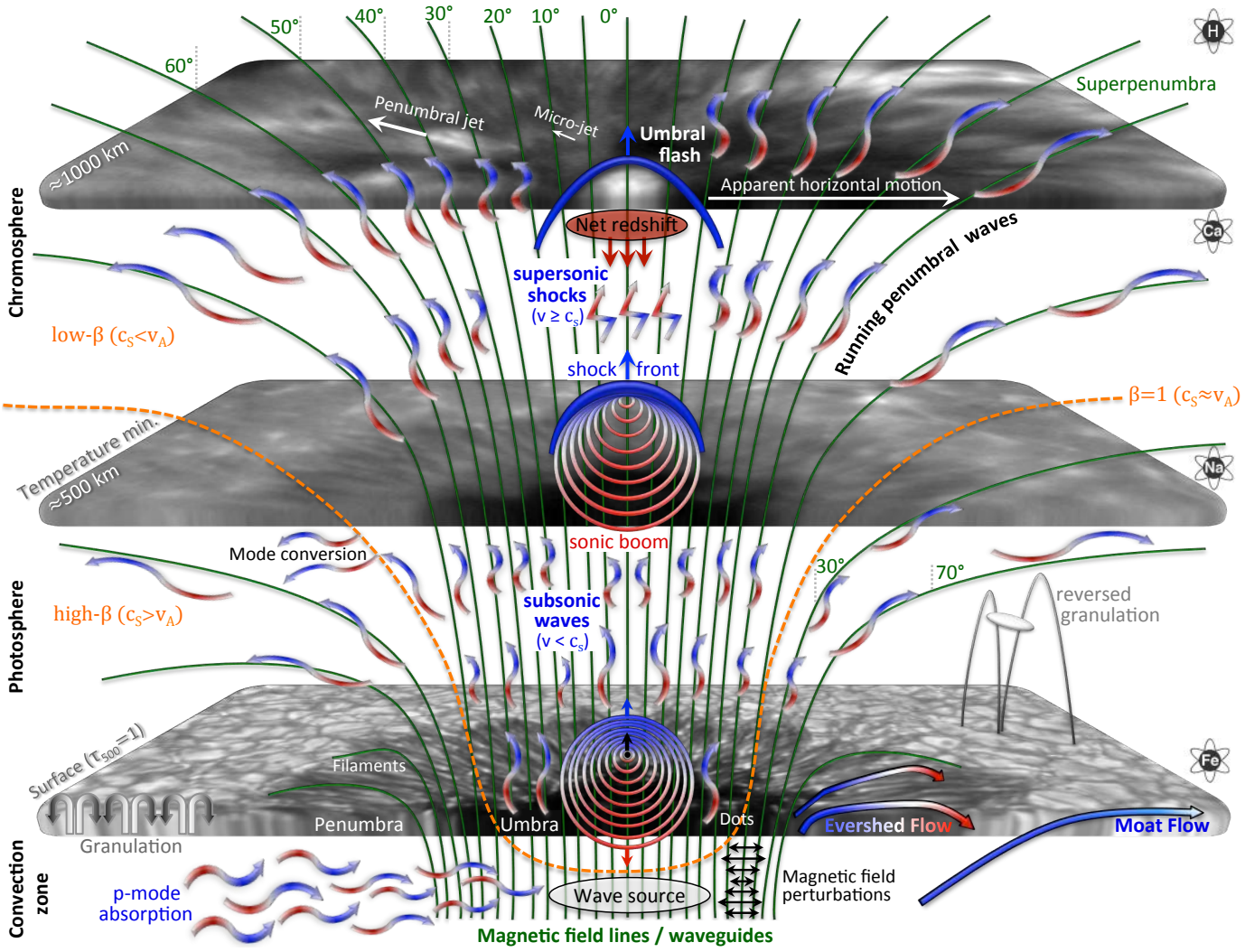

Figure 7.1.: Sketch of sunspot dynamics and wave propagation.

waves in the atmospheric layers support the upward propagation of magnetoacoustic waves in sunspots. In the upper photosphere and chromosphere, umbral flashes propagate with vertical velocities of up to $8 - 15\,\mathrm{km\,s^{-1}}$. The analysis of Doppler velocities in the lower sunspot atmosphere shows that the oscillatory amplitude of the wave modes increases for higher atmospheric layers. In particular, umbral waves in the 2.5–3 min band propagate unhindered along the umbral magnetic field. From the lower photosphere to the lower chromosphere, the Doppler velocities increase by a factor of 6–7 up to $1\,\mathrm{km\,s^{-1}}$. Since waves with longer periods than the acoustic cut-off period are evanescent in the upper atmosphere, the velocity power at these periods increase only slightly or hardly from the photosphere to the chromosphere. The findings are in general agreement with the power distribution reported from other observations (e.g., Lites and Thomas 1985; Lites et al. 1998; Centeno et al. 2006; Felipe et al. 2010b).

The gas density in the sunspot atmosphere decreases exponentially with increasing geometrical height. When the coherent photospheric waves propagate upward to the chromosphere, their acoustic energy flux has to be maintained by the relative oscillatory motion. Consequently, the oscillatory amplitude of an upward propagating wave steepens. In the relatively cool upper photosphere and lower chromosphere, umbral short-period waves can form a magnetoacoustic shock front (Centeno et al. 2006; Bard and Carlsson 2010). The adiabatic compression of the plasma at the shock front is extreme and leads to a rise in temperature by a thousand Kelvin and more (de la Cruz Rodríguez et al. 2013). This induces an increase of the atomic ionization and radiative brightness (Havnes 1970; Kneer et al. 1981).

Umbral flashes: Umbral flashes dominate the dynamics in the umbral chromosphere. They appear at an average period of 2.5 min as bright shock waves which amplify the spectral intensity at quiescence by up to three times. The area of maximum brightness ($2 - 4''$) of the flash coincides with the maximum red-shift of the spectral Na I D1 line indicating a downward motion of the plasma. At the advent of shock wave, the Ca II 854.21 nm line exhibits a blue-shifted emission peak which indicates upward propagation of the shock front. The apparently conflicting results are brought into line by the nature of acoustic shock waves which consist of two components of motion along the line-of-sight (Socas-Navarro et al. 2000). The first component of shock propagation is the upward motion of the shock front toward the observer. The second component is the sonic boom behind the shock front which points in the opposite direction. Additional evidence for the shock wave nature of umbral flashes is given by the measured wave function of Doppler velocities. Whereas the umbral oscillations in the photosphere describe a sinusoidal wave function, umbral flashes in the chromosphere transform the sinusoidal shape into a saw-tooth wave function with rapidly occurring blue-shifts (in line with Centeno et al. 2006). The temporal evolution of the umbral flash appearance at the smallest scales supports the geometrical configuration of a shock cone. Since the zenith inclination of the magnetic field increases toward the penumbra, the umbral flash performs an apparent horizontally outward-directed motion. The analysis of oscillations in the upper chromosphere, transition region, and corona demonstrates that umbral flashes can propagate unhindered to the upper atmosphere.

Running penumbral waves: The nature of running penumbral waves is proven. The obtained wave characteristics of running penumbral waves provide evidence for the scenario of slow-mode magnetoacoustic wave propagation along the inclined magnetic field lines (see Section 2.5). Consequently, umbral flashes and running penumbral waves share the same wave nature and possibly the same driving source in the sub-photospheric umbra. The comprehensive observations reveal that running penumbral waves are present from the middle photosphere to the transition region. The wave signal is most prominent in the chromospheric penumbra and extends to the superpenumbra. In spectroscopic data corresponding to a distinct atmospheric layer, running penumbral waves appear as bright largely coherent bands which propagate radially outward from the inner to the outer penumbra. With increasing distance from the umbra, the apparent horizontal velocity slows down and the dominant wave period increases. This visual pattern is observed

at all atmospheric layers. The inclination of the sunspot's magnetic field explains the super-sonic velocities at the outer umbra and inner penumbra and the radial decrease of the apparent horizontal velocity (Bloomfield et al. 2007a; Madsen et al. 2015). As illustrated in Fig. 6.19, the magnetic field lines incline against the zenith with increasing distance from the umbra. The path length and travel time of a coherent wave front to a distinct atmospheric height increase from the umbra to the outer penumbra. The shift in wave period from 3 min in the umbra to 10 min in the outer penumbra is accounted to the modified acoustic cut-off period. Bel and Leroy (1977) proposed that the acoustic cut-off period, which blocks the upward propagation of long-period waves, decreases where the magnetic field lines are more inclined against the zenith. Therefore, the more inclined penumbra also channel waves with longer periods. The observed wave power, peak periods and acoustic cut-off modifications are in best agreement with the findings of other observational studies (e.g., De Pontieu et al. 2005; McIntosh and Jefferies 2006; Bloomfield et al. 2007a; Jess et al. 2013; de la Cruz Rodríguez et al. 2013; Yuan et al. 2014b).

Reconstruction of the magnetic field topology: The proposed proportionality between the zenith inclination of the magnetic field lines and the acoustic cut-off period was employed to reconstruct the magnetic field topology from the measured wave periods in the sunspot atmosphere. As presented in Section 6.5, the inference of the zenith inclination yields consistent results. To my best knowledge, a reconstruction of the chromospheric magnetic field inclination, based on oscillations in non-polarimetric spectroscopic data, is performed for the first time.

Waves in irregular sunspots, pores and light bridges: The omnipresence of sunspot waves is substantiated by the observation of an irregular sunspot. One side of the sunspot is lacking a photospheric penumbra. Nevertheless, the chromosphere above that region exhibits an inclined superpenumbra which features the propagation of running penumbral waves. As stated by Sobotka et al. (2013) and Freij et al. (2014), also pores can show such a chromospheric superpenumbra with apparently outward propagating waves. Above light bridges, umbral waves cannot propagate to the neighboring umbra. They approach each other from both sides and break or merge above the center of the light bridge.

The observations support the scenario of sunspot waves being slow-mode magnetoacoustic waves which propagate upward along the magnetic field lines. The wave scenario is illustrated in Fig. 7.1. The sunspot of active region NOAA11823 is shown in spectral intensity from the bottom photosphere at the optical depth $\tau_{500} = 1$ (bottom layer), temperature minimum layer at an altitude of around 500 km (middle layer), and chromosphere at around 1000 km above the optical depth unity. The magnetic field lines (green lines), which represent the magnetic waveguides, are sketched according to the inferred zenith inclinations. In the convection zone, p-modes propagate toward the sunspot umbra. The acoustic character of the waves is indicated by the shape of the wave and changing Doppler velocity (blue- and red-shifts). The p-modes are fractionally absorbed by the sunspot. Magnetic field perturbations are drawn as a series of black arrows. Mode conversion acts at the layer at which the sound speed equals the Alfvén speed ($\beta = 1$, orange dashed line). Slow-mode magnetoacoustic waves in the low-β regime of the sunspot describe a field-guided quasi-acoustic propagation. In the photosphere, the waves have a slightly sub-sonic phase velocity (indicated by the sinusoidal waves and the acoustic compression and rarefaction). When the umbral waves propagate upward, they steepen and form into super-sonic shocks (indicated by the saw-tooth waves and the shock front). In the chromosphere, the shock wave is visible as a bright umbral flash. A net red-shift is present in the umbra. The projection of running penumbral waves in the chromosphere describes an apparent horizontal motion. Further dynamics are highlighted in the illustration, e.g., the Evershed and moat flow, granular convection and reversed granulation, umbral micro-jets and penumbral jets.

8. Outlook

"The important thing is not to stop questioning. Curiosity has its own reason for existence. One cannot help but be in awe when he contemplates the mysteries of eternity, of life, of the marvelous structure of reality. It is enough if one tries merely to comprehend a little of this mystery each day. Never lose a holy curiosity."

— Albert Einstein, *statement in LIFE magazine*

There are still many unresolved questions in solar physics and it will need curious people to discover their answers. It will require vision, imagination and pioneering spirit for the investigation of the Sun. As today, future solar physicists will have to embrace a wide field of disciplines. They will have to understand the dynamical processes and the nature of events from the smallest to the largest scales, from quantum physics over nuclear physics and magnetohydrodynamics to classical physics.

For more than four centuries, sunspots have been a persistent source of fascination and insight for solar physicists. Though we have gathered a profound knowledge on their nature and dynamics, a number of fundamental questions still remains unanswered. Especially, improved high resolution observations of the smallest scales will help to complete the overall picture of sunspots. In hands with with the technological progress of the 21st century and ground-breaking observations, new features and unexpected dynamical phenomena will become visible. They will bring light into the magnetic small-scale structure of the umbra and penumbra. The small-scale appearance and propagation of umbral flashes and running penumbral waves will become apparent. Yet unresolved components of shock waves will be resolved. Future space observation might answer the question on the supersonic down-flow above umbrae. Is it really a constant mass-flow or the blowback of umbral shock waves? The resolution of the umbral and penumbral fine scale structure will answer as many questions as new ones will posed. The nature of umbral dots and umbral micro-jets will reveal themselves. With improved helioseismic studies of active regions, the subsurface structure of sunspots and the mechanisms of p-mode absorption and mode conversions in sunspots might be clarified. Maybe light is even brought to the ongoing discussion about the heating of the upper atmosphere, specifically above sunspots. Not only the investigation of sunspot dynamics and phenomena on the spatial scales, but also on the temporal scale will make its contribution to the future insight. High-cadence observations with rates of seconds or even milliseconds will feature the rapidly occurring events in sunspots. Continuous sunspot recordings at time scales of hours to a week will illuminate the relation between the different dynamical events. Of course telescope at Earth and in the Earth's orbit can only record the processes on the front side of the solar disk. Future space missions and elaborate helioseismological investigation will probable allow to observe the entire solar atmosphere simultaneously and investigate the global wave phenomena on the Sun. By way of example, does the evolution of a sunspot influence its wave properties, or do flows and waves in sunspots interact with each other? From another perspective, long-term statistical studies of sunspot waves over a sunspot cycle or even many decades will shed light into the connection between the properties of sunspot waves and the overall magnetic activity.

Solar physics of the 21st century will be dominated by the rapid technological progress. Large ground-based telescopes and ingenious solar satellite missions will provide us with the capability to observe the Sun at its smallest spatial scales. New state-of-the-art instruments will permit us to study its magnetic activity at highest spectral precision and polarimetric accuracy. With this potential, the

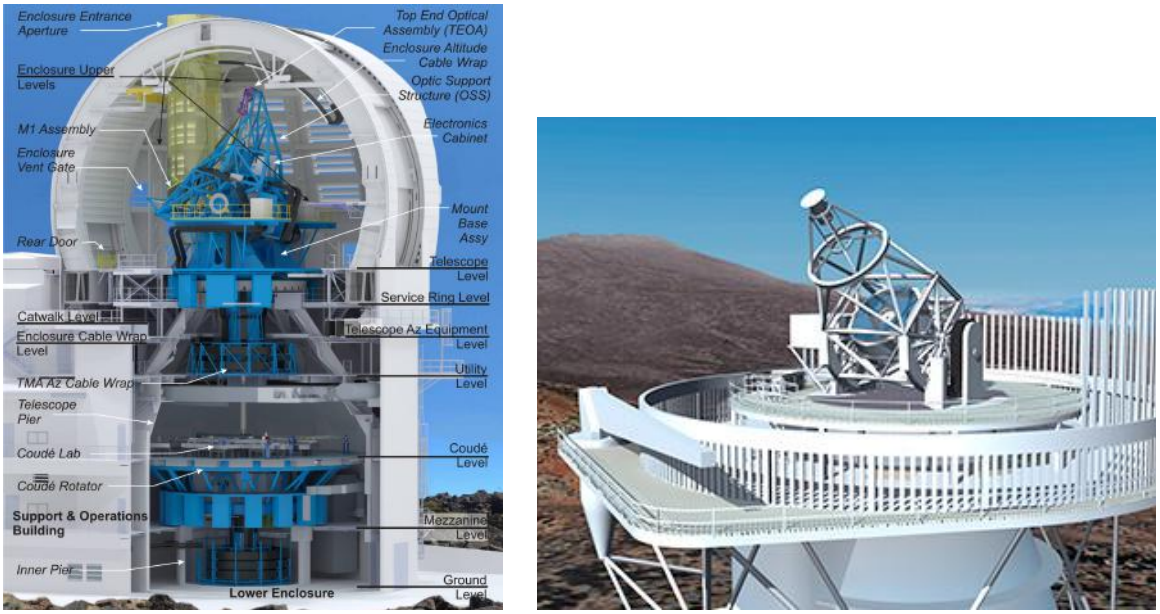

Figure 8.1.: Future 4 m-class solar telescopes. Left panel: The Daniel K. Inouye Solar Telescope (DKIST) on Maui will start its operations in 2019. Image from Tritschler et al. (2015). Right panel: The European Solar Telescope to be located on the Canary Islands has finished the conceptual design study. Image from European Commission (2013).

pace of solar research will even increase, keeping the field prosperous for the next decades. Already in the last years, the pioneering spirit of the solar community has created a new class of ground-based solar telescopes with apertures of around 1.5 m. At the beginning of the 2010's, operation has started for two ultramodern telescopes, the GREGOR telescope under the lead of the Kiepenheuer-Institut and the *New Solar Telescope* of the Big Bear Solar Observatory. The first is located on Tenerife, the latter in California. Equipped with high-order adaptive optics systems, both telescopes manage to resolve solar structures smaller than 100 km. Together with the successful solar space telescopes – Solar Dynamics Observatory (SDO), HINODE and the Interface Region Imaging Spectrograph (IRIS) – these observatories will dominate the current decade. But the time does not stand still. The next generation of solar telescopes is planned or already in construction. The Daniel K. Inouye Solar Telescope (DKIST) is will start its operation in 2019 (see left panel in Fig. 8.1). This 4.2 m-aperture telescope on the Hawaiian island Maui is expected to deliver landmark observations and will dominate solar observation for the following decades. It will be operated under the lead of the National Solar Observatory (NSO). Its European counterpart, the European Solar Telescope (EST) has finished its conceptual design study (see right panel in Fig. 8.1). It is planned as a 4 m aperture telescope and will be placed on the Canary islands. Both telescopes, equipped with adaptive optics systems can reveal solar features as small as 20 km wide. Beyond, an even bigger solar telescope is planned in China. When completed, the Chinese Giant Solar Telescope could deliver a spatial resolution equivalent to an 8 m-diameter telescope. In addition to Earth-based telescopes, a number of brilliant future space mission will deliver continuous high-performance observation of the Sun. Data in the spectral range from X-rays to infrared will complete the overall picture of our star. To name one, the Solar Orbiter is an ambitious ESA mission which will be launched in 2018. The satellite telescope will orbit the Sun coming as close as 0.28 astronomical units to the solar surface. By its inclined orbit to the solar ecliptic, it will be able to observe the polar region of the Sun in full detail.

However, the best telescope is worth nothing without its scientific instruments. Also here, numerous advanced technologies guide the way to the next generation of observational instruments. Imaging spectro-polarimeters based on Fabry-Pérot interferometers like the Visible Tunable Filter

(VTF) instrument for the DKIST will deliver beautiful observations for the different atmospheric layers. Simultaneously operating powerful spectrographs will provide the highest spectral precision and polarimetric accuracy possible. Laser frequency combs attached to spectrographs will guarantee an absolute wavelength calibration allowing an accurate and reliable velocity determination throughout the solar atmosphere. One example for this pioneering type of instrument is the Laser Absolute Reference Spectrograph (LARS; Doerr et al. 2012) attached to the Vacuum Tower Telescope on Tenerife. All in all, these observational devices will create an enormous amount of data. Professional data centers will have to create effective and powerful data calibration pipelines to provide the solar community with science-ready observations. High processing speeds, fast transmission rates and big storage media will be needed to deal with the exponentially increasing amount of information. The field is pacing with the time. Solar physics is ready to enter another golden age.

A. Additional figures and tables

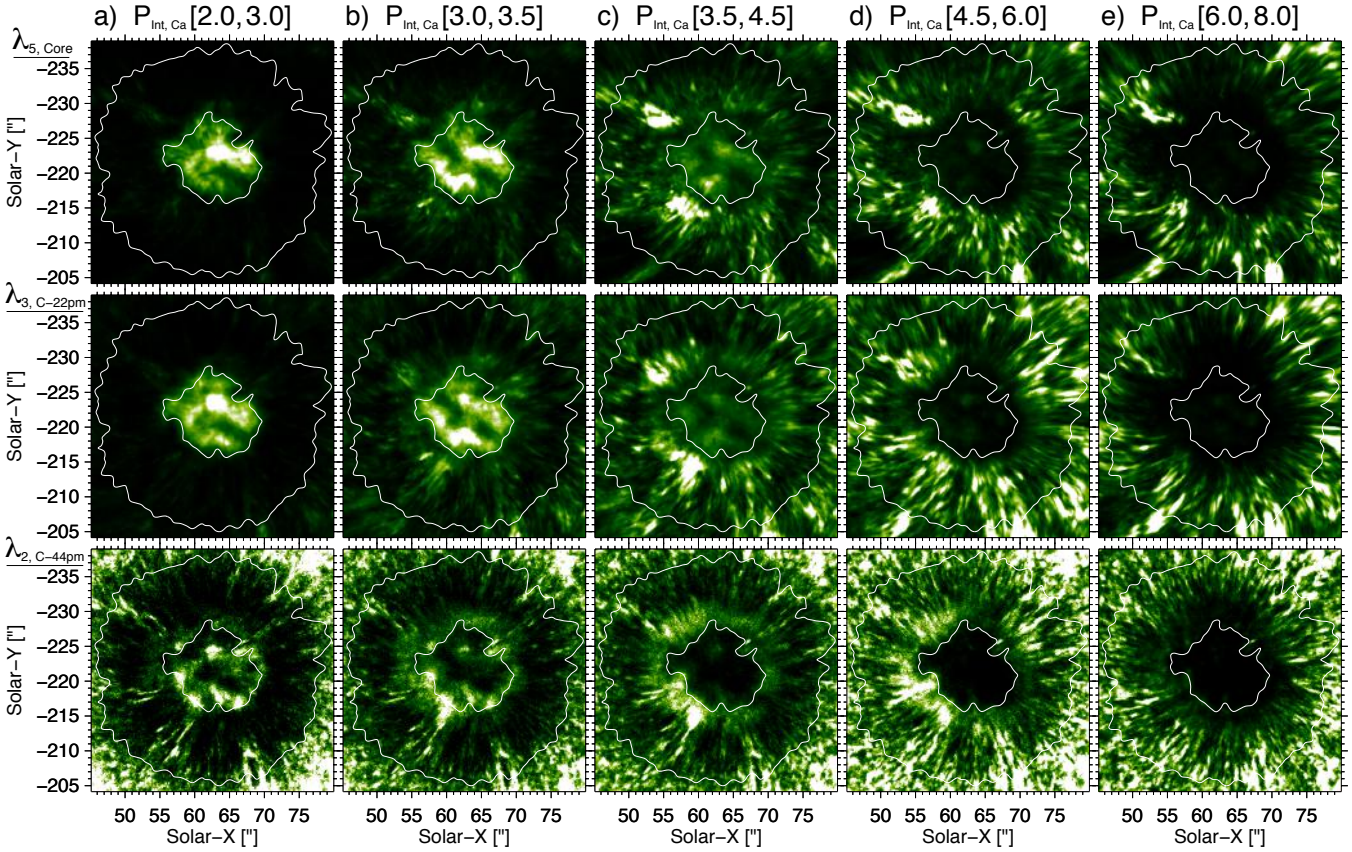

Figure A.1.: Distribution of the scaled wavelet power $P_{\mathrm{Int,\,Ca}}$ in the sunspot NOAA 11823 (see Sec. 4.3.1). The three rows display the power obtained from three characteristic spectral positions of the Ca II 854.212 nm line, namely the line minimum $\lambda_{5,\mathrm{Core}}$ (top row), blue line core $\lambda_{3,\mathrm{C-22pm}}$ (middle row), and blue line wing $\lambda_{2,\mathrm{C-44pm}}$ (bottom row) at the line bend. The averaged power for period ranges (in min) are shown from 2–3 min to 6–8 min (left to right panel). The power was scaled for best visibility of sunspot wave power. Bright colors indicate high power.

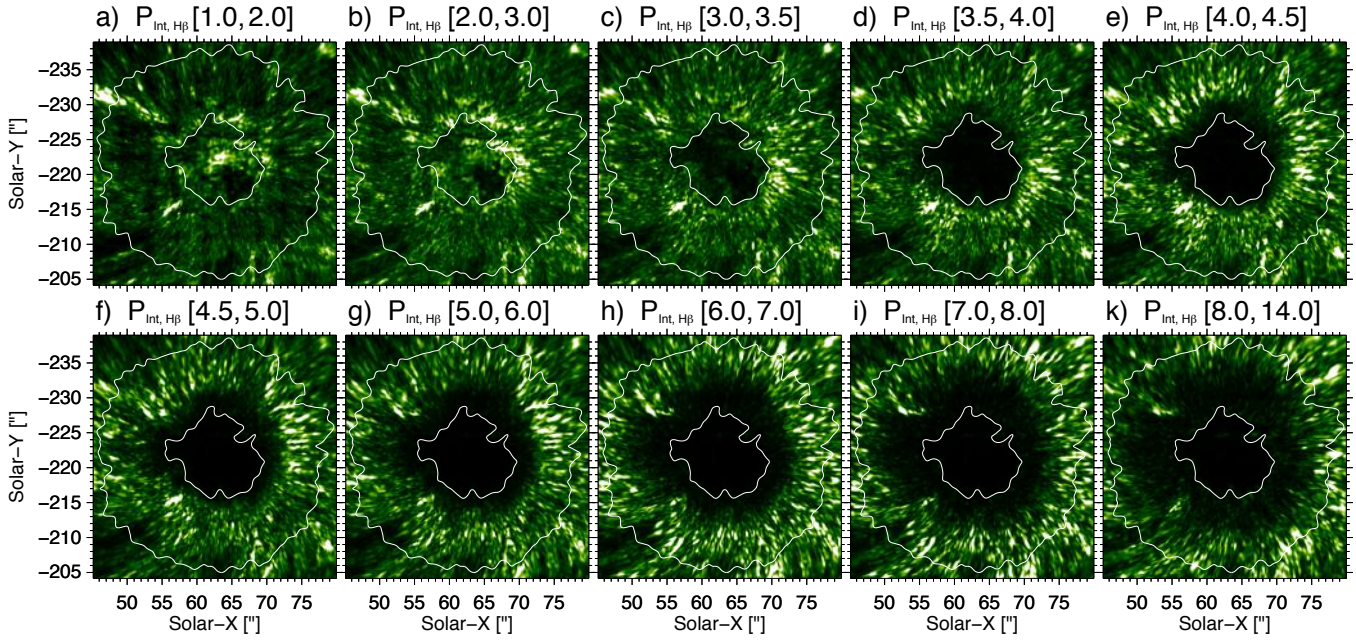

Figure A.2.: Distribution of the scaled wavelet power $P_{\mathrm{Int},\mathrm{H}\beta}$ in the sunspot NOAA 11823 (see Sec. 4.3.1). The intensities power of the spectrometric H_β observations at 486.1 nm was filtered for period ranges from 1–2 min (panel a) to 8–14 min (panel k). The power was scaled for the best visibility of sunspot wave power. Bright colors indicate most power.

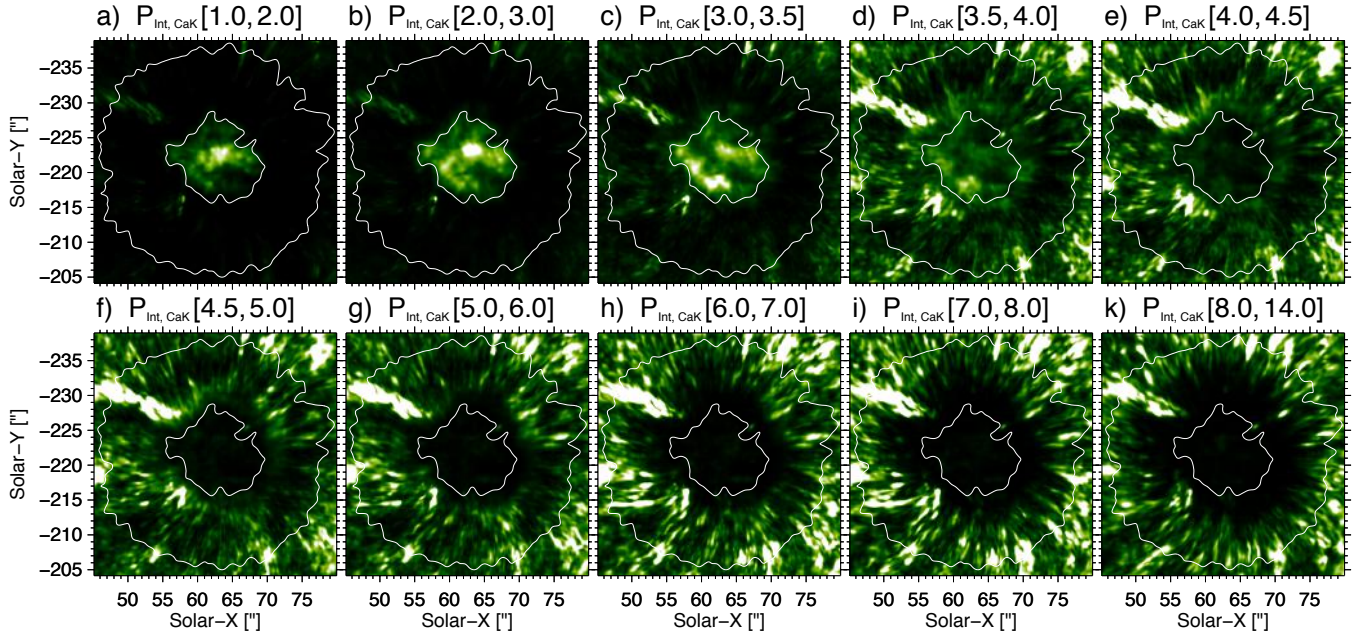

Figure A.3.: Distribution of the scaled wavelet power $P_{\mathrm{Int},\mathrm{CaK}}$ in the sunspot NOAA 11823 (see Sec. 4.3.1). The intensities power of the spectrometric Ca K observations at 393.4 nm was filtered for period ranges from 1–2 min (panel a) to 8–14 min (panel k). The power was scaled for the best visibility of sunspot wave power. Bright colors indicate most power.

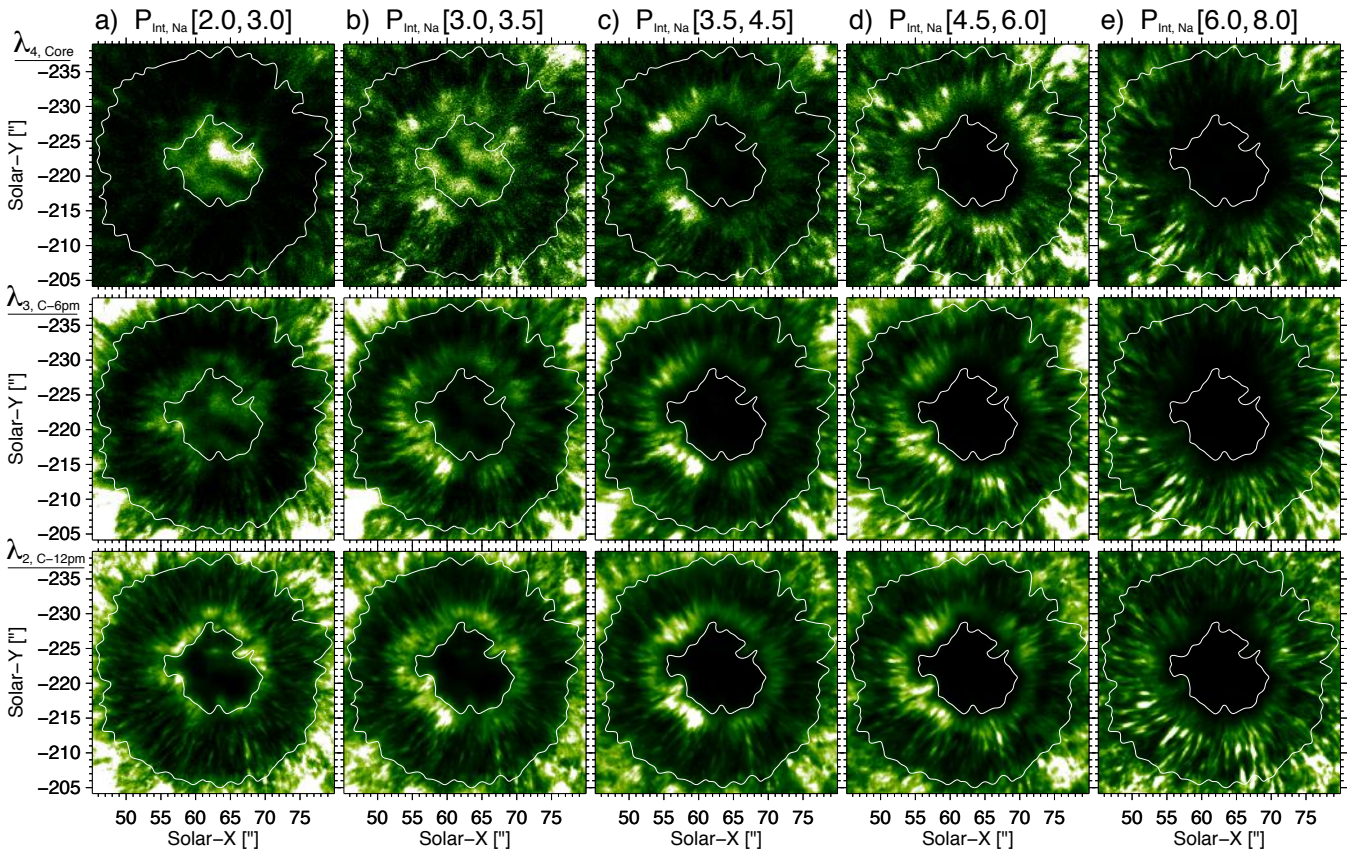

Figure A.4.: Distribution of the scaled wavelet power $P_{\mathrm{Int,\,Na}}$ in the sunspot NOAA 11823 (see Sec. 4.3.1). The three rows display the power obtained from three characteristic spectral positions in the Na I 589.59 nm line, namely the line minimum $\lambda_{4,\mathrm{Core}} = 589.590$ nm (top row), blue line core $\lambda_{3,\mathrm{C-6pm}}$ (middle row), and blue line wing $\lambda_{2,\mathrm{C-12pm}}$ (bottom row) at the line bend. The averaged power for period ranges (in min) are shown from 2–3 min to 6–8 min (left to right panel). The power was scaled for best visibility of sunspot wave power. Bright colors indicate most power.

Table A.1.: Average time delays $\overline{\Delta t_{\mathrm{U}}}$ for the umbral area between the oscillations in spectral brightness. E.g., the oscillation at the blue wing Na I position at $\lambda_{2,\,\mathrm{c-12pm}}$ precedes the oscillation at the line minimum at $\lambda_{4,\,\mathrm{Core}}$ by 45 s. The estimated average formation height H_{form} of the spectral positions above the respective optical depth unity is given in km.

$\overline{\Delta t_{\mathrm{U}}}$ [s]	Fe I 630.15 nm		Na I 589.59 nm			Ca II 854.21 nm		
	$\lambda_{3,\,\mathrm{c-8pm}}$	$\lambda_{5,\,\mathrm{Core}}$	$\lambda_{2,\,\mathrm{c-12pm}}$	$\lambda_{3,\,\mathrm{c-6pm}}$	$\lambda_{4,\,\mathrm{Core}}$	$\lambda_{2,\,\mathrm{c-44pm}}$	$\lambda_{3,\,\mathrm{c-22pm}}$	$\lambda_{5,\,\mathrm{Core}}$
$\lambda_{3,\,\mathrm{c-8pm}}$	—	52 (±50)						
$\lambda_{5,\,\mathrm{Core}}$	−52 (±50)	—	−6 (±84)			−12 (±75)		
$\lambda_{2,\,\mathrm{c-12pm}}$		6 (±84)	—	18 (±6)	45 (±24)	0 (±11)		
$\lambda_{3,\,\mathrm{c-6pm}}$			−18 (±6)	—	16 (±18)			
$\lambda_{4,\,\mathrm{Core}}$			−45 (±24)	−16 (±18)	—			−23 (±22)
$\lambda_{2,\,\mathrm{c-44pm}}$		12 (±75)	0 (±11)			—	24 (±34)	
$\lambda_{3,\,\mathrm{c-22pm}}$						−24 (±34)	—	1 (±2)
$\lambda_{5,\,\mathrm{Core}}$					23 (±22)		−1 (±2)	—
H_{form} [km]	100	300	250	600	1000	250	900	950

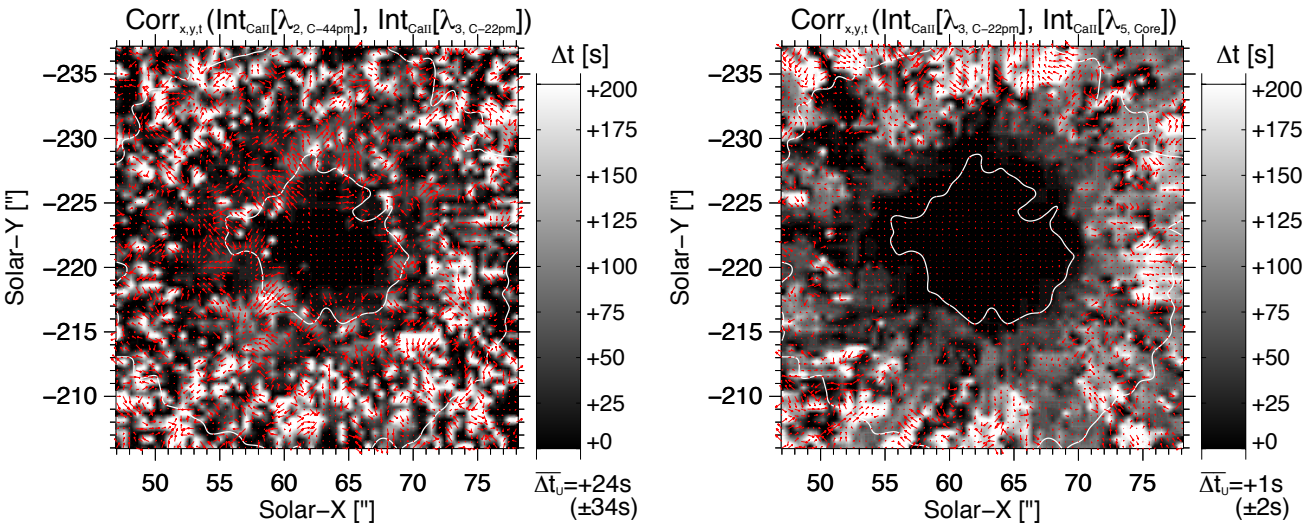

Figure A.5.: Phase difference maps for the sunspot NOAA11823. The time delays of oscillations in spectral intensities between the line wing ($\lambda_{2,\,\mathrm{C-44pm}}$), blue line core ($\lambda_{3,\,\mathrm{C-22pm}}$), and line minimum ($\lambda_{5,\,\mathrm{Core}}$) of Ca II 854.21 nm are displayed. The grayscale indicates the time differences, the red arrows hint at the spatial displacements. The penumbral boundaries are contoured in white. Further information in Section 5.4.1.

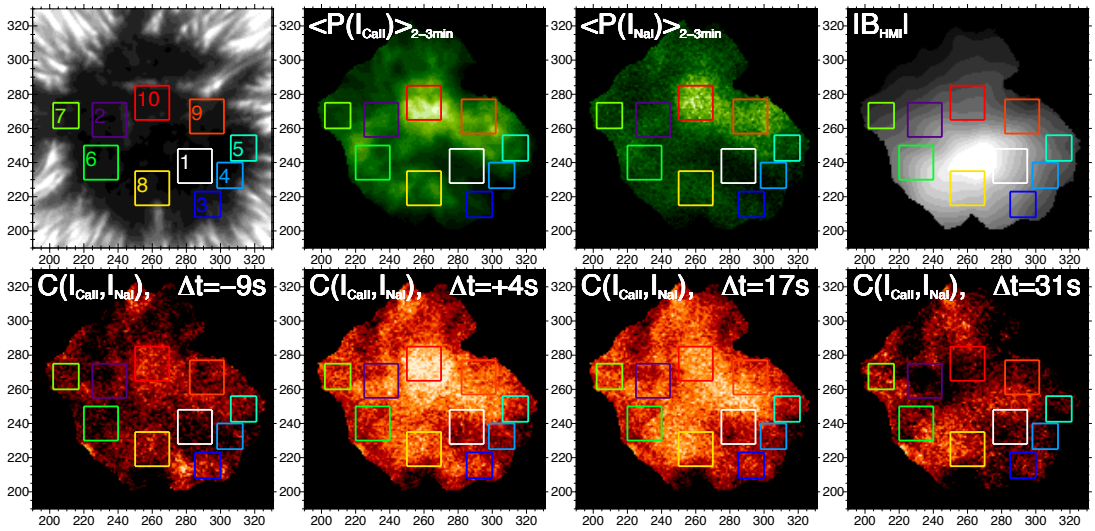

Figure A.6.: Time delays between intensity oscillations in the line minima of Na I at 589.59 nm (I_{NaI}) and Ca II at 854.21 nm (I_{CaII}). The analysis was performed for the umbral area sunspot NOAA11823. In the lower panels, the relative correlation coefficients $C(I_{\mathrm{CaII}}, I_{\mathrm{NaI}})$ are shown for four time delays Δt. High positive correlations are displayed in brighter color. In the upper panels, the umbra is shown in continuum intensity (left), global wavelet power in the 2–3 min range (middle), and magnetic field strength. Stronger power and magnetic field is displayed brighter. Ten umbral regions are highlighted in color. Compare Figs. 5.7 and 6.17.

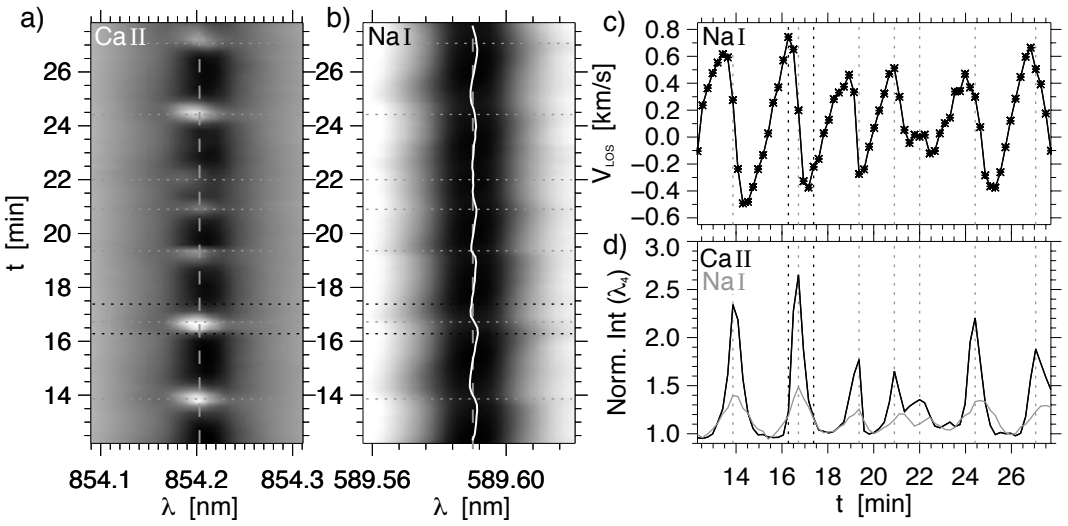

Figure A.7.: Umbral flash appearance in spectroscopic lines. Caption as in Fig. 5.8. The analyzed region is marked by the green quadrate in Fig. A.8.

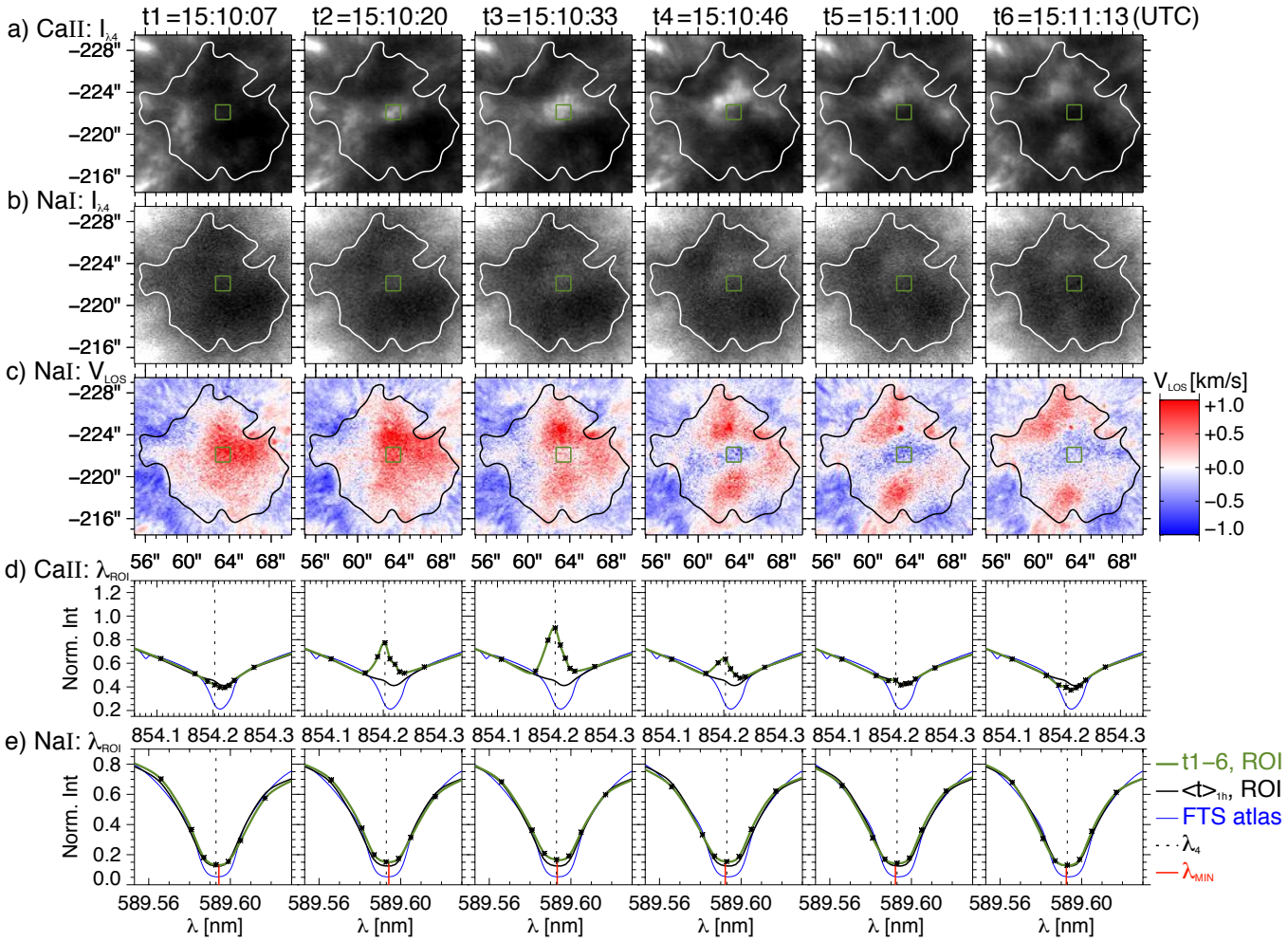

Figure A.8.: Umbral flash appearance in spectral intensities and Doppler velocities. Caption like in Fig. 6.15. The time steps corresponds the bright emission at $t = 17$ min in Fig. A.7.

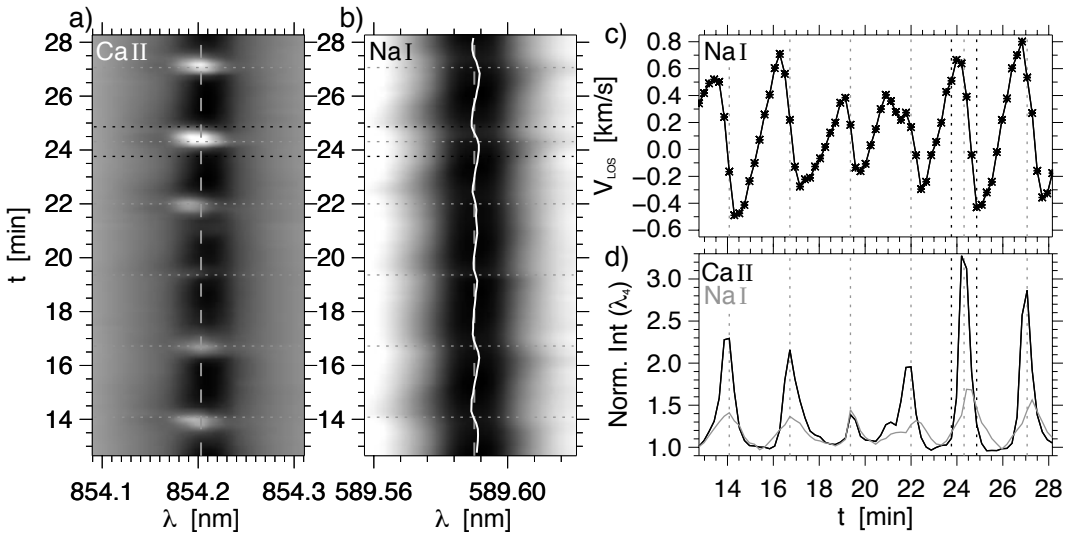

Figure A.9.: Umbral flash appearance in spectroscopic lines. Caption as in Fig. 5.8. The analyzed region is marked by the green quadrate in Fig. A.10.

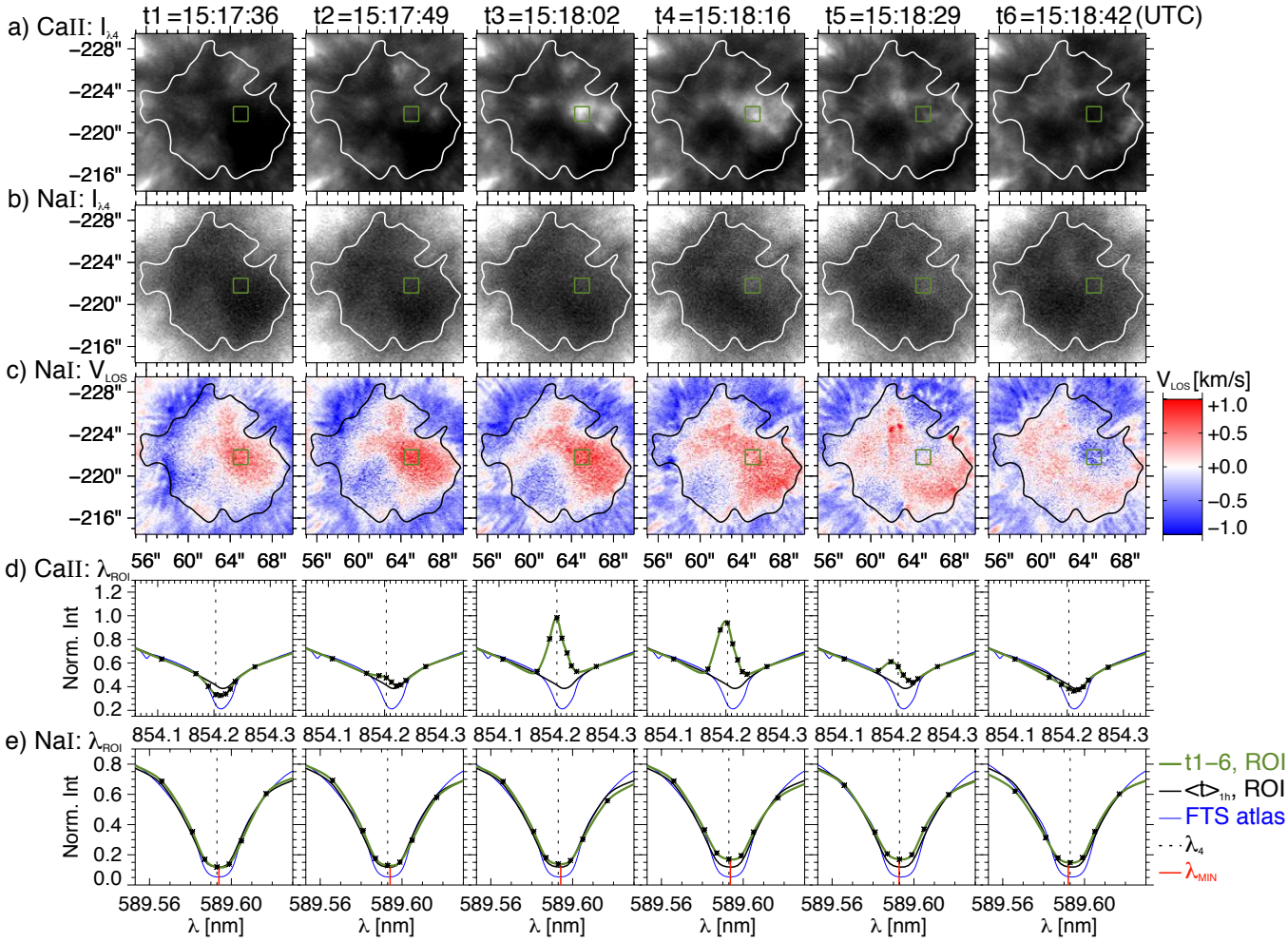

Figure A.10.: Umbral flash appearance in spectral intensities and Doppler velocities. Caption like in Fig. 6.15. The time steps corresponds the bright emission at $t = 24$ min in Fig. A.9.

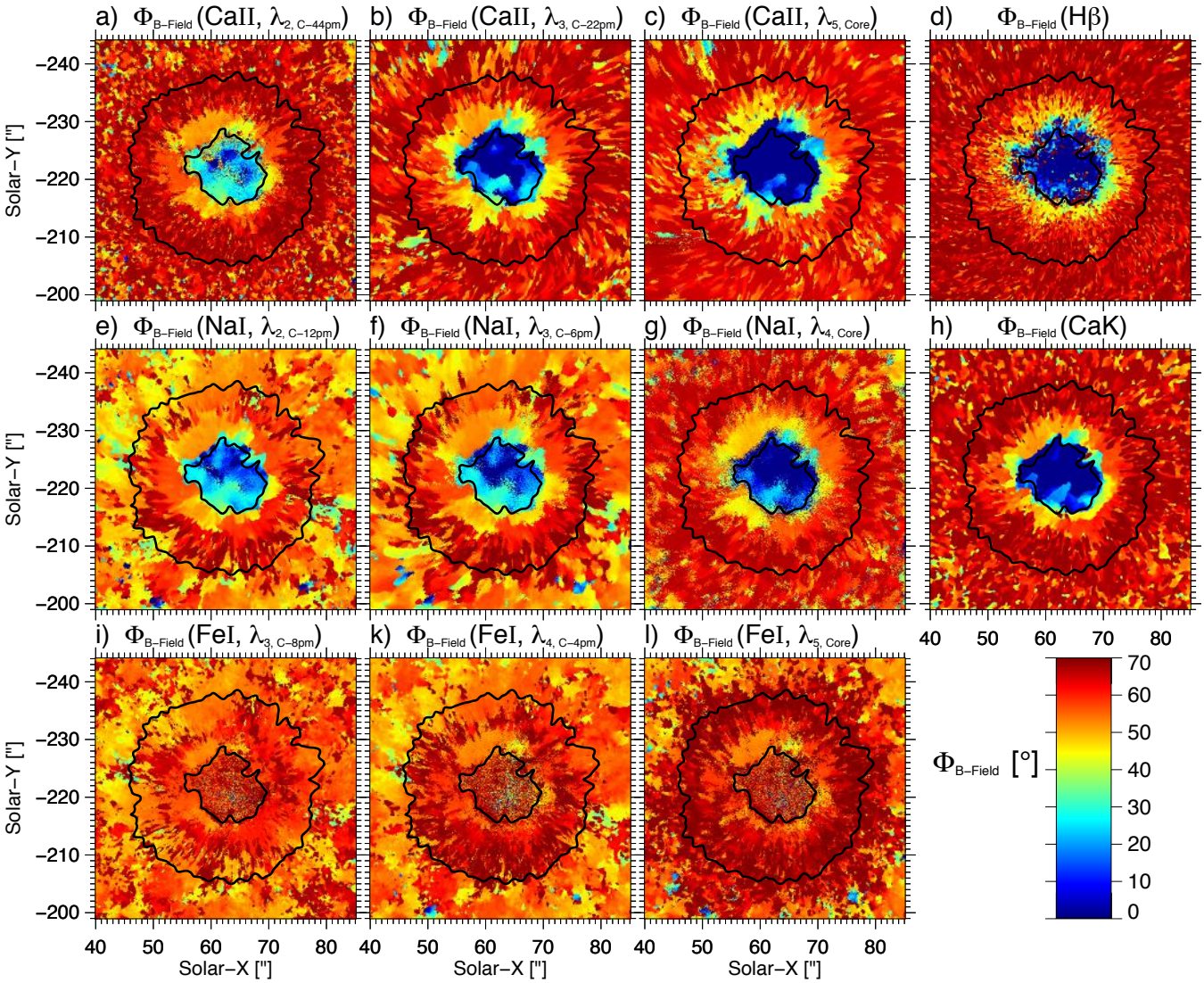

Figure A.11.: Magnetic field inclination angles Φ_B of sunspot NOAA11823 at various wavelength positions corresponding to photospheric and chromospheric layers. The zenith angles (in deg) were retrieved using the umbral atmospheric model of Maltby et al. (1986). The peak periods were displayed in Fig. 6.12. The inclination angles are scaled from 0° (dark blue) to 70° (dark red). The black contours indicate the location of the inner and outer penumbral boundary in continuum intensity. A detailed description of the various line positions is given in the caption of Fig. 6.29.

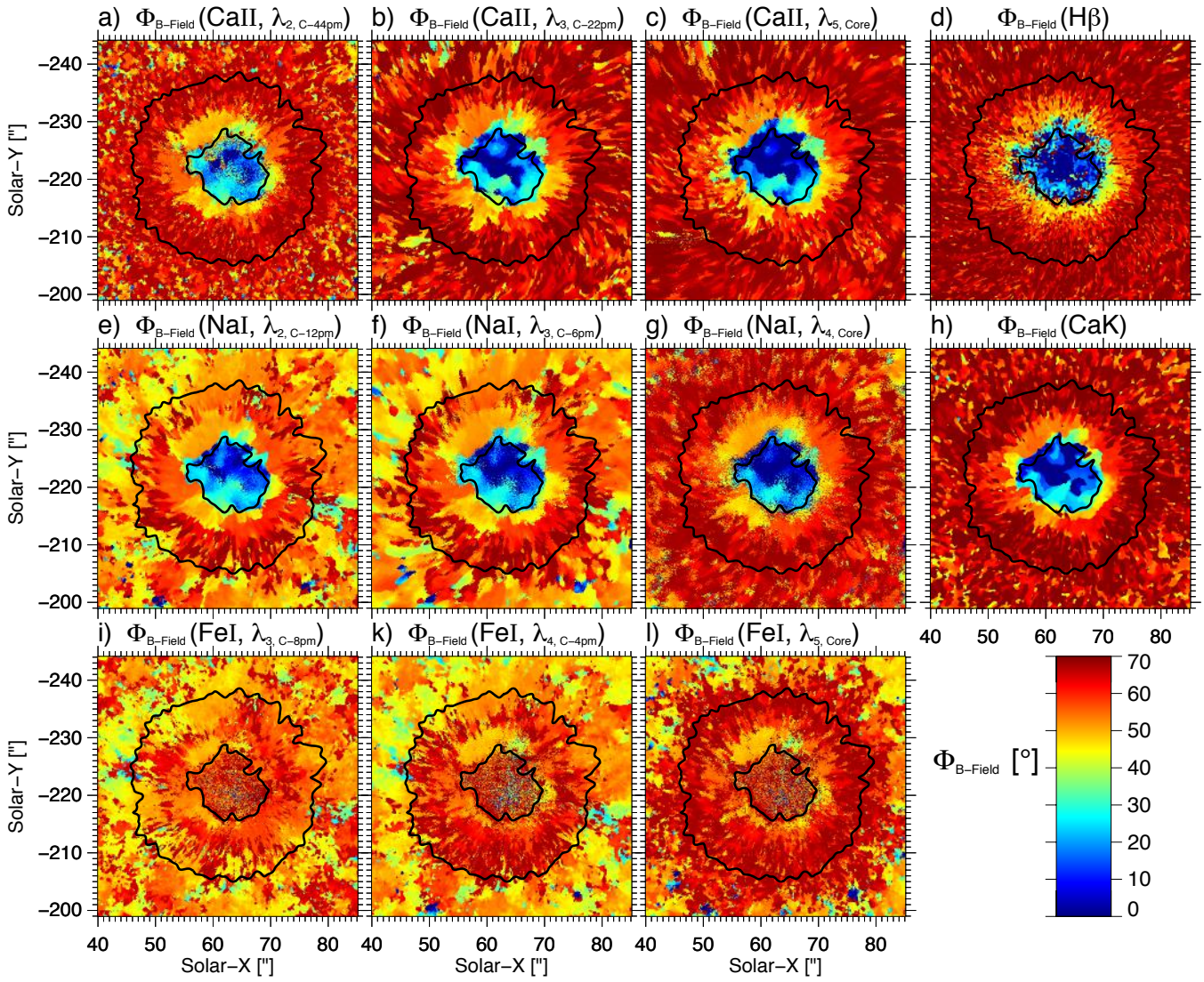

Figure A.12.: Same as Fig. A.11 but with magnetic field inclination angles Φ_B (in deg) retrieved with the quiet sun atmospheric model of Maltby et al. (1986).

B. CASSDA – Center for Advanced Solar Spectro-polarimetric Data Analysis

B.1. The project

The Center for Advanced Solar Spectro-polarimetric Data Analysis (CASSDA) is a work project at the Kiepenheuer Institute for Solar Physics. CASSDA was initiated for the development of automated data calibration pipelines for the German solar telescopes at the Teide Observatory on Tenerife.

Figure B.1.: The logo of the Center for Advanced Solar Spectro-polarimetric Data Analysis with a sunspot at high spatial resolution in the background.

In modern times, complex calibration procedures allow for the retrieval of the highest quality of observational data made with ground-based solar telescopes. To ensure the highest scientific output of the sophisticated astronomical instruments, the scientist has to be provided with software packages for an accurate data reduction or, even better, with science-ready data. To deal with the large amounts of observational data, efficient and automated data calibration pipelines are indispensable. To fulfill these needs for the German solar telescopes on Tenerife, the Kiepenheuer Institute for Solar Physics, as the leading institute operating the GREGOR telescope and the Vacuum Tower Telescope (shown in Fig. B.2), has established the Center for Advanced Solar Spectro-polarimetric Data Analysis. The project is funded by the Senate Competition Committee (SAW) of the Leibniz Association (Ref.-No. SAW-2012-KIS-5). CASSDA has started its activities in July 2012 with a starting project duration of three years.

The CASSDA working team is part of the Experimental Solar Physics Department of the Kiepenheuer Institute and consists of four scientific members. The coordinator and project scientist (Nazaret Bello González) is supported by two post-doctoral scientists (Catherine Fischer and Christian Bethge) and one Ph.D. student (Johannes Löhner-Böttcher). Besides the duties on data processing, the group's scientific research program focuses on the coupling and dynamics of the solar photosphere and chromosphere. Based on spectro-polarimetric measurements, the evolution of the quiet sun magnetic field as well as flows and oscillations in sunspots are investigated. This Ph.D. thesis about wave phenomena in sunspots is integrated within the CASSDA project.

Figure B.2.: The German solar telescopes, GREGOR (upper left) and the Vacuum Tower Telescope (upper right), at the Teide Observatory on Tenerife (Image: KIS).

The aim of CASSDA is to provide accurate spectroscopic and spectro-polarimetric datasets from the prestigious German telescopes at the Teide Observatory (Schroeter et al. 1985) to the international solar physics community. Therefore, young scientists are trained to acquire expertise in the observing procedures and the post-observational data handling. Advanced data calibration techniques and software packages are developed, revised and unified. Automated data calibration pipelines are developed in close cooperation with the international community, partner institutes[1] and in coordination with the affiliated SOLARNET project[2]. The different data levels are archived and will be provided in due time to the community on public databases like the Solar Virtual Observatory (SVO). This is done for the major astrophysical instruments at the VTT and GREGOR, namely TESOS (Triple Etalon SOlar Spectrometer), TIP (Tenerife Infrared Spectrograph), GFPI (GREGOR Fabry-Pérot Interferometer), GRIS (GREGOR Infrared Spectrograph) and LARS (Laser Absolute Reference Spectrograph).

In 2014 and 2015, the CASSDA team organized two international meetings on solar observations and data processing. In February 2014, the 1st CASSDA-SOLARNET Workshop was held in Freiburg. At this 3-day workshop on scientific data processing, many of the world's leading solar scientists discussed about the challenges of retrieving ready-for-science data from ground-based solar observations. Key aspects were image reconstruction techniques, accurate data calibration, concepts of data pipelines and the integration of solar observations in data archives. One year later, in April 2015, the 1st CASSDA School for young solar observers took place at the Observatorio del Teide on Tenerife. Within one week, expert telescope users and solar observers lectured and instructed 14 students and young postdocs in the capabilities and operation of the German solar telescopes and their attached scientific instruments. The students were supervised at real observations with GREGOR and the VTT. Subsequently, they learned how to calibrate the observational data and to use existing data pipelines. I contributed to the organization and was involved very actively in both events as oral contributor and lecturer, respectively.

The data calibration of imaging solar spectrometers and the development of a processing pipeline for the TESOS instrument were two essential tasks of my work as a Ph.D. student. In the next two section, I will devote myself to these topics and present their application in the CASSDA GUI – TESOS.

[1] Collaborating institutes were the Leibniz-Institut für Astrophysik (AIP) in Potsdam, the Department of Astronomy at Stockholm University, the Max Planck Institute for Solar System Research (MPS) in Göttingen, and the Instituto de Astrofísica de Canarias (IAC) on Tenerife.

[2] A network to coordinate and integrate the major European research institutions and infrastructures in the field of high-resolution solar physics. Several joint research activities are be carried out as work packages, like WP50 for the development of data-reduction pipelines and archive databases for the solar instruments.

B.2. Data processing of spectro-polarimetric data

An imaging spectrometer is a scientific instrument which produces a two-dimensional image at a single instant of time within a filtered spectral band. As described in Sect. 4.1.2, this very narrow and precise bandwidth is filtered by a combination of an interference pre-filter and two or three Fabry-Pérot interferometers (FPIs or etalons). An exemplary optical setup is shown in Fig. 4.8. By piezo-electric tuning and relative motions of the etalons, the filtered wavelength position is changed. To make a spectral scan, the etalons are calibrated so that images at successive positions of a spectral line are recorded. In addition to the spectral information which is yielded by the 'narrow-band' channel, a second accompanying 'broad-band' channel performs simultaneous observations in continuum intensity. This broader spectral band is chosen close to the observed spectral line. The continuum data serves as spatial context information and will be used for image reconstructions.

In the last years, the number and quality of solar spectrometers has increased steadily. In combination with additional polarimetric devices (see Fig. 4.8), these instruments became powerful imaging spectro-polarimeters. The three-dimensional data cubes of spectral scans in the spatial domain are extended by a fourth dimension, the polarimetric state. The most important etalon-based solar spectro-polarimeters are TESOS (Triple Etalon SOlar Spectrometer; Kentischer et al. 1998) at the Vacuum Tower Telescope, IBIS (Interferometric Bidimensional Spectrometer; Cavallini 2006) at the Dunn Solar Telescope, CRISP (CRisp Imaging Spectro Polarimeter; Scharmer et al. 2008) at the Swedish Solar Telescope on La Palma, and the GFPI (GREGOR Fabry-Pérot Interferometer; Puschmann et al. 2012) at GREGOR. Except for TESOS, all instruments use two etalons for the spectral filtering. One FPI serves as a narrow filter and is considered as the high-resolution etalon. The other FPI yields a broader transmission and therefore serves as the low-resolution etalon. An example of transmission curves and their product is shown in the left panel of Fig. B.6. In the case of TESOS – as the name Triple Etalon SOlar Spectrometer indicates – the system was upgraded by a third synchronized high-resolution etalon (Tritschler et al. 2002).

All in all, the mentioned imaging spectrometers resemble each other in their optical setup and characteristics. They feature spectral resolutions[3] up to 300,000 and operate in the optical to near-infrared range at typical wavelength between 500 nm and 860 nm. For quasi-simultaneous observations of multiple spectral lines, often up to six pre-filters can be mounted on a rotating filter wheel. In hand with automated rapid adjustments of the FPI settings during an observational cycle, the observed spectral line can be switched within few seconds and less. The frame rate of the observation depends on the reaction time of the etalons, on the image size and the recording rate. For typical image sizes between $40''$ and $90''$ at spatial scales of $0.04 - 0.09''$ pixel^{-1}, a frame rate of up to 6 images per second is achieved. Imaging spectrometers aim to study the rapid and small-scale dynamics of the solar atmosphere. The high spatial resolution is ensured by the imaging technique, the high temporal resolution has to be reached by a critical sampling of the spectral positions and the observational frame rate. Each data cycle (see Fig. B.4) consists of the number of spectrally filtered lines, their number of wavelength positions, the accumulation of observation at each spectral position, and the number of polarimetric degrees. Exemplary, a data cycle of two spectral lines, both sampled with 15 spectral positions in spectroscopic mode would yield a temporal cadence of around 5 s for the repetitive observation. For the polarimetric observation of the full-Stokes vector, the cycle time would increase by a factor of four to six to at least 20 s. If one would like to apply reconstruction techniques to the spectral scans, the temporal cadence would again multiply by a factor of 6 or more to at least two minutes. Comparing the time-scales, it is therefore important to clarify the dynamical time-scales of solar events and to adopt the necessary observational settings. This is kept in mind for the design and construction of the next-generation imaging spectro-polarimeters. The Visible Tunable Filter (VTF;

[3]The spectral resolution $\mathcal{R}$ describes how fine the instrument can sample the solar spectrum. It is calculated as the ratio $\mathcal{R} = \frac{\lambda}{\delta\lambda}$ between the observed spectral wavelength λ and the transmission width $\delta\lambda$. A smaller spectral width leads to a higher resolution. For a wavelength of 600 nm, a step size of 2 pm is needed to achieve a spectral resolution of 300,000.

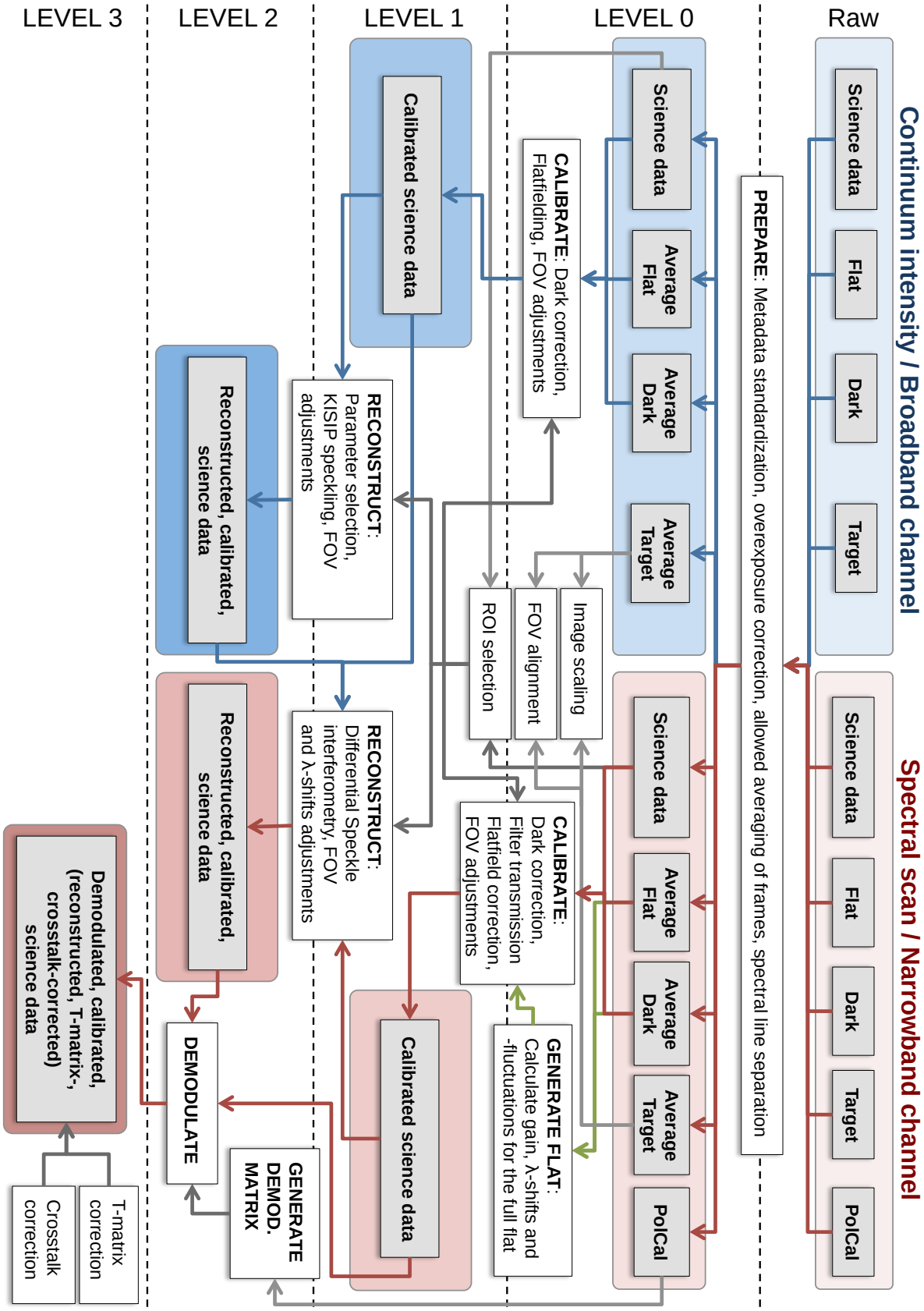

Figure B.3.: Flowchart for the processing of etalon-based spectro-polarimetric data. The data results for different processing levels (0–3) are highlighted, in blue for the broad-band channel (left side), and in red for the narrow-band channel (right side). The processing steps between the different levels are described in the white boxes.

Schmidt et al. 2014) instrument will perform the high-resolution spectro-polarimetric observations at the 4 m-class telescope DKIST (Daniel K. Inouye Solar Telescope) from 2019 on. As the great descendant of TESOS, the developers at the Kiepenheuer Institute for Solar Physics will have to put all their effort in making the instrument as effective and fast as possible.

To make an spectro-polarimetric instrument successful, it is essential to perfect the design of the instrument and the utilized optical components. Then, of course, experimental expertise is needed to achieve an excellent instrumental accuracies for the observations. These instruments demand a very deep knowledge about their inner workings to efficiently exploit the scientific information hidden in the data. Thus, it is inevitable to bring together the instrument builders and expert scientists working with Fabry-Pérot interferometers to develop programs for an accurate calibration of the data. This advanced data processing has to include the correction for instrumental effects like intensity errors due to the pre-filter transmission, dust, background noise and the roughness of the etalon surfaces. In addition, it has to implement an exact calibration of the telescopic and instrumental polarization. Complex image reconstruction techniques have to be integrated and applied to retrieve the highest spatial resolution. Finally, advanced data analysis procedures are applied to infer the atmospheric parameters, like velocities, temperatures and the magnetic field vector. They will provide science-ready data to the non-expert user.

In this section, I will describe the necessary processing steps for etalon-based imaging spectrometers. The calibration procedure will be explained exemplarily for the sunspot region in NOAA11455 (Section 4.3.2) observed with the Triple Etalon SOlar Spectrometer (Kentischer et al. 1998; Tritschler et al. 2002; Beck et al. 2010) at the VTT. The processing steps are shown in Fig. B.3 and can be applied to all solar imaging spectrometers. In Fig. 4.8, the optical setup of TESOS and a short specification of the instrument are given.

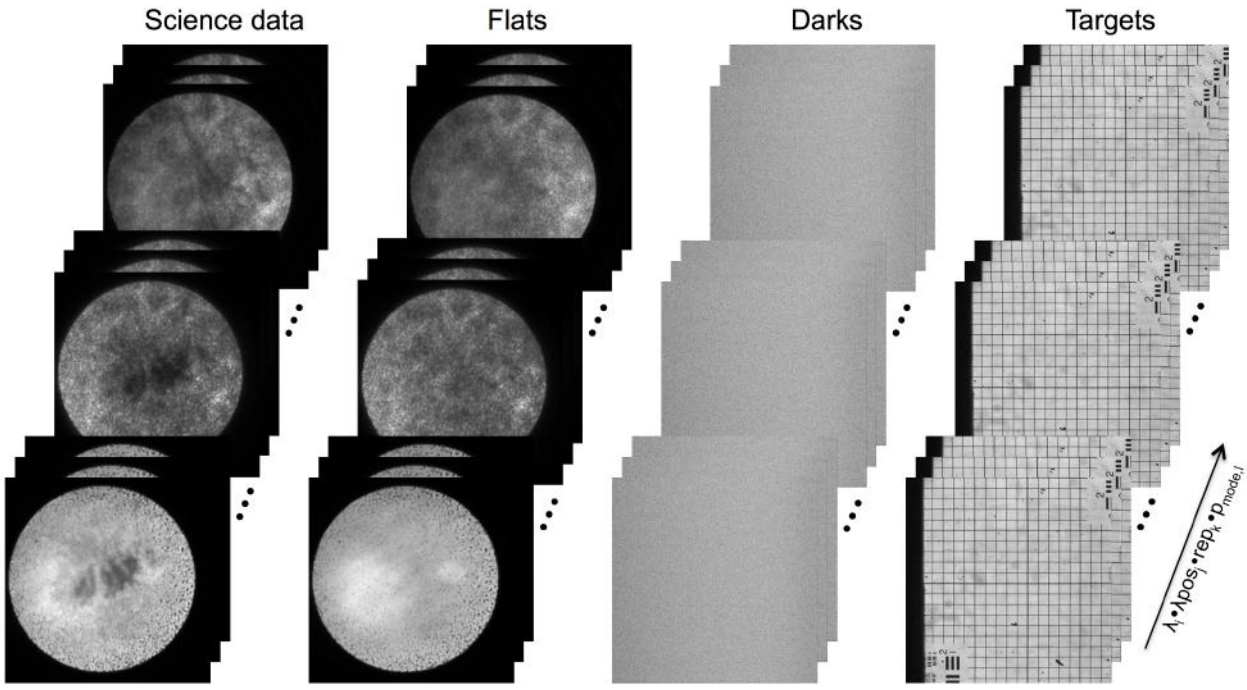

Figure B.4.: Raw data from the narrow-band channel. The spectral scans of a sunspot (left column), flat-field images (second left column), background intensities (second right column) and target grids (right column) were recorded in three different wavelength bands with TESOS at the VTT.

Raw data: The scientific observation with imaging spectro-polarimeters yields a big amount of raw data (see Fig. B.3). Besides the science data which contain the actual solar observations, a hand full of data has to be incorporated to accurately calibrate the scientific observations. As shown in Fig. B.4, this includes Flats (flat-field images), Darks (background intensity images) and Targets (Resolution Test Chart and grids). Their data cubes consist of two-dimensional images recorded at various spectral positions and polarimetric states. In detail, it composes of several spectral wavebands λ_{i} sampled at various wavelength positions λpos_{j} in defined polarimetric states $p_{\mathrm{mode,l}}$. The number is multiplied by the repetitive observation rep_{k}. The narrow-band (NB) channel is accompanied by the simultaneous observation of the continuum intensity within a close-by waveband in the broad-band (BB) channel. Therefore, the overall amount of data doubles.

Flats: The flat-field calibration data are recorded to determine and correct for the instrumental effects which superimpose the solar structures. From the observational point of view, the same instrumental setting has to be used as for the recording of the science data. Yet, the pointing of the telescope is changed to a quiet sun region, preferably at disk center. Then, the telescope performs a random walk motion within that region. This kind of observation is performed for several observation cycles. Later the flat-field data are averaged for the respective wavelength positions and polarimetric states. The solar structures should have vanished by the smearing and reveal the systematic errors of the instrument. The intensity pattern of a flat-field image (as shown in the right panel of Fig. B.7) contains the dust and dirt particles in the foci of the telescope and instrument, as well as the background intensity and dead-pixels recorded by the camera. Large-scale and small-scale variations in spectral intensity are caused by nano-roughness of the FPI surfaces. These errors are represented by prominent 'Orange peel pattern'.

Darks: The dark current or background intensity (see Fig. B.4) superimposes the real signal coming from the Sun. The camera detects a weak signal consisting of the background radiation, the electric current of the camera itself and the read-out noise. To measure this dark intensity, the light path to the instrument has to be blocked. Then, the signal is measured for several cycles and averaged to one two-dimensional image.

Targets: Target images are recorded to determine the image scale and align the images of both instrumental channels. As shown in Fig. B.4, they consist of a calibration grid and a resolution test chart invented by the U.S. Air Force. The known bar dimensions of the chart (better seen in the upper panel of Fig. B.10) are analyzed to obtain the resolving power of the instrument. The resolution limit is reached if the imager cannot discern a group of three bars anymore. With the line grid next to the chart, the images can be aligned. Often a dot pattern is added for a fine alignment of the image rotation.

Pre-filter transmission: Imaging spectrometers are a system of one pre-filter and two or more etalons to filter a narrow spectral bandwidth. The optical pre-filter uses interference to narrow down the transmitted spectral signal to a few nanometers or even less. The profile of the transmitted intensity with respect to the wavelength is not flat but often resembles a Gaussian curve with one central maximum. Good filters can have a profile with an flattened high transmission level of up to 95% followed by a rapid smeared decrease in transmission intensity. In the recorded science data, this pre-filter transmission overlays the profile of the spectral line. To determine the pre-filter transmission, a broader and finer sampling of the spectral line is selected. Then, several scan cycles are recorded in the random-walk motion in a quiet sun region close to the disk center. The average spectral profile is calculated and the envelope of the profile is determined and normalized. To correct for the pre-filter transmission, the spectral profiles of the science data are divided by the normalization values at the corresponding positions of the envelope profile.

Polarization calibration: When sunlight is reflected or transmitted by an optical surface like from a mirror or prism, the polarization of the light is affected. In the case of spectro-polarimetric observation, the polarizing effects of the telescope and instrument can falsify the scientific results. It is therefore

inevitable to accurately determine the polarizing effects and correct the observations from these effects. The calibration is based on a polarization measurement and model for the telescope. The recording of polarization calibration data has to be performed close to the scientific observations. I will not go further into detail here, but refer the interested reader to the description of telescope polarization models by Beck et al. (2005), the general calibration of spectro-polarimetric data by Collados (1999), and in case of the Visible Imaging Polarimeter of TESOS by Beck et al. (2010).

Data preparation: The first step of calibrating the raw data is the preparation of the data. In the flowchart of data processing (Fig. B.3), this is summarized under PREPARE. This step can be used for the standardization of the data structure and metadata. With an unified data standard, observation from other imaging spectro-polarimeters than TESOS can serve as input for an automated data pipeline, too. Like in the case of the TESOS data pipeline (see Fig. B.9), the preparation of the data can include the separation of data from different spectral lines and the correction of overexposures and dead pixels of the camera. To reduce the amount of data, the necessary averaging steps for the Flats, Darks, Targets and pre-filter transmissions can be performed at this stage. The data are then stored in a unified FITS (Flexible Image Transport System) data standard, including significant metadata in an adapted FITS-header. As shown in the flowchart (Fig. B.3), the outcome is labeled as Level 0 data.

Flat-field calibration: The most important step in post-observational data treatment is an accurate correction for the instrumental errors in spectral intensity. If the instrumental effects are flattened across the imager's field-of-view, the process is called 'flat-field calibration' or simply 'flat-fielding'. For imaging spectrometers, these effects are strongly dependent on the wavelength. I will briefly explain the necessary calibration steps for an advanced flat-fielding. In Fig. B.3, the operation steps are charted.

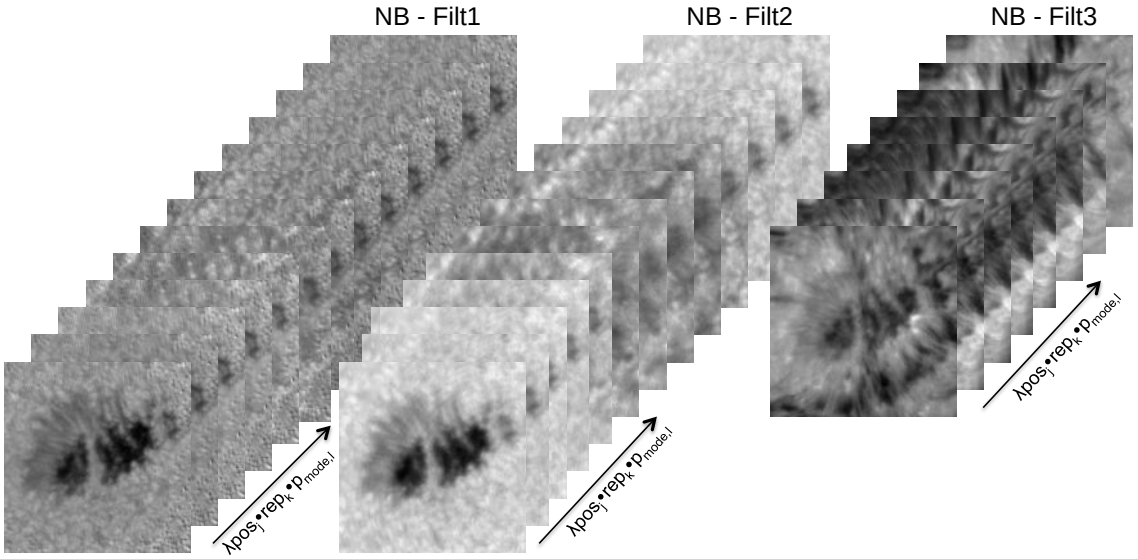

Figure B.5.: Spectral scans of a sunspot after flat-field calibration (Level 1). The narrow-band data are sorted according to the three different wavelength bands (Filt1-3). The raw data from the narrow-band channel are shown in Fig. B.4.

Broad-band: In the case of the continuum intensity in the broad-band channel, the flat-field calibration is easy. Since only a single, broad waveband is filtered, a simple correction for the intensity defects is sufficient. The defects result from dust and dirt in the instruments foci and from camera

defects like dead-pixels or gradients in the camera's sensitivity. These effects are stable enough at time scales of several hours to assume them as constant for the scientific observations. The same holds for the dark current and the position of the target images. For this reason, the raw calibration data are averaged to a single two-dimensional Flat $F_{\mathrm{BB,\,Level\,0}}\,(\mathrm{x},\mathrm{y})$ (or $F_{\mathrm{BB,\,L0}}$), and Dark $D_{\mathrm{BB,\,Level\,0}}\,(\mathrm{x},\mathrm{y})$ (or $D_{\mathrm{BB,\,L0}}$). Every image $S_{\mathrm{BB,\,Level\,0}}\,(\mathrm{x},\mathrm{y},\mathrm{i}) = S_{\mathrm{BB,\,L0}}(\mathrm{i})$ of the broad-band science data is then reduced by the average Flat and Dark like

$$S_{\mathrm{BB,\,L1}}(\mathrm{i}) = \frac{S_{\mathrm{BB,\,L0}}(\mathrm{i}) - D_{\mathrm{BB,\,L0}}}{F_{\mathrm{BB,\,L0}} - D_{\mathrm{BB,\,L0}}} \cdot \langle F_{\mathrm{BB,\,L0}} - D_{\mathrm{BB,\,L0}} \rangle \tag{B.1}$$

to obtain the background corrected, flat-fielded data (in Fig. B.3 labeled as Level 1 data). The resulting structures are from the Sun with minor statistical errors from the instrument, as shown in the left side of Fig. B.8.

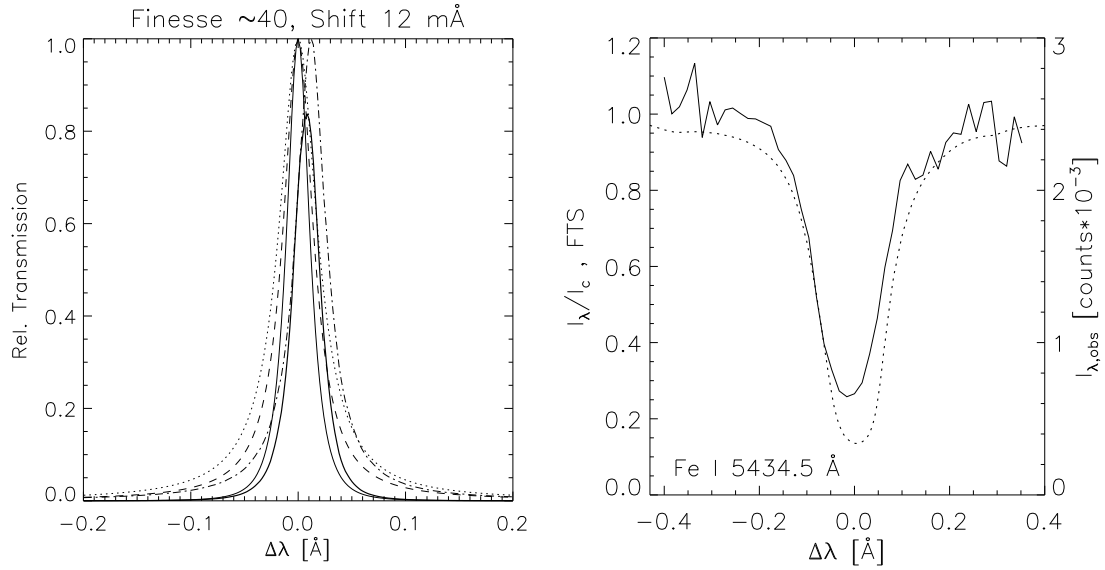

Figure B.6.: Left panel: Relative transmission of a spectrometer with two etalons of different plate separation. The black solid curves show the transmission products for two cases: 1) Thin solid line: Both transmission profiles (dotted and dashed) are perfectly centered. 2) Thick solid line: The transmission of the second etalon (dash-dotted) undergoes a wavelength shift of 1.2 pm against the first (dotted). The product is shifted and reduced in transmission. Right panel: The observed line profile (solid; here Fe I 543.4 nm line) is shifted against its atlas profile (dotted) of the Fourier Transform Spectrometer (FTS). The intensity is given in relative number to the continuum intensity and in absolute counts. Images: Bello González et al. (2013b)

Narrow-band: The flat-field calibration of the spectral scans from the narrow-band channel is by far more involved. In addition to the constant intensity defects mentioned in the last paragraph, the system of Fabry-Pérot interferometers (FPIs) introduces several wavelength-dependent effects which have to be corrected.[4] They are caused by the roughness of the etalon surfaces and inter-etalon reflections. Every Fabry-Pérot interferometer works as a narrow wavelength filter (as displayed in Fig. 4.5) and has its own spectral transmission profile. An example is shown in the left panel of Fig. B.6. The first of the FPI's serves as a low-resolution filter and characterizes through the broader profile (dotted curve) with lower Finesse[5]. To achieve a high spectral resolution a second high-finesse etalon is mounted in series.

[4] This paragraph was written on the basis of Bello González et al. (2013b).

[5] The Finesse characterizes the resonator and is calculated as the ratio between the free spectral range (the distance to

It has a sharper transmission profile. In the perfect case, the maximum of its profile is located at the same wavelength position (dashed curve) as the first FPI profile. Then, their transmission product (thin solid) possesses the same maximum position in wavelength and intensity. To achieve this case, the reflecting surfaces of the etalons would have to be perfectly flat. From the developer's point of view this is almost impossible, the absolute roughness would have to be at the atomic scale.

Let us assume a scenario with a small flatness defect of $\Delta d = 2\,\mathrm{nm}$ (which is around 20 atomic radii) and calculate the effect on the transmission profile. The refractive index of air is neglected and the attack angle at the etalon surface is chosen as vertical. The interference condition for the etalon then becomes

$$m \cdot \lambda = 2 \cdot d \tag{B.2}$$

for the maximum transmission at order m and wavelength λ. The spacing between the etalon plates is set to a typical value of $d = 1\,\mathrm{mm}$. The filtered wavelength is chosen as $\lambda = 600\,\mathrm{nm}$. The changed light path directly affects the transmission by

$$\frac{\Delta\lambda}{\lambda} = \frac{\Delta d}{d} \tag{B.3}$$

and results in a wavelength shift of $\Delta\lambda = 1.2\,\mathrm{pm}$. Transformed in Doppler velocities[6], this introduces an already large defect of $600\,\mathrm{m\,s^{-1}}$. The red-shifted profile of the second etalon is shown as the dash-dotted curve in the left panel of Fig. B.6. When the shifted transmission profile of the second etalon is multiplied with the first one (dotted curve), their product (thick solid) is a spectrally shifted, slightly asymmetric transmission profile with a reduced maximum intensity. These changes have to be applied to the nano-roughness which is present allover the FPIs surfaces. At the detector plane of an imaging spectrometer in telecentric mounting, the pixel-wise change of maximum transmission appears as the so-called 'orange peel pattern'. An example for such an intensity pattern is shown in the left panel of Fig. B.7. The corresponding absolute wavelength shifts are shown in the right panel and range between $\Delta\lambda_{\mathrm{max}} \approx \pm 2\,\mathrm{pm}$.

The effect of the etalon transmission on a full line profile is illustrated in the right panel of Fig. B.6. The dashed curve shows the normalized spectral profile I_λ / I_c of the Fe I line at 543.4 nm from the Fourier Transform Spectrometer (FTS) Atlas (Neckel 1999). The solid curve plots a shifted line profile $I_{\lambda,\mathrm{obs}}$ as observed (in 10^3 counts) with TESOS. Caused by an etalon roughness of only some nm, the line is 1) blue-shifted by $\Delta\lambda = -2\,\mathrm{pm}$, 2) has a reduced line depth due to reflectivity effects, 3) has an additional intensity gradient caused by the pre-filter transmission, and 4) exhibits intensity fluctuations along the wavelength range. Consequently, an accurate calibration of these effects is indispensable for a correct interpretation of the spectral information. For a wavelength of 543.4 nm, a line shift of 2 pm translates into a Doppler velocity offsets of more than $1\,\mathrm{km\,s^{-1}}$. A neglect of this effect can lead to the misinterpretation of atmospheric velocities and can even falsify the conclusions for prominent solar phenomena like sunspot flows and waves.

The advanced flat-field calibration of the spectral narrow-band data has to include all effects mentioned in the last paragraphs. Summarized under GENERATE FLAT and CALIBRATE in Fig. B.3, these are: the background intensity recorded by the camera, dust and dirt particles lowering the intensity, the pre-filter transmission, the intensity variation and wavelength shifts caused by the etalons, and the intensity fluctuations along the wavelength. There are many ways to achieve a reliable calibration of the scientific data. In any case, the instrument developer and observer have to ensure that the corrupting effects are fairly stable in space, magnitude, and time, at least at the scales covering the data acquisition. The calibration process can be divided into several steps. The dark correction can be done at first. Then the line shifts of the spectral profiles against an average profile can be calculated for every pixel. In the next step, the observed profiles are fitted with a Voigt function. Thereby,

the next transmission maximum) and the full-width at half-maximum of the transmission profile.

[6] Calculated by $\frac{\Delta\lambda}{\lambda} = \frac{\Delta v}{c}$, with Doppler velocity v and speed of light c.

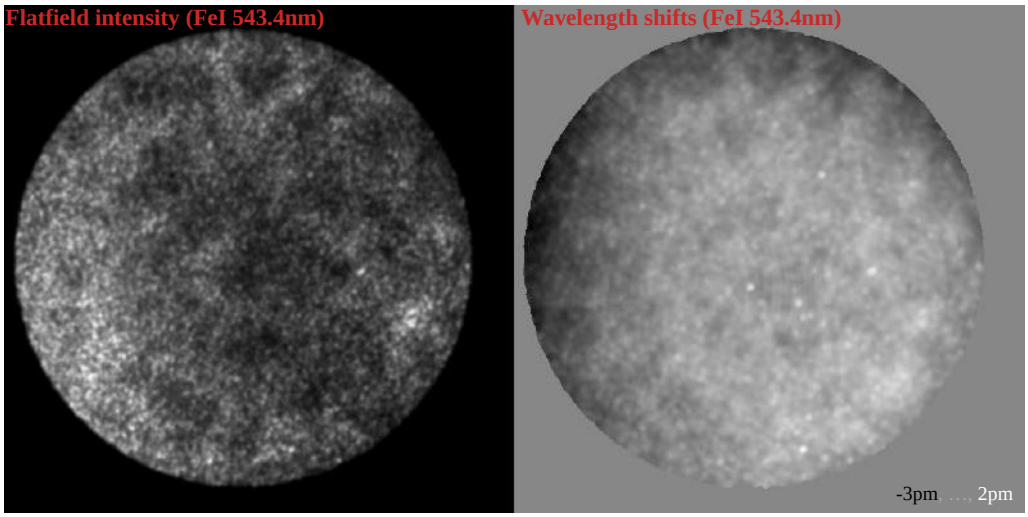

Figure B.7.: Flat-field intensity pattern (left) and wavelength shifts (right) introduced by flatness defects of the surfaces of the TESOS etalons. The intensity transmission and shifts show the typical 'orange peel pattern' for a telecentric setup. The information has to be applied to the science data. The shifts range from −3 pm (black) to 2 pm (white). For a given wavelength of 543.4 nm, a shift of 1 pm corresponds to a velocity of 550 m s^{-1}.

the intensity fluctuations in wavelength are reduced. The pixel-wise profiles can then be shifted and interpolated to the originally selected wavelength positions. The ratio of the spectral intensities of the single profiles to the average unshifted profile yields a data cube of intensity patterns for each spectral position. The line broadening is included in these data as well. For the actual data calibration, the accurately extracted effects are reduced from the science data. Fig. B.5 shows the resulting flat-fielded images from a sunspot observation performed with TESOS. The raw science data can be seen in Fig. B.4. The sunspot was scanned at various positions in three spectral lines, Fe I at 709.0 nm (NB-Filt1), Fe I at 543.4 nm (NB-Filt2) and H_α at 656.3 nm (NB-Filt3).

The description of the narrow-band reconstruction was given for an imaging spectrometer with the etalons in a telecentric mounting (see Fig. 4.7). As the FPIs are located close to the focal plane, the roughness effects are focussed and can be distinguished for the correction of the line-shifts. For the collimated mounting of the etalons, such an 'orange peel' pattern does not exist. As the FPIs are out of focus, the flatness defects are smeared out allover the field. The result is a radially symmetrical decrease in intensity and wavelength. The blue-shifts of the spectral lines increase as a function of distance from the optical axis. Both mounting systems have their advantages and disadvantages. A detailed investigation is given in Kentischer et al. (1998). Whereas GFPI and IBIS are based on a collimated setup, the instruments TESOS, CRISP and VTF are developed with a telecentric mounting. An extensive description of imaging spectrometers is given by Feller (2007). An elaborate spectral flat-field calibration is presented by de la Cruz Rodríguez et al. (2015).

Image alignment: To provide an inherently consistent set of calibrated data, the images have to be adjusted also spatially. Target images have been recorded to achieve a precise image scaling and alignment. As shown in Fig. B.4 and the upper panel of Fig. B.10, they consist of 1) a bar chart to define the resolving power of the telescope and instrument, and 2) a line grid with a known line spacing. The incoming light beam is split for the broad-band and narrow-band channel. There the two beams are influenced by different optical elements. The recorded images can be transposed, mirrored, displaced, twisted or enlarged with respect to each other. The bar chart and line grid are used to define these orientations, image scales and misalignments. The necessary resizing, rotation and horizontal

and vertical shifts are applied. The contortions are performed with a precise cross-correlation routine and a well-working interpolation. After the field of view of the two channels have been aligned, also the superposition of the target images at different spectral bands has to be checked and corrected. As the light path is wavelength dependent and as different spectral pre-filters are used, the images can also harbor internal misalignments. Therefore, the target images have to be recorded in the spectral setting of the scientific data. In addition to the image alignment, a congruent region of interest (ROI) within the field of view (FOV) of both channels can be selected. An example for this is shown in Fig. B.10) with the spectral intensity on the left and continuum intensity on the right. The respective region of interest is shown in Figs. B.5 and B.8. For an overview of the discussed steps, see the flowchart in Fig. B.3.

Image reconstruction: The heated atmosphere of the Earth is turbulent. When a coherent wavefront of incoming light from the Sun travels through the turbulent patches of air in the atmospheric layers, it becomes distorted. When observing the Sun with a ground-based telescope, the temporarily sharp solar features in the focal plane of the telescope jump around and are smeared across the field of view within milliseconds. This motion is comparable to an object observed through the flickering air above a heated road. Of course, this effect lowers the spatial resolution of the observations. To make full use of large-aperture telescopes and their high resolving power, instruments and techniques were developed to overcome the atmospheric turbulences. The pre-observational way to correct for the wavefront errors is to use an adaptive optics (AO) system. A wavefront sensor detect the shape of the wavefronts and provides the information to two correcting mirrors, a first mirror to tip and tilt the incoming light beam and a second thin deformable mirror (DM) with backside actuators to adjust the finer and more rapid distortions. To approach the resolution limit of the telescope, several techniques for the post-observational data treatment have been established. A detailed review and comparison of the well-established image restoration methods is given by Löfdahl et al. (2007) and by Puschmann and Beck (2011). In the following, I will briefly discuss the different image reconstruction techniques and point the interested reader to the mentioned articles and the references therein.

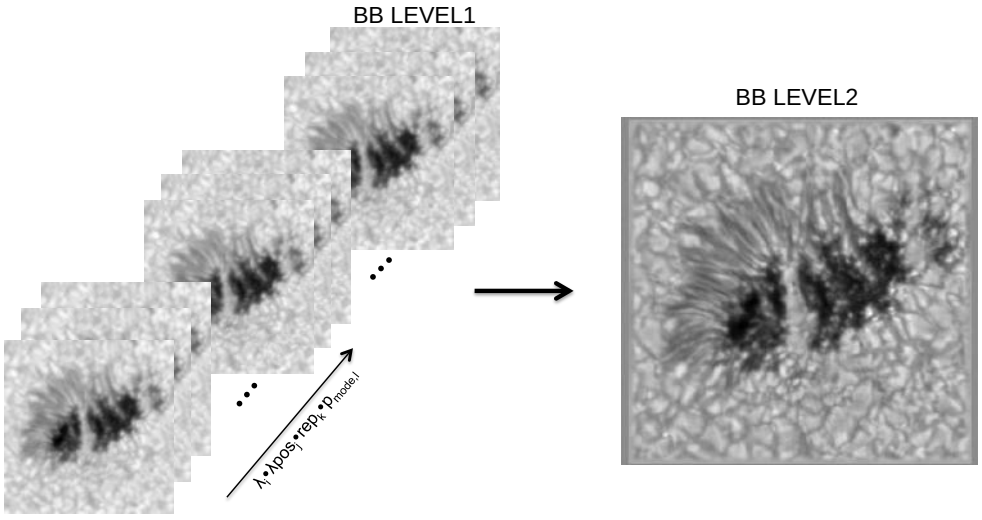

Figure B.8.: Broad-band image reconstruction. By speckle imaging, the sequence of calibrated data (Level 1; left panels) is merged into a high-resolution reconstruction (Level 2; right panel).

Broad-band speckle imaging: The two most elaborated and employed reconstruction methods are the speckle imaging and the Phase Diversity or Multi-Frame Blind Deconvolution. For the speckle reconstruction, a sequence of up to 100 shortly exposed (only few milliseconds) two-dimensional images is observed very fast (within a few seconds) in one waveband. The solar features are assumed as

constant at this time-scale, so the real solar image should be always the same. From the changes in time, the image distortion can be calculated and corrected. A fractional sequence of frames can yield a convincing reconstruction as well, but the statistical significance would decrease by far. The data sequence is Fourier-transformed into the frequency domain in which the Fourier amplitudes are determined (von der Luhe 1985) and in which the phases are estimated. The latter was initially done with the Knox-Thompson algorithm (Knox and Thompson 1974) and speckle masking method (Weigelt 1977) for the general use. Later, specific speckle reconstruction methods (von der Luehe 1993; de Boer 1993) were developed for the application to solar observations. In this field, the reconstruction was improved by the speckle imaging with an extended Knox-Thompson algorithm (Mikurda and von der Lühe 2006). This reconstruction technique was integrated into the automated speckle code KISIP (Kiepenheuer Institute Speckle Interferometry Package) by Wöger and von der Lühe (2008). Further documentation is given in Wöger et al. (2008). To perform a reconstruction, KISIP just needs a sequence of spectrometric images as input while the user can define a number of parameters like the apodisation index or the subfield size. The latter is preferably the size of the isoplanatic patch of around 5 arcsec. At the end, the speckle reconstructed subfields are recombined automatically. Fig.B.8 shows the final calibrated and reconstructed science data (BB Level 2 in Fig. B.3) made from the sequence of calibrated broad-band data.

Narrow-band differential speckle interferometry: The spectral scans in the narrow-band channel of the imaging spectrometer are recorded simultaneously to the images in continuum intensity. These co-temporal images have suffered from the same atmospheric distortions. The sequence of broad-band data is speckle reconstructed. An instantaneous optical transfer function Keller and von der Luehe (1992) yields the transition information of every single observed image to the final reconstruction. For the speckle reconstruction of the broad-band data, the images have been divided into subfields. For the narrow-band images the same subfields are cut with preferentially the size of the isoplanatic patch of around 5 arcsec. In case of TESOS with an image scale of around 0.09 arcsec per pixel, the subfield size is chosen so that the number of pixels per axis is a power of low prime numbers, e.g., $2^6\,px = 64\,px = 5.7''$. The subfield point spread functions obtained from the broad-band reconstructions can be applied to the corresponding narrow-band subfields. It is crucial that the deconvolution at this differential speckle interferometry requires the repetitive observation at the selected wavelength positions during one sequence. Usually six to eight accumulations are valid. For every wavelength position, one reconstructed image is obtained as the re-composition of the reconstructed subfields. Besides, several other aspects have to be noted to attain a good image restoration. For instance, the exposure times for the spectral frames have to be short ($\leq$ 30 ms). Furthermore, if the adjustment of the spectral intensity and wavelength shifts due to the etalon roughness has not been done together with the flat-field calibration, it can still be included at this stage. A detailed mathematical description of the narrow-band reconstruction for the case of TESOS data is given in Bello González et al. (2013b). It deals with the adapted 'Göttingen Codes' (e.g., Janssen 2003) for the reconstruction of spectral data. They were developed at the institute for astrophysics at the University of Göttingen. In the flowchart (Fig. B.3), the steps for the narrow-band reconstruction (Level 2) are summarized under RECONSTRUCT.

Multi-Object Multi-Frame Blind Deconvolution: The second technique of image reconstruction is the Multi-Object Multi-Frame Blind Deconvolution (MOMFBD, van Noort et al. (2005)). Like at the differential speckle interferometry, the narrow-band frames have to be deconvolved with an optical transfer function to obtain the reconstructed image. As the name tells, it is a blind deconvolution at which the real image and the point spread function are estimated. The pupil phases for the successive frames are constructed interactively with a set of increasing polynomials while the differences between observed data and model are minimized. The ambiguity of the possible combinations with a good fitting is decreased by the number of multiple frames. Usually a number of 5 to 20 frames is sufficient. Initially, this Multi-Frame Blind Deconvolution was developed for a time-series using one single object Schulz (1993). Later, the techniques was extended to multiple objects (Löfdahl 2002).

This add-on was off great value especially for imaging spectro-polarimeters. It allows the simultaneous reconstruction of solar features during the scanning through the wavelength positions or polarization states. The method was automated to an exposable code (van Noort et al. 2005).

Destretching: An additional restoration of the temporal image distortions is the so-called 'de-stretching'. The image shifts of the single frames are mapped with respect to an average or highest-contrast image. The two-dimensional distortions are then applied to the sequence of frames. This method can be performed instead or in addition to image reconstruction techniques. This holds for example, when the exposure times of the images were too long or when no accumulation were performed at the wavelength positions.

B.3. CASSDA GUI – TESOS pipeline

As discussed in the previous section, the accurate calibration of data acquired with etalon-based imaging spectrometers is very involved. It requires a professional expertise in the functioning of the instrument and its effects on the data. To guarantee a verified calibration of the data, the instrument developers and experimental scientists provide elaborated processing programs or already fully-calibrated data to the scientific community. In this sense, automated data pipelines are developed to deal with the large amounts of observations. Examples are the CASSDA GUI – TESOS pipeline for the processing of TESOS data acquired at the Vacuum Tower Telescope, as well as CRISPRED (de la Cruz Rodríguez et al. 2015), a data pipeline for the CRISP instrument at the Swedish Solar Telescope.

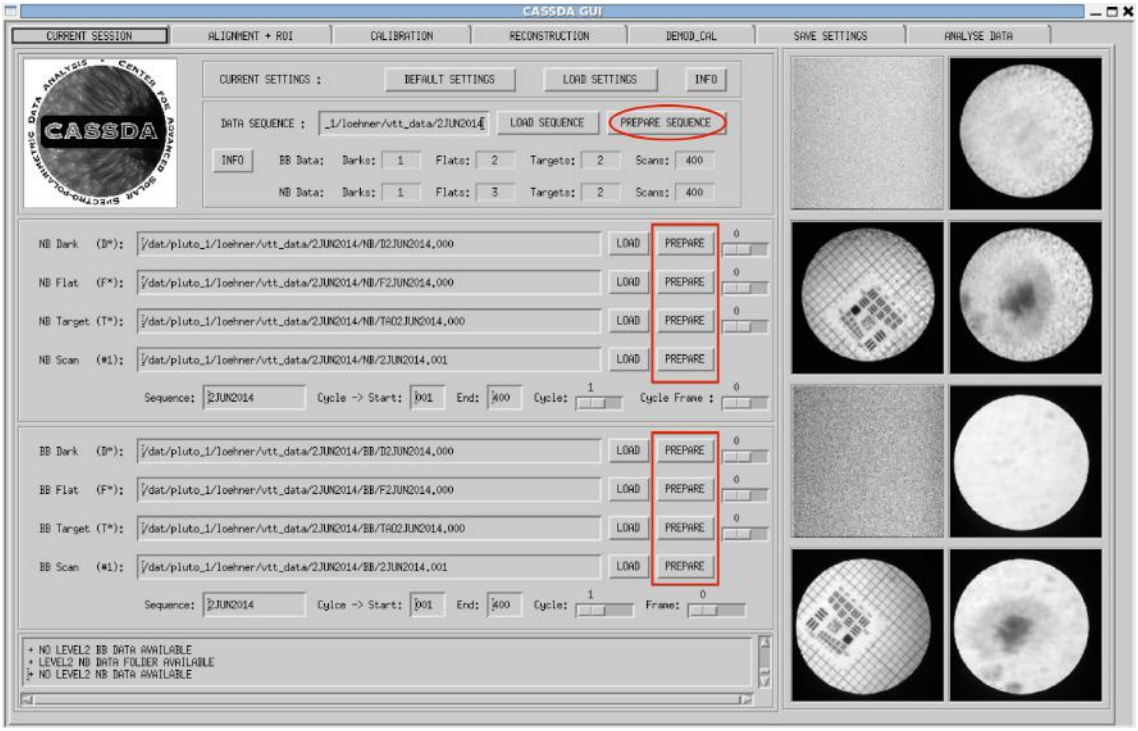

Figure B.9.: The CASSDA GUI – TESOS. A data sequence of TESOS observation from June 2014 was loaded. The file paths and several sequence informations are displayed. With integrated image sliders one can scan through the data visualized in the right panels. The `PREPARE` function (highlighted in red) is used to standardize the raw data.

For the fast and easy post-observational treatment of spectroscopic and spectro–polarimetric TESOS data[7], a plethora of existing data processing software packages were unified and standardized. A

[7]For a description of TESOS and its data please see Section 4.1.3 and Fig. 4.8.

calibration tool was designed which includes all the necessary steps mentioned in Section B.2. The CASSDA GUI – TESOS is a graphical user interface (GUI) programmed with widgets in IDL (Interactive Data Language). As shown in Fig. B.9, it provides the user with quick-look images of the input to the data pipeline. In addition, the tool gives previews of the processed data for all output levels (see Fig. B.3). For the scientific observer at the telescope, the CASSDA GUI – TESOS can serve for quality inspection and on-site data calibration. The user friendly visualization and handling of the advanced processing techniques make it a powerful and reliable tool for the post-observational data treatment. On the one hand, it can be used very interactively to define the calibration settings and parameters while each level of calibration can be executed separately. On the other hand, it generates data configuration files with the chosen settings of the current session. These files contain the file paths of the input and output data as well as all alignment, flat-fielding and reconstruction parameters. The configuration files can then be used as input for an automated data pipeline. In the following, I will explain the features for the calibration of spectrometric data within the CASSDA GUI – TESOS.

Load data: In Fig. B.9, the front page (`CURRENT SESSION`) of the CASSDA GUI – TESOS is shown. With the `LOAD SEQUENCE` option, a sequence of TESOS observations can be selected and loaded. Thereby a specific folder structure and file naming is mandatory. The raw data has to be ordered according to the instrument channel. The initial letter of the filename (F*:Flat, D*:Dark, T*:Target) classifies the type of calibration data. The last three digits give the number of the scan cycle. The standardized header information[8] of the files provides the basis for an automated identification and processing of the data. When a sequence of raw observations is loaded, the data types are ordered automatically. Yet, the data can also be loaded manually. The sequence information is listed in the upper left part in Fig. B.9, the file information is given below. The corresponding images of the science data, Darks, Flats and Targets (see also Fig. B.4) are displayed in small windows on the right side. With image sliders, it is possible to check the sequence cycle by cycle and frame by frame. With this tool, a first consistency check can be performed. If a sequence has been defined or calibrated before, it is possible to load its configuration file with `LOAD SETTINGS` and read in the saved session again.

Prepare: As described in Section B.2, a precise preparation and standardization of the raw data toward an intermediate calibration level (see Fig. B.3) increases the reliability and capability of a data calibration pipeline. The function `PREPARE` within the CASSDA GUI – TESOS is highlighted in Fig. B.9 in red color. It performs several pre-calibrational steps for the data sequence and the single files. A first accuracy check is performed for the file paths, data values and the metadata. Overexposures and dark pixels are corrected. The data cubes are partitioned according to the different spectral lines of a multi-wavelength observation. Where applicable, the frames of the calibration data are averaged for the wavelength positions. Thereby the data volume is reduced. The adapted and standardized metadata are saved in the file headers. The prepared data are stored in the automatically generated Level 0 folders (see Fig. B.3). During operations, the German solar telescopes send information about ambiance parameters of the air and the telescope to an integrative database. At this point, these context metadata can be imported to the file headers. Furthermore, the data standardization within the preparation provides the future user with the possibility to process also data from other imaging spectro-polarimeters like the Visible Tunable Filter at the DKIST (see Section 8). Therefore, the pipeline was coded as universal as possible.

Image alignment: As discussed in Section B.2, the two light beams of an imaging spectro-polarimeter can be shifted, descaled and rotated with respect to each other. A perfect and stable fine-adjustment of the optics in the broad-band and narrow-band channel is hard to achieve. Therefore target grids consisting of lines, bars and dots are recorded in both channels with the settings of the scientific observation. In the CASSDA GUI – TESOS, a half-automated tool for the image alignment and adjustment is implemented. The upper panel of Fig. B.10 shows a target grid in the sub-window `NB IMAGE SCALE`

[8] The metadata from an imaging spectrometer should contain information about the spatial dimensions, the time stamp, relevant solar parameters, the telescope, current seeing values, camera settings, spectral line positions and other relevant observational settings.

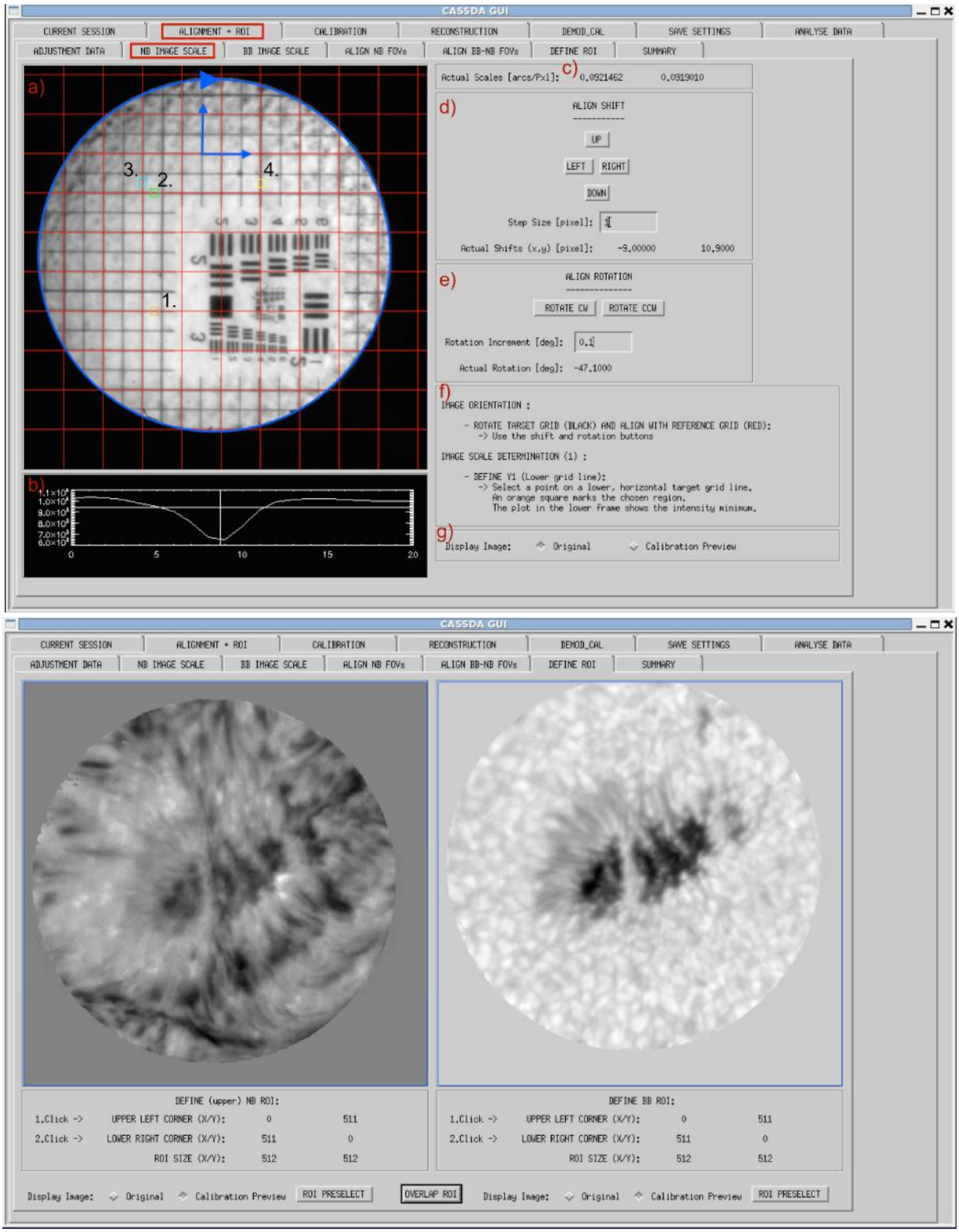

Figure B.10.: Fast and easy image adjustment using the CASSDA GUI – TESOS. Upper panel: With target grids, the images of the narrow-band and broad-band channel are scaled and aligned. Lower panel: When the image channels (here spectral scan on the left, continuum intensity on the right) are aligned an scaled, coincident regions of interest can be selected.

which serves for the determination of the image scale of the narrow-band channel. It is part of the image adjustment in `ALIGNMENT + ROI` (highlighted in red color). By shifts and rotations (panels d and e), the line grid of the target is aligned with the vertical and horizontal lines reference lines (red color). The motions in panel a) are marked by the blue arrows. By the manual selection of grid lines in a distance of six lines (1–2: vertical, 3–4: horizontal) and an automated fitting to the line center (panel b), the image scales are calculated (panel c). For TESOS observations with the longer light path, it amounts to around 0.09 arcsec px^{-1}. The scale ratio of the broad-band images is determined analogous in the sub-window `BB IMAGE SCALE`. In the next step, the images of both channels are equalized in spatial scale. In the sub-window `ALIGN BB-NB FOVs`, the broad-band and narrow-band targets and thereby the field of views of both channels are aligned. This is done by shifts and rotations which can be performed manually or with an automated image cross-correlation. In case of polarimetric observations with a split field of view in the narrow-band channel, the spectral scans have to be co-aligned also internally. After the image alignment, the region of interest (ROI) within the field of view can be selected. As shown in the lower panel of Fig. B.10, the sub-window `DEFINE ROI` displays the adjusted fields of the narrow-band (left) and broad-band (right) channel. The desired region (blue rectangle) is defined in an automated way or manually by mouse-clicks. The data from the final coinciding region can be compared in Figs. B.5 and B.8. The image adjustment parameters are saved in the configuration files and applied to the data during the automated calibration.

Calibrate: The data calibration of imaging spectrometers was described elaborately in Section B.2. All calibration steps[9] are performed automatically, solely the input information and output paths are listed in the `CALIBRATION` window. The output is stored as Level 1 data (see Fig. B.3) in an automatically generated folder. However, an additional option to the normal flat-field calibration is available, if the results are not satisfying. This can happen if the etalons were not stable enough in time or if the intensity fluctuation in wavelength are to large or unstable. Then a simple intensity flat-fielding with a line shift determination can be selected for the data set. Because of processing time issues of the first method, only the latter method is applied for the calibration preview within the CASSDA GUI – TESOS. In the lower panel of Fig. B.10, the previews of the flat-fielded sunspot images are shown for a spectral position in the core of H_α (left) and in continuum intensity (right).

Reconstruct: Techniques have been developed to converge to the highest spatial resolution one can achieve with large-aperture telescopes. The image distortions caused by the Earth's turbulent atmosphere have to be corrected. The image reconstruction can be done with different approaches, each one yields advantages and disadvantages. In the CASSDA GUI – TESOS, the reconstruction is done with the broad-band speckle imaging and the narrow-band differential speckle interferometry. The techniques were described in Section B.2. For the speckle reconstruction of the continuum intensities, the KISIP code Wöger and von der Lühe (2008) was integrated into the data pipeline. First, the user has to define the region within the field of view which has to be reconstructed. If it is not defined, then the selected region for the data calibration is taken. In the next step, a reconstruction preview can be generated. In the sub-window `BB RECONSTRUCTION`, the reconstruction parameters can be changed. These are variables like the subfield size, the maximum number of iterations, a percentage for apodisation window of the phase reconstruction and the limiting number of frames with the highest contrast. A result of a successful broad-band reconstruction is shown in B.8. For the reconstruction of the spectral scans in the narrow-band channel, the differential speckle interferometry (Keller and von der Luehe 1992) was chosen. Therefore, the 'Göttingen Codes' (e.g., Janssen 2003) were adapted and included in the data pipeline. The necessary input for the narrow-band reconstruction is provided automatically by the broad-band speckle reconstruction and the deconvolved optical transfer functions. The output is saved as Level 2 data (see Fig. B.3) in the automatically generated folders.

[9] This includes the correction for the background intensity and the pre-filter transmission, the application of intensity and wavelength shifts as well as intensity fluctuations, and the spatial adjustment of the images.

Bibliography

Abdelatif, T. E., Lites, B. W., and Thomas, J. H.: 1986, *The Astrophysical Journal* **311**, 1015, [URL] 21, 22, 102, 103, 123, 159

Albregtsen, F. and Maltby, P.: 1978, *Nature* **274**, 41, [URL] 19

Alfvén, H.: 1942, *Nature* **150**, 405, [URL] 6, 34

Alissandrakis, C. E., Georgakilas, A. A., and Dialetis, D.: 1992, *Solar Physics* **138**, 93, [URL] 25, 130

Alissandrakis, C. E. and Kundu, M. R.: 1984, *Astronomy and Astrophysics* **139**, 271, [URL] 14, 157

Asensio Ramos, A., Trujillo Bueno, J., and Landi Degl'Innocenti, E.: 2008, *The Astrophysical Journal* **683**, 542, [URL] 147

Asplund, M., Grevesse, N., Sauval, A. J., and Scott, P.: 2009, *Annual Review of Astronomy and Astrophysics* **47**, 481, [URL] 19

Balthasar, H.: 1999, *Solar Physics* **187**, 389, [URL] 104, 160

Balthasar, H., Martínez Pillet, V., Schleicher, H., and Wöhl, H.: 1998, *Solar Physics* **182**, 65, [URL] 21, 22, 65, 103

Balthasar, H. and Schmidt, W.: 1993, *Astronomy and Astrophysics* **279**, 243, [URL] 13, 14

Balthasar, H., Wiehr, E., and Kueveler, G.: 1987, *Solar Physics* **112**, 37, [URL] 21, 65

Bard, S. and Carlsson, M.: 2010, *The Astrophysical Journal* **722**, 888, [URL] 24, 122, 123, 126, 161

Beck, C., Bellot Rubio, L. R., Kentischer, T. J., Tritschler, A., and Del Toro Iniesta, J. C.: 2010, *Astronomy and Astrophysics* **520**, A115, [URL] 179, 181

Beck, C., Schlichenmaier, R., Collados, M., Bellot Rubio, L., and Kentischer, T.: 2005, *Astronomy and Astrophysics* **443**, 1047, [URL] 181

Beckers, J. M. and Tallant, P. E.: 1969, *Solar Physics* **7**, 351, [URL] 6, 20, 23, 61, 68, 122

Bel, N. and Leroy, B.: 1977, *Astronomy and Astrophysics* **55**, 239, [URL] 28, 43, 44, 133, 135, 142, 162

Bello González, N., Danilovic, S., and Kneer, F.: 2013a, *Astronomy and Astrophysics* **557**, A102, [URL] 13

Bello González, N., Flores Soriano, M., Kneer, F., Okunev, O., and Shchukina, N.: 2010, *Astronomy and Astrophysics* **522**, A31, [URL] 66, 90

Bello González, N., Kneer, F., and Löhner-Böttcher, J.: 2013b, *TESOS - Speckle Reconstruction of Narrow-band Data, Technical Note* 182, 186

Bello González, N., Okunev, O. V., Domínguez Cerdeña, I., Kneer, F., and Puschmann, K. G.: 2005, *Astronomy and Astrophysics* **434**, 317, [URL] 65

Bellot Rubio, L. R., Balthasar, H., Collados, M., and Schlichenmaier, R.: 2003, *Astronomy and Astrophysics* **403**, L47, [URL] 13

Bellot Rubio, L. R., Collados, M., Ruiz Cobo, B., and Rodríguez Hidalgo, I.: 2000, *The Astrophysical Journal* **534**, 989, [URL] 21, 66, 104, 107, 160

Berkefeld , T., Schmidt, D., Soltau, D., von der Lühe, O., and Heidecke, F.: 2012, *Astronomische Nachrichten* **333**, 863, [URL] 49

Bharti, L., Hirzberger, J., and Solanki, S. K.: 2013, *Astronomy and Astrophysics* **552**, L1, [URL] 16, 25

Bloomfield, D. S., Lagg, A., and Solanki, S. K.: 2007a, *The Astrophysical Journal* **671**, 1005, [URL] 25, 27, 28, 111, 130, 131, 133, 134, 137, 138, 162

Bloomfield, D. S., Solanki, S. K., Lagg, A., Borrero, J. M., and Cally, P. S.: 2007b, *Astronomy and Astrophysics* **469**, 1155, [URL] 102

Boerner, P., Edwards, C., Lemen, J., Rausch, A., Schrijver, C., Shine, R., Shing, L., Stern, R., Tarbell, T., Title, A., Wolfson, C. J., Soufli, R., Spiller, E., Gullikson, E., McKenzie, D., Windt, D., Golub, L., Podgorski, W., Testa, P., and Weber, M.: 2012, *Solar Physics* **275**, 41, [URL] 79

Bogdan, T. J.: 2000, *Solar Physics* **192**, 373, [URL] 21, 22, 34, 61, 67, 101, 102, 121

Bogdan, T. J., Brown, T. M., Lites, B. W., and Thomas, J. H.: 1993, *The Astrophysical Journal* **406**, 723,

[URL] 102

Bogdan, T. J. and Judge, P. G.: 2006, *Philosophical Transactions of the Royal Society of London Series A* **364**, 313, [URL] 21, 28, 101, 112, 121, 132, 137, 143

Borrero, J. M., Tomczyk, S., Kubo, M., Socas-Navarro, H., Schou, J., Couvidat, S., and Bogart, R.: 2011, *Solar Physics* **273**, 267, [URL] 79, 92, 93

Borrero, J. M., Tomczyk, S., Norton, A., Darnell, T., Schou, J., Scherrer, P., Bush, R., and Liu, Y.: 2007, *Solar Physics* **240**, 177, [URL] 92

Braun, D. C., Duvall, Jr., T. L., and Labonte, B. J.: 1987, *The Astrophysical Journal Letters* **319**, L27, [URL] 13, 22, 102

Bruls, J. H. M. J., Lites, B. W., and Murphy, G. A.: 1991, in L. J. November (ed.), *Solar Polarimetry*, p. 444, [URL] 65, 66

Brynildsen, N., Leifsen, T., Kjeldseth-Moe, O., Maltby, P., and Wilhelm, K.: 1999, *The Astrophysical Journal Letters* **511**, L121, [URL] 23, 121

Cabrera Solana, D., Bellot Rubio, L. R., and del Toro Iniesta, J. C.: 2005, *Astronomy and Astrophysics* **439**, 687, [URL] 64, 65, 66, 88

Cally, P. S., Bogdan, T. J., and Zweibel, E. G.: 1994, *The Astrophysical Journal* **437**, 505, [URL] 102

Cally, P. S., Crouch, A. D., and Braun, D. C.: 2003, *Monthly Notices of the Royal Astronomical Society* **346**, 381, [URL] 102

Canfield, R. C., Reardon, K. P., Leka, K. D., Shibata, K., Yokoyama, T., and Shimojo, M.: 1996, *The Astrophysical Journal* **464**, 1016, [URL] 116

Carlsson, M. and Stein, R. F.: 1992, *The Astrophysical Journal Letters* **397**, L59, [URL] 24, 98

Carlsson, M. and Stein, R. F.: 1997, *The Astrophysical Journal* **481**, 500, [URL] 19, 24, 68, 122, 123, 126

Cauzzi, G., Reardon, K. P., Uitenbroek, H., Cavallini, F., Falchi, A., Falciani, R., Janssen, K., Rimmele, T., Vecchio, A., and Wöger, F.: 2008, *Astronomy and Astrophysics* **480**, 515, [URL] 68, 69

Cavallini, F.: 2006, *Solar Physics* **236**, 415, [URL] 54, 56, 57, 177

Cavallini, F., Berrilli, F., Cantarano, S., and Egidi, A.: 2000, in A. Wilson (ed.), *The Solar Cycle and Terrestrial Climate, Solar and Space weather*, Vol. 463 of *ESA Special Publication*, p. 607, [URL] 56

Centeno, R., Collados, M., and Trujillo Bueno, J.: 2006, *The Astrophysical Journal* **640**, 1153, [URL] 23, 25, 28, 110, 112, 122, 123, 161

Centeno, R., Collados, M., and Trujillo Bueno, J.: 2009, *The Astrophysical Journal* **692**, 1211, [URL] 22, 23, 24, 25, 124

Centeno, R., Socas-Navarro, H., Collados, M., and Trujillo Bueno, J.: 2005, *The Astrophysical Journal* **635**, 670, [URL] 25

Christopoulou, E. B., Georgakilas, A. A., and Koutchmy, S.: 2000, *Astronomy and Astrophysics* **354**, 305, [URL] 25, 28, 130

Christopoulou, E. B., Georgakilas, A. A., and Koutchmy, S.: 2001, *Astronomy and Astrophysics* **375**, 617, [URL] 25, 28

Collados, M.: 1999, in B. Schmieder, A. Hofmann, and J. Staude (eds.), *Third Advances in Solar Physics Euroconference: Magnetic Fields and Oscillations*, Vol. 184 of *Astronomical Society of the Pacific Conference Series*, pp 3–22, [URL] 92, 181

Collados, M., Martinez Pillet, V., Ruiz Cobo, B., del Toro Iniesta, J. C., and Vazquez, M.: 1994, *Astronomy and Astrophysics* **291**, 622, [URL] 19, 107

Couvidat, S., Schou, J., Shine, R. A., Bush, R. I., Miles, J. W., Scherrer, P. H., and Rairden, R. L.: 2012, *Solar Physics* **275**, 285, [URL] 79

de Boer, C. R.: 1993, *Ph.D. thesis*, PhD-Thesis, Göttingen, (1993), [URL] 186

de la Cruz Rodríguez, J., Löfdahl, M. G., Sütterlin, P., Hillberg, T., and Rouppe van der Voort, L.: 2015, *Astronomy and Astrophysics* **573**, A40, [URL] 184, 187

de la Cruz Rodríguez, J., Rouppe van der Voort, L., Socas-Navarro, H., and van Noort, M.: 2013, *Astronomy and Astrophysics* **556**, A115, [URL] 23, 24, 25, 28, 69, 122, 123, 124, 127, 129, 133, 161, 162

De Moortel, I., Ireland, J., Hood, A. W., and Walsh, R. W.: 2002, *Astronomy and Astrophysics* **387**, L13, [URL] 23, 102, 121

De Pontieu, B., Erdélyi, R., and De Moortel, I.: 2005, *The Astrophysical Journal Letters* **624**, L61, [URL] 121,

133, 162

De Pontieu, B., Erdélyi, R., and James, S. P.: 2004, *Nature* **430**, 536, [URL] 44, 102, 135, 142

Delbouille, L., Roland, G., and Neven, L.: 1973, *Atlas photometrique du spectre solaire de [lambda] 3000 a [lambda] 10000*, [URL] 64, 65, 68

Denker, C.: 1998, *Solar Physics* **180**, 81, [URL] 15

Dere, K. P., Landi, E., Mason, H. E., Monsignori Fossi, B. C., and Young, P. R.: 1997, *Astronomy and Astrophysics Supplement Series* **125**, 149, [URL] 70

Dere, K. P., Schmieder, B., and Alissandrakis, C. E.: 1990, *Astronomy and Astrophysics* **233**, 207, [URL] 13

Doerr, H.-P., Steinmetz, T., Holzwarth, R., Kentischer, T., and Schmidt, W.: 2012, *Solar Physics* **280**, 663, [URL] 90, 165

Dwivedi, B. N. and Parker, F. b. E. N.: 2003, *Dynamic Sun*, [URL] 45

Efremov, V. I. and Parfinenko, L. D.: 1996, *Astronomy Reports* **40**, 89, [URL] 104

Eibe, M. T., Mein, P., Roudier, T., and Faurobert, M.: 2001, *Astronomy and Astrophysics* **371**, 1128, [URL] 70

Eisberg, J.: 2002, in M. J. Nye (ed.), *The Cambridge History of Science Vol. 5: The Modern Physical and Mathematical Sciences*, pp 505–521, Cambridge University Press 1, 7

Esteban Pozuelo, S., Bellot Rubio, L. R., and de la Cruz Rodríguez, J.: 2015, *The Astrophysical Journal* **803**, 93, [URL] 137

European Commission: 2013, *EST: Understanding our sun*, http://ec.europa.eu/research/infrastructures/pdf/success_stories/EST_FP7_successes_story.docx.pdf 164

Evershed, J.: 1909, *Monthly Notices of the Royal Astronomical Society* **69**, 454, [URL] 90

Federspiel, M. and Mattig, W.: 1993, *Astronomy and Astrophysics* **276**, 227, [URL] 68

Felipe, T., Khomenko, E., and Collados, M.: 2010a, *The Astrophysical Journal* **719**, 357, [URL] 122

Felipe, T., Khomenko, E., Collados, M., and Beck, C.: 2010b, *The Astrophysical Journal* **722**, 131, [URL] 23, 110, 112, 122, 161

Felipe, T., Socas-Navarro, H., and Khomenko, E.: 2014, *The Astrophysical Journal* **795**, 9, [URL] 25, 107

Feller, A.: 2007, *Ph.D. thesis*, Cuvillier Verlag, Eidgenössische Technische Hochschule ETH Zürich, Nr. 17333, 2007, [URL] 56, 184

Fontenla, J. M., Avrett, E. H., and Loeser, R.: 1993, *The Astrophysical Journal* **406**, 319, [URL] 17, 69

Freij, N., Scullion, E. M., Nelson, C. J., Mumford, S., Wedemeyer, S., and Erdélyi, R.: 2014, *The Astrophysical Journal* **791**, 61, [URL] 22, 27, 29, 71, 121, 140, 162

Fujimura, D. and Tsuneta, S.: 2009, *The Astrophysical Journal* **702**, 1443, [URL] 104

Georgakilas, A. A., Christopoulou, E. B., and Koutchmy, S.: 2000, *Astronomy and Astrophysics* **363**, 306, [URL] 25

Gingerich, O., Noyes, R. W., Kalkofen, W., and Cuny, Y.: 1971, *Solar Physics* **18**, 347, [URL] 17

Giovanelli, R. G.: 1972, *Solar Physics* **27**, 71, [URL] 20, 25, 130

Gurman, J. B. and House, L. L.: 1981, *Solar Physics* **71**, 5, [URL] 104

Hale, G. E.: 1908a, *The Astrophysical Journal* **28**, 315, [URL] 12

Hale, G. E.: 1908b, *The Astrophysical Journal* **27**, 204, [URL] 1, 5

Hale, G. E., Ellerman, F., Nicholson, S. B., and Joy, A. H.: 1919, *The Astrophysical Journal* **49**, 153, [URL] 5, 6

HAO's Solar Physics Historical Timeline, *Education webpage of the High Altitude Observatory*, https://www2.hao.ucar.edu/Education/SolarPhysicsHistoricalTimeline 1

Hathaway, D. H.: 2015, *Living Reviews in Solar Physics* **12**, 4, [URL] 12

Havnes, O.: 1970, *Solar Physics* **13**, 323, [URL] 123, 161

Hawking, S.: 2002, *On the shoulders of giants : the great works of physics and astronomy*, [URL] 1

Hawking, S. W.: 1988, *A brief history of time. From the Big Bang to Black Holes*, [URL] 1

Hernandez, G.: 1986, *Fabry-Perot interferometers*, [URL] 51, 56

Horn, T., Staude, J., and Landgraf, V.: 1997, *Solar Physics* **172**, 69, [URL] 104, 160

Hufbauer, K.: 1991, *Exploring the sun : solar science since Galileo*, Baltimore : Johns Hopkins University Press, c1991., [URL] 1

Janssen, K.: 2003, *Ph.D. thesis*, Universitäts-Sternwarte Göttingen, Geismarlandstrasse 11, D-37083 Göttingen, Germany, [URL] 186, 190

Jess, D. B., De Moortel, I., Mathioudakis, M., Christian, D. J., Reardon, K. P., Keys, P. H., and Keenan, F. P.: 2012, *The Astrophysical Journal* **757**, 160, [URL] 67

Jess, D. B., Mathioudakis, M., Christian, D. J., Keenan, F. P., Ryans, R. S. I., and Crockett, P. J.: 2010, *Solar Physics* **261**, 363, [URL] 59

Jess, D. B., Morton, R. J., Verth, G., Fedun, V., Grant, S. D. T., and Giagkiozis, I.: 2015, *Space Science Review* **190**, 103, [URL] 101

Jess, D. B., Reznikova, V. E., Van Doorsselaere, T., Keys, P. H., and Mackay, D. H.: 2013, *The Astrophysical Journal* **779**, 168, [URL] 25, 26, 27, 28, 44, 67, 110, 115, 116, 130, 131, 133, 137, 148, 162

JSOC webpage, *Webpage of the Joint Science Operations Center*, http://jsoc.stanford.edu 75, 76, 79, 85, 93

Judge, P. G., Tritschler, A., Uitenbroek, H., Reardon, K., Cauzzi, G., and de Wijn, A.: 2010, *The Astrophysical Journal* **710**, 1486, [URL] 56

Jurčák, J., Bello González, N., Schlichenmaier, R., and Rezaei, R.: 2015, *Astronomy and Astrophysics* **580**, L1, [URL] 12

Keller, C. U. and von der Luehe, O.: 1992, *Astronomy and Astrophysics* **261**, 321, [URL] 186, 190

Kentischer, T. J., Schmidt, W., Sigwarth, M., and Uexkuell, M. V.: 1998, *Astronomy and Astrophysics* **340**, 569, [URL] 51, 53, 54, 55, 57, 58, 177, 179, 184

Keppens, R. and Martinez Pillet, V.: 1996, *Astronomy and Astrophysics* **316**, 229, [URL] 14, 157

Khomenko, E. and Cally, P. S.: 2012, *The Astrophysical Journal* **746**, 68, [URL] 42, 43

Khomenko, E. and Calvo Santamaria, I.: 2013, *Journal of Physics Conference Series* **440(1)**, 012048, [URL] 101, 102

Khomenko, E. and Collados, M.: 2009, *Astronomy and Astrophysics* **506**, L5, [URL] 29

KIS, *Webpage of the Kiepenheuer-Insitute für Sonnenphysik*, http://www.kis.uni-freiburg.de 49, 50, 176

Kneer, F., Mattig, W., and v. Uexkuell, M.: 1981, *Astronomy and Astrophysics* **102**, 147, [URL] 23, 68, 69, 70, 123, 161

Knox, K. T. and Thompson, B. J.: 1974, *The Astrophysical Journal Letters* **193**, L45, [URL] 186

Kobanov, N., Kolobov, D., Kustov, A., Chupin, S., and Chelpanov, A.: 2013a, *Solar Physics* **284**, 379, [URL] 67, 69

Kobanov, N. I.: 1990, *Solar Physics* **125**, 25, [URL] 22

Kobanov, N. I.: 2000, *Solar Physics* **196**, 129, [URL] 25, 27, 68

Kobanov, N. I., Chelpanov, A. A., and Kolobov, D. Y.: 2013b, *Astronomy and Astrophysics* **554**, A146, [URL] 22, 71, 121

Kobanov, N. I., Kolobov, D. Y., and Makarchik, D. V.: 2006, *Solar Physics* **238**, 231, [URL] 25, 28, 130, 131, 137

Kobanov, N. I. and Makarchik, D. V.: 2004, *Astronomy and Astrophysics* **424**, 671, [URL] 22, 26, 102

Kramida, A., Yu. Ralchenko, Reader, J., and NIST ASD Team: 2014, NIST Atomic Spectra Database (ver. 5.2), [Online]. Available: http://physics.nist.gov/asd [2015, September 7]. National Institute of Standards and Technology, Gaithersburg, MD. 62, 65

Krishna Prasad, S., Jess, D. B., and Khomenko, E.: 2015, *The Astrophysical Journal Letters* **812**, L15, [URL] 102

Kucera, A., Balthasar, H., Rybak, J., and Woehl, H.: 1998, *Astronomy and Astrophysics* **332**, 1069, [URL] 65, 66

Kupke, R., Labonte, B. J., and Mickey, D. L.: 2000, *Solar Physics* **191**, 97, [URL] 104

Landgraf, V.: 1997, *Astronomische Nachrichten* **318**, 129, [URL] 107

Landi, E., Del Zanna, G., Young, P. R., Dere, K. P., and Mason, H. E.: 2012, *The Astrophysical Journal* **744**, 99, [URL] 70

Landolfi, M. and Landi Degl'Innocenti, E.: 1982, *Solar Physics* **78**, 355, [URL] 93

Leenaarts, J., Carlsson, M., Hansteen, V., and Rouppe van der Voort, L.: 2009, *The Astrophysical Journal Letters* **694**, L128, [URL] 69

Leenaarts, J., Carlsson, M., Hansteen, V., and Rutten, R. J.: 2007, *Astronomy and Astrophysics* **473**, 625,

[URL] 19

Leenaarts, J., Carlsson, M., and Rouppe van der Voort, L.: 2012, *The Astrophysical Journal* **749**, 136, [URL] 67

Leenaarts, J., Rutten, R. J., Reardon, K., Carlsson, M., and Hansteen, V.: 2010, *The Astrophysical Journal* **709**, 1362, [URL] 70

Leighton, R. B., Noyes, R. W., and Simon, G. W.: 1962, *The Astrophysical Journal* **135**, 474, [URL] 6, 20, 61, 102

Leka, K. D.: 1997, *The Astrophysical Journal* **484**, 900, [URL] 15, 140

Lemen, J. R., Title, A. M., Akin, D. J., Boerner, P. F., Chou, C., Drake, J. F., Duncan, D. W., Edwards, C. G., Friedlaender, F. M., Heyman, G. F., Hurlburt, N. E., Katz, N. L., Kushner, G. D., Levay, M., Lindgren, R. W., Mathur, D. P., McFeaters, E. L., Mitchell, S., Rehse, R. A., Schrijver, C. J., Springer, L. A., Stern, R. A., Tarbell, T. D., Wuelser, J.-P., Wolfson, C. J., Yanari, C., Bookbinder, J. A., Cheimets, P. N., Caldwell, D., Deluca, E. E., Gates, R., Golub, L., Park, S., Podgorski, W. A., Bush, R. I., Scherrer, P. H., Gummin, M. A., Smith, P., Auker, G., Jerram, P., Pool, P., Soufli, R., Windt, D. L., Beardsley, S., Clapp, M., Lang, J., and Waltham, N.: 2012, *Solar Physics* **275**, 17, [URL] 60, 70

Lites, B. W.: 1984, *The Astrophysical Journal* **277**, 874, [URL] 22, 66, 69, 112

Lites, B. W.: 1986, *The Astrophysical Journal* **301**, 1005, [URL] 123

Lites, B. W.: 1992, in J. H. Thomas and N. O. Weiss (eds.), *NATO Advanced Science Institutes (ASI) Series C*, Vol. 375 of *NATO Advanced Science Institutes (ASI) Series C*, pp 261–302, [URL] 20

Lites, B. W., Elmore, D. F., Seagraves, P., and Skumanich, A. P.: 1993, *The Astrophysical Journal* **418**, 928, [URL] 94

Lites, B. W. and Thomas, J. H.: 1985, *The Astrophysical Journal* **294**, 682, [URL] 66, 112, 161

Lites, B. W., Thomas, J. H., Bogdan, T. J., and Cally, P. S.: 1998, *The Astrophysical Journal* **497**, 464, [URL] 16, 21, 22, 27, 65, 66, 104, 107, 112, 134, 161

Lites, B. W., White, O. R., and Packman, D.: 1982, *The Astrophysical Journal* **253**, 386, [URL] 25, 27, 130

Livingston, W.: 2002, *Solar Physics* **207**, 41, [URL] 12

LMSAL webpage, *Webpage of the Lockheed Martin Solar Astrophysics Laboratory for SDO data*, `http://sdowww.lmsal.com` 75, 98, 151

Löfdahl, M. G.: 2002, in P. J. Bones, M. A. Fiddy, and R. P. Millane (eds.), *Image Reconstruction from Incomplete Data*, Vol. 4792 of *Society of Photo-Optical Instrumentation Engineers (SPIE) Conference Series*, pp 146–155, [URL] 186

Löfdahl, M. G., van Noort, M. J., and Denker, C.: 2007, in F. Kneer, K. G. Puschmann, and A. D. Wittmann (eds.), *Modern solar facilities - advanced solar science*, p. 119, [URL] 185

Löhner-Böttcher, J. and Bello González, N.: 2015, *Astronomy and Astrophysics* **580**, A53, [URL] 25, 71, 130, 134, 136

Löhner-Böttcher, J. and Schlichenmaier, R.: 2013, *Astronomy and Astrophysics* **551**, A105, [URL] 13, 79, 90

López Ariste, A., Socas-Navarro, H., and Molodij, G.: 2001, *The Astrophysical Journal* **552**, 871, [URL] 14, 127

Mackay, D. and Yeates, A.: 2012, *Living Reviews in Solar Physics* **9**, 6, [URL] 98

Madsen, C. A., Tian, H., and DeLuca, E. E.: 2015, *The Astrophysical Journal* **800**, 129, [URL] 23, 25, 28, 130, 131, 137, 162

Maltby, P., Avrett, E. H., Carlsson, M., Kjeldseth-Moe, O., Kurucz, R. L., and Loeser, R.: 1986, *The Astrophysical Journal* **306**, 284, [URL] 17, 18, 19, 148, 173, 174

Maltby, P., Brynildsen, N., Fredvik, T., Kjeldseth-Moe, O., and Wilhelm, K.: 1999, *Solar Physics* **190**, 437, [URL] 23

Marco, E., Aballe Villero, M. A., Vazquez, M., and Garcia de La Rosa, J. I.: 1996, *Astronomy and Astrophysics* **309**, 284, [URL] 25, 27, 134, 137

Marsh, M. S. and Walsh, R. W.: 2006, *The Astrophysical Journal* **643**, 540, [URL] 23, 121

Martínez González, M. J., Asensio Ramos, A., Manso Sainz, R., Khomenko, E., Martínez Pillet, V., Solanki, S. K., López Ariste, A., Schmidt, W., Barthol, P., and Gandorfer, A.: 2011, *The Astrophysical Journal Letters* **730**, L37, [URL] 104

Martínez González, M. J., Collados, M., and Ruiz Cobo, B.: 2006, *Astronomy and Astrophysics* **456**, 1159,

[URL] 65

Martinez Pillet, V. and Vazquez, M.: 1993, *Astronomy and Astrophysics* **270**, 494, [URL] 19

Mathew, S. K., Solanki, S. K., Lagg, A., Collados, M., Borrero, J. M., and Berdyugina, S.: 2004, *Astronomy and Astrophysics* **422**, 693, [URL] 19, 148

McIntosh, P. S.: 1990, *Solar Physics* **125**, 251, [URL] 12, 72, 80

McIntosh, S. W. and Jefferies, S. M.: 2006, *The Astrophysical Journal Letters* **647**, L77, [URL] 133, 135, 162

Mein, N. and Mein, P.: 1980, *Astronomy and Astrophysics* **84**, 96, [URL] 68, 69, 157

Mikurda, K. and von der Lühe, O.: 2006, *Solar Physics* **235**, 31, [URL] 186

Mogilevskii, É. I., Obridko, V. N., and Shel'Ting, B. D.: 1973, *Radiophysics and Quantum Electronics* **16**, 1043, [URL] 104

Moore, R. L.: 1973, *Solar Physics* **30**, 403, [URL] 28

Morton, R. J.: 2012, *Astronomy and Astrophysics* **543**, A6, [URL] 13, 116

Morton, R. J., Verth, G., Jess, D. B., Kuridze, D., Ruderman, M. S., Mathioudakis, M., and Erdélyi, R.: 2012, *Nature Communications* **3**, 1315, [URL] 40, 104

Murdin, P.: 2001, *Encyclopedia of astronomy and astrophysics*, [URL] 15, 19

Nagashima, K., Sekii, T., Kosovichev, A. G., Shibahashi, H., Tsuneta, S., Ichimoto, K., Katsukawa, Y., Lites, B., Nagata, S., Shimizu, T., Shine, R. A., Suematsu, Y., Tarbell, T. D., and Title, A. M.: 2007, *Publications of the Astronomical Society of Japan* **59**, 631, [URL] 116

NASA, *Solar Science Webpage of NASA*, http://solarscience.msfc.nasa.gov 8

NASA, *Space Place Webpage of NASA*, http://spaceplace.nasa.gov/review/solar-tricktionary/photosphere.en.jpg 8

Neckel, H.: 1999, *Solar Physics* **184**, 421, [URL] 128, 183

Norton, A. A., Ulrich, R. K., Bush, R. I., and Tarbell, T. D.: 1999, *The Astrophysical Journal Letters* **518**, L123, [URL] 104, 160

NSO/AURA, *Webpage of the National Solar Observatory / AURA*, http://www4.nso.edu/staff/ali/dlsp_man/index_dlsp.html, http://nsosp.nso.edu/instruments 48

Nye, A. H. and Thomas, J. H.: 1974, *Solar Physics* **38**, 399, [URL] 25, 28, 130

O'Shea, E., Muglach, K., and Fleck, B.: 2002, *Astronomy and Astrophysics* **387**, 642, [URL] 22, 121

Penn, M. J. and Labonte, B. J.: 1993, *The Astrophysical Journal* **415**, 383, [URL] 102

Perot, A. and Fabry, C.: 1899, *The Astrophysical Journal* **9**, 87, [URL] 52

Pesnell, W. D., Thompson, B. J., and Chamberlin, P. C.: 2012, *Solar Physics* **275**, 3, [URL] 50, 51

Priest, E. and Forbes, T.: 2000, *Magnetohydrodynamics*, p. 1983 31

Puschmann, K. G. and Beck, C.: 2011, *Astronomy and Astrophysics* **533**, A21, [URL] 185

Puschmann, K. G., Denker, C., Kneer, F., Al Erdogan, N., Balthasar, H., Bauer, S. M., Beck, C., Bello González, N., Collados, M., Hahn, T., Hirzberger, J., Hofmann, A., Louis, R. E., Nicklas, H., Okunev, O., Martínez Pillet, V., Popow, E., Seelemann, T., Volkmer, R., Wittmann, A. D., and Woche, M.: 2012, *Astronomische Nachrichten* **333**, 880, [URL] 55, 177

Reardon, K. P. and Cavallini, F.: 2008, *Astronomy and Astrophysics* **481**, 897, [URL] 56, 58

Reznikova, V. E. and Shibasaki, K.: 2012, *The Astrophysical Journal* **756**, 35, [URL] 23, 71, 116, 121, 157

Rimmele, T. R.: 2004, in D. Bonaccini Calia, B. L. Ellerbroek, and R. Ragazzoni (eds.), *Advancements in Adaptive Optics*, Vol. 5490 of *Society of Photo-Optical Instrumentation Engineers (SPIE) Conference Series*, pp 34–46, [URL] 48

Rimmele, T. R. and Radick, R. R.: 1998, in D. Bonaccini and R. K. Tyson (eds.), *Adaptive Optical System Technologies*, Vol. 3353 of *Society of Photo-Optical Instrumentation Engineers (SPIE) Conference Series*, pp 72–81, [URL] 48

Roberts, B.: 2000, *Magnetohydrodynamic Waves*, p. 2225 34, 41

Rouppe van der Voort, L. and de la Cruz Rodríguez, J.: 2013, *The Astrophysical Journal* **776**, 56, [URL] 16, 25

Rouppe van der Voort, L. H. M., Rutten, R. J., Sütterlin, P., Sloover, P. J., and Krijger, J. M.: 2003, *Astronomy and Astrophysics* **403**, 277, [URL] 23, 24, 25, 28, 68, 122, 126, 131

Rüedi, I. and Cally, P. S.: 2003, *Astronomy and Astrophysics* **410**, 1023, [URL] 107

Rüedi, I. and Solanki, S. K.: 1999, in B. Schmieder, A. Hofmann, and J. Staude (eds.), *Third Advances in Solar Physics Euroconference: Magnetic Fields and Oscillations*, Vol. 184 of *Astronomical Society of the Pacific Conference Series*, pp 131–135, [URL] 107

Rueedi, I., Solanki, S. K., and Livingston, W.: 1995a, *Astronomy and Astrophysics* **302**, 543, [URL] 15, 140

Rueedi, I., Solanki, S. K., and Livingston, W. C.: 1995b, *Astronomy and Astrophysics* **293**, 252, [URL] 14

Rueedi, I., Solanki, S. K., Stenflo, J. O., Tarbell, T., and Scherrer, P. H.: 1998, *Astronomy and Astrophysics* **335**, L97, [URL] 104, 107, 160

Ruiz Cobo, B. and del Toro Iniesta, J. C.: 1992, *The Astrophysical Journal* **398**, 375, [URL] 147

Ruiz Cobo, B. and del Toro Iniesta, J. C.: 1994, *Astronomy and Astrophysics* **283**, 129, [URL] 64

Rutten, R. J.: 2003, *Radiative Transfer in Stellar Atmospheres*, [URL] 61, 70

Rutten, R. J. and Uitenbroek, H.: 1991, *Solar Physics* **134**, 15, [URL] 98

Scharmer, G. B., Narayan, G., Hillberg, T., de la Cruz Rodríguez, J., Löfdahl, M. G., Kiselman, D., Sütterlin, P., van Noort, M., and Lagg, A.: 2008, *The Astrophysical Journal Letters* **689**, L69, [URL] 55, 177

Schleicher, H.: 1976, *Ph.D. thesis*, Thesis, University Göttingen, (1976), [URL] 69

Schlichenmaier, R. and Collados, M.: 2002, *Astronomy and Astrophysics* **381**, 668, [URL] 16

Schlichenmaier, R., Rezaei, R., Bello González, N., and Waldmann, T. A.: 2010, *Astronomy and Astrophysics* **512**, L1, [URL] 12

Schlichenmaier, R. and Schmidt, W.: 2000, *Astronomy and Astrophysics* **358**, 1122, [URL] 13

Schmidt, W.: 2002, in H. Sawaya-Lacoste (ed.), *SOLMAG 2002. Proceedings of the Magnetic Coupling of the Solar Atmosphere Euroconference*, Vol. 505 of *ESA Special Publication*, pp 167–174, [URL] 13

Schmidt, W. and Balthasar, H.: 1994, *Astronomy and Astrophysics* **283**, 241, [URL] 15

Schmidt, W., Bell, A., Halbgewachs, C., Heidecke, F., Kentischer, T. J., von der Lühe, O., Scheiffelen, T., and Sigwarth, M.: 2014, in *Society of Photo-Optical Instrumentation Engineers (SPIE) Conference Series*, Vol. 9147 of *Society of Photo-Optical Instrumentation Engineers (SPIE) Conference Series*, p. 0, [URL] 55, 179

Schmidt, W., Hofmann, A., Balthasar, H., Tarbell, T. D., and Frank, Z. A.: 1992, *Astronomy and Astrophysics* **264**, L27, [URL] 16, 156

Schmidt, W., Stix, M., and Wöhl, H.: 1999, *Astronomy and Astrophysics* **346**, 633, [URL] 88

Schmidt, W., von der Lühe, O., Volkmer, R., Denker, C., Solanki, S. K., Balthasar, H., Bello Gonzalez, N., Berkefeld, T., Collados, M., Fischer, A., Halbgewachs, C., Heidecke, F., Hofmann, A., Kneer, F., Lagg, A., Nicklas, H., Popow, E., Puschmann, K. G., Schmidt, D., Sigwarth, M., Sobotka, M., Soltau, D., Staude, J., Strassmeier, K. G., and Waldmann , T. A.: 2012, *Astronomische Nachrichten* **333**, 796, [URL] 49

Schou, J., Borrero, J. M., Norton, A. A., Tomczyk, S., Elmore, D., and Card, G. L.: 2012a, *Solar Physics* **275**, 327, [URL] 79

Schou, J., Scherrer, P. H., Bush, R. I., Wachter, R., Couvidat, S., Rabello-Soares, M. C., Bogart, R. S., Hoeksema, J. T., Liu, Y., Duvall, T. L., Akin, D. J., Allard, B. A., Miles, J. W., Rairden, R., Shine, R. A., Tarbell, T. D., Title, A. M., Wolfson, C. J., Elmore, D. F., Norton, A. A., and Tomczyk, S.: 2012b, *Solar Physics* **275**, 229, [URL] 59, 79

Schrijver, C. J.: 2001, *The Astrophysical Journal* **547**, 475, [URL] 98

Schrijver, C. J. and De Rosa, M. L.: 2003, *Solar Physics* **212**, 165, [URL] 98, 151

Schroeter, E. H., Soltau, D., and Wiehr, E.: 1985, *Vistas in Astronomy* **28**, 519, [URL] 49, 176

Schulz, T. J.: 1993, *Journal of the Optical Society of America A* **10**, 1064, [URL] 186

Schunker, H. and Cally, P. S.: 2006, *Monthly Notices of the Royal Astronomical Society* **372**, 551, [URL] 102

Settele, A., Sigwarth, M., and Muglach, K.: 2002, *Astronomy and Astrophysics* **392**, 1095, [URL] 104, 107

Sigwarth, M. and Mattig, W.: 1997, *Astronomy and Astrophysics* **324**, 743, [URL] 25, 70

Smirnova, V., Efremov, V. I., Parfinenko, L. D., Riehokainen, A., and Solov'ev, A. A.: 2013, *Astronomy and Astrophysics* **554**, A121, [URL] 107

Sobotka, M., Bonet, J. A., and Vazquez, M.: 1993, *The Astrophysical Journal* **415**, 832, [URL] 15

Sobotka, M., Švanda, M., Jurčák, J., Heinzel, P., Del Moro, D., and Berrilli, F.: 2013, *Astronomy and Astrophysics* **560**, A84, [URL] 15, 25, 27, 29, 66, 69, 140, 141, 162

Socas-Navarro, H.: 2015, *NICOLE: NLTE Stokes Synthesis/Inversion Code*, Astrophysics Source Code Library 147

Socas-Navarro, H., McIntosh, S. W., Centeno, R., de Wijn, A. G., and Lites, B. W.: 2009, *The Astrophysical*

Journal **696**, 1683, [URL] 25, 118

Socas-Navarro, H., Trujillo Bueno, J., and Ruiz Cobo, B.: 2000, *The Astrophysical Journal* **544**, 1141, [URL] 14, 24, 25, 69, 127, 161

Solanki, S. K.: 2003, *Astronomy and Astrophysics Reviews* **11**, 153, [URL] 12, 13, 14, 15, 19

Solanki, S. K., Rueedi, I., and Livingston, W.: 1992, *Astronomy and Astrophysics* **263**, 339, [URL] 14

Solanki, S. K., Walther, U., and Livingston, W.: 1993, *Astronomy and Astrophysics* **277**, 639, [URL] 148

Spruit, H. C.: 2013, *ArXiv e-prints*, [URL] 31, 34, 36, 37, 38, 41

Spruit, H. C. and Bogdan, T. J.: 1992, *The Astrophysical Journal Letters* **391**, L109, [URL] 102

Stangalini, M., Giannattasio, F., Del Moro, D., and Berrilli, F.: 2012, *Astronomy and Astrophysics* **539**, L4, [URL] 22, 66, 124

Staude, J.: 2002, *Astronomische Nachrichten* **323**, 317, [URL] 104, 107, 160

Staude, J. and Horn, T.: 1997, in F. P. Pijpers, J. Christensen-Dalsgaard, and C. S. Rosenthal (eds.), *SCORe'96 : Solar Convection and Oscillations and their Relationship*, Vol. 225 of *Astrophysics and Space Science Library*, pp 235–238, [URL] 66

Stix, M.: 2002, *The sun: an introduction*, [URL] 9, 13, 19, 20, 51

Straus, T., Fleck, B., and Andretta, V.: 2015, *Astronomy and Astrophysics* **582**, A116, [URL] 13

Suetterlin, P. and Wiehr, E.: 1998, *Astronomy and Astrophysics* **336**, 367, [URL] 16

Sych, R. and Nakariakov, V. M.: 2014, *Astronomy and Astrophysics* **569**, A72, [URL] 22, 121

Thomas, J. H.: 1981, in L. E. Cram and J. H. Thomas (eds.), *The Physics of Sunspots*, pp 345–358, [URL] 22, 102

Thomas, J. H., Cram, L. E., and Nye, A. H.: 1984, *The Astrophysical Journal* **285**, 368, [URL] 20, 21, 22, 65, 68, 103, 123

Thomas, J. H., Weiss, N. O., Tobias, S. M., and Brummell, N. H.: 2002, *Nature* **420**, 390, [URL] 14

Tian, H., DeLuca, E., Reeves, K. K., McKillop, S., De Pontieu, B., Martínez-Sykora, J., Carlsson, M., Hansteen, V., Kleint, L., Cheung, M., Golub, L., Saar, S., Testa, P., Weber, M., Lemen, J., Title, A., Boerner, P., Hurlburt, N., Tarbell, T. D., Wuelser, J. P., Kankelborg, C., Jaeggli, S., and McIntosh, S. W.: 2014, *The Astrophysical Journal* **786**, 137, [URL] 22, 23, 25, 121, 126

Title, A. M., Frank, Z. A., Shine, R. A., Tarbell, T. D., Topka, K. P., Scharmer, G., and Schmidt, W.: 1993, *The Astrophysical Journal* **403**, 780, [URL] 16, 156

Torrence, C. and Compo, G. P.: 1998, *Bulletin of the American Meteorological Society* **79**, 61, [URL] 90, 91, 92

Tritschler, A., Bellot Rubio, L. R., and Kentischer, T. J.: 2004, in *American Astronomical Society Meeting Abstracts #204*, Vol. 36 of *Bulletin of the American Astronomical Society*, p. 794, [URL] 56, 58

Tritschler, A., Rimmele, T. R., Berukoff, S., Casini, R., Craig, S. C., Elmore, D. F., Hubbard, R. P., Kuhn, J. R., Lin, H., McMullin, J. P., Reardon, K. P., Schmidt, W., Warner, M., and Woger, F.: 2015, in G. T. van Belle and H. C. Harris (eds.), *18th Cambridge Workshop on Cool Stars, Stellar Systems, and the Sun*, Vol. 18 of *Cambridge Workshop on Cool Stars, Stellar Systems, and the Sun*, pp 933–944, [URL] 164

Tritschler, A. and Schmidt, W.: 2002, *Astronomy and Astrophysics* **388**, 1048, [URL] 15

Tritschler, A., Schmidt, W., Langhans, K., and Kentischer, T.: 2002, *Solar Physics* **211**, 17, [URL] 55, 58, 177, 179

Tsiropoula, G., Alissandrakis, C. E., Dialetis, D., and Mein, P.: 1996, *Solar Physics* **167**, 79, [URL] 25

Tziotziou, K., Tsiropoula, G., Mein, N., and Mein, P.: 2006, *Astronomy and Astrophysics* **456**, 689, [URL] 25, 44, 130, 132, 137, 143

Tziotziou, K., Tsiropoula, G., Mein, N., and Mein, P.: 2007, *Astronomy and Astrophysics* **463**, 1153, [URL] 23, 25, 28, 67, 69, 117, 131, 133, 157

Tziotziou, K., Tsiropoula, G., and Mein, P.: 2002, *Astronomy and Astrophysics* **381**, 279, [URL] 23

Uexkuell, M. V., Kneer, F., and Mattig, W.: 1983, *Astronomy and Astrophysics* **123**, 263, [URL] 68, 70

Uitenbroek, H.: 2006, in J. Leibacher, R. F. Stein, and H. Uitenbroek (eds.), *Solar MHD Theory and Observations: A High Spatial Resolution Perspective*, Vol. 354 of *Astronomical Society of the Pacific Conference Series*, p. 313, [URL] 68, 69

Uitenbroek, H.: 2011, in J. R. Kuhn, D. M. Harrington, H. Lin, S. V. Berdyugina, J. Trujillo-Bueno, S. L. Keil, and T. Rimmele (eds.), *Solar Polarization 6*, Vol. 437 of *Astronomical Society of the Pacific Conference Series*, p. 439, [URL] 156

van Noort, M., Rouppe van der Voort, L., and Löfdahl, M. G.: 2005, *Solar Physics* **228**, 191, [URL] 186, 187

Vernazza, J. E., Avrett, E. H., and Loeser, R.: 1981, *The Astrophysical Journal Supplement Series* **45**, 635, [URL] 17, 67, 68

Viticchié, B., Del Moro, D., Berrilli, F., Bellot Rubio, L., and Tritschler, A.: 2009, *The Astrophysical Journal Letters* **700**, L145, [URL] 56

Volkmer, R., von der Lühe, O., Kneer, F., Staude, J., Balthasar, H., Berkefeld, T., Caligari, P., Collados, M., Halbgewachs, C., Heidecke, F., Hofmann, A., Klvaña, M., Sobotka, M., Nicklas, H., Popow, E., Puschmann, K. G., Schmidt, W., Soltau, D., Strassmeier, K., and Wittmann, A. D.: 2007, in F. Kneer, K. G. Puschmann, and A. D. Wittmann (eds.), *Modern solar facilities - advanced solar science*, p. 39, [URL] 50

von der Luehe, O.: 1993, *Astronomy and Astrophysics* **268**, 374, [URL] 186

von der Luehe, O., Soltau, D., Berkefeld, T., and Schelenz, T.: 2003, in S. L. Keil and S. V. Avakyan (eds.), *Innovative Telescopes and Instrumentation for Solar Astrophysics*, Vol. 4853 of *Society of Photo-Optical Instrumentation Engineers (SPIE) Conference Series*, pp 187–193, [URL] 49

von der Luhe, O.: 1985, *Astronomy and Astrophysics* **150**, 229, [URL] 186

von der Lühe, O., Schmidt, W., Soltau, D., Kneer, F., and Staude, J.: 2000, in A. Wilson (ed.), *The Solar Cycle and Terrestrial Climate, Solar and Space weather*, Vol. 463 of *ESA Special Publication*, p. 629, [URL] 50

Weigelt, G. P.: 1977, *Optics Communications* **21**, 55, [URL] 186

Westendorp Plaza, C., del Toro Iniesta, J. C., Ruiz Cobo, B., Martinez Pillet, V., Lites, B. W., and Skumanich, A.: 1997, *Nature* **389**, 47, [URL] 137, 142

Westendorp Plaza, C., del Toro Iniesta, J. C., Ruiz Cobo, B., Martínez Pillet, V., Lites, B. W., and Skumanich, A.: 2001, *The Astrophysical Journal* **547**, 1130, [URL] 14, 155

Wittmann, A.: 1974, *Solar Physics* **36**, 29, [URL] 14, 107, 160

Wöger, F., von der Lühe, O., and Reardon, K.: 2008, *Astronomy and Astrophysics* **488**, 375, [URL] 186

Wöger, F. and von der Lühe, II, O.: 2008, in *Society of Photo-Optical Instrumentation Engineers (SPIE) Conference Series*, Vol. 7019 of *Society of Photo-Optical Instrumentation Engineers (SPIE) Conference Series*, p. 1, [URL] 50, 79, 186, 190

Yuan, D., Nakariakov, V. M., Huang, Z., Li, B., Su, J., Yan, Y., and Tan, B.: 2014a, *The Astrophysical Journal* **792**, 41, [URL] 15, 25, 139, 140, 141

Yuan, D., Sych, R., Reznikova, V. E., and Nakariakov, V. M.: 2014b, *Astronomy and Astrophysics* **561**, A19, [URL] 104, 121, 133, 157, 162

Yurchyshyn, V., Abramenko, V., and Kilcik, A.: 2015, *The Astrophysical Journal* **798**, 136, [URL] 67

Yurchyshyn, V., Abramenko, V., Kosovichev, A., and Goode, P.: 2014, *The Astrophysical Journal* **787**, 58, [URL] 16, 25, 67

Zhao, J., Chen, R., Hartlep, T., and Kosovichev, A. G.: 2015, *The Astrophysical Journal Letters* **809**, L15, [URL] 27, 104, 134

Zirin, H. and Stein, A.: 1972, *The Astrophysical Journal Letters* **178**, L85, [URL] 20, 25, 130

Acknowledgements

First of all, I want to thank my lovely wife Bella. Without her caring support, this work would not have been possible. She is always there for me, provides me with the necessary balance, and makes my life rich. As my soulmate, she understands me like no one else. As my muse, she inspires and motivates me. I apologize for the great privations in the last month in both of our lives. She bravely went through with me. Thank you, Bella!

Now, it is the turn of my nearest and dearest. I want to thank my parents Christine and Helge. They have always supported me with devotion. With wisdom, affection and backing, they guided and secured me on my way. You two are the best! I also thank my grandmother Adelheid, who always believed in me. She was proud of me ever since, and I know she would be now as well. Of course, I want to thank my grandfather Walter, from whom I learned to handle tools, to fiddle around and to be insistent. As I know by now, these are the essential skills for a successful experimental physicist. I want to thank my brother Matthias and my sister Katharina. I can always count on them and I am very proud of them. Many thanks also go to Benjamin, Susanne, and Leon, who supported Bella and me so much with their generosity and advice. I owe all of you so much and hope to return the favor one day.

In the last three years, I had a wonderful time at the Kiepenheuer-Institut in Freiburg. Everybody was so friendly and supportive, that it was a pleasure to work with them. First of all, I want to thank Nazaret and Wolfgang for being such fantastic supervisors. From their scientific instinct, profound knowledge and remarkable expertise I have learned so much. Their door was always open for me and it was a delight talking to them and discussing the solar mysteries. They beaconed and sometimes corrected me, but also gave me the freedom to find my own ways and solutions. I always found the support I needed and was provided with all opportunities I wanted. I thank Nazaret with her warm-hearted nature for the many happy moments and teaching me the importance of 'checking', 'double-checking' and 'cross-checking'.

I want to thank all of my colleagues at the Kiepenheuer-Institut. First of all, Rolf. Without his initial support, I wouldn't stand where I am today. I want to thank Christian and Catherine, who were wonderful colleagues in our little CASSDA group. Many thanks go to Matthias, who became a good friend and with whom I enjoyed my coffee breaks and passionate discussions. He and Klaus literally saved my gluteus maximus at the telescope. I want to give thanks to my office mates, Morten and Christoph. It was great fun having these two excellent guys around. For nice conversation and help, I want to thank Vincent, René K., René S., Wiebke, Kolja, Reza, Vigeesh, Irina, Ariane, Oski, Kenti, Sebastian, and Hanna. For a great week in India, his lecture on radiative transfer, and his patience answering my questions, I want to thank Juan Manuel. I want to thank Markus for his nice welcome when I joined the institute. Especially, I want to thank Oskar von der Lühe, who fired my passion for solar physics and gave me the opportunity to start my state examination thesis at the institute. Thanks also to Svetlana who encouraged the CASSDA project. I want to thank also the IT guys who managed to get everything fixed within a glimpse or two. For a marvelous time on Tenerife and their support at the telescopes, I want to thank Oliver, Stefan, Thomas Keller, Mirsad, and Jürgen. Over and over, I have to thank Sylvia, Tanja, Bettina, who arranged the travels, money, and organizations. I will pay it back with a cake or two. Thanks also go to Roland, Christine and Melanie for taking care.

I want to acknowledge the Senatsausschuss of the Leibniz Association, which funded the Centre for Advanced Solar Spectro-polarimetric Data Analysis, Ref.-No. SAW-2012-KIS-5, and my Ph.D. project. I thank SOLARNET, an EU-FP7 integrated activity project under Grant Agreement 312495, for the service mode operation at the Dunn Solar Telescope within the transnational ACCESS pro-

gram. Observations were obtained at the National Solar Observatory, operated by the Association of Universities for Research in Astronomy, Inc. (AURA), under cooperative agreement with the National Science Foundation. The instruments IBIS and ROSA were operated by personnel from the Istituto Nazionale Di Astrofisica and the Queens University Belfast, with special thanks to Gianna Cauzzi and Peter Keys. HMI and AIA data were used by courtesy of NASA/SDO and science teams. Additional thanks goes to Alexandra Tritschler and Christian Beck for the IBIS and DST service mode operation of the National Solar Observatory. I want to thank the Kiepenheuer-Institut for the operation of the telescopes at the Teide Observatory and the support for my observation runs.

In my Ph.D. time I had many fruitful discussion with colleagues about my work. I want to thank all of them and apologize if I have forgotten anybody: Manolo Collados, Elena Khomenko, Rebecca Centeno Elliot, Tobias Felipe, Matthias Rempel, Rob Rutten, Mats Carlsson, Jaime de la Cruz Rodríguez, Berhard Fleck, Luis Bellot Rubio, Edgar Carlin Ramírez, Hardi Peter, Rehka Jain, Marc deRosa, Carsten Denker, Horst Balthasar, Christoph Kuckein, Torsten Waldmann, and many more. Especially, I want to thank Franz Kneer who guided me on my first steps in spectroscopic data calibration and was always willing to be on hand with help and advice.

I want to thank my fiends for the most welcome distraction in my spare free time. I am grateful for the delicious cooking with Jonas and Julia, the nice evenings and travels with Michael and Fabian, and the time travels with Derya. I also want to thank Rebecca and Stelios for switching my brain off at sport.

At the end, I want to thank my dear colleagues, Nazaret, Irina, Wolfgang, Rolf, Juan Manuel, Markus, Jo, Matthias, and Bella, for taking the time to read the manuscript and providing me with many fruitful comments and corrections.

Publications and scientific contributions

Articles in peer-reviewed journals

Löhner-Böttcher, J. and Bello González, N.: 2015, "Signatures of running penumbral waves in sunspot photospheres". In: Astronomy and Astrophysics 580, A53

Technical notes

Bello González, N., Kneer, F. , and Löhner-Böttcher, J.: 2013, "TESOS – Speckle Reconstruction of Narrow-band Data", Technical note

Articles in preparation for peer-reviewed journals

Löhner-Böttcher, J. and Bello González, N.: 2015, "Shock wave characteristics of sunspot umbral flashes". In: Astronomy and Astrophysics

Löhner-Böttcher, J. and Bello González, N.: 2015, "Magnetic field reconstruction based on sunspot oscillations'. In: Astronomische Nachrichten

Löhner-Böttcher, J.: 2015, "CASSDA GUI TESOS – User manual for TESOS data processing", Technical note

Scientific contributions to conferences and seminars

Löhner-Böttcher, J. and Bello González, N.: 2015, "Magnetic field reconstruction based on sunspot oscillations", 12th Potsdam Thinkshop "The Dynamic Sun – Exploring the Many Facets of Solar Eruptive Events", 26 – 29 Okt 2015, Potsdam (Talk)

Löhner-Böttcher, J. and Bello González, N.: 2015, "Magnetic field reconstruction based on sunspot oscillations", 3rd SOLARNET / 7th HELAS / SpaceInn conference "The Sun, the stars, and Solar-stellar relations", 31 Aug – 4 Sep 2015, Freiburg (Talk)

Löhner-Böttcher, J.: 2015, "Solar observation with VTT and TESOS", 1st CASSDA School for Solar Observers, 20–25 Apr 2015, Observatorio del Teide, Tenerife (Lecture)

Löhner-Böttcher, J.: 2015, "Solar Spectroscopy", master seminar "Spectroscopy in Astrophysics", Kiepenheuer-Institut für Sonnenphysik, 13 Feb 2015, Freiburg (Talk)

Löhner-Böttcher, J. and Bello González, N.: 2014, "Study of wave phenomena in sunspots", IUCAA conference "Coupling and Dynamics of the Solar Atmosphere", 10–14 Nov 2014, Pune, India (Poster)

Löhner-Böttcher, J. and Bello González, N.: 2014, "Wave phenomena in sunspots", 14^{th} European Solar Physics Meeting, 8–12 Sep 2014, Dublin (Contributed talk)

Löhner-Böttcher, J. and Schlichenmaier, R.: 2014, "Correlations between sunspots and their moat flows", 14^{th} European Solar Physics Meeting, 8–12 Sep 2014, Dublin (Poster)

Löhner-Böttcher, J.: 2014, "CASSDA GUI TESOS – Fast and easy processing of TESOS data", Albanova data pipeline meeting, 17–19 Jun 2014, Stockholm (Talk)

Löhner-Böttcher, J.: 2014, "CASSDA GUI – TESOS", 1st CASSDA-SOLARNET workshop on data processing, 18–20 Feb 2014, Freiburg (Contributed talk)

Löhner-Böttcher, J. and Schlichenmaier, R.: 2013, "Correlations between sunspots and their moat flows", Forum of the Leibniz Association, 6–7 Jun 2013, Berlin (Poster)

Löhner-Böttcher, J. and Bello González, N.: 2013, "CASSDA – Center for Advanced Solar Spectropolarimetric Data Analysis", 10th Thinkshop on "High resolution optical spectroscopy", 28–31 May 2013, Potsdam (Poster)